



*Third Asia-Pacific  
Symposium  
on  
Wind Engineering*

December 13-15, 1993

Hong Kong

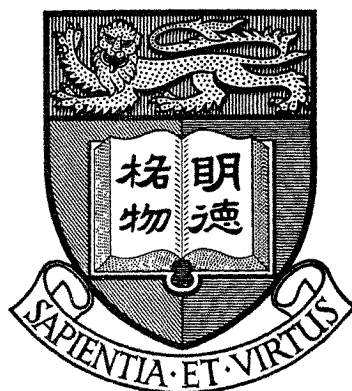
PROCEEDINGS

Volume II

Edited by

K.M. Lam  
Y.K. Cheung

UNIVERSITY OF HONG KONG  
LIBRARY



*This book was a gift  
from*

Faculty of Engineering  
University of Hong Kong

PROCEEDINGS  
OF  
THE THIRD ASIA-PACIFIC SYMPOSIUM  
ON  
WIND ENGINEERING

December 13-15, 1993

Hong Kong

*Edited by* K.M. Lam and Y.K. Cheung  
*The University of Hong Kong*

*VOLUME II*

*Organized by*

Department of Civil and Structural Engineering, The University of Hong Kong  
The Hong Kong Institution of Engineers

*Sponsored by*

Australian Wind Engineering Society  
Chinese Society for Wind Engineering and Industrial Aerodynamics  
Hong Kong Institute of Architects  
Japan Association for Wind Engineering

Copies of the Proceedings are available from

Professor Y.K. Cheung  
Department of Civil and Structural Engineering  
The University of Hong Kong  
Pokfulam Road  
Hong Kong  
Telephone: (852) 859 2666  
Fax. No.: (852) 559 5337

## FOREWORD

The Third Asia-Pacific Symposium on Wind Engineering (APSOWE III) is jointly organized by the Department of Civil and Structural Engineering, The University of Hong Kong and The Hong Kong Institution of Engineers from December 13 to 15, 1993 in Hong Kong. The choice of Hong Kong as the location for the Symposium is by no means accidental. As we all know, Hong Kong is one of the great cities in Asia on the Pacific rim, and this region is the only area in the world that is experiencing rapid economic growth and infrastructure development. With her clusters of ultra-tall buildings, her many steep slopes, the frequent onslaught of tropical cyclones or typhoons, her concern for air pollution from factory and vehicle emissions, Hong Kong is definitely the ideal city to hold such a meeting on wind engineering. In addition, Hong Kong is now receiving worldwide attention for her replacement airport at Chek Lap Kok which also includes other core projects such as the Tsing-Ma Bridge which is going to be one of the longest suspension bridges in the world.

Following the objectives of the previous two Symposiums in Roorkee and Beijing, this Symposium aims to bring together scientists and engineers in Asia-Pacific area as well as other parts of the world to discuss and exchange ideas and experience related to the research and practice of wind engineering. In the past decade, there has been rapid development on wind engineering research and practice in the Asia-Pacific region. Learned bodies representing wind engineers and scientists have been formed in many countries. Among which, the Australian Wind Engineering Society, the Chinese Society for Wind Engineering and Industrial Aerodynamics and the Japan Association of Wind Engineering are kindly sponsoring the present Symposium. We are confident that the Asia-Pacific Symposium has become and will remain an important conference for wind engineers and scientists regionally as well as internationally.

This year, the organizing committee has received over 250 abstracts covering all topics of wind engineering from over 20 countries. Based on the submitted abstracts, about 180 papers were selected and authors were invited to submit six-page manuscripts for inclusion in the Proceedings. The present Proceedings in two volumes contain these contributing papers, together with three keynote papers and three invited papers. A noticeable feature is the large number of papers on bridges, probably due to the importance of infrastructure development in the coastal cities in the Asia-Pacific rim. We would like to take this opportunity to thank the authors of all papers as well as those who have submitted abstracts.

In addition, we would like to thank the precious assistance of members of the Scientific Advisory Board and the Organizing Committee. Special appreciation goes to Professor T.F. Sun and the Chinese Society for Wind Engineering and Industrial Aerodynamics who organized the paper submission in China and the participation of the members of his society. We would also like to thank the Hong Kong Institute of Architects for being an honorary sponsor of this Symposium.

Last but not least, the success of the Symposium also depends on the generous support of various organizations. The donations are largely used to subsidize those participants from the developing countries, and we would like to acknowledge their kindness with our deepest gratitude.

Y.K. Cheung  
Chairman  
Organizing Committee



## SCIENTIFIC ADVISORY BOARD

J.E. Cermak	Colorado State University, U.S.A.
C.M. Cheng	Tamkang University, Taipei, China
Y.K. Cheung	The University of Hong Kong, Hong Kong
A.N.L. Chiu	University of Hawaii at Manoa, U.S.A.
E.C.C. Choi	Nanyang Technological University, Singapore
E.J. Cui	Beijing Institute of Aerodynamics, China
A.G. Davenport	The University of Western Ontario, Canada
A.J. Dutt	National University of Singapore, Singapore
J. Gandemer	Centre Scientifique et Technique du Batiment, France
H.J. Gerhardt	Fachhochschule Aachen, Germany
D.X. He	China Aerodynamics Research and Development Centre, China
M. Ito	Saitama University, Japan
P. Krishna	University of Roorkee, India
B.E. Lee	University of Portsmouth, U.K.
W.H. Melbourne	Monash University, Australia
S. Murakami	University of Tokyo, Japan
R.H. Scanlan	John Hopkins University, U.S.A.
N. Shiraishi	Kyoto University, Japan
T.F. Sun	Peking University, China
G.R. Walker	CSIRO Division of Building, Construction and Engineering, Australia
H.F. Xiang	Tongji University, China

## ORGANIZING COMMITTEE

Y.K. Cheung (Chairman)	The University of Hong Kong
B.J. Stubbings (Vice-Chairman)	Mitchell, McFarlane, Brettnall and Partners International Limited
K.M. Lam (Secretary)	The University of Hong Kong
K.M. Cheung	Buildings Department, Hong Kong Government
S.C. Kot	Hong Kong University of Science and Technology
A.K.H. Kwan	The University of Hong Kong
P.K.K. Lee	The University of Hong Kong
A.Y.T. Leung	The University of Hong Kong
J. MacArthur	Ove Arup and Partners Hong Kong Limited
H.K. Ng	Buildings Department, Hong Kong Government
H.T. Poon	Royal Observatory, Hong Kong Government
Y.C. So	Housing Department, Hong Kong Government
P.K. Tse	Mott MacDonald Hong Kong Limited
H.S.H. Wu	Leighton Asia Limited

# CONTENTS

## VOLUME I

### *Keynote Papers*

- Progress in Physical Modeling for Wind-Engineering 3  
*J.E. Cermak, Colorado State University, U.S.A.*
- How Can We Simplify and Generalize Wind Loads? 15  
*A.G. Davenport, University of Western Ontario, Canada*
- The Response of Large Roofs to Wind Action 27  
*W.H. Melbourne, Monash University, Australia*

### *Invited Papers*

- Wind Loads on Low Rise Buildings 39  
*P. Krishna, University of Roorkee, India*
- On Turbulent Vortex Shedding Flow Past 2D Square Cylinder Predicted by CFD 41  
*S. Murakami and A. Mochida, University of Tokyo, Japan*
- Interference between Wind Loading on Group of Structures 57  
*T.F. Sun and Z.F. Gu, Peking University, China*

### *Bridges*

- The Effect of Section Model Details on Aeroelastic Parameters 71  
*N.P. Jones, R.H. Scanlan, P.P. Sarkar and L. Singh, Johns Hopkins University, U.S.A.*
- Improvements of Aerodynamic Behaviors for Box Girder Bridges with Triangular Fairings 77  
*F. Nagao, H. Utsunomiya, S. Manabe and A. Kawase, University of Tokushima, Japan*
- Effects of Turbulence on Torsional Flutter of a Bridge Deck 83  
*H. Kobayashi, A. Hatanaka and T. Ueda, Ritsumeikan University, Japan*
- Tsing Ma Bridge - Superstructure Evolution 89  
*A.S. Beard, A.G. Simpson and S.A. Coleman, MacDonald Group, Hong Kong*
- Methods of Wind Response Investigation Employed for the Kap Shui Mun Bridge 95  
*R.H. Scanlan, S.L. Stroh and J.D. Raggett, Johns Hopkins University, U.S.A.*
- Study on Aerodynamic Selection of Cross Section for Suspension Bridges in China 101  
*H.F. Xiang, Z.X. Lin and J.Z. Song, Tongji University, China*
- Wind Tunnel Testing for the Second Severn Bridge 107  
*P.A. Irwin and J. Xie, Rowan Williams Davies & Irwin Inc., Canada*



Aerodynamic Stability of Self-Anchored Double Deck Suspension Bridge <i>S.D. Kwon, S.P. Chang, Y.S. Kim and S.Y. Park, Seoul National University, Korea</i>	113
Analysis of Experimental Data from Wind-Induced Response of a Long Span Bridge <i>J.M.W. Brownjohn, A. Zasso, G.A. Stephen and R.T. Severn, Nanyang Technological University, Singapore</i>	119
Identification of Flutter Derivatives of Bridge Deck from Free Vibration Data <i>M. Iwamoto and Y. Fujino, Nagoya Institute of Technology, Japan</i>	125
Comparisons between Wind Tunnel Tests on a Full Aeroelastic Model of the Proposed Bridge over Stretto di Messina and Numerical Results (Part I) <i>G.L. Larose, A. Damsgaard, M. Falco and A. Cigada, Danish Maritime Institute, Denmark</i>	131
Comparison between Wind Tunnel Test on a Full Aeroelastic Model of the Proposed Messina Bridge and Numerical Results (Part II) <i>G. Diana, F. Cheli, S. Bruni, A. Collina and G.L. Larose, Politecnico di Milano, Italy</i>	137
Extensive Identification of Bridge Deck Aeroelastic Coefficients: Average Angle of Attack, Reynolds Number and Other Parameter Effects <i>A. Curami and A. Zasso, Politecnico di Milano, Italy</i>	143
Consideration of the Typhoon Behaviour of the Kao Ping Hsi Bridge in Taiwan <i>Helmut Wenzel, Vienna Consulting Engineers, Austria</i>	149
Damping Effects of Cable Cross Ties in Cable-Stayed Bridges <i>H. Yamaguchi and H. D. Nagahawatta, Saitama University, Japan</i>	155
Aeroelastic Characteristics of a Stressed Ribbon Pedestrian Bridge Spanning 252m <i>M. Pirner, Institute of Theoretical and Applied Mechanics, Czechoslovakia</i>	161
 <i>Bridge Analysis</i>	
Wind Resistant Design for Long Span Suspension Bridges <i>K. Kazama, H. Yamada and T. Miyata, Yokohama National University, Japan</i>	169
System Identification Procedure for Structural Parameters and Wind Characteristics in Ambient Vibration Surveys <i>Nicholas P. Jones, Tinghui Shi, J. Hugh Ellis and Robert H. Scanlan, Johns Hopkins University, U.S.A.</i>	175
An Analysis Method for Buffeting Responses of Flexible Bridge with Aerodynamic Coupling between Modes <i>W.L. Qu and H.F. Xiang, Wuhan University of Technology, China</i>	181
Comparative Study in Coupled Flutter Analysis Methods of a Long Span Suspension Bridge <i>Hitoshi Yamada and Toshio Miyata, Yokohama National University, Japan</i>	187
Predicting Aerodynamic Response of Retrofitted Deer Isle Bridge to Turbulent Wind <i>Chun-Sheng Cai, Pedro Albrecht and Harold R. Bosch, University of Maryland, U.S.A.</i>	193
Wind-Induced Lateral-Torsional Instability of Cable-Stayed Bridges during Erection <i>Vivote Boonyapinyo, Toshio Miyata and Hitoshi Yamada, Yokohama National University, Japan</i>	199

Study on Buffeting Response Spectrum Method for Long Span Bridges <i>W. Chen, M. Gu and H.F. Xiang, Tongji University, China</i>	205
Gust Response of a Long Span Bridge by the Time Domain Approach <i>Jovito C. Santos, Toshio Miyata and Hitoshi Yamada, Yokohama National University, Japan</i>	211
Damping in Suspension Bridges: Sources, Measurements and Errors <i>J.M.W. Brownjohn, Nanyang Technological University, Singapore</i>	217
A Practical Method of Passive TMD for Suppressing Wind Induced Vertical Buffeting of Long-Span Bridges <i>M. Gu, H.F. Xiang and A.R. Chen, Tongji University, China</i>	223
State-Space Method of Wind-Induced Response Analysis for Suspension Bridge <i>Sun Bingnan, Zhou Qiang and Tang Jinchun, Zhejiang University, China</i>	229
Vortex-Excited Vibration Control of Bridges Using TMD <i>A.R. Chen, H.F. Xiang and M. Gu, Tongji University, China</i>	235
Numerical Simulation of Flow around Bridge Deck by the Penalty-Hybrid/Mixed FEM <i>B. Zhu and D.P. Chen, Southwest Jiaotong University, China</i>	241
A Study of Wind-Resistant Stability of Long-Span Cable-Stayed Steel Bridge <i>Hou Wen-Wei, China Academy of Railway Sciences, China</i>	247
 <i>Tall Buildings</i>	
A Parametric Study of Dynamic Wind Loads on Buildings <i>B.E. Lee, S. Lui, Q. Wang and C. Xie, University of Portsmouth, U.K.</i>	255
An Assessment of Dynamic Wind Loads on a Series of CAARC-Like Slender Buildings <i>Liu Shangpei, Wang Qizhi and Lee, B.E., China Aerodynamics Research &amp; Development Center, China</i>	261
Equivalent Wind Spectrum for Torsional Response of Symmetrical Buildings <i>T. Balendra, C.G. Koh and R. Ramanathan, National University of Singapore, Singapore</i>	267
Stochastic Stability of Wind Excited Structures <i>Y.K. Lin and Q.C. Li, Florida Atlantic University, U.S.A.</i>	273
Simulation Method of Simultaneous Time-Series of Multi-Local Wind Forces on Tall Buildings by Using Dynamic Balance Data <i>K. Yoshie, T. Ohkuma, H. Marukawa, H. Niwa, T. Teramoto and H. Kitamura, Tokyo Structural Office, Japan</i>	279
Random Response Analysis of Multi-Story and Tall Buildings under Pulsating Wind <i>M.K. Xiao, M. Lai and Ch. Zhang, Chongqing Institute of Architecture &amp; Engineering, China</i>	285
Damping Estimate from Full-Scale Measurement of the Dynamic Response of a High-Rise Building under Wind Loads <i>J. Jong Lou and Kang-Ning Lou, Polytechnic University, U.S.A.</i>	291

A Computer Program for the Evaluation of Dynamic Response of Structures to Wind Turbulence <i>M. Attou, Ecole Centrale de Nantes, France</i>	297
Equivalent Modal Damping Ratios of a Composite Tube-Type Tall Building under Dynamic Wind Loading <i>B.C. Huang, K.M. Lam, A.Y.T. Leung and Y.K. Cheung, Tongji University, China</i>	305
Observations and Responses of Occupants in High-Rise Buildings during Severe Typhoon <i>Edmund C.C. Choi, Nanyang Technological University, Singapore</i>	311
The Investigation of Wind-Induced Dynamic Response on a Square-Section Tall Building <i>Zhang Liangliang and Xie Changtian, China Aerodynamics Research and Development Center, China</i>	317
Effect of Angle of Attack on Vortex Induced Vibration and Galloping of Tall Buildings in Smooth and Turbulent Boundary Layer Flows <i>H. Kawai, Tokyo Denki University, Japan</i>	323
Response of Multistorey Buildings Subjected to Wind Loading <i>M. Qamaruddin, A.L.M. Mauroof and H.K.R. Al-Hatimi, Sultan Qaboos University, Sultanate of Oman</i>	329
Reliability of Tall Buildings and High-Rise Structures Based on Comfortable Requirement of Residents <i>Li Guiqing, Cao Hong, Li Qiusheng and Ou Siyuan, Wuhan University of Technology, China</i>	335
An Estimation Procedure for Wind Induced Torsion of Tall Buildings <i>D.L. Beneke and K.C.S. Kwok, University of Sydney, Australia</i>	341
Dynamic Behaviour of High-Rise Structures <i>Cao Hong, Li Qiusheng, Ou Siyuan and Li Guiqing, Wuhan University of Technology, China</i>	347
The Wind Tunnel Model Testing of Tall Buildings of Haijiang Garden at the Chinese Town in Shenzhen <i>G.H. Cai, Beijing Institute of Aerodynamics, China</i>	353
Study on the Exponential Model of the Fluctuation Wind Load <i>Zhou Bicheng and Tao Qibin, Hefei University of Technology, China</i>	359
 <i>Towers and Chimneys</i>	
Dynamic Characteristics and Wind Induced Response of a Steel Frame Tower <i>M.J. Glanville and K.C.S. Kwok, University of Sydney, Australia</i>	367
Full-Scale Measurements of Vortex-Induced Vibrations <i>Hans Ruscheweyh and Thomas Galemann, University of Technology Aachen, Germany</i>	373
Analytical Determination of Equivalent Modal Damping Ratios of a Composite Tower in Wind-Induced Vibrations <i>B.C. Huang, A.Y.T. Leung, K.M. Lam and Y.K. Cheung, Tongji University, China</i>	379

Effects of Soil-Structure Interaction and Cracking on Gust Factor of R.C. Chimneys <i>N. Lakshmanan, S.V.S. Balakrishna Rao and B. Venkateswarlu, Structural Engineering Research Centre, India</i>	385
Dynamic Reliability of Wuhan T.V. Tower under the Action of Wind Load <i>Li Qiusheng, Cao Hong and Li Guiqing, Wuhan University of Technology, China</i>	391
An Analysis of Galloping Oscillation for the Mast of the Central TV Transmission Tower <i>Liang Shuguo, Le Junwang and Qu Weilian, Wuhan University of Hydraulic and Electric Engineering, China</i>	397
An Investigation of Aerodynamic Loading for Huge Luminous Lighthouse <i>Y.H. Ren, Beijing Institute of Aerodynamics, China</i>	403
 <i>Wind Characteristics</i>	
Was the Harris and Deaves Velocity Profile a Step in the Wrong Direction? <i>D.A. Paterson, CSIRO Division of Building, Construction and Engineering, J Australia</i>	411
Wind Tunnel Study of the Wind Flow over Auckland City and Comparison with Full-Scale Data <i>R.G.J. Flay and R.J. Andrews, University of Auckland, New Zealand</i>	417
Full-Scale Measurements of Windspeeds at a Suburban Area <i>Koichi Miyashita, Yukio Tamura, Yutaka Asami and Syunichi Naito, Wind Engineering Institute Co., Ltd., Japan</i>	423
An Æolian Geographical Informative System for Structural Engineering: Some Results <i>Gianni Bartoli, Vittorio Gusella and Paolo Spinelli, Universita di Firenze, Italy</i>	429
SODAR - A Useful Remote Sounder to Measure Wind and Turbulence <i>S. Vogt and P. Thomas, Universitat Karlsruhe, Germany</i>	435
Research on the Characters of Land-Sea Breeze and Environmental Planning <i>Lin Kongguang, Fujian Provincial Institute for Science of Environmental Protection, China</i>	441
A Study on the Characteristics of Steady Mountain Wind <i>Y.M. Li, M. Lai, X.L. Wang and J.H. Wang, Chongqing Institute of Architecture &amp; Engineering, China</i>	447
Characteristics of Wind Direction Meander at the Site of Guangdong Nuclear Power Station <i>Zhou Ruming, Yang Zhongqin and Yu Wenzhuo, Suzhou Thermal Engineering Research Institute, China</i>	453
A Study on Characteristics and Simulation Method of Pulsating Wind <i>Y.M. Li, M. Lai and Q. Zhao, Chongqing Institute of Architecture &amp; Engineering, China</i>	459
Theoretical Study on Cold-Air Damming of the Qinling Mountains <i>Qi Ying and Zhou Jiangnan, Institute of Mechanics, CAS, China</i>	465
Theoretical Study on Atmospheric Boundary Layer and the Interaction with Free Atmosphere over Local Heating <i>Qi Ying and Zhou Jiangnan, Institute of Mechanics, CAS, China</i>	471

Numerical Simulation of the Thermal Internal Boundary Layer in Coastal Area - Application of E-ε Closure Model <i>W.G. Wang and W.M. Jiang, Nanjing University, China</i>	477
Experimental and Numerical Simulation of Flow around Two-Dimensional Hills <i>A.D. Ferreira, A.M.G. Lopes, D.X. Viegas and A.C.M. Sousa, Universidade de Coimbra, Portugal</i>	483
Flow Blocking on Windward Slope <i>Sang Jianguo, Zhang Boyin and Niu Zhennan, Peking University, China</i>	489
Numerical Simulation of the Local Wind Field and Turbulent Characteristics for Sun- Radiation Heated, Unstable Stratified Atmospheric Boundary Layer around a Two- Dimensional Hill <i>Du Guoliang, Institute of Chemical Defence, China</i>	493
Study on Turbulent Flow over a Two-Dimensional Ridge by a Non-Hydrostatic Higher-Order Closure Model <i>H.N. Liu and X.M. Wu, Nanjing University, China</i>	499
The Numerical Prediction of a Turbulent Flow over a Curved Hill <i>Xu Cheng, Wu Xiaosong, Fa Lixia and Wang Zhugao, ast China Institute of Technology, China</i>	505
 <i>Extreme Wind</i>	
Analysis of Peak Gust vs. Fastest-Mile Wind Statistics <i>Richard E. Peterson, Steven D. Goldstein and K.C. Mehta, Texas Tech University, U.S.A.</i>	513
Estimating Design Wind Speeds from Short-Term Records <i>Edmond D.H. Cheng and Arthur N.L. Chiu, University of Hawaii at Manoa, U. S.A.</i>	519
Interannual Variability of Tropical Cyclones Making Landfall over China <i>Johnny C.L. Chan and Clarence C.K. Fong, City Polytechnic of Hong Kong, Hong Kong</i>	525
The Study of Classification of Typhoon Landing on China <i>Zhu Ruizhao, Ji Juzhi and Ma Shuhong, Chinese Academy of Meteorological Sciences, China</i>	531
Probability-Based Wind Speed in India <i>M.J. Alam and A.R. Santhakumar, Anna University, India</i>	537
Stochastic Modelling of Cyclones <i>K. Balaji Rao, K.C. Thomas and T.V.S.R. Appa Rao, Structural Engineering Research Centre, India</i>	543
Research on the Wind Feature of Typhoon Landing on the Surface <i>Zheng Zhihua and Ma Wendou, Kunming Institute of Technology, China</i>	549
 <i>Bluff Bodies-Cylinders</i>	
Mechanism of Interference Galloping of Two Identical Cylinders in Cross Flow <i>B. Dielen and H. Ruscheweyh, University of Technology Aachen, Germany</i>	557

Numerical Study of Pressure Fluctuations on Rectangular Cylinder in Aerodynamic Oscillation <i>T. Tamura, Y. Itoh, A. Wada and K. Kuwahara, Tokyo Institute of Technology, Japan</i>	563
Numerical Study of Flow Interaction behind Two Circular Cylinders of Equal Diameters <i>C.W. Ng and N.W.M. Ko, University of Hong Kong, Hong Kong</i>	569
Effects of Turbulence Characteristics on Vortex-Induced Oscillation of Two-Dimensional Cylinders with Various Structural Dampings <i>M. Kawatani, O. Suzuki, H. Kim and H. Kobayashi, Osaka University, Japan</i>	575
Aerodynamic Behavior of Multiple Elastic Circular Cylinders with Vicinity Arrangement <i>Y. Kubo, T. Nakahara and K. Kato, Kyushu Institute of Technology, Japan</i>	581
Effect of Horizontally Inclined Wind on the Vortex Induced Oscillation of a Rectangular Cylinder <i>H. Utsunomiya, F. Nagao, K. Asano and T. Matsumoto, University of Tokushima, Japan</i>	587
Flow Characteristics of Two Square Cylinders of Different Size in Side-by-side Arrangement <i>P.T.Y. Wong, N.W.M. Ko and A.Y.W. Chiu, University of Hong Kong, Hong Kong</i>	593
Flow over Partially Grooved Cylinder with and without Acoustic Excitation <i>K.W. Lo, Y.C. Leung, C.H. Wong and N.W.M. Ko, University of Hong Kong, Hong Kong</i>	599
Vibration-Induced Wind Forces on the Two Dimensional Rectangular Models <i>Y. Momomura, T. Ohkuma, H. Marukawa and T. Tsurumi, Izumi Sohken Engineering, Co., Ltd., Japan</i>	605
The Vortex Shedding of a Group of Three Equispaced Circular Cylinders <i>Xu Youheng and Cheng Zhao, Fudan University, China</i>	611
A Study of Wake Galloping of Bridge Stay-Cables <i>T. Yoshimura, M.G. Savage, H. Tanaka and D. Urano, Kyushu Sangyo University, Japan</i>	617
Flow around and Mean Pressure Field on a Circular Cylinder Placed Downstream of a Blunt-Based Flat Plate in Staggered Arrangement <i>H. Ibrahim Keser and M. Fevzi Unal, Istanbul Technical University, Turkey</i>	623

## VOLUME II

### *Bluff Body Aerodynamics and Separation*

An Experimental Investigation of the Effects of Free-Stream Turbulence on Streamwise Surface Pressures in Separated and Reattaching Flows <i>Q.S. Li and W.H. Melbourne, Monash University, Australia</i>	631
Turbulence Scale Effects on Buffeting Forces of a Flat Hexagonal Section <i>K. Kimura and Y. Fujino, University of Tokyo, Japan</i>	637

An Experimental Study of Flow Structure around a Rankine Body <i>S.J. Lee and K.J. Kwon, Pohang Institute of Science &amp; Technology, Korea</i>	643
Study on Aerostatic Characteristics and Aeroelastic Instability of Structural L-Shaped, T-Shaped and Cross-Shaped Sections <i>Atsushi Okajima, Hisanori Ueno and Donglai Yi, Kanazawa University, Japan</i>	649
Effects of the Incident Flow on the Motion Downstream a Backstep <i>A. Aroussi, University of Nottingham, U.K.</i>	655
Control of Bluff Body Flow Separation <i>D.A. Shah, S.H. Winoto and W.C. Ou, National University of Singapore, Singapore</i>	661
Effects of Aspect Ratio and Surface Roughness on the Time-Averaged Aerodynamic Forces on Cantilevered Circular Cylinders at High Reynolds Numbers <i>Y. Uematsu and M. Yamada, Tohoku University, Japan</i>	667
Navier-Stokes Calculation of Flow Field around Three-Dimensional Blunt Body <i>Zhu Guolin, Wang Kaichun and Guo Yingjun, China Aerodynamics Research and Development Center, China</i>	673
Separation Characteristics of Flows over Blunt Structure in Shear Flows <i>X.Y. Zhu, X.T. Yu, Z.C. Shi and E.J. Cui, Beijing Institute of Aerodynamics, China</i>	679
Mean Velocity Profiles in the Wake of Two Prismatic Bodies in Tandem Arrangement <i>B.H. Lakshmana Gowda and M. Mohamed Sitheeq, Indian Institute of Technology, India</i>	685
 <i>Roofs and Low Rise</i>	
Analysis of Wind-Induced Roof Pressure Data Acquired in the Field <i>K.C. Mehta, B.B. Yeatts and D.A. Smith, Texas Tech University, U.S.A.</i>	693
Aerodynamic Instability and Damping of a Suspension Roof <i>J.E. Cermak, H.G.C. Woo, M.L. Lai, J. Chan and S.L. Danielson, Colorado State University, U.S.A.</i>	699
Wind Tunnel Testing of Houses with Large Overhangs in the West Indies <i>Paul W.M. Tam and Virender K. Handa, Meinhardt (C &amp; S) Ltd., Hong Kong</i>	705
Proper Orthogonal Decomposition and Reconstruction of Multi-Channel Roof Pressure <i>B. Bienkiewicz, Y. Tamura, H.J. Ham, H. Ueda and K. Hibi, Colorado State University, U.S.A.</i>	711
Pressure Factors for Edge Regions on Low Rise Building Roofs <i>J.D. Ginger and C.W. Letchford, University of Queensland, Australia</i>	717
Effect of Free-Stream Turbulence on Peak Suctions Observed below Corner Vortices <i>H.W. Tieleman, E.C. Panzer, O.K. Rediniotis and R.E. Akins, Virginia Polytechnic Institute and State University, U.S.A.</i>	723
Effect of Aspect Ratio on Roof Wind Loads of Low-Rise Rectangular Buildings <i>R. Sankaran, James Cook University of North Queensland, Australia</i>	729

Wind Loads on a Horizontal Grandstand Roof of Large Aspect Ratio <i>K.M. Lam and A.P. To, University of Hong Kong, Hong Kong</i>	735
Analysis of a Tension Membrane Hypar Roof Subjected to Fluctuating Wind Loads <i>P.K.F. Pun and C.W. Letchford, University of Queensland, Australia</i>	741
Parametric Study of Wind Pressure Distribution on Sloping Roofs <i>Rajeev Gupta and A.K. Ahuja, University of Roorkee, India</i>	747
The Mean Pressure on Shell Structure Roof <i>Chen Qin hao, Guangdong Provincial Building Research &amp; Design Institute, China</i>	753
The Effect of Directional Variations on the Observed Mean and Rms Pressure Coefficients <i>P.J. Richards, R.P. Hoxey and B.S. Wanigaratne, University of Auckland, New Zealand</i>	759
Wind Tunnel Study of Water Tanks <i>J. Parthiban, A.R. Santhakumar and K. Padmanaban, Anna University, India</i>	765
 <i>Wind Codes and Wind Damage</i>	
The New European Wind Load Code <i>H. Ruscheweyh, University of Technology Aachen, Germany</i>	773
Recommended Improvements in the South Florida Building Code <i>Herbert S. Saffir, Herbert Saffir Consulting Engineers, U.S.A.</i>	781
An Experimental Investigation and Code Validation of the Wind Behaviour for a Square-Edged Tapered Building <i>Z.J. Lu, M.H. Sheu, J.H. Chou, C.H. Ding, S.K. Zen and J.J. Miao, National Cheng Kung University, Taiwan</i>	787
Development of Wind Load Standard for Chinese Bridge Code <i>Yingjun Chen, Xizhe Yu, Jianming Yin and Guangcheng Niu, Northern Jiaotong University, China</i>	793
Wind Loading and Serviceability of Tall Buildings in Tropical Cyclone Regions <i>P.A. Irwin and J. Xie, Rowan Williams Davies &amp; Irwin Inc., Canada</i>	799
Wind Damage Expert System for Insurance Industry <i>Kishor C. Mehta and Ronald H. Cheshire, Texas Tech University, U.S.A.</i>	805
Damage Assessment and Vulnerability Analysis of Structures Subjected to Cyclones <i>T.L. Murlidharan, J. Durga Prasad and T.V.S.R. Appa Rao, Structural Engineering Research Centre, India</i>	811
Cyclone Resistant Low Cost Houses in Coastal Regions in Developing Countries <i>G.C. Mathur, National Buildings Organisation, India</i>	817
 <i>Dampers and Active Control</i>	
Modelling of Tuned Mass Dampers for Wind Tunnel Tests on a Full-Bridge Aerolastic Model <i>G.L. Larose, A. Larsen and E. Svensson, Danish Maritime Institute, Denmark</i>	823
Vibration Control of Wind-Excited Tall Buildings with Passive Dampers <i>B. Samali and K.C.S. Kwok, University of Technology, Australia</i>	829



Effect of Liquid Dampers on Along-Wind Response of Structures <i>Keming Sun, H.F. Cheong and T. Balendra, National University of Singapore, Singapore</i>	835
Design Aspects of Tuned Mass Dampers for the Great Belt East Bridge Approach Spans <i>A. Larsen, E. Svensson and H. Andersen, COWI Consult A/S, Denmark</i>	841
Test and Research of Control for Alongwind and Acrosswind Responses of Tall Building by Cylindric Deep-Water Tank <i>W.L. Qu, S.G. Liang, Z.Y. Li, K.S. Sheng and G.Q. Li, Wuhan University of Technology, China</i>	847
Wind Tunnel Investigation of Active Vibration Control of Tall Buildings <i>R.J. Facioni, K.C.S. Kwok and B. Samali, University of Sydney, Australia</i>	853
On Control of Along-Wind and Across-Wind Vibrations of Structure by Crossed Dampers <i>X.T. Zhang and R.C. Zhang, Tongji University, China</i>	859
Control for Turbulence Wind Vibration Responses of Nanjing TV Tower by Semi-Active TMD <i>W.L. Qu and W.R. Cheng, Wuhan University of Technology, China</i>	865
<i>Wind Tunnel Techniques</i>	
Wind-Tunnel Modelling of the Atmospheric Surface Layer <i>Jack E. Cermak, Leighton S. Cochran and Russ D. Leffler, Colorado State University, U.S.A.</i>	873
A Large Australian Dynamic Weather Testing Facility (DWTF) <i>David Paterson and Geoff Farrance, CSIRO Division of Building, Construction and Engineering, Australia</i>	879
Computer-Controlled Wind Tunnel for Wind-Engineering Applications <i>A. Nishi and H. Miyagi, Miyazaki University, Japan</i>	885
On the Design of Wind Tunnel Inlet <i>Furman F.M. Fang and Kenny W.M. Gan, National Chung-Hsing University, Taiwan</i>	891
Design of a Low-Cost Stratified Boundary Layer Wind Tunnel <i>M. Schatzmann, J. Donat and S. Hendel, University of Hamburg, Germany</i>	897
Basic Study on Blockage Effects in Turbulent Boundary Layer Flows <i>M. Noda, H. Utsunomiya and F. Nagao, University of Tokushima, Japan</i>	905
Optimization of Pressure Measurement System for Wind Tunnel Experiments <i>B. Bienkiewicz and Y. Sun, Colorado State University, U.S.A.</i>	911
Geometric Similitude Applied to Model and Full-Scale Pressure Tap Sizes <i>Leighton S. Cochran, Marc L. Levitan, Jack E. Cermak and Byron B. Yeatts, Colorado State University, U.S.A.</i>	917
Design and Calibration of High Frequency Base Balances Used for Dynamic Wind Load on Building Models <i>Chen Feng, Hu Guofeng and Lee, B.E., China Aerodynamics Research and Development Center, China</i>	923

A Simple Five-Component Base Balance for Measurement of Mean Wind Loads on Building Models <i>A.K.H. Kwan and K.M. Lam, University of Hong Kong, Hong Kong</i>	929
A Numerical Investigation of a Proposed Force Balance Technique to Improve the Wind Response Predictions of Tall Buildings with Coupled 3-D Mode Shapes <i>D.Y.N. Yip and R.G.J. Flay, Ove Arup &amp; Partners, New Zealand</i>	935
The Constant Temperature Hot-Wire (Film) Anemometer System with Main Bridge Prephas -Shift Circuit <i>Sheng Senzhi and Zhuang Yongji, Peking University, China</i>	941
Wind Tunnel Modeling Test on Mechanism of Weakening Typhoon's Damage to Rubber Forest by Tea-Rubber Community <i>L.S. Lou and K. Zhao, Central Research Institute of Building and Construction of MMI, China</i>	947
Physical Modelling of Natural Wind and Its Guide in a Large Open Pit Mine <i>Peng Xi and Lu Guorong, Safety and Environmental Protection Research Institute, MIM, China</i>	953
 <i>Pedestrian Level Winds</i>	
Pedestrian Comfort Including Wind and Thermal Effects <i>Michael J. Soligo, Peter A. Irwin and Colin J. Williams, Rowan Williams Davies &amp; Irwin Inc., Canada</i>	961
Infrared-Thermography Technique for Pedestrian Wind Evaluation <i>Hanqing Wu and Theodore Stathopoulos, Concordia University, Canada</i>	967
Wind Environment Assessment: A Case Study in the Brisbane CBD <i>C.W. Letchford and J.D. Ginger, University of Queensland, Australia</i>	973
Generic Models for Pedestrian-Level Winds in Built-up Regions <i>Theodore Stathopoulos and Hanqing Wu, Concordia University, Canada</i>	979
Evaluation of Pedestrian Level Wind Environment Around a Row of Tall Buildings <i>A.P. To, K.M. Lam and D.K.T. Thung, University of Hong Kong, Hong Kong</i>	985
 <i>Atmospheric Dispersion</i>	
Computational Atmospheric Dispersion of a Pollutant over a Complex-Shaped Terrain <i>M.J.S. Morais and L.A. Oliveira, University of Coimbra, Portugal</i>	993
Field Study of Roof Top Dispersion in Urban Area <i>K.S. Lam and S.C. Kot, Hong Kong Polytechnic, Kowloon</i>	999
Effects of Model Scale in Estimating Pollutant Dispersion near Buildings <i>P.J. Saathoff, T. Stathopoulos and M. Dobrescu, Concordia University, Canada</i>	1005
Building Downwash of Plumes and Plume Interactions <i>J.C.K. Cheung and W.H. Melbourne, Monash University, Australia</i>	1011
Models of Urban Air Diffusion and Their Application <i>Wang Shufang, Peking University, China</i>	1017
Plume Diffusion Model of Internal Boundary Layer <i>Jie Xuan, Wenhu Ye and Tianfeng Sun, Peking University, China</i>	1023

A New Research Method of Atmospheric Environmental Capacity <i>Liu Baozhang, Peking University, China</i>	1029
Study on the Thermal Internal Boundary Layer and Dispersion of Air Pollutant in Coastal Area by Numerical Simulation <i>W.M. Jiang and H.B. Yu, Nanjing University, China</i>	1035
A Puff Model under Changing Meteorological Condition Used in a Real Time Dose Assessment System for Qinshan Nuclear Power Plant <i>Erbang Hu and Han Wang, China Institute for Radiation Protection, China</i>	1041
Wind-Tunnel Simulation on the Thermal Buoyancy Plume Rise and Dispersion from Multipipe Stack <i>G.L. Xie and W.M. Jiang, Nanjing University, China</i>	1047
Wind Tunnel Modeling of Dust Emission and Deposition in Lower Atmosphere: Similarity Principles <i>Jie Xuan and Wenhu Ye, Peking University, China</i>	1053
Experimental Studies of Dispersion near Building Complex <i>Zhang Maoshuan, Yao Rentai, Liu Jinfeng and Tao Shuwang, China Institute for Radiation Protection, China</i>	1059
Low-Altitude Wind Structure and Atmospheric Pollutant Diffusion <i>Zheng Xiong, Liuzhou Environment Protection Research Institute, China</i>	1065
 <i>Transportation</i>	
Drag Reduction of Trucks through Boundary-Layer Control <i>V.J. Modi, S. St. Hill and T. Yokomizo, University of British Columbia, Canada</i>	1073
Environment over Helideck of Offshore Platform <i>Qiang Chen, Zhifu Gu, Tianfeng Sun and San Song, Peking University, China</i>	1079
Some Wind Tunnel Experiments on Three-Dimensional Effects of Circulation Control Sail Wing <i>Pan Weiming, Wang Xianfu and Zhang Shaoqing, Wuhan University of Water Transportation Engineering, China</i>	1085
Wake Survey and Analysis on the Scaled Car Models <i>Wang Maoxun, Zhou Yuping and Zhu Wei, China Aerodynamics Research and Development Center, China</i>	1091
Numerical Simulation and Characteristic Analysis of Flow around Embankment of Railway Line <i>Zhang Jianbo, Cui Erjie and Fu Guangming, Beijing Institute of the Aerodynamics, China</i>	1097
Study on the Numerical Method for Surrounding Flow Field of Coaches <i>G.Y. Gong, Y.S. Chen, Q.F. Li and L. Gao, Xian Highway Transportation University, China</i>	1103
100 Passenger Air Foil Craft Type AF-2 <i>Hu An-ding, Marine Design &amp; Research Institute of China, China</i>	1109

## *Wind Breaks, Wind Power and Others*

- Full-Scale Measurements of the Effect of a Porous Windbreak on Wind Spectra 1117  
*G.M. Richardson and P.J. Richards, Silsoe Research Institute, U.K.*
- Measurement of the Reynolds Stress Structure behind the Multiple Windbreaks  
Across-Wind 1123  
*Bao-Shi Shiau, Institute of Physics, Academia Sinica, Taiwan*
- Modelling the Flow Field around Windbreaks with Surface Vorticity Method 1129  
*C.R. Chou, John Z. Yim and C.C. Yu, National Taiwan Ocean University, Taiwan*
- The Deposition of Sand Particles on and around Structures with Domed Roofs 1135  
*A. Aroussi, University of Nottingham, U.K.*
- Wind Powered Treatment of Waste Water - FRED's WATER Process 1141  
*J.S. Shrimpton, D.A. Janes and N.H. Thomas, FRED Ltd., U.K.*
- Flow Visualization of a Rotating Wind Turbine Blade 1147  
*Jan-Ake Dahlberg, Goran Ronsten, He Dexin and Chen Ming, Aeronautical Research  
Institute, Sweden*
- A Research and Exploitation on Wind Energy Resources along  
the Coast of Guangdong Province 1155  
*Luo Jinlin, Applied Climate Institute, GRMC, China*
- The Stable Position of a Radar Antenna System and Application of  
the Aerodynamic Compensator to an Array Antenna 1159  
*Bian Zongshan and Wu Zhicheng, Nanjing Research Institute of  
Electronic Technology, China*
- Comparative Study of the Storm Surge Models Proposed for Bangladesh:  
Last Developments and Research Needs 1165  
*J.A. As-Salek and T. Yasuda, Gifu University, Japan*
- Comparative Study for Assessment Code of Transport of  
Radioactive Materials and Research of Model 1171  
*Li Jikai and Wang Jiaming, China Institute for Radiation Protection, China*
- The Mechanism of Unfavorable Effects of Wind on Efficiency of  
Dry Cooling Towers 1177  
*Wei Qingding, Zhang Boyin, Liu Keqi, Du Xiangdong and Meng Xianzhong,  
Peking University, China*
- Weakly Nonlinear Deep Water Waves under Wind Action 1183  
*John Z. Yim, C.R. Chou and P.E. Liu, National Taiwan Ocean University,  
Taiwan*
- Aspects of the Wind Energy Potential in the Former Soviet Union 1189  
*Nikolai N. Kukharkin, Princeton University, U.S.A.*
- Learning from Hurricane Iniki 1195  
*Arthur N.L. Chiu and Gregory L.F. Chiu, University of Hawaii at Manoa,  
U.S.A.*

## **Bluff Body Aerodynamics and Separation**



## **An experimental investigation of the effects of free-stream turbulence on streamwise surface pressures in separated and reattaching flows**

Q. S. Li and W. H. Melbourne

Department of Mechanical Engineering  
Monash University, Clayton 3168, Australia

**Abstract:** An experimental investigation was conducted to study the effects of free-stream turbulence on surface pressures on a flat plate with rectangular leading-edge geometry using turbulence-producing grids. The measured mean, standard deviation and peak pressure coefficients as well as lateral cross-correlation of fluctuating pressures are presented and discussed.

### **1. Introduction**

Numerous wind tunnel studies have been carried out to investigate the effects of turbulence intensity and scale on the surface pressures on flat plates and rectangular cylinders over the last three decades. In particular these include Vickery (1966), Bearman (1971), Gartshore (1973), Melbourne (1975, 1979), Lee (1975), Hillier and Cherry (1981, 1987), Kiya and Sasaki (1983, 1985), Nakamura and Ohya (1984, 1987). However, much of these studies have involved extensive measurements in the reattachment zone where the maximum rms pressure occurs. Saathoff and Melbourne (1987, 1989) focused their investigation on the peak pressures which occur in the forward part of the bubble and which are of primary concern in wind engineering. But the largest ratio of turbulence scale to plate thickness in their studies was less than 2.0. More work is required over a much larger range of turbulence scale to be relevant to the wind engineering field. Although Nakamura and Ozono (1987) investigated the effects of turbulence on streamwise pressures over a large range of turbulence scale, only mean pressures were measured in their study.

This paper describes a study of the effects of free-stream turbulence on mean, fluctuating and peak pressures as well as lateral cross-correlation of fluctuating pressures on a flat plate over a larger range of turbulence intensity and scale.

### **2. Experimental Arrangements**

The experiments were carried out in a 450kw closed-circuit wind tunnel with a working section 2.0m wide and high in the Department of Mechanical Engineering, Monash University. Free-stream turbulence was generated by using grids, and three grids were used, which had bar widths of 300mm, 100mm, and 35mm, respectively. The ratio of mesh size to bar width was 4.0 for each grid. A blunt flat plate with rectangular cross-section was used for experimental model which had a thickness,  $D$ , of 50mm and a chord/thickness ratio,  $L/D$ , of 20. The spanwise dimension was 1.6m, giving an aspect ratio of 32. The model was mounted between endplates located 200mm from the each side wall of the tunnel. Wind tunnel solid blockage was 2.5% and the data have not been corrected. The Reynolds number based on plate thickness was approximately  $4.5 \times 10^4$ . Pressure data on the model were collected using Honeywell

163pc transducers connected to pressure tapings with 60mm lengths of PVC tubing with an internal diameter of 1.5mm. Restrictors placed in the tubing provided a flat frequency response within 10% up to 250Hz. Streamwise pressure distributions were measured using a row of tapings on the centreline of the bottom surface on the model.

### 3. Experimental Results

Distributions of mean pressure coefficient,  $C_p$ , in turbulence and smooth flows are presented in Figure 1. The turbulent flows have two values of turbulence intensity,  $I_u$ , of about 8% and 15%, and the ratio of turbulence integral scale to plate thickness,  $L_x/D$ , are over the range from 1.4 to 8.4. It can be seen from Figure 1 that an increase in free-stream turbulence intensity reduces the size of the separation bubble and reduces the minimum value of  $C_p$ , as noted by previous researchers. The data presented in Figure 1 also show little effect of turbulence scale on mean pressure distribution, as observed by Saathoff and Melbourne(1989). However, investigation by Nakamura and Ozono(1987) indicated that mean pressure distributions are scale-dependent for  $L_x/D > 2.0$ . Figure.2 shows the distribution of reduced pressure coefficients which was proposed by Roshko and Lau(1965) are defined as follows.

$$\bar{C}_p = \frac{C_p - C_{p_s}}{1 - C_{p_s}} \quad (1)$$

where  $C_{p_s}$  is the mean pressure coefficient at the separation point. It is more clearly seen in Figure 2 that little scale effect is evident in the mean pressure distributions over the wide range of scale. Data measured by Saathoff and Melbourne(1989) are also presented in Figure 3.

Streamwise distributions of standard deviation of pressures,  $C_{\sigma_p}$ , are shown in Figure.4. An increase in turbulence intensity causes fluctuating pressures to increase and the location of maximum  $C_{\sigma_p}$  to move closer to the leading edge. An increase in turbulence intensity from 8% to 15% moves the position of maximums  $C_{\sigma_p}$  upstream from 1.7D to 0.9D. Also  $C_{\sigma_p}$  increases with increasing scale. Saathoff and Melbourne(1987) have shown that  $C_{\sigma_p}$  correlates well with the parameter  $\eta = (\sigma_u/u)(Lx/D)^{0.15}$ , except at large scales. Figure 5 shows data from Cherry, Saathoff and the present study. Although the amount of data obtained in this study is not sufficient to draw firm conclusions, reasonable correlation was provided by the parameter  $\eta$  over the range of larger turbulence scale.

Streamwise distributions of negative peak pressure coefficient,  $C_{\bar{p}}$  are shown in Figure.6 for smooth and turbulent flows. Since the value of  $C_{\bar{p}}$  depends on the length of sampling record, Figure 6 is presented mainly to show the effects of turbulence intensity and scale on the negative peak pressures. The peak pressure coefficients also show a dependence on both turbulence intensity and scale. In particular, the effect of turbulence scale on peak pressures becomes greater as turbulence increases. The minimum value of  $C_{\bar{p}}$  measured in the large-scale turbulence is about four times lower than that obtained in smooth flow. The peak pressures occur in the forward part of the bubble, and as turbulence intensity increases to produce a contraction of the bubble length, the position of minimum peak pressure also moves closer to the leading edge.

Figure 7 shows the cross-correlation of fluctuating pressures as a function of lateral displacement near separation. It can be seen that the turbulence scale significantly affects the distribution of lateral cross-correlation of fluctuating pressures. An increase in turbulence



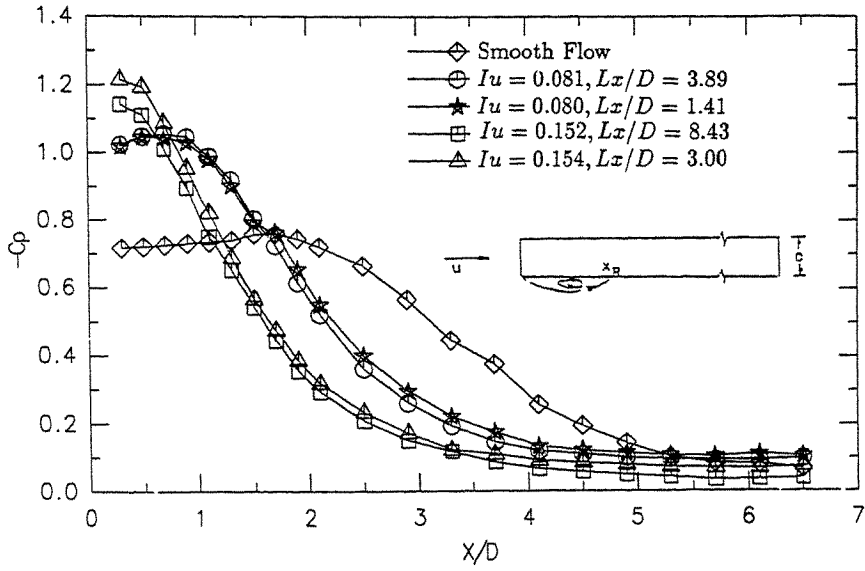


Figure 1. Mean Pressure Distributions On Model Surface In Turbulent and Smooth Flows

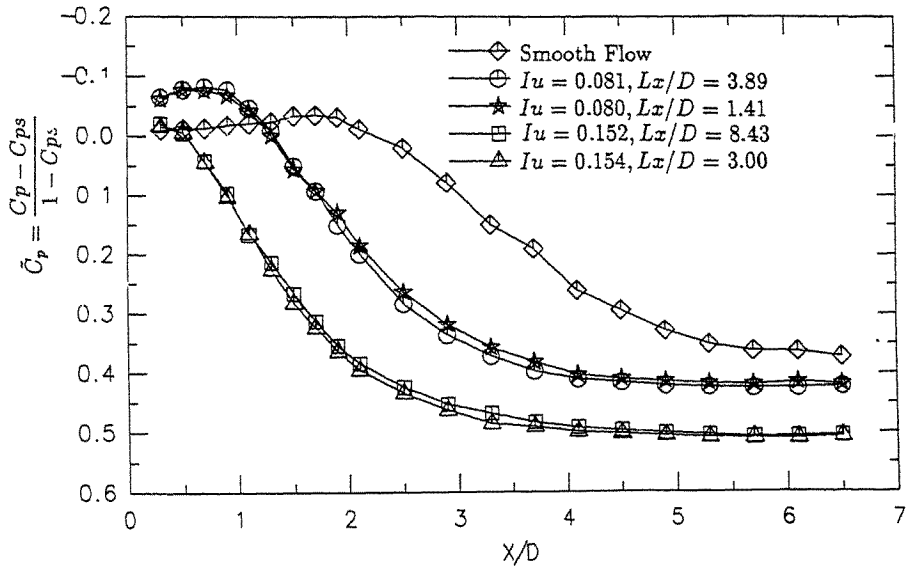


Figure 2. Reduced Mean Pressure Distributions On Model Surface In Turbulent and Smooth Flows

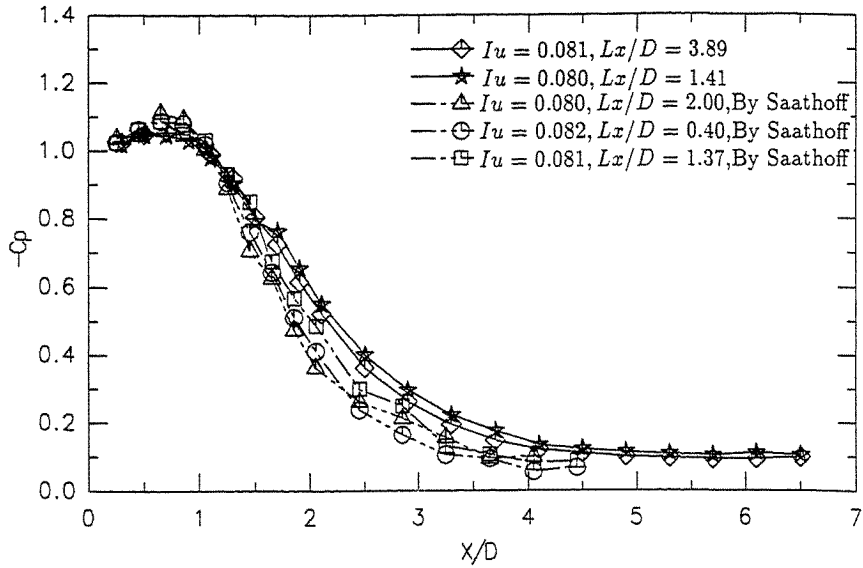


Figure 3. Mean Pressure Distributions On Model Surface In Turbulent and Smooth Flows

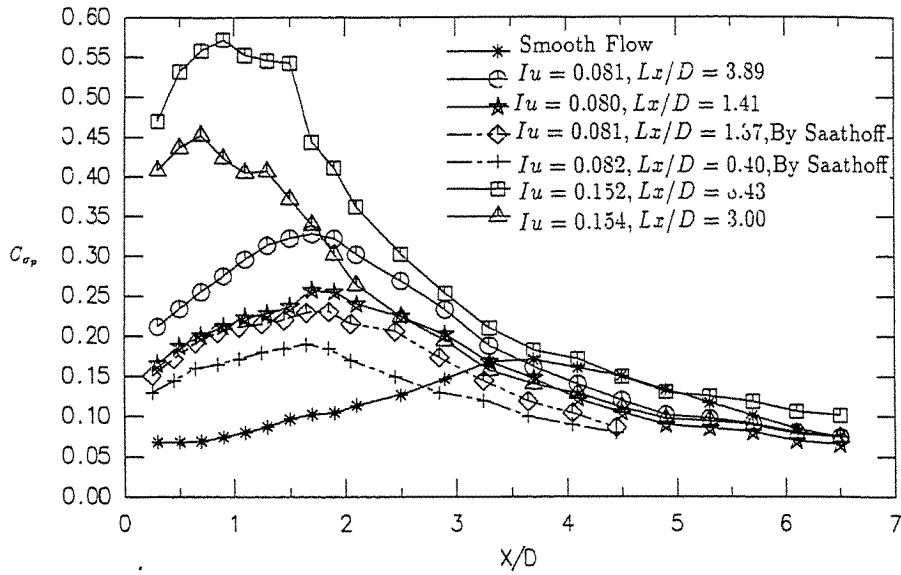


Figure 4. Distributions of Fluctuating Pressure Coefficient In Turbulent and Smooth Flows

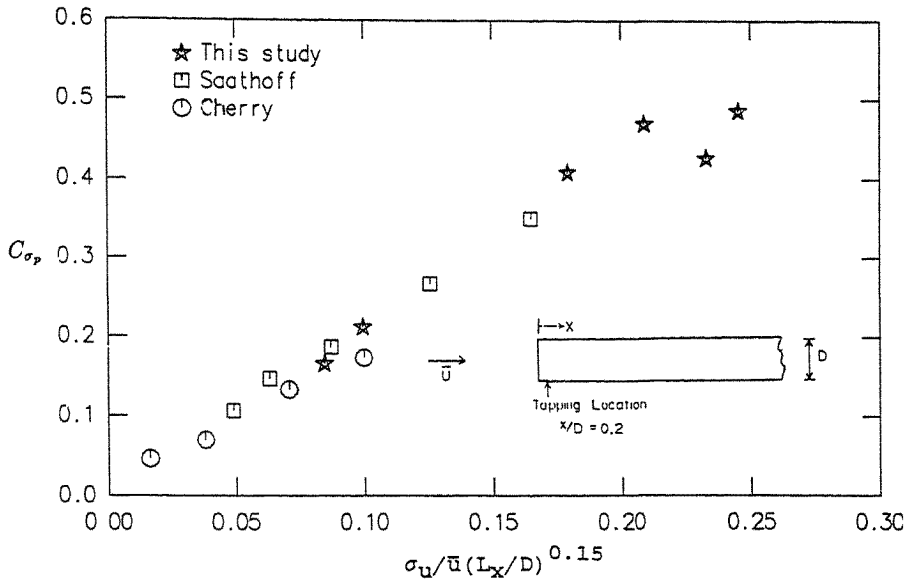


Figure 5. Fluctuating Pressure Coefficient Near Separation As a Function of the Turbulence Parameter,  $\eta$

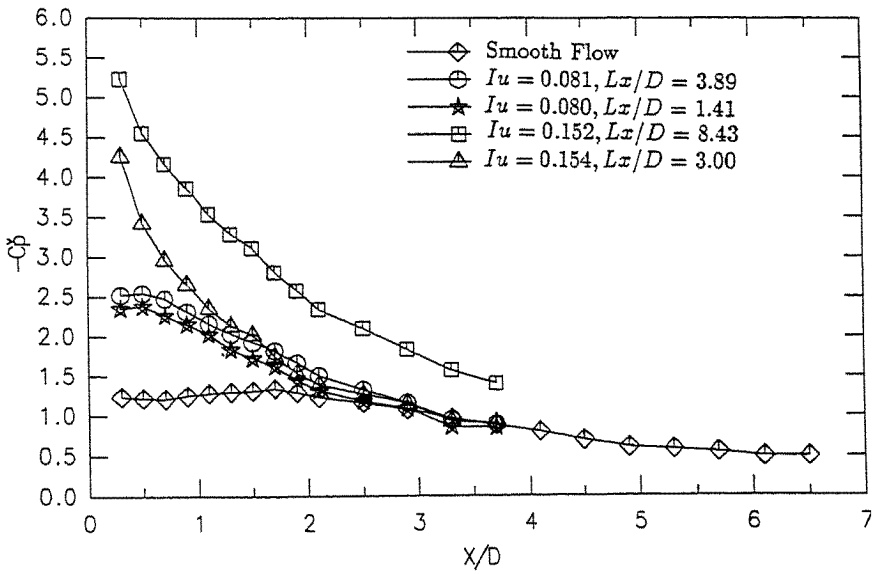


Figure 6. Distributions of Negative Peak Pressure Coefficient In Turbulent and Smooth Flows

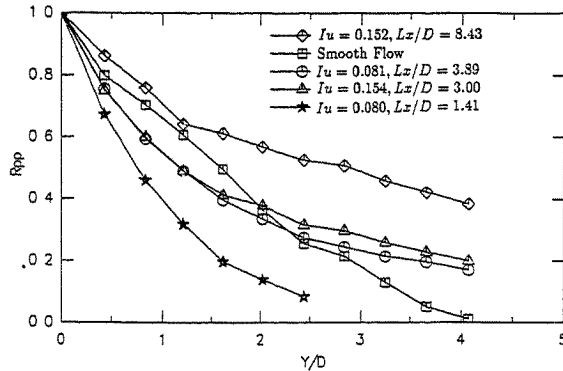


Figure 7 Cross-Correlation of Fluctuating Pressure As a Function of Lateral Displacement

on streamwise surface pressures on a flat plate. Experimental data have indicated that mean pressure distributions are strongly dependent on free-stream turbulence intensity but are not significantly affected by turbulence scale over a wide range of scale. On the other hand, fluctuating pressures are dependent on both turbulence intensity and scale and pressure fluctuations near separation correlate well with the parameter,  $(\sigma_u/u)(L_x/D)^{0.15}$ , even when  $L_x/D \gg 1.0$ . The magnitude of large negative peak pressures also increases with turbulence intensity and scale. The effect of turbulence scale on peak pressures becomes greater as turbulence intensity increases. The lateral cross-correlation of fluctuating pressures near separation are significantly affected by the free-stream turbulence scale. An increase in turbulence scale causes the lateral cross-correlation to become greater.

It is clear that correct modelling of both turbulence intensity and scale is necessary when endeavouring to estimate the highest magnitude of design pressure on structures.

#### Acknowledgement

The support of the Australian Research Council is gratefully acknowledged.

#### References:

1. N.J. Cherry, R. Hillier and M.E.M.P. Latour, Unsteady measurements in a separated and reattaching flow, *J. Fluid Mech.*, Vol.144, pp 123-146.
2. Q.S. Li and W.H. Melbourne, A study of turbulence effect on surface pressures in separated and reattaching flows, *Proceedings of Third Workshop on Wind Engineering*, B5-B8, Brisbane, July, 1993.
3. Y. Nakamura and S. Ozono, The effects of turbulence on a separated and reattaching flow, *J. Fluid Mech.*, Vol.178, pp 477-490, 1987.
4. P.J. Saathoff and W.H. Melbourne, Freestream turbulence and wind tunnel blockage effects on streamwise surface pressures, *J. Wind Eng. & Ind. Aerodyn.*, Vol.26, pp 353-370, 1987.
5. P.J. Saathoff and W.H. Melbourne, The generation of peak pressures in separated and reattaching flow, *J. Wind Eng. & Ind. Aerodyn.*, Vol.32, pp 121-134, 1989.

## Turbulence scale effects on buffeting forces of a flat hexagonal section

K. Kimura and Y. Fujino

Department of Civil Engineering  
The University of Tokyo, Tokyo, 113, Japan

**Abstract:** The characteristics of the buffeting lift forces on a finite length model with a flat hexagonal cross-section were studied experimentally. It was found that as the turbulence scales became larger, the magnitude of the power spectrum of the buffeting lift forces became larger, the peak of the power spectrum became steeper, and it shifted to lower frequency. These characteristics could not be explained by the conventional buffeting analysis that uses the strip theory approximation. It was discussed that the modification of the analysis may be necessary where the buffeting forces acting on a cross-section are determined by considering the effect of the flow over other spanwise locations.

### 1. Introduction

Buffeting responses of structures are often predicted by wind tunnel experiments. However, it is not easy to generate large scale turbulence in a wind tunnel especially if the wind tunnel has a relatively short test section. The similitude of the turbulence scale to the size of the structure sometimes cannot be therefore satisfied. Then, in order to predict the actual buffeting response of the prototype structure, it is necessary to correct the experimental results by considering the turbulence scale effects.

For line-like structures such as long-span bridges, buffeting responses may also be predicted by the conventional buffeting analysis. It assumes the strip theory approximation, where the aerodynamic forces acting on a cross-section of line-like structures are treated as the two-dimensional aerodynamic forces which are determined by the velocities of the approaching wind at the cross-section. Thus the correlation of the fluctuating aerodynamic forces acting on cross-sections at different locations becomes approximately the same as that of the fluctuation of the velocities of the approaching wind. However, the applicability of the strip theory approximation has been questioned by some experimental studies [1,2,3,4], where the correlation of the fluctuating pressures or aerodynamic forces has been observed to be higher than that of the fluctuating wind velocities. Because the strip theory approximation applies exactly to buffeting forces if the turbulence scales are infinite, it is reasonable to think that the applicability of the approximation depends on the ratio of the turbulence scales to the size of the structure.

Therefore, it is important to clarify the effects of the turbulence scales on the buffeting aerodynamic forces in order to either experimentally or analytically evaluate the more accurate buffeting forces. In this study, the effects of scales of turbulence on the buffeting lift forces are studied by using a section model with a flat hexagonal cross-section. The overall buffeting lift force acting on a portion of the model is measured, and the effects of the turbulence scale, wind speed, and spanwise length of the portion are examined by comparing the power spectra of the forces. Also some discussions are given on the characteristics of the buffeting forces that are not represented by the conventional buffeting analysis.

## 2. Wind Tunnel Experiment

The model was a 1.05 m long section model with a flat hexagonal cross-section of 148 mm wide and 15 mm thick (Fig. 1). The model had a movable portion at the middle of its span. This movable portion was supported by two or four flat plate springs that were rigid enough to avoid the resonance vibration of the movable portion in the interested frequency range. Three types of the movable portion were used with the different spanwise length,  $W$ , of 20, 50, and 100 mm, respectively. Four strain gauges each were attached to the flat plate springs to make up a full Wheatstone bridge per a spring. High frequency component of the output from dynamic strain amplifiers was truncated by low pass filters with the cut-off frequency of 700 Hz, and the signal was then digitized by AD converter at 1 kHz sampling rate. The calibration was done by putting weights in the center of the movable portion. It was assumed that the same loading was acting on each spring during the calibration, and the calibration factor of the output from each strain amplifier was determined. Then the outputs multiplied by the calibration factors were added together to give the overall lift force acting on the movable portion.

The model was placed in an open circuit wind tunnel with a test section of 1.09 m wide and 1.80 m high. Three types of turbulent flow were generated by coarse square mesh grids. The mesh size of the grids was four times larger than the bar size. The grids were set upstream of the model location with a distance 10 times larger than the mesh size. With this configuration, flow with different scales of turbulence but almost the same turbulence intensities were generated. The configurations of the grids are shown in Table 1.

Table 1. Grid configurations and flow characteristics.

	Grid 1			Grid 2			Grid 3		
$B$ (mm)	20			50			80		
$M$ (mm)	80			200			320		
$D/B$	10			10			10		
$U$ (m/s)	4.0	8.0	12.0	4.0	8.0	12.0	4.0	8.0	12.0
$I_w$ (%)	8.8	7.4	7.5	8.0	7.4	8.0	7.7	8.3	7.3
$L_w^z$ (mm)	21	25	27	38	47	57	49	60	68
$L_w^y$ (mm)	25	25	25	30	30	30	40	40	50

where,  $B$ : bar size,  $M$ : mesh size,  $D$ : grid to model distance,  $I_w$ : turbulence intensity of  $w$ , and  $L_w^z$  and  $L_w^y$ : integral scales of turbulence of  $w$

The flow characteristics were measured mainly for the vertical component of the fluctuating velocity,  $w$ , which plays a dominant role on the buffeting lift forces. A hot wire anemometer with x probes was used. By adjusting the parameters  $L_w^z$  and  $L_w^y$  that correspond to the scales of turbulence, the measured power spectra and the cross-spectra of the  $w$ -component were fitted to the following expressions that are based on the Kármán spectra [5].

$$S_w(f) = \frac{(2 \cdot \sigma_w^2 \cdot L_w^z / U) \cdot [1 + 188.8 \cdot (f \cdot L_w^z / U)^2]}{[1 + 70.78 \cdot (f \cdot L_w^z / U)^2]^{11/6}} \quad (1)$$

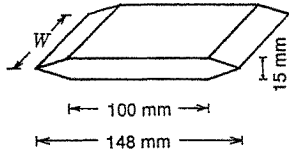


Fig. 1. Dimensions of the movable portion.

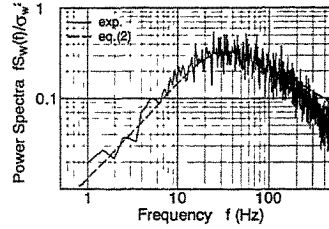


Fig. 2. Dimensionless power spectrum of  $w$ -component (Grid 2,  $U = 8$  m/s)

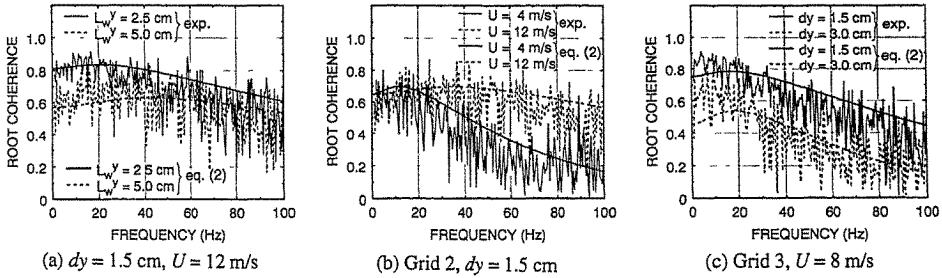


Fig. 3. Root coherence of  $w$ -component at the locations separated normal to the mean flow direction with distance  $dy$ .

$$S_{ww}(f, y, y') = \frac{2^{1/6} \cdot S_w(f)}{\Gamma(5/6)} \times \left[ \eta^{5/6} \cdot K_{5/6}(\eta) - \frac{\eta^{11/6} \cdot K_{11/6}(\eta)}{1 + \frac{8}{3} \cdot (2 \cdot \pi / B_1)^2 \cdot (f \cdot L_w^y / U)^2} \right] \quad (2)$$

where,  $\eta = \frac{|y - y'|}{L_w^y} B_1 \cdot \sqrt{1 + (2 \cdot \pi / B_1)^2 \cdot (f \cdot L_w^y / U)^2}$ ,  $B_1 = \sqrt{\pi} \cdot \frac{\Gamma(5/6)}{\Gamma(1/3)}$ ,  $\sigma_w$  is r.m.s. of  $w$ ,  $K$  is the

modified Bessel function of the second kind, and  $\Gamma$  is the gamma function. In the buffeting analysis conducted for comparison, these expressions were used as the wind velocity spectra. Some examples of the measured power spectra and root coherences are shown in Figs. 2 and 3 with the fitted expressions of  $S_w(f)$  and  $S_{ww}(f, y, y')/S_w(f)$ . The scales of turbulence from the expression above and the intensity of turbulence are shown in Table 1. The flow characteristics had some dependence on the wind speed.

Figs. 4, 5, and 6 show the power spectra of the measured buffeting lift forces. Each of them indicates the effects of the turbulence scale, wind speed, and spanwise length of the movable portion, respectively. The peak around 40 Hz of some spectra seemed to be caused by an overall model vibration that resulted an inertia force of the movable portion to act on the flat plate springs, and it should be disregarded. With these figures, the following characteristics can be pointed out, where

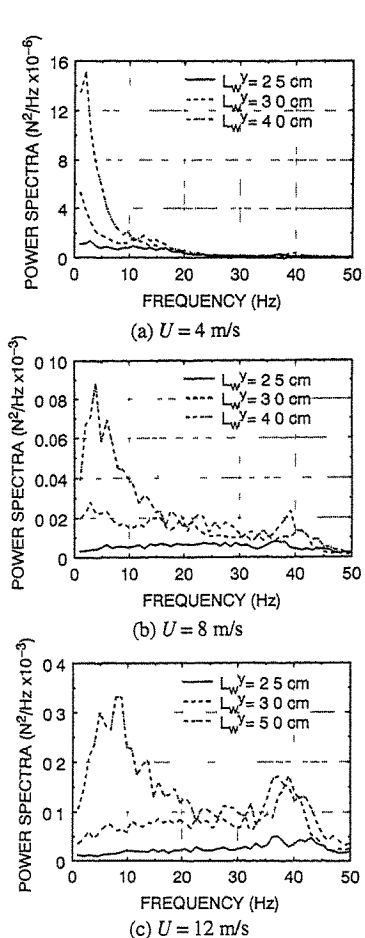


Fig 4 Effects of turbulence scales ( $W = 5$  cm)

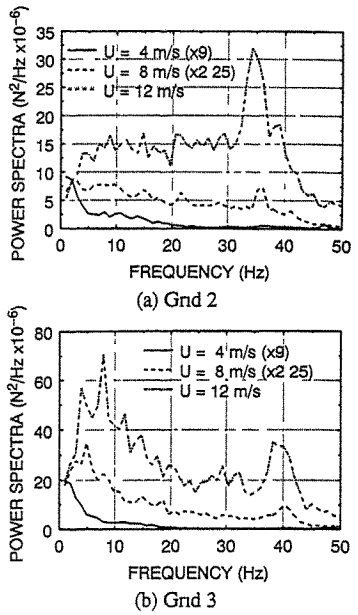


Fig 5 Effects of wind speed ( $W = 2$  cm).

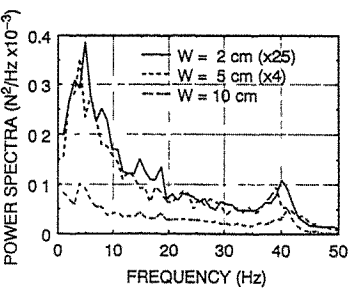


Fig. 6. Effects of spanwise length of the movable portion (Grd 3,  $U = 8$  m/s).

the word 'spectral peak' corresponds to the peak or rise of the spectra other than what was mentioned above

- 1) With the increase of turbulence scales of approaching flow, the magnitude of the power spectrum becomes larger, the spectral peak becomes steeper, and the frequency of the spectral peak location becomes lower (Figs 4)
- 2) With the increase of the wind speed, the frequency of the spectral peak location becomes higher and the spectral peak becomes less steep (Figs 5) Note that the power spectra are multiplied by  $(12 \text{ m/s} / U \text{ m/s})^2$  in the figures to have converted values at  $U = 12 \text{ m/s}$  for all spectra



3) Difference of the spanwise length of the movable portion has little influence on the magnitude of the power spectrum per the same area between the cases of  $W = 2$  cm and  $W = 5$  cm (Fig. 6). For  $W = 10$  cm case, however, the magnitude becomes smaller. Note that the power spectra are multiplied by  $(10 \text{ cm} / W \text{ cm})^2$  in the figure to have converted values per the same area of  $W = 10$  cm case.

### 3. Comparison with the Analytical Results

The power spectra of the buffeting lift force acting on the movable portion were also obtained by the conventional buffeting analysis. In the analysis, a) an approximate expression of the Sears function [6] was used as the aerodynamic admittance; b) eq. (2) was used as the expression of the cross-spectrum of  $w$ -component; c) the measured slope of the lift coefficient in the same flow condition as the experiment was used. The results of the analysis are shown in Figs. 7. By comparing with the corresponding experimental results (Figs. 4(b), 5(a), and 6), it is clear that the analytical results cannot reproduce the characteristics of the experimental results of buffeting lift force power spectra:

- 1) With the decrease of the turbulence scales, the magnitude of the power spectra by the analysis does not become as small as that by the experimental results especially in the very low frequency region (less than 10 Hz, say).
- 2) With the increase of the wind speed or the decrease of the turbulence scales, the spectral peak shifts to the higher frequency in the experiment. However the spectra in the analysis always take the maximum value at the lowest frequency.

### 4. Discussion

The reason of these inconsistencies of the experimental and analytical results may be attributed to the strip theory approximation used in the conventional buffeting analysis. With this approximation, the flow characteristics of the approaching wind that is needed to determine the buffeting forces acting on a cross-section are only that at the location of the cross-section. However, the buffeting lift forces acting on a cross-section or narrower strip than the turbulence scale are also affected by the vortices generated over other spanwise locations [7]. In other words, in turbulent flow which has inherently three-dimensional characteristics, the strip theory approximation does not apply exactly even if the line-like structure on which the buffeting forces are considered has a uniform cross-section along its span.

The contribution to the buffeting forces on a cross-section from the flow over other spanwise locations may be taken into account by considering the turbulence scale taken normal to the mean flow direction in the analysis. This means that the turbulence scale taken normal to the mean flow direction may be used as a parameter to define not only the correlation of the buffeting forces at different spanwise locations but also the magnitude of the buffeting forces acting on a cross-section. A two-dimensional aerodynamic admittance with two wave number spectrum could be utilized for

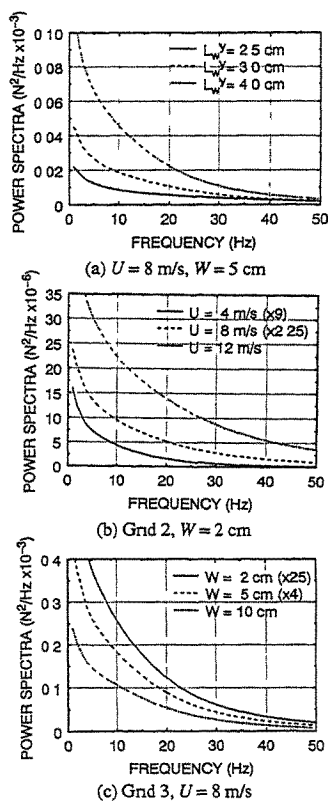


Fig. 7 Analytical results.

this purpose as in the case of buffeting analysis of wings [8]. Actually, the rise of the coherence of the  $w$ -component at the locations separated normal to the mean flow direction moves toward the higher frequency direction with decrease of turbulence scale (Fig. 3(a)) and with increase of wind speed (Fig. 3(b)). Therefore, it may be possible to reproduce the experimental results by including the turbulence scale taken normal to the mean flow direction for the evaluation of the buffeting forces acting at a cross-section.

The reason of the previous finding that the correlation of the buffeting forces is higher than that of the fluctuation of the velocities of the approaching wind [1,2,3,4] may also be attributed to the contribution to the buffeting forces on a cross-section from the flow over other spanwise locations, because the contribution from other spanwise locations makes the correlation of the buffeting forces at different spanwise locations higher. Sankaran and Jancauskas [3] have attributed this higher correlation to the flow separation, but the consideration above which applies to streamlined cross-section may explain the phenomena. The present experimental results showed little difference in the buffeting lift force spectra between  $W = 2$  and  $5$  cm case (Fig. 6), although the coherence of the  $w$ -component for  $dy = 3$  cm case was considerably smaller than that for  $dy = 1.5$  cm case (Fig. 3(c)). This may be another evidence that the correlation of the buffeting forces is higher than that of the fluctuation of the velocities of the approaching wind.

### 5. Concluding Remarks

An experiment was conducted where the effects of turbulence scales on the buffeting lift forces were mainly studied. The experimental buffeting lift force spectra were compared with the analytical results that were based on the conventional buffeting analysis. It was shown that the analysis cannot reproduce the actual characteristics of the buffeting lift forces in some cases.

In the present analysis, turbulence scales were comparatively small with the width of the model. It is therefore needed to measure the effects on the buffeting forces under larger turbulence scales. The strip theory gives better approximations with larger turbulence scales, but it is still important to clarify the accuracy of the approximation. Also the larger correlation of the buffeting forces has to be taken into account in the analysis. For more detailed study such as the evaluation of the correlation of the buffeting forces, the buffeting force distribution over the model has to be measured as conducted by Larose, Davenport, and King [4].

The authors acknowledge the financial support of the Honshu-Shikoku Bridge Authority. Much of the experimental work was conducted by M. Okayama (Kajima Corp., formerly undergraduate student at the University of Tokyo) and his effort is gratefully acknowledged.

### References:

1. W.H. Melbourne, Proc. Workshop on Wind Tunnel Modeling Criteria & Techniques in Civil Eng. Applications (1982) 637.
2. H. Kawai, J. Wind Eng. Ind. Aerody., 13 (1983) 197.
3. R. Sankaran and E.D. Jancauskas, Proc. BBAA2 (1992).
4. G.L. Larose, A.G. Davenport, and J.P.C. King, Proc. 7th US National Conf. on Wind Eng. (1993).
5. H.P.A.H. Irwin, National Research Council Canada, Lab. Tech. Rep. LTR-LA-210 (1977).
6. H.W. Liepmann, J. Aeronautical Sci., 19 (1952) 793.
7. P. Lamson, NACA TN 3880 (1957).
8. R. Jackson, J.M.R. Graham, and D.J. Maull, Aero. Quart., 24 (1973) 155.

## An Experimental Study of Flow Structure Around a Rankine Body

S.J. Lee and K.J. Kwon

Department of Mechanical Engineering  
Pohang Institute of Science & Technology, Pohang, Korea

**Abstract:** An experimental study was made of the flow structure of the wake behind a Rankine body for two incidence angles of attack. Surface pressure, total pressure and streamwise velocity fluctuation of the turbulent wake were measured. Mean velocity, turbulence intensity, skewness and flatness distributions of the wake were presented using a flow field imaging technique.

The results show that at  $5^\circ$  angle of attack, the circumferential pressure gradient increased on the forebody of the model and the flow accelerated toward the leeward side. The pressure on the leeward surface increased as the flow progresses downstream. Total pressure, mean velocity and turbulence intensity distributions at zero angle of attack showed no evidence of a vortex pair. However, at  $5^\circ$  angle of attack, a strong counter-rotating vortex pair was descending downstream. The leeward side of the model at  $5^\circ$  angle of attack had low skewness and high flatness values, suggesting an energetic entrainment from the free stream.

### 1. Introduction

From an aerodynamics' viewpoint, many moving vehicles can be idealized as Rankine bodies. The wake behind a moving vehicle often contains twin vortices which cause an increase in drag. When twin vortices rotate in an opposite direction about the parallel rotational axes, they move normal to the vortex axes. Fig. 1 shows a sketch of the flow around a Rankine body and a formation of twin vortices.

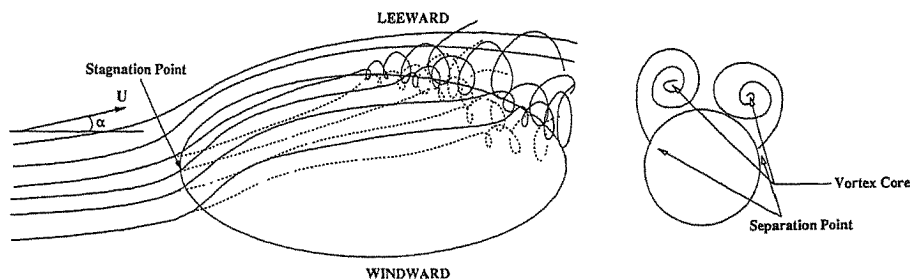


Fig. 1. A sketch of the flow around a Rankine body

The flow characteristics and vortex structure of the wake behind a sphere have been investigated by many researches. Uberoi and Freymuth[1] experimentally investigated the axisymmetric turbulent wake behind a sphere 50 to 300 diameter downstream from the sphere. They measured the turbulent energy decay from a one-dimensional energy spectra of the three velocity components of the turbulent wake. Achenbach[2] measured the Strouhal number up to  $3 \times 10^5$ . He found that the separation point rotates around the sphere. Pao and Kao[3] visualized a shedding of the vortex behind a sphere and suggested that the wake have a closed-end double helical structure for

Reynolds numbers from  $4 \times 10^4$  to  $2 \times 10^5$ .

Recently several investigations have been made of the flow visualization and separation mechanism on the surface of spheroids and Rankine bodies. Perry and Watmuff[4] investigated the wake structure of the three-dimensional elliptical body using a flying hot-wire probe and phase averaging technique. They found two regular critical points; a center point coincides with a minimum pressure point and a saddle point corresponds to a maximum pressure point. Using a PDV(Particle Displacement Velocimetry) method Fu et al.[5] measured the velocity and vorticity profiles around the leeward side of prolate spheroid at an incidence. They found that a boundary layer tripping greatly changes the overall flow structure, and that the size and magnitude of the counter-rotating secondary vortices near the body surface substantially vary and in some cases they are comparable to those of the primary vortices. The vortex formation has a close relation with the flow separation in the body surface, and for the axisymmetric bodies, the flows along the side surface are difficult to analyze.

Most of the experimental studies for the inclined prolate spheroids were limited to the measurements of surface shear stresses[9] and surface flow visualization[10]. However, little attention has been given to the wake behind a spheroid or a Rankine shaped body. The main objectives of the present research are to attain a better understanding of the flow structure behind a Rankine body and to develop a computer-driven flow visualization technique for the flow field.

## 2. Experimental Apparatus and Procedure

In the present study, a Rankine body model having an aspect ratio,  $AR(= a/b)$ , of 2.5, with the major axis radius of  $a = 100$  mm and the minor axis radius of  $b = 40$  mm was installed in the 2' x 2.4' subsonic wind tunnel with 6 piano-wires of 0.3 mm diameter. During the experiment free stream velocity was maintained at 10m/s and Reynolds number(based on the minor axis radius,  $b$ ) was  $5.3 \times 10^4$ . Experiments were carried out for two angles of attack( $\alpha = 0^\circ$  and  $5^\circ$ ).

For surface pressure measurements 33 pressure taps of 0.4 mm diameter were installed along the perimeter of the model and connected to a 48-channel Scanivalve.

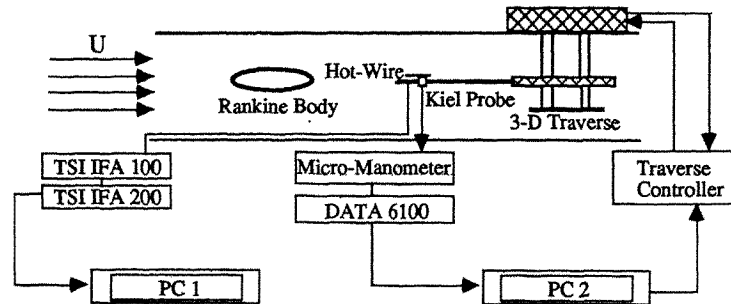


Fig. 2. Schematic diagram of the data acquisition system

Fig. 2 shows a schematic diagram of the data acquisition system for the wake measurement. The Kiel probe designed to minimize the effect of yaw angle was used to measure the total pressure distribution in the wake. To measure the streamwise velocity fluctuation a single hot-wire probe(TSI 1210 - T1.5) was used and the hot-wire probe was traversed following a predetermined scanning route. The voltage outputs from the hot-wire anemometer were digitized at a sampling rate of 2kHz after passing through 1kHz low-pass filter and the data length at each measurement point was 4096.

From the measured velocity signals, mean velocity, turbulence intensity, skewness, and flatness were calculated.

Total pressure and instantaneous velocity were measured by scanning probes in the sections of  $X/a = 2, 3$  and  $4$ , where  $X$  is a distance from the model center along the streamwise direction. The flow field area tested was  $150 \times 150$  mm and  $150 \times 165$  mm for  $\alpha = 0^\circ$  and  $5^\circ$  respectively. Since counter-rotating vortices at  $\alpha = 5^\circ$  descend as the flow progresses downstream, the field test area was rectangular with a long vertical scanning and the test area was shifted by 25mm downward from the center of the model.

A computer controlled three-axis traverse system was used to traverse the Kiel probe and the single hot-wire probe. By vertically incrementing the probe by a small amount ( $\Delta = 5$ mm) at the end of each spanwise scan, a two-dimensional sheet of the flow field data at a given section was obtained.

These flow field data were presented using an image processing flow visualization technique. This technique provides information on a given flow field by reconstruction, point by point, of the local values of total pressure, mean velocity and turbulence statistics, etc. In this technique, the flow field data are processed through a computer which codes the data in certain color and displays the results on a color video monitor. In the shading of regions of the survey plane, a linear interpolation scheme was used to increase a spatial resolution by filling in empty areas between discrete data points. The multi-colored display technique would help to qualitatively and/or quantitatively interpret large quantities of data.

### 3. Results and Discussion

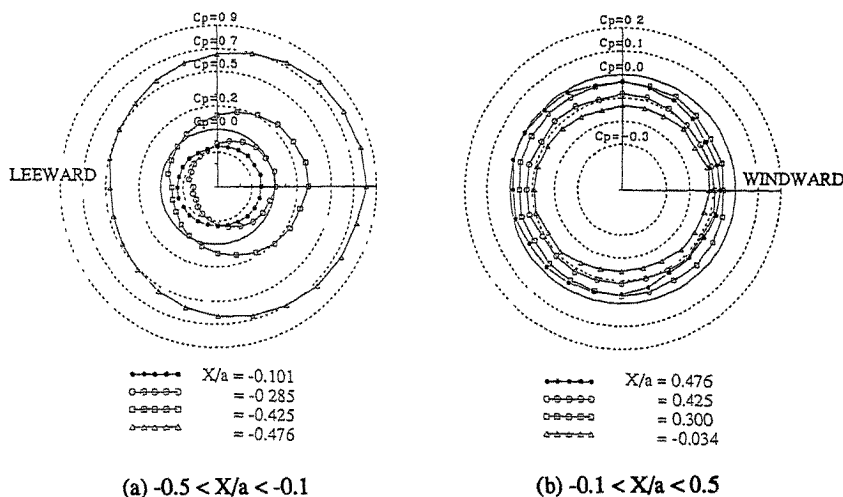


Fig. 3. Polar plots of surface pressure distribution at an angle of attack  $\alpha = 5^\circ$

The surface pressure distributions at an angle of attack of  $\alpha = 5^\circ$  are shown in Fig. 3. The results show locations where the boundary layer separates from the model surface to form a vortex pair. It is shown from Fig. 3(a) that the separation on the leeward side occurs about  $X/a = -0.1$ . While the separation on the windward side occurs in the vicinity of  $X/a = 0.2$ .

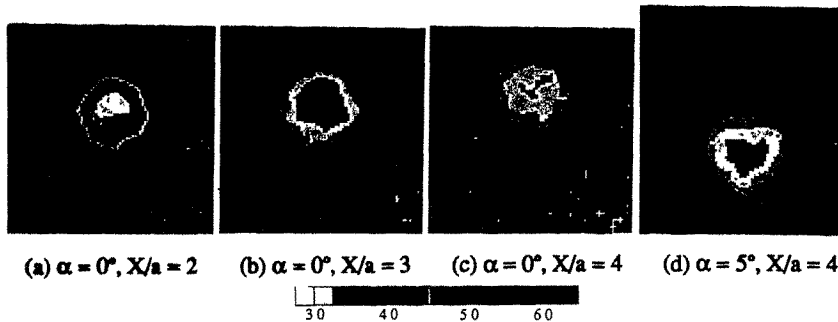


Fig. 4. Total pressure distributions (mmH<sub>2</sub>O)

Fig. 4 shows the total pressure distributions in the wake region at  $X/a = 2, 3$  and  $4$  downstream from the center of the Rankine body. The colors bar chart ranges from white for the minimum pressure to red and blue, and to black for the maximum pressure. One color represents a range of  $0.25\text{mmH}_2\text{O}$ .

At  $\alpha = 0^\circ$ , the wake region heavily diffuses and total pressure is rapidly recovered compared to that at  $\alpha = 5^\circ$ . From this figure, we can see a weak vorticity at  $X/a = 4$  and  $\alpha = 0^\circ$ . When the vorticity is strong the vortex size is small, but the pressure at the center point is very low. At  $\alpha = 0^\circ$ , the vortex shed from the model surface is composed of a lot of small vortices around the circumference of the model and smoothly follows the free stream flow. But at a higher angle of attack ( $\alpha = 5^\circ$ ), two large vortex nuclei are formed on the body surface and develop to a pair of two strong vortices (twin vortices). As the flow progresses downstream, these twin vortices descend perpendicular to the free stream. The right side vortex of the vortices rotates counterclockwise and the left side vortex clockwise.

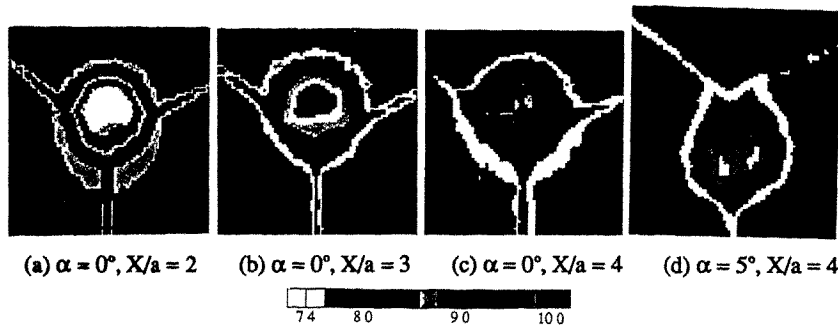


Fig. 5. Velocity distributions (m/s)

The mean streamwise velocity distributions are shown in Fig. 5. The displayed data are highly qualitative due to the unsteady three-dimensional reversed flow in the separated region. In this figure one color represents a velocity range of  $0.2\text{m/s}$ . The velocity images show a similar behavior to the total pressure results. But the velocity defects diffuse in a slower rate than those of the total pressure. Since the velocity and dynamic pressure are equivalent physical quantities, this behavior implies a high decrease of static pressure in the outer region adjacent to the free stream.

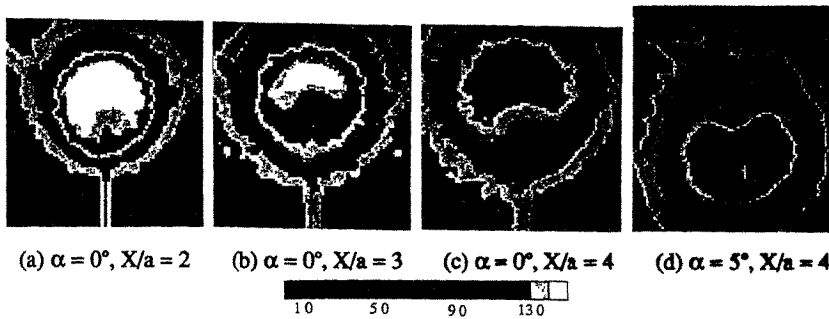


Fig. 6. Turbulence intensity distributions (%)

Images of the color mapped turbulence intensity are shown in Fig. 6. One color in the color-bar chart indicates a 1% range of the turbulence intensity. The turbulence intensity distribution in a wide region has more sensible values than the mean velocity distribution. If the turbulent wake is divided into two regions (central continuous turbulent region and intermittent outer region), the latter has relatively little influences on the time-averaged total pressure and mean velocity distributions. Turbulence intensity distributions show large values in the outer wake region where mean velocity has a maximum gradient. The region of the valuable turbulence intensity largely expands as the flow goes downstream. At  $\alpha = 5^\circ$ , we can confirm the effects of twin vortices on the turbulence intensity distribution. In addition, contour maps of the total pressure, streamwise mean velocity and turbulence intensity distributions are plotted from the field survey data. The typical contour plots at  $X/a = 2$  and  $\alpha = 5^\circ$  are shown in Fig. 7. This clearly shows the twin vortices and sensible regions of each physical quantity previously stated.

The skewness is a dimensionless measure of the asymmetry, i.e., the lack of symmetry ( $s=0$ ) in the probability density distribution. The flatness is a measure of large fluctuating values from the mean velocity. Fig. 8 and Fig. 9 show the skewness and the flatness distributions respectively. One color band represents a range of skewness value of 1 in the skewness distribution and flatness value of 10 in the flatness distribution. Unlike the total pressure, mean velocity, and turbulence intensity distributions, the vortex structure of the wake is not clearly shown in the skewness and flatness images, but the free stream entrainment and mixing phenomena can be drawn from them.

At  $\alpha = 0^\circ$ , skewness values are low around the circumference of a circle whose diameter is almost the same as the minor axis diameter of the Rankine body. For the Rankine body at incidence, very low skewness values exist on the leeward side of the body. Here, low negative skewness value means energetic entrainment from the free stream. At  $\alpha = 5^\circ$ , the skewness has smaller values than those at  $\alpha = 0^\circ$ . The flatness distribution shows very low values in the central region and very large values in the intermittent region. This implies the energetic entrainment and strong mixing in the intermittent region.

#### 4. Conclusion

The flow characteristics and vortex structure of the wake behind a Rankine body at two angles of attack were investigated using an image processing flow visualization technique.

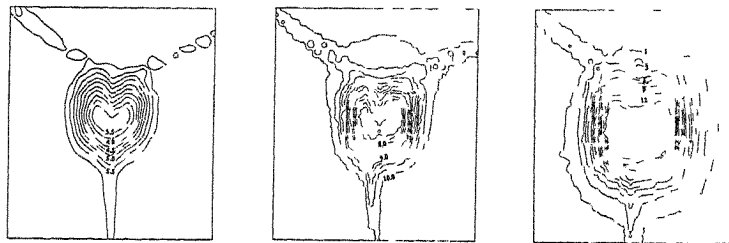
The wake behind the Rankine body contains vortices whose strength decreases as the flow progresses downstream. At an angle of attack  $\alpha = 5^\circ$ , a descending counter rotating vortex pair exists in the wake. The flow field data show that the mean velocity and turbulence intensity diffuse more rapidly in the intermittent region than in the central turbulent region. The skewness and flatness distributions indicate the flow entrainment and mixing in the wake behind a Rankine body.

### Acknowledgements

The authors gratefully acknowledge the support of Advanced Fluids Engineering Research Center, POSTECH.

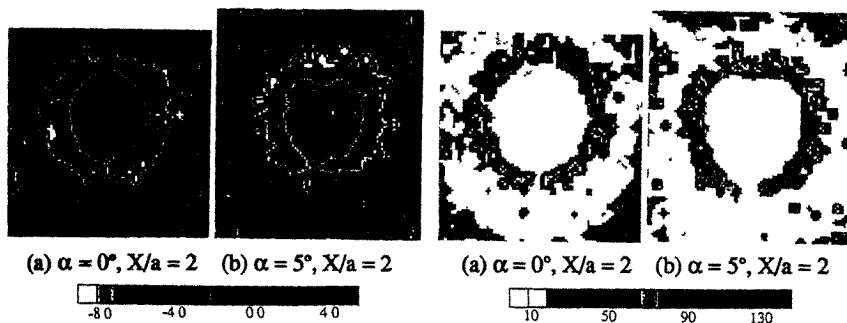
### References:

1. M.S. Uberoi and P. Freymuth, *Physics of Fluids*, Vol. 13, No. 9 (1970), 2205.
2. E. Achenbach, *J. Fluid Mech.*, Vol. 62 (1974), 204.
3. H.P. Pao and T. W. Kao, *Physics of Fluids*, Vol. 20, No. 2 (1977), 187.
4. A.E. Perry and J.H. Watmuff, *J. Fluid Mech.*, Vol. 103 (1981), 33.
5. T.C. Fu, A. Shekarriz, J. Katz and T.T. Huang, 19th Symposium on Naval Hydrodynamics, (1992), 113.
6. H.U. Meier and H.P. Kreplin, *Z. Flugwiss. Weltraumforschung*, Vol. 4, No. 2 (1980), 65.
7. T. Han and V.C. Patel, *J. Fluid Mech.*, Vol. 92 (1979), 643.
8. C.E. Costis, N.T. Hoang and J. Telionis, *Aircraft*, Vol. 86, No. 9 (1989), 810.
9. K.C. Wang, H.C. Zhou, C.H. Hu and S. Harrington, *Proc. R. Soc. London, A* 421 (1990), 73.
10. A.E. Winkelmann and P.T. Chen, *AIAA Journal*, Vol. 23, No. 9 (1985), 1381.



(a) Total pressure (mmH<sub>2</sub>O) (b) Mean velocity (m/s) (c) Turbulence intensity (%)

Fig. 7. Contour maps of total pressure, mean velocity and turbulence intensity distributions



(a)  $\alpha = 0^\circ$ ,  $X/a = 2$  (b)  $\alpha = 5^\circ$ ,  $X/a = 2$

Fig. 8. Skewness distributions

(a)  $\alpha = 0^\circ$ ,  $X/a = 2$  (b)  $\alpha = 5^\circ$ ,  $X/a = 2$

Fig. 9. Flatness distributions



## STUDY ON AEROSTATIC CHARACTERISTICS AND AEROELASTIC INSTABILITY OF STRUCTURAL L-SHAPED, T-SHAPED AND CROSS-SHAPED SECTIONS

Atsushi OKAJIMA\*, Hisanori UENO\*\*, Donglai YI \*\*\*

\* Professor, \*\* Associate Professor, \*\*\*Graduate Student  
Department of Mechanical Engineering, Kanazawa University  
Kodatsuno 2-40-20, Kanazawa, Japan 920

**Abstract:** *Aerostatic characteristics and aeroelastic instability of structural angle section (L-shaped) and their combined sections, that is, T-shaped and cross-shaped sections are studied using a wind tunnel. Firstly, lift and drag forces, moment and Strouhal number of various structural sections are measured against an angle of attack. Secondly, the amplitude of an oscillating motion of a structural model and the Strouhal frequency of a wake are measured. The bending resonance exhibits the familiar vortex excitation near the critical wind velocity and the galloping-oscillation in the range of high wind velocities. It is found that aerostatic characteristics and aeroelastic behaviors of cross-shaped and T-shaped section models are very similar to those of square and L-shaped section models at the corresponding angles rotated by 45 degrees, respectively. The results should prove useful in structural designs such as high voltage transmission towers, antenna mast, bridges, etc. where the angle sections and their combined sections are often used as secondary members.*

### 1. Introduction

The aerostatic and aerodynamic characteristics of structures with L-shaped section and the combination of L-shaped sections such as T-shaped and cross-shaped sections which are widely used as structural components in electrical transmission towers, antenna masts, bridges and etc. have not been well known so far. In recent years, only Modi and Slater[1] reported the results concerning the aerostatic and aerodynamic characteristics of structure with L-shaped section. Here in this paper, on basis of experiments in wind tunnel, we first get clear about the aerostatic characteristics concerning the lift and drag forces, the moment and the Strouhal number of L-shaped, T-shaped and cross-shaped sections when the structures are exposed to free stream flow with various angles of attack, and then, by changing the mass-damping ratio (Scruton number), we have made a series of free oscillation test for the aerodynamic characteristics of vibrations at various angles of attack of flow over each section. It is found that aerostatic characteristics and aeroelastic behaviors of cross-shaped and T-shaped section models are very similar to those of square and L-shaped section models at the corresponding angles rotated by 45 degrees, respectively.

### 2. Experimental Facilities and Procedures

An Eiffel type of wind tunnel of which measuring section is 300 mm in width and 1200 mm in height is used in the experiment. The uniformity of flow is limited within 0.3%, and the turbulence intensity of flow inside the measuring section is within 1.0%. In the experiment, the testing models can be installed between the two end plates at any angle between 0° to 360° to get any angle  $\alpha$  of attack of flow over them and, as shown in figure 1, can vibrate transversely (figure 1, a) and torsionally (figure 1, b), respectively, with the natural vibrating frequency to be from 5 to 6 Hz. Figure 2 shows the sketches of structural sections and the definition of angle  $\alpha$ . The testing models all which have a span of  $L=294$  mm are made of acryl and have been made to be as acute as possible in

corners. In order to make it identical the change of damping coefficient (logarithmic damping ratio  $\delta$ ) of vibrating system, a same electromagnetic damper which is installed outside the measuring section is used for both transverse and torsional vibrating models. Testing models are supported by springs of which natural frequency is  $33\text{ Hz}$  and the lift and drag forces and moment are measured by strain gauges attached on the springs. The displacement of model of transverse vibration is measured by a Laser Displacement Detector outside the measuring section, and the angular deformation of model in torsional vibration is measured by strain gauges set on the springs. Moreover, in order to reduce the end effect of flow on testing, a plate of  $200\text{ mm}$  diameter and  $1\text{ mm}$  thick is equipped on each end of model. Considering the different symmetry of the sections in flow, the ranges of attack angle of flow over each model are different as such:  $-45^\circ \sim 0^\circ$  for cross-shaped section and  $-90^\circ \sim 90^\circ$  for T-shaped section and  $-45^\circ \sim 135^\circ$  for L-shaped section, and the data are obtained every  $5$  degrees for static characteristics and every  $15$  degrees in free oscillation tests. The amplitude of response transverse vibration ( $\eta$ ) which is expressed by the percentage of root-mean-square value of displacement to model height  $H$  and the amplitude of response torsional vibration ( $\theta$ ) which is expressed by the root-mean-square value of response angular deformation are measured in the experiment through changing the angle of attack and Scruton numbers. The Scruton numbers of transverse vibration ( $S_{CT} = 2m\delta / \rho H^2$ , where  $\rho$  is air density) and of torsional vibration ( $S_{CT} = 2I\delta / \rho H^4$ , where  $I$  is the equivalent inertia moment of model) are showed in each summary figure of the experiments. Furthermore, the drag and lift forces, by compared with  $\rho U^2 HL/2$  where  $U$  is the velocity of upstream flow, and the moment by  $\rho U^2 H^2 L/2$  are made dimensionless and become  $C_D$ ,  $C_L$ ,  $C_M$ , respectively. In the paper, the range of Reynolds number is  $(0.32 \sim 5.2) \times 10^4$  where  $\nu$  is the viscosity coefficient of air.

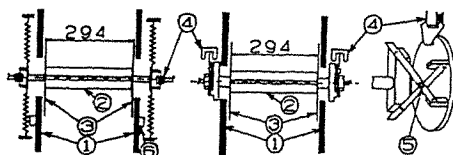


Fig. 1. The vibrating model system at wind tunnel (a) transverse vibrating model; (b) torsional vibrating model; ① the inner of wind tunnel; ② vibrating model; ③ end plates; ④ electromagnetic damper; ⑤ strain gauges; ⑥ laser displacement detector

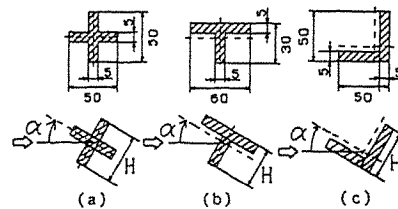
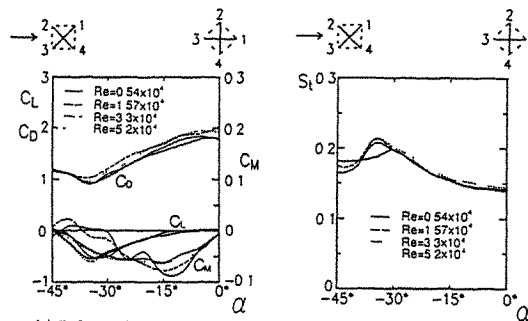


Fig 2. The angles of attack of flow over model sections (a) cross-shaped section; (b) T-shaped section; (c) L-shaped section

### 3. The Characteristics of Structural Cross-shaped Section

#### 3.1 Aerostatic characteristics

Figure 3 shows the static characteristics of drag  $C_D$ , lift  $C_L$ , moment  $C_M$  and Strouhal number  $S_t$  of structural cross-shaped section against the angle of attack in a range of  $-45^\circ \sim 0^\circ$ . For the angle range of greater than  $-35^\circ$ , referring to the top instruction of figure 3 showing the position of structure towards free stream flow, the shear layer shedding from point 3 reattaches at upstream surface of point 4 and then separates from the point 4 downstream, which causes the



(a) Lift  $C_L$ , Drag  $C_D$  and Moment  $C_M$  along angle  $\alpha$   
(b) Strouhal number  $S_t$  along angle  $\alpha$   
Fig.3. Aerostatic characteristics of cross-shaped section

rapid change of flow pattern and results in the sharp curves of  $C_D$ ,  $C_L$ ,  $S_r$ . For the angle range of  $-45^\circ \sim -35^\circ$ , such static characteristics that the slope of  $C_L$  curve in range of  $-45^\circ \sim -35^\circ$  is almost the same as that of rectangular cylinder in range of  $0^\circ \sim 10^\circ$ [2] let us to conclude that the flow pattern around cross-section structure is similar in essence to that of around square cylinder whose outline is drawn by the dash lines as in the top of figure 3. It is also shown in the figure that the static characteristic curves of different Reynolds numbers are almost the same, which suggests that the influence of Reynolds number on static characteristics is small here.

### 3.2 Aeroelastic characteristics of transverse vibration

Figure 4 shows the amplitude  $\eta$  of flow-induced transverse vibration of cross-section structure against the reduced velocity  $\bar{U}$  ( $=U/f_nH$ ) at following angles of attack: (a)  $\alpha=-45^\circ$ , (b)  $\alpha=-40^\circ$ , (c)  $\alpha=-20^\circ$ , (d)  $\alpha=0^\circ$ . The black arrows in the figure show the critical wind velocity  $\bar{U}_{cr}$  obtained from Strouhal number of the wake. For angles less than  $-35^\circ$  as shown in (a)  $\alpha=-45^\circ$  and (b)  $\alpha=-40^\circ$ ,  $\eta$  begins to increase with  $\bar{U}$  from around  $\bar{U}=8$  and  $\bar{U}=12$  respectively and then galloping vibrations occur, which corresponds to  $\partial C_L / \partial \alpha < 0$  as in figure 3. In particular for  $\alpha=-45^\circ$  and  $S_{CP}=45.19$ , the response amplitude  $\eta$  is increasing with  $\bar{U}$ , which is exactly the same as the case of galloping vibration of square cylinder at  $\alpha=0^\circ$ . For  $\alpha=-20^\circ$  as in figure 4(c), and there is no galloping vibration, and the region of a limit-cycle confined by the dotted line is found also. For  $\alpha=0^\circ$  as in figure 4(d), only vortex-induced vibrations of quite large amplitude occur from  $\bar{U}_{cr}$  to the low-velocity side. Deducing from figure 4 (c) and (d), it can be got that in the angle range of  $\alpha=-35^\circ \sim 0^\circ$  in which  $\partial C_L / \partial \alpha > 0$  as in figure 3 there occurs no galloping vibrations but only vortex-induced vibrations;  $\eta$  decreases with the increase of Scruton number and the reduction of  $\alpha$ ; and the unsteady region of vortex-induced vibrations shafts from the right of  $\bar{U}_{cr}$  to the left when  $\alpha$  increases.

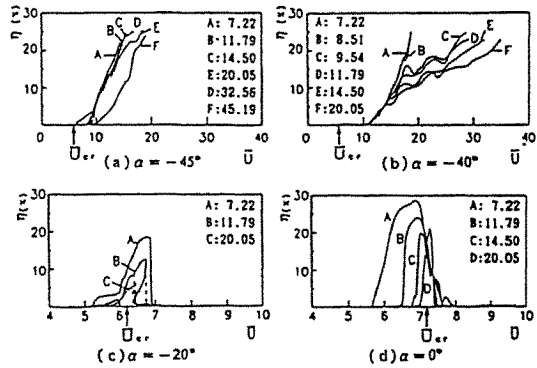


Fig. 4. The response aeroelastic characteristics of transverse vibrations of cross-shaped section

## 4. The Characteristics of Structural T-shaped Section

### 4.1 Aerostatic characteristics

Figure 5 shows the static characteristics of T-shape-section structure in the angle range of

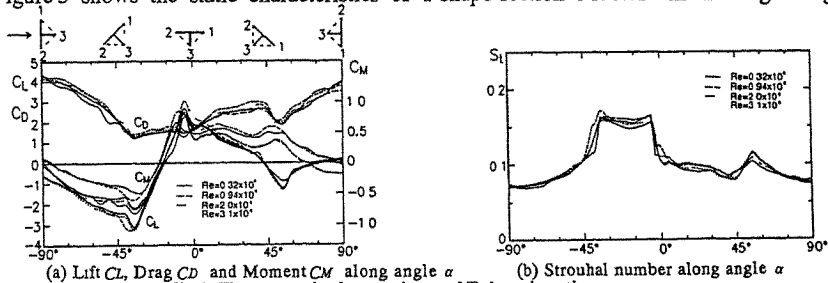


Fig. 5. The aerostatic characteristics of T-shaped section

$-90^\circ \sim 90^\circ$ . Referring to the profiles in the top of figure 5(a) showing the position of structure towards flow, the flow separates from point 1 and point 2 in the angle range of  $\alpha = -90^\circ \sim -35^\circ$ , and the shear layer shedding from point 2 reattaches on the upstream surface of point 3 and then separates from point 3 downstream if  $\alpha$  is in the range of  $-35^\circ \sim -5^\circ$ . For the angle range  $\alpha = -5^\circ \sim 55^\circ$ , the flow separates from only point 2 and point 3, and for  $\alpha > 55^\circ$  the shear layer shedding from point 3 reattaches on the upstream surface of point 1 and then separates from point 1 downstream. This frequent change of flow patterns thus results in the sharp variation of  $C_D$  and  $C_L$ . For lift force  $C_L$  as in figure 5(a),  $\partial C_L / \partial \alpha < 0$  keeps in the angle ranges of  $\alpha = -90^\circ \sim -35^\circ$  and  $\alpha = -5^\circ \sim 55^\circ$  and at the same time Strouhal number considerably changes in such ranges. Here also, the curves of different Reynolds numbers as given are almost the same.

#### 4.2 Aeroelastic characteristics of transverse vibration

Figure 6 shows the transverse vibration characteristics of T-shape structure at attack angles of (a)  $\alpha = -75^\circ$ , (b)  $\alpha = 0^\circ$ , (c)  $\alpha = 30^\circ$  and (d)  $\alpha = 45^\circ$ . For  $\alpha = -75^\circ$  as in figure 6(a), the vortex-induced vibrations of large amplitude occur around the critical wind velocity  $\bar{U}_{cr} = 14$ , and it is expected that the amplitude of vibration will increase gradually with  $\bar{U}$  when  $\bar{U} > 50$  and galloping vibration will happen finally at upper wind velocities. For  $\alpha = 0^\circ$  as in figure 6(b), there is no vortex-induced vibration observed around the critical wind velocity  $\bar{U}_{cr}$  but occurs transverse galloping vibration at velocity  $\bar{U} = 20$  whose amplitude ( $\eta$ ) tends to decrease somewhat at the velocity of  $\bar{U} = 33$  to resonate with the twisting vibration happening simultaneously. For  $\alpha = 30^\circ$  and  $\alpha = 45^\circ$  as in figure 6(c) and (d), the vortex-induced vibrations start to occur at velocity  $\bar{U}_{cr}$  and then become the galloping vibration. Considering the curve C of  $\alpha = 30^\circ$  and  $\alpha = 45^\circ$  as an example, the vortex-induced vibrations occurring at  $\bar{U}_{cr}$  gradually change into galloping vibrations as velocity increases.

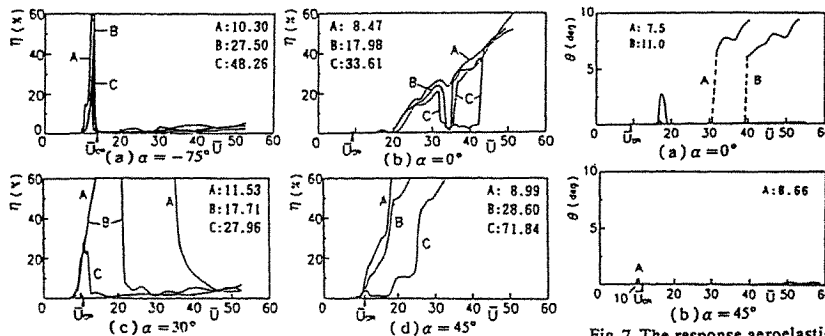


Fig. 6. The response aeroelastic characteristics of transverse vibrations of T-shaped section

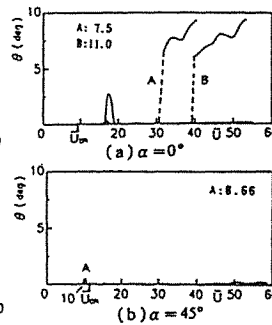


Fig. 7. The response aeroelastic characteristics of torsional vibrations of T-shaped section

#### 4.3 Aeroelastic characteristics of torsional vibration

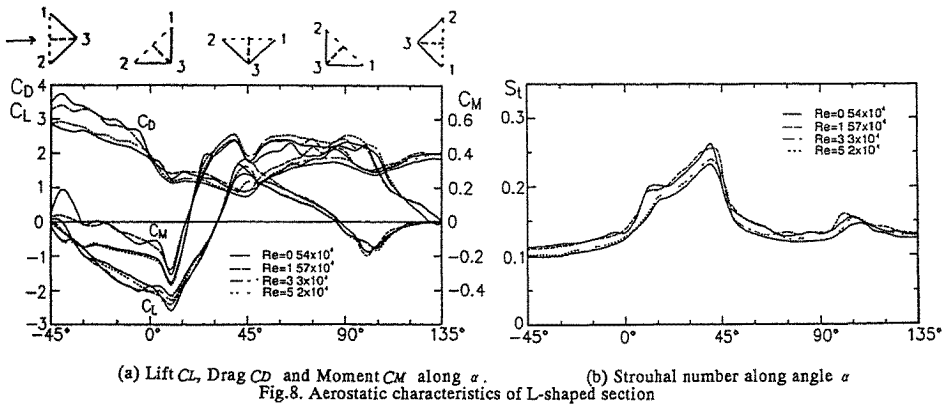
Figure 7 shows the response amplitude of torsional deformation ( $\theta$ ). When  $\alpha = 0^\circ$  as in figure 7(a), the hysteresis phenomenon peculiar to hard flutter happens, i.e., if an initial amplitude is given at the wind velocity  $\bar{U} = 30$  for curve A, torsional flutter will occur along the dotted line as in the figure. For  $\alpha = 45^\circ$  as in figure 7(b), there is no torsional vibration almost in the whole range of attack angle although around  $\bar{U} = 10$  some small vibrations do occur.

### 5. The Characteristics of Structural L-shaped section

#### 5.1 Aerostatic characteristics

Figure 8 shows the static characteristics of L-shape structures in the angle range of  $-45^\circ \sim$

135°. When  $\alpha = -45^\circ \sim 10^\circ$ , referring to the sketches in the top of figure 8 showing the position of structure towards flow, the flow separates from point 1 and point 2, although when  $\alpha = 10^\circ$  the flow separating from point 2 seems to slide along the side surface of 2-3. For  $\alpha = 10^\circ \sim 40^\circ$ , the flow from point 2 reattaches at upstream surface of point 1 and then separates from point 1 downstream and there also exists flow separating from point 3. As for the flow pattern in the range of  $\alpha = 45^\circ \sim 100^\circ$ , the flow separates from point 2 and point 3, and here again when  $\alpha = 100^\circ$ , the flow shedding from point 3 slides along the side surface of 3-1 and then separates from point 1 downstream. Judging from the  $C_L$  curve, galloping vibrations should occur in the ranges of  $-40^\circ \sim 10^\circ$  and  $40^\circ \sim 100^\circ$  where  $\partial C_L / \partial \alpha < 0$  and the change of flow pattern usually results in the abruptly change of  $C_L$  curve. The static characteristic curves of L-shape section as shown in figure 8 are almost the same as those of T-shape section as shown in figure 5 if only the attack angle  $\alpha$  rotates  $-45^\circ$ , i.e., the variations of  $C_D$ ,  $C_L$ ,  $S_t$  in the range of  $\alpha_T = -90^\circ \sim 90^\circ$  for T-shape section are almost the same as that of L-shape section in the range of  $\alpha_L (= \alpha_T + 45^\circ) = -45^\circ \sim 135^\circ$  (where the footnotes  $L, T$  represent L-shape, T-shape sections respectively). Comparing figure 5 and figure 8 which show the flow patterns corresponding to the sketches on the top of each figure, it can be seen that the black-line-shape section has the same flow pattern around it as the dash-line-shape section and so is the case for  $C_D$ ,  $C_L$  and  $S_t$ , i.e., the variations of flow pattern and fluid force are almost identical only if the outlines of structural sections are the same.



### 5.2 Aeroelastic characteristics of transverse vibration

Figure 9 shows the response vibration amplitude of L-shape structure at the angles of (a)  $\alpha = -45^\circ$ , (b)  $\alpha = -15^\circ$ , (c)  $\alpha = 45^\circ$  and (d)  $\alpha = 75^\circ$ . For the cases of (a)  $\alpha = -45^\circ$  and (b)  $\alpha = -15^\circ$ , vortex-induced vibrations occur around the critical wind velocity  $\bar{U}_{cr}$  and the amplitude increases with velocity, which agrees well with the experiment of Modi and Slater[1]. For  $\alpha = 0^\circ$  which is in the range of  $\partial C_L / \partial \alpha < 0$  as shown in figure 8, vortex-induced vibrations with small amplitudes occur around  $\bar{U}_{cr}$  and galloping vibrations happen around  $\bar{U} = 10$ . Considering (c)  $\alpha = 45^\circ$  alike, galloping vibrations occur from around  $\bar{U} = 16$  for curve A, and the hysteresis phenomenon emerges again for curve B. For (d)  $\alpha = 75^\circ$ , around the critical wind velocity there emerge large amplitude vibrations which amplitude declines sharply and then increases gradually as velocity develops, which displays serious nonlinear characteristics.

### 5.3 Aeroelastic characteristics of torsional vibration

Figure 10 gives the results of the response torsional vibrations of L-shape section, which

shows that vortex-induced vibrations occur around  $\bar{U}_{cr}$  when  $\alpha = -30^\circ$  as in figure 10(a) and quite complicated hard flutters happen at  $\alpha = 5^\circ$  as in figure 10(b). Here the same hysteresis phenomenon as that of figure 7 happens at  $\bar{U} = 10$  for curve A and this phenomenon becomes more complicated as Scruton number increases.

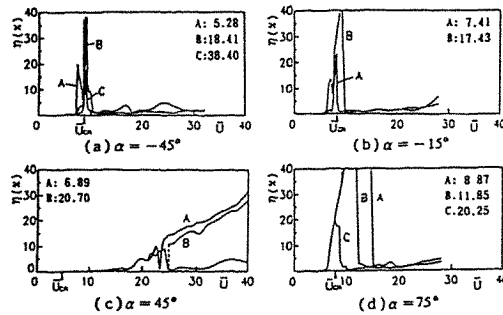


Fig.9. The response aeroelastic characteristics of transverse vibrations of L-shaped section

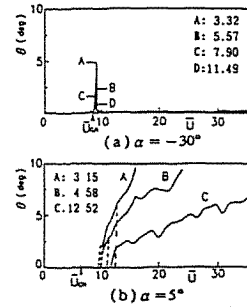


Fig.10. The response aeroelastic characteristics of torsional vibrations of L-shaped section

#### 5.4 Influence of the angles of attack

The static characteristics of L-shape structure in figure 8 is almost identical to that of T-shape structure as in figure 5 when we let  $\alpha_L = \alpha_T + 45^\circ$  (where the footnotes  $L, T$  represent L-shape, T-shape structures respectively). In almost the same way for transverse vibration, the  $\eta - \bar{U}$  curves of L-shape structure in figure 9(a)  $\alpha_L = -45^\circ$ , (b)  $\alpha_L = -15^\circ$ , (c)  $\alpha_L = 45^\circ$  and (d)  $\alpha_L = 75^\circ$  are almost identical to the curves of T-shape structure in figure 6 of (a)  $\alpha_T = -75^\circ$ , (b)  $\alpha_T = 0^\circ$  and (c)  $\alpha_T = 30^\circ$ , respectively, and the equation  $\alpha_L = \alpha_T + 45^\circ$  which displays the relation of static characteristics between L-shape and T-shape sections also can be applicable to the response vibration characteristics between L-shape and T-shape structures.

## 6. Conclusion

The variations of lift, drag and Strouhal number of structures with L-shape, T-shape and cross-shape sections against the angle  $\alpha$  of attack have been measured, and some researches have been made on the aeroelastic characteristics of each structure by changing the angle  $\alpha$  of attack and Scruton number. It has been proved that the angle  $\alpha$  has great influence on the static and dynamic characteristics of structures. In particular, when T-shape versus L-shape and cross-shape versus square-shape structures are put towards upstream flow in a relationship position where the relationship is  $\alpha_L = \alpha_T + 45^\circ$  for T-shape and L-shape structures, the static characteristics of the couple structures along the angle  $\alpha$  of attack are found to be almost the same. Furthermore, the response vibration characteristics of the couples are also identical to one another when the stated angle relationship does be kept.

### References:

- (1). Modi, V.J. and Slater, J. E., Unsteady aerodynamic and vortex induced aeroelastic instability of a structural angle section, J.Wind Eng. and Indu. Aerodyn., Vol.11(1983), pp. 321-334.
- (2). Nakamura, Y., Mizota, T., Yoshimura, T., Aerodynamic Forces and Moment Characteristics of Rectangular and H-shaped Cylinders (in Japanese), Bulletin of the Research Institute for Applied Mechanics, Kyushu University, Japan, Vol.40(1973), pp. 245-255.
- (3). Nakamura, Y. and Mizota, T., Unsteady lifts and wakes of oscillating rectangular prism, J. Eng. Mech. Div. ASCE Vol.101, No. EM6(1957), pp. 855-871.

## Effects of the incident flow on the motion downstream a backstep

A Aroussi

Department of Mechanical Engineering, University of Nottingham, Nottingham, U.K

**Abstract:** The size of the reattachment length downstream a step is examined as a function of the incident boundary layer. The effects investigated are the degree of turbulence and the shape of the velocity profile at the inlet. It is found that the reattachment length decreases with increasing turbulence and that the steeper the inlet velocity profile specified the greater the reattachment length. The study is computational validated with non-intrusive measurements.

### 1. Introduction

The majority of practical flows are of the bluff body type; this is where the flow separates from the surface of an object due to a sharp edge. In many cases, this separated flow reattaches to the body further downstream, and these types of flow are encountered in numerous engineering devices such as turbomachines, heat exchangers and chemical process equipments. The simplest case where this occurs is the flow behind a rearward facing step; which is often used to test numerical techniques and mathematical models of turbulence. The presence of fixed geometry with just two free boundaries and the certain presence of vortices makes an efficient environment for computational work and the testing of numerical techniques. A review of such studies is given by Aroussi & Senior (1992). These reviews have shown the unreliability and the limited applicability of some of the experimental work and most of the analytical methods. However, three numerical studies are found to be particularly useful in that they review the influence of turbulence on the reattachment length. The studies by Baker & Moss (1978) and Isomato & Honami (1989) are used as a comparison with the present results.

The flow pattern behind a typical rearward facing step is shown in Fig 1. The important features of this flow are the separation point, at the corner of the step, the recirculation zone behind the step, and the reattachment point. The turbulent intensities and shear stress reach maxima in the reattachment zone, and decay rapidly after the reattachment. The reattachment length is taken as the distance from the back of the step to the reattachment point. The structure of the fluid motion resulting from this complex interaction between the separated shear layer and the adjacent flow depends on the characteristics of the approach flows. consequently, comparisons of data on the reattachment length must take into account the characteristics of the flow approaching the step.

The reattachment point is an important property of any reattaching flow. Practically it may indicate deposition of fluid particles; particularly in two phase flows. For comparison with other work, the reattachment length gives a quantitative result which is easier to correlate than a general flow pattern.

It is how this reattachment length varies with different inlet conditions which this paper investigates experimentally, using LDA and PIV, and numerically using a model of turbulence. The inlet conditions specifically examined are the velocity, and the degree of turbulence in the approaching flow. The aim of this study is to find a relationship between inlet conditions and the reattaching length. The paper concentrates on the effect of inlet velocity profiles and inlet turbulence on the reattachment length. For the purposes of this investigation a two-dimensional step is modelled. The length of the numerical solution domain is set to 15 step heights. This is to ensure that the effects at outlet do not interfere with the flow in the region of reattachment.

### 3. Experimental programme

The measurements are conducted in an open circuit wind tunnel and in a water channel. The wind tunnel has a maximum speed  $10\text{ms}^{-1}$  and an adjustable flow profile in the working section. This is made of perspex to allow access to the laser beams of the LDA system. Similarly, the flume has an adjustable

flow to the test section, but the maximum speed is only  $2\text{ms}^{-1}$ . The water is driven by a submerged pump which provides a maximum flow rate of  $90\text{m}^3\text{h}^{-1}$ . The working section is built of 4mm glass. In both devices, the incident flow is controlled by the introduction of screens upstream of the test section. These are flow smoothing screens and slatted screens for the generation of turbulence. These are located downstream of the honeycomb flow straighteners. The model of the step is made of perspex and mounted on the floor of the flow channel. The optical anemometers used to acquire the flow properties are a two component Laser Doppler Anemometer (LDA) and a Particle Image Velocimeter (PIV).

PIV is used in conjunction with the water channel and involves the recording of multiple images of scattering particles on a single photographic negative. If the displacement of separate scattering particles images and the time between consecutive exposures can be measured, the velocity of the flow local to each such particle can be calculated.

The light source for the PIV system used is provided by an 18W, continuous wave, Argon Ion laser. This type of laser is employed because the light produced is in the blue-green region of the spectrum, and has the lowest absorption-attenuation characteristics in water. The arrangement used is such that the beam passes through a chopper in the form of a rotating disk with a transparent segment, which allows the generation of the required discrete images, and then a glass rod to produce a light sheet, 2mm thick, in the investigated flow area. The water is seeded by a powder of naturally buoyant particles.

The second anemometer in the form of a digital correlator based two component LDA system is used with the wind tunnel to obtain the longitudinal and vertical components of the mean velocity. These are obtained on a rectangular grid at intervals of 3 to 5mm, depending on the size of the step. This system uses a 15mW HeNe laser and a back-scatter arrangement mounted on a traversing mechanism.

#### 4. Computational programme

The turbulent and recirculating fluid flows generated downstream of the step by the separation of the free stream are elliptic in nature. The primary eddy is formed when the separated shear layer reattaches downstream of the step after which the flow returns to its normal boundary layer state. Between the step and the reattachment point a large vortex is maintained by the energy in the shear layer above it. As the primary vortex sweeps backwards it is forced upwards by the vertical boundary generating a recirculation zone in the bottom corner. These flow features are mathematically approximated by most one and two equation models of turbulence (Launder and Spalding 1972).

The aim is to simulate the flows measured with the optical anemometers and assess the accuracy of the solution of the  $K\epsilon$  model and evaluate the dependence of such a solution on the inlet boundary conditions. Furthermore, establish a relationship between the degree of turbulence at the inlet boundary, the shape of the inlet velocity profile and the reattachment length downstream of the step.

The  $K\epsilon$  effective viscosity model This is the simplest mathematical model of turbulence for with elliptical equations that govern the flow associated with backward facing steps. The dependent variables

$$\epsilon = \frac{C_D K^{3/2}}{l}$$

solved for are the turbulence energy  $K$  and its dissipation rate  $\epsilon$ . These quantities are related by

The  $K\epsilon$  model expresses the Reynolds shear stresses according to the Boussinesq hypothesis, that is a product of the mean velocity gradient and the turbulent viscosity  $\mu_t$

$$(-\rho \bar{u}_i \bar{u}_j) = \mu_t \left( \frac{\partial U_i}{\partial x_j} + \frac{\partial U_j}{\partial x_i} \right)$$

The turbulent viscosity is calculated from the local values of  $K$  and  $\epsilon$  :

$$\mu_t = \frac{C_\mu \rho K^2}{\epsilon}$$

In many applications the empirical constant of the  $K\epsilon$  model are varied "to tune" the predictions to fit the experimental results. However for bluff body flows, other workers found that predictions did not



improve by changing these constants (Vasilic-Melling 1977); therefore the values of these constants have not been altered in this study and are those specified by Launder and Spalding (1972).

## 5. Results and discussions

This study concentrates on the effect of increasing the amount of turbulence and varying the shape of the velocity profile in the flow approaching the step on the reattachment length downstream. Numerically, the turbulence is specified as a uniform profile at inlet, just above the back face of the step and covers a range from 1% to 90%. Experimentally, the turbulence intensity range at the inlet is 5% to 40%.

The changes in flow pattern caused by increasing the inlet turbulence are such that at low turbulence intensities the vortex is long and slender giving a long reattachment length (Fig 2), but at high turbulence level the vortex shrinks in size, resulting in the reattachment point being closer to the step. The centre of the vortex is also nearer to the back face of the step.

This is illustrated in the comparison of the predicted vertical profiles of the U-velocity at various inlet turbulence intensities (Figs 3 and 4). Each of these profiles represents a degree of turbulence at the inlet boundary. The profiles are taken at two different locations downstream of the step; namely at  $X/H=1$  and  $X/H=5$  (where  $H$  is the step height). At  $X/H=1$ , corresponding to  $H$  downstream the step, the profiles show the expected features of a recirculation zone; namely positive flow at the top and reversing flow at the bottom. The flow changes polarity at  $Y/H=0.6$ . All the profiles merge together except that at 0% turbulence which changes polarity at  $Y/H=0.8$  and has a faster positive flow and a slower negative flow; indicating the start of a larger recirculation zone than the others (Fig 3).

At  $X/H=5$ , the profiles show the same trend, but no longer merge (Fig 4). The lower the inlet turbulence the faster the positive and reversing flows. Thus indicating larger eddies at lower turbulence levels. This means that the higher the inlet turbulence, the higher the degree of mixing and the sooner the flow downstream returns to the normal wall boundary layer; that is the smaller the recirculation zone.

At values of  $Y=0$  on the floor of the domain, both sets of profiles, obtained numerically, indicate a negative velocity. This is impossible due to the no slip condition at walls; the velocity at these points should be zero. The reason for this error is poor treatment of the wall region. As explained earlier, the region close to the wall is bridged by a "wall function". The distance covered by the wall function is taken as one cell height. Although the profiles are shown to  $Y=0$ , they do in fact stop one cell height short of this level. The error in these profiles is due to the dense grid close to  $Y=0$ ; hence the wall function only bridges a small gap.

The above effect can also be seen in figures 5 and 6 which show vertical profiles of the turbulence energy taken at  $X/H=1$  and 5. Low inlet turbulence give thinner initial shear layers in comparison to higher inlet turbulence levels (Fig 5). At  $X/H=5$  these shear layers have expanded significantly to cover the area occupied by the recirculation zone. However, the shear layer is still thinner for low inlet levels of turbulence, which indicate longer reattachment lengths (Fig 6).

To validate the use of the computational results over the whole flow domain, profiles of velocity are compared with present experimental results and those reported by other researchers. For example, a comparison of the present vertical profiles of the longitudinal velocity at 10% turbulence intensity are compared with the present LDA measurements and with the hot wire results of Baker and Moss (Fig 7). The shapes and maximum values of the profiles compare well indicating that the turbulence energy is well modelled. The  $K\epsilon$  is known to underpredict behind a step by up to 20% (Kim et al 1980). Here it underpredicts at  $X/H=2$  and 4. The maximum error in the present predictions in comparison to Baker's results at  $X/H=4$  is 16%. There is a larger error between the profiles at  $X/H=2$  for low values of  $Y$  (around  $0.5H$ ). This is due to different inlet conditions.

A study of the effect of the thickness of the approach boundary layer on the reattachment length is also conducted. The approach profile obeys the power law equation  $U=U_\infty(y/\delta)^\alpha$  where the power law index ( $\alpha$ ) is varied from 0.1 to 1. The variation of the reattachment length with this parameter is shown in figure 8. An almost linear relationship is obtained, where the reattachment length increases proportionally with the power law index. This should be expected since the recirculation zone is formed by the overlapping of the faster fluid over the slower fluid underneath.

This project concentrates on determining a relationship between the reattachment length and inlet turbulence. By varying the uniform inlet turbulence profiles from 1% to 90% a relationship is obtained.

Overall, the results show that at low turbulence levels the reattachment point decreases rapidly with increasing inlet turbulence. As the turbulence increases, the reattachment length decreases more slowly in an exponential form. At 60% turbulence a steady state is reached. Even with increasing turbulence the reattachment length remains at 3.5 step height downstream of the step. The present LDA results cover the inlet turbulence range 5% to 40% only. The measurements compare extremely well to the predictions and also show an exponential decay of the reattachment length with increases in the turbulence energy. These findings are plotted against the experimental results obtained by Isomota and Honami (1989), (Fig 9). Their study examines the effect of inlet turbulence between 10% and 12% on the reattachment length. A very strong linear relationship between turbulence and the reattachment length is indicated. Increasing the turbulence by 2% moves the reattachment point upstream by two step heights. Although the present study does indicate a lower value of reattachment length at 10% turbulence, the values at 12% compare well. If the results of Isomota and Honami are interpolated to slightly high turbulence, the curves indicated by present predictions and those of Isomota would join to form a reasonably smooth curve of exponential form. This shows that the present predictions closely agree with the trend indicated by the experiments, and the exponential form of the graph is correct.

## 6. Conclusions

This study demonstrates that higher inlet turbulence results in great mixing in the flow. This causes the profiles of the variables to become uniform more quickly in high turbulence flows and the reattachment point can form further upstream. At very high turbulence the flow is saturated with mixing and an increase in the inlet turbulence has no effect on the reattachment length.

In modelling the rearward facing step some simplifications have been made. All the cases which have been considered have modelled 2-dimensional effects only. In any practical situation of flow behind a step, the step would have a finite width and it is known that cyclic three dimensional effects exist in the flow. These have been found to affect the reattachment length.

## References

- 1) Launder and Spalding, Academic Press, 1972.
- 2) Kim, C S and Chang, P K, Jnl of the Franklin Inst, 1980, pp 547-570.
- 3) Moss, W D and Baker, S, Aeronautical Quarterly, 1978, pp 151-170.
- 4) Isomoto, K and Honami, S, 1989.
- 5) Aroussi A and Senior A, 4th Int. Sym. on Turbulence, USA (1992)
- 6) Vasilic-Melling D ,Phd thesis, Imperial College, London (1977).

## NOMENCLATURE

U	Longitudinal velocity	$\rho$	Density of fluid	V	Vertical velocity
K	Turbulence kinetic energy	$U_\infty$	Free stream velocity	$\epsilon$	energy dissipation rate
$\mu_t$	turbulent viscosity	H	Step height	X	Longitudinal direction
Y	Vertical direction	$C_p$	Constant	$\delta$	layer thickness

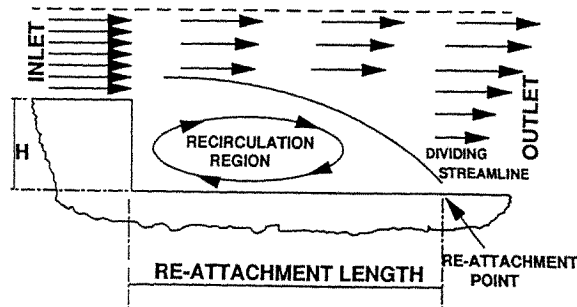
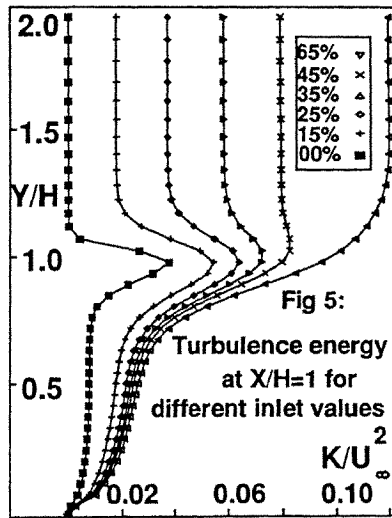
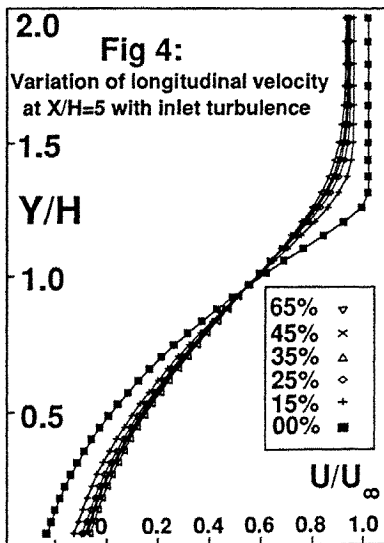
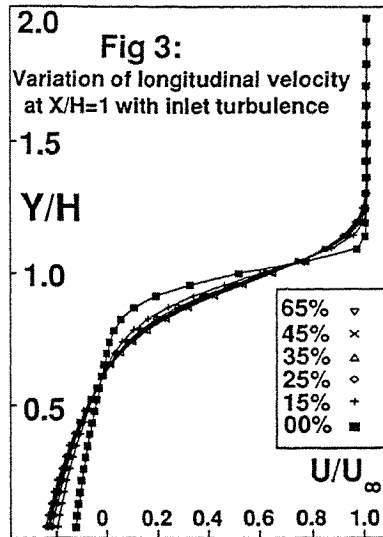
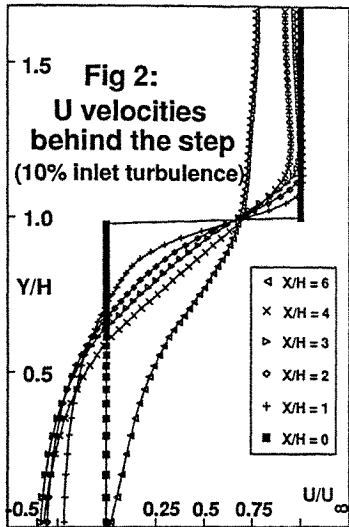
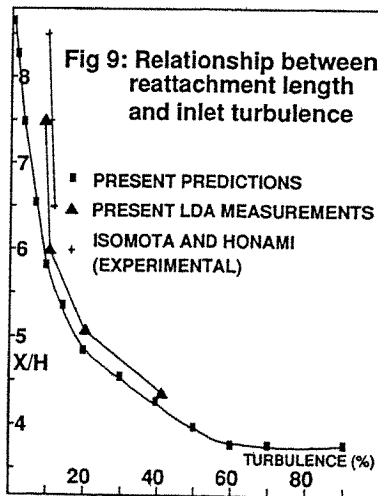
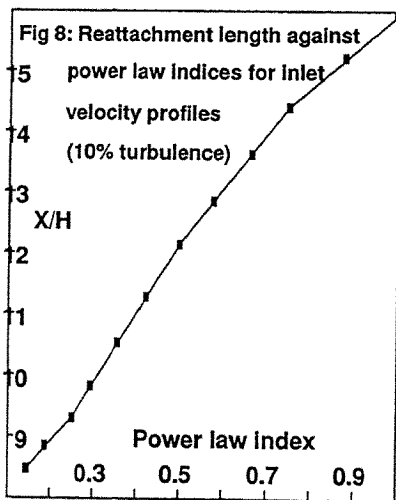
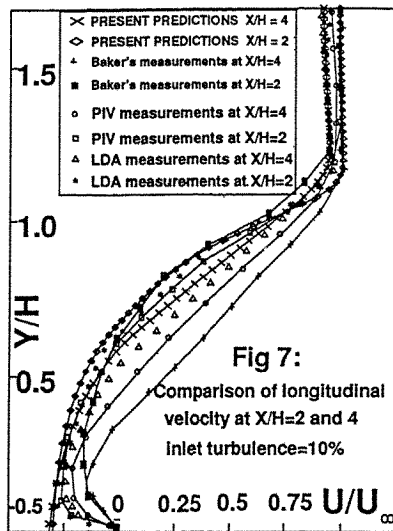
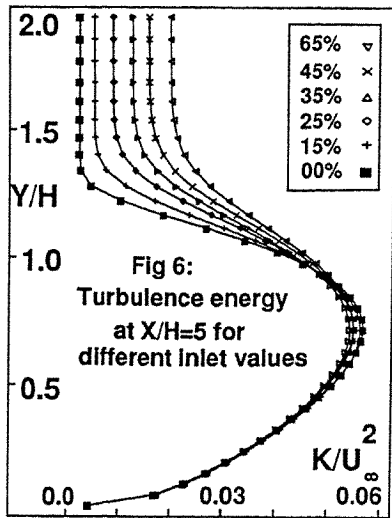


Fig 1: Flow regime behind a rearward facing step





## CONTROL OF BLUFF BODY FLOW SEPARATION

D. A. SHAH, S. H. WINOTO AND W. C. OU

Department of Mechanical and Production Engineering  
National University of Singapore  
10 Kent Ridge Crescent, Singapore 0511  
Republic of Singapore.

**Abstract:** Measurements have been made at a sub-critical Reynolds number range (20000 - 60000) on a plain and a slatted cylinder to study and document the changes in flow characteristics due to the presence of slat device. The measurements include static pressure distributions, drag forces and mean and fluctuating velocity distributions at several downstream locations in the wake. The results clearly demonstrate the ability of slat device to suppress the vortex-induced oscillations and reduce the body drag as has been reported in the literature. Importantly, results from the detailed wake measurements behind the cylinders help to understand and explain a plausible mechanism leading to the effectiveness of the slat device.

### 1. Introduction

Separation control using different techniques for the viscous fluid flow past a bluff body has been an active area of research for many years [1-3]. Broadly, a control technique can belong to either a passive or an active system. In the passive system, the geometrical configuration is manipulated to invigorate the weak boundary layer whereas an active system relies on external power such as suction, blowing or acoustic means to bring about desired changes in the flow field.

The flow control technique employed for the present study belongs to passive category originally introduced by Price [4] and subsequently modified, explored and studied by others [3,5,6]. The device considered by Price [4] was essentially a shrouded cylinder where it was clearly demonstrated that a perforated shroud can effectively suppress vortex-excited vibrations. Using a similar device, the experiments of Zdravkovich [7] conducted at sub-critical Reynolds number indicated a dramatic changes in the mean static pressure distribution around a cylinder due to application of shroud. Following these studies, a modified passive system known as slat system was proposed and effectively tested by Wong [3]. Essentially it is a self-regulating and stabilizing flow system device consisting of a number of slats which are disposed around the cylinder at a fixed distance from the cylinder surface and are placed longitudinally spanning the length of the cylinder. The set-up proposed by Wong was employed in the studies of Galbraith [5] and Kokkalis [6]. These studies include static pressure distributions, cylinder drag measurements and flow visualization experiments on plain and slatted cylinders and in general have concluded that the slat device is effective in suppressing vortex-induced oscillations and in reducing drag of the cylinder.

The aim of the present experiments using a plain and slatted cylinders is to gain more insight and sought an explanation for the effectiveness of the device. To this end, after preliminary measurements of mean static pressure distributions and drag force measurements, detailed measurements in the wake behind plain and slatted cylinders are carried out and spectral analysis of the fluctuating wake velocity signals is performed.

## 2. Experimental details

The experiments were conducted in a subsonic, open-circuit, suction type wind tunnel with a square test section of 0.45m x 0.45m. The wind tunnel was operated at different speeds to provide a range of Reynolds numbers ( $Re = U_f D/\nu = 20000 - 60000$ ;  $U_f$  is the freestream speed and  $D$  is the plain cylinder diameter). A 52.5 mm outer diameter and 400 mm long circular cylinder made of 6.5 mm thick perspex was mounted vertically in the wind tunnel supported by two rectangular end plates. The slat device configuration has an open area ratio of 40%, width of the slat is 0.087D and the gap between slats and the cylinder outer surface is 0.143D. The parameters adopted for the slat configuration are identical to those employed by Wong [3] for ease of comparison.

The mid-section of the cylinder has 30 pressure tapings of 1.2mm dia flushed to the surface along its circumference to enable the measurements of static pressure distribution. A Setra Model 239  $\pm$  0.1 psi pressure transducer in conjunction with DAS 20 A/D card was used to measure the differential pressure between the pressure tapping and the tunnel wall static pressure.

The drag force acting on the model was measured directly using a six-component load cell. It was ensured that drag measurements does not include drag of the end plates.

Mean velocity measurements in the wake region were carried out using a pitot-static tube and a hot-wire anemometer and fluctuating velocity measurements were carried out using hot-wire anemometer. A RMS meter and a spectrum analyzer were used to measure RMS velocity fluctuation and spectrum respectively. The downstream measurements were carried out up to  $X/D = 10$ .

## 3. Results and discussion

The mean static pressure measured around the circular cylinders with and without the slat device and expressed in terms of mean pressure coefficient  $C_p (= (p - p_\infty) / 0.5 \rho U_f^2)$  is presented in Figure 1. Although the results presented are only for  $Re = 40000$ , the results obtained at  $Re = 20000$  and  $60000$  are no different and the results do not show any significant Reynolds number dependence for the  $Re$  range covered in the experiments. It is evident from Figure 1 that the slat device drastically changes the pressure distribution around the cylinder. At the upstream portion, up to about  $60^\circ$ , the  $C_p$  values of the plain cylinder are higher than those of the slatted cylinder. The situation is reversed beyond  $60^\circ$ . A significant increase in pressure (from  $60^\circ$  to  $180^\circ$ ) results in reduced pressure drag in case of slatted cylinder as will be discussed further. The present trends of  $C_p$  distributions are in good agreement with those reported earlier [3,7].

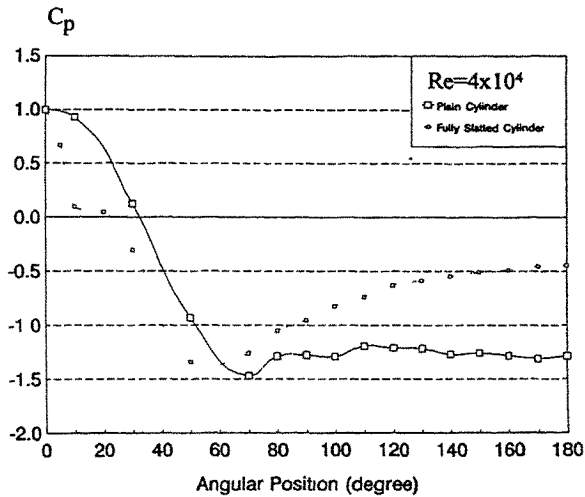


Figure 1 Mean pressure coefficient Vs circumferential angle at  $Re = 40000$ .

The results obtained from the direct drag measurements expressed in terms of drag coefficient  $C_d$  (based on plain cylinder diameter) indicate a reduction in body drag due to presence of slats by about 15% for the range of  $Re$  considered. This reduction mainly comes from the reduction in pressure drag and is consistent with results obtained from Figure 1.

Typical mean and fluctuating velocity profiles in the near wake regions of cylinders are presented in Figure 2. It is observed that there is a high loss of momentum and turbulence intensity in the near wake region and also a reduction in wake thickness behind the slatted cylinder. At  $X/D = 3.0$ , the mean velocity on the wake centreline of the slatted cylinder is about 85% smaller and the corresponding turbulence intensity is smaller by about 80%. The differences in velocity profiles and the extent of the wake decreases with increasing streamwise distance and are very small at  $X/D = 10.0$ . These quantitative observations are corroborated by the flow visualization results of Galbraith [5]. The loss in momentum for the case of slatted cylinder is seen to recover in regions outside the wake where higher velocities (about 7% higher) are recorded. A plausible explanation for these higher velocities is that high momentum fluid is ejected through the slots around the sides of the cylinder and flows into the regions outside the wake leading to increased momentum.

The spectral results were obtained at several values of  $X/D$  and  $y/D$  but the results are presented in Figure 3 for only one value of  $y/D$  and three values of  $X/D$  at  $Re = 40000$ . The spectral peak for the plain cylinder occur at about 45 Hz which is close to the calculated Strouhal frequency of 48 Hz ( $=f D / U_f = 0.216$ ).

The spectral peak for the slatted cylinder occurs at about 39 Hz. The observed reduction in Strouhal frequency is in agreement with

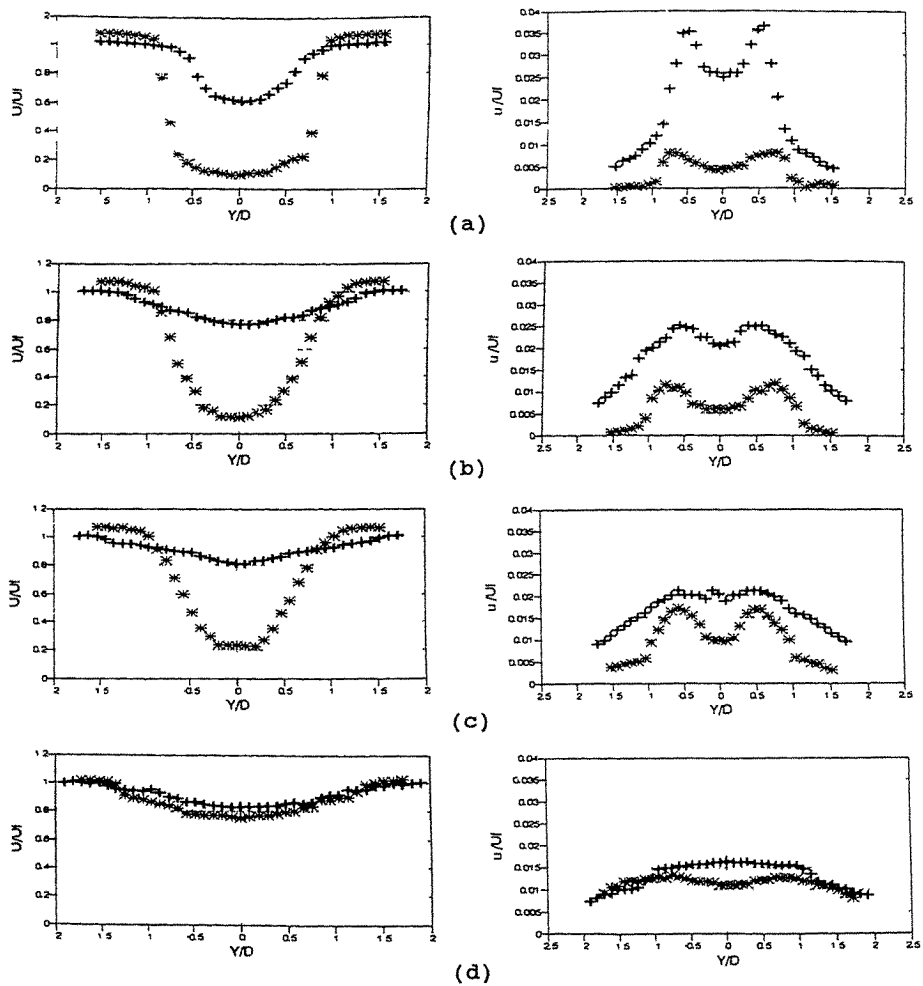


Figure 2 Mean and fluctuating velocity profiles behind plain and slatted cylinders at  $Re = 40000$ . (a)  $X/D = 1.0$ ; (b)  $X/D = 3.0$ ; (c)  $X/D = 5.0$ ; (d)  $X/D = 10.0$ . + ; Plain cylinder; \* ; Slatted cylinder.

reported results [6]. For the slatted cylinder case, spectral peak appears at  $X/D = 4.0$  at the strouhal frequency (Figure 3). This in contrast to the plain cylinder case where a peak was observed at



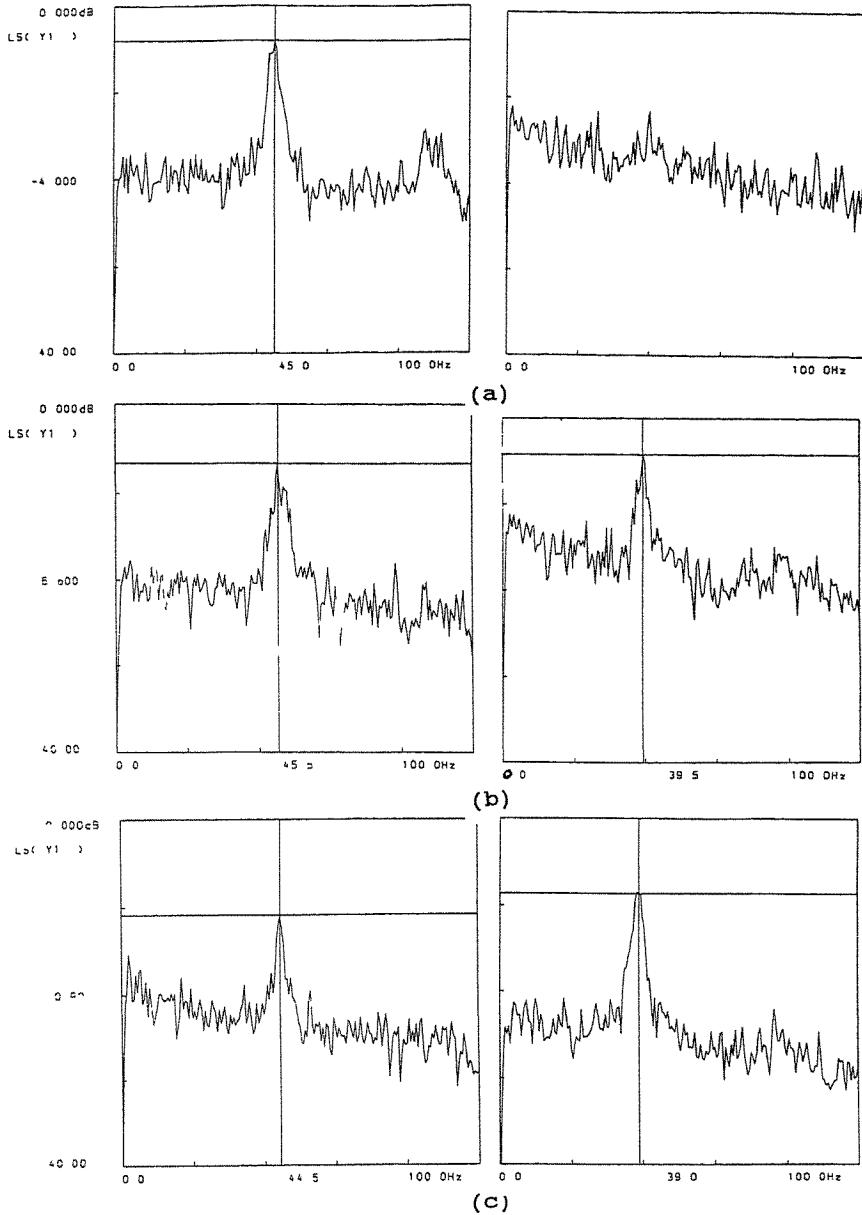


Figure 3 Power density spectra ( $Re = 40000$ ) for plain and slatted cylinders at  $y/D = 0.667$  and (a)  $X/D = 3.0$ ; (b)  $X/D = 5.0$ ; (c)  $X/D = 10.0$ .

With the employment of the slat device, the pressure distribution changes drastically and the drag coefficient of the model is observed to reduce significantly despite the likely increase in viscous friction due to the presence of slats. Vortex formation at the Strouhal frequency is found to delay due to presence of the slats and occurs at about  $3.5 D$  leading to suppression of vortex-induced oscillations. A substantial reduction in mean velocities and turbulence intensities is observed in the wake region leading to loss of momentum in this region. This loss of momentum is however seen to recover in the regions outside the wake where higher free stream velocities are registered.

**References:**

1. Kline, S.J. Trans. A.S.M.E., Basic Engr., 81 (1959) 305.
2. Dean, R. C., Handbook of Fluid Mechanics, McGraw-Hill, London, (1961) Section 11.
3. Wong, H. Y., J. Wind Eng. and Ind. Aerodyn., 4 (1979) 183.
4. Price, P. J. Engr. Mech. Div. Am. Soc. Civ. Engrs., 82 (1956) Paper 1030.
5. Galbraith, R. A., J. Wind Eng. and Ind. Aerodyn., 6 (1980) 227.
6. Kokkalis, A., J. Wind Eng. and Ind. Aerodyn. 24 (1986) 253.
7. Zdravkovich, M. M. and Volk, J. R., J. Sound Vib., 20 (1972) 451.

## Effects of aspect ratio and surface roughness on the time-averaged aerodynamic forces on cantilevered circular cylinders at high Reynolds numbers

Y. Uematsu and M. Yamada

Department of Architecture, Tohoku University, Sendai, Japan

**Abstract:** Time-averaged wind loads on cantilevered circular cylinders at high Reynolds numbers have been studied in a wind tunnel by using rough-walled models. The primary purpose of this study is to construct models of the aerodynamic coefficients for full-scale application. Measurements were made of the wind pressure distributions on the cylinder surface. Data gathered from a number of experiments concerned with this subject are also reviewed. The results indicate that the aerodynamic coefficients in the transcritical regime are functions primarily of the aspect ratio and the surface roughness of the cylinder. For the drag coefficient and the circumferential pressure distribution, quantitative descriptions of their behavior are provided as functions of these two factors.

### 1. Introduction

The flow past circular cylinders at high Reynolds numbers has been a subject of intense attention from a practical point of view in relation to designing huge engineering structures, such as tall buildings and stacks. Hence, a number of papers have been published on this subject; an extensive review of the previous experimental data was made by Basu [1, 2]. However, as he pointed out, most of the previous experiments were conducted under two-dimensional conditions, and there are only limited data on the flow past cantilevered cylinders, particularly for high Reynolds numbers. Some available data suggest that the aerodynamic forces on such cylinders at high Reynolds numbers are primarily affected by the aspect ratio and surface roughness of the cylinders.

This paper presents the results of a series of wind-tunnel experiments undertaken to elucidate the effects of these two factors as well as of the shear in the approaching flow on the time-averaged aerodynamic coefficients in the transcritical regime; the terminology and definition of the Reynolds-number regime are based on Nakamura and Tomonari [3]. Based on the results together with those of previous investigations, we provide quantitative descriptions of the drag coefficient and the circumferential pressure distribution as functions of the aspect ratio and the relative roughness.

### 2. Experimental Arrangements and Procedures

The experiments were conducted in an Eiffel-type wind tunnel with a working section of 6.5m length and 1.4 by 1.0m cross-section. Three kinds of flows were used; that is, a smooth flow with a turbulence intensity of  $I_u = 0.7\%$ , a grid-produced turbulent flow with  $I_u = 6.4\%$ , and a turbulent boundary layer with a power law exponent of  $\alpha = 0.25$  and a thickness of  $z_G = 52\text{cm}$ . The experiments conducted in the former two flows without shear are hereafter referred to as "Case I", and those in the turbulent boundary layer as "Case II".

The diameter  $D$  of the test cylinder was 11.3cm in Case I and was 6.0cm in Case II. The aspect ratio  $H/D$  was varied from unity to 4 and from unity to 5 in Cases I and II, respectively. Surface roughness was provided by gluing sand paper to the cylinder surface in order to obtain a transcritical flow in the wind tunnel. The standard roughness used is based on the equivalent sand roughness  $k_s$  (see Achenbach [4], for example). The relative roughness  $k_s/D$  of each cylinder was evaluated in the same way as Achenbach [5] did; the value of  $k_s/D$  was in a range from  $282 \times 10^{-5}$  to  $1070 \times 10^{-5}$  in Case I and from  $420 \times 10^{-5}$  to  $750 \times 10^{-5}$  in Case II.

Pressure taps were provided along a generator of the cylinder and the pressure distributions were measured by rotating the cylinder about its axis. No correction for the blockage effect on the pressure distribution was applied to the results.

In the experiments, the variation of the base pressure coefficient  $C_{pb}$  at mid-height with the Reynolds number  $Re$  was first measured and the transition of the flow regimes was identified. Then, the pressure measurements were made at some specific subcritical and transcritical Reynolds

numbers. The Reynolds number, in terms of the cylinder diameter  $D$  and the wind velocity  $U_H$  at cylinder height ( $z = H$ ), was in a range from  $3.8 \times 10^4$  to  $1.4 \times 10^5$  in Case I and from  $4.4 \times 10^4$  to  $5.8 \times 10^4$  in Case II. The local and mean drag coefficients,  $C_{Dz}$  and  $C_D$ , were obtained from the distribution of the mean pressure coefficient  $C_p$ .

### 3. Results in Smooth and in Turbulent Flow

#### 3.1. Mean drag coefficient

Figure 1 summarizes measurements [6–9] of mean drag coefficient  $C_D$  in the subcritical regime as a function of the reciprocal aspect ratio  $D/H$ . The value of  $C_D$  is minutely affected by the free-stream turbulence in this regime. The major influence on  $C_D$  is the aspect ratio  $H/D$ ; however, for  $H/D < 5$  the value of  $C_D$  becomes less sensitive to  $H/D$  also. The scatter of the data for longer cylinders, say  $H/D > 5$ , is greater than for shorter cylinders, which is probably due to the differences in the experimental conditions. In our previous work [10], it was found that our data, as well as the data of Okamoto and Yagita [6], agreed well with the results of the Wieselsberger's classic experiment (1922), not shown in this figure; he measured  $C_D$  using a finite cylinder with both ends immersed in the free-stream. Based on these results, we obtained an empirical equation as a simple function of  $H/D$ . As shown in Fig. 1, the equation is expressed as the product of the two-dimensional  $C_D$  value ( $C_{D0} = 1.2$ ) and a function  $k_1$  of  $H/D$ .

The transcritical  $C_D$  values are plotted against  $D/H$  in Fig. 2. The data on two-dimensional cylinders are quoted from Basu [1]; a representative value of  $C_D$  may be 0.52 obtained by Schewe [11] which results in  $C_D/C_{D0} = 0.43$ . Sakata et al. [12] and Sabransky and Melbourne [13] used nominally smooth cylinders. Regarding the dependence of  $C_D$  on  $H/D$ , we observe a trend similar to that observed in the subcritical regime (solid line in Fig. 2). For smooth cylinders, the value of  $C_D$  may be given by  $0.43 \times C_{D0} \times k_1(H/D)$  (dashed line in Fig. 2). On the other hand, for rough cylinders, the surface roughness effect should be incorporated into the model. As shown in Fig. 2, the value of  $C_D$  generally increases with an increase in  $k_s/D$ . Figure 3 shows the influence of  $k_s/D$  on  $C_D$ ; the data for two-dimensional cylinders are again quoted from Basu [1]. The reduction in  $C_D$  shown in the figure was calculated by taking the ratio of the mean drag coefficient and the corresponding subcritical value  $C_{D0}$  presented by the aforementioned empirical equation (Fig. 1). By introducing such a reduction to  $C_D$ , the data for a wide range of  $H/D$  collapse into a narrow region. The solid line indicates a representative equation obtained by using the least squares method. Accordingly, the value of  $C_D$  in the transcritical regime can be presented by multiplying the subcritical value ( $= C_{D0} \cdot k_1(H/D)$ ) by a function  $k_2$  of  $k_s/D$ .

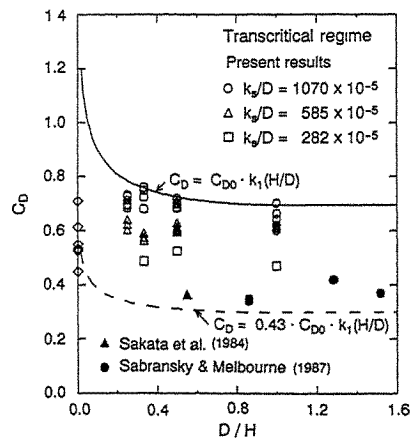
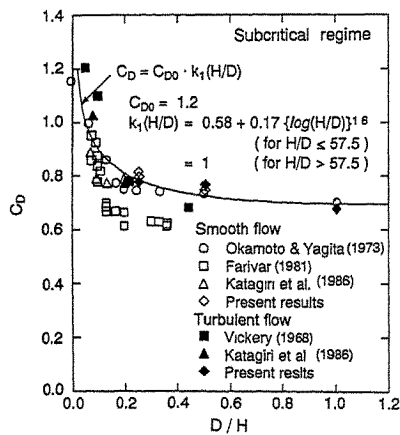


Fig. 1. Variation of  $C_D$  with  $D/H$ (subcritical regime). Fig. 2. Variation of  $C_D$  with  $D/H$ (transcritical regime).

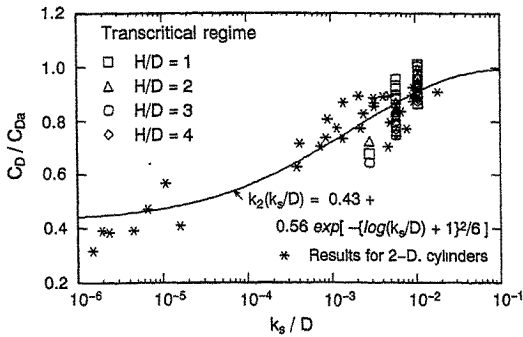


Fig. 3. Influence of  $k_s/D$  on  $C_D$  in the transcritical regime.

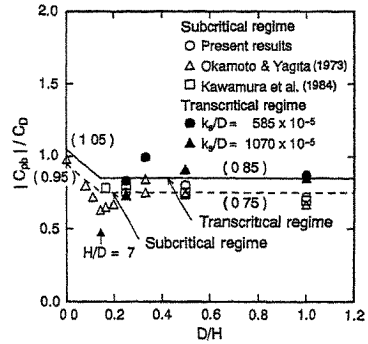


Fig. 4. Plot of  $|C_{pb}|/C_D$  vs.  $D/H$ .

### 3.2. Mean pressure coefficient

The circumferential distribution of  $C_p$  is characterized by the six typical values which are the maximum pressure coefficient  $C_{ps}$  at stagnation point ( $\theta = 0^\circ$ ), the angle  $\theta_0$  of zero crossing, the minimum pressure coefficient  $C_{pm}$  and its position  $\theta_m$  and the base pressure coefficient  $C_{pb}$  with the position  $\theta_s$  of its beginning. In a uniform flow without shear, such as the grid-produced turbulent flow, it is reasonably expected that  $C_{ps} = 1.0$  except in the regions near the top and the base. An attempt is made to obtain quantitative descriptions of the other five parameters as functions of  $H/D$  and/or  $k_s/D$ . It should be noted that the values of these parameters measured at the mid-height ( $z = H/2$ ) are used hereafter in this section, unless mentioned.

**Base pressure coefficient.** — Arranging the data obtained by many researchers [14–21] with two-dimensional cylinders, we found an approximately linear relationship between  $C_D$  and  $|C_{pb}|$ . The  $|C_{pb}|/C_D$  ratio depends somewhat on  $Re$ ; representative values of 0.95 and 1.05 were obtained for the subcritical and transcritical regimes, respectively. The present data on  $|C_{pb}|/C_D$  are plotted against  $D/H$  in Fig. 4, together with some available data [6, 22]. Although scatter is present, both in the subcritical and in the transcritical regime, the  $|C_{pb}|/C_D$  ratio seems approximately independent of  $H/D$  for smaller aspect ratios, say  $H/D < 7$ . This corresponds to the Okamoto and Yagita's [6] finding that the flow pattern around a cantilevered cylinder in the subcritical regime changes significantly at an aspect ratio in a range from 6 to 7. The solid and dashed lines in Fig. 4 represent a general trend of  $|C_{pb}|/C_D$  against  $D/H$  in the subcritical and transcritical regimes, respectively. Using these relations, we can calculate the values of  $C_{pb}$  through  $C_D$  for given  $H/D$  and  $k_s/D$  ratios.

**Minimum pressure coefficient.** — Many researchers have studied the surface roughness effects on the circumferential  $C_p$ -distribution using two-dimensional cylinders. A review on this subject was made by Güven et al. [19]. According to their results, the pressure rise  $C_{pb} - C_{pm}$  is primarily a function of  $k_s/D$ . Figure 5 summarizes measurements of  $C_{pb} - C_{pm}$  from a variety of sources. The data for the two-dimensional cylinders either with distributed roughness or with vertical ribs are quoted from Ref. [19], and those for cooling tower models from Farrell et al. [23]. For the ribbed models, the values of  $k_s/D$  are not given in the publications. Therefore, it was necessary to assume a value of  $k_s/k$  for such models, with  $k$  being the rib height. Plotting the results on the ribbed models together with those on other models, we found that the data are consistent with each other, as shown in Fig. 5, when we assumed that  $k_s/k = 2.0$ . It is of interest to note that the data for a wide range of  $H/D$  as well as for a variety of configurations collapse into a narrow region. The solid line in the figure shows a representative equation obtained by using the least squares method. Using this equation, we can calculate the value of  $C_{pm}$  because the value of  $C_{pb}$  has already been presented.

For cylinders with a free end, the flow is disturbed to an extent that the magnitude of the aerodynamic coefficients, and their axial distribution, are altered. In particular, the magnitude of  $C_{pm}$  is increased in a tip region up to  $z'/D \approx 2$ , with  $z'$  being the distance from the tip. The maximum value of  $|C_{pm}|$  was generally found at  $z'/D \approx 0.5$ . Figure 6 shows a tip-flow effect on the

axial variation of  $C_{pm}$ , where the increase  $\Delta C_{pm}$  in  $|C_{pm}|$  from the mid-height value is plotted against  $H/D$ . Because of the scarcity of measurements in the transcritical regime, the data obtained in the subcritical regime are also included [6, 7, 22]. Despite the scatter in the results, a general trend does emerge; the value of  $\Delta C_{pm}$  first increases with an increase in  $H/D$  up to  $H/D \approx 7$ , and then shows a nearly constant value of about 0.7 for  $H/D > 7$ . This implies that the tip-flow effect becomes greater as the aspect ratio increases up to about 7. The solid line in the figure shows a model of such a behavior. In constructing the model, larger values of  $\Delta C_{pm}$  were emphasized.

**Angular parameters.**  $\theta_0$ ,  $\theta_m$  and  $\theta_s$  — The values of the angular parameters,  $\theta_0$ ,  $\theta_m$  and  $\theta_s$ , in the transcritical regime are plotted against  $D/H$  in Fig. 7. Also shown are the available measurements with smooth and rough-walled two-dimensional cylinders by many researchers [3, 4, 5, 14, 19, 20, 24]. It can be seen that all of these parameters are minutely affected by  $k_s/D$ . Furthermore, in common with  $|C_{pb}|/C_D$ , they become less sensitive to  $H/D$  for  $H/D < 7$ . The three dashed lines in the figure represent the general trends for  $\theta_0$ ,  $\theta_m$  and  $\theta_s$ , respectively.

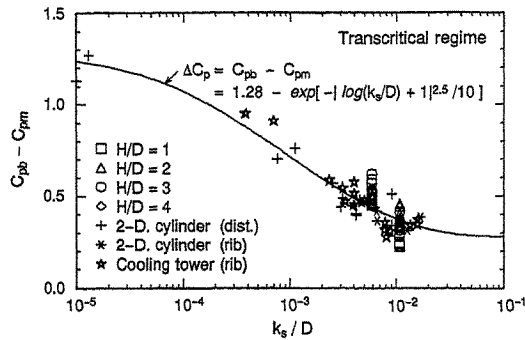


Fig. 5. Influence of  $k_s/D$  on  $C_{pb} - C_{pm}$ .

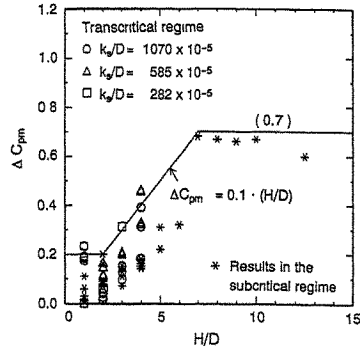


Fig. 6. Increase in  $|C_{pm}|$  in the tip region.

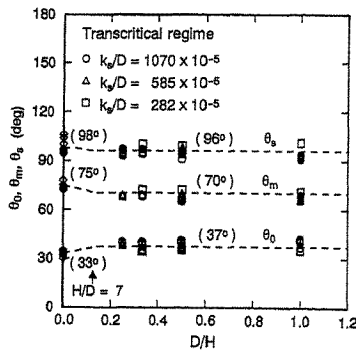
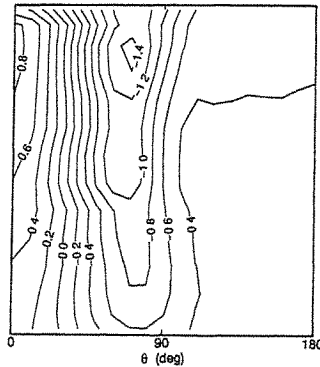


Fig. 7. Angular parameters  $\theta_0$ ,  $\theta_m$  and  $\theta_s$  vs.  $D/H$ . Fig. 8. Distribution of  $C_p$  ( $H/D = 4$ ,  $k_s/D = 560 \times 10^{-5}$ ).



#### 4. Results in the Turbulent Boundary Layer

An example of the  $C_p$  distribution is shown in Fig. 8, where  $C_p$  is defined in terms of the dynamic pressure  $q_H$  of the approaching flow at  $z = H$ . In general, the distribution along the stagnation line is similar to that of the dynamic pressure  $q_s$  in the undisturbed turbulent boundary layer, except in the regions near the top and the base where the flow is influenced by the separated tip-flow and by the horseshoe vortex, respectively. On the other hand, the pressure coefficient in the

wake region is fairly constant despite the shear in the approaching flow. The value of  $C_{pm}$  shows a slight change in the vertical direction. The angular positions of  $\theta_0$ ,  $\theta_m$  and  $\theta_s$  obtained from the circumferential  $C_p$ -distribution do not change significantly in the vertical direction. The variation of local mean drag coefficient  $C_{Dz}$  in the vertical direction obtained from the  $C_p$ -distribution is shown in Fig. 9. The experimental results show a general trend of increasing  $C_{Dz}$  with height except in a tip-region up to  $z'/D \approx 0.5$ ; the form of the variation looks similar to that of  $q_z$ .

Considering the aforementioned features of  $C_p$ - and  $C_{Dz}$ -distributions, we made the following assumptions to apply the empirical equations obtained above to a boundary layer case:

- (1) The wind pressure on the stagnation line is equal to  $q_z$ . Therefore, the maximum pressure coefficient  $C_{ps}$  is presented by  $1.0 \cdot (q_z/q_H)$ .
- (2) The base pressure coefficient  $C_{pb}$  does not change with height. The value is calculated from the relation between  $C_{pb}$  and  $C_D$  (see Fig. 4).
- (3) The pressure rise  $C_{pb} - C_{pm}$ , or the minimum pressure coefficient  $C_{pm}$  does not change with height, either. However, an increase in  $|C_{pm}|$  in the tip-region up to  $z'/D = 2$  is taken into account by the model in Fig. 6.
- (4) The values of  $\theta_0$ ,  $\theta_m$  and  $\theta_s$ , are constant regardless of height, and are presented by the model in Fig. 7.
- (5) The local drag coefficient defined in terms of the dynamic pressure  $q_z$  of the approaching flow at the corresponding height is equal to the mean drag coefficient  $C_D$  obtained in the uniform flow. Therefore,  $C_{Dz}$ , when defined in terms of  $q_H$ , is given by  $C_{Dz} = C_D \cdot (q_z/q_H)$ .

The solid lines in Fig. 9 show the predicted distributions of  $C_{Dz}$ , which are generally consistent with the experimental results. Figure 10 shows a comparison between the experimental and predicted results for the six parameters which describe the circumferential  $C_p$ -distribution; the predicted results are expressed by the solid lines, and the experimental results by circles etc. Both results agree relatively well with each other, which indicates that not only the representations obtained above but also the assumptions made here are generally satisfactory at least for  $H/D \leq 5$ .

For applying the empirical equations to full-scale structures, it is necessary to know the relationship between  $k_s$  and the representative physical height  $k$  of the surface roughness. In our previous work [24], we discussed the  $k_s/k$  ratio for several kinds of roughness. As mentioned above, it is reasonably assumed that  $k_s/k = 2.0$  for sharp-edged vertical ribs. Furthermore, the values of  $k_s/k$  are about 1.0 and 1.5 for closely-packed spheres and sand paper, respectively.

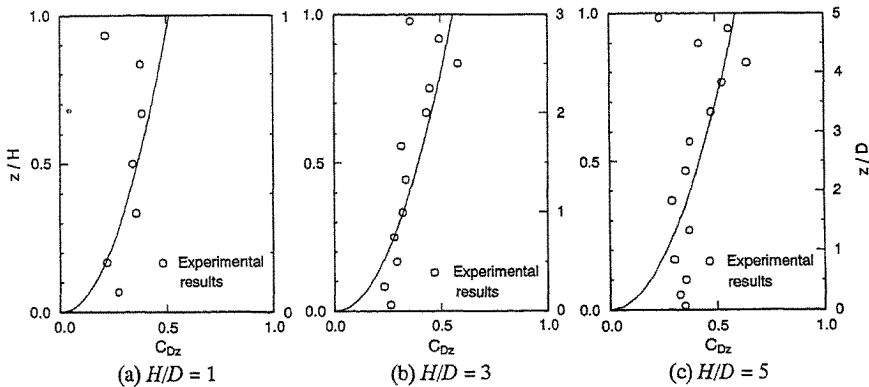


Fig. 9. Vertical distribution of  $C_{Dz}$  ( $k_s/D = 750 \times 10^{-5}$ ).

## 5. Concluding Remarks

The time-averaged aerodynamic forces on cantilevered circular cylinders in the transcritical regime are dependent primarily on the aspect ratio  $H/D$  and the relative roughness  $k_s/D$  of the cylinder. For the drag coefficient and the circumferential pressure distribution, quantitative descriptions

of their behavior as functions of  $H/D$  and  $k_s/D$  were provided based on the data obtained in the uniform flows. A discussion was made of the applications of these representative equations to a cylinder immersed in a turbulent boundary layer. By comparing the experimental data obtained in a turbulent boundary layer with the predicted results, the validity of the equations was confirmed. Using these equations, we can estimate the design wind loads on buildings and structures of circular cross-section when the values of  $H/D$  and  $k/D$  are given.

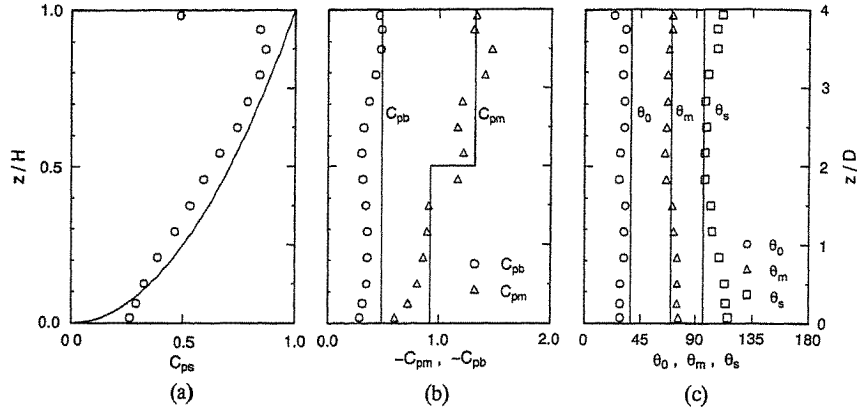


Fig. 10. Vertical distributions of  $C_{ps}$ ,  $C_{pm}$ ,  $C_{pb}$ ,  $\theta_0$ ,  $\theta_m$  and  $\theta_s$  ( $H/D = 4$ ,  $k_s/D = 560 \times 10^{-5}$ ).

#### References

1. R.I. Basu, *J. Wind Engrg. Ind. Aerodyn.*, 21 (1985) 273.
2. R.I. Basu, *J. Wind Engrg. Ind. Aerodyn.*, 24 (1986) 33.
3. Y. Nakamura and Y. Tomonari, *J. Fluid Mech.*, 123 (1982) 363.
4. E. Achenbach, *J. Fluid Mech.*, 46 (1971) 321.
5. E. Achenbach, *Int. J. Heat Mass Transfer*, 20 (1977) 359.
6. T. Okamoto and M. Yagita, *Bull. Japan Soc. Mech. Engrs.*, 16 (1973) 805.
7. Dj. Farivar, *ALAA J.*, 19 (1981) 275.
8. J. Katagiri, H. Marukawa, O. Nakamura, Y. Tamura and T. Ohkuma, *Proc. 9th Nat. Symp. on Wind Engrg.*, Tokyo, (1986) 103.
9. B.J. Vickery, *J. Engrg. Mech. Div.*, ASCE, 94 (1968) 31.
10. Y. Uematsu, M. Yamada and K. Ishii, *J. Wind Engrg. Ind. Aerodyn.*, 33 (1990) 43.
11. G. Schewe, *J. Fluid Mech.*, 133 (1983) 265.
12. I. Sakata, M. Kiya and M. Arie, *Trans. Jpn. Soc. Mech. Engrs.*, 457 (1984) 2050.
13. L.J. Sabransky and W.H. Melbourne, *J. Wind Engrg. Ind. Aerodyn.*, 26 (1987) 65.
14. A. Roshko, *J. Fluid Mech.*, 10 (1961) 345.
15. P.W. Bearman, *J. Fluid Mech.*, 37 (1969) 577.
16. D. Surry, *J. Fluid Mech.*, 52 (1972) 543.
17. J.P. Batham, *J. Fluid Mech.*, 57 (1973) 209.
18. H.H. Bruun and P.O.A.L. Davies, *J. Sound and Vibration*, 40 (1975) 535.
19. O. Güven, C. Farrell and V.C. Patel, *J. Fluid Mech.*, 98 (1980) 673.
20. M. Kiya, Y. Suzuki, M. Arie and M. Hagino, *J. Fluid Mech.*, 115 (1982) 151.
21. C. Farrell and J. Blessmann, *J. Fluid Mech.*, 136 (1983) 375.
22. T. Kawamura, M. Hiwada, T. Hibino, I. Mabuchi and M. Kumada, *Bull. Japan Soc. Mech. Engrs.*, 27 (1984) 2142.
23. C. Farrell, O. Güven and F. Maisch, *J. Engrg. Mech. Div.*, ASCE, 102 (1976) 1059.
24. W.D. James, S.W. Paris and G.N. Malcolm, *ALAA J.*, 18 (1980) 1066.
25. Y. Uematsu, M. Yamada and M. Fukushi, *Proc. 12th Nat. Symp. on Wind Engrg.*, Tokyo, (1992) 219.



## Navier-Stokes Calculation of Flow Field Around Three-Dimensional Blunt Body

*Zhu Guolin Wang Kaichun Guo yingjun*

*China Aerodynamics Research and Development Center*

**Abstract:** The Reynolds-averaged, three dimension steady Navier-Stokes equations are solved numerically by a finite-volume method and these equations are applied to study flow around three-dimensional blunt body and car-like body. The finite volume equations are formulated in the strong conservative form on a general, non-orthogonal grid system. The mixed difference scheme is used to form the difference equations. In order to improve the stability of the solution procedure, only the parts of the convection flux and diffusion terms are treated implicitly. Numerical predictions of the turbulence are obtained with the k-ε model. The resulting equations are solved by the pressure-correction algorithm.

The calculation results for blunt body and for a car-like body are presented in this report. The calculation results for the blunt body have been compared with experiment results.

### 1. Method of Computation

• **Governing Equations**

The Reynolds-averaged, three dimension steady Navier-Stokes equations can be expressed in general vector form as follows;

$$\text{div}(\rho \vec{V} \Psi - \Gamma \nabla \Psi) = q_v \quad \dots\dots\dots (1)$$

• **Grid Generation**

Using the algebraic method generates the grids of H form.

• **Control Volume and Discretization**

The governing equation is discretized by the finite volume method. Fig. 1 shows the coordinate system and a typical control volume.

• **Discretization of The Continuity Equation**

The cell face fluxes are represented by  $I_e, I_n, I_s, I_w, I_x, I_y$ . The subscripts 'e', 'n' etc. denote the finite volume boundary locations between grid points P and E, between grid points P and N, etc.

$$I_e - I_w + I_s - I_n + I_r - I_b = 0 \quad \dots\dots\dots (2)$$

where

$$I_e = F_{1e} = \rho_e \cdot \vec{V}_e \cdot \vec{S}_e^+$$

$\vec{V}_e$  is the velocity vector through 'e' cell face.

$\vec{S}_e^i$  is geometric vector and it is perpendicular to  $\eta-\zeta$  plane.

$$\vec{S}_e^i = \vec{e}_b, \vec{e}_t \times \vec{e}_n, \vec{e}_s$$

$I_w, I_n, I_s, I_t$  and  $I_b$  have the similar formulations.

- Discretization of The Momentum Equation
- The Discretization of The Convection Terms

$$\begin{aligned} \int_{(\omega)_P} \text{div}(\rho \cdot \vec{V} \cdot \Psi) d\omega &= \int_{(\omega)_P} (\rho \vec{V} \Psi) \vec{d}s \\ &= \sum_c \Psi_c (\rho \vec{V})_c \cdot \vec{S}_c = (\sum_c \Psi_c \cdot F_c)_P \end{aligned} \quad \dots\dots\dots (3)$$

$c = e, w, n, s, t, b$

- The Discretization of The Diffusion Terms

$$- \int_{(\omega)_P} \text{div}(\Gamma \nabla \text{grad} \Psi) d\omega = - \int_{(\omega)_P} \Gamma \nabla \text{grad} \Psi \vec{d}s = - (\sum_c (\Gamma \nabla \text{grad} \Psi)_c \cdot \vec{S}_c)_P \quad \dots\dots\dots (4)$$

where

$$\begin{aligned} (I_e^D)_P &= - (\Gamma \nabla \text{grad} \Psi)_e \cdot \vec{S}_e \\ &= - \left\{ \frac{(\Gamma \nabla)_e}{(dV)_e} [(\Psi_E - \Psi_P) \cdot \vec{S}_E^i \cdot \vec{S}_E^i \right. \\ &\quad \left. + (\Psi_n - \Psi_m) \cdot \vec{S}_E^i \cdot \vec{S}_E^i + (\Psi_n - \Psi_w) \right. \\ &\quad \left. \cdot \vec{S}_E^i \cdot \vec{S}_E^i \right\}_P \end{aligned}$$

$(I_w^D)_P, (I_n^D)_P, (I_s^D)_P, (I_t^D)_P, (I_b^D)_P$  have the similar formulations.

- The Discretization of The Pressure Term

$$\int_{(\omega)_P} \frac{\partial P}{\partial X_i} d\omega \approx [(P_e - P_w) \cdot \vec{S}_E^i + (P_n - P_s) \cdot \vec{S}_E^i + (P_t - P_b) \cdot \vec{S}_E^i] \cdot \vec{i}_i \quad \dots\dots\dots (5)$$

where  $\vec{i}_i$  is the unit vector,  $i=1, 2, \text{ and } 3$  represent the  $x, y, z$  direction respectively.

- The Discretization of The Second Source Term

$$\int_{(\omega)_P} \text{div}(\mu_{eff} \frac{\partial \vec{V}}{\partial x_i}) d\omega \approx (\sum_c \mu_{eff} \frac{\partial \vec{V}}{\partial x_i} \cdot \vec{S}_c)_P \quad \dots\dots\dots (6)$$

$c = e, w, n, s, t, b$

where

$$\begin{aligned} (I_e^{D''})_P &= (\mu_{eff} \frac{\partial \vec{V}_e}{\partial x_i} \cdot \vec{S}_e)_P \\ &= \frac{\mu_{eff}}{(dV)_e} \{ (\vec{V}_E - \vec{V}_P) \cdot \vec{S}_E^i \cdot \vec{S}_E^i + (\vec{V}_n - \vec{V}_m) \cdot \vec{S}_E^i \cdot \vec{S}_E^i \\ &\quad + (\vec{V}_n - \vec{V}_w) \cdot \vec{S}_E^i \cdot \vec{S}_E^i \} \cdot \vec{i}_i \end{aligned}$$

$I_w^{D''}, I_n^{D''}, I_s^{D''}, I_t^{D''}, I_b^{D''}$  have the similar formulations.

- Differencing Schemes

The mixed differencing scheme of the central difference scheme (CDS) and the upwind difference

scheme (UDS) is used in this calculation.

The convection flux is expressed as following form:

$$I_i^* = I_i^{UDS} + r(I_i^{CDS} - I_i^{UDS}) \quad \dots\dots\dots(7)$$

If  $r=0$ , the convection fluxes are calculated from UDS expressions, and if  $r=1$ , the CDS expressions are employed; for  $0 < r < 1$ , the two fluxes are blended.

For the diffusion terms using coefficients  $D_e, D_n, D_t, D_w, D_s, D_b$  represents implicit parts.

where

$$(I_i^D)_f = -D_i(\Psi_f - \Psi_f) - S_i \quad \dots\dots\dots(8)$$

$S_i$  is the source term;  $D_e, D_t, D_w, D_s, D_b$  have the similar formulations.

• Final Form of Discretized Equations

When all flux components are introduced in equation (1), an algebraic counterpart of the differential equation is obtained. values of dependent variable at cell boundary locations have to be expressed by nodal values.

$$a_p \Psi_p = \sum_{nb} a_{nb} \Psi_{nb} + S_p \quad \dots\dots\dots(9)$$

where

$$\begin{aligned} nb &= E, N, T, W, S, B \\ a_E &= D_e + \max(-F_E, 0) \\ a_W, a_N, a_S, a_T, a_B &\text{ have the similar formulations.} \\ S_p &= S^* \Psi_p + S^{**} \\ a_p &= a_E + a_W + a_S + a_N + a_T + a_B + S^{**} \end{aligned}$$

The equation (9) is solved by plane-relaxation iteration procedure.

• Pressure-Correction Equation

The pressure-correction method belongs to SIMPLE algorithm.

**2. Boundary Conditions**

No-slip boundary conditions are employed along the walls or moving walls. So this method can calculate the effects of the moving wall or ground effects.

The gradients along the streamwise direction are set to zero for all the variables at the exit boundary. At the symmetry plane, the velocity component that is perpendicular to the symmetry plane and the gradients next to the plane of symmetry are set to zero. At the inlet, a uniform velocity profile is specified together with the free stream turbulent quantities  $k$  and  $\epsilon$ . Near the wall, the logarithmic wall function is used to provide the near-wall boundary conditions for the momentum and turbulence transport equations. The effect of pressure gradients on the wall function formulation is ignored in the present study.

**3. Calculation Results**

We present three dimensional computational results for Ahmed' s body (Fig. 2) and car-like body (Fig. 3). The grids are  $28 \times 24 \times 18$  for Ahmed' s body flow field and the incoming velocity is 12m/sec. The grids are  $50 \times 30 \times 22$  for car-like body flow field and the incoming velocity is 36m/sec.

In order to proof the validity of this method, the Ahmed' s body has been calculated by present method and the comparison between present results and the experiment or computational results from Ref. 3 has been carried out. Fig. 4 shows the comparison of the experimental and computational wake velocity vector

distribution in the symmetry plane behind the Ahmed' s body. There are two recirculating flow regions. It forms two vortices, and the above vortex is bigger than the beneath vortex, the agreement with the experiment and calculational result from Ref. 3 is good although the grids for Ref. 3 are much more than that of present method (for Ref. 3, the body surface grids are  $31 \times 51 \times 97$ ). Fig. 5 presents the comparison of the cross-flow velocity distribution in the transverse plane behind Ahmed' s body. Ref. 3 shows the calculation result on left half plane and the experiment result on left half plane; this calculation gives the cross-flow velocity distribution on the right half plane and the left half plane. The agreement with experimental result and calculational result from Ref. 3 is also good. Fig. 6 shows the velocity vector distribution in the symmetry plane around car body. It can be seen that the two vortices in the wake region are different from the Ahmed' s body wake region. The reason is that the bottom surface of the after-body for the car has declination and the bottom surface for the Ahmed' s body is flat. Fig7 gives the cross-flow velocity vector distribution behind the car. It can be seen from this figure that four vortices are formed because of the declinations of the top surface and bottom surface for the car' s after-body. Fig. 8 presents the pressure distributions on the top and bottom surface in the symmetry plane. Fig. 9 shows the pressure contour in the symmetry plane. Fig. 10 shows the pressure contour in the cross plane behind car.

#### 4. Conclusions

The present study illustrated the capabilities of the present method. The program based on this method can get plenty of information about the aerodynamics. It is suitable to analyse the flow field around the blunt body and analyse the vortices for the wake regions. present report is our preliminary research work, so there are some areas which require further study.

#### References;

1. Zhu Guolin, Wang Kaichun, and Guo Yingjun, "Finite volume method for solving three-dimensional Navier-Stokes Equations," CARDG report, 1991. (No publication).
2. Zhu Guolin, M. kronast, "The Calculation of Ground Effect on a Car Flow Field Using Two Dimensional Navier-Stokes Equation," ACTA AERODYNAMICA SINICA 1/1993.
3. Taeyoung Han, "A Navier-Stokes Analysis of Three-Dimensional Turbulent Flows around a Bluff Body in Ground Proximity," ALAA/ASME/SIAM/APS, First National Fluid Dynamics Congress July 25-28, 1988.
4. S. Parameswaran and Richard L. Sun, "Numerical Aerodynamic Simulation of Turbulent Flows Around a Car-Like Body Using the Non Staggered Grid System," AIAA paper 89-1984, 1989.
5. Patankar, S,V, "Numerical Heat Transfer and Fluid Flow," MCGraw-Hill, New York, 1980.

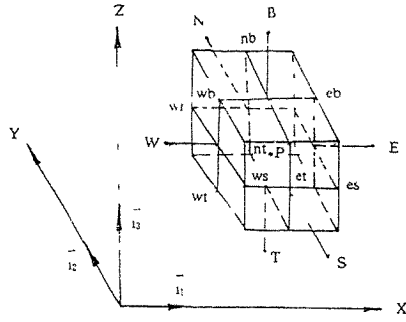


Fig. 1 coordinate system and typical control volume

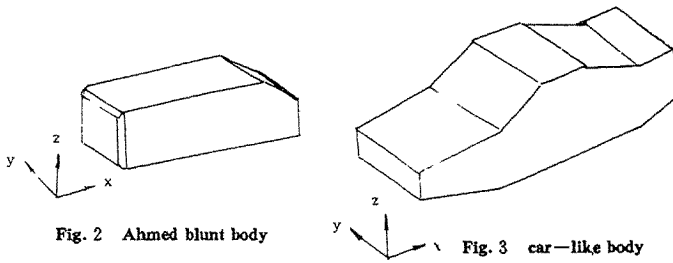
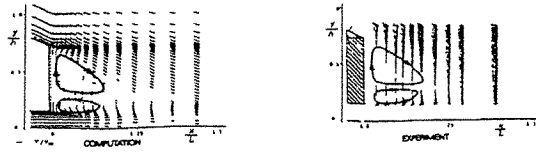
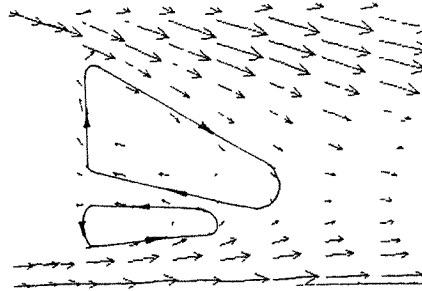


Fig. 2 Ahmed blunt body

Fig. 3 car-like body

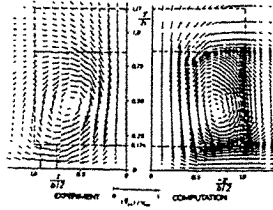


a. experimental and computational result from Ref. 3

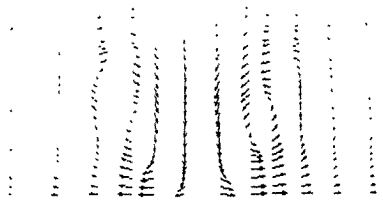


b. computational result from present method

Fig. 4 comparison of the experimental and computational wake velocity vector distribution in the symmetry plane behind Ahmed's body.



a. experimental and computational result from Ref. 3



b. computational result from present method

Fig. 5 comparison of cross flow velocity distribution in the transverse plane

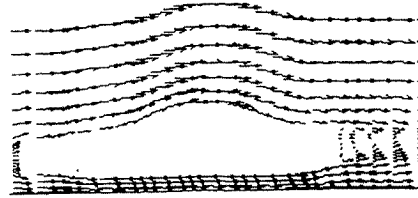


Fig. 6 computational result of velocity vector distribution in the symmetry plane

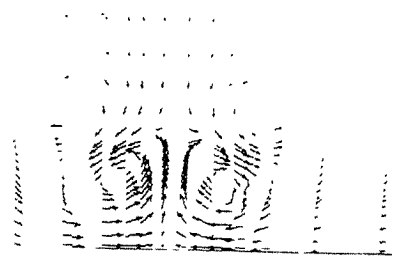


Fig. 7 computational result of cross flow velocity distribution in the transverse plane.

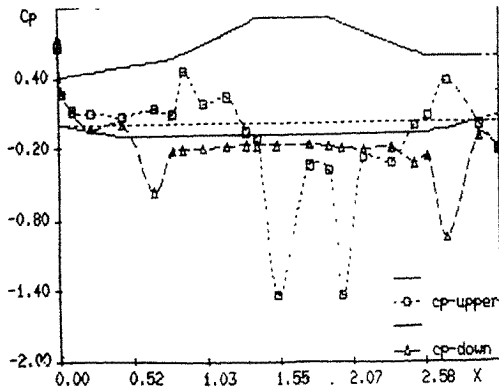


Fig. 8 computational pressure distribution on the car surface.

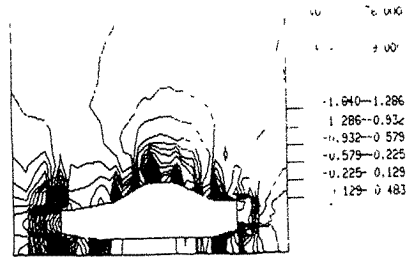


Fig. 9 computational pressure contour in the symmetry plane around car.

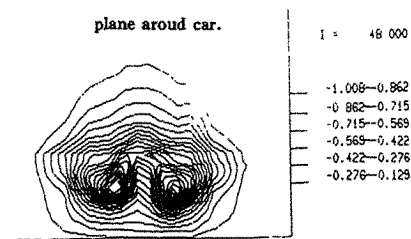


Fig. 10 computational pressure contour in the transverse plane behind car.

## Separation Characteristics of Flows Over Blunt Structure in Shear Flows

X. Y. Zhu <sup>†</sup>, X. T. Yu <sup>†</sup>, Z. C. Shi <sup>\*\*\*</sup>, E. J. Cui <sup>\*\*</sup>

<sup>†</sup> Beijing Institute of Aerodynamics

<sup>\*\*</sup> Beijing Institute of Aerodynamics, Head of the Research Group

<sup>\*\*\*</sup> Dept. of Bridge Eng., Tongji University

**Abstract:** The study is only a part of a series of research on flow separation characteristics of cylinder and square prism in an atmospheric boundary layer wind tunnel, focusing on flow around these models, their vortex shedding characteristics and the effect of turbulence in shear flows are also investigated. Pressure scanning valve and hot-wire anemometer have been used to measure the fluctuation velocity distributions at different positions downstream of the models and surface pressure of the cylinder.

Through the analysis of power spectrum density at wakes, the law of shedding frequency change with incident flow turbulence is obtained. The results clearly have revealed the separation characteristics of flows around blunt structure in uniform and shear flows together with the difference in these cases.

### 1. Introduction

Flow over blunt bodies and the vortex shedding in wakes may induce longitudinal and lateral aerodynamic loads acting on the bodies. Sometimes the structure may be destroyed by the flow induced vibrations.

For the flow over cylinder in shear flow, quite a few people have researched on it and have revealed some main characteristics of vortex shedding under this condition <sup>[1]</sup>. In this paper, the measurement methods of surface pressure and wake velocity field traversing have been performed to further study the detailed flow structure, and carry out a series of experimental research, focusing on the flow over square prism model.

The pressure on model surface were measured with pressure scanning valve, the vortex shedding frequency is measured by using hot-wire anemometer and "Conditional Sampling Techniques", the power spectrum density of velocity fluctuation in the wake was analysed. The measured results clearly reveal the law of vortex shedding occurrence and the characteristics of flow separation, and also reveal the difference between the flow fields of a shear flow and a uniform flow over blunt bodies.

### 2. Testing model and Testing Wind Tunnel

Two testing models are used in the experiments: one is a square prism, with section area  $100 \times 100 \text{mm}^2$ ,  $L/B=1/4$ ; another is a cylinder,  $d=100 \text{mm}$ ,  $L/B=14.7$ . The setup of models in wind tunnel is shown in Figure 1. The square prism model is used only for wake measurement, and the cylinder model can be used either for pressure measurement or wake measurement.

The testing wind tunnel is a low-speed wind tunnel in Tongji University (Shanghai) for building and bridge research. This wind tunnel is closed-jet, blow-down type, the test section is  $1.2 \text{m} \times 1.2 \text{m} \times 18 \text{m}$ , the maximum wind speed can reach up to  $32.5 \text{m/s}$ , the flow turbulence level is  $\epsilon=0.5\%$ . The power of motor driving the fan is  $55 \text{Kw}$  <sup>[2]</sup>.

As the wind tunnel test section is as long as  $18 \text{m}$ , it can be used to simulate shear flow characteristics of the atmospheric boundary layer. In our test, two kinds of atmospheric boundary layer simulation technologies are used: one is grill with two towers (Figure 2); the other is roughness elements with two towers (Figure 3).

For pressure measurement, SCANSO pressure scanning valve is used to gather data, the scanning speed is 48 points / second. For fluctuation velocity field of wake flow, TFA100 hot-wire anemometer is used to gather data and to analyse the power spectrum density.

### 3. Test method

First, test on the two kinds of models is made in uniform field. In the test, the incident flow velocity is  $V_\infty=10m/s$ ,  $Re_\infty=0.7\times 10^5$ . These test results are compared to that obtained shear flow field.

Secondly, the test is made in shear flow field of high turbulence induced by grill with two towers. The steepness parameter used in test analysis is defined by

$$\bar{\beta} = \frac{D}{Vr} \frac{dV}{dz}$$

Where  $D$ ,  $Vr$  and  $\frac{dV}{dz}$  respectively is the cylinder diameter or characteristic transverse diameter, reference velocity in the mid-height of cylinder, and its velocity gradient in the position.

In this tests, for the incident flow,  $\bar{\beta}=0.125$ , averaged turbulence  $\epsilon_{cp}=14.8\%$ ,  $V_\infty=10m/s$ ,  $Re_\infty=0.7\times 10^5$ .

Finally, the test is made in shear flow field of lower turbulence induced by the roughness elements with two towers. For the shear flow field, in the position about half height of the cylinder,  $\bar{\beta}\leq 0.05$ ,  $\epsilon_{cp}=1.5\%$ ,  $V_\infty=10m/s$ ,  $Re_\infty=0.7\times 10^5$ .

In both uniform field and shear flow field, fluctuation velocity distribution in wake flow has been measured at 7 cross sections of the square prism model, fluctuation distribution in wake flow at 5 cross sections and pressure distribution at 10 cross sections of cylinder have been measured.

### 4. Test results and analysis

#### 4.1 For uniform flow field

The pressure distribution curve in Figure 4a clearly shows that the airflow separation and vortex shedding occurred in the position  $60^\circ\sim 70^\circ$  from the stagnation point, which is in line with the vortex shedding phenomenon shown by power spectrum curve of the cylinder. Figure 4a also shows obvious end-effect in the region  $h\geq 2D$  away from the end.

Figure 5 gives the power spectrum curves of cylinder and square prism in the uniform flow field. For the cylinder, the single-peak of vortex shedding frequency is wide, the Strouhal Number  $S_r\approx 0.20$  (Figure 5a). For the square prism, the wake traversing measurement shows single-peak near the center-line of the model, and double-peaks at  $y=30mm$  away from center line, which is caused by the vortex shedding simultaneously by the leading and trailing edges. With the outside movement of the hot-wire away from the center-line, the double-peaks change into single-peak, showing the disappearance of effect separation at trailing edges (Figure 5b, 5c, 5d, 5e). For the square prism,  $S_r\approx 0.1$ .

#### 4.2 For shear flow field of high turbulence

The shear flow field induced by the grill with two towers is the flow with high turbulence ( $\bar{\beta}=0.125$ ,  $\epsilon_{cp}=14.8\%$ ). In this flow field, the vortex shedding from cylinder and square prism is constrained, the power spectrum curve has flat form similar to typical turbulent fluctuation [3], there is no peak, which shows that no remarkable separation and vortex shedding occur.

Figure 6a gives the power spectrum curves for the cylinder, while Figure 6b gives out that for the square prism. They reveal that the wake flow in shear flow of high turbulence is complex and multi-vortex structure.

For the cylinder, the pressure distribution curve shows no flow separation along the body surface and disappearance of end effect, which is different obviously from the result of uniform flow field (Figure 4b).

#### 4.3 For shear flow of lower turbulence

The shear flow field induced by roughness elements with two tower is of lower turbulence. In the position near  $z=\frac{1}{2}H$  ( $H$  is height of prism),  $\bar{\beta}\leq 0.05$ ,  $\epsilon_{cp}\leq 1.5\%$ . In this flow field, the vortex shedding



over the cylinder and the square prism reoccurs (Figures 7a and 7b). The cylinder is of cellular structure, and  $S_t$  in each cell is about constant [4] (Figure 8), which is in line with the test results by Kiya, et al [5]. That is, at  $\bar{\beta} < 0.1$ , the shear flow has no obvious influence on  $S_t$ .

Figure 7b shows that the vortex shedding over the square prism has peak frequency, but the spectrum peak is wide, which reflects the characteristics of multi-vortices and complex fluctuation composition. In this figure, no obvious cellular structure has been observed. The transverse measured results of wake flow over the square prism shows that the double-peaks have disappeared and all is single peak in y direction.

## 5. Conclusions

With all the above test results and analysis, the conclusions are drawn as follows:

(1) In shear flow field of lower turbulence ( $\epsilon_{sp} \leq 1.5\%$ ,  $\bar{\beta} \leq 0.05\%$ ), cellular structure of vortex shedding over cylinder could still be observed. In each cell,  $S_t$  is about constant. For square prism under the same condition, no obvious phenomenon of cellular could be observed and furthermore, the phenomenon of cellular is disappears at high turbulence.

(2) In shear flow field of high turbulence, ( $\epsilon_{sp} = 14.8\%$ ,  $\bar{\beta} = 0.1$ ,  $Re_\infty \approx 10^5$ ), the peak value in power spectrum curve corresponding to the become more flat turbulent fluctuation. This is in conformity with the opinion in Reference [3], which reflects that the turbulence has obvious constraint on the phenomenon of vortex shedding.

(3) For flow over square prism, the corner of the leading edge is the fixed flow separation point, and there also exists separation and vortex shedding in the trailing edge, so the wake flow and vortex structure are more complex. In uniform flow field, double peaks occur in the power spectrum curve on square prism. In shear flow field of lower turbulence, there occurs obvious single peak, but not prominent compared with the phenomenon on cylinder. This is because that the increase of the turbulence of incident flow constraints the vortex shedding in the trailing edge.

(4) End effect of cylinder. In uniform flow field, the obvious region of end influence can be observed, its influence region is obvious in 2D region away from the end. In shear flow field, no obvious region of end influence exists.

This study is a part of the research on aerodynamic characteristic of blunt buildings in atmospheric boundary layer shear flow field. The research plans to carry out more test for flow over blunt structure in shear flow field of different  $\bar{\beta}$  value, and to make flow visualization of these flow in water tunnel, to establish theoretical calculation model and give out the engineering calculation method determining wind loading and wind vibration on buildings in atmospheric boundary layer shear flow.

This study has received support by the civil engineering antidisaster laboratory of Tongji University, the authors thank you for all the colleagues in the laboratory them help.

## References

- 1 Griffin, O. M., ASME J. Fluids Eng. 107, (1985), 298-306.
- 2 Cai Guohua, Report on TJ-I Atmospheric Boundary Layer Building Wind Tunnel Flow Field Calibration. BIA (China), T. R. 8726137, 1991
- 3 Sun T. F., Cui E. J., Research on the Flow Around The Blunt Bodies and Flow Induced Vibrations, ACTA Aerodynamics Sima 1 (1985), 62-75
- 4 Kiga, M. J., Fluid Mech, 101, (1980), 721-736
- 5 Mair, M. A., SIAM J. of Appl. Math. 28, (1975), 519-540.



Figure 1 Square Model

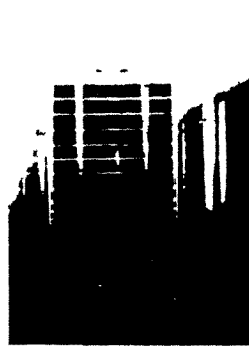


Figure 2 Grill with Two Towers

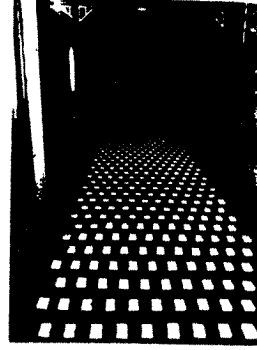


Figure 3 Roughness Elements with Two Towers

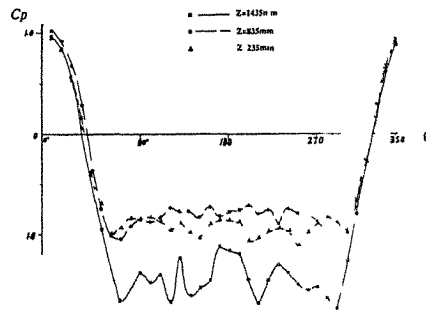


Figure 4a. Curves of Pressure Distribution on Cylinder in Uniform Flow

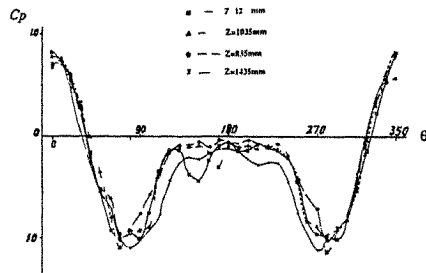


Figure 4b Pressure Distribution on Cylinder in Shear Flow ( $\beta=0.1$ ,  $\epsilon_{cp}=14.8\%$ ,  $Re_w=10^5$ )

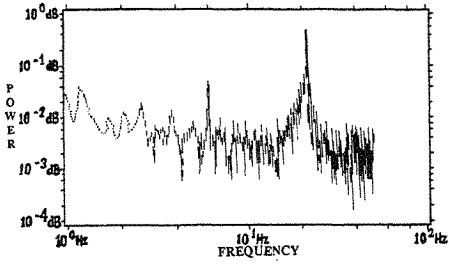


Figure 5a. Drawing of Power Spectrum on Cylinder in Uniform Flow ( $Z=735mm$ ,  $Y=90mm$ )

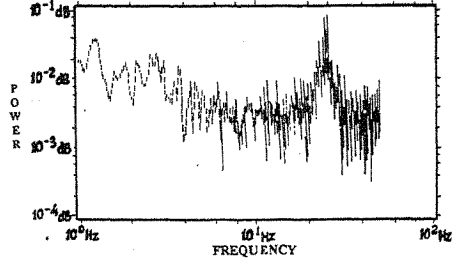


Figure 5b. Drawing of Power Spectrum on Square Prism in Uniform Flow ( $Z=600mm$ ,  $Y=0mm$ )

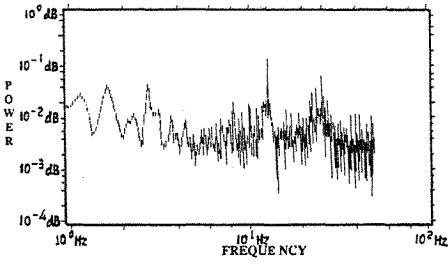


Figure 5c. Drawing of Power Spectrum on Square Prism in Uniform Flow ( $Z=600mm$ ,  $Y=30mm$ )

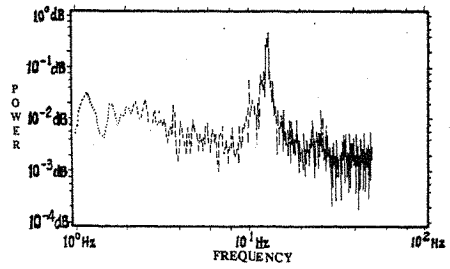


Figure 5d. Drawing of Power Spectrum on Square Prism in Uniform Flow ( $Z=600mm$ ,  $Y=90mm$ )

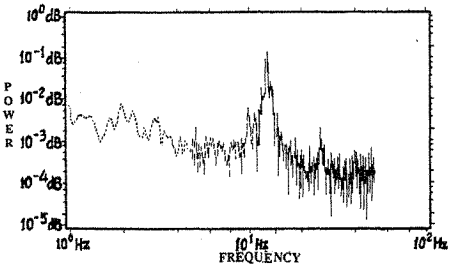


Figure 5e. Drawing of Power Spectrum on Square Prism in Uniform Flow ( $Z=600mm$ ,  $Y=150mm$ )

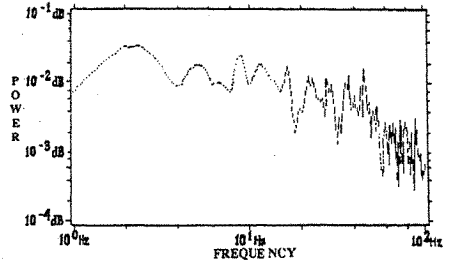


Figure 6a. Drawing of Power Spectrum on Cylinder ( $Z=780mm$ ,  $Y=30mm$ ) in Shear Flow ( $\beta=0.1$ ,  $\epsilon_{cp}=14.8\%$ )

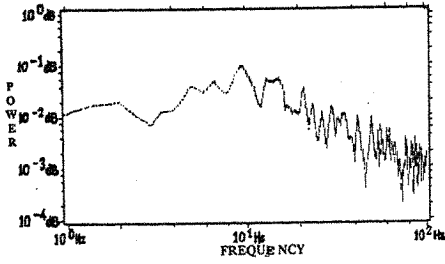


Figure 6b. Drawing of Power Spectrum on Square Prism ( $Z=850\text{mm}$ ,  $Y=120\text{mm}$ ) in Shear Flow ( $\bar{\beta} \approx 0.1$ ,  $\epsilon_{cp} = 14.8\%$ )

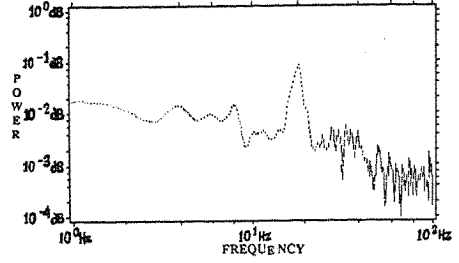


Figure 7a. Drawing of Power Spectrum on Cylinder ( $Z=780\text{mm}$ ,  $Y=90\text{mm}$ ) in Shear Flow ( $\bar{\beta} \leq 0.05$ ,  $\epsilon_{cp} \leq 1.5\%$ )

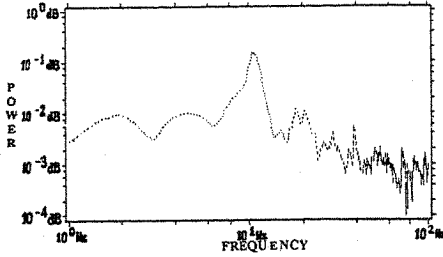


Figure 7b. Drawing Power Spectrum on Square Prism ( $Z=1280\text{mm}$ ,  $Y=120\text{mm}$ ) in Shear Flow ( $\bar{\beta} \leq 0.05$ ,  $\epsilon_{cp} \leq 1.5\%$ )

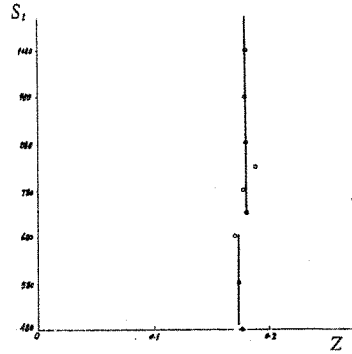


Figure 8. Variation of  $S_i$  on Cylinder With  $Z$  in Shear Flow ( $\bar{\beta} \leq 0.05$ ,  $\epsilon_{cp} \leq 1.5\%$ )

MEAN VELOCITY PROFILES IN THE WAKE OF TWO PRISMATIC  
BODIES IN TANDEM ARRANGEMENT

B.H. Lakshmana Gowda and M. Mohamed Sitheeq

Fluid Mechanics Laboratory, Department of Applied Mechanics,  
Indian Institute of Technology, Madras - 600 036, India.

**Abstract:** The mean velocity profiles in the gap between two bluff bodies in tandem arrangement and in the wake of the rear body are presented in this paper. The results are presented when the gap between the bodies is systematically varied from a low value to a large value. The reattachment point within the gap between the bodies and behind the rear body, the shear layer distortion due to the interference effects are revealed by the study.

### 1. Introduction

The understanding of the flow around prismatic bodies is of importance in building aerodynamics and environmental aerodynamics. The wind flow gets distorted due to the presence of the structure in its path and the wake created may cause considerable discomfort to the pedestrians and also influence the wind loads on other structures around. If the structure is located near an aerodrome, the movement of the aircrafts will be affected by the turbulence generated in the wake. Further, buildings usually occur in various combinations with different relative spacings. In all such cases the interference effects become important in deciding both the fluid motion and the wind loading.

There are relatively few investigations dealing with the measurement of mean and turbulence quantities in the wake of three-dimensional bluff bodies. The characteristics of the mean flow field behind a leading edge obstacle was investigated by Sforza and Mons [1]. The decay of the axial component of mean velocity and the longitudinal component of turbulence intensity in the wake of three-dimensional bluff bodies with different relative dimensions is investigated by Peterka and Cermak [2]. Castro and Robins [3] have reported some wake measurements in their study on the flow around a surface mounted cube in uniform and turbulent streams. Ogawa and Oikawa [4] have presented the results of a field investigation of the flow and diffusion around a model cube. Gowda et.al [5] have carried out the mean flow and turbulence measurements in the wake of a three-dimensional bluff body. But there appears to be hardly any information on the mean flow and the turbulence characteristics under conditions of interference between two prismatic bodies. In the present study the mean velocity profiles behind two cubical bodies ( $h/b = 1$  and  $l/b = 1$ ;  $h$  is the height,  $l$  is the length and  $b$  is the width) arranged in tandem position are presented. The gap ( $g$ ) between the bodies is varied ( $g/b = 1$  to 7) and the velocity profiles are presented in the gap between the bodies and in the wake of the rear body at each gap ratio.

### 2. Experimental Arrangement

The experiments are carried out using the wind tunnel facility shown in Fig.1. Air from a blower passes through a set of screens and a settling chamber which terminates in a nozzle conforming to DIN 1952 standards. The dimensions of the nozzle exit are 130 mm x 240 mm. The velocity at exit is very uniform, the variation both in the horizontal and vertical planes (taken at the central section of the nozzle exit) being less than 0.5 per cent. The turbulence level at exit is 0.4 per cent. A stand designed and fabricated out of mild steel angles is used to support the surface plate on which the bodies are placed. A smooth hylam sheet 12 mm in thickness with a length of 1140 mm and a width of 655 mm is used as the surface plate. Pressure tappings (1mm in

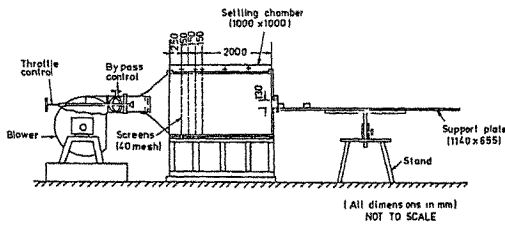


Fig 1 Experimental set-up

diameter) are provided all along the length of the plate (on the central line) with a centre to centre distance of 6 mm. There is provision for levelling the surface plate and also varying its position in the vertical direction. The plate is positioned in front of the nozzle so that its leading edge abuts with the lower edge of the nozzle as shown in Fig.1. The uniform pressure distribution on the surface plate without the bodies confirmed the proper alignment of the surface plate. Prismatic bodies with  $b$  equal to 30 mm made out of fine teak wood and finished to have smooth surface and sharp edges (to eliminate Reynolds number effect) are utilized. There is sufficient length of the surface plate behind the bodies for all relative positions (i.e.  $g/b$  ratios) investigated. A standard pitot tube with a tip diameter of 1 mm is made use of for the velocity measurements and the ambient static pressure is taken to be atmospheric. At all stations, traverses were made extending up to the ground plate. But in certain regions within the gap and behind the rear body the velocities could not be obtained with sufficient accuracy and confidence up to some height from the ground plane. This is because of the highly recirculating nature of the flow in these regions. In all such cases, that portion of the velocity profile which could be measured with sufficient accuracy only is shown. The pitot pressure is measured using micromanometer Type FC 012 (Make: Furness Controls, U.K.) with an accuracy of 0.01 mm water column. The measurement accuracy of the velocities in the present study is within 3 per cent taking into consideration the fluctuations in the mean flow close to the bodies.

All measurements are carried out at a exit velocity of 14 m/s which gives a Reynolds number (referred to the width of the body) of 30000. As bodies with sharp edges are made use of, the dependence of the results on the Reynolds number is only marginal and they can be used for analysing practical situations. The limitations of the present study are pointed out in the last section.

### 3. Results and Discussion

#### 3.1. Mean Velocity Profiles

The velocity profiles at various stations without the body and with a single body (i.e. without the interfering body) are presented in Figs.2 and 3 respectively. In these figures (and also other figures)  $U$  is the velocity at any distance  $y$  measured from the ground plane and  $U$  is the velocity in the free stream approaching the bodies. This is the same in all cases (and hardly differed from the dynamic pressure at nozzle exit) as only the region close to nozzle exit has been utilised for the measurements. Results at Figs.2 and 3 enable one to get an idea of the comparative distortion of the velocity profiles with and without interference. From Fig.3, it can be seen that the shear layer separating from the front top edge of the body reattaches behind, at a distance of about twice the width of the body. The profiles at various  $x/b$  indicate that the growth of the outer edge of this shear layer is restricted and extends from amount 0.5  $h$  above the height of the body (at  $x/b = 0$ ) to 0.75  $h$  even at large downstream distances. There is very little change in the profiles beyond  $x/b = 9$  and they have very nearly the same shape as those in Fig.2 at these large  $x/b$  values.

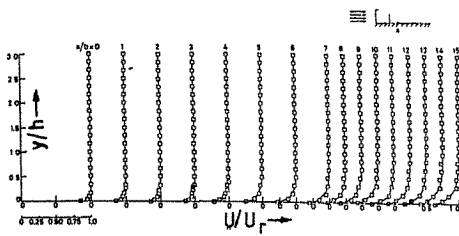


Fig. 2 Mean velocity profiles without body

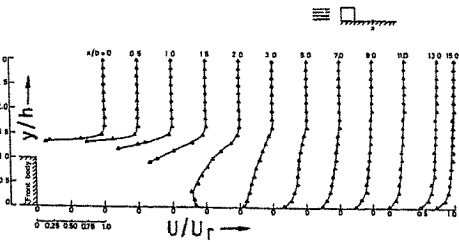


Fig 3 Single body ( $h/b=1$ )

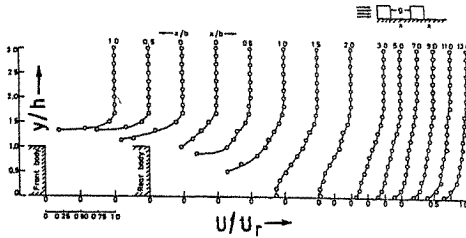


Fig 4.  $h/b=1, g/b=1$

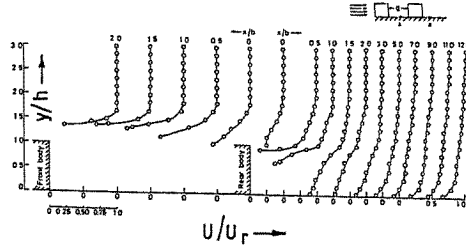
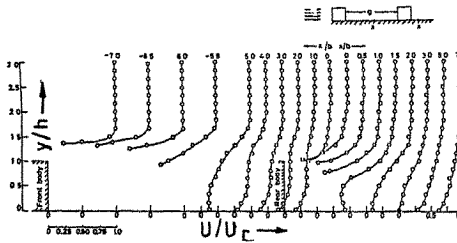
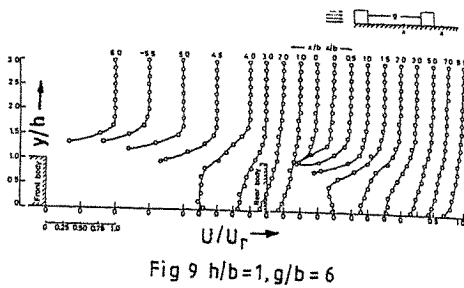
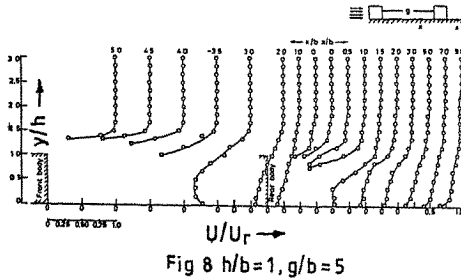
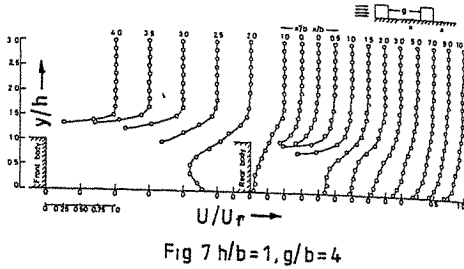
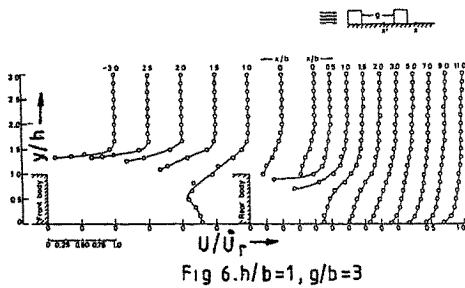


Fig 5.  $h/b=1, g/b=2$

Referring to Fig. 4 where the results for  $g/b = 1$  are presented, it is seen from the shape of the velocity profiles within the gap that the thickness of the shear layer separating from the front body extends up to about  $0.75h$  above the body height. The flow is highly disturbed even up to the height of the body. (This is the reason why the velocity profiles could be measured and presented for  $y/h \geq 1$ ). Considering the profile at  $x/b = 0$  (the location corresponds to the rear face of the downstream body), the shear layer is seen to be sufficiently thick. Another interesting feature is that the velocity profile could be measured even up to the top edge of the body unlike at  $x'/b = -1$  (the location corresponds to the rear face of the front body). This is because of the presence of the recirculating region on top of the front body at  $x'/b = -1$  whereas such a region appears to be non-existent on top of the rear body at  $x/b = 0$ . It can be conjectured that there is no shear layer originating due to separation at the front top edge of the rear body. Rather, the shear layer generated due to the separation at the front top edge of the upstream body is enveloping the downstream body. The reattachment of this layer occurs on the top of the rear body between  $x'/b = 0$  and  $x/b = 0$  which is reflected in the shape of the velocity profiles and the extent of the height up to which the velocity measurement could be carried out at these two locations. The rear body appears to have a streamlining effect on the flow separating from the front body. Further the velocity profiles behind the rear body indicate flow reattachment of the flow on the ground plane to occur within a distance of  $1.5b$  from the rear face. After reattachment, the shape of the velocity profiles change gradually and beyond  $x/b = 9$ , the profiles can be expected to remain unaltered.

The results shown at Fig. 5 ( $g/b = 2$ ) indicate that there is still no reattachment of the shear layer within the gap. But the shear layer thickness grows within the gap which can be seen from comparing the profiles at  $x'/b = 0$  in Figs. 5 and 4. The other features are similar to those observed in Fig. 4.



As the spacing between the bodies increases, the shear layer separating from the top edge of the front body reattaches to the ground plane within the gap (Fig.6 to 10). After reattachment there is a rapid change in the velocity profiles as can be seen in Figs.7 to 10. Considering the results at  $g/b = 7$  (Fig.10) for a detailed discussion, the velocity profiles within the gap reveal the reattachment of shear layer to occur at about a distance of  $2b$  behind the front body. It is interesting to compare the velocity profile at  $x'/b = 0$  in Fig.10 with the corresponding profile in Fig.4. In the later case the thickness of the shear layer is much larger than in the former. This is because what is seen at  $x'/b = 0$  in Fig.4 is the shear layer which is generated due to the flow separation at the top edge of the front body and which is growing in thickness along the flow. Whereas, at  $x'/b = 0$  in Fig.10 the shear layer has been generated due to the flow separation at the front top edge of the rear body itself and hence its thickness is sufficiently small. The velocity profiles behind the rear body reveal the flow reattachment on the ground plane to occur around  $1.5b$  behind the rear face. Obviously at this gap ratio (i.e.  $g/b = 7$ ) the rear body does not have any streamlining effect as at  $g/b = 1$  (Fig.4) and the features observed behind the rear body in Fig.10 could be attributed to the increased turbulence levels generated because of the front body, though turbulence measurements are needed to obtain a conclusive answer. These are planned for the future.



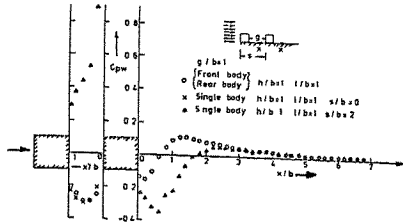


Fig 11 Interference effects on pressure distribution:  $g/b=1$

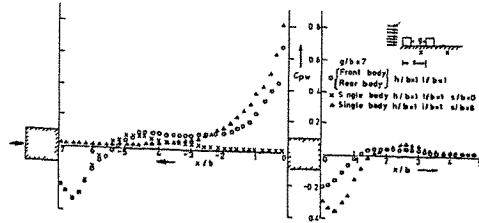


Fig 12.  $g/b=7$

### 3.2. Pressure Measurements

The pressure measurements on the ground plane along the centre line for two cases i.e.  $g/b = 1$  and  $7$  are presented in Figs.11 and 12. In these figures  $C_{pw} = (p - p_r) / \frac{1}{2} \rho U_r^2$  is the pressure coefficient on the ground plane,  $p$  is the pressure at any point on the surface plane with the body and  $p_r$  is the pressure at the same point on the surface plate without the body. The detailed pressure distribution for all the values of  $g/b$  are given in Gowda and Sitheeq [6]. The two cases are given to highlight the correspondence between the mean velocity profiles and the pressure distribution. The pressure distribution is obtained for the cases : a) when the single body is at the leading edge ( $s/b = 0$ , Fig.11) b) when the single body is at some distance from the leading edge ( $s/b = 2$ , Fig.11) and c) under conditions of interference with two bodies. For the present purpose, considering case (c) in Fig.11, it is seen that the reattachment behind the rear body occurs around  $x/b = 1.5$  (which is indicated by the position of the peak value of  $C_{pw}$ ). The velocity profiles behind the rear body in Fig.4 indicate also that the reattachment is occurring around the same  $x/b$  value. A constant pressure in the gap between the bodies in Fig.11 indicates a trapped recirculating flow which was the reason for the difficulty in extending the velocity profile measurements further downwards than that shown in Fig.4. The results shown in Fig.12 for  $g/b = 7$  indicate also a reattachment of flow behind the rear body around  $x/b = 1.5$ . The velocity profiles for this  $g/b$  value (Fig.10) also indicate flow reattachment around  $x/b = 5$ . In the gap between the bodies the pressure measurements show reattachment to occur around  $x'/b = 4.75$  which is in agreement with the trend indicated by the velocity profiles in the gap in Fig.10. Thus there is good agreement between the velocity measurements and the pressure distribution on the ground plane.

### 3.3. Flow Visualisation Results

To corroborate the results of the mean velocity measurements some flow visualisation results are given in Fig.13. For this purpose a aluminium surface plate is utilized and a homogeneous mixture of lamp black and kerosene is applied uniformly on the surface plate. Runs are made at the same Reynolds number as earlier i.e.  $Re = 3 \times 10^4$ .

Fig.13a shows that the reattachment behind the body (without interference) occurs around  $h/b = 2$  which agrees well with that indicated by the velocity profiles shown in Fig.3. There is correspondence between the results presented in the previous section and those revealed by Figs.13b to g for various  $g/b$  values. For example the reattachment within the gap is not evident for  $g/b = 1$  and  $2$  (Figs.13b and c) which is also the case from Figs.4 and 5. In Fig.13b ( $g/b = 3$ ) the reattachment within the gap (in front of the rear body) can be made out which is also revealed from Fig.6. At all  $g/b$  values (Figs.13b

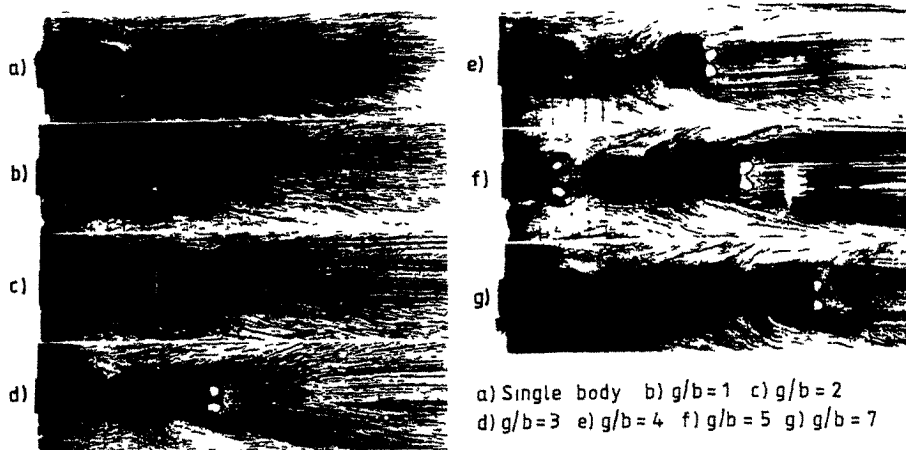


Fig 13 Flow patterns

to g) the size of the vortices behind the rear body are smaller compared to that without interference (Fig.13a). This indicates a smaller reattachment length behind the rear body which is borne out by the results at Figs 4 to 10 where the velocity profiles indicate a reattachment distance of about  $1.5b$  behind the rear body compared to  $2b$  behind the front body which is also revealed by the pressure measurements. Thus there is good correspondence between the flow visualisation results, pressure distribution and the velocity measurements.

#### 4. Concluding Remarks

The mean velocity profiles presented reveal the flow to be highly distorted within the gap between two cubical bodies. The reattachment within the gap occurs for  $g/b \geq 3$ . The maximum outer extent of the shear layer appears to be restricted to about one body height from the top surface. The reattachment length behind the rear body ( $\approx 1.5b$ ) for all  $g/b$  ratios is less than that without interference ( $\approx 2b$ ). The mean velocity profiles behind the rear body can be expected to become similar beyond  $x/b = 9$ .

#### References:

1. P.M. Sforza and R.F. Mons., "Wall wake flow behind a leading edge obstacle", AIAA, Vol 8, 1970, pp.2162-2167
2. J.A. Peterka and J.E. Cermak, "Turbulence in building wakes", 4th International conference on Wind Effects on Buildings and Structures, Heathrow, 1975, pp.447-463.
3. I.P. Castro and A.C. Robins, "The flow around a surface mounted cube in uniform and turbulent streams", J. Fluid Mech., Vol.79, 1977, pp.307-336.
4. Y. Ogawa and S. Oikawa., "A field investigation of the flow and diffusion around a model cube", Atmospheric Environment, Vol 16, No.2, 1982, pp.207-222.
5. B.H.L. Gowda, H.J. Gerhardt and C. Kramer., "Mean flow and turbulence measurements in the wake of a three-dimensional bluff body", J Aero. Soc. of India, Vol.39, No.1, 1987, pp.29-32.
6. B.H.L. Gowda and M.M. Sitheeq, "Effect of interference on the pressure distribution on the ground plane around two low-rise prismatic bodies in tandem arrangement", Applied Scientific Research, Vol.47, 1990, pp.129-149.

## **Roofs and Low Rise**



## **Analysis of wind-induced roof pressure data acquired in the field**

K.C. Mehta, B.B. Yeatts, and D.A. Smith

Wind Engineering Research Center  
Texas Tech University, USA

**Abstract:** A field research facility has been constructed at Texas Tech University to study wind effects on low-rise buildings. A variety of research is being pursued at the facility including wind loads on building surfaces, internal pressures, performance of roofing materials, and wind flow around the building. Much of the past and present work has focused on the analysis of roof pressure data collected at the field facility. The results of a study to determine the degree of correlation between internal and roof pressures and an introduction to an area averaging of roof pressures experiment are presented.

### **1. Introduction**

Severe wind-induced damage to low-rise structures has demonstrated a need for a greater understanding of wind pressures on and inside buildings. One part of buildings which is highly susceptible to wind damage is the roof. The Wind Engineering Research Field Laboratory (WERFL) at Texas Tech University (TTU) is providing an excellent opportunity to study roof pressures through field experiments. This paper presents the results of a study involving the correlation of internal and roof pressures. An introduction to an area averaging influence of pressures on a roof purlin is also included.

### **2. Field site description**

The WERFL consists of a 30 x 45 x 13 ft (9.1 x 13.7 x 4 m) test building which is fully rotatable and a 160 ft (49 m) meteorological tower. The test building and tower are located in a flat, open field on the TTU campus in Lubbock, Texas. The test building is equipped with instrumentation to record both internal and external pressures during high winds. The tower is located about 150 ft (46 m) west of the test building. Wind speed and direction instruments are placed at several heights of the tower to measure wind characteristics. Details of the field facility, instrumentation, and data acquisition system have been published [1,2,3].

Characteristics of the test building which are of particular interest for the research presented here include the location and size of openings and the location of roof framing members. Internal pressure of buildings is highly dependent on opening size and location. The test building has a door and a window which provide 5% and 2% openings in the walls, respectively. The roof of the building is supported by purlins running parallel to the long dimension. Figure 1 shows the opening locations and the location of the instrumented purlin and pressure transducers used in the area averaging experiment.

The data presented here were collected using Mode 15 data acquisition. The record duration for Mode 15 was 15 minutes with pressures sampled at 40 Hz and anemometry sampled at 10 Hz. Over 800 records were collected in this mode.

### **3. Correlation of internal and roof pressure**

The correlation between internal and roof pressure data collected at the WERFL has been studied for selected data records. Since internal pressures have a maximum value when a windward opening is present, the three data records analyzed have either a 2% or a 5% windward wall opening. Roof pressures were measured at locations approximately 1 ft (0.3 m) from the windward edge of the roof in each record. The internal pressure was measured near the volumetric center of the test building.

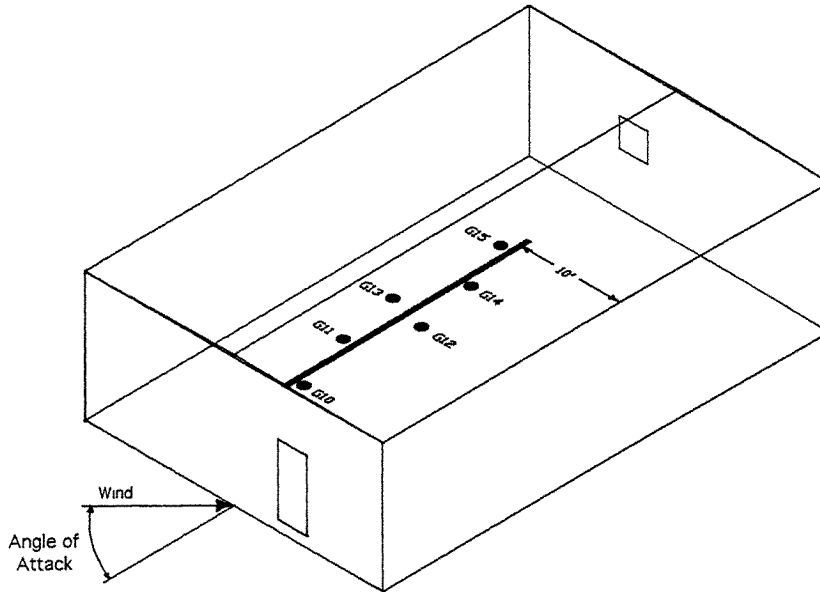


Figure 1. Test building showing opening locations and location of the instrumented purlin and pressure transducers used in the area averaging experiment.

Only 5 minute segments of the full 15 minute pressure coefficient time histories were used in the correlation analysis to reduce computation time. The internal and roof pressure coefficients are plotted simultaneously for part of one of the data records used in the correlation study in Figure 2. There is a visible correlation between the two time histories.

Cross-correlation coefficient functions were calculated to a time lag of 25 seconds. Results of this analysis show that internal pressure is very highly correlated with roof pressure as cross-correlation coefficients were in the range of -0.7 to -0.9 for near zero lag time. Figure 3 depicts the calculated cross-correlation coefficient function for one of the three data records analyzed. The correlation is negative because roof pressures are negative and internal pressure is positive for windward openings. The high correlation of internal and roof pressure is significant because it implies that the outward acting surface pressures applied to a roof component by wind can be greatly magnified if there is a windward opening.

#### 4. Area averaging experiment

The Metal Building Manufacturer's Association has sponsored an experiment at the WERFL to assess the area averaging effects on pressures for a roof purlin. The purlin chosen for the experiment is shown in Figure 1. The purlin is an 8 inch deep, cold formed Z-shaped member, 25 ft long, spans 23.5 ft between rigid support frames, and has a 1.5 ft overhang adjacent to the building wall.

The purlin displacement can be related to an average pressure acting on the tributary area using a uniform pressure-purlin displacement curve. This curve is developed by pressurizing the inside of the building using a high pressure moderate flow fan. The tributary area of the roof purlin is developed by applying point loads on the roof and measuring the purlin centerline displacement to the applied load.

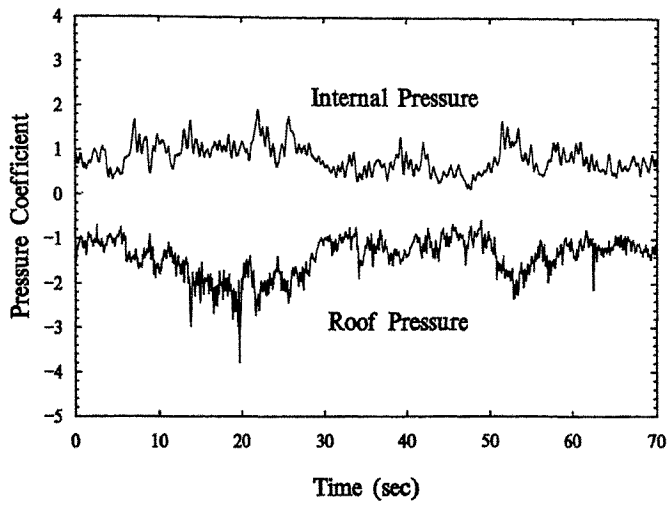


Figure 2. Simultaneous time histories for internal and roof pressure coefficients.

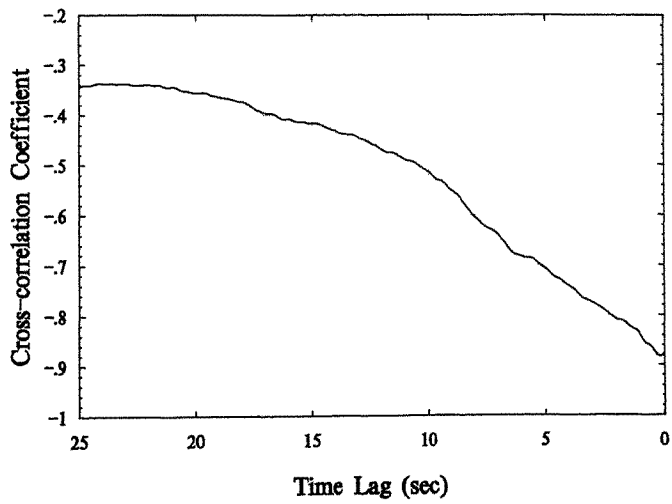


Figure 3. Cross-correlation function for internal and roof pressure.

Six pressure transducers are used to measure the pressures in the purlin tributary area. To provide redundancy, two direct current displacement transducers (DCDT) measure the purlin centerline displacement. The sampling rate for the pressure transducers is 40 hertz and for the DCDT's is 10 hertz.

Analysis of the purlin response to cyclic daily temperature fluctuations under zero wind conditions indicate that the purlin-metal deck system exhibit a slip-stick behavior. The purlin-metal deck system exhibits linear response to a thermal gradient across the system up to a point where sufficient shear flow forces are developed between the purlin and the deck to overcome the clamping force provided by the self tapping screws which connect the members. At this point, the roof deck "slips" relative to the purlin and then "sticks" in a new equilibrium position. The position which the roof purlin sticks after slipping is not deterministic. This slip-stick phenomena has made obtaining reliable zero reading for the purlin displacement (from which to measure the purlin mean response) difficult. As a result, only the fluctuating component of the purlin response to wind pressures is analyzed.

The spectrum for the fluctuating response of the purlin, the spectra of the measured u-component speed, and the wind induced pressure at transducer G12 are shown in Figures 4 and 5 for two records. Figure 4 shows the purlin response for record M15N609 which is for an angle of attack of 23.9 degrees and Figure 5 show comparable results for record M15N787 at an angle of attack of 257.3 degrees. The summary statistics for these two records are shown in Table 1.

Statistic	Record	
	M15N609	M15N787
15-Minute Mean Wind Speed	22.9 mph	17.1 mph
Angle of Attack	23.9 deg	257.3 deg
$z_0$	0.028 ft	0.122 ft
$u^*$	1.517 mph	1.518 mph
$a$	0.149	0.211

Table 1. Summary statistics for the two records shown in Figures 4 and 5.

These results indicate that the purlin does not respond to the high frequency component of the wind pressures at taps. In fact, it indicates that the purlin spectral response follows closely the wind spectra. This implies that the high frequency component of the wind-induced pressure is averaged out in the purlin response.

## 5. Conclusions

The objective of this paper is to give information on full-scale research being conducted on roof pressure data collected at the WERFL of Texas Tech University. Conclusions from the two studies discussed in the paper are as follows:

1. A high correlation exists between internal pressure and roof pressure. The magnitudes of cross-correlation coefficients are in the range of 0.7 to 0.9 for time lags up to one second.
2. Preliminary results of the area averaging experiment show that the response of a purlin to wind loading closely follows the wind spectra.
3. The purlin does not appear to respond significantly to the high frequency component of the wind-induced pressures at taps.



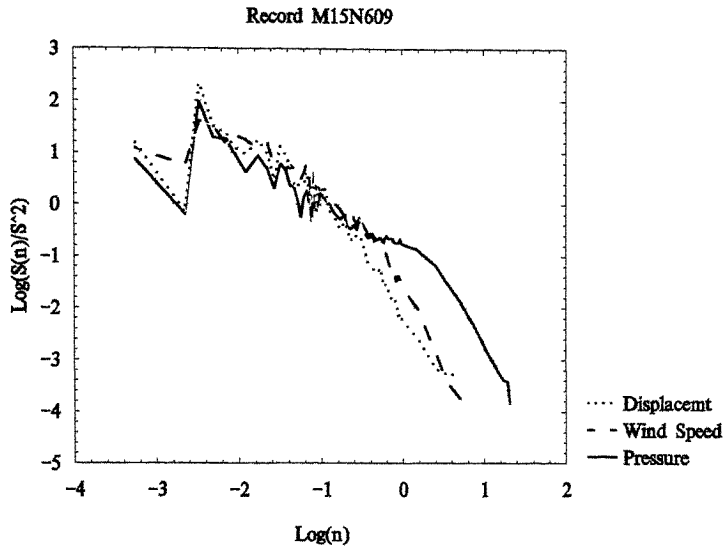


Figure 4. Spectral results for record M15N609.

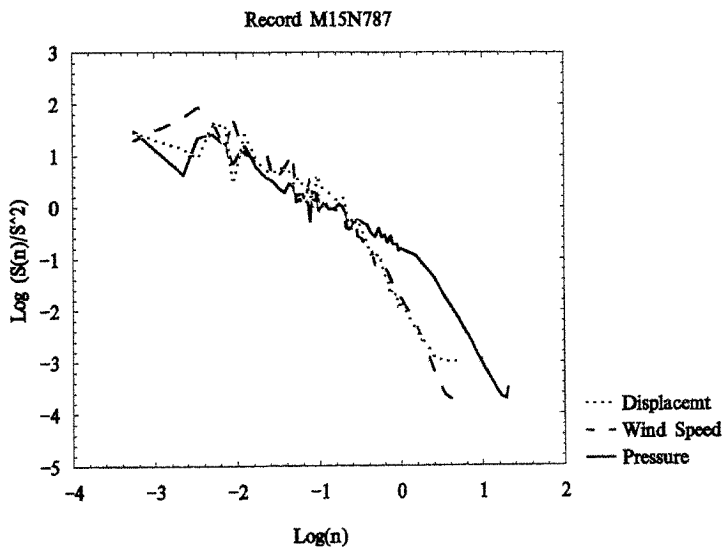


Figure 5. Spectral results for record M15N787.

## 6. Acknowledgments

The WERFL project has been guided from the beginning by an external advisory committee. Dave Surry, Robert Scanlan, and Joe Minor, current members of the committee, have contributed significantly to the progress at WERFL. Financial support from the U.S. National Science Foundation (Grants BCS-8821163 and CES-8611601) and the Metal Building Manufacturer's Association is acknowledged.

## References:

1. Levitan, M.L., and Mehta, K.C., 1991a: "Texas Tech Field Experiments for Wind Loads Part I: Building and Pressure Measuring System," Proceedings, Eighth International Conference on Wind Engineering, London, Ontario, Canada, July 8-12.
2. Levitan, M.L., and Mehta, K.C., 1991b: "Texas Tech Field Experiments for Wind Loads Part II: Meteorological Instrumentation and Terrain Parameters," Proceedings, Eighth International Conference on Wind Engineering, London, Ontario, Canada, July 8-12.
3. Yeatts, B.B., and Mehta, K.C., 1992: "Field Experiments for Building Aerodynamics," presented at the Second International Colloquium on Bluff Body Aerodynamics and Applications, Melbourne, Australia, December 7-10.

## Aerodynamic instability and damping of a suspension roof

J. E. Cermak, H.G.C. Woo, M. L. Lai<sup>+</sup>, J. Chan<sup>++</sup>, and S. L. Danielson<sup>+++</sup>

Department of Civil Engineering, Colorado State University, Fort Collins, CO USA

<sup>+</sup>3M Company, St. Paul, MN USA

<sup>++</sup>T. Y. Lin International, San Francisco, CA USA

<sup>+++</sup>Parsons Brinckerhoff, San Francisco, CA USA

**Abstract:** A series of wind-tunnel studies with a passive viscoelastic damper system connected to a full aeroelastic roof model was conducted to develop an effective damping system. The structural responses and damping ratios were included in the measurements. Results indicate that the damping ratio, 8% in the vertical mode and 4% in the torsional mode, should be adequate and practical for the prototype structure. A continuous damper system for the prototype roof structure was designed based on the wind-tunnel test results and frequency shift theory derived from the model strain energy method.

### 1. Introduction

Construction of the Chientan Station (R18A) roof of the Taipei Mass Rail Transit system has been completed. The station which bears heavy traditional Chinese architectural style has a curved roof shell 187.6 m in length, 16.6 m in width and weight of approximately 2,800 metric tons. Unique design of the roof structure is that, instead of supporting by columns, the whole roof shell is suspended below two main cables by 26 pairs of suspenders. The two main supporting cables are back stayed by a ground anchor and supported by an inclined concrete pylon at each end of the station.

Three phases of wind-tunnel studies were conducted at the Fluid Dynamics and Diffusion Laboratory of Colorado State University after the preliminary design of the entire station structure was completed. In Phase I of the investigations, a 1:75 sectional model of the roof shell with two degrees of freedom (vertical and torsional) was investigated [1]. Effects including roof geometry, geometrical details, damping and the fundamental torsional-to-vertical frequency ratio on the roof shell aerodynamic performance were investigated. Based on the test results, the geometry of the roof shell was modified and the fundamental frequency ratio

(torsional/vertical) was increased to 1.69 to improve the aerodynamic performance. In Phase II, a 1:120 full aeroelastic model (Fig. 1) with natural vertical damping ratio  $\zeta_v = 0.6\%$  and torsional damping ratio  $\zeta_t = 1.1\%$  was built to study the three-dimensional aerodynamic response and stability problems associated with turbulence, topography, surrounding structures and positions of train(s) under the roof [2]. Among many characteristics of the roof-shell response that have been identified,

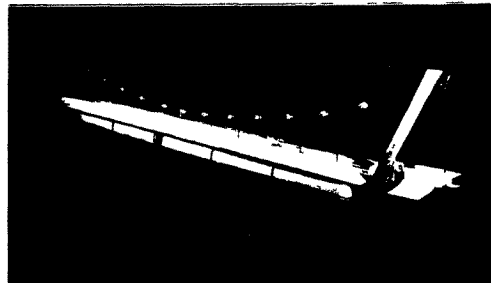


Fig. 1. An 1:120 scale full aeroelastic roof model of Chientan (R18A) Station.

the most critical case is with one train parked on the upstream track of the station. The air flow through the gap between the train roof and the station-roof tip creates an aerodynamic effect which bears resemblance to that of the mouth piece of a wind instrument. The instability commences suddenly after 112.7 km/hr (70 mph) wind speed is reached and the roof begins to vibrate violently in both the vertical and torsional modes. This dynamic response obviously cannot satisfy the criteria of satisfactory performance at 146 km/hr (90.7 mph) hourly wind speed set for Tamshui, Taipei [3]. In Phase III, further studies were performed to provide the vital information necessary for the design of a suitable damping device for the roof-shell structure [4].

## 2. Viscoelastic Damper and Wind-Tunnel Test

Three yoke-shape light weight metallic plates (Fig. 2) were attached at the center and the quarter spans of the model roof shell for the installation of the passive damper system. This arrangement is directed at controlling both the first and second modes of vertical bending and transverse torsional motions [2]. Viscoelastic material cut into elements with a dimension of 5 x 6 mm in cross section and with a certain predetermined length were attached between the end tip of the yoke-shape plate and another L shape plate which was glued to the station platform. The dampers were centered along the center axis of the roof-shell and its center is 22 mm below the elastic center of the roof.

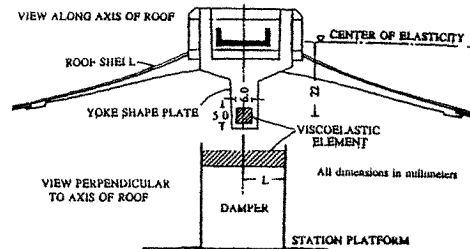


Fig. 2. Cross section of roof-shell model and damper system.

A series of studies with wind blowing normal to the roof span was conducted in the Industrial Aerodynamics Wind Tunnel of CSU to determine a preferable damping for the structure. Both the vertical and torsional damping ratios and the structural response were included in the measurement. Deflection of the roof shell were measured using the Kaman Proximity Meters - noncontact type displacement transducers. Output signals from the displacement transducers were first fed into an 8-channel signal conditioner and then recorded with an oscillograph chart recorder for analysis. Adjustment of damping provided by the viscoelastic element was carried out by changing the length (and hence the stiffness) of the viscoelastic element and by adhering the viscoelastic element to either one side or both sides of the yoke-shape plate. This was done in a trial and error manner.

Tests conducted to evaluate the roof peak-to-peak responses were all carried out under two conditions: 1) with no train at the station, and 2) with a train parked on the upwind track. Table 1 summarizes some of the related parameters and test results. For comparison, results of tests 2, 3, and 4 are selected and presented in Figs. 3, 4, and 5, respectively. For test 4 case, results indicate the dampers do not adequately stabilize the roof response. For test 2 and test 3, the results show a substantial suppression in the roof-shell response. The displacement data and visual observation all indicate that the entire roof shell remains stable

Test	Dampers	Viscoelastic Elements	Element Size L x W x H mm	Damping Ratio		Stability
				Vertical (%)	Torsional (%)	
Part II	0	0	—	0.6	1.1	no
1	3	6	15 x 6 x 5	18	17	yes
2	3	3	15 x 6 x 5	8	8	yes
3	3	6	25 x 6 x 5	8	4	yes
4	3	3	25 x 6 x 5	4	4	no

Table 1. Results of roof-shell response with various damper sizes and the related parameters.

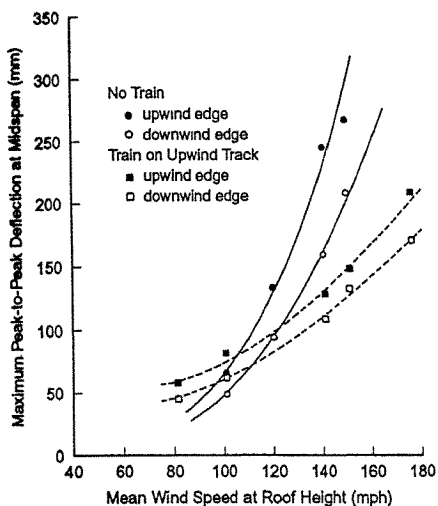


Fig. 3. Peak-to-peak maximum response of Chientan (R18A) Station model with a passive viscoelastic damper system ( $\zeta_v = 8\%$ ,  $\zeta_t = 8\%$ ).

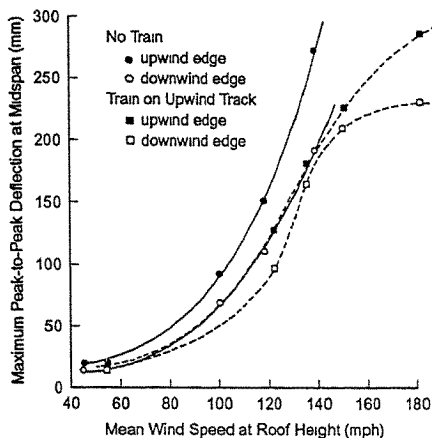


Fig. 4. Peak-to-peak maximum response of Chientan (R18A) Station model with a passive viscoelastic damper system ( $\zeta_v = 8\%$ ,  $\zeta_t = 4\%$ ).

even when a train is parked on the upwind track at wind speed exceeding 240 km/hr (150 mph). It is interesting to note that in both cases, except in the region below 161 km/hr (100 mph) in Fig. 3, for the train-in-upwind position, the results show that the roof is not only stabilized but the response becomes smaller than for the no-train case. The results below 161 km/hr (100 mph) in Fig. 3 should be interpreted with caution. The reason that there is a cross over in the roof response between the with- and without-train cases can be due to nonlinear responses of the damper and/or some experimental uncertainties.

It has been concluded that the damping ratios,  $\zeta_v = 8\%$  and  $\zeta_t = 4\%$ , should be adequate and practical for the prototype structure. Within the resolution of the experimental technique adopted in this study, with the dampers attached to the roof shell in test 3, there is no significant change in both the vertical and torsional frequency of the roof shell.

### 3. Damper Design

Viscoelastic damper system is designed to provide the necessary damping for the prototype roof structure using the model strain energy method [5,6]. The added damping ratio of a viscoelastic damped structure can be estimated according to

$$\zeta = \frac{\eta}{2} \frac{\phi^T K' \phi}{\phi^T K_s \phi}, \quad (1)$$

where  $\eta$  is the loss factor of the damper,  $\phi^T$  is the transpose of the mode shape vector,  $K'$  is the stiffness matrix due to the damper storage stiffness, and  $K_s$  is the stiffness matrix of the structure including contribution from the damper storage stiffness. When the damper stiffness is small

compared to the structure, Eq. 1 can be simplified [7] as

$$\zeta = \frac{\eta}{2} \left( 1 - \left( \frac{f_0}{f_s} \right)^2 \right), \quad (2)$$

where  $f_0$  and  $f_s$  are the natural frequencies of the structure without and with added dampers, respectively. This frequency shift is assessed by placing spring elements into the structure. For this roof structure, eight springs are placed at eight pre-determined damper locations in a finite element analysis shown in Fig. 6. The calculated added damping ratios and natural frequencies for the first torsional and vertical modes versus damper storage stiffness are shown in Fig. 7(a)-7(d). The loss factor,  $\eta$ , of the damper is assumed to be one.

The structural inherent damping ratios are assumed to be 1% and 0.6% for the torsional and vertical mode respectively. The required additional damping ratios are then 3% for the torsional and 7.4% for the vertical mode. From Figs. 7(a) and 7(c), the damper stiffnesses should be 82.15 t/m (4.6 kips/in) for the torsional mode and 60.72 t/m (3.4 kips/in) for the vertical mode. The frequency increases slightly from 1.13 to 1.17 Hz for torsional and 0.67 to 0.76 Hz for the vertical mode. Change of the structural stiffness due to dampers is small.

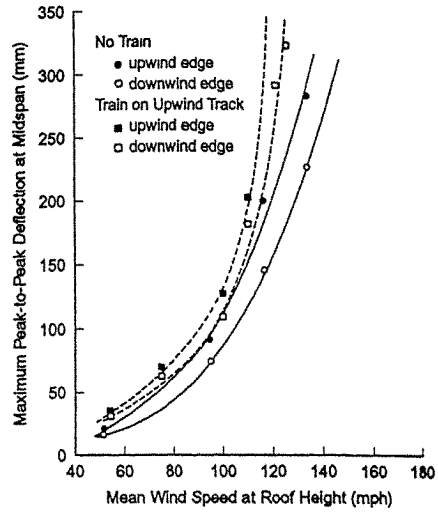


Fig. 5. Peak-to-peak maximum response of Chientan (R18A) Station model with a passive visco-elastic damper system ( $\zeta_v = 4\%$ ,  $\zeta_t = 4\%$ ).

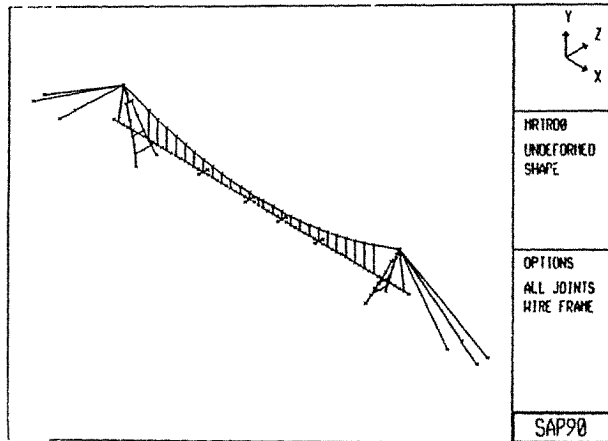


Fig. 6. Finite element analysis and damper locations for prototype roof structure.

Since the dampers work for both torsional and vertical modes, with the viscoelastic material used, the damper storage stiffness has changed to 67.87 t/m (3.8 kips/in) for the vertical mode, and 82.15 t/m (4.6 kips/in) for the torsional mode. The design is slightly on the conservative side.

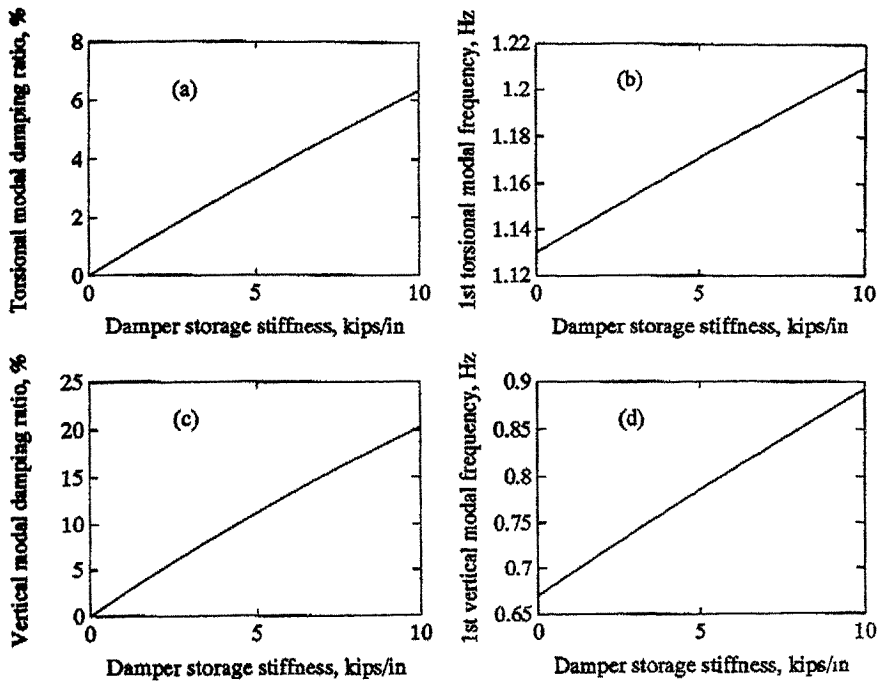


Fig. 7. (a) Added 1st torsional modal damping ratio versus damper storage stiffness, (b) 1st torsional modal frequency versus damper storage stiffness, (c) added 1st vertical modal damping ratio versus damper storage stiffness, (d) 1st vertical modal frequency versus damper storage stiffness.

#### 4. Damper Configuration

Once the damper stiffness is determined, size of the damper can be calculated using the following equation:

$$K' = G'A/h, \tag{3}$$

where A is the area of the viscoelastic material and h is the thickness. The viscoelastic material will work in shear. The thickness of the viscoelastic material has to be large enough to limit the shear strain. It is determined that 8.4 cm (3.3 in) is appropriate. The total shear area of the viscoelastic material is 15x102 cm (5.9 x 40 in). The damper consists of two sub-dampers connected in series to fit into the light post. Forty aluminum fins each 0.16 cm (0.063 in) in thickness are used to dissipate the heat generated in the viscoelastic material during strong wind.

## 5. Concluding Remarks

Wind-induced loading and response have been recognized as important elements to be considered during the design of new or modifications for existing long-span suspended structures. This issue is most critical for typhoon frequent zones such as Taiwan. Suitably designed damper devices can be used effectively to dissipate the excessive energy and thus prevent undesirable violent vibrations of the structure. Identification of potential problems through aeroelastic model investigations and detailed damper studies and laboratory tests to determine an effective damping ratio can provide architects and structural engineers with valuable guidance and design data.

### References:

1. Bienkiewicz, B., Kawakita, S., Cermak, J.E. and Peterka, J.A. Tech. Rep. for American Transit Consultants, Inc., Taipei, Taiwan, (1991) CER90-91BB-SK-JEC-JAP1a.
2. Bienkiewicz, B., Kawakita, S., Cermak, J.E. and Peterka, J.A. Tech. Rep. for American Transit Consultants, Inc., Taipei, Taiwan, (1991) CER90-91BB-SK-JEC-JAP91b.
3. Tsai, I.C. and Lin, Z.S., Proc. of the ROC-Japan Joint Seminar on Multiple Hazards Mitigation, National Taiwan University, Taipei, Taiwan, (1985).
4. Cermak, J.E. and Woo, H.G.C. Tech. Rep. for 3M Company, St. Paul, MN, (1993) CER90-91JEC-HGCW1c.
5. Johnson, C.D. and Kienholz, D.A., AIAA J, 20, No.9 (1982),1284.
6. Chang, K.C., Soong, T.T., Oh, S.T. and Lai, M.L. ASCE J. Struc. Engng, 118, No.7(1992),1955.
7. Oh, S.T., Chang, K.C., Lai, M.L. and Nielsen, E.D. 10th World Conf. on Earthquake Engng. Madrid, Spain, July 19-24, 1992.



## **Wind Tunnel Testing of Houses with Large Overhangs in the West Indies**

Paul W M Tam, BSc, PhD, MICE, CEng, MHKIE, FGS  
and

Virender K Handa<sup>†</sup>, BSc, MASc, PhD, PEng, MASCE

Executive Engineer, Meinhardt (C & S) Ltd, Hong Kong

<sup>†</sup>Professor, Department of Civil Engineering,  
University of Waterloo, Waterloo, Ontario, N2L 3G1

**Abstract:** Houses in the West Indies are subject to large tropical cyclones from time to time and large scale damages often results after such cyclones. Wind tunnel testing of typical houses was undertaken as part of a joint research program to enable the University of the West Indies, St. Augustine to develop recommendations for the use of appropriate wind pressures for the structural design of houses with large eaves and large overhangs that are typical in the area. Very little wind pressure has existed for such houses until this time.

### **1. Introduction**

In order to provide accurate wind pressure information for the design of houses in the West Indies, it was decided that wind tunnel testing be carried out on typical houses in the area. Survey of existing houses was carried out to provide typical building shape. Models were made on these typical houses and were then tested in the University of Waterloo Flexible Wall Wind Tunnel.

### **2. Method**

#### **2.1 Survey of Building Configurations**

In order to come up with a general recommendation for the wind pressure coefficients for design of houses in the West Indies, it is necessary first of all to conduct a survey of typical houses in the area. The survey was done by the University of the West Indies and passed onto the University of Waterloo.

#### **2.2 Building Types Chosen for Testing**

Houses generally have large eaves and large overhangs which make them particularly vulnerable to wind uplift forces. To assess the effects of cyclone wind forces on these houses, six typical houses were chosen and models were made for testing at the wind tunnel of the University of Waterloo. Details of two of these are shown on Figures 1 and 2. Figure 3 shows the wind direction and nomenclature for Model WI-3.

#### **2.3 Wind Velocity Profiles**

It would have been ideal if three types of velocity profiles namely, urban, sub-urban and open country are produced by in the tunnel for model testing. This will give a more comprehensive understanding of the wind pressure effects of different houses under different areas of the country. However, only the urban and open country profiles were generated as it would be too costly to generate all the profiles. It was considered sufficient to test models under the two profiles and the wind pressure effects due to the sub-urban profile would be interpolated from the other two profiles.

The wind pressure profiles were generated using a combination of floor roughness (using 25 x 25 x 25 mm cubes regularly placed on tunnel floor) and spires

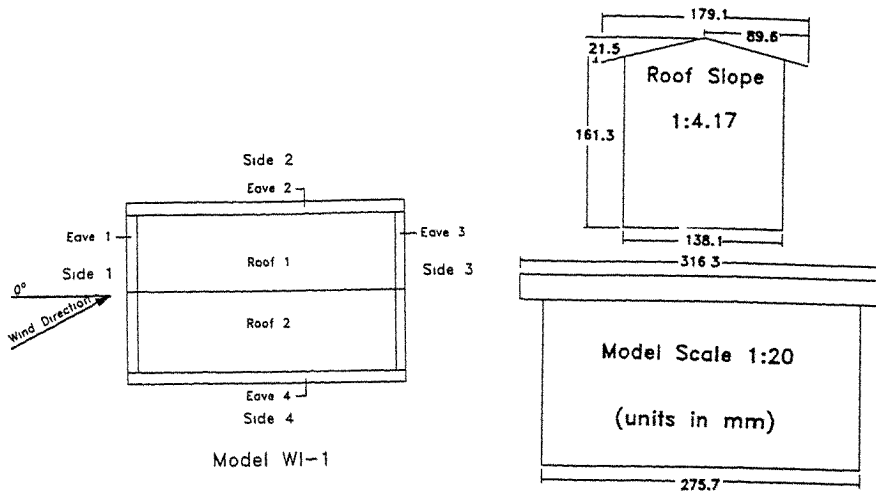


Figure 1: Model WI-1:  
Plan and Sections

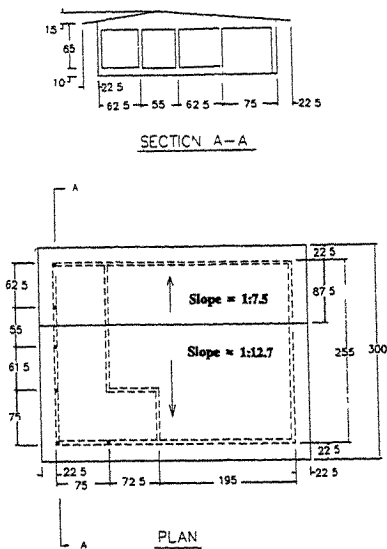


Figure 2: Model WI-3  
Plan and Section

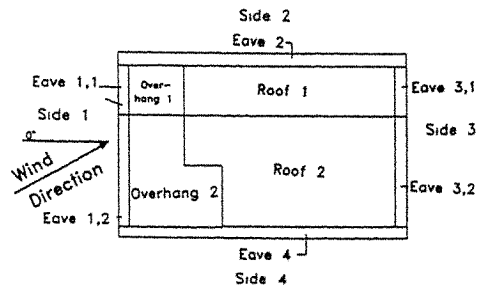


Figure 3: Model WI-3  
Wind Direction and  
Nomenclature

(see Figure 4). The experimental profiles generated were compared to the theoretical ones and the agreement was good for both profiles (see Figure 5).

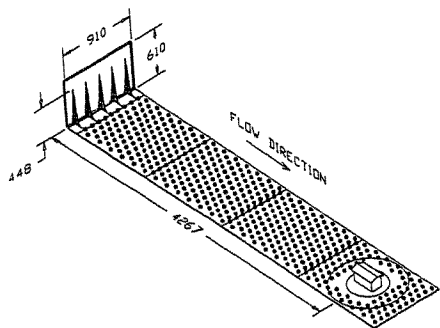


Figure 4: Spires and Floor Roughness for Urban Profile

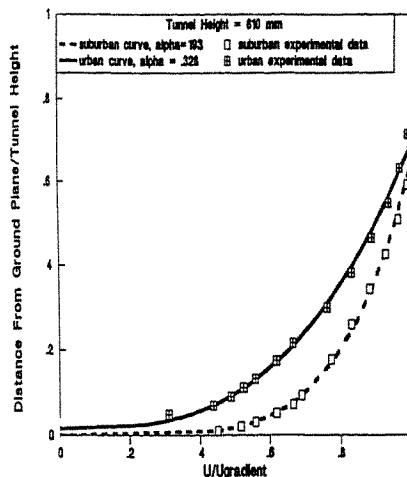


Figure 5: Urban and Open Country Wind Profiles

#### 2.4 Wind Tunnel Testing and Data Analysis

Six plexiglass models at a scale of 1:20 to 1:40 were made for the six houses chosen. Wind pressure were measured using pressure taps formed by drilling holes onto the 3mm thick clear plexiglass at places where wind pressure data would be of interest. The holes are then connected to the plastic tubing which in turn are connected to the scani values for pressure monitoring. In order to avoid the effects of tubing on wind current, all tubing is contained inside the models. Where pressure readings are required from the eaves and from the overhangs, special troughs (or tunnels) are formed inside the plexiglass sheet by first forming troughs onto a sheet and subsequent laminating by a very thin sheet, or by drilling into the sheet (see Figure 6).

One of the most important considerations in model construction is to determine the optimal amount of pressure taps required. It was indicated from a study of optimization of pressure taps on a calibration cube that for any surface a sparse matrix of 20 to 30 pressure taps when tactfully arranged could provide a pressure coefficient contours with accuracy up to within 1% of that from a full matrix of 150 or more taps [2]. The sparse matrix arrangement requires the inclusion of a few central taps with the remainder positioned along the outer edge of the surface. Based on this finding, the pressure taps were carefully arranged to produce an optimal result.

The models were placed onto a rotating disk at the test section of the tunnel and the disk was rotated every 22.5 degrees automatically. Wind tunnel pressure data were collected by a automatic data collection system. Software was written to convert the raw wind tunnel data into wind pressure coefficients. Commercially available software is used to convert wind tunnel data into wind pressure profiles.

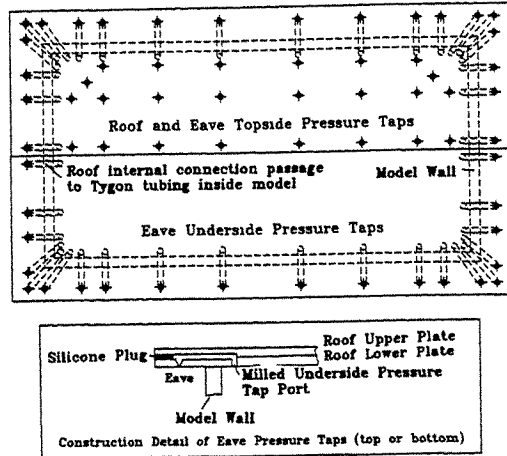


Figure 6: Typical Pressure Tap Details

All six models were tested under the urban wind velocity profile and the open country wind velocity profile.

### 3. Results and Recommendations

In general the wind pressure coefficients on the roofs are comparable to other published data, which confirms the accuracy of data and laboratory procedure used. The wind pressure coefficients for eaves and under the overhangs are valuable for the structural design of houses as not much data exist at those areas. Depending on the angle of wind, the eaves and the overhangs may be under positive or negative wind pressures. Hence, a house may be stable to wind at a particular angle, but it may be unstable at another angle. The wind tunnel data demonstrated this fact. In the design of houses, these should be taken into account and the all possible combinations of wind effects should be considered.

#### 3.1 Roof Top Pressure Coefficients

##### Model WI-1 (Figure 1)

This symmetrical model has a roof slope of about 1:4.17. The eaves contribute to 23% of the total roof area. The floor plan length to width ratio was 2:1 and the eave height to floor plan width ratio was 1:1. The minimum  $c_p$  values obtained for wind directions at 0 degree, 45 degrees and 90 degrees were -1.3, -2.2 and -1.6 respectively. Due to the 2:1 length to width ratio, the approach streamlines were somewhat affected and resulting in greater suction pressures for wind direction of 90 degrees than that of 0 degree.

##### Model WI-3 (Figures 2 and 3)

This asymmetrical model has a slope of 1:7.5 and 1:12.7 for roofs 1 and 2 respectively. The eaves contribute to 24.9% of the total roof area and the overhang 21.1%. Figure 2 shows the plan and sections and Figure 3 shows the wind direction and nomenclature of roof elements. The roof is exposed to high positive underside wind pressures for wind directions for the range from 135 degrees to zero

and to 315 degrees. The minimum  $c_p$  value obtained was -1.8 for wind direction at 0 and 315 degrees. At 270 degrees, the minimum  $c_p$  value was -1.4.

Table 1 shows the wind pressure coefficients for Models WI-1 and WI-3 for all wind directions. This table shows that the negative (suction) pressures are higher with the open country wind profile than the urban one. It should be clear in the later discussion that design of building based simply on these  $c_p$  values may be erroneous.

Table 1: Averaged Roof Pressure Coefficients for All Wind Directions ( $c_p$ )

Model	Urban Profile	Open Country Profile	Percent Increase
WI-1 Roof 1	-0.598	-0.670	+12%
WI-1 Roof 2	-0.472	-0.675	+43%
WI-3 Roof 1	-0.463	-0.533	+15.1%
WI-3 Roof 2	-0.427	-0.481	+12.6%

### 3.2 Roof Top and Underside Pressure Coefficients Combined

#### Model WI-1

Figure 7 shows the wind pressure coefficients obtained by averaging the pressure taps results on Eave 1 and the vector sum coefficients for the roof top and the underside. Diamond symbols and downward triangle symbols respectively are used for the Eave 1 top surface and down surface respectively. Upward triangle symbols are used to indicate the underside pressure coefficients and diamond cross symbols are used to indicate the vector sum topside pressure coefficients. It can be seen that there is good symmetry for wind directions from 0 to 180 degrees and the vector sum topside pressure coefficients (diamond cross symbols) are reduced by the suction pressures on the underside and becoming nearly zero when Eave 1 is downstream.

#### Model WI-3

The large areas of the eaves and overhangs 1 and 2 had significant contribution to the underside pressure. Figure 8 shows the averaged roof top pressure coefficients and the vector sum pressure coefficients. It can be seen that the suction on the roof top is partially cancelled by the suction pressure at the overhangs and the eaves and the suction pressure is almost entirely cancelled by the underside pressure for wind directions at 180 to 200 degrees.

The results of Model WI-3, when compared to those of Model WI-1, illustrates that the larger eaves and large overhand areas of model WI-3 have induced large positive pressure coefficients on the underside for some wind directions. However, this situation is not found in Model WI-1.

### 3.3 Use of Wind Tunnel Data

The wind tunnel testing data are being used by the University of the West Indies for design of new houses. The wind force data obtained is currently being used in laboratory testing of roof and building frame connections. Using wind pressure data which resemble closely to the actual wind conditions in the area permit an optimal building design be achieved. This would ensure efficient use of material and in this day when environmental concerns are of such paramount importance, the contribution of this work can be seen as a possible step toward this goal.

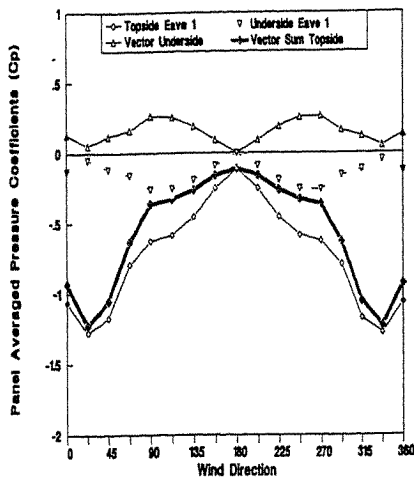


Figure 7: Urban  $c_p$  Values vs. Wind Direction Plot for Eave 1 and Vector Sum  $c_p$  on Roof for Model WI-1

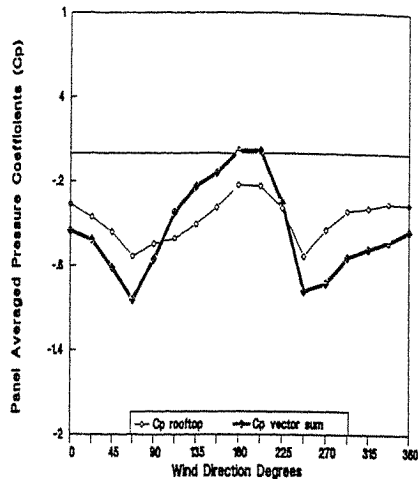


Figure 8: Urban  $c_p$  Values vs. Wind Direction Plot for Roof Top and Vector Sum  $c_p$  for Model WI-3

### Conclusion

Wind induced pressures on houses due to cyclones have been examined for two typical Caribbean houses. Model WI-1 represents one which has a small floor plan with significant eaves on all four sides and a moderate roof slope. Model WI-3 has a larger floor plan, shallower roof slopes and has 46% of the roof area contributed by the eaves and overhangs.

The surface pressure coefficients and vector sums are presented to show how underside pressures may affect the total uplift force on a building. The effects the underside suction pressure on the eaves of Model WI-1 on the overall uplift is much less than that for Model WI-3, which has a much larger percentage of roof made up by the overhang and the eaves.

### Acknowledgment

We are grateful to Professor Brundrett, Head, Tunnel Testing Facility of the University of Waterloo, for assisting us in data presentation. Funding for this work was provided by the International Research Development Centre, Ottawa, through a Cyclone-Resistant Housing (Trinidad) Research Contract.

### References

1. Tam, P. W. M., Handa, V. K. and Brundrett, E. (1992), "Wind Tunnel Analysis for Housing in the West Indies, Construction Management of Civil Engineering and Fluid Mechanics Division of Mechanical Engineering, University of Waterloo, Volumes I, II and III, 723 pages, Waterloo, Ontario, Canada N2L 3G1.
2. Tam, P. W. M., Handa, V. K. and Brundrett, E. (1992), "Wind Forces on Roofs of Residences with Large Eave and Overhang Areas", submitted to the Journal of Wind Engineering for publication.

## Proper orthogonal decomposition and reconstruction of multi-channel roof pressure

B. Bienkiewicz, Y. Tamura<sup>+</sup>, H.J. Ham, H. Ueda<sup>++</sup>, and K. Hibi<sup>++</sup>

Department of Civil Engineering, Colorado State University, Fort Collins, Colorado 80523, U.S.A.

<sup>+</sup> Department of Architectural Engineering, Tokyo Institute of Polytechnics, 1583 Iiyama, Atsugi, Kanagawa 243-02, Japan

<sup>++</sup> Institute of Technology, Shimizu Corporation, 3-4-17 Etchujima, Koto-ku, Tokyo 135, Japan

**Abstract:** The proper orthogonal decomposition and reconstruction of pressure on the roof of a low-rise building is described. The point pressures acquired simultaneously at 204 taps, uniformly distributed on the roof, were used in the analysis. The pressure space covariance was computed and employed to calculate the eigenvectors (modes) and the principal coordinates. These quantities were employed next to reconstruct the pressure and to perform the convergence study of the time series of the reconstructed roof loading. The results show that approximately 30% and 2% of the computed modes are needed to represent the largest negative peak of point and area-averaged roof pressure, respectively.

### 1. Introduction

It has been recognized that the extreme temporal fluctuations of the aerodynamic loading are associated with flow events of relatively large spatial scales. The notion of organized (coherent) structures has been developed and accepted in turbulence research and new tools have been developed for their analysis. One of the proposed methods is the proper orthogonal decomposition (POD), known also as the Karhunen-Loeve expansion. This technique has been successfully employed in investigations of turbulent boundary-layer flows.

Bienkiewicz et al [1] applied the POD in analysis of the area-averaged pressure in a corner region of the roof of a low-rise building. Due to hardware limitations, only ten channels of the pressure data were used in the study. In this paper, a data set consisting of 204 simultaneously acquired pressure channels is considered. In addition to the POD analysis and reconstruction, the effects of spatial averaging on the convergence of the pressure reconstruction are discussed.

### 2. Background

The main objective of the POD is to identify a deterministic function which have a structure typical of a random field. Given random pressure  $p(x,y,t)$ , the maximum of the projection of  $p(x,y,t)$  on a deterministic function  $\Phi(x,y)$  is sought. This leads to the following condition

$$\frac{\int p(x, y, t) \phi(x, y) dx dy}{\sqrt{\int \phi^2(x, y) dx dy}} = \max. \quad (1)$$

When the operation implied by Eq. 1 is performed in the mean-square sense, an eigenvalue problem

$$\int R_p(x, y, x', y') \Phi(x', y') dx' dy' - \lambda \Phi(x, y) \quad (2)$$

is established, where  $R_p(x, y, x', y')$  is the space covariance of pressure. For a spatially discrete data set, the integration is performed numerically and Eq. 2 is used to compute the eigenvalues  $\lambda_n$  and the eigenvectors  $\Phi_n(x, y)$ . The eigenvectors, also denoted herein as modes, are used as the base functions in a series expansion of the pressure

$$p(x, y, t) = \sum a_n(t) \Phi_n(x, y) \quad (3)$$

where the principal coordinates are

$$a_n(t) = \frac{\int p(x, y, t) \Phi_n(x, y) dx dy}{\int \Phi_n^2(x, y) dx dy} \quad (4)$$

### 3. Wind Tunnel Test

The experimental study was carried out in a boundary-layer wind tunnel at Institute of Technology, Shimizu Corporation. The tunnel is of a closed-circuit type and it has a 2.6m x 2.4m test section which is 15m long. A model of a generic low-rise building, depicted in Figure 1, was used in the study. The building geometrical proportions are similar to those of the Texas Tech University test building. The roof of the building was furnished with 204 uniformly distributed pressure taps, shown in Figure 1 as circles. An open circle (in Figure 1) represents the pressure tap at which the largest negative peak pressure occurred. The power law index of the mean approach flow was 1/6, and the geometrical scale was estimated to be 1/250, based on the longitudinal scale of turbulence. The multi-channel pressure measurement system, described by Ueda et al [2], was used to acquire the pressure at a sampling rate of 667 Hz. The record length of the pressure time series used in the analysis was 3.07 seconds.

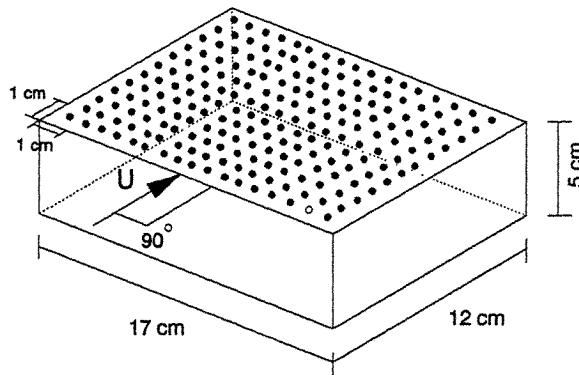


Fig. 1. Model of building and pressure tap location



#### 4. Results and Discussion

Figures 2 and 3 show the distribution of the mean, and the mean square of the roof pressure coefficient, computed using the dynamic pressure at the roof elevation.

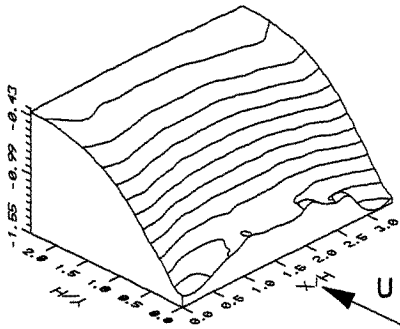


Fig. 2. Mean pressure

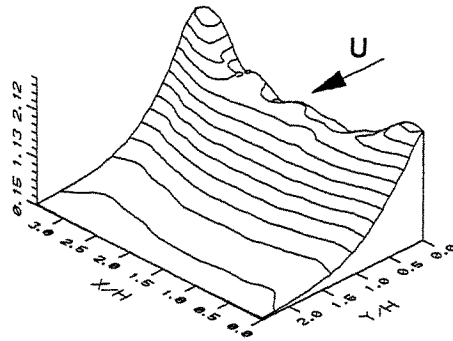


Fig. 3. Mean square of pressure

The first ten computed eigenvalues are listed in Table 1. The distribution of all the 204 normalized eigenvalues is depicted in Figure 4. It can be seen that the first eigenvalue exceeds by approximately two orders of magnitude the remaining eigenvalues.

Mode	Eigenvalue
1	160.287
2	1.714
3	1.603
4	1.165
5	0.623
6	0.578
7	0.530
8	0.412
9	0.372
10	0.298

Table 1. First 10 eigenvalues

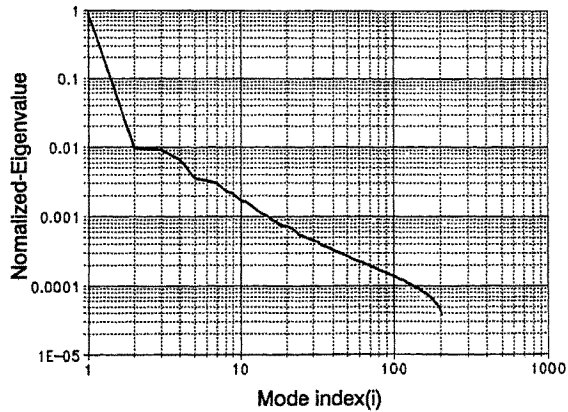


Fig. 4. Normalized eigenvalues  $\lambda^0 / \sum_j \lambda^0$  versus  $i$

The eigenvectors (modes) associated with the first four eigenvalues are shown in Figure 5. The dominant participation of the first mode is apparent when the plots of the pressure mean square, Figure 3, and the first mode, Figure 5, are compared. This is in agreement with observations for a smaller data set, Bienkiewicz et al [1], and for the one-dimensional covariance analysis, Holmes and Best [3], and Macdonald et al [4].

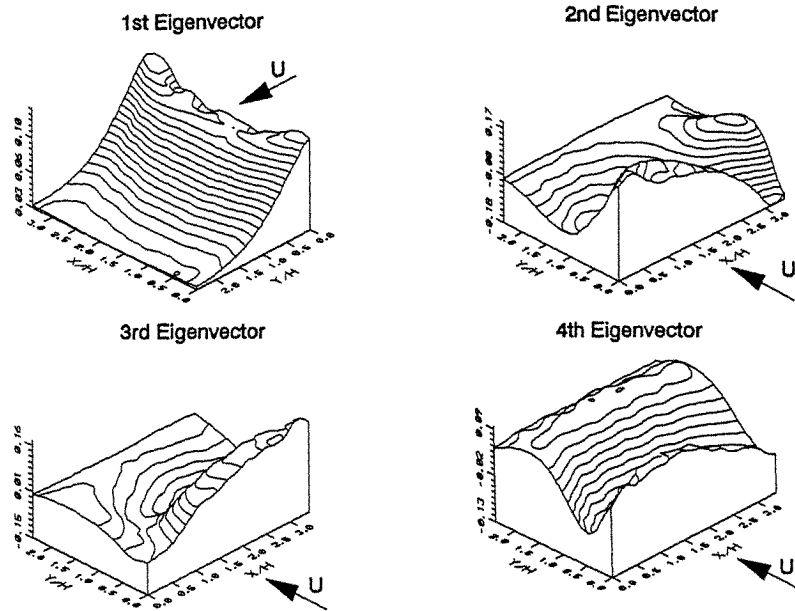


Fig. 5. Eigenvectors of roof pressure

The POD results can be used to reconstruct the original pressure field, Eqs. 3 and 4. This process is illustrated in Figure 6.

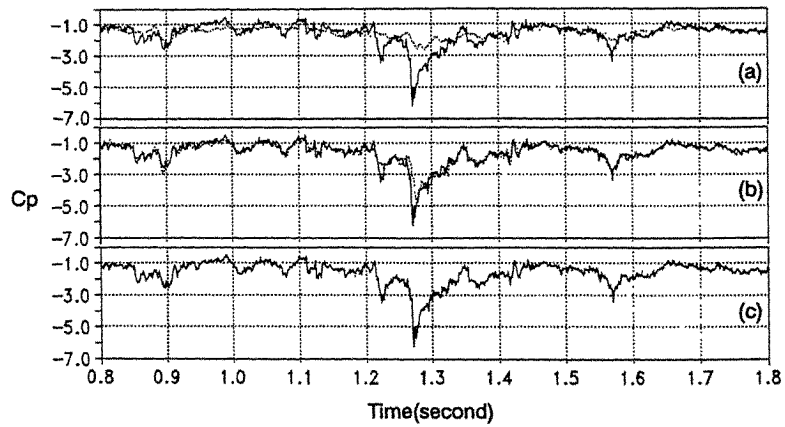


Fig. 6. Original (solid line) and reconstructed (dotted line) pressure using one (a), ten (b), and sixty (c) modes

The original time series of point pressure is compared with the pressure resulting from modal reconstruction. A pressure tap exhibiting the largest magnitude of the negative pressure (tap marked with an open circle in Figure 1) is considered and the depicted time series is centered on the measured largest negative peak pressure.

A similar comparison for the area-averaged pressure is shown in Figure 7. The pressure time series averaged over six taps (a tap marked with an open circle, Figure 1, and five solid-circle taps surrounding that tap) is considered. As shown, an excellent representation of the pressure, averaged over the tributary area associated with the considered taps, is obtained using only three modes.

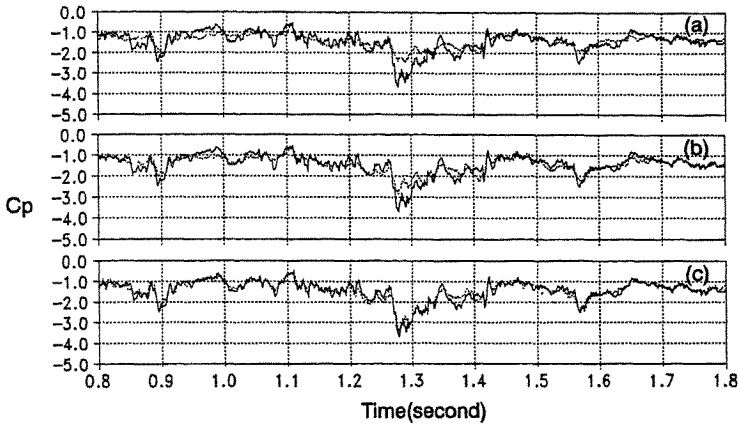


Fig. 7. Area-averaged original (solid line) and reconstructed (dotted line) pressure using one (a), two (b), and three (c) modes

The pressure reconstruction error is depicted in Figure 8 and 9.

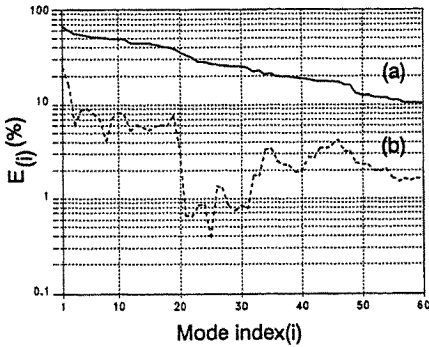


Fig. 8. Reconstruction error for point (a) and area-averaged (b) peak pressure

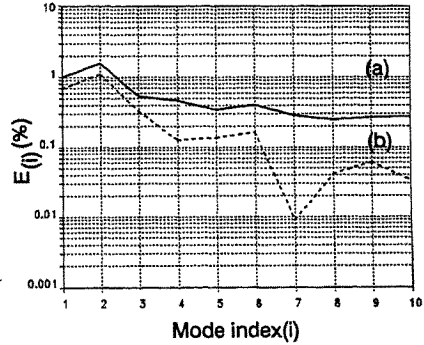


Fig.9. Reconstruction error for point (a) and area-averaged (b) mean pressure

The error is computed by calculating the difference between the original and reconstructed pressure and by normalizing it using the original pressure. The effect of the number of modes on the error associated with reconstruction of the largest negative peak (Figures 6 and 7, time instant of 1.27 sec) are illustrated in Figure 8. It can be seen that 60 modes are required to represent the peak point pressure with the error of approximately 10%. Thus approximately 30% of the computed modes (60 out of the total of 204) are needed in this case. As shown in Figure 8, reconstruction of the area-averaged peak pressure requires 3 modes, i.e. less than 2% of the total number of modes.

The reconstruction error for the mean pressure is shown in Figure 9. Only the first mode is needed for representation of the mean point and area-averaged roof pressure with the error of approximately 1%.

## 5. Conclusions

The presented data show that the results of the proper orthogonal decomposition of the multi-channel roof pressure exhibit properties similar to those reported for smaller data sets. The first mode makes the most significant contributions and its shape resembles the distribution of the pressure mean square. It is shown that modal reconstruction of point peak pressure can be obtained with the error of 10 % when approximately 30% of the computed (204) modes are used in the pressure reconstruction. Only one mode is needed for reconstruction of the mean pressure with the error of 1%.

## Acknowledgments

Work described in this paper has been conducted as part of Task 3 of the CSU/TTU Cooperative Program in Wind Engineering. Support for the Program has been provided by the U.S. National Science Foundation through a Cooperative Agreement BCS-8821542. Partial support of the described effort has been also provided by Shimizu Corporation, Japan.

## References:

1. B. Bienkiewicz, H.J. Ham and Y. Sun, "Proper orthogonal decomposition of roof pressure", Preprints of the Second Colloquium on Bluff Body Aerodynamics and Applications, Melbourne, Australia, December 1992.
2. Ueda, H., K. Hibi, Y. Tamura and K. Fujii, "Multi-channel simultaneous fluctuating pressure measurement system and its applications", submitted to *J. of Wind Eng. and Ind. Aerodyn.*
3. J.D. Homes and R.J. Best, "An approach to the determination of wind load effects on low-rise buildings", *J. Wind Eng. Ind. Aerodyn.*, 7 (1981) 273-287.
4. P.A. Macdonald, J.D. Holmes and K.C.S. Kwok, "Wind loads on circular storage bins, silos and tanks. III. Fluctuating and peak pressure distributions", *J. Wind Eng. Ind. Aerodyn.*, 34 (1990) 319-337.

## Pressure factors for edge regions on low rise building roofs

J. D. Ginger and C. W. Letchford

Department of Civil Engineering  
The University of Queensland  
Brisbane Queensland Australia 4072

### Abstract

Point and area-averaged pressures are presented for enclosed low rise (height (h) / breadth (b) = 1/3) building roof, based on 1:100 scale wind tunnel measurements obtained in a simulated suburban atmospheric boundary layer. Large magnitude mean and peak suction pressures were measured close to the leading edges under the separating shear layer. Significantly larger magnitude mean and peak pressures were measured on 0.2h (wide) by 1.0h (long) rectangular edge strips compared to the pressures on 1.5h by 1.0h roof sections. Pressure factors of the order 3.0 for suction pressures and 1.4 for positive pressures were obtained for these regions.

### 1. Introduction

Wind tunnel tests carried out on low rise (height (h) / breadth (b) < 1/3) building roofs by Kind [1] and Ginger [2] amongst others have shown that the largest pressures were experienced close to edge discontinuities (ie. leading edges), in regions of flow separation. Ginger [2] and Ginger and Letchford [3] also studied the spatial and temporal characteristics of the pressures in these regions.

Flow mechanisms over sharp edged roofs are characterized by shear layer separation and subsequent vortex formation. Ginger [2] measured large magnitude mean and fluctuating pressures under the 2D separation bubble for wind flow normal to the separating edge (ie.  $\beta = 0^\circ$ ) and under the 3D conical vortex for oblique wind directions (ie.  $\beta = 15^\circ$  to  $75^\circ$ ) in simulated suburban atmospheric boundary layer flow conditions. Large magnitude mean and peak suction pressures were measured within a 0.2h wide region from the separating edges. The largest magnitude point suction pressures were measured for  $\beta \sim 30^\circ$  close to the apex of the 3D conical vortex.

Most wind loading codes (eg. AS1170.2 [4]), prescribe the quasi-static design approach for determining peak wind loads on low rise buildings. In this method the fluctuating surface pressures depend entirely on the fluctuating wind velocity in the atmospheric boundary layer. Although the quasi-static design is satisfactory for regions where the flow impinges directly, it is not suitable for determining peak pressures where flow separation and vortex formation takes place. Local pressure factors are prescribed to account for the highly intermittent larger magnitude pressures in the flow separation regions.

Ginger [2] and Ginger and Letchford [3] showed that fluctuating suction pressures were spatially well correlated over a length of 1.0h, on 0.2h wide rectangular strips along the separating edges under the 2D separation bubble and the 3D conical vortex. The larger magnitude pressure fluctuations under the 3D conical vortex for  $\beta \sim 30^\circ$  to  $60^\circ$  were better correlated than the pressure fluctuations under the 2D separation bubble for  $\beta = 0^\circ$ . Furthermore, for a particular wind direction, conditionally sampled data showed that the peak suction pressures were better correlated than the time averaged pressures. The regions appropriate for applying pressure factors on low rise building roofs in turbulent boundary layer flow conditions are identified as 0.2h by 1.0h rectangular edge strips along the separating edges.

## 2. Experimental procedure

Tests were carried out in the 3 m wide by 2 m high by 12 m long Boundary Layer Wind Tunnel in the Department of Civil Engineering, University of Queensland. A terrain category 3 (AS1170.2 [4])  $z_0 = 0.2\text{m}$  boundary layer was simulated at a length scale of 1/100 as described by Ginger [2]. A 300mm by 300mm square planform 100mm high (h) flat roof enclosed building model with pressure tappings on the roof was tested in this flow. Area-averaged pressures were measured on six 100mm by 150mm panels (labelled A, B, C, D, E, F) using six uniformly spaced tappings, as shown in Figure 1. Area averaged pressures were also measured on 100mm by 20mm rectangular edge strips (labelled  $A_s$  to  $F_s$ ) surrounding the parent panels using five uniformly spaced tappings also shown in Figure 1. The effect of wind orientation ( $\beta$ ), was studied over the range  $0^\circ$  to  $360^\circ$ . The point and area-averaged pressure measurement systems had good frequency response beyond 100Hz at which point they were lowpass filtered and sampled at 250 Hz for 30s. The positive direction was defined as downwards. The results presented here are the average of five runs.

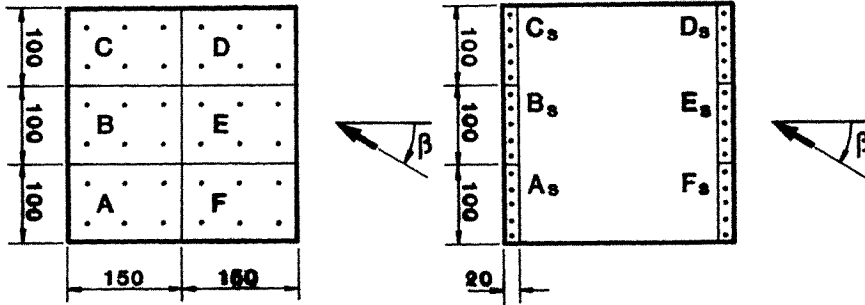


Figure 1. Roof panels A to F and edge strips  $A_s$  to  $F_s$

## 3. Results

The mean pressure coefficient contour plots for  $\beta = 0^\circ$  and  $30^\circ$  presented in Figure 2, identify the large suction pressure regions under the separated shear layers. The large magnitude mean and peak suction pressures are within a 0.2h wide region close to the leading edges for all wind directions.

Ginger [2] and Ginger and Letchford [3] also showed that the time averaged and peak suction pressures under the separated shear layer were well correlated over a distance greater than 1.0h and for  $\beta = 30^\circ$  progressively larger suction pressures were shown to be progressively better correlated. The pressures were also increasingly better correlated with increased elongation of the separated shear layer in the axial direction of the 3D conical vortex, as the wind orientation was increased from  $0^\circ$  to  $75^\circ$ . The variation of mean, standard deviation, maximum and minimum area-averaged pressure coefficients with wind direction on the six panels (A to F) is summarized in two cases: a roof corner panel F and a roof middle panel E in Figures 3 and 4 respectively.

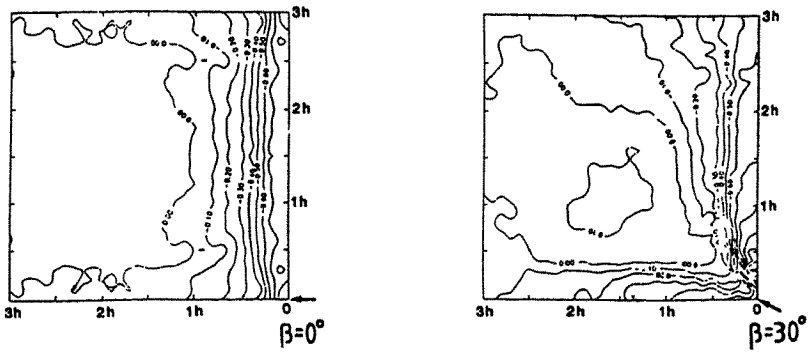


Figure 2. Mean pressure coefficient contours on building roof,  $\beta = 0^\circ$  and  $30^\circ$  respectively.

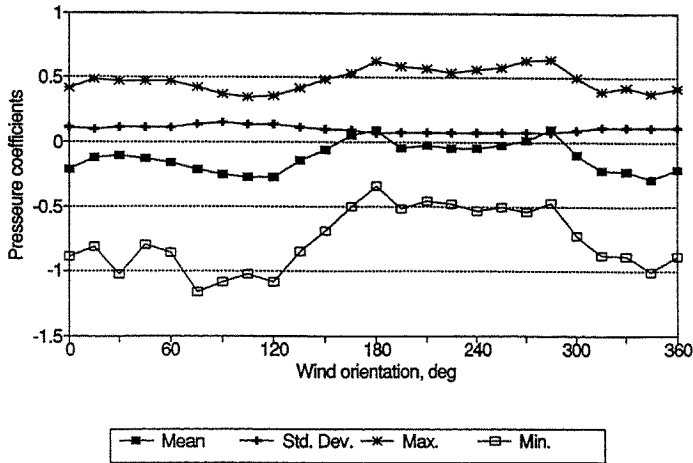


Figure 3. Pressure coefficient variation for roof corner panel F.

For roof corner section F, Figure 3 shows that the formation of a 2D separation bubble for  $\beta = 0^\circ$  and  $90^\circ$  and 3D conical vortices for other wind directions generate large magnitude mean and fluctuating suction pressures. The location of the pressure tappings in relation to the flow separation regions generate the largest magnitude mean, maximum and minimum pressure coefficients of -0.29, 0.64 and -1.16, for  $\beta = 345^\circ$ ,  $285^\circ$  and  $75^\circ$  respectively.

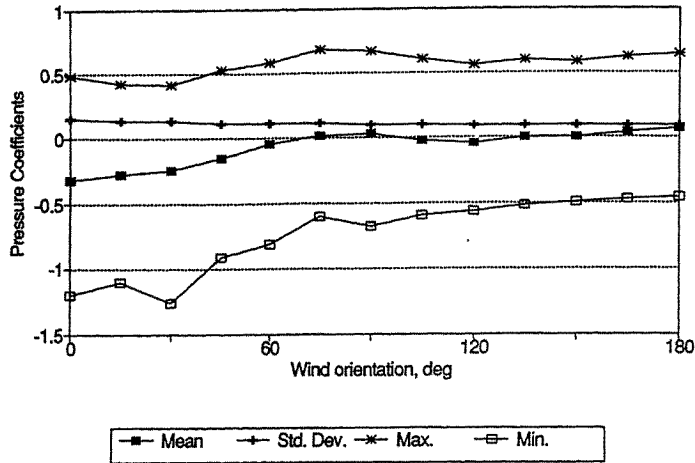


Figure 4. Pressure coefficient variation for roof middle panel E.

For roof middle panel E, Figure 4 shows that the formation of a 2D separation bubble for  $\beta = 0^\circ$  and 3D conical vortices for other wind directions again generate large magnitude mean and fluctuating suction pressures. The largest magnitude mean, maximum and minimum pressure coefficients of -0.32, 0.68 and -1.26, were measured for  $\beta = 0^\circ, 75^\circ$  and  $30^\circ$  respectively. The variation of mean, standard deviation, maximum and minimum area averaged pressure coefficient with wind direction on the six edge strips ( $A_s$  to  $F_s$ ) is summarized in two cases: a roof corner edge strip  $F_s$  and a roof middle edge strip  $E_s$  in Figures 5 and 6 respectively.

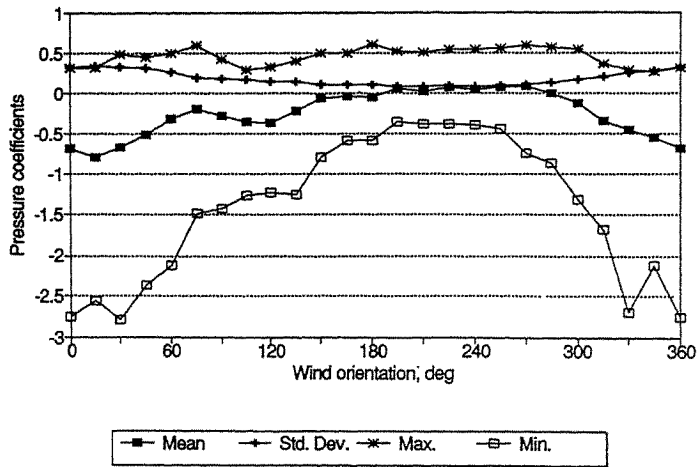


Figure 5. Pressure coefficient variation for roof corner strip  $F_s$ .

For roof corner edge strip  $F_s$ , Figure 5 shows the familiar formation of a 2D separation bubble for  $\beta = 0^\circ$  and 3D conical vortices for other wind directions. The largest magnitude mean, maximum and minimum pressure coefficients of -0.79, 0.57 and -2.75 were measured for  $\beta = 15^\circ, 285^\circ$  and  $0^\circ$  respectively.



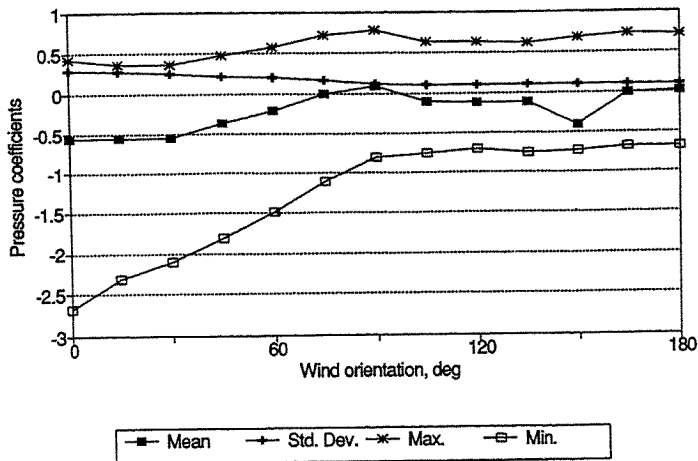


Figure 6. Pressure coefficient variation for roof middle strip  $E_5$ .

For roof middle edge strip  $E_5$ , Figure 6 again shows the formation of a 2D separation bubble for  $\beta = 0^\circ$  and 3D conical vortices for other wind directions. The largest magnitude mean, maximum and minimum pressure coefficients of -0.56, 0.77 and -2.68 were measured for  $\beta = 0^\circ, 90^\circ$  and  $0^\circ$  respectively.

AS1170.2 [4] suggests a local pressure factor  $K_1$  of 1.5 for areas of size  $a^2$  within  $a$  of the edge and 2.0 for areas of size  $a^2/4$  within  $a/2$  of the edge. The definition of  $a$  is the lesser dimension of 20% of plan dimension or the roof height. Here  $a$  takes the value  $0.2 * 300\text{mm} = 60\text{mm}$ , and  $a^2 = 3600\text{mm}^2$  and  $a^2/4 = 900\text{mm}^2$ . The pressure factors prescribed in AS1170.2 [4] are used with mean pressure coefficients and gust dynamic pressures, i.e. *peak suction pressures* applied on the entire roof. This paper determines local pressure factors ( $K_1$ ) for the 0.2h by 1.0h edge strips using the area-averaged pressure data on the parent panel. The strips shown in Figure 1 have areas of  $2000\text{mm}^2$ , thus lying between the provisions of the code[4]. Values of  $K_1$  can be estimated from the ratios of the peak strip pressure to peak panel pressure (maxima/maxima and minima/minima) and are shown in Figures 7 and 8 respectively.

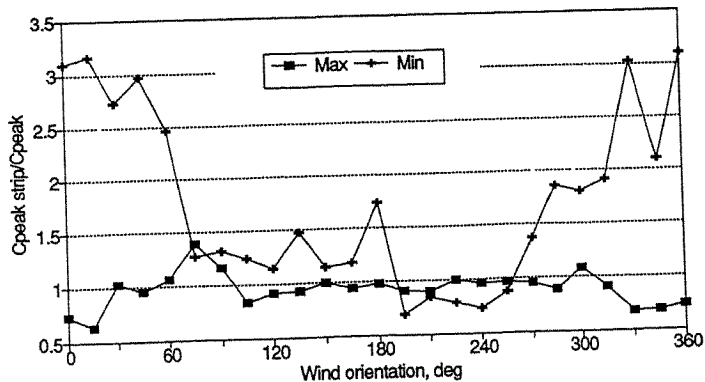


Figure 7. Estimated local pressure factors for corner strip regions

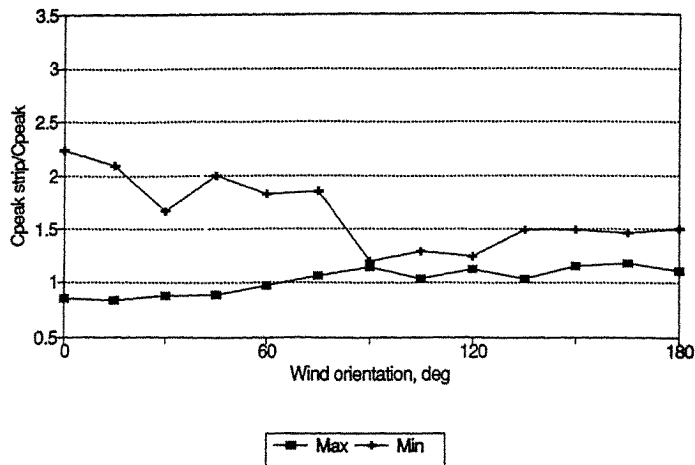


Figure 8. Estimated local pressure factors for middle strip regions

Figure 7 shows that a  $K_1$  of  $\sim 3.0$  is appropriate for suction pressures for  $\beta = 0^\circ$  to  $60^\circ$  and  $\sim 1.4$  for positive pressures for  $\beta = 90^\circ$  for the roof corner edge strip regions. Figure 8 shows that a  $K_1$  of  $\sim 2.0$  is appropriate for suction pressures for  $\beta = 0^\circ$  to  $60^\circ$  and  $\sim 1.2$  for positive pressures for  $\beta = 90^\circ$  for the roof middle edge strip regions. These pressure factors are to be used with peak suction pressures acting on  $1/6$  the roof area within which the respective edge strips are contained. It is important to note that the peak suction pressure acting on  $1/6$  the roof area is of a larger magnitude than the peak pressure acting on the entire roof. Thus the code [4] values appear to underestimate the pressure factors for suction pressures on  $0.2h$  by  $1.0h$  edge strips in separation regions.

#### 4. Conclusions

Large magnitude mean and fluctuating pressures were measured within regions of flow separation on low rise building roofs. In turbulent boundary layer flows, the large magnitude mean and peak suction pressures were measured within a region  $0.2h$  from the separating edge. These pressures were well correlated over a distance of  $1.0h$ . In adopting a quasi-static design approach local pressure factors are required for separated flow regions along edges. Appropriate factors on  $0.2h$  by  $1.0h$  edge strips referenced to  $1.5h$  by  $1.0h$  roof panels encompassing these edge strips are  $1.4$  and  $3.0$  for positive and suction pressures respectively for the worst wind directions.

#### 5. References

1. R.J. Kind, Worst suction near edges of flat roof tops on low-rise buildings, *J. Wind Eng. Ind. Aerodyn.*, 25, (1986) 31-47.
2. J.D. Ginger, Characteristics of large pressures in regions of flow separation on low rise building roofs, PhD Thesis, University of Queensland, 1992.
3. J.D. Ginger and C.W. Letchford, Characteristics of large pressures in regions of flow separation, 2nd Int. Coll. on Bluff Body Aerodynamics and Applications, Dec. 1992, Melbourne, Australia.
4. Australian standard, SAA loading code Part 2: Wind loads AS1170.2 (1989).

## EFFECT OF FREE-STREAM TURBULENCE ON PEAK SUCTIONS OBSERVED BELOW CORNER VORTICES

H. W. Tieleman, E. C. Panzer, O. K. Rediniotis and R. E. Akins\*

Department of Engineering Science and Mechanics  
Virginia Polytechnic Institute and State University  
Blacksburg, Virginia, U.S.A. 24061-0219

\*Department of Physics and Engineering  
Washington and Lee University  
Lexington, Virginia, U.S.A. 24450

**Abstract:** Extremely high suction pressures on the top surface of surface-mounted prisms occur for oblique angles of attack and are believed to be associated with the existence of the conical corner vortices. Evidence is presented that incident small scale turbulence produced by small circular rods placed upstream of a surface mounted prism has an appreciable effect on the observed pressure distributions. For angles of varying incidence between  $0^\circ$  and  $40^\circ$ , incident small scale turbulence increases the magnitude of the mean and fluctuating pressure coefficients. With incident small scale turbulence, typical pressure distributions associated with the conical vortices exist.

### 1. Introduction

Unsteady aerodynamic forces on rigid prisms depend primarily on the nature of the incident flow and the prism geometry. These forces can be felt in two different ways [1].

a. Unsteady *buffeting* wind loads, where the surface pressures respond to large scale wind gusts as if they were unsteady flows. Many wind engineers assume that the dynamic interaction of large scale wind gusts with a structure is the primary cause of the large pressure peaks (positive or negative) experienced by the structure. Consequently, they argue that successful prediction of surface pressures and wind loads from wind tunnel simulation experiments should be based on the careful scaling of the turbulence integral scale [2]. However, this approach fails to predict the extreme suction pressures (rms and peak) on the sides and roofs, especially in regions of flow separation and strong vortex formation.

b. *Interaction* of the incident turbulence with different flow regions adjacent to the surface of bluff bodies. This interaction modifies boundary and shear layer development, changes the position of flow reattachment and is responsible for changes in vortex behavior. The latter being directly associated with the observed high suction pressures which exist in areas of flow separation and flow reattachment [3] and strong vortex flows observed on roofs near corners for cornering wind directions [4].

### 2. The Effect of Small Scale Turbulence

Surface pressures on the sides and leeward surface of two dimensional rectangular cylinders are affected primarily by the turbulence intensity of the incident flow. Gartshore in 1973 [5] and with his co-workers in 1975 [6] demonstrated that increased levels of small-scale turbulence led to increased entrainment and growth of the separated shear layers, resulting in the well known modification of the drag and base pressure depending on the dimensions of the cylinder relative to its critical length-to-width ratio. Many other investigators have come to similar conclusions, also demonstrating that the integral scale of the incident turbulence has little effect on the pressure distributions on the side and rear faces of two-dimensional rectangular cylinders.

### 3. Surface-Mounted Prisms

Experimental results presented in References 7 and 8 demonstrate clearly that the pressure distribution on the side and leeward faces of surface-mounted prisms are primarily correlated with the incident small-scale turbulence content. The latter being quantified by the modified small-scale spectral parameter as originally introduced by Melbourne in 1978 [9].

Results from surface pressure observations on the top surfaces of rectangular surface mounted prisms (plan dimensions larger than the prism height) submerged in a variety of turbulent boundary layers have indicated that extreme suction pressures exist near the corner and along the edges for oblique azimuth angles. Systematic experimental studies conducted at the University of Western Ontario [8,10] revealed the following general conclusions:

- a. Mean pressure coefficients decrease in magnitude while the fluctuating pressure coefficients increase in magnitude with increasing turbulence intensity.
- b. The magnitude of all pressure coefficients generally increase with prism height,  $H$ .
- c. For near cornering flow, pressure coefficients with the largest magnitudes occur along two lines (rays) which intersect with the corner and make an angle of approximately 17 degrees with either leading edge. Along these rays, the magnitude of the pressure coefficients decreases rapidly with increasing normalized distance ( $s/H$ ) from the prism corner.

It is obvious that vortex dynamics plays an important role in the understanding of the flow inside the corner (delta wing) vortex and of the associated pressure distribution below these vortices. Presently, a complete understanding of these phenomena and how they are affected by the prism geometry and the nature of the incident flow is lacking.

### 4. Experimental Plan

#### 4.1 Basic Principles

As discussed before, surface pressures (mean and fluctuating) on the sides and base of surface mounted prisms are primarily controlled by the level of incident small scale turbulence and correlate poorly with integral scales. Therefore it must be suspected that surface pressures on the top surface of surface-mounted prisms are also affected by the content of the small scale turbulence in the incident flow. The correctness of this idea must be tested by studying the effect of small scale turbulence on the surface pressure distribution. This can be achieved experimentally by creating incident small-scale turbulence by placing a small diameter rod upstream of the prism in otherwise smooth flow.

#### 4.2 Experimental Equipment and Procedures

For this experiment a 51 cm  $\times$  51 cm suction wind tunnel was used with an open circuit and capable of speeds in the test section (2.5 m long) up to 20 m/s. The background turbulence in the test section is less than 0.5%, while the boundary layer thickness on the tunnel floor is less than 20 mm, so that the top surface of the prism is exposed to nonturbulent flow unless a rod was in place. A prism ( $H = 84\text{mm}$ ,  $W = 105\text{mm}$  and  $L = 86\text{mm}$ ) was mounted on the tunnel floor. Pressure taps (1mm diameter) are located in the top surface along two lines perpendicular to the leading edge at distances  $x_1/H = 0.379$  and  $x_2/H = 0.681$  respectively (Fig. 1). Pressure observations at angles of attack of  $\alpha = 0, 30, 35, 40$  and 45 degrees were made along these lines as well along the 17 degree ray. Each of four different circular rods (4.8, 3.2, 2.4 and 1.6 mm in diameter) was mounted approximately 30mm upwind of the prism to create the small scale incident turbulence. A free stream air speed of approximately 10m/s was used for all tests. A Pressure System solid state pressure scanner (model ESP-16TL) was used to make the high-frequency observations. The analog outputs are multiplexed within the sensor unit and amplified internally to provide a full scale output of  $\pm 5$  VDC. The accuracy rating of the system falls within  $\pm 0.1\%$  of full scale output. The observed pressure signals were

sampled at a rate of  $200\text{Hz}$  for a duration of 40 seconds. Mean, RMS and negative peak pressure coefficients are extracted from the observed pressure records observed at each pressure tap. All coefficients are based on the dynamic pressure associated with the free stream velocity.

## 5. Experimental Results

### 5.1 Flow Observations Downstream of the Circular Rods

These observations were made in a small wind tunnel located at Washington and Lee University. A single hot film probe was located approximately  $30\text{mm}$  behind the rod and aligned with the edge of the rod. Data were sampled at  $10\text{kHz}$ . The mean and standard deviation of each record was computed in order to obtain a turbulence intensity. The spectral density function of each record was computed to verify the frequency content of the signal. The ambient flow had a background turbulence intensity of less than 1%. Turbulence intensity, actual frequency measured in the wake, Reynolds Number for the cases run are listed in Table 1. The Strouhal Number for each case was nominally 0.2.

Diameter mm	Turbulence Intensity %	Actual Frequency kHz	Re
1.6	10	3.28	2800
2.4	11	2.25	4200
3.2	15	1.64	5600
4.8	20	1.06	8400

Table 1. Flow properties in the wakes of circular rods

The wavelengths of the observed velocity fluctuations relative to the prism height ( $H = 84\text{mm}$ ) varied between 0.3 and 0.1 depending on the rod diameter and are in agreement with the wavelength suggested by Melbourne [9] in the definition of his small scale spectral density parameter. Figure 2 presents the turbulence intensities downstream of the rod including the Gartshore results [5].

### 5.2 Pressure Observations

Figures 3 and 4 represent the distribution of pressure coefficients along the line  $x/H = 0.681$  (see Fig. 1) for azimuth angles of zero and 35 degrees respectively. For both cases the lowest magnitudes are observed without the upstream rod in place while larger magnitudes (lower mean and peak pressure coefficients) are observed with any of the upstream rods in place. Similar observations can be made from Figure 5 which represents the variation of the pressure coefficients along a ray for which  $b = 17$  degrees (see Fig. 1). Maximum effect on the pressure coefficients is observed with rods placed approximately  $30\text{mm}$  upstream from the prism corner and approximately  $25\text{mm}$  below the top surface of the prism. Also the largest effect on the pressure coefficients is noticeable with the largest diameter rod in place. Based on these preliminary results of this experiment, evidence is presented that incident small scale turbulence affects the surface pressures on the top surface of surface-mounted rectangular prisms for either normal or oblique angles of attack.

## 6. Conclusions

As Gartshore [5] pointed out small scale incident turbulence influences the base pressure coefficients of rectangular 2-D cylinders. These observations are the result of increased entrainment into the separated shear layers together with a reduced radius of curvature of these layers.

Based on the observed increases in magnitude of the pressure coefficients on the top surface of the surface-mounted prism, it can be concluded that similar effects are experienced by separated shear layers for oblique angles of attack bringing the vortices closer to the top surface of the prism resulting in increased magnitudes of both mean and fluctuating pressure coefficients.

**References**

1. P. W. Bearman, Proc. 3rd U.S. National Conference on Wind Engineering, Florida, (1978) 265-272.
2. N. J. Cook, Proc. International Workshop on Wind Tunnel Modeling Criteria and Techniques in Civil Engineering Applications, Gaithersburg, Maryland, (1982) 126-136.
3. P. J. Saathoff and W. H. Melbourne, *J. Wind Eng. Ind. Aerodyn.*, 32 (1989) 121-134.
4. K. C. Mehta, M. L. Levitan, R. E. Iverson and J. R. McDonald, *J. Wind Eng. Ind. Aerodyn.*, 41-44 (1992) 181-192.
5. I. S. Gartshore, Boundary Layer Wind Tunnel, Rep. 4-73, University of Western Ontario, London, Canada, 1973.
6. A. Laneville, I. S. Gartshore and G. V. Parkinson, Proc. 4th International Conference of Wind Effects on Structures, London, U.K., (1975) 333-341.
7. H. W. Tieleman, *J. Wind Eng. Ind. Aerodyn.*, 41-44 (1992) 923-934.
8. H. W. Tieleman, Proc. Bluff Body Aerodynamics and Application II, Melbourne, (1992).
9. W. H. Melbourne, Proc. 5th International Conference on Wind Engineering, Fort Collins, Colorado, (1979) 541-552.
10. H. W. Tieleman, D. Surry and J. X. Lin, Proc. Inaugural Conference of the British Wind Engineering Society, Cambridge, England (1992).

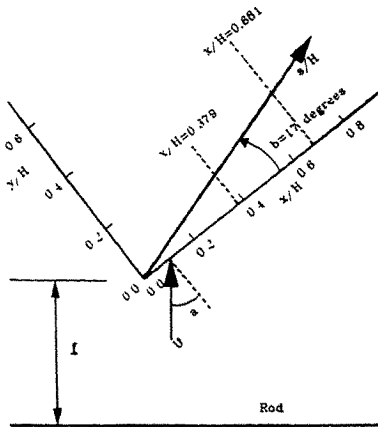


Fig. 1 Definition diagram.

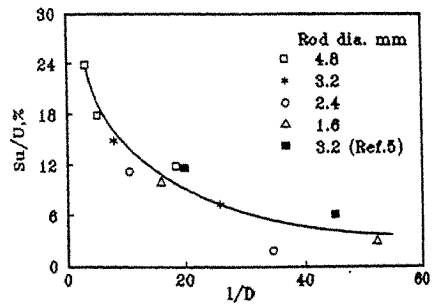
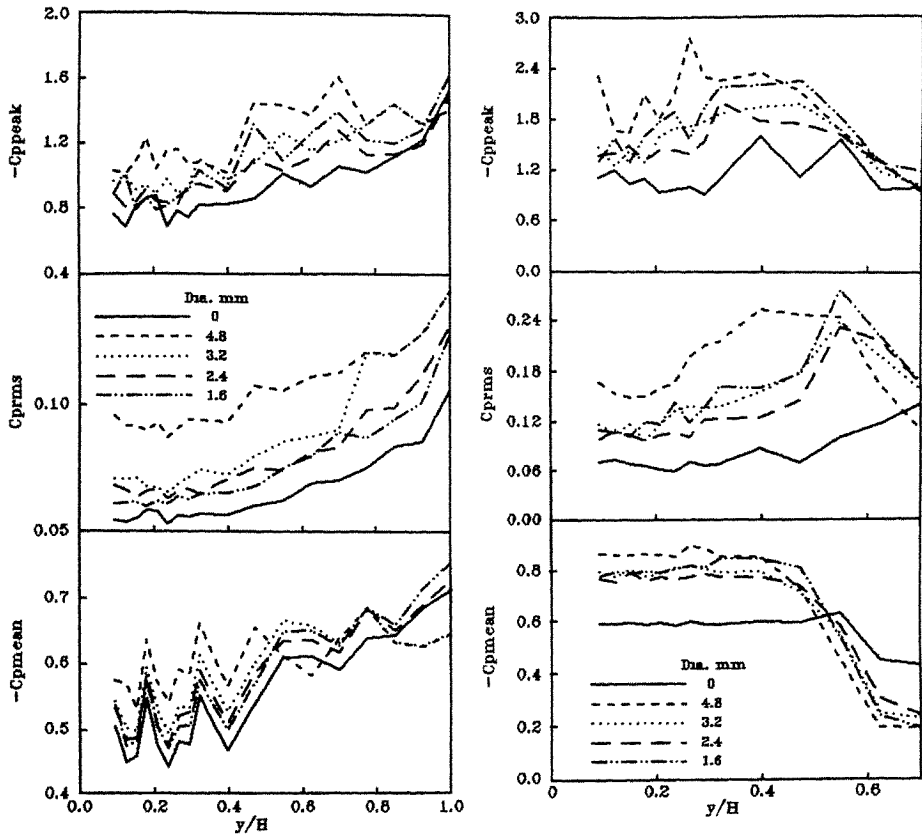


Fig. 2 Turbulence intensities behind circular rods.



Figs. 3 and 4. Distribution of mean, rms and peak pressure coefficients along the line  $x/H = 0.681$  for azimuth angles of 0 and 35 degrees respectively. Incident flow modified by turbulence from upstream circular rods.

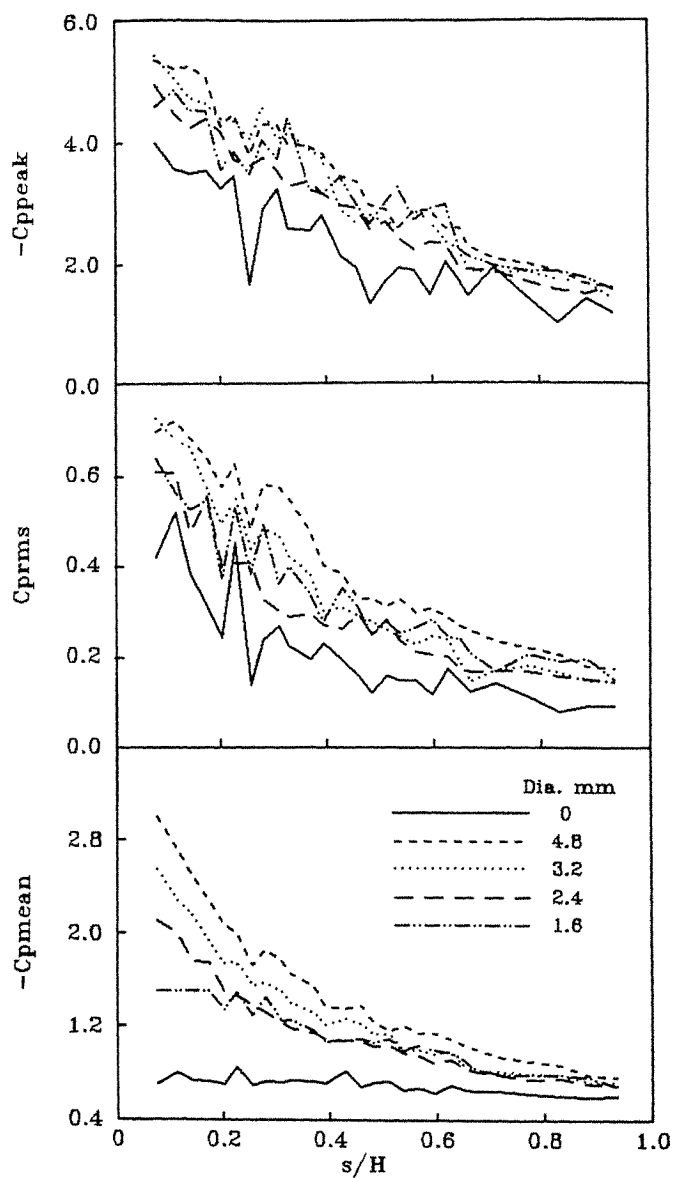


Fig. 5 Distribution of mean, rms and peak pressure coefficients along the line with ray angle of 17 degrees and for an azimuth angle of 35 degrees. Incident flow modified by turbulence from upstream circular rods.



## Effect of Aspect Ratio on Roof Wind Loads of Low-Rise Rectangular Buildings

R. Sankaran

James Cook Cyclone Structural Testing Station  
James Cook University of North Queensland  
Townsville, Q 4811 Australia.

**Abstract:** A wind tunnel study has been conducted to evaluate the effect of building aspect ratio on roof wind loads. Various rectangular building models with different aspect ratios and roof pitches were used to obtain mean and peak pressure co-efficients at various locations of the roof. A comparison of these pressure co-efficients with those obtained from the Australian Wind Loading Code (AS 1170.2-1989) suggests that the aspect ratio of buildings has a significant effect on roof wind loads.

### Introduction

The external pressures on various components (e.g. the walling, roofing etc.) of a low-rise enclosed structure such as a house can be readily calculated using a Standard or Code (for example, Australian Wind Loading Code [1]). However, the effect of aspect ratio (= length/width) of buildings is not fully addressed by Codes or Standards. Full-scale measurements obtained on agricultural buildings by Hoxey and Moran [2] indicate that, in general, low rise building's roof pressure distribution is significantly affected by its length. However, these measurements involved several full-scale buildings situated at different sites. Therefore, these results may have been influenced by site conditions as well as multiple parameter changes. More recently, Holmes and Paterson [3] conducted a computational study on arched-roof buildings which showed that increasing the aspect ratio of a building produces an increase in magnitude of positive and negative pressures on both windward and leeward walls as well as roof.

A systematic wind tunnel study is described here which investigates the effect of building aspect ratio on roof wind loads. Measurements of pressure co-efficients are presented for buildings with different aspect ratios and roof pitch angles for different wind directions. The measured pressures are compared to the Code values.

### Experimental Arrangement

All the measurements were carried out in the Boundary Layer Wind Tunnel, James Cook University of North Queensland. The test section measurements are 17.5 m long, 2.5 m wide and 2 m high. A maximum speed of about 22 m/s can be achieved at the measurement location.

A scale of 1:200 was used for the wind tunnel models. All the models had same width and height (200 mm and 150 mm respectively) and only their lengths were varied to 200 mm, 400 mm, 800 mm, and 1600 mm which provided aspect ratios of 1, 2, 4, and 8 respectively. A schematic diagram of the model is shown in Figure 1. The models were manufactured in modules so that their aspect ratios and roof pitch angles can be changed easily. Three different roof pitches ( $\theta=7.5^\circ$ ,  $22.5^\circ$  and  $45^\circ$ ) were considered in the present study. Each model was fixed on the 1.7 m diameter turntable which could be rotated through  $360^\circ$  to vary the relative angle of attack of the wind.

External pressures were measured using pressure taps distributed both at end and mid length sections of the models. Two Setra 237 pressure transducers mounted within "Scanivalves" were used for this purpose. The "Scanivalves" were mounted within the models and connected to the pressure taps using 450 mm long p.v.c. tubings, which incorporated two restrictors to get a flat frequency response within  $\pm 10\%$  up to 200 Hz. This response is adequate for the present testing.

The atmospheric boundary layer corresponding to terrain category 2 was simulated in the wind tunnel using a 300 mm high fence mounted across the entrance of test section on carpeted floor. The

mean velocity and turbulence intensity profiles, measured at the model location (without the model), are shown in Figure 2. Profiles, predicted using the semi-theoretical equations of Deaves and Harris [4], are also included in Figure 2. The agreement between the experiments and theoretical predictions is good as seen from Figure 2.

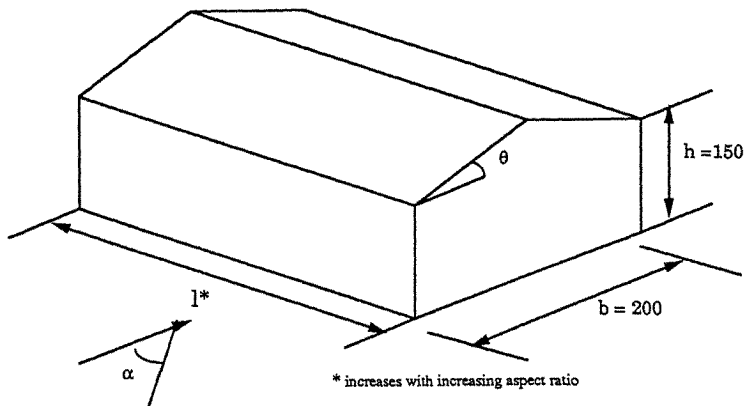


Figure 1. Schematic diagram of the low-rise building

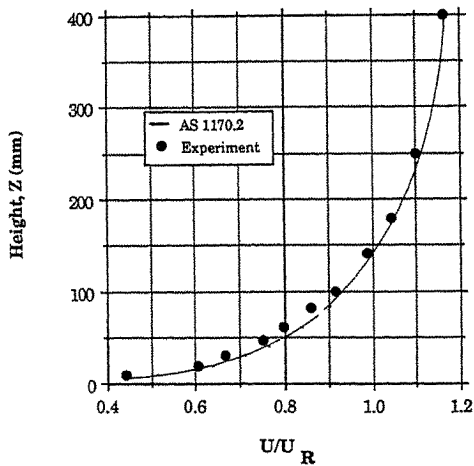


Figure 2a. Comparison of measured and predicted velocity profiles

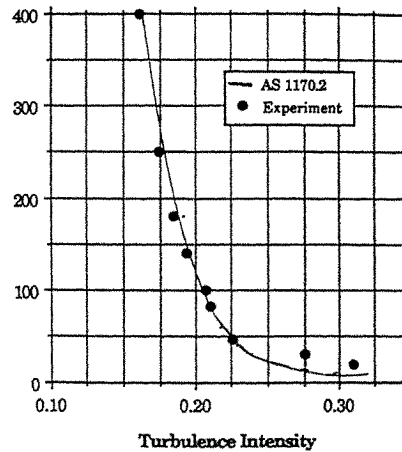


Figure 2b. Comparison of measured and predicted turbulence intensity profiles

The velocity and turbulent intensity profiles were measured using a TSI 1210-10 hot film probe in conjunction with a TSI IFA 100 constant temperature anemometer. The anemometer voltages were linearised using TSI model 1072 lineariser before sampling. All the data were sampled at 1000 Hz for a duration of 32 Sec, which corresponds to about 60 minutes in full-scale.

Static pressure and freestream velocity were measured using a pitot-static tube, mounted about 1 m above the wind tunnel floor. The pitot-static tube was also used for calibrating the hot film probe at the beginning and end of each run.

## Results and Discussion

### Effect of Aspect ratio

The measured external point pressures and “pneumatically averaged” pressures (obtained using manifolds) were reduced to non-dimensional pressure co-efficients to enable direct comparison with the Australian Wind Loading Code, AS1170.89.

The effect of building aspect ratio on mean pressure co-efficients is given in Figure 3a. The variation of mean pressure is plotted at six discrete locations between the eaves and ridge of models of roof pitch angle  $7.5^\circ$ . It can be seen that the mean pressure increases systematically with an increase in the aspect ratio. While the increase is maximum around the midway point between eaves and ridge, the minimum increase occurs close to the ridge. Although the Code values are not shown, mean pressure co-efficients were well below the Code values for all cases. The present results are generally consistent with the observations of [2] and [3]. While increasing the aspect ratio of an arched roof building from 0.3 to 5, the computational study of Holmes and Paterson showed an increase in roof mean pressures by a factor of 2.7. In the present study, as can be seen from Figure 3a, the mean pressures increase by a factor of 3.4 (Maximum) while the aspect ratio is increased from 1 to 8.

Figure 3b shows the effect of aspect ratio on minimum pressure co-efficients measured at mid-length section for the same model ( $7.5^\circ$  pitch) for  $0^\circ$  wind angle of attack. The Code recommended values are also plotted in this figure as solid lines. It can be seen that, once again, there is a systematic increase in minimum pressure co-efficients as the aspect ratio of the building is increased from 1 to 8. For aspect ratios of 1 and 2, the measurements are well within those specified by the Code. When the aspect ratio is increased to 4, the pressure co-efficients are higher than for aspect ratios 1 and 2 but well within the Code limit except near the ridge. A further increase in aspect ratio to 8, increases the pressure co-efficients significantly; all the measured pressure co-efficients (between eaves and ridge) exceed the Code limit with the difference being small near the eaves and maximum around the midway point between eaves and ridge.

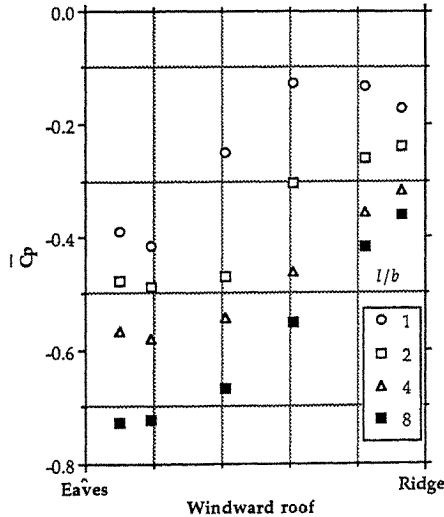


Figure 3a. Effect of aspect ratio on mean pressure co-efficient for  $7.5^\circ$  roof pitch building

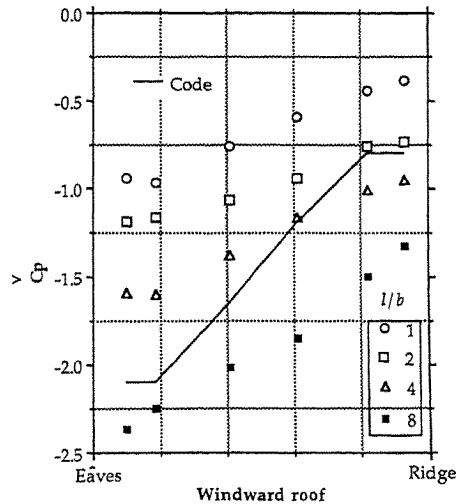


Figure 3b. Effect of aspect ratio on minimum pressure co-efficient for  $7.5^\circ$  roof pitch building

### Effect of Roof pitch angle

The measured minimum pressure co-efficients for buildings with constant eaves height but various roof pitch angles are plotted in Figures 4a, 4b and 4c for aspect ratios 2, 4 and 8 respectively. The air flow is at an angle of attack of  $0^\circ$ .

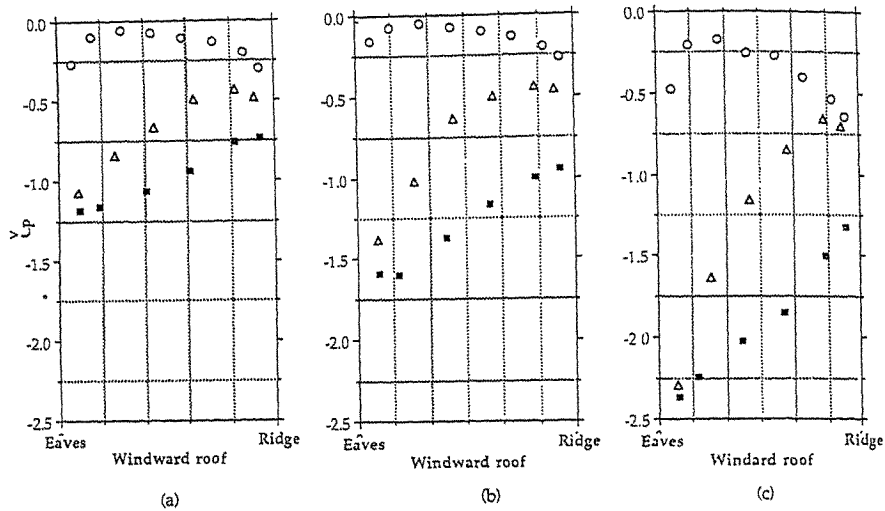


Figure 4. Comparison of minimum roof pressure co-efficients for various roof pitch angles.  
(a)  $l/b = 2$ , (b)  $l/b = 4$ , (c)  $l/b = 8$ . ■  $7.5^\circ$  ▲  $22.5^\circ$  ○  $45^\circ$

Several interesting observations can be made from these figures. In general, for a given building aspect ratio, as the roof pitch angle is increased the roof pressures decrease. In particular, there is a small reduction in pressures near the eaves, when the roof pitch angle is increased from  $7.5^\circ$  to  $22.5^\circ$ . Further, the minimum pressures decrease monotonically as the ridge is approached and substantial reduction occurs around the ridge. In contrast, when the roof pitch angle is increased from  $22.5^\circ$  to  $45^\circ$ , significant reduction in roof pressure occurs near the eaves with very little change near the ridge. This can be explained as follows: for both  $7.5^\circ$  and  $22.5^\circ$  roof pitches, flow separates at the leading edge, inducing higher suction pressures near the eaves. However, for  $22.5^\circ$  pitch angle, flow re-attaches earlier, as compared to  $7.5^\circ$  case, thus yielding a reduction in negative pressures (at locations away from the leading edge). When the roof pitch angle is increased further to  $45^\circ$ , the flow does not separate at the leading edge as evident from the small suction pressure near the eaves. The flow remains attached to about 75% of the length of the windward roof and has a tendency to separate near the ridge, especially for the higher aspect ratio building. All these observations are consistent with the results of Kanda and Maruta, 1992 [5]. Since the results of [2] may have been influenced by multiple geometric parameter variation (the eaves height of various buildings was *not* constant in [2]) results of this study were not directly compared to those in [2].

When the measured pressures were compared with the Code values (not shown), it was clear that *all measurements* were higher than the Code for a building with aspect ratio of 8 for roof pitches of  $7.5^\circ$  and  $22.5^\circ$ . However, for  $45^\circ$  roof pitch, only the ridge region experiences higher than Code recommended pressure. For a building with aspect ratio of 4 and  $7.5^\circ$  roof pitch, the minimum pressures are well within the Code's limit except near the ridge. For  $22.5^\circ$  pitch, the pressures are higher than the Code upto about midway between the eaves and ridge but becomes equivalent to the Code for the remaining length. For  $45^\circ$  roof pitch, all the measured minimum pressures are significantly lower than those provided in the Code.

### Effect of angle of attack of wind

Figures 5a and 5b show the measured minimum pressure co-efficients for wind directions 0° and 30° and for buildings with roof pitches of 7.5° and 22.5° respectively. These figures contain data obtained at mid length section of buildings with aspect ratios of 4 and 8.

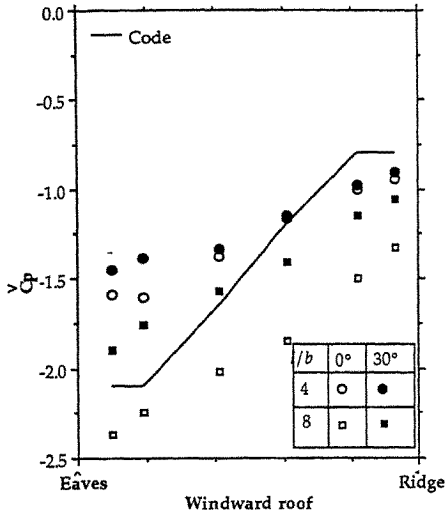


Figure 5a. Comparison of minimum pressure co-efficients for wind angles 0° and 30°. Roof Pitch = 7.5°

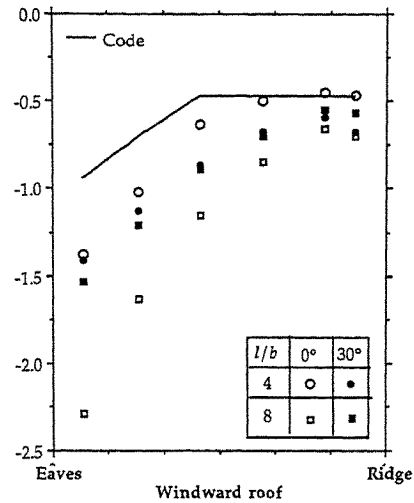


Figure 5b. Comparison of minimum pressure co-efficients for wind angles 0° and 30°. Roof pitch = 22.5°

Both the figures show that roof pressures increase as the aspect ratio is increased, as noted previously. For buildings with roof pitches of 7.5° and 22.5° and an aspect ratio of 8, as the wind angle of attack is increased from 0° to 30°, there is a small reduction in roof pressures. When the angle of attack of wind is changed from 0° to 30°, for the model of aspect ratio 4, opposite trends are produced for roof pitch angles 7.5° and 22.5°. For a roof pitch of 7.5°, the roof pressures are slightly lower for 30° wind direction as compared to 0°. However, with a roof pitch of 22.5° roof pressures for 30° wind direction are marginally higher than 0° wind. This observation is consistent with the conclusion of [5] that peak pressures on building roofs need not occur at 0° wind direction. It is conjectured here that the conical vortex, originating from the leading edge of the building at oblique wind angles, may be increasing the roof pressures for the building with aspect ratio of 4 but may not be strong enough to influence the roof pressures at mid length section of the building with aspect ratio of 8. This aspect will be investigated in detail in a future study.

### Pneumatically Averaged Pressures

In addition to the point pressures, pneumatically averaged pressures were measured at mid length section and end section of the models with aspect ratios of 4 and 8 at 0° wind angle. The manifold and tubing system, used for these measurements, was designed using the guidelines provided by Holmes and Lewis [6]. Figures 6a and 6b show the pneumatically averaged pressures for aspect ratios 4 and 8 respectively. It is clear that all previous comments made with respect to the effect of roof pitch angle on minimum pressures are valid for these figures for both end section and mid length section. It is interesting to note that mid length pressures are greater than end section pressures for 7.5° roof pitch model. However, this trend is reversed with an increase in roof pitch angle. For 22.5° the mid length pressure is about the same as end section pressure and for 45° the end section pressures are lower than mid section pressures. These trends are same for both aspect ratios (Figures 6a and 6b). While the limited data collected at the end section does not enable the

identification of the precise mechanism behind this behaviour, it is believed that three dimensional effects associated with end section play a dominant role in creating the observed trends. Future work will address this aspect.

All the measured pneumatically averaged pressure co-efficients are well within the Code limits except that of 45° roof pitch model with aspect ratio of 8. For this case, the positive pressure just behind eaves is about 15% higher than that suggested in the Code.

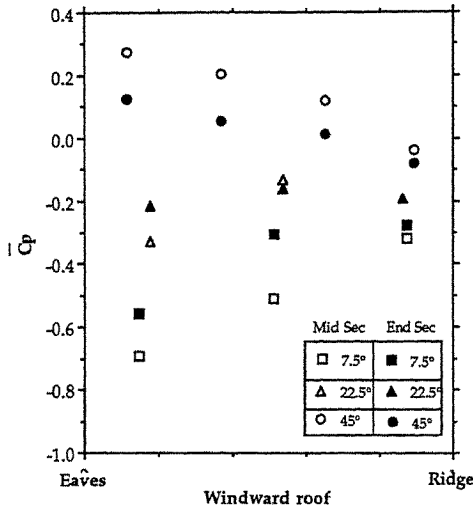


Figure 6a. Pneumatically averaged pressures  $l/b = 4$

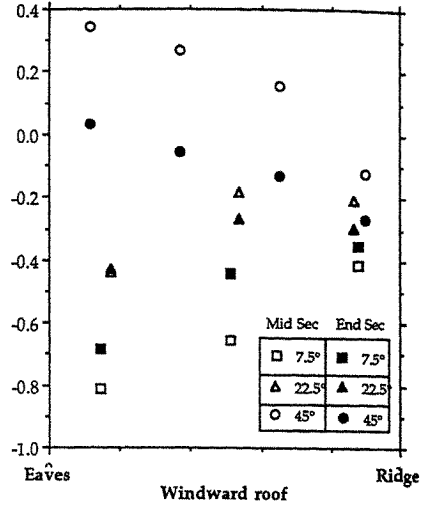


Figure 6b. Pneumatically averaged pressures  $l/b = 8$

### Conclusions

A wind tunnel study has been carried out which explored the effect of building aspect ratio on roof wind pressures. Results of the study indicate significant increase in windward roof pressures as the building's aspect ratio is increased. However, for a given aspect ratio, the measured roof pressures decrease with an increase in roof pitch angle. When the measured pressures are compared to the Code, it is noted that the Code does not adequately cover design pressures for large buildings with high aspect ratios (>8). Therefore, a wind tunnel investigation is required to obtain realistic design pressures for such buildings.

A comparison of peak pressures obtained for wind from various directions support the earlier suggestion that occurrence of critical pressures depends on various building parameters (such as the roof pitch angle, aspect ratio etc.) and does not always occur at 0° wind direction.

### References

- Standards Australia, Australian Standard 1170, Part 2: Wind Loads, 1989, Sydney, NSW.
- Hoxey, R.P. and Moran, P. : A Full-Scale Study of the Geometric Parameters that Influence Wind Loads on Low rise Buildings, Journal of Wind Engineering and Industrial Aerodynamics, Vol. 13, pp 277-288, 1983.
- Holmes, J.D. and Paterson, D.A. : Mean Wind Pressures on Arched-roof Buildings by Computation, Proc. of Second International Colloquium on Bluff Body Aerodynamics and Applications, Melbourne, 7-10 Dec. , 1992.
- Deaves, D.M. and Harris, R.I. : A Mathematical Model of the Structure of Strong Winds, Construction Industry Research and Information Association (U.K) Report 76, 1978.
- Kanda, M. and Maruta, E. : Characteristics of Fluctuating Wind Pressure on Long Low-rise Buildings with Gable roofs, Proc. of Second International Colloquium on Bluff Body Aerodynamics and Applications, Melbourne, 7-10 Dec. , 1992.
- Holmes, J.D. and Lewis, R.E. : Optimization of Dynamic Pressure Measurement Systems. II Parallel tube-manifold systems. Journal of Wind Engineering and Industrial Aerodynamics, Vol. 25, pp 275-290, 1987.

## Wind loads on a horizontal grandstand roof of large aspect ratio

K.M. Lam and A.P. To

Department of Civil and Structural Engineering  
The University of Hong Kong, Pokfulam Road, Hong Kong

**Abstract:** We measured wind pressures on the wind tunnel model of a horizontal rectangular grandstand roof of aspect ratio 6.6:1. Forces on panels of the roof were obtained from real time integration of pressures. The results suggested that distributions of roof pressures and panel forces attributed largely to flow separation on the top surface of the roof. Spatial coherence measurements revealed large-scale organised fluctuations associated with the separation, which were suggested to play an important role in the generation of roof loads.

### 1. Introduction

Grandstand roofs are usually designed as large roof structures cantilevered at the rear of the grandstands. As a result, they demand particularly critical analysis of wind effects. All wind loading codes, however to our knowledge, treat grandstand roofs under the category of canopy roofs [1]. This presents practical difficulties to design engineers relying solely on wind codes because most grandstand roofs possess aspect ratios larger than those of the canopy roofs covered in the codes. Moreover, grandstand roofs are usually much larger in size than common canopy roofs.

On the other hand, codification of wind loads on canopy roofs is itself much less mature than codification for roofs of enclosed buildings. This is due to the relatively scarce amount of wind tunnel and full scale data on canopy roofs or grandstand roofs [2,3,4].

This paper describes the wind tunnel results of wind pressures and panel loads on the grandstand roof of a proposed stadium in Hong Kong. The roof laying almost horizontally is 13.7 m above ground. Its rectangular form of 90.2 m by 13.7 m gives an aspect ratio of 6.6:1. The sloping sitting area of grandstand rises to a height of 9.6 m, presenting a blockage of 70%. A 1:100 rigid model of the grandstand and roof was tested in simulated wind of the open to suburban terrain type, without any other structures in the vicinity (Fig. 1). The simple geometry of the grandstand roof and the general testing conditions may allow our wind tunnel data to be added to the small database of wind loads on grandstand roofs.

The structural design of the roof is that it will be supported by a truss with all the loads transmitted to the ground via a row of columns arranged along the longer span of the grandstand. Hence, it is convenient to divide the roof laterally into a row of parallel panels (Fig. 2). In this paper, we shall present and discuss the wind pressure data, followed by the panel loads. We shall also look into correlations among the wind pressures and with the panel loads, with a view to explore the generation mechanism of wind loads on the roof.

### 2. Experimental Procedures

The investigation was carried out at the boundary layer wind tunnel of the Department of Civil and Structural Engineering at the University of Hong Kong. The wind tunnel is of the recirculating type with a working section of 3 m wide by 1.8 m high and 12 m long. Spires and roughness elements were used to provide at the model location a simulated atmospheric boundary layer of the general type terrain in the Hong Kong Wind Code [5]. This terrain type, which specifies a power law exponent of 0.19 for the wind speed profile, corresponds somewhere

between the open land and suburban terrain in other codes.

The 1:100 rigid model of the grandstand roof is shown in Fig. 1. The roof was built of an acrylic sheet with 180appings installed on one side only. Two sets of test were run, one with theappings on the top and the other with theappings on the bottom surface of the roof.

The 180appings were grouped into 30 parallel panels, each with sixappings (Fig. 2). Wind pressures at the sixappings in a panel were measured simultaneously with six pressure transducers, each of which being connected to the tapping through flexible tubing and a scanivalve. The six scanivalves were synchronized so that wind pressure measurements on each panel were performed simultaneously and the instantaneous wind force on each panel could be obtained from pressure integration.

Acquisition of wind pressures from the transducers was performed with an analog-to-digital convertor in a 486 computer. The computer also performed computation of statistical properties of wind pressures and panel forces. Wind loads acting downwards on the roof were defined positive. The dynamic pressure at the roof height was monitored with a pitot-static tube and used as the reference pressure.

### 3. Results and Discussion

#### 3.1. Roof pressure distributions

Time-averaged mean net wind pressures on the roof were obtained from the combination of mean pressures measured on the top and bottom surfaces. Results are shown in Fig. 3 as contours of mean net pressure coefficients.

For a roof structure, flow separates at the leading edge and may reattach downstream. The separation bubbles are usually characterized by high suction. For  $\theta = 0^\circ$ , a large region of suction (negative) pressure extends from the leading edge to almost the trailing edge. Flow visualisation smoke pictures, not reported here, have shown that a separation bubble formed on the top surface and that no well-organised separation was observed on the bottom surface. Thus, we believe that the region of net suction for  $\theta = 0^\circ$  is due to the separation bubble on the top surface of the roof, which extends almost to the trailing edge at the central portion of the roof span. Towards the lateral edges, the extent of the bubble is decreasing; and secondary separations of a smaller scale seem to occur at a further downstream location at the edges.

For  $\theta = 30^\circ$  and  $60^\circ$ , changes in shape of the extent of the main separation bubble with wind directions are observed from the pressure contours. It is also observed that the other region of suction pressures gains significance, with the suggestion of patterns resembling the delta-wing vortices found on roofs of enclosed buildings.

When wind comes from the rear of the grandstand, the pressure contours for  $\theta = 180^\circ$  and other angles not shown here suggest a smaller extent of suction pressures induced by the separation bubble. This may be due to the blunt vertical rear wall of the sitting area providing accelerated flow right in the windward edge of the roof.

For  $\theta = 90^\circ$  when wind blows parallel to the longer span of the roof, a much smaller region of suction is observed, suggesting that the flow reattaches shortly downstream of the windward edge. The net pressure on a large part of the roof downstream is close to zero.

#### 3.2. Panel forces

As mentioned earlier, our tapping arrangement enabled the roof be divided into 30 panels. On each panel, we were able to obtain the real time history of the force on its top surface from integration of six pressure signals. The force signal on the bottom surface was also obtained, but not simultaneously with the force on the top surface. For the two forces, their mean values and extreme values, minimum and maximum, were calculated. The time-averaged mean net downward force can be obtained from a combination of mean values of the two surface forces. Extreme values of the net force, however, cannot be known exactly. Nevertheless, the two



combinations of extreme values of the two surface forces will give the bounds for the maximum and minimum values of the net downward force on the panel.

Distributions of mean, minimum and maximum values of the panel force coefficients along the roof span are shown in Fig. 4 for some wind angles. The reference dynamic pressure and areas of the panels are used in the force coefficients. For  $\theta = 0^\circ$ , the big separation bubble on the top surface leads to upward lift (negative force) occurring at all times over all parts of the roof except the two outermost panels on either side. For  $\theta = 60^\circ$ , large lifting forces occur on panel number 1, that is the most windward panel, probably due to the effect of both separation bubbles there. For other panels, the extreme values of net forces cover most downward loading and upward lift, with the maximum uplift much bigger in magnitude than the maximum downward load. The force distribution for  $\theta = 90^\circ$  suggests the occurrence of a separation bubble over the small-numbered panels. Forces on other panels have mean values close to zero, with fluctuations between  $C_F = -0.3$  to  $0.3$ . When wind comes from the rear of the grandstand, smaller uplifts are found and "maximum" bounds of the net forces cover some downward loadings.

Variations of panel forces with wind angles are shown in Fig. 5 for some selected panels, namely panel 1 on the edge, panel 15 at the middle and the panel 8 at quarter span of the roof.

### 3.3. Spectra and coherence

Fig. 6a shows the power spectra of the top surface panel force on panels 1, 8 and 15 at  $\theta = 0^\circ$ . The bulk of energy is found in a broad spectral peak roughly centred roughly at 8 Hz. This can be due to coherent fluid actions associated with the separation bubble. The Strouhal number corresponding to this peak is  $St = fh/U_h = 0.16$ , where  $U_h$  is the mean wind speed at the height  $h$  of the roof. Similar broad peaks at  $St = 0.12$  were found for the panel forces on a stadium roof of an elliptical form and it was suggested that the peaks are due to vortex shedding at the upstream sector of the stadium [6]. For  $\theta = 90^\circ$ , when the separation bubble does not cover panels 8 and 15, the 8 Hz peak in the spectra in Fig. 6b show much cleaner appearance. This supports that the peak is due to the separation bubble so that the fluctuations are induced on panels 8 and 15, without the fine-scale turbulent motions. For  $\theta = 180^\circ$ , the spectra in Fig. 6c show weaker effect of the separation bubble. In all spectra in Fig. 6, two less pronounced broad peaks around 0.8 Hz and 2 Hz are also observed. We are not certain of the cause of these peaks. There is also a sharp peak at 16 Hz, which is due to the resonance vibration of the model roof.

For  $\theta = 0^\circ$ , coherence spectra between pressures on top surface of panel 15 are shown in Fig. 7a. The three coherence spectra shown are formed between the wind pressure on the most upwind tapping  $a$  and those at tapping  $b$  next downwind, tapping  $d$  near the middle and the most downwind tapping  $f$  respectively. For the close separation  $a-b$ , coherence above 50% is found concentrated within two broad frequency ranges around 8 Hz and 2 Hz. With increasing separating distances, coherence falls probably due to the violent turbulent motion inside the separation bubble. Fig. 7b shows the coherence between the top surface panel force of this panel 15 with the pressures at the three tapping locations  $b$ ,  $d$  and  $f$ . No significant coherent contribution to force generation is observed from the wind pressures, neither is any concentration of coherence on particular frequencies observed. This suggests a large proportion of fine-scale turbulent components in the wind pressure signals at locations under the separation bubble.

For wind direction across the panels,  $\theta = 90^\circ$ , coherence among pressures on a panel represents the lateral correlation of wind pressures. For panel 8, coherence spectra in Fig. 8a of pressure at tapping  $a$  with those at tappings  $b$  and  $f$  respectively show that frequencies within the two broad peaks at 8 Hz and 2 Hz are well correlated laterally, with coherence remaining above 60% at the peaks. Correlation of pressures at these three tapping locations with the top surface force is shown in Fig. 8b. The high coherence of 80% at the two peaks suggests large contribution of wind pressures to the generation of wind loads at these frequencies. Fig. 8c shows the power spectra of the three pressure signals. The clear peak at 8 Hz attributes itself to fluctuations induced by the separation bubble at the upstream panels, which may also account for

the high spatial correlation in the absence of violent turbulence.

#### 4. Concluding Remarks

We present wind pressure and panel force data of a grandstand roof of a large aspect ratio. For wind direction perpendicular to the longer span of the roof, strong uplifting loads are measured, which are suggested to be caused by the occurrence of a large separation bubble on the top surface of the roof. With wind coming from the grandstand front, the spatial effect of the bubble extends almost over the entire roof. For wind direction along the longer span, the flow reattaches rapidly on the roof surface. The separation bubble leads to high suction pressures on the top surface, with violent pressure fluctuations resulting in large peak suction. However, these violent wind pressure fluctuations connected with fine-scale turbulent actions are not well correlated spatially; thus contribute little to the generation of wind loads. On the other hand, large-scale coherence pressures which are induced outside the separation bubble at a few broad frequency ranges seem to play an important role in the generation of wind loading on the roof.

#### References:

1. N.J. Cook, "The designer's guide to wind loading of building structures. Part 2: Static structures" (1990), Butterworths Press.
2. R.H. Bernard, *J. Wind Eng. Ind. Aerodyn.*, 8 (1981) 21-30.
3. W.H. Melbourne and J.C.K. Cheung, *J. Wind Eng. Ind. Aerodyn.*, 28 (1988) 401-410.
4. C.W. Letchford and J.D. Ginger, *J. Wind Eng. Ind. Aerodyn.*, 45 (1992) 25-45.
5. E.C.C. Choi, "Wind loading in Hong Kong, Commentary on the Code of Practice on wind effects, Hong Kong" (1983).
6. B.J. Vickery and M. Majowick, *J. Wind Eng. Ind. Aerodyn.*, 42 (1992) 1447-1458.

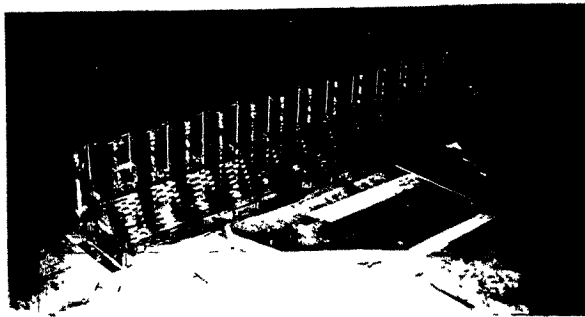


Fig. 1.  
Wind tunnel model  
of grandstand and  
roof.

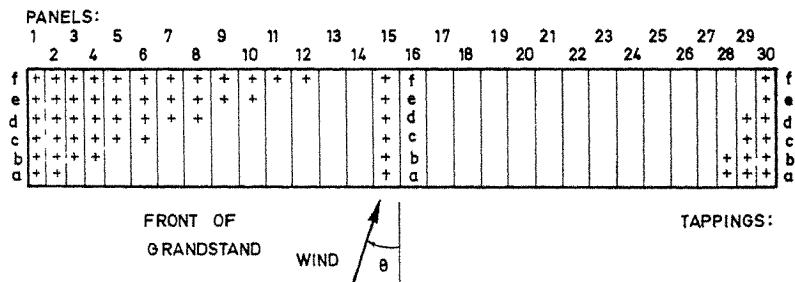


Fig. 2. Tapping and panel arrangement on roof.

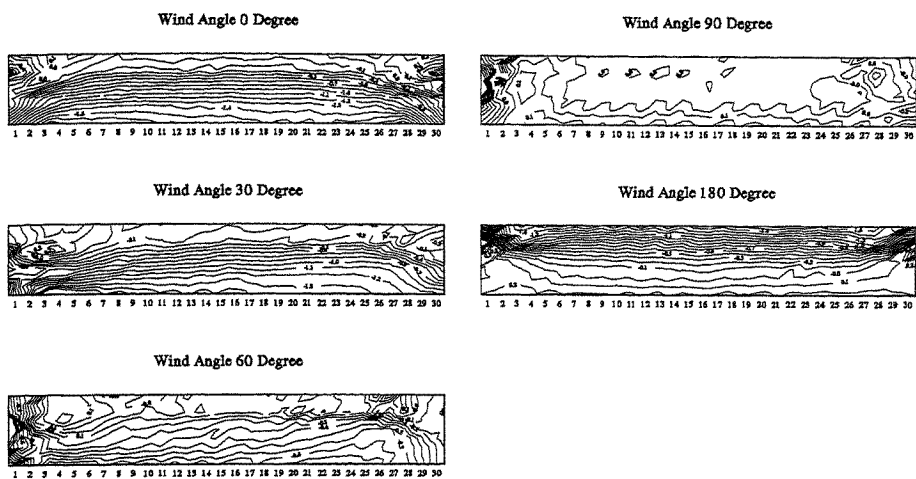


Fig. 3. Distribution of mean net pressure coefficients on roof.

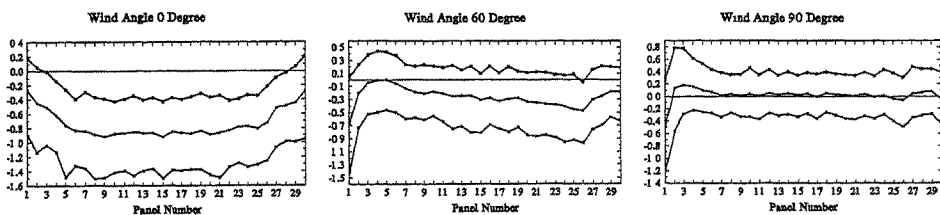


Fig. 4. Distribution of mean, minimum and maximum force coefficients on panels.

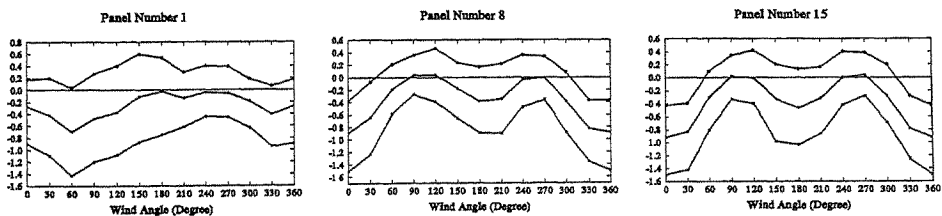


Fig. 5. Distribution of panel force coefficients with wind angle.

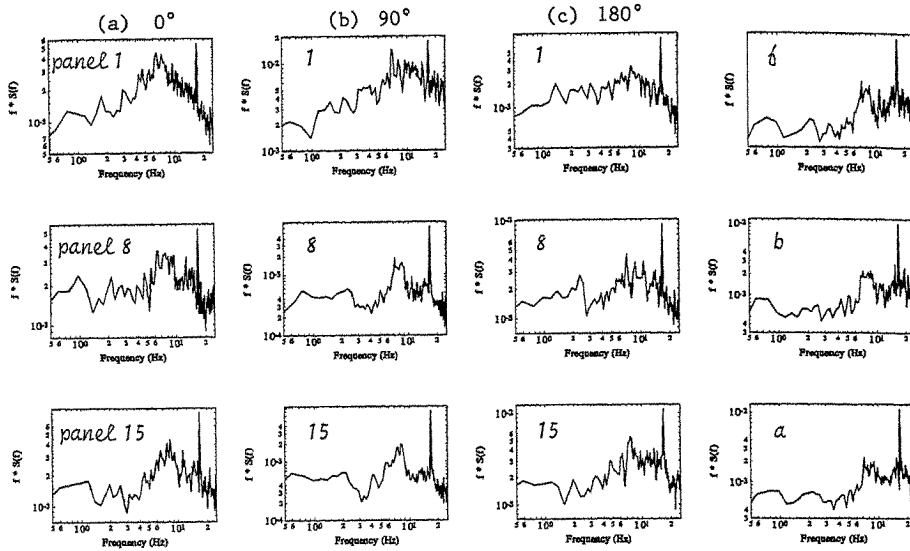


Fig. 6. Power spectra of top surface panel forces.

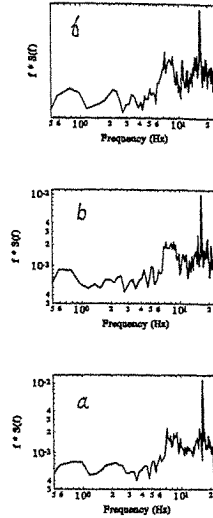


Fig. 9. Power spectra of pressure on panel 8.

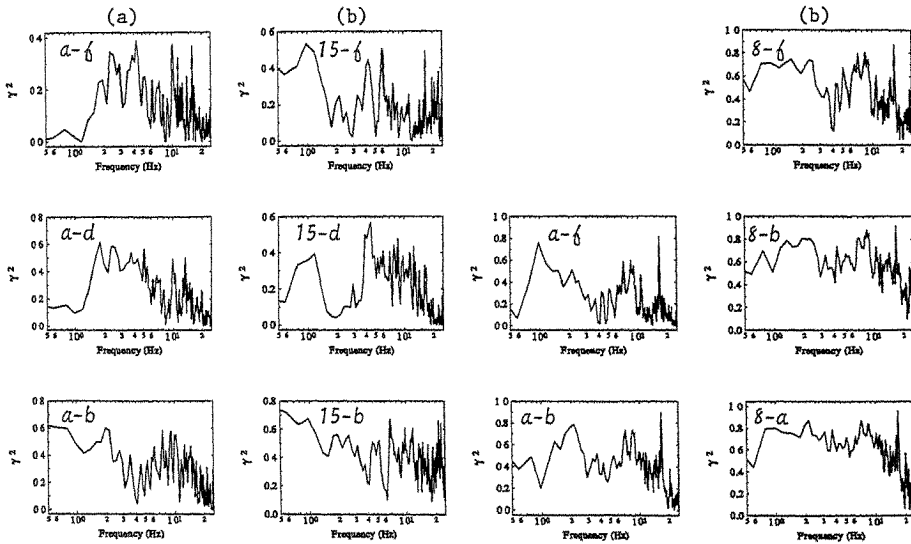


Fig. 7. Coherence spectra of wind pressure on panel 15 at 0° (a) with tapping a; (b) with panel force.

Fig. 8. Coherence spectra of wind pressure on panel 8 at 90° (a) with tapping a; (b) with panel force.

## **ANALYSIS OF A TENSION MEMBRANE HYPAR ROOF SUBJECTED TO FLUCTUATING WIND LOADS**

By P.K.F. Pun and C.W. Letchford

Department of Civil Engineering  
University of Queensland, Australia

### **1 Introduction**

Tension membrane structures can be thought of as thin prestressed fabric surfaces. Like cable net structures, tension membrane structures carry and transmit loads by direct tensile stress without bending or compression. They are large displacement structures that rely on geometrical stiffness and prestress to resist loads. The prestress is achieved either by using edge cables or pneumatics. Edge prestressed structures assume anticlastic shapes. A common anticlastic shape is that of the hyperbolic paraboloid, or hypar, which is a doubly curved saddle shape (Fig.1).

In warmer climates, the dominant loading for tension membrane structures is wind, due to their flexibility, light weight and large span, the very characteristics that make them so appealing. Yet, not much is known about the wind loads on these structures because of the uniqueness of each individual structure. This study aims to characterise the wind loads on a tension membrane hypar and to estimate the peak load effects of the structure due to wind load. The prototype is a free-standing 15mx15m in plan hypar roof. The curvature of the hypar is set by two high support points 7.5m high and two low support points 5m high. Using wind loads determined from boundary layer wind tunnel tests, estimates of the peak reactions at the corner supports were determined with the aid of the non-linear finite element package SHAPE. The covariance integration method was used for these estimates in order to obtain a more accurate description of the fluctuating load effects than that produced using the highly conservative quasi-steady method recommended by most wind codes.

### **2 Wind Tunnel Tests**

The wind tunnel tests were carried out in a 3mx2mx12m recirculating type boundary layer wind tunnel at the University of Queensland. All tests were carried out in a simulated Terrain Category 3 atmospheric boundary layer at a length scale of 1:100 and a velocity scale of 1:2. The boundary layer was formed using roughness elements upstream of the model and a grid and fence at the upstream end of the tunnel.

A rigid 1:100 scale model of the hypar was used. The model was made using two 2mm thick layers of perspex sandwiching a 1.5mm thick acrylic sheet. Eight pockets or manifolds were machined out from both the top and bottom perspex layers, each top and bottom pocket corresponding to a patch on the hypar as shown in Figure 2. Eight pressure tappings were made in each pocket, the tapping locations being chosen as the centroids of equal area triangles subdividing each patch. This arrangement for pressure measurement amounts to an area-averaging technique, which takes into account the spatial correlation of pressures over the patches.

PVC tubes transmit the pressures in each manifold to pressure transducers via Scanivalve switches. The model was mounted on a turntable in the wind tunnel with the

transducers and switches fixed beneath. The Scanivalve switches allowed top and bottom manifold pressures from each patch to be sent in turn to the transducers. The signals from the transducers were analog differenced to obtain nett (top-bottom) pressure differences on the roof. The signals were low pass filtered at 100Hz and sampled at 250Hz for 30s by a high speed data acquisition system.

Area averaged pressures were measured for the hypar to obtain mean, RMS and peak pressure coefficients for angles of attack from  $0^\circ$  to  $90^\circ$  in steps of  $15^\circ$ . The coefficients are referenced to the eaves dynamic pressure with eaves height at the level of the low support points of the hypar (5cm model height). Point pressure measurements were also obtained. Cross correlation coefficients for the patches were obtained using a spectrum analyser. As well as this, area averaged measurements were obtained with 40% and 60% blockages located underneath the hypar and for a grouped arrangement of four hypars. Oil surface flow visualisation tests were also conducted on models of 1.5mm and 6.0mm thicknesses to determine whether the incorrectly scaled thickness of the model would significantly affect the flow patterns and therefore the pressure measurements.

For the  $0^\circ$  angle of attack (Fig.3), high negative panel pressures were measured on panels adjacent to the windward high point, indicating the presence of conical vortices on the top surface edges near this high point. This was confirmed by the point pressure measurements and the flow visualisation tests. Flow over the rest of the surface was attached. For the  $90^\circ$  angle of attack, by symmetry, the vortices formed on the edges adjacent to the windward low point on the bottom surface. However these vortices were much weaker than the ones on the top surface at  $0^\circ$  because the velocity at the level of the low points (eaves height) was much smaller than that at the level of the high points.

The highest single mean panel pressure was found to be at  $45^\circ$  on panel A. However, the most severe overall loading would seem to occur near  $0^\circ$  with large opposing pressures occurring at the front and back of the roof or near  $90^\circ$  with large nett upward pressures over nearly the entire roof.

### 3 Structural Analysis

The structural analysis of the tension membrane hypar roof was carried out using the 'SHAPE' package. SHAPE is a non-linear finite element analysis package developed by Meek and Ho [1] for shape-finding and membrane analysis of shell and membrane structures.

Once a satisfactory shape of the hypar roof had been determined, load analysis was carried out on it. Fabric exhibits complex biaxial and non-linear stress-strain behaviour. Elastic properties of fabric differ in the warp and weft directions of weave. For this analysis, the SHAPE program was modified to accommodate an orthotropic model of the fabric. The fabric used for the analysis of the hypar was a TYPE II fabric with elastic moduli of 670kN/m(warp) and 300kN/m(weft) and tensile strengths of 88kN/m(warp) and 79kN/m(weft). A uniform prestress of 2kN/m was prescribed over the whole of the roof fabric. Patch loads varying from -1.0kPa to 1.0kPa were applied separately on a high and a low patch of the hypar. Reactions at each of the corners (Fig.2) were obtained and plotted against the patch loads. Figure 4 is a sample of these plots. From the results, reactions at each corner due to unit positive or negative patch loads at each patch could be worked out by symmetry, thus giving the influence coefficients for the support reactions. It must be noted here that the load effect for these influence coefficients is actually the change in support reactions from the prestress condition due to the applied loads because even with no applied load, support reaction forces still exist due to prestress. Thus, if

pressure  $p$ (kPa) on a patch of area  $A$  causes support reactions  $R_p$ , then the influence coefficient  $\beta$  can be defined as

$$\beta = \frac{R_p - R_{0,0}}{A * p} \quad \dots(1)$$

$p = \pm 0.2$  if the influence coefficients are defined at the level of realistic wind loads

This equation implies that the change in support reactions varies linearly with the applied load. As can be seen from Figure 4, this is a reasonable and conservative approximation for most support reactions. Due to the geometric non-linearity in the behaviour of the structure, the assumption that superposition applies is not totally accurate either.

The stiffness matrix for the structure was obtained and used to evaluate the natural frequencies of the whole prototype. The lowest or fundamental frequency of the prototype was found to be almost 3Hz which is well above the energy containing frequency of fluctuating wind, so there is little danger of lock-in leading to instability. This confirms that the prototype is sufficiently stiff and small to be considered a static structure.

#### 4 Estimation of Peak Reactions Using Quasi-Steady and Covariance Integration Theory

The results of the wind tunnel tests and the structural analysis were combined to estimate the peak reactions at the corner supports. Most wind codes recommend the use of a quasi-steady design approach for determining peak wind loads on static low-rise structures. That is, peak pressures are obtained by multiplying mean pressure coefficients by the eaves height dynamic pressure due to gust wind velocity. This implies that fluctuating pressures depend entirely on upwind fluctuating velocity. Pressure fluctuations are assumed to be perfectly correlated everywhere.

The covariance integration method, developed by Holmes and Best [2], takes into account the correlation of pressures between different points or sections of a structure. Therefore, a more accurate description of the fluctuating pressure distribution over a structure is sought.

The varying load effects are obtained from the varying pressures using the influence coefficients  $\beta$  such that

$$\text{Load effect} \quad L(t) = \int_A p(t)\beta \, dA \quad \dots(2)$$

$$\text{Coefficient of load effect} \quad C_L(t) = \frac{L(t)}{\frac{1}{2}\rho U^2 A} \quad \dots(3)$$

The mean load effect coefficient can then be written as

$$[\bar{C}_L] = [\beta_i][\bar{C}_{pi}] \quad \dots(4)$$

in matrix form for discretised pressures (patch pressures)

$\beta_i$  = influence coefficient for load effect due to pressure on general patch  $i$

$C_{pi}$  = mean pressure coefficient (referenced to eaves dynamic pressure) on general patch  $i$

Quasi steady theory then estimates the peak load effect coefficient as

$$\hat{C}_L = \bar{C}_L * G_u^2 \quad \text{.....(5)}$$

where  $G_u$ , the gust factor, was measured as 2.03

Covariance integration estimates the variance of the load effect coefficient as

$$\sigma_{CL}^2 = [\beta^T] [\sigma_{cp}] [r] [\sigma_{cp}] [\beta] \quad \text{.....(6)}$$

$r$  = normalised cross-correlation of pressure coefficients

$\sigma_{cp}$  = standard deviation of pressure coefficients at each location

and the peak load effect coefficient as

$$\hat{C}_L = \bar{C}_L + g \sigma_{CL} \quad \text{.....(7)}$$

$g$  = statistical peak factor (measured as  $\approx 4$  for low-rise structures by Holmes [2])

The matrix calculations above were used to estimate the peak reaction coefficients for the tension membrane hypar roof. The results are summarised in Table 1 which compares the quasi-steady and covariance integration estimates of peak support reaction coefficients for each support for several wind directions. For the most part, the covariance integration estimates were found to be larger than the quasi-steady estimates. This is surprising given that quasi-steady theory makes the very conservative assumption that peak pressures occur everywhere simultaneously. The measured cross correlation coefficient values are certainly small due to the different flow mechanisms on the roof. However, the standard deviation pressure coefficients are all very high. This appears to be the main reason behind the large covariance integration peak estimates. It should be noted here that quasi-steady theory fails when dealing with very small coefficient values, so not all the comparisons in Table 1 are valid. Ideally, also, the statistical peak value  $g$  should have been determined by analysing the time history of the pressure fluctuations.

## 5 Conclusions

The mean and fluctuating pressure distributions over a typical hypar roof have been obtained from a wind tunnel study. Analysis of the results indicate that covariance integration, although much more sophisticated, produces similar estimates of peak load effects as the quasi-steady method for the tension membrane hypar. There would be some logic in this given the non-linearity of the structure's response to applied load. However, this conclusion has to be qualified by noting that the unusually high RMS coefficients measured substantially increased the covariance integration estimates. Tests using a larger model may help clarify these RMS pressures.

## 6 References

- 1 J.L. Meek and P.T.S. Ho, 'SHAPE: (A membrane shape-finding program for tension structures)', Adv. Eng. Software, v7 n1 (1985) 2-7
- 2 J.D. Holmes and R.J. Best, 'An approach to the determination of wind load effects on low rise buildings', J. Wind Eng. Ind. Aerodyn., 7 (1981) 273-287



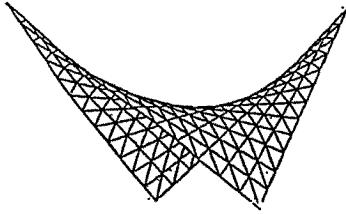


Fig.1 The hyperbolic paraboloid

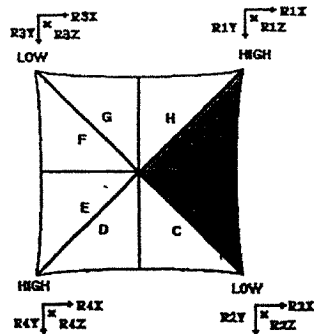
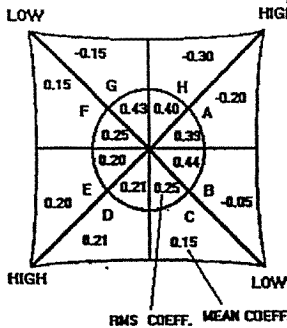


Fig.2 Model patch divisions and support reactions

PANEL PRESSURES -  
SINGLE HYPAR .NO BLOCKAGE

0 degrees



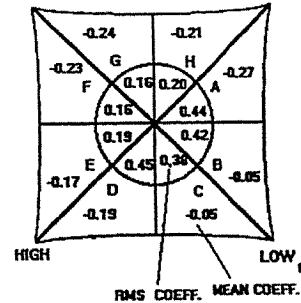
(ALL VALUES ARE PRESSURE COEFFICIENTS)

CROSS CORRELATION COEFFICIENTS  
ANGLE OF ATTACK- 0 DEGREES

	A	B	C	D	E	F	G	H
A	1.00	0.63	0.57	0.47	0.43	0.49	0.51	0.57
B		1.00	0.72	0.41	0.36	0.31	0.26	0.34
C			1.00	0.43	0.39	0.34	0.28	0.29
D				1.00	0.35	0.35	0.28	0.24
E					1.00	0.33	0.27	0.26
F						1.00	0.51	0.37
G							1.00	0.47
H								1.00

PANEL PRESSURES -  
SINGLE HYPAR .NO BLOCKAGE

90 degrees



(ALL VALUES ARE PRESSURE COEFFICIENTS)

CROSS CORRELATION COEFFICIENTS  
ANGLE OF ATTACK- 90 DEGREES

	A	B	C	D	E	F	G	H
A	1.00	0.58	0.40	0.29	0.29	0.11	0.10	0.65
B		1.00	0.61	0.45	0.42	0.17	0.13	0.50
C			1.00	0.62	0.51	0.13	0.19	0.44
D				1.00	0.66	0.10	0.14	0.31
E					1.00	0.17	0.18	0.28
F						1.00	0.32	0.23
G							1.00	0.23
H								1.00

Fig.3 Sample wind tunnel test results

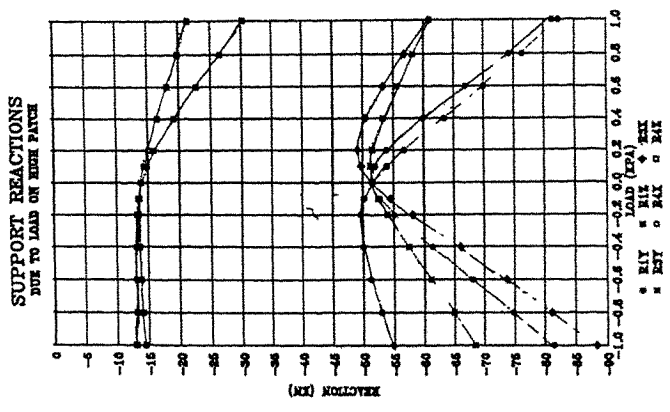


Fig.4 Sample structural analysis results

ANGLE (DEGS)	REACT.	MEAN COEF	VAR COEF	PEAK COEF COV INT	PEAK COEF Q-STEADY	
0.0	R1X	1.2	0.5	3.9	5.0	
	R1Y	-1.2	0.5	-4.0	-5.1	
	R2X	1.2	0.8	3.8	5.0	
	R2Y	-1.2	0.8	-4.0	-5.1	
	R3X	0.2	0.1	0.1	0.1	
	R3Y	-0.2	0.1	-0.1	-0.1	
	R4X	0.2	0.4	2.7	3.4	
	R4Y	-0.2	0.4	-2.7	-3.4	
	R5X	0.1	0.3	2.4	3.1	
	R5Y	-0.1	0.3	-2.4	-3.1	
	R6X	0.1	0.1	1.6	2.1	
	R6Y	-0.1	0.1	-1.6	-2.1	
	45.	R1X	0.6	0.2	2.6	3.4
		R1Y	-0.6	0.2	-2.6	-3.4
		R2X	0.1	0.1	1.5	2.0
		R2Y	-0.1	0.1	-1.5	-2.0
R3X		0.6	0.4	3.0	4.0	
R3Y		-0.6	0.4	-3.0	-4.0	
R4X		0.3	0.3	2.4	3.2	
R4Y		-0.3	0.3	-2.4	-3.2	
R5X		0.4	0.2	2.3	3.1	
R5Y		-0.4	0.2	-2.3	-3.1	
R6X		0.1	0.1	1.1	1.5	
R6Y		-0.1	0.1	-1.1	-1.5	
90.		R1X	0.3	0.5	3.1	4.1
		R1Y	-0.3	0.5	-3.1	-4.1
		R2X	0.1	0.0	0.7	0.9
		R2Y	-0.1	0.0	-0.7	-0.9
	R3X	1.4	2.5	7.7	10.1	
	R3Y	-1.4	2.5	-7.7	-10.1	

Table 1 Comparison of peak reaction coefficients (Covariance integration vs Quasi-steady)

**Parametric study of wind pressure distribution on sloping roofs**

Rajeev Gupta and A.K. Ahuja

Department of Civil Engineering  
University of Roorkee, Roorkee  
India

**Abstract:** A review of the literature for wind loads on industrial building roofs indicates that only average wind pressure coefficients for certain wind directions and slopes of roof are available in code of practice of few countries. The present paper describes the details and the results of the experimental study carried out on rigid models of industrial buildings with skylight. Results of the study are presented in the form of local, average and maximum values of wind pressure coefficients.

**1. Introduction**

Residential buildings generally have flat or sloping roofs. But large span buildings for industrial or public use have either sloping or curved roofs (Fig. 1). Specially in case of industrial buildings, where entry of natural light through roof is of importance, saw-tooth roofs or roofs with skylight (Figs. 1d to 1f) are generally used. Data in the present Indian Standard on wind loads [1] and national codes of other countries [2] are rather fragmentary regarding wind loads on such roofs. For instance, external pressure coefficients for saw-tooth roofs of multispan buildings are given in Table 17 of Indian Standard [1], but only for 4 wind directions namely 0°, 90°, 180° and 270°. Similarly, Table 20 gives pressure coefficients on sloping roofs with skylight for wind normal to the ridge only, and skew winds are not included. Also the effects of variation in roof slope, building height ratio, and building plan ratio on pressure coefficients are not shown. Further, values of local pressure near edges which are expected to be greater in many cases than the average values on the surface are also not available. Thus the available information is not enough to prepare a set of recommendations for the designers to arrive at a safe but economical design of such roof systems.

This paper describes the extensive experimental programme carried out at University of Roorkee in order to complete the above information to the extent best possible. Rigid models of industrial buildings with skylight (Fig. 1f) were tested in the boundary layer wind tunnel to study the influence of certain structural and flow parameters namely wind incidence angle, slope of roof, model size, openings on wall and terrain roughness on the values of mean wind pressure coefficients on the roof surface. The work in this direction was initiated by Singh [3] at University of Roorkee and the present work is an extension of the earlier work. Results presented herein in the form of tables and figures can easily be used by the designers.

**2. Experimental details**

**Building models**

Models of the sloping roof building were made of timber and perspex

sheet. Dimensions of the prototype were assumed as length = 25 m, width = 12.5 m and height = 12.5 m. Models were made with 3 different scales namely 1:50, 1:100 and 1:200. Roof angles were kept as 15° and 25°. In all 6 models were prepared. Salient features of these models are listed in Table 1. A typical model is shown in Fig. 2. All the models except one with 1:200 scale were provided with 70 pressure points to measure external pressure on 6 surfaces namely A, B, C, D, E and F. All models had solid walls except one which was used to study the internal pressure distribution, in which openings representing doors and windows were provided on two long walls. In this model 60 pressure points were provided to measure internal pressure in addition to 70 external pressure points by making roof with 2 layers of perspex sheet.

Each pressure tapping on the building models was connected with a plastic tube so as to connect it to a multi U-tube manometer. These tubes were then drawn from the bottom of the models into the working chamber of the wind tunnel.

#### **Wind characteristic**

The building models were tested in a turbulent boundary layer developed with the help of vortex generators and cubical blocks placed on the upstream side of models. A total of three velocity profiles were generated having power law index (n) of 1/10, 1/8 and 1/5.5.

#### **Parameters of study**

The purpose of the present work was to study the influence of various structural and flow parameters on wind pressure distribution. Values of these parameters used during the study are given in Table 2.

### **3. Results and discussions**

Individual point pressure measurements were made at all the tapping locations on each model. Only mean pressures were measured. From the measured values of pressures, face average pressure coefficients, centre-line average pressure coefficients and local maximum pressure coefficients were obtained. Effect of the above mentioned parameters on pressure coefficients are discussed below. However, due to paucity of space, results of only few cases are reported herein.

#### **Effect of wind incidence angle ( $\theta$ )**

To study the effect of wind incidence angle on wind pressure coefficients, perspex model of roof slope ( $\alpha$ ) 25° and model scale 1:100 was tested for 7 wind directions namely 0°, 15°, 30°, 45°, 60°, 75° and 90° under a wind with velocity profile of 1/10 power law index. Mean values of local pressure coefficients are shown in Table 3. (Due to limitation of space, pressure values at only few tapping positions are shown.) It is observed that at 0° wind incidence angle, all faces namely A to F are subjected to suction, suction being more for upstream points compared to down stream points. As wind incidence angle increases from 0° to 30°, suction increases at most of the points. With further increase in the value of wind angle, suction decreases on windward face A and B, and becomes pressure at 45°. On faces C, D, E and F it remains suction at almost all the points for all directions of wind, with small variation in the values of suction.

Variation of the face average and centre-line average values, which were obtained from the local values, can be seen in Tables 4 and 5. It is noticed that variation of coefficients on faces A and B is identical where it increases with wind incidence angle. Maximum value of average pressure on

these faces lie between 0.4 and 0.7. On faces C to F, coefficients fluctuate with wind angle with maximum suction occurring around  $\theta = 30^\circ$  and minimum around  $\theta = 75^\circ$ . These values are further compared with the values given in IS Code [1] for wind normal to ridge. Values of pressure coefficients obtained experimentally on few faces are comparable with code values, but there is a difference of sign in the pressure values for lower sloping part on windward side. Whereas code indicates a suction of 0.6, a pressure of 0.377 (face average) and 0.515 (centre-line average) were obtained experimentally.

#### **Effect of slope of roof ( $\alpha$ )**

To study the effect of roof slope on wind pressure coefficients, two perspex models of scale 1:100 were used. These were having roof slope of  $15^\circ$  and  $25^\circ$  respectively. The models were tested for 3 wind directions namely  $0^\circ$ ,  $45^\circ$  and  $90^\circ$  under a wind with velocity profile of 1/10 power law index. It is observed that at  $0^\circ$  wind incidence angle, all faces namely A to F are subjected to suction on both the models. Further, the suction is found to decrease with increase in roof slope except at few points on face A. However, at other angles there is increase in pressure or decrease in suction almost at all pressure points with increase in roof slope. Numerical values of pressure at representative points are shown in Table 6.

#### **Effect of other parameters**

Whereas, the effects of all the parameters listed in Table 2 were studied as part of this work, due to limitation of space the results of other parameters are not included in this paper.

#### **4. Conclusions**

Following conclusions are drawn from the present study.

- (i) Mean wind pressure coefficients vary significantly with wind incidence angle.
- (ii) There are the areas of high suction on the roof near windward corners with skew wind directions.
- (iii) It is not the normal direction of wind as specified in the code of practice, but the skew wind directions which have critical values for roof pressures.
- (iv) Face average pressure coefficients differ significantly from centre line average pressure coefficient on some faces.
- (v) Values of the pressure coefficients given in the code of practice do not match with observed data in all the cases.

#### **5. Further scope of work**

In order to make the results obtained from the present study more comprehensive, further research can be done by considering (i) a row of buildings with skylight, (ii) openings on the skylight portion, and (iii) roof resting on columns (i.e. building with no side walls).

#### **6. Acknowledgement**

The work presented herein forms part of the research work done by the first author under the supervision of the second author for his Master's dissertation during 1990-91.

#### **References**

1. IS: 875 (Part-3) - 1987, "Indian Standard Code of Practice for Design Loads (other than Earthquake) for Buildings and Structures, Part-3 Wind Loads", Bureau of Indian Standards, New Delhi, India, 1987.
2. "Wind Resistant Design Regulations : A World List -- 1975", Published by

- Gakujutsu Bunken Fukyu-Kai, Oh-Okayama, Meguroku, Tokyo, Japan, 1975.
3. Sumer Singh, "Wind Loads on Sloping Roofs with Skylight", M.E. Thesis, Deptt. of Civil Engg., Univ. of Roorkee, Roorkee, India, November 1990.

Table 1 Salient features of models

Model Identi- fication	Size of model (mm)			Model scale	Roof angle ( $\alpha$ )	No. of pressure tapping		Material used
	Length	Width	Height			Ext.	Int.	
I	500	250	250	1:50	15°	70	-	Timber
II	500	250	250	1:50	25°	70	-	Timber
III	250	125	125	1:100	25°	70	-	Perspex sheet
IV	250	125	125	1:100	15°	70	-	Perspex sheet
V	125	62.5	62.5	1:200	25°	30	-	Perspex sheet
VI	500	250	250	1:50	25°	70	60	Perspex sheet

Table 2 Values of parameters

Sl. No.	Parameter	Values
1	Wind incidence angle ( $\theta$ )	0°, 15°, 30°, 45°, 60°, 75°, 90°
2	Roof slope ( $\alpha$ )	15°, 25°
3	Model scale	1:50, 1:100, 1:200
4	Openings on walls	0%, 5%, 10%, 20%, 25%
5	Power law index (n) (Terrain roughness)	1/10, 1/8, 1/5.5

Table 3 Variation of mean wind pressure coefficients with wind incidence angle (n = 1/10,  $\alpha$  = 25°, model scale = 1:100)

Pressure point no.	Wind incidence angle ( $\theta$ )						
	0°	15°	30°	45°	60°	75°	90°
A1	-0.145	-0.127	-0.245	+0.119	+0.299	+0.648	+0.249
A2	-0.169	-0.266	-0.368	-0.310	-0.149	-0.025	+0.124
A13	-0.677	-0.784	-0.249	+0.447	+0.698	+0.455	+0.202
A14	-0.722	-0.911	-0.399	+0.329	+0.524	+0.354	+0.101
B5	-0.203	+0.025	-0.050	+0.259	+0.374	+0.506	+0.556
B6	-0.290	+0.078	+0.123	+0.141	+0.310	+0.572	+0.848
B9	-0.895	-1.020	-0.147	+0.376	+0.620	+0.548	+0.299
C5	-0.096	-0.261	-0.810	-0.965	-0.811	-0.787	-0.748
C6	-0.167	-0.540	-1.414	-0.023	+0.188	+0.353	-0.973
F14	-0.659	-0.788	-0.683	-0.762	-0.574	-0.430	-0.531
F15	-0.729	-0.834	-0.556	-0.688	-0.549	-0.379	-0.379

Table 4 Variation of face average wind pressure coefficients with wind incidence angle ( $\theta$ ) ( $n = 1/10$ ,  $\alpha = 25^\circ$ , model scale = 1:100)

Face	Wind incidence angle ( $\theta$ )						
	0°	15°	30°	45°	60°	75°	90°
A	-0.380	-0.263	-0.134	+0.104	+0.309	+0.403	+0.377
B	-0.391	-0.267	-0.070	+0.249	+0.428	+0.496	+0.515
C	-0.379	-0.575	-0.857	-0.687	-0.403	-0.685	-0.878
D	-0.372	-0.533	-0.720	-0.576	-0.424	-0.415	-0.536
E	-0.325	-0.590	-0.635	-0.602	-0.404	-0.414	-0.494
F	-0.367	-0.542	-0.669	-0.633	-0.450	-0.414	-0.536

Table 5 Variation of centre-line average wind pressure coefficients with wind incidence angle ( $\theta$ ) ( $n = 1/10$ ,  $\alpha = 25^\circ$ , model scale = 1:100)

Face	Wind incidence angle ( $\theta$ )						
	0°	15°	30°	45°	60°	75°	90°
A	-0.249	-0.008	-0.008	+0.119	+0.282	+0.449	+0.515
B	-0.247	-0.052	+0.037	+0.200	+0.342	+0.539	+0.702
C	-0.132	-0.401	-1.112	-0.494	-0.312	-0.217	-0.861
D	-0.108	-0.298	-0.977	-0.282	-0.259	-0.126	-0.449
E	-0.214	-0.635	-0.777	-0.328	-0.247	-0.175	-0.474
F	-0.259	-0.517	-0.801	-0.663	-0.698	-0.523	-0.590

Table 6 Variation of mean wind pressure coefficients with roof slope ( $\alpha$ ) ( $n = 1/10$ , model scale = 1:100)

Pressure point no.	Wind incidence angle ( $\theta$ )					
	0°		45°		90°	
	$\alpha = 15^\circ$	$\alpha = 25^\circ$	$\alpha = 15^\circ$	$\alpha = 25^\circ$	$\alpha = 15^\circ$	$\alpha = 25^\circ$
A1	-0.111	-0.145	-0.392	-0.210	+0.138	+0.256
A2	-0.089	-0.169	-0.346	-0.189	-0.069	+0.149
A3	-0.089	-0.121	-0.346	-0.253	-0.185	-0.064
B5	-0.326	-0.203	+0.369	+0.145	+0.499	+0.485
B6	-0.235	-0.290	+0.217	+0.262	+0.552	+0.649
C5	-0.149	-0.096	-1.108	-0.847	-0.859	-0.626
C6	-0.195	-0.167	-1.260	-1.281	-0.989	-1.269
D5	-0.130	-0.071	-0.825	-0.688	-0.646	-0.491
D6	-0.214	-0.145	-0.850	-0.706	-0.626	-0.511
E9	-0.977	-0.871	-0.842	-0.868	-0.551	-0.519
E10	-0.652	-0.706	-0.796	-0.787	-0.551	-0.519
F13	-0.608	-0.659	-0.796	-0.767	-0.529	-0.548
F14	-0.652	-0.659	-0.774	-0.726	-0.551	-0.548
F15	-0.652	-0.729	-0.842	-0.706	-0.529	-0.548

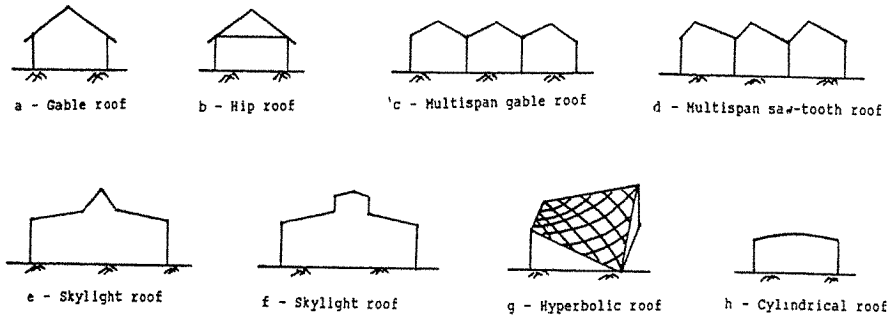


Fig. 1 Various roof forms for industrial and public buildings

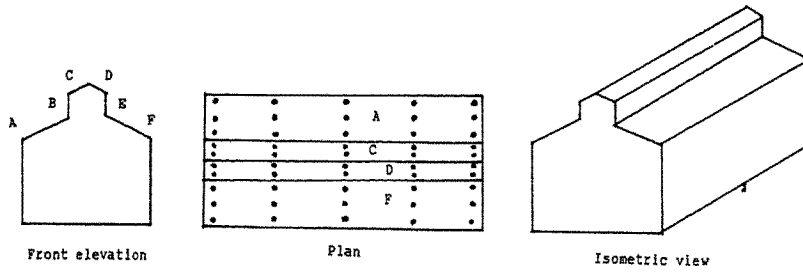


Fig. 2 Typical model of sloping roof with skylight with locations of pressure points ( $\alpha = 25^\circ$ , model scale = 1:100)

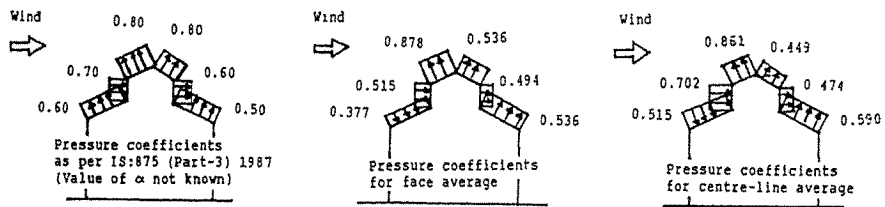


Fig. 3 Comparison of average wind pressure coefficients for wind normal to ridge ( $n = 1/10$ ,  $\alpha = 25^\circ$ , model scale = 1:100)



## The Mean Pressure on Shell Structure Roof

Chen Qin hao\*

Guangdong Provincial Building Research & Design Institute, China

**Abstract:** The shell structure roof is characterized by extraordinary shape and lower gravitational load. The wind load, therefore, is predominant in design loads. The pressure tests were carried out on four building models with shell roofs in CGB—1 Building Aerodynamics Wind Tunnel, Guangdong Provincial Building Research & Design Institute, China. Some typical results were reported in this paper, and the influence of roof configuration on pressure distribution was discussed.

### 1. Introduction

The shell structure roof is one of attractive new designs by its aesthetic shape. The light and thin roof shell is, generally, supported by frame network, hence characterized by lower gravitational loads. The wind load, therefore, is predominant in design loads. On the other hand, the wind load on such roofs is hardly referred to design code due to its extraordinary shape. The Guangdong Provincial Building Research & Design Institute has the fortune to have tested several shell-roof models with various shape in its Building Aerodynamics Wind Tunnel CGB—1, to measure the mean pressure distribution. Some typical results are reported in this paper.

### 2. Facility and Test Procedure

The tests were carried out in the wind tunnel CGB—1, a close-circuit boundary layer wind tunnel with two tandem test sections. The pressure tests on roof models were conducted in the larger test section of 3m wide, 2m high and 10m long. The atmosphere boundary layer was simulated with fence, spire and roughness elements. The pressure was measured by distributed tapping and scanivalve, and acquired and processed by PC computer based system. The roof models were made of light wooden plates and epoxy.

### 3. Typical Results

#### 3.1 *Hyperbolic Paraboloid Shell Roof*

Xinhai Concert Hall, Guangzhou, is a building with hyperbolic paraboloid shell roof of 48m×48m square platform. The roof corners in south and north are 40m and 25m high, respectively, and both in east and west touch ground (Fig. 1). The building was surrounded by the side walls. A 1/150 scaled model was tapped by 289 (17×17) pressure holes, and the mean pressure was measured under eight wind angles in wind tunnel. The pressure measured on the upper surface of roof was shown in Figs. 2~6, for N, NE, E, SE, and S wind directions, respectively, where the twice larger scale was used on SE and NW sides intentionally to be clear.

In N-wind case (blew diagonally), the positive pressure occurred on the higher southern upturned corner, covering about a quarter roof area, and the suction on remaining larger area (Fig. 2). In NE-wind case (blew against the edge), it was seen in Fig. 3 that only lower pressure occurred near SE edge of the roof, and suction almost covered whole roof surface and peak suction along NE edge. When E-wind blew (Fig. 4) the pressure region moved towards eastern corner, and higher suction was applied on both

\* President of Wind Engineering Department, Senior engineer.

SE and NE edges of peak coefficient  $-1.39$ . In both SE- and S-wind cases (Figs. 5-6), the suction covered the whole roof.

### 3.2 *Compound Dome-like Shell Roof*

Nanshan Amusement and Sports Center, Shenzhen City, has a main building with shell roof consisting of twenty dome-like sub-roofs in square platform ( $14\text{m} \times 14\text{m}$ ). Each sub-roof, called "umbrella" from its shape, is formed with 64 pieces of same right isosceles triangles shown in Fig. 7.

Based on the roof platform configuration in Fig. 8, two different flow conditions were considered during the tests, one was 2D flow typical in central portion of main roof (e. g. B, M and F in the figure) and the other was 3D flow near side end (e. g. L and R). A 1/20 scaled roof model consisted by three umbrellas was used as a section model during tests. For 2D flow study, two endplates were added to simulate the flow condition.

#### 3.2.1 *2D Flow Results*

The pressure (suction) coefficients on upper roof surface of three umbrellas with endplates were shown in Fig. 8, where the frontal (windward), middle and backward (leeward) umbrellas were denoted by F, M and B, respectively. It was found that on umbrella M and B, the suction tended to recovery from apex to either edge, with peak suction at apex. On umbrella F, however, much stronger suction (about  $C_p = -2.00$ ) occurred along the frontal edge, and continued to recovery through apex till leeward edge (about  $C_p = -0.47$ ). The same suction recovery trends were from apex ( $C_p = -1.03$ ) to both side edges ( $C_p = -0.85$ ) as on M and B mentioned above. For the combination F-M-B, the strongest suction occurred along the windward edge of the umbrella F. It was concluded from the 2D tests that among three umbrellas, the highest wind load was on the frontal one, and the lowest load on the middle one, which agreed with the results from the force tests.

The influence of the eaves in height and shape on pressure distribution was also studied. The results indicated the significant effects of the eaves on the pressure over frontal umbrella F to suppress a concentrated stronger suction near windward edge and to smooth the pressure distribution. However, there is a compromise with aesthetics on eave height effect.

#### 3.2.2 *3D Flow Results*

The wind pressure coefficients on upper surface of umbrella R were shown in Fig. 10 with varied wind directions. In general, the suction was not much high, even positive pressure could be seen on a few points on some occasions. On such umbrellas, the influence of eaves height was less than in 2D case mentioned above.

## 4. Other Studies and Conclusion

The similar tests completed in CGB-1 wind tunnel included the pressure measurement on the canopy of Zhuhai Stadium, Zhuhai Economic Special Zone, and on the shelter roof of dry coal store in the Zhanjiang Power Plants. The results from both tests showed the suction over the upper roof surfaces at any wind directions.

It is concluded from the results obtained in CGB-1 wind tunnel up to date that the suction on the upper surface was the predominant wind load exerted on the shell structure roof, and the peak suction normally occurred along the frontal edges.

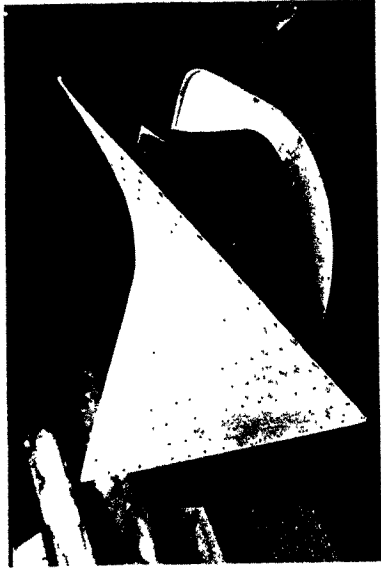


Fig. 1 Xinhai Concert Hall with hyperbolic paraboloid shell roof

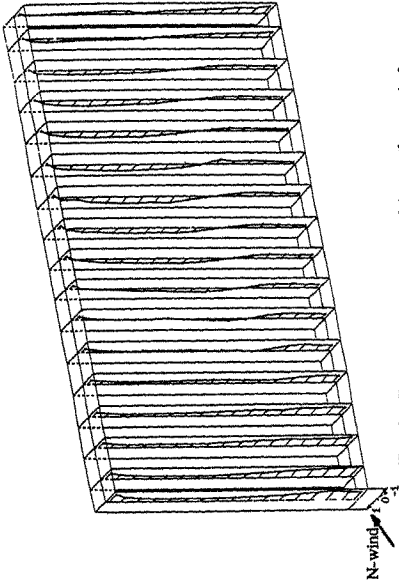


Fig. 2 Pressure on supper roof in northern wind

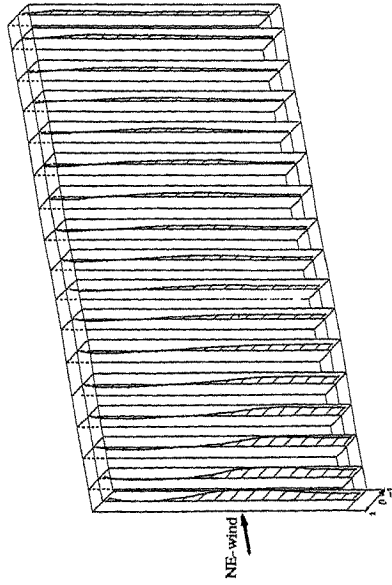


Fig. 3 Pressure on supper roof in northeast wind

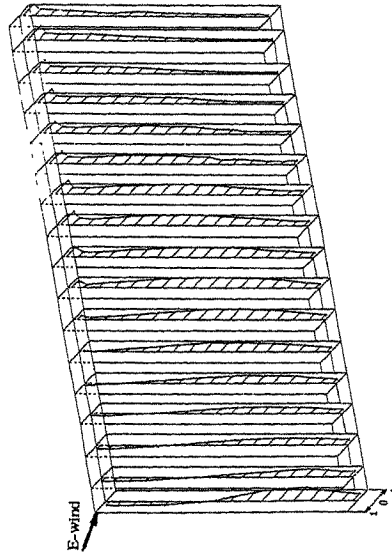


Fig. 4 Pressure on supper roof in eastern wind

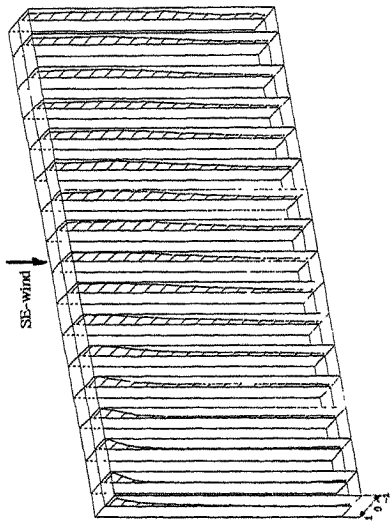


Fig. 5 Pressure on supper roof in southeast wind

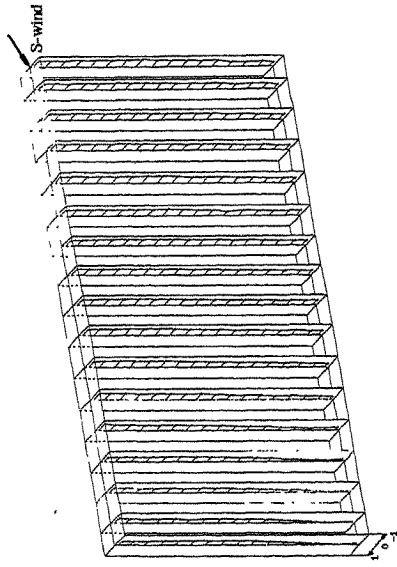


Fig. 6 Pressure on supper roof in southern wind

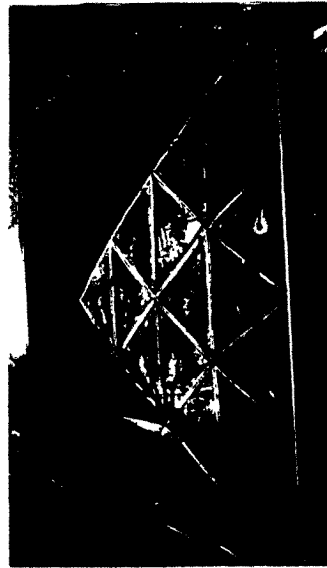


Fig. 7 Umbrella formed with 64 triangles

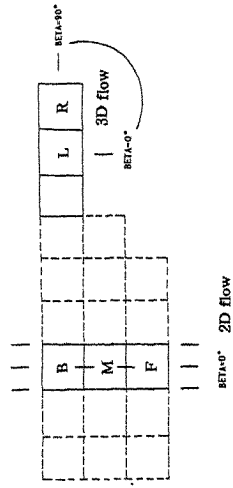


Fig. 8 Compounded domelide shell roof configuration

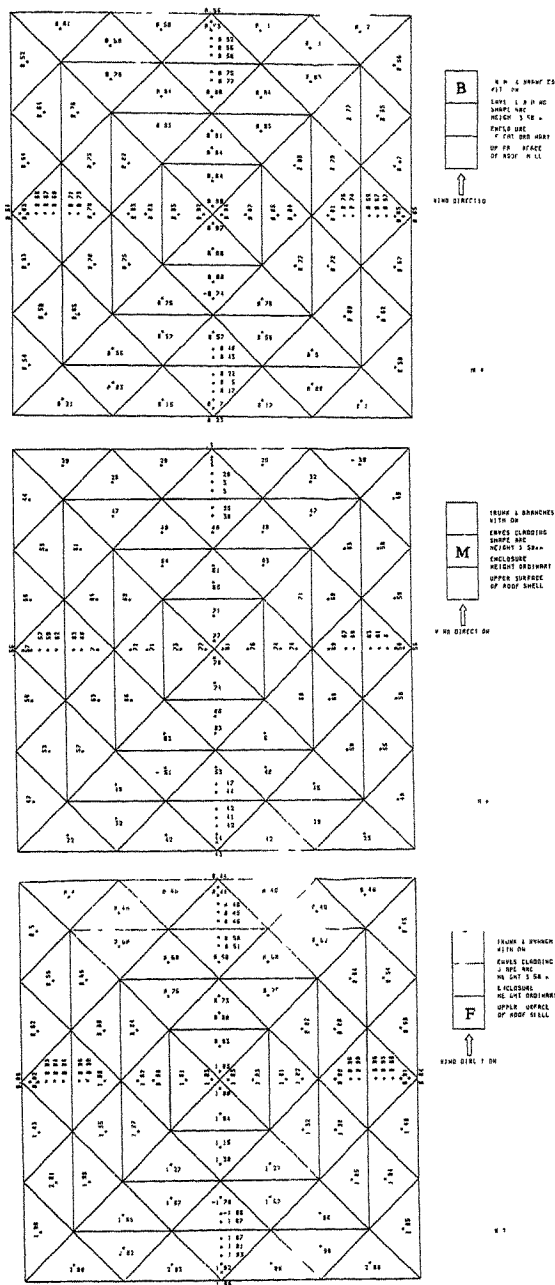


Fig. 9 Pressure coefficients on roof in 2D flow condition

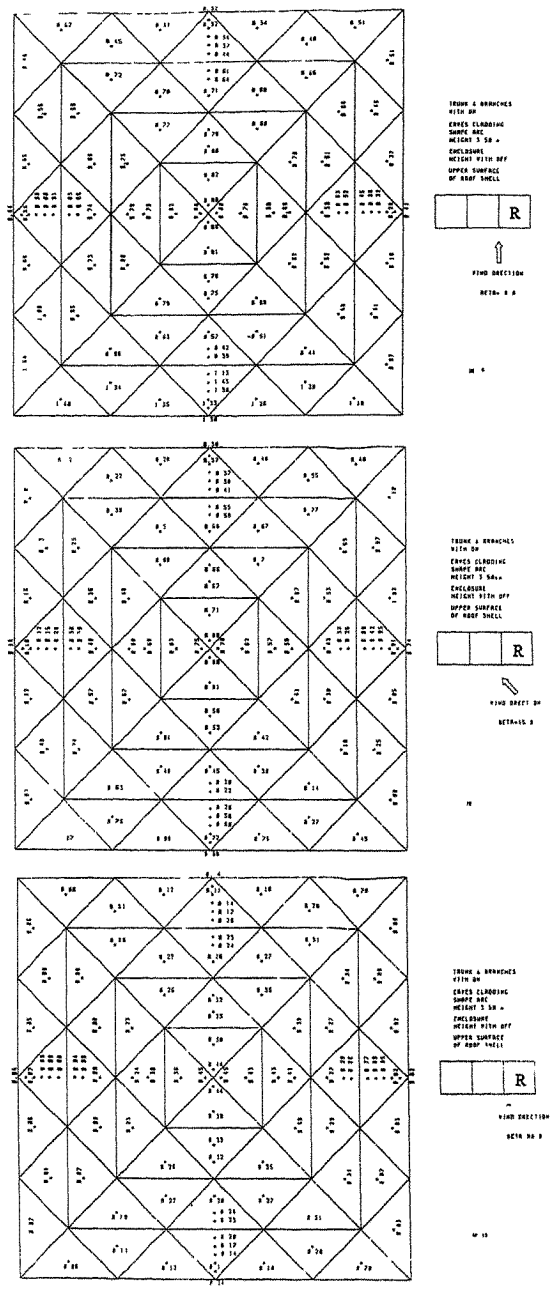


Fig. 10 Pressure coefficients with wind angle in 3D flow condition

## The effect of directional variations on the observed mean and rms pressure coefficients

P.J. Richards<sup>†</sup>, R.P. Hoxey\* and B.S. Wanigaratne<sup>†</sup>

<sup>†</sup>Department of Mechanical Engineering  
University of Auckland, Private Bag 92019, Auckland, N.Z.

\*Silsoe Research Institute  
Wrest Park, Silsoe, Bedford MK4S 4MS, U.K.

**Abstract:** A Fourier series is fitted to a set of mean pressure coefficient data for the Silsoe Structures Building. Corrections made to this function illustrate the effect of directional variations in rounding the  $C_p(\theta)$  relationship. It is shown that in a region of local extreme the difference may be more than 0.25 in  $C_p$ . These series are also used to give an estimate of the contribution to the fluctuating pressures resulting from directional variations. It is shown that this estimate closely matches observed data.

### 1. Introduction

In both full-scale and wind-tunnel measurements of pressures on buildings the mean pressure coefficient is usually assumed to be a function of the mean wind direction  $\bar{\theta}$ . However, during an observation period of say 10 minutes (full-scale), the wind direction will vary significantly either side of the mean and so the observed mean pressure coefficient is the average effect of a band of wind directions. The consequence of this is a smoothing of the  $C_p(\theta)$  relationship. For example, if the pressure coefficient reaches a particularly extreme value over a very narrow range of wind directions, then this peak will be rounded by directional variations and a lower value observed.

In addition directional variations will cause the pressures on the building to fluctuate even if the wind speed is constant. Consequently directional variations make a direct contribution to the variance of pressure and hence to the rms pressure coefficient.

### 2. Full-scale Measurements

The data used for assessing the concepts presented in this paper were obtained from measurements on the Silsoe Structures Building [1] during 1990 and 1991.

Surface pressures were sensed at tapping points flush with the surface of the building. The tapping points were positioned at 3 transverse sections of the building, with 11 tapping points in each section. (Tap 22 was not monitored.) Reference pressure was obtained from a static probe mounted near the anemometer at the ridge height of the building and 20m west of the North-West corner of the building.

The three components of windspeed were sensed using a sonic anemometer type Gill 1012R. The anemometer produced a digital output (RS232) at a digitisation rate of approximately 21 Hz. A 32-channel CED 1401 data acquisition system together with a Compaq 386 PC was used. The output from the pressure transducers was connected directly to the CED 1401, whereas the sonic anemometer was connected to the RS232 port on the PC. Since the requirement was to record the 32 pressure signals simultaneously with windspeed, the logging PC had to interleave information from the CED 1401 and the sonic anemometer and this restricted data acquisition to a rate of 5 Hz.

The standard recording method adopted was to record 10 seconds of zero - 4 minutes of calibration - 60 minutes of surface pressure - 4 minutes of calibration - 10 seconds of zero, making a total record length of 1 hour 8 minutes and 20 seconds (a total of 20,500 data points). Each scan consisted of the 32 pressure readings and 4 readings from the sonic anemometer. To allow time for settling when the solenoid valves were activated, a 2 second pause followed each switching event.

The one hour records were subdivided into six ten minute records. Mean and rms pressure coefficients were deduced for each ten minute record by dividing the mean and rms pressures by the mean dynamic pressure  $\bar{q}$ . The rms value of the dynamic pressure  $\sigma_q$  was also recorded. Fig. 1 shows the mean pressure coefficients obtained from tapping 5 over the range of mean directions ( $\bar{\theta}$ ) which occurred during the recorded period. Values for  $\sigma_\theta$  were also recorded.

### 3. Fourier series

Since the mean pressure coefficient data is periodic in  $\theta$  a Fourier series of order N taking the form

$$C\bar{p}(\bar{\theta}) = \sum_{k=0}^N \bar{a}_k \cos k\bar{\theta} + \bar{b}_k \sin k\bar{\theta} \quad (1)$$

can be fitted to the data by using the least squares method. For each tapping the order N was chosen on the basis of keeping it as small as possible while trying to minimise the standard error. An example of the fitted curve is shown in Fig. 1 and reproduced as the solid line in Fig. 2.

It can be noted that this represents the relationship between the ten minute mean pressure coefficient and the ten minute mean wind direction. If it is assumed that a more instantaneous relation exists such that

$$C\bar{p}(\theta) = \sum_{k=0}^N a_k \cos k\theta + b_k \sin k\theta \quad (2)$$

and if the wind direction is normally distributed with a variance  $\sigma_\theta^2$  then the observed mean pressure coefficient function

$$C\bar{p}(\bar{\theta}) = \sum_{k=0}^N a_k e^{-\frac{k^2 \sigma_\theta^2}{2}} \cos k\bar{\theta} + b_k e^{-\frac{k^2 \sigma_\theta^2}{2}} \sin k\bar{\theta} \quad (3)$$

By equating equations (1) and (3) it is then possible to obtain estimates for  $a_k$  and  $b_k$  and construct a curve for  $C\bar{p}(\theta)$ . An example of this is shown in Fig. 2 (dashed line). It may be noted that in the region of the lowest pressure coefficient the difference is of the order of -0.25. It may also be observed that this new curve now fits most of the more extreme results.

### 4. Fluctuating Pressures

If it is similarly assumed that the instantaneous pressure is related to the reference mean pressure  $\bar{p}_0$ , the instantaneous reference dynamic pressure  $q$  and instantaneous wind direction  $\theta$  by

$$p = \bar{p}_0 + C_p(\theta)q \quad (4)$$

where  $C_p(\theta)$  is approximately equivalent to  $C\bar{p}(\theta)$  as given in equation 2, then it follows that the rms pressure coefficient

$$C_p(\text{rms})^2 = C\bar{p}(\bar{\theta})^2 \frac{\sigma_q^2}{\bar{q}^2} + \sigma_{C_p}^2 \left( 1 + \frac{\sigma_q^2}{\bar{q}^2} \right) \quad (5)$$



where the variance of  $C_p$  can be estimated from

$$\sigma_{C_p}^2 = \sum_{j=0}^N \sum_{k=0}^N A_j A_k E1 (E2 + E3 - 1) + B_j B_k E1 (E2 - E3)$$

in which

$$A_k = a_k \cos k\bar{\theta} + b_k \sin k\bar{\theta}$$

$$B_k = -a_k \sin k\bar{\theta} + b_k \cos k\bar{\theta}$$

$$E1 = e^{-\frac{(j^2 + k^2)\sigma_q^2}{2}}, \quad E2 = \frac{1}{2} e^{jk\sigma_q^2} \text{ and } E3 = \frac{1}{2} e^{-jk\sigma_q^2}$$

Equation (5) has been used to estimate the rms pressure coefficient for tapping 2 (a wall tapping at a height of 2 m and 0.6 m from the NW corner). The mean pressure coefficient data shown in Fig. 3 was fitted by a Fourier series and the rms pressure coefficients estimated. Fig 4 shows the sets of measured and estimated rms pressure coefficients for the directions  $190^\circ < \bar{\theta} < 300^\circ$ . A reasonable correlation is observed.

The contributions to  $C_p(\text{rms})$  are more obvious in Fig. 5 where in the region around  $C_{\bar{p}} = 0$  the first term in equation (5) is small and the dominant contribution results from the variation in  $C_p$  with direction. It may therefore be observed that the magnitude of the directional variation term around  $C_{\bar{p}} = 0$  is of the same order of magnitude as the velocity fluctuation term ( $C_{\bar{p}}^2 \sigma_q^2 / \bar{q}^2$ ) at  $C_{\bar{p}} = -0.6$  (where  $\sigma_{C_p}^2$  is small).

Fig. 6 shows a plot of the estimated (from equation (5)) and measured values for  $C_p$  (rms) for all 32 tappings and wind direction between  $190^\circ$  and  $300^\circ$ . The values for  $\sigma_q$ ,  $\bar{q}$  and  $\sigma_\theta$  used for the estimate are those recorded at the time of measurement. This plot includes 14 885 data points. The fitted regression has a slope of 1.0125 and intercept of 0.0133 which is very close to a one-one matching but with some scatter.

## 5. Discussion and Conclusions

It has been shown that direction variations during an observation period result in a rounding of the observed  $C_p(\theta)$  relationship. In a region of local extremes this may result in a difference of more than 0.25 in  $C_p$ . It has also been illustrated that the rms pressure coefficient may be accurately estimated by including the effects of variation in the winds dynamic pressure and variations in wind direction. This has implication for computation fluid dynamic modelling of wind loads on buildings where it is reasonably easy to predict the mean pressure coefficients variation with direction [2] but this information would be more useful if it can be used to estimate the rms or possibly even the extreme pressures. Previous work in this direction has either ignored the directional effects [3] or has used a crude estimate for these [4]. The use of Fourier series enables a much more accurate estimate to be obtained.

## Acknowledgements

The experimental data used in this paper was obtained with the support of the UK Ministry of Agriculture, Fisheries and Food and the UK Building Research Establishment.

## References:

1. A.P. Robertson and A.G. Glass, Silsoe Research Institute Divisional Note 1482 (1988).
2. P.J. Richards and R.P. Hoxey, *J. Wind Eng. Ind. Aerodyn.* 41-44 (1992) 1641-1652.
3. D.A. Paterson, *J. Wind Eng. (Japan)* 52 (1992) 24-29.
4. P.J. Richards and B.S. Wanigaratne, *J. Wind Eng. (Japan)* 52 (1992) 30-35.

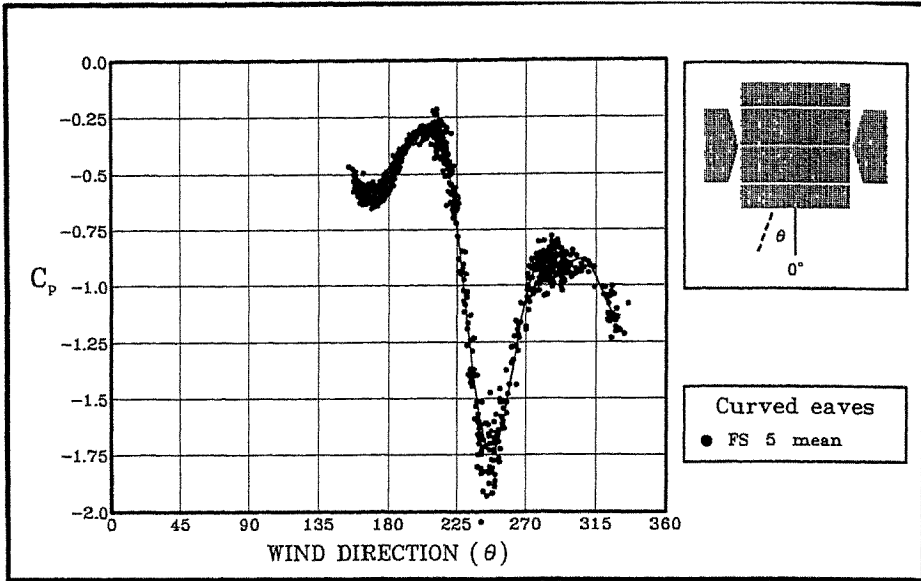


Fig.1. Mean pressure coefficient as a function of wind direction for tap 5.

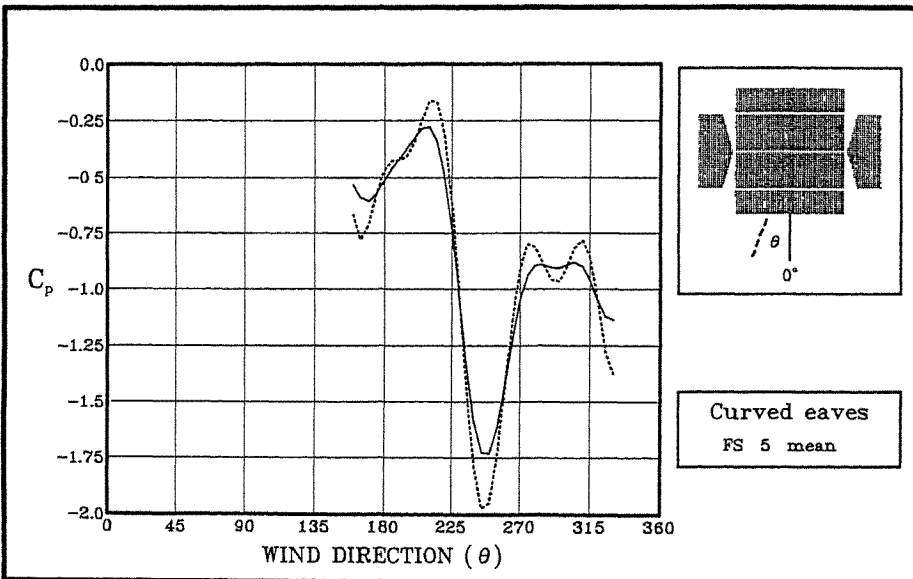


Fig.2. The Fourier fitted function, equation (1), (—) and the instantaneous function, equation (2), (----) for tap 5.

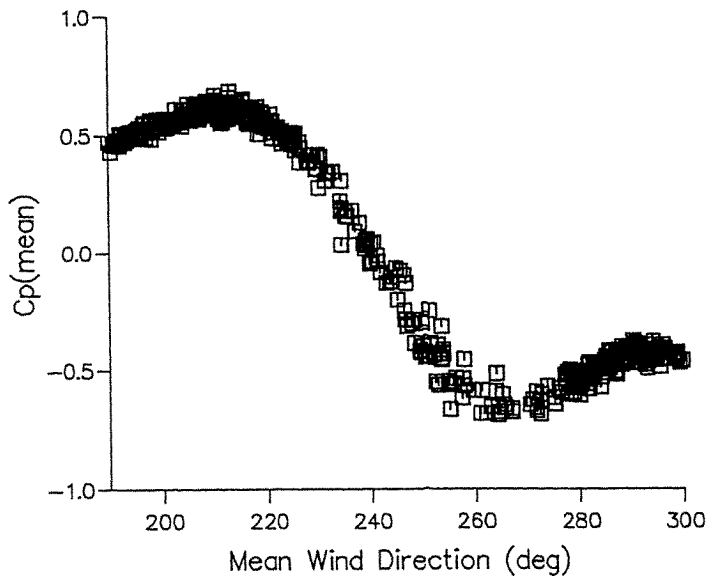


Fig.3. Measured mean pressure coefficient variation with direction for tap 2.

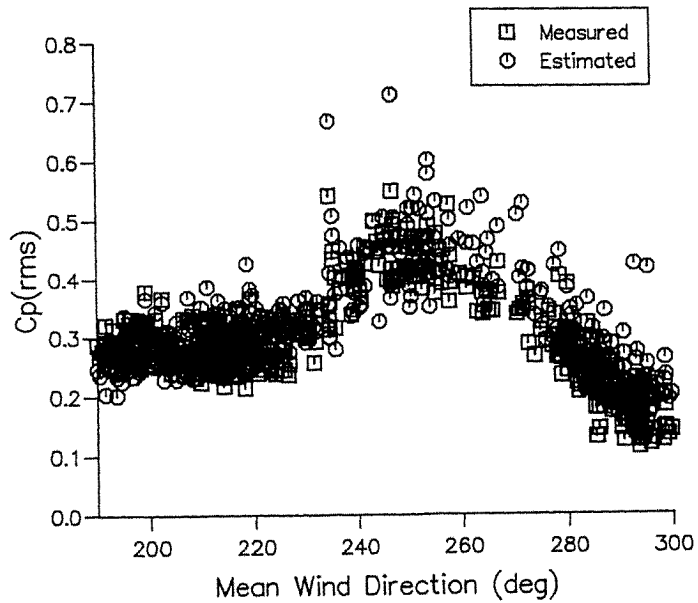


Fig.4. Measured and estimated (equation (5)) rms pressure coefficient data for tap 2.

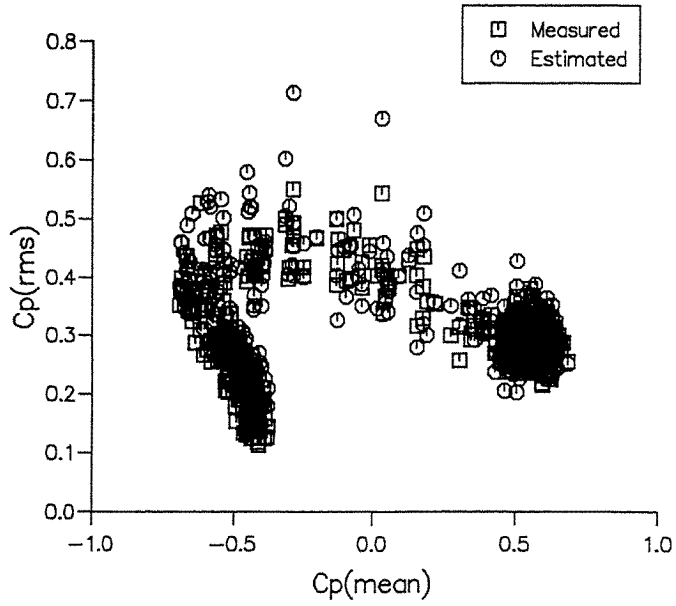


Fig.5. Measured and estimated rms pressure coefficient as related to mean pressure coefficient for tap 2.

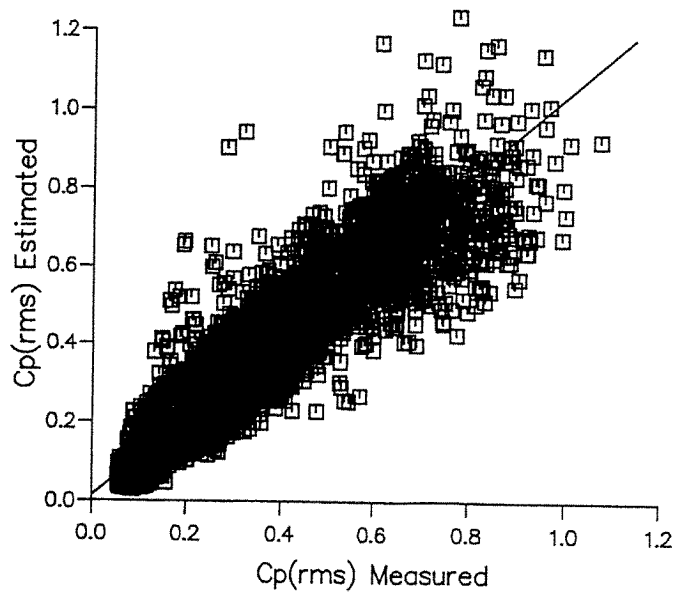


Fig.6. Estimated versus measured rms pressure coefficients from all 32 tappings.

## WIND TUNNEL STUDY OF WATER TANKS

J.Parthiban, A.R.Santhakumar & K.Padmanaban

Department of Structural Engineering  
& Department of Aeronautical Engineering  
Anna University, Madras 600 025, India.

**Abstract:** This experimental work is a systematic study of wind loads on a 1 in 100 scale model of a water tank with cylindrical stem and conical top, in a wind tunnel of short test section, with proper simulation of terrain. Pressure distribution thus obtained is used to arrive at drag coefficients over different regions of the model resulting in the estimation of the overall drag coefficient of the tank. Influence of the presence of one water tank over the other with spacings as multiples of maximum diameter of the cone and stagger angles up to  $10^\circ$  have been considered. Present experimental data suggest that the current practice of assuming wind loads on water tanks as recommended by the existing codes of practice, even allowing for terrain factors, results in considerable over estimate of the wind loads and over design of these structures.

### 1. Introduction

Water tanks are tall slender structures with large masses on top. This type of structure is put up in all terrains mainly to ensure adequate supply of water to colonies built sometimes in far flung areas. The existing codes of practice in India have been suggesting allowances to be made for wind loads in the structural design of water tanks. The well known case of failure of a water tank on account of the cyclonic winds in recent times was the structural failure of the tank in Sriharikota island in India due to the Bay of Bengal Cyclone of 1984.

There are many references in literature to research carried out on wind loads acting on tall structures like chimneys, towers and masts, but very little attention has been paid to wind loads on water tanks. Many slender water tanks with huge mass at top are being built. It is felt that, as of today, there is some amount of arbitrariness in assuming the wind loads in the current codes of practice. The lack of information on the variation of the coefficient of drag with height poses difficulties to the designers in optimizing the structural design. Thus the estimation of the pressure distribution round a tank and the calculation of drag coefficient have assumed importance.

### 2. Terrain simulation

The use of naturally grown rough wall boundary layer to simulate the atmospheric boundary layer in long test section wind tunnels makes sure that accurate representation of the atmospheric boundary layer can be obtained. Saw tooth roughness, Vortex generator array and Spire array for boundary layer thickness augmentation are some of the boundary layer

tripping techniques at the entrance of the test section as suggested by Cermak<sup>1</sup>.

Not every laboratory can afford the cost or space for a boundary layer wind tunnel of sufficient length. Since early seventies tremendous amount of work has been done to devise methods of accelerating the growth of natural boundary layers by passive devices to obtain simulation giving similar accuracy in shorter wind tunnels.

The wind tunnel at the Aeronautical Engineering Department of Madras Institute of Technology (Anna University), India has a test section length of 2m and hence falls into the category of wind tunnels of short test section.

Cook<sup>2</sup> in his work has proposed the combined usage of roughness, barrier and mixing device to generate the atmospheric boundary layer in short test sections. The role of the surface roughness in representing the rough surface of the ground is identical to that in the natural growth boundary layer simulation. Barrier is to provide an initial momentum deficit, representing the effect of a longer stretch of roughness upwind. The role of the mixing device is to distribute this momentum deficit through the developing boundary layer.

The work done by Cowdrey<sup>3</sup> has helped in creating the required boundary layer by tripping the velocity profile by means of a grid at the entrance to the test section. The grid consists of circular rods at specific spacings.

Rao and Garg<sup>4</sup> have modified the above method by adding roughness elements downwind of the grid to accelerate the growth of the boundary layer.

Cowdrey has suggested a formula for spacing of rods in test section as

$$Y/s = \left( \frac{n}{1+n} \right)^n \left[ \frac{1 + K_1}{1 + \frac{d/l}{(1-d/l)^2}} \right]^{n/2}$$

- Y - height of a point in the velocity profile above the ground
- s - height of the wind tunnel
- n - reciprocal of the power law index.
- K<sub>1</sub> - overall pressure drop coefficient of the grid
- d - diameter of the grid rod.
- l - distance of separation between axes of two rods.

A program to compute the spacing of the bars in the grid as per Cowdrey's formula with the terrain roughness factor and the diameter of the rods as the input data was used in the present case.

The input data are

n = 3, k = 0.05, s = 90cm, d = 1cm.

### 3. Experimental Details and Data Reduction:

The Layout of the water tank is given in Fig.1. Models of given dimensions have been made to a scale of 1:100 in metal

sheet. The model can be split into five parts - the shaft consists of three parts; container cone and the roofdome are the other two parts. In the model there is provision for a total of ninety one pressure pick ups. Pressure pick ups have been minimised by staggering. From the recorded readings the distribution of the coefficient of pressure was computed at different heights. A typical plot is given in Fig.2.

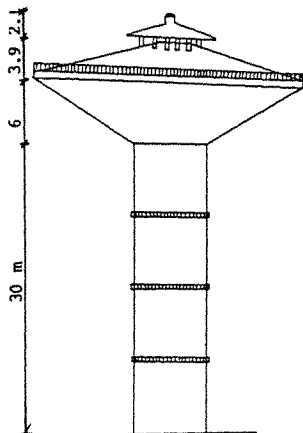


Fig.1 Layout of the water tank.

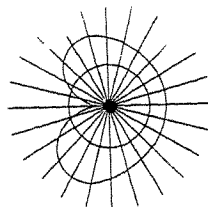


Fig.2 Cp. plot at typical section.

The coefficient of drag ( $C_d$ ) was obtained by resolving the coefficient of pressure in the direction of the flow at every level. The forces at every height are estimated as  $F_z(\text{experiment}) = C_d \cdot P_z \cdot A_e \cdot G$

$F_z(\text{code}) = C_f \cdot P_z \cdot A_e \cdot G$

where  $C_f$  = Recommended values of Coefficient of pressure as per code<sup>5</sup> IS 875

$P_z = 0.6 V_z =$  as in IS 875

$C_d$  = Coefficient of drag

$A_e$  = effective area

$G$  = Gust factor as per IS 875

$V_z$  = Design wind speed as per IS 875.

Shear force at a level is the summation of the nodal forces at that level and at levels above. Bending moment at a level is the summation of the moments created by the nodal forces above the level, about the level.

The wind tunnel tests covered runs in different speeds. The effect on one tank in the lee of another was also studied by having two models in tandem with different spacings (in terms of maximum diameter) and angles of stagger.

#### 4. Conclusions:

The following conclusions have been drawn based on the wind tunnel study of a water tank model.

**(a) Effect of terrain simulation:**

A hilly terrain has been simulated during the test using a grid at the entrance to the test section and surface roughness elements in the tunnel. Tests were conducted with and without terrain simulation. It was noticed that drag coefficient values were 50% to 100% higher when the terrain was simulated as against the case with no terrain simulation.

**(b) For single tank in the test section:**

(i) The Cd values obtained by experiment were on the overall lower than those suggested by the wind code. This consequently gave lower values of shear force and bending moment at the base of the tank estimated by experiment than by wind code. (Table 1)

(ii) There is no significant effect on Cd values due to variation of test section speed suggesting that the flow is completely turbulent even at the lowest speed. This is in keeping with the behaviour of a bluff body in full turbulent flow.

(iii) One of the findings of the present investigation is the presence of a force opposite to the wind direction at the tip of the tank as seen in table 1. A possible reason for this is the three dimensional effect at the tip in a turbulent flow. The existence of this negative force explains the reason for getting less bending moment and shear force by experiment compared to the ones based on wind code.

---

LEVEL	Ht (m)	Cd	Ae (Sq.m)	FN <sub>E</sub> (KN)	FN <sub>C</sub> (KN)	SF <sub>E</sub> (KN)	SF <sub>C</sub> (KN)	BM <sub>E</sub> (KN.M)	BM <sub>C</sub> (KN.M)
1	40.67	-0.6610	20.980	-22.931	26.609	-22.93	26.60	0.00	0.00
2	39.37	0.3730	59.470	36.357	74.761	13.42	101.37	-29.81	34.59
3	35.56	0.9900	52.000	82.703	64.074	96.12	165.44	21.34	420.81
4	33.02	0.7460	55.290	65.376	67.217	161.50	232.66	265.50	841.03
5	29.21	0.3490	15.450	8.355	18.362	169.86	251.02	880.84	1727.47
6	26.67	1.0900	19.050	31.591	22.230	201.45	273.25	1312.28	2365.07
7	24.13	0.5240	19.050	14.909	21.823	216.36	295.07	1823.97	3059.13
8	21.59	1.1120	23.775	38.848	26.795	255.20	321.87	2373.53	3808.62
9	17.78	0.6260	28.610	25.040	30.680	280.24	352.55	3345.87	5034.95
10	13.97	0.3460	33.540	15.380	34.094	295.62	386.64	4413.62	6378.17
11	8.89	0.9440	28.540	32.948	26.770	328.57	413.41	5915.41	8342.32
12	6.35	0.6960	23.810	20.266	22.333	348.84	435.74	6749.99	9392.40
13	2.54	0.4480	33.840	18.540	31.741	367.38	467.48	8079.08	11052.59

---

**Table 1. Comparison of Forces by Code and Experiment (Single tank)**

FN - Nodal Force; SF - Shear Force; BM - Bending Moment  
Suffix: E - Experimental Values; C - Calculated by Code.



(c) For tanks kept in tandem and at stagger:

(i) When the rear tank is very close to the front one (spacing of one D, where 'D' is the maximum diameter of the conical portion). and with no stagger, complete shielding seems to occur. The rear tank registers practically no drag.

(ii) However even with a spacing of one D, the Cd values are significant when the tanks are staggered.

(iii) When the spacing is progressively made more the Cd values also are increased, with a maximum recorded at a spacing of 3D. At spacings higher than 3D the Cd values show a downtrend.

(iv) The balconies also seem to have an effect on Cd since at balcony locations the local Cd values are lower.

(d) Note on shear force and bending moment values:

(i) The terrain simulation gives nearly 100% extra moment and about 80% increase of shear force at root as against the respective values with no terrain simulation.

(ii) Beyond a spacing of 3D and with good stagger there is no marked difference in bending moment and shear force values between the experiment and as calculated by wind code.

(iii) But in moderate spacings and stagger the values of shear force and bending moment arrived at through experimented data are lower than those calculated by the use of the wind code.

References:

1. J.E. CERMAK. Proc. of Int. workshop on wind tunnel modeling for Civil Engg. applications, Ed.T.A. Reinhold, Cambridge University Press 1982.
2. N.J. COOK *ibid.*
3. G.N.V. RAO & R.K. GARG Asian Congress on Fluid mechanics, Seoul, August 1992.
4. C.F. COWDREY (1967), " Note-1055", Aero Div, NPL,U.K., May 1967.
5. Indian Standard Code of Practice for Design Loads for Buildings and other Structures., IS-875 part 3 wind loads.



## **Wind Codes and Wind Damage**



## The New European Wind Load Code

H. Ruscheweyh

Wind Engineering  
Institute for Steel Structures  
University of Technology Aachen (RWTH) Germany

### Abstract

The final draft of the new European Wind Load code is explained and some background informations are given about the format, the calculation procedures and the basic values of wind and aerodynamic coefficients. The static wind load as well as dynamic wind effects are presented.

### 1. Introduction

For the harmonization of the actions on buildings and structures within the European Community a new Wind Load Code has been drafted. The drafting work has been finished in April 93 by an expert group and has been sent to the Committee TC 250/SC1 for voting to become an ENV-state. While this paper is being written, the technical content of the draft has been approved by the SC 1 Committee. Within two years this ENV-Wind Load Code will be used and checked by the engineers. Corrections and/or editorial changes may be made after this period to come to the final code, which will be legally binding for all memberstates of Europe, including the EFTA-states.

### 2. Principles

The present draft of the Eurocode "WIND ACTION", has been started from the ISO T 98 "Wind Action" and it has been developed to a working paper which can be applied to most of the common buildings and structures. To achieve the design aims of a structure account shall be taken of

- turbulent wind acting over part or all of the structure
- static and fluctuating pressures induced by the wake behind the structure
- fluctuating forces induced by the motion of the structure

The response of structures due to wind action is divided into the following types:

- static response, stochastic and resonant response due to turbulence and wake effects, vortex resonance, galloping, interference, divergence and flutter

The wind load is presented either as a wind pressure or a wind force resp. wind moment.

### 3. Wind pressure and wind forces

#### 3.1 Wind pressure on surfaces, $w_{e,i}$

The wind pressure on surfaces given in this code is valid for surfaces which are sufficiently rigid to neglect their resonant vibration caused by the wind. The pressure is described as an

$$\begin{aligned} - \text{ external pressure } w_e &= q_{\text{ref}} \cdot c_e \cdot (z_e) \cdot c_{pe} & (1) \\ - \text{ internal pressure } w_i &= q_{\text{ref}} \cdot c_e \cdot (z_i) \cdot c_{pi} & (2) \end{aligned}$$

and the net pressure is

$$w_{\text{net}} = w_e - w_i \quad (3)$$

where:

$$\begin{aligned} q_{\text{ref}} &= \text{reference mean wind velocity pressure} = \rho/2 v_{\text{ref}}^2 \text{ (see 4.1)} \\ c_e(z_e, z_i) &= \text{exposure coefficient (see 4.2.2) which includes the effects of the wind profile} \\ &\quad \text{and of the topography} \\ c_{pe,i} &= \text{external (e) and internal (i) pressure coefficients derived from a coefficient} \\ &\quad \text{catalogue} \\ z_{e,i} &= \text{reference height defined together with the } c_{pe,i} \text{-values.} \end{aligned}$$

### 3.2 Wind force, $F_w$

The global force,  $F_w$ , which results from the pressure distribution (without friction forces) shall be obtained from the following expression

$$F_w = q_{\text{ref}} \cdot c_e(z_e) \cdot c_f \cdot A_{\text{ref}} \cdot c_d \quad (4)$$

where:

$$\begin{aligned} c_f &= \text{force coefficient} \\ A_{\text{ref}} &= \text{reference area for } c_f \\ c_d &= \text{dynamic factor, which takes into account the aerodynamic admission and the} \\ &\quad \text{resonant gust response and is } \leq 1 \text{ for structures which are not sensitive to vibrations} \\ q_{\text{ref}} c_e(z_e) &= \text{defined as before} \end{aligned}$$

### 3.3 Friction force, $F_{fr}$

For structures with large areas swept by the wind (i.e. large free standing roofs), friction forces,  $F_{fr}$ , may be important. They shall be obtained from:

$$F_{fr} = q_{\text{ref}} \cdot c_e(z_e) \cdot c_{fr} \cdot A_{fr} \quad (5)$$

where:

$$\begin{aligned} c_{fr} &= \text{friction coefficient} \\ A_{fr} &= \text{area swept by the wind} \\ q_{\text{ref}} c_e(z_e) &= \text{defined as before.} \end{aligned}$$

## 4. Reference wind and wind coefficients

### 4.1 Reference wind velocity

The reference wind velocity,  $v_{\text{ref}}$ , is defined as

- the 10 min mean wind velocity
- at 10 m above ground of terrain category II (see 4.2.1)
- with an annual probability of exceedence of 0,02 (50 year return period).

### 4.2 Wind coefficients

#### 4.2.1 Coefficients for the reference wind velocity

$$v_{\text{ref}} = c_{\text{DIR}} \cdot c_{\text{TEM}} \cdot c_{\text{ALT}} \cdot v_{\text{ref},0} \quad (6)$$

where:

$$v_{\text{ref},0} = \text{basic value of the reference wind velocity at 10 m above sea level given in the national wind maps which are presented in an Annex.}$$

- $c_{DIR}$  = direction factor, which takes into account the probability of wind speed depending on the wind direction. It is taken as 1,0 unless otherwise specified in the national wind maps.
- $c_{TEM}$  = temporary (seasonal) factor which takes into account the probability of wind speed for structures which are
- structures during construction and which may require temporary bracing supports
  - structures whose life time is known and less than one year.
- Unless otherwise specified in the national wind maps,  $c_{TEM}$  is taken as 1,0.
- $c_{ALT}$  = altitude factor which takes into account the altitude level of the site and is to be taken as 1,0 unless otherwise specified in the national wind maps.

#### 4.2.2 Coefficients for the mean wind velocity at height z

The mean wind velocity at height, z, at the site of the structure depends on the roughness of the terrain in the direction from where the wind is blowing and on topographical effects (hills, escarpments etc.). It is given by

$$v_m(z) = v_{ref} \cdot c_r(z) \cdot c_t(z) \quad (7)$$

where:

$c_r(z)$  = roughness coefficient at height z

$c_t(z)$  = topography coefficient at height z

The roughness coefficient describes the effect of the terrain roughness and is defined by a logarithmic law. It shall be calculated by

$$\begin{aligned} c_r(z) &= k_r \cdot \ln(z/z_0) && \text{for } z_{min} \leq z \\ c_r(z) &= c_r(z_{min}) && \text{for } z < z_{min} \end{aligned} \quad (8)$$

Four different terrain categories are defined and given in Table 1 together with the parameters  $k_r$  = terrain factor,  $z_0$  = roughness length,  $z_{min}$  = minimum height.

When there is any doubt about the choice between two categories in the definition of a given area, the worst case should be taken.

	terrain category	$k_r$	$z_0$ [m]	$z_{min}$ [m]	$\epsilon$
I	Rough open sea Lakeshore with at least 5 km fetch upwind and smooth flat country without obstacles	0,17	0,01	2	0,13
II	Farmland with boundary hedges, occasional small farm structures, houses or trees	0,19	0.05	4	0,26
III	Suburban or industrial areas and permanent forests	0,21	0,3	8	0,37
IV	Urban areas in which at least 15% of the surface is covered with buildings and their average height exceeds 15 m	0,23	1	16	0,46

Table 1: Terrain categories and related parameters

If a structure is situated near a change of terrain roughness, a simple procedure is given in the Code.

The topography coefficient,  $c_t(z)$ , accounts for the increase of mean wind velocity over isolated hills and escarpments. It is given in the code by a formula and two diagrams. Otherwise it is set to 1,0.

#### 4.2.3 The exposure coefficient, $c_e(z)$

The exposure coefficient,  $c_e(z)$ , takes into account the effects of terrain roughness, topography, turbulence and height above ground on the mean wind speed.

It is developed from the gust response factor,  $G$ , which itself is not used in its classical expression in the Eurocode. Starting from the basic expression for the quasi static design wind pressure,  $q(z)$ , in the height,  $z$ , above ground:

$$q(z) = q_{\text{ref}} \cdot c_r^2(z) \cdot c_t^2(z) \cdot G \quad (9)$$

$$G = 1 + 2 \cdot g \cdot I_v(z) \cdot \sqrt{Q_o^2 + R_x^2} \quad (10)$$

where:

- $g$  = peak factor
- $I_v$  = turbulence intensity in the height  $z$  above ground
- $Q_o^2$  = background part of the gust response
- $R_x^2$  = resonant part of the gust response
- $c_r(z)$ ,  $c_t(z)$ ,  $q_{\text{ref}}$  defined as before

and expanding the equation with  $(1 + 2 \cdot g \cdot I_v(z))$  we receive the following expression for  $q(z)$ :

$$q(z) = q_{\text{ref}} \cdot c_r^2(z) \cdot c_t^2(z) \cdot (1 + 2 \cdot g \cdot I_v(z)) \frac{1 + 2 \cdot g \cdot I_v(z) \cdot \sqrt{Q_o^2 + Q_x^2}}{1 + 2 \cdot g \cdot I_v(z)}$$

In the first bracket the turbulence intensity  $I_v(z)$  is replaced by

$$I_v(z) = \frac{k_r}{c_r(z) \cdot c_t(z)} \quad (11)$$

thus:

$$q(z) = q_{\text{ref}} \cdot c_r^2(z) \cdot c_t^2(z) \cdot \left( 1 + 2 \cdot g \cdot \frac{k_r}{c_r(z) \cdot c_t(z)} \right) \frac{1 + 2 \cdot g \cdot I_v(z) \cdot \sqrt{Q_o^2 + Q_x^2}}{1 + 2 \cdot g \cdot I_v(z)}$$

$$q(z) = q_{\text{ref}} \cdot [c_r^2(z) \cdot c_t^2(z) + 2 \cdot g \cdot k_r \cdot c_r(z) \cdot c_t(z)] \frac{1 + 2 \cdot g \cdot I_v(z) \cdot \sqrt{Q_o^2 + Q_x^2}}{1 + 2 \cdot g \cdot I_v(z)} \quad (12)$$

The expression in the first bracket is called "exposure coefficient",  $c_e(z)$ :

$$c_e(z) = c_r^2(z) \cdot c_t^2(z) + 2 \cdot g \cdot k_r \cdot c_r(z) \cdot c_t(z) \quad (13)$$

and the quotient is called "dynamic factor",  $c_d$ :



$$c_d = \frac{1 + 2 \cdot g \cdot I_v(z) \cdot \sqrt{Q_0^2 + R_x^2}}{1 + 2 \cdot g \cdot I_v(z)} \quad (14)$$

The dynamic factor,  $c_d$ , is described in chapter 6.2 in more detail.

The peak factor,  $g$ , can be approximated by  $g = 3.5$ , thus

$$c_e(z) = c_r^2(z) \cdot c_t^2(z) + 7 \cdot k_r \cdot c_r(z) \cdot c_t(z) \quad (15)$$

For the most common cases,  $c_t(z) = 1$ , the exposure coefficient is illustrated in Figure 1.

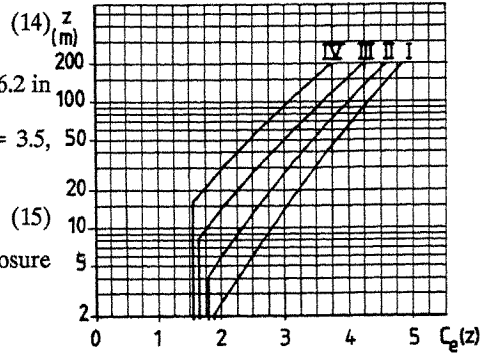


Fig. 1: Exposure coefficient  $c_e(z)$  as a function of height  $z$  above ground and terrain roughness category for  $c_t = 1$ .

## 5. Aerodynamic coefficients

The Eurocode presents aerodynamic coefficients for the following structures, structural elements and components:

- buildings, including building walls, different types of roofs, internal pressure
- canopy roofs and multispan roofs
- free standing boundary walls, fences and signboards
- structural elements with rectangular, sharp edged and regular polygonal section
- circular cylinders and spheres
- lattice structures and scaffolding
- bridges
- flags
- slenderness effect

Each coefficient is referred to a reference area and a reference height, which are defined for that particular coefficient.

## 6. Dynamic factor for gust response

As shown in chapter 4.2.3 the dynamic factor,  $c_d$ , takes into account the reduction effect due to the lack of correlation of pressures over surfaces and the magnification effects due to the frequency content of turbulence close to the fundamental frequency of the structure.

In order to evaluate the dynamic factor,  $c_d$ , two procedures can be applied:

- (i) simple procedure
- (ii) detailed procedure.

The simple procedure has been developed for buildings and structures which are less sensitive to dynamic response. The dynamic factor,  $c_d$ , for those structures is less or near 1.

### 6.1 Field of application

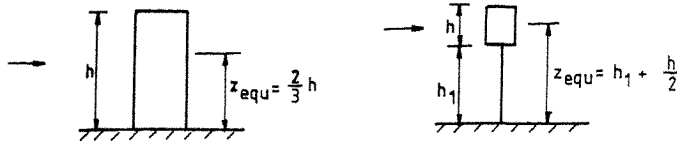
Based on the detailed procedure and with approximations of natural frequencies and damping, criteria have been developed for the field of application of the simplified procedure, which provides conservative results.

### 6.2 The detailed procedure for $c_d$

The dynamic factor,  $c_d$ , is defined by /1/

$$c_d = \frac{1 + 2 \cdot g \cdot I_v(z_{equ}) \cdot \sqrt{Q_0^2 + R_x^2}}{1 + 7 \cdot I_v(z_{equ})} \quad (16)$$

where:  $z_{equ}$  = equivalent height of the structure



The quantities  $g$  = peak factor,  $I_v$  = turbulence intensity,  $Q_0$  = background part of the gust response,  $R_x$  = resonant part of the gust response are presented by mathematical expressions which allow a numerical calculation with computers. For a quick check and for illustration the parameters are presented in diagrams, too.

In order to evaluate the serviceability of the structure in respect to alongwind vibration an expression is given to calculate the displacements and accelerations.

Finally, interference factors are presented for high-rise buildings in tandem or grouped arrangement effected by wake buffeting.

### 7. Vortex shedding

Slender structures such as chimneys, observation towers, elements of open frames and trusses, bridges and in some cases high rise buildings shall be designed to resist the dynamic effect of vortex shedding. The shedding of vortices from unstiffened cylindrical shells may in addition excite ovaling oscillations. The field of application is given by criteria which implies the limit of

$$v_{cnt} \leq 1,25 v_m$$

where  $v_m$  = design wind speed (see chapter 4.2.1).

In order to calculate the critical wind speed

$$v_{cnt} = (b \cdot n_p) / St \quad (17)$$

the Strouhal numbers,  $St$ , are given for different cross sections and the natural frequency,  $n_p$ , may be estimated by using the formulae given in a special Annex.

For the calculation of the maximum vortex resonance amplitude the correlation length model is presented /2/

$$\frac{\max y_F}{b} = K_w \cdot K \cdot c_{lat} \cdot \frac{1}{St^2} \cdot \frac{1}{Sc} \quad (18)$$

where:

- $b$  = reference width of the cross section
- $K_w$  = effective correlation length factor;  $0,1 \leq K_w \leq 0,6$
- $K$  = mode shape factor;  $0,1 \leq K \leq 0,14$
- $c_{lat}$  = aerodynamic force coefficient, given for the cross sections as listed in chapter 5
- $St$  = Strouhal number
- $Sc$  = Scruton number =  $2 m \delta / (\rho b^2)$

The most important point of the correlation length model is the calculation of the effective correlation length factor,  $K_w$ . For large amplitudes ( $\max y_F/b > 0,1$ )  $K_w$  must be calculated by an iterative procedure. Simple formulae are presented for common cases. The correlation length model cannot be applied only to cantilevered or simple supported structures but also to more complicated structures, like spatial lattice structures, frame structures or guyed masts. The handling for those systems is described in the Eurocode.

#### **8. Aeroelastic instabilities and interference effects**

The following phenomena are described

- galloping instability, interference galloping, bridge flutter, divergence. Criteria and calculation procedures are presented for the onset velocity resp. divergence velocity for galloping, interference galloping and divergence. Bridge flutter stability should be calculated by solving the flutter equation or with model tests and is not presented in detail.

#### **9. Final remarks**

The new draft of the Eurocode "Wind Action" presents calculation procedures of wind pressure and wind forces for the most common buildings and structures for static loads as well as for dynamic effects. It was the aim to draft a code with includes modern calculation procedures and verified aerodynamic coefficients which produce realistic load values. The structure of the code enables to add or to reduce values as available and to follow an increase of knowledge and experiences in the field of wind action.

For the description of the wind characteristics a format is given and the regional values are presented in different national wind maps. Every country may introduce simplifications or more sophisticated descriptions of wind parameters, if available.

For structures which are less sensitive to dynamic effects, the calculation procedure becomes simple and is restricted to only a few calculation steps.

All design codes of the Eurocode will refer to this wind action code, so that the wind load will be calculated in an identical manner for all buildings and structures.

During the following ENV period it may happen, that some supplements will be included if the design codes request for it.

#### **References**

1. Solari, G.: Turbulence modelling for gust loading, J. Struct. Eng., ASCE, 113, 7, 1550-1569
2. Ruscheweyh, H.: Vortex excited vibrations, Proc. Course "Wind-excited vibrations on structures, CISM, Udine, Italy, 1992



## RECOMMENDED IMPROVEMENTS IN THE SOUTH FLORIDA BUILDING CODE

Herbert S. Saffir, P.E., F, ASCE

Herbert Saffir Consulting Engineers  
Coral Gables, Florida 33134

**Abstract:** After Hurricane Andrew struck the area south of Miami on August 24, 1992, a Building Code Evaluation Task Force was formed. This Task Force was established by the County Manager, Joaquin Aviño, P.E., and was charged with the responsibility of reevaluating current requirements of the South Florida Building Code and making recommendations for changes, as a result of Hurricane Andrew's lessons. The Task Force is an eight member group made up of consulting engineers, university professors of engineering, and building code specialists. The author is a member of the Task Force and subsequently established Building Code Committee. This paper covers the main recommendations for revisions to the Building Code.

### 1. BUILDING CODE

The South Florida area is governed by the South Florida Building Code, which is a specification-type code, strong on prescriptive detail, and pointed toward prevalent building practices in South Florida which use masonry (concrete block) types of construction extensively. The present wind load requirements call for a design storm of 120 mph ( 53 m/s) at 30 feet (9.14 m) above grade, with velocity increases in conformance with the 1/7th power law, to a maximum of 198 mph (89 m/s) at 1000 feet (305m) above grade. The South Florida Building Code is a regional code used by the permanent population of over 4 million people residing in South Florida.

### 2. OBSERVED DEFICIENCIES AFTER HURRICANE ANDREW

Although the Building Code in use is a hurricane-resistant code, the South Florida area had not had a major hurricane - Category 3 or greater on the Saffir-Simpson Hurricane Scale - for almost 40 years. Observed damage to buildings and other structures after Hurricane Andrew can be attributed to these factors:

The storm's severity, which was conservatively estimated to be 145 mph ( 65 m/sec.) sustained wind velocity for 1 minute, at 30 feet (9.14 m.) above grade, and 175 mph (78 m/sec.) gust wind velocity, at 30 feet (9.14 m.) above grade. This exceeded the design storm specified in the South Florida Building Code, although working stresses given in the building code permit some overload without failure.

Some code and installation deficiencies left building envelopes unprotected and vulnerable to windborne debris.

Failures to follow the building code in all respects especially applied to roof sheathing and roof bracing.

Inadequate building code enforcement, inadequate plans reviews by various

building departments involved and inadequate inspections by building department inspectors.

Inadequate training and poor supervision at all levels of building contractors' staffs.

Inadequate training of building departments' inspection personnel.

Use of substitute materials without proper controls for compliance with the performance requirements of the building code.

### 3. RECOMMENDATIONS FOR BUILDING CODE IMPROVEMENTS

The Task Force made these recommendations for improving the South Florida Building Code, since adopted by the governing board.

For wind load requirements, the sections covering wind loads in ASCE Standard 7-88 (formerly ANSI A58.1) will be adopted in place of the present wind load requirements in the South Florida Building Code, with certain qualifications. Only Exposures C and D were adopted:  
D for coastal areas up to a distance of 1500 feet (457 m.) back of the high water line on the coast, and C for interior coastal areas.\*

#### Definitions:

Exposure C: Open terrain with scattered obstructions have heights generally less than 30 feet (9.14 m.). This category includes flat open country and grasslands.

Exposure D: Flat, unobstructed areas exposed to wind flowing over large bodies of water. This exposure shall apply only to those buildings and other structures exposed to the wind coming from over the water. Exposure D extends inland from the shoreline a distance of 1500 feet (457 m.) or 10 times the height of the building or structure, whichever is greater.

Wind loads for the design of the main wind force resisting systems shall be designed for the exposure category at the site of the building or structure.

For the design of components and cladding, Exposure C shall be used for all buildings less than or equal to 60 feet (18 m.) in height.

For all buildings in South Florida except those listed below the basic fastest-mile design storm will be 110 mph (49 m/s)  $\times 1.05 = 115.5$  mph (52 m/s) @ 30 feet (9.14m) above grade. (1.05 is taken from the Table of Importance Factors for areas on hurricane coasts).

For those buildings where more than 300 people congregate in one area, or for essential facilities such as hospitals, fire and police stations, communication

---

\* See Table 1 giving velocity pressures for design purposes.

centers, power stations, stations, stations having critical defense capabilities, and designated shelters for hurricanes, the basic fastest-mile design storm will be 110 mph ( 49 m/s)  $\times 1.11 = 122.1$  mph ( 55 m/s) 30 feet (9.14 m.) above grade (1.11 is taken from the Table of Importance Factors).

Clarify and fully enforce code requirements for submission of truss bracing details by the architect of record (non-engineered buildings) especially since many failures were due to poor or improper residential roof truss bracing.

Clarify and fully enforce the code requirements as to responsibility for the design and inspection of curtainwall panels, using the new ASCE 7-88 Standard for wind loadings. This will increase the design loading for such components of buildings. All systems shall be designed by a Registered Engineer.

Adopt mandatory protection of building envelope in new construction by requiring that the components of exterior walls such as glazing, doors and windows of enclosed buildings be specifically designed and constructed to preserve the enclosed building envelope against wind pressure and impact loads from windborne debris or be protected by fixed, operable or portable demountable storm shutters.

Require mandatory testing of shingles and tiles as a system at 110 mph ( 49 m/s) and adopt a testing standard for incorporation into the building code.

Re-examine the use of wall systems other than concrete block in multi-story residential and commercial buildings and ban prefabricated systems if necessary.

Strengthen the role of the structural engineer in the design of residential and commercial structures.

Require that the architect or engineer-of-record participate in the structural inspection process and sign an affidavit prior to the issuance of the Certificate of Completion by the Building Official certifying that to the best of his/her knowledge the building construction fully complies with the design intent and the building code, and the approved permit plans reflect the structural "as-built" conditions.

Require as part of the permit set of plans that all drawings and specifications for building component items, such as windows, doors, roof trusses, etc., that have received product control approval, be included, so that thorough conforming inspections can be performed by the building inspectors.

Clarify design responsibility for loads transmitted to the structure by mechanical equipment mounted on the roof.

For pre-engineered metal buildings, which fared poorly during Hurricane Andrew, the following requirements are recommended:

a. Require roof and wall lateral and cross bracing in addition to panel and deck diaphragm action for wind bracing.

- b. Require that doors be anchored as part of the frame in the closed position. Require that all doors meet the performance requirements of the code.
- c. Require a heavier metal siding (minimum gage of 24) (0.06 c.m.).
- d. Institute a quality control program for all steel fabrication and installation.
- e. Re-examine the use of self-tapping screws for fastening siding and roof panels and ban, if necessary.
- f. Require that metal siding be designed continuously; decrease allowable deflection and require that siding be subjected to an impact load test consistent with the criteria established for the protection of building envelopes.
- g. Eliminate the use of cables for tension members.

#### 4. IN SUMMARY

The tremendous amount of structural damage caused by Hurricane Andrew can be attributed to many factors, with, in general, no one factor outstanding as a cause. However, some building code improvements and better methods of enforcement of code requirements are warranted, and recommendations of the Building Code Evaluation Task Force have been made to improve the code in response to the lessons of Hurricane Andrew.



Table 1

Velocity pressures, with basic wind of 110 mph (49 m/s)  
 computed for 1.05 and 1.11 Importance factors

Importance Factor = 1.05

Height above ground	0-15' (0-4.57 m)	30' (9.14 m)	50' (15.24 m)	100' (30.48 m)	200' (60.96 m)	300' (91.44 m)	400' (121.92 m)	500' (152.41m)
Exposure C (1.29 kN/m <sup>2</sup> )	27 psf (1.63)	34 (1.63)	39 (1.87)	47 (2.25)	57 (2.73)	64 (3.06)	70 (3.35)	75 (3.59)
Exposure D (1.96 kN/m <sup>2</sup> )	41 psf (2.25)	47 (2.25)	52 (2.49)	60 (2.87)	69 (3.30)	75 (3.59)	79 (3.78)	82 (3.93)
Importance Factor = 1.11								
Exposure C (1.48 kN/m <sup>2</sup> )	31 psf (1.77)	37 (1.77)	43 (2.06)	53 (2.54)	64 (3.06)	72 (3.45)	78 (3.73)	83 (3.97)
Exposure D (2.20 kN/m <sup>2</sup> )	46 psf (2.49)	52 (2.49)	58 (2.78)	67 (3.21)	77 (3.69)	83 (3.97)	88 (4.21)	92 (4.40)



#1 Steel hangar building showing roof failure



#2 One-story residential construction showing result of lack of roof truss bracing, and breaching of exterior building envelope



#3 Commercial building windows and store front panels failed, with subsequent failure of roof



#4 Failure of steel rolling slat door, opening building to high internal pressures

An Experimental Investigation and Code Validation of the Wind  
Behaviour for a Square-Edged Tapered Building

Z.J. Lu, M.H. Sheu, J.H. Chou\*, C.H. Ding\*, S.K. Zen and J.J. Miau+

Department of Architectural Engineering  
National Cheng Kung University, Taiwan  
\*Department of Engineering Science  
National Cheng Kung University, Taiwan  
+Institute of Aeronautics and Astronautics  
National Cheng Kung University, Taiwan

**ABSTRACT:**Experiments are conducted to study the wind behaviour of a square-edged tapered building. The aspect ratio is 5 and the tapered angle is about 3 degrees. The Reynolds numbers are 1180 and 15385 for the water table and the wind tunnel experiments, respectively. The wind profile corresponds to a turbulent boundary layer in an open country. The pedestrian wind exists up to a height of about 1/10 building height. Codes comparison show that ANSI code gives good comparison for the windward surface, conservative for the side surface and poor for the upper level of the building for the leeward surface. On the other hand, Taiwan code prediction is conservative for the windward surface and too small for the leeward surface.

## 1. Introduction

Taiwan is a small island with a very large population. Thus it is natural for her to have high-rise buildings. On the other hand, due to her geological location, Taiwan is constantly under the threat of typhoons and strong seasonal winds which could lead to building and structural damages. In addition to structural damages, buildings subjected to winds could also have adverse effects such as flow-induced vibrations, curtain wall breakages and unbearable noise levels, just to name a few [1,2], which could cause discomfort to building dwellers. In order to provide a safe and comfort living environment for building dwellers, there are design regulations that a designer must follow. However, because of complex interactions between buildings and winds, and limited design data base, current building codes are rather inadequate [3,4]. Most high rise buildings have to go through a series of wind tunnel testings before being constructed. Wind tunnel tests still play an important role in building designs.

The main purpose of this study is to check the validity of two building codes, namely, ANSI and Taiwan building code. Two test models are used. One is a rectangular cylinder and the other is tapered rectangular cylinder. Both water table and wind tunnel test are conducted. The water table experiments are used mainly to study the physical aspects of the building behavior while the wind tunnel tests are used to check the validity of building codes.

## 2. Experimental Approach

The water table used is of a circulated type. City water driven by a 3-HP water pump runs through the facility continuously. The rectangular cross sectional area of the test section is 30 cm by 20 cm. Typical water depth for the experiment was 18 cm. The working fluid goes through a series of screens before entering the test section. Care was also taken to prevent the wave reflection from the downstream side of the test section so that good flow quality can be maintained. Flow visualization was made by two methods. One is the introducing of food coloring dye solution into the flow field through hypodermic needle. The Reynolds number of the needle based on its diameter was less than 40. Thus disturbances caused by the needle can be neglected. The other was by painting coloring paint onto the surface of the building models so that surface flow patterns and vortex shedding behavior can be observed. The flow structures were recorded by video recording systems for further analysis. The Reynolds number of the water table experiment was 1180. The observed phenomena included surface flow patterns, vortex shedding behaviors, wake regions and horseshoe vortex flows.

The wind tunnel used was a continuous blowing, open-loop type with a contraction ratio of 9:1. The test section is rectangular with a cross sectional area of 19.5 cm by 16.4 cm. Laboratory air was the working fluid. The Reynolds number was 15385. The surface pressure distributions were measured by surface pressure taps installed on the model surface and diaphragm type pressure transducer through a 48-port scanivalve. Data were taken and stored in a personal computer for later analysis. Two types of wind conditions are tested. One is an atmospheric turbulent boundary layer with a 1/7 power law velocity distribution. This wind profile was created by putting roughness element at the upstream of the test section inlet. The other is a uniform wind just for comparing purposes.

Two building models are studied. One is a rectangular cylinder and the other is a tapered rectangular cylinder as shown in Fig. 1. The aspect ratio, height to width, is 5:1. A height of 150 m corresponds to about 60-story building which is the current attention in Taiwan. Due to the size of the test section, scale-down models are used. They are 1/1000 and 1/1500 models for the water table and wind tunnel test, respectively. Experiments were conducted for every 10-degree change in wind direction from 0 degree to 90 degrees.

## 3. Results and Discussion

Fig. 2 shows a typical vortex shedding process for both models at zero angle of incidence. It can be seen that vortex shedding process for both models is fairly two dimensional except at the top and bottom locations where three dimensionality is very evident. It should be pointed out that the shedded vortices have two scales. One is smaller scale vortices come from the separated shear layer and has higher frequency. These smaller scale vortices tend to form larger scale vortices in the wake region and shed with a much lower frequency. This is the principal source of flow-induced vibration for buildings.

Furthermore, the shedding frequency for the rectangular cylinder is slightly larger than that of the tapered cylinder. The shedding behavior for both models at other angle of incidence shows similar results. This is expected since the models have sharp corners which tend to fix the separation locations on the models.

Surface flow patterns corresponding to flow conditions shown in Fig. 2 is depicted in Fig. 3 where surface A is the windward surface and surface B is the side surface. From the flow pattern on the front surface, it can be seen that the gross features for both models are very similar except the location of the stagnation point which is an indication of the scale of the horseshoe vortex. The tapered cylinder has a smaller scale horseshoe vortex. From the flow pattern on the side surface, one can observe that tapered cylinder is more three dimensional. Thus tapering can increase three dimensionality and reduce the scale of the horseshoe vortex. Therefore flow-induced vibration can be reduced by tapering.

The results of code comparison is shown in Fig. 4. Fig. 4a, 4b and 4c are the results for the windward surface, side surface and leeward surface, respectively. Both the results for the turbulent atmospheric boundary layer and the uniform wind distribution are shown in Fig. 4. In the figure, model A represents rectangular cylinder and model B represents tapered cylinder, and B.L. denotes the case for the 1/7 power law mean wind velocity profile. From Fig. 4a, it is clear that for the 1/7 power law wind profile, the pressure for the tapered cylinder is smaller than that of the rectangular cylinder as expected since the flow field for the former is more three dimensional. It can also be seen that ANSI code prediction is very close to the experimental result except at the top and bottom locations where three dimensional effects are large. On the other hand, Taiwan code prediction is much more conservative and is closer to the results of uniform wind distribution.

As for the results on the side surface shown in Fig. 4b, ANSI code gives a conservative estimate and Taiwan code provides no information at all. From the figure, it also can be observed that tapered cylinder has a larger suction pressure which is consistent with the results of Fig. 3b and 3d.

For the leeward surface, ANSI code prediction is more conservative and Taiwan code estimate is less conservative. Both codes can not account for the three dimensional effect at the top level of the buildings.

Overall speaking, ANSI code gives better prediction than Taiwan code. For the calculation of static wind load, Taiwan code result is acceptable because the load is due to the pressure difference between the windward surface and the leeward surface. But for the curtain wall design, which is very popular in Taiwan, the pressure on the leeward surface is too small for the Taiwan code. In this regard, ANSI code is also not adequate for the top level curtain wall design.

#### 4. Conclusions

An experimental study was conducted to investigate the wind behavior of a rectangular cylinder and a tapered rectangular cylinder. Comparison with both ANSI code and Taiwan code are also made. Key results are:

- a. Tapered cylinder has less static wind load due to its more three dimensional flow pattern.
- b. The shedding behavior for both tapered and rectangular cylinder is fairly two dimensional except at the top and bottom part of the buildings.
- c. For both models, shedded vortices have two scales, a smaller scale from the separated shear layer and an accumulated larger scale from the wake region.
- d. ANSI code provides better results than Taiwan code. For the static load calculation, Taiwan code can be used but not for the curtain wall design. However, none of codes can predict the effect due to three dimensional flow structures.

#### References:

1. E. L. Houghton and N. B. Carruthers, *Wind Forces on Buildings and Structures, An Introduction*. John Wiley & Sons (1976).
2. H. Liu, *Wind Engineering, A Handbook for Structural Engineers*. Prentice Hall (1991).
3. American National Standards Institute, ANSI, A 58.1-1982 (1982).
4. Ministry of Interior, ROC. *Building Technology Regulations* (1990).

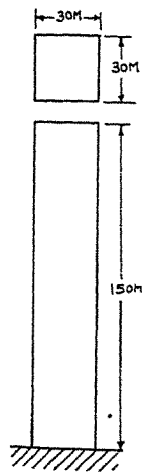


Fig. 1a. Rectangular building.

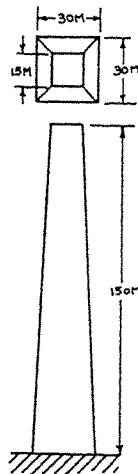


Fig. 1b. Tapered rectangular building.

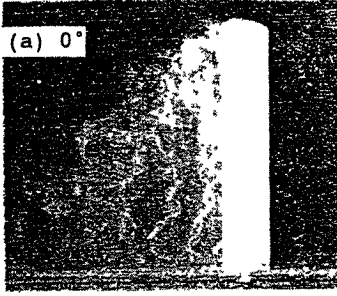


Fig. 2a. Shedding process for the rectangular model.

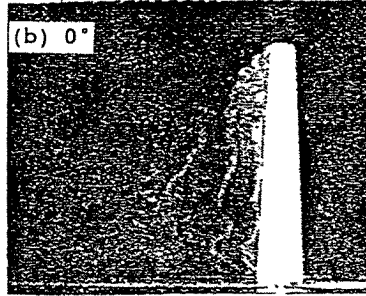


Fig. 2b. Shedding process for the tapered model.

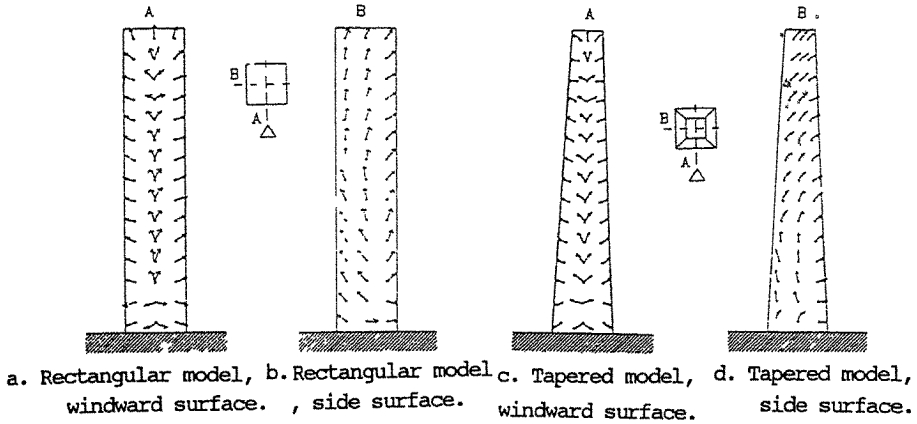
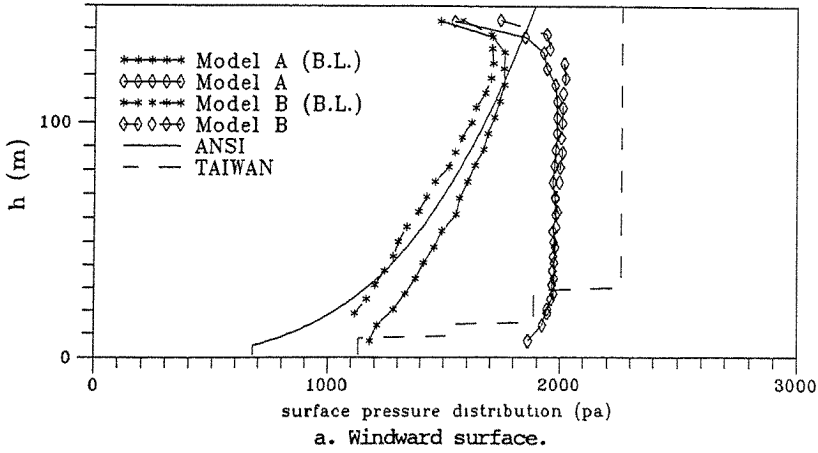
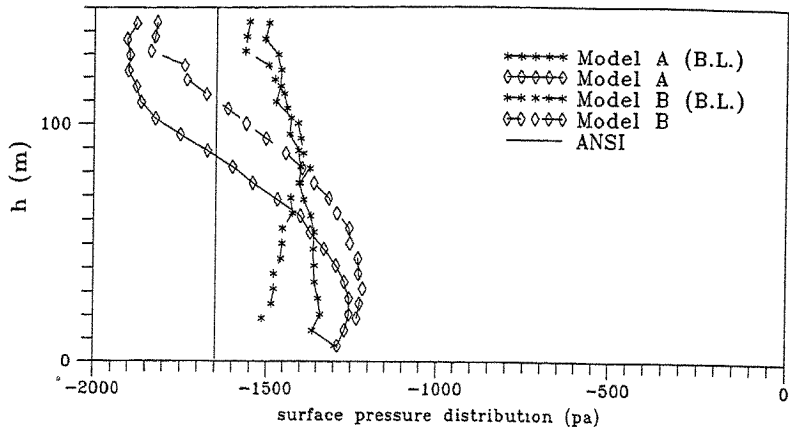
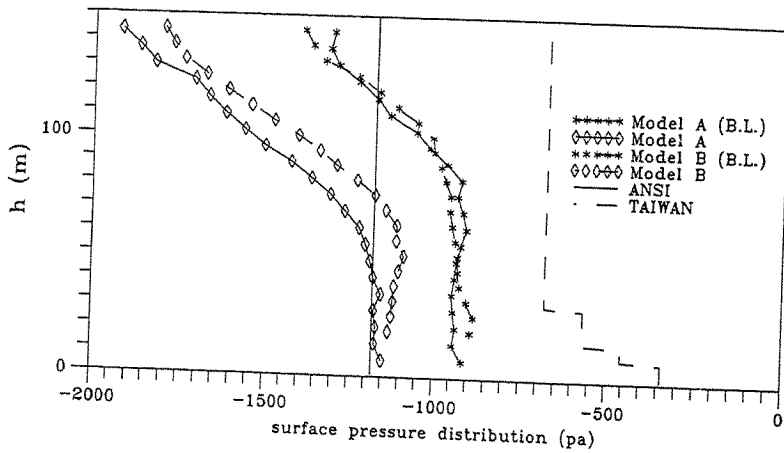


Fig. 3. Surface flow patterns.





b. Side surface.



c. Leeward surface.

Fig. 4. Comparisons among code predictions and experimental results.



## Development of wind load standard for Chinese bridge code

Ying-Jun Chen Xizhe Yu Jianming Yin Guangcheng Niu  
Civil Engineering Dept., Northern Jiaotong University, Beijing 100044, China

**Abstract:** In order to revise the Chinese wind load standard for bridge code, some researches are carried out. The main subjects discussed in this paper are: (1) Basic wind speed and design wind load; (2) Gust factor and gust pressure coefficient; (3) Scope of application; (4) The derivation of gust pressure coefficient and the interaction of wind and train loading, etc are discussed in the appendices.

### 1. Introduction

The wind load standard for Chinese Highway Bridge Code (JTJ 021-85) does not differ essentially from that for Chinese Railway Bridge Code (TBJ2-85). They are published in 1986 by the Ministry of Communications and the Ministry of Railways of the People's Republic of China, respectively. The standard specifications for bridges are applied to ordinary bridges with span lengths less than 160 m for railway bridges and 200 m for highway bridges. For these bridges, the magnitude of wind load has been not significant comparing with other live loads, such as vehicle loading.

However, with the increase of flexible structures, the wind effect has become increasingly important. On the other hand, according to the unified standard of reliability-based design of railway engineering structures published by the China Ministry of Railways (1992), the more detailed and systematic study of wind load is necessary in order to revise the bridge code.

### 2. Basic Wind Pressure

The basic or reference wind speed refers to the reference elevation, that is, 10 m above sea or ground level, standard exposure, averaging time 10 min. In bridge code 1986, the reference elevation was 20 m above sea or ground level, but 10 m is convenient for statistics.

The yearly maximum wind speed  $x_{max}$  can be considered as an independent random variable for every year. The probabilistic distribution function of which is  $F_x(x)$ , let  $x_T$  be the expectation value of return period T years. The probability  $q = P[x_{max} < x_T] = F_x(x_T)$ . The mean return period  $\bar{T}$  is also a random variable. If a bridge is designed for wind return period  $\bar{T}$ , and let the probability of non-exceedance in expected lifetime N years be Q, then

$$Q = q^N = \{F_x(x_T)\}^N = \left(1 - \frac{1}{\bar{T}}\right)^N \quad (1)$$

that is

$$\bar{T} = \frac{1}{1 - Q^{\frac{1}{N}}} \quad (2)$$

This is the relation between the wind return period and the expected lifetime of a bridge for the specified value of  $Q$ . But we have no so much data on statistic characteristics of load and resistance in this time, therefore, according to the presently used code, the return period is taken the same as the expected lifetime of the bridge, that is,  $\bar{T} = 100$  years for railway bridges,  $\bar{T} = 50$  years for highway bridges, and take the probability of exceedance level of 63%. The target reliability index may be determined by the specification calibration method.

According to the above mentioned principles, from the Chinese Meteorological Bureau records about 20–40 years(1951-1988) of 490 meteorological stations, a new wind map of basic wind pressures of China is newly carried out. It is known that the wind pressure was over-estimated in the wind map of previous code, as there were not enough meteorological data to draw isopleths at that time. The Fisher-Tippet Type I (Gumbel) distribution is used in extreme wind analysis. The basic wind pressure  $w_0 = v^2 / 1600$ (in  $kN / m^2$ ) and  $v$  is in  $m / s$ .

It should be noted that a number of meteorological records are less than 30 years at some stations, they do not accept the type I distribution, and the type II or the type III distribution is more appropriate. According as the data size increases, the type I distribution is fitted. As a result, the use of type I distribution is statistically reasonable at most of the stations in China. Of course, it may be more reasonable to consider longer return period than the expected lifetime, and the extreme wind analysis can be made by taking the difference of wind climate into account, if we have more reliability-based data in the future[2].

### 3. Design Wind Load

The transverse load is taken as acting in horizontal direction and perpendicular to the direction of bridge length unless local conditions change the direction of the wind. The transverse wind load per unit area is calculated by the following expression

$$w_i = k_0 k_1 k_2 k_3 w_0 \text{ (in } kN / m^2 \text{)} \quad (3)$$

where  $k_0$  is a factor refers to the return period  $\bar{T}$ , the basic wind pressure  $w_0$  is calculated for  $\bar{T} = 100$  years, that is  $k_0 = 1$ , for  $\bar{T} = 50$  years,  $k_0 = 0.88$ ,  $k_1$  is drag coefficient, in addition to the data of previous bridge code, wind tunnel experiments are carried out for some section shapes.  $k_2$  is a coefficient refers to the topography and terrain condition,  $k_3$  is gust coefficient. Expression (3) is quite differ from the previous conventional Chinese bridge codes. Especially for  $k_3$ , it is explained in the next section.

### 4. Gust Factor

The Chinese conventional bridge codes did not consider the gust effect. In the British

standards BS5400 (1978)[1], a gust velocity factor is used. The maximum design wind velocity  $V_m$  is

$$V_m = \bar{v} \left( 1 + \mu \frac{\sigma_v}{\bar{v}} \right) \equiv \bar{v} G \quad (4)$$

Where  $\bar{v}$  is mean wind velocity,  $\sigma_v$  is rms turbulent wind velocity,  $\frac{\sigma_v}{\bar{v}}$  is turbulence velocity coefficient,  $\mu$  is statistical peak factor, and  $G$  is called the gust velocity coefficient. In our case, a gust pressure coefficient  $k_3$  is defined, after some calculations, the gust pressure coefficient for superstructures  $k_{3s}$  and that for bridge piers  $k_{3p}$  can be expressed as followings

$$k_{3s} = \mu_z(z) \left[ 1 + \mu_f \sqrt{\frac{1}{l^2} \int_0^l \int_0^l \exp\left(-\frac{|x-x'|}{L_x}\right) dx dx'} \right] \quad (5)$$

$$k_{3p} = \mu_z(z) \left[ 1 + \mu_f \sqrt{\frac{1}{H^2} \int_0^H \int_0^H \exp\left(-\frac{|z-z'|}{L_z}\right) dz dz'} \right] \quad (6)$$

Where  $\mu_z(z)$  is a coefficient refers to the altitude  $z$  of the structure above the ground level.

The gust wind consists of mean and turbulent components, for the spatial correlation of the turbulence, the expressions of ECCS are used

$$\lambda(x, x') = \exp\left(-\frac{|x-x'|}{L_x}\right), \quad L_x = 42 \left(\frac{z}{20}\right)^{\frac{1}{4}} \quad (7)$$

$$\lambda(z, z') = \exp\left(-\frac{|z-z'|}{L_z}\right), \quad L_z = \sqrt{37z} \quad (8)$$

$\mu_f = \mu \sigma_w / \bar{w}$  is turbulence pressure coefficient, in general,  $\bar{z}$  is the average value of  $z$  and  $z'$ .

The derivation of expressions (5) and (6), is stated in appendix(A) of this paper. The expressions are differ from those of BS5400 for they are gust pressure factors. The aerodynamic admittance is not considered in these expressions, hence for flexible high piers and long span girders greater than 160–200 m, the dynamic response effects must be considered by another coefficients. It is simple to use expressions (5) and (6) by some table, from the parameters of site terrain roughness coefficient, the altitude of the structure above the ground level, span length or pier height, the coefficient  $k_3$  can be directly found from the table.

## 5. Conclusion

As pointed by Prof. M. Ito[2], the wind-resistant design codes for bridges are now in a period of transition and evolution, in particular on the criteria for dynamic response. Prof. A.G. Davenport proposed a dynamic response factor accounting for not only gust response but also other dynamic actions of wind[3]. But further investigation and data accumulation are necessary for this kind of factor.

The present Chinese Bridge Design Codes are applicable to ordinary bridges, the span lengths of which are less than 160 m for railway bridge and 200 m for highway bridge. In order to expand the scope, some studies are going on now.

#### Appendix A Effect of wind turbulence

For ordinary bridges, the superstructure is considered as one dimensional rigid structure, the wind force on element  $dx$  of a girder at height  $z$  above ground is (Fig.1)

$$dp(x,z,t) = C_D w(x,z,t) dx \quad (A1)$$

The wind pressure can be written as

$$w(x,z,t) = w(x,z) f(t) \quad (A2)$$

$$w(x,z,t) = \frac{1}{2} \rho V^2 = \frac{1}{2} \rho (\bar{v} + v_f)^2 \approx \frac{1}{2} \rho \bar{v}^2 + \rho \bar{v} v_f = \bar{w} + W_f \quad (A3)$$

Where  $\bar{w}$  is average wind pressure,  $W_f$  is turbulent wind pressure.

The mean square of turbulent force is

$$\overline{(f_a + f_b)^2} = \int_0^l \int_0^l \overline{d f d f'}, \quad \overline{d f d f'} = \rho^2 C_D^2 \bar{v}^2 \overline{v_f v_f'} dx dx' \quad (A4)$$

The spatial correlation factor of turbulent force is expressed by eqs.(7) and (8), and

$$\overline{v_f v_f'} = \sigma_v^2 \exp\left(-\frac{|x-x'|}{L_x}\right) \quad (A5)$$

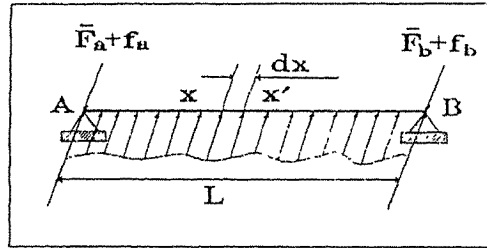


Fig.1. A girder under wind force

From these equations we have

$$\overline{(f_a + f_b)^2} = \int_0^l \int_0^l \rho^2 C_D^2 \bar{v}^2 \sigma_v^2 \exp\left(-\frac{|x-x'|}{L_x}\right) dx dx'$$

$$\sigma_v^2 = \frac{\sigma_w^2}{\rho^2 \bar{v}^2}$$

then

$$\overline{(f_a + f_b)^2} = C_D^2 \sigma_w^2 \int_0^l \int_0^l \exp\left(-\frac{|x-x'|}{L_x}\right) dx dx' \quad (A6)$$

Supposing that the turbulence velocity is expressed by Gaussian process, and the reaction force also fits normal distribution, the total wind force is

$$P = \bar{F}_a + \bar{F}_b + \mu\sqrt{(f_a + f_b)^2}$$

Where  $\bar{F}_a = \bar{F}_b = \bar{F} = \frac{1}{2} c_D \bar{W}l$ .

Substitute eq.(A6) into above equation, we have

$$P = c_D \bar{W}l \left[ 1 + \mu \frac{\sigma_w}{\bar{W}} \sqrt{\frac{1}{l^2} \int_0^l \int_0^l \exp\left(-\frac{|x-x'|}{L_x}\right) dx dx'} \right] \quad (A7)$$

Where  $\mu \frac{\sigma_w}{\bar{W}} = \mu_f$  is called the turbulent fluctuating factor, from the Chinese code of building construction

$$\mu_f = \frac{1}{2} \times 35^{1.8(\alpha-0.16)} \left(\frac{z}{10}\right)^{-\alpha}$$

The relation between  $\bar{W}$  and basic wind pressure  $\bar{W}_0$  is

$$\frac{\bar{W}}{\bar{W}_0} = \left(\frac{z}{10}\right)^{2\alpha} (35)^{0.32} \left(\frac{H_T}{10}\right)^{-2\alpha} \quad (A8)$$

Where  $H_T$  is gradient wind height,  $\alpha$  is the terrain roughness factor, in Chinese code, it has three categories, for category A,  $\alpha = 0.12, H_T = 300m$ , for category B,  $\alpha = 0.16, H_T = 350m$ , for category C,  $\alpha = 0.20, H_T = 400m$ . Let

$$\mu_z(z) = \left(\frac{z}{H_T}\right)^{2\alpha} (35)^{0.32} \quad (A9)$$

then eq.(A7) can be expressed as follows

$$P = c_D \bar{W}_0 l \mu_z(z) \left[ 1 + \mu_f \sqrt{\frac{1}{l^2} \int_0^l \int_0^l \exp\left(-\frac{|x-x'|}{L_x}\right) dx dx'} \right] \quad (A10)$$

Finally, we have the gust pressure coefficient

$$k_{3S} = \mu_z(z) \left[ 1 + \mu_f \sqrt{\frac{1}{l^2} \int_0^l \int_0^l \exp\left(-\frac{|x-x'|}{L_x}\right) dx dx'} \right] \quad (5)$$

It can be seen that the gust pressure coefficient is dependent on turbulent fluctuating factor, spatial correlation characteristic, height of the girder above ground, girder length and terrain roughness factor, under the assumption of one dimensional rigid structure. The code highlights that the method of evaluating across-wind and other components of structural response to wind loading are very complex and have not as yet reached a stage that successful codification can be attempted. For special bridge, a case study is necessary. For example, a truss bridge stiffened by flexible arch under the combined action of train and wind loading, according to the Davenport power spectrum, the time history curve of turbulence is gotten by Monte-Carlo method, the dynamic deflection of the bridge considering the aerodynamic

admittance is 15% greater than that by the static method of the code[4]. The dynamic reliability problem under wind action is also studied by stochastic process extreme analysis[5].

#### Appendix B Effect of wind direction

The effect of wind direction was not considered in current Chinese wind load provision. The data of three meteorological stations located at coastal, inland and border district respectively are studied. Fig.2 is an example, the graphs from inside to outside indicate the data of different return periods of 30, 50, 100 years. As pointed by Y.K.Wen(1983, ASCE, Str. Eng. Vol.109, No.4), the effect of wind direction must be considered on structural reliability study.

#### Acknowledgment

This study is supported in part by Chinese NSF and Ministry of Railways.

#### References

1. BS5400, Steel, Concrete and Composite Bridge, Part 2, Specification for Loads, British Standards Inst., 1978.
2. M. Ito, Codification of Wind-Resistant Design—with Particular Reference to Bridge Codes, Recent Advances in Wind Engineering, Vol. I, International Academic Publishers, 1989, Beijing.
3. A.G Davenport, Proposed New International(ISO) Wind Standard, idem.
4. He Xia, Ying-Jun Chen, Xifeng Duan, Dynamic Response Analysis of Truss Bridge Stiffened by Flexible Arch under the Combined Action of Train and Wind Loading, Proc. Bridge Structure Science, 1992, Tongji Univ. Press. (in Chinese)
5. He Xia, Ying-Jun Chen, Dynamic Reliability of Train-Bridge System Under Wind Action by Stochastic Process Extreme Analysis, accepted by the Fourth East Asia-Pacific Conference on Structural Engineering and Construction, Korea, 1993.

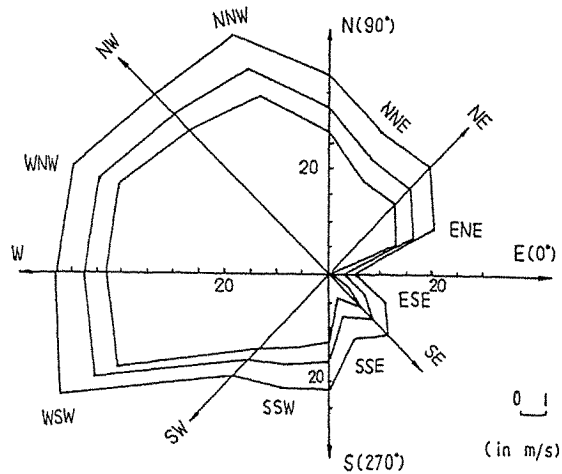


Fig.2. Change of yearly max. wind velocity of a station where winds show strong directionality

## Wind Loading and Serviceability of Tall Buildings in Tropical Cyclone Regions

P.A. Irwin and J. Xie

Rowan Williams Davies and Irwin Inc. (RWDI)  
650 Woodlawn Road West, Guelph, Ontario, Canada N1K 1B8

**Abstract:** A discussion is given of wind speed profiles and turbulence intensities in Typhoons/Hurricanes and the use of this information in wind tunnel tests. Also methodology for using the high frequency force balance technique to determine the wind response of buildings with complex modes of vibration is described. Serviceability criteria for motions are also discussed.

### 1. Introduction

This paper discusses several topics relating to wind tunnel testing of buildings for the determination of wind loads and motion effects. The first is specific to areas subject to Typhoons or Hurricanes (assumed to be the same phenomenon) and concerns the variation of mean wind speed with height in the parts of these storms where wind speeds are highest. A related question is that of the turbulence intensity in these storms. Another topic of concern for all regions is the use of the high frequency force balance technique on buildings with offset mass and stiffness centres. These buildings have modes of vibration in which sway and torsional motions participate simultaneously. To predict accurate loadings and motion effects for such modes requires modification of the original force balance technique. The methodology is described below.

### 2. Wind Profiles and Turbulence in Typhoons/Hurricanes

The phrase in the second sentence of the introduction, "in the parts of the storm where wind speeds are highest", bears repeating and emphasis. Since it is the eyewall region of the Typhoon that produces the highest winds it is very important to use a wind profile that is consistent with what actually occurs in the eyewall region and not, as a number of authors have done, to make the assumption that profiles measured at some undefined point elsewhere in the Typhoon are applicable throughout the storm. As pointed out by Simiu<sup>[1]</sup> in 1974, there are theoretical reasons for expecting a larger ratio  $U_{10}/U_{UL}$  near the centre of Hurricanes or Typhoons than for normal winds, or for winds further out from the eye of the same storm. Here  $U_{UL}$  is the "upper level" wind, meaning wind at about the 500 m height, and  $U_{10}$  is the mean wind speed near ground level (taken as at the 10 m height). Measurements verify this theoretical expectation. Figure 1, which uses results from Powell, Marks and Black<sup>[2]</sup>, shows this ratio as a function of radius from the storm centre for Hurricane Alicia after it passed over the coastline. The ratio is on the order of 0.70 in the eyewall whereas it would typically be about 0.56 in normal winds in open country. Figure 2 shows the exponent  $\alpha$ , in the assumed velocity profile power law  $U/U_{10} = (z/10)^\alpha$ , as a function of mean speed derived from Powell et al's data from Hurricane Alicia. The downwards trend in  $\alpha$  as the mean wind speed increases is very noticeable, implying that in the highest wind region of these types of storm the exponent is smaller and the profile correspondingly flatter than for normal winds. A number of authors (e.g. Georgiou et al<sup>[3]</sup>, Vickery and Twisdale<sup>[4]</sup>) have examined the available data on velocity profiles in Typhoons/Hurricanes and concluded that typically over water the eyewall surface winds are about 0.80 to 0.85 of upper level winds and that this drops to about 0.70 over open terrain land.

For tall buildings in Typhoon or Hurricane regions recognition of the different velocity profile in the eyewall region is important. A conservative approach appears to be to assume the power law exponent

is about 0.1 for mean wind speeds (averaging time 10 minutes) above about 30 m/s in open country, compared with the exponent of 0.14 for normal winds in open country. For a building 200 m high this difference in assumed velocity profile can result in over 20% difference in wind load at the top (a 20% reduction if the reference wind is given at the usual 10 m height). The other wind property that is important for wind loading is the turbulence intensity. It appears that the turbulence intensity tends to be higher in Typhoons/Hurricanes than for normal winds. Krayner and Marshall<sup>[5]</sup> have recommended modified gust factors specific to Hurricanes to account for this. Their increase in gust factor implies an increase in turbulence intensity by a factor of about 1.3. Again this needs to be considered in wind tunnel testing. In the tests the important parameters are the wind speed and turbulence intensity near the top of the building. A precise duplication of the vertical gradient of wind velocity is less important.

### 3. Force-Balance Technique for Buildings with Complex Modes

In strong winds, tall slender buildings sway and twist and this motion has two effects. First, it results in large structural loads simply because of the great inertial forces generated by the building's moving mass. The second important effect is that the motion may become perceptible to the building's occupants. To assess and quantify these effects through wind tunnel tests, the high-frequency force-balance technique is widely used, it being relatively economical compared with aeroelastic model tests.

This approach is suitable in cases where the building motion does not itself affect the aerodynamic forces. In practice, it is applicable to many buildings for determining the structural loads. For local peak wind loads on the cladding more detailed pressure model tests such as described by Irwin<sup>[6]</sup> are required.

The high-frequency force-balance technique, in its initial form, was applied to the high rise buildings with linear uncoupled mode shapes for which the generalized dynamic forces are directly proportional to the overturning moments and thus can be easily measured in the wind tunnel tests. However, a number of buildings have irregular shapes, and the mass centre does not coincide with the centre of stiffness. Therefore, although the lower mode shapes typically are still approximately linear, each mode of vibration involves coupled sway and torsional motions. The following analysis may be applied to these buildings<sup>[7]</sup>.

As a general form, the equation of motion of the building in its  $j$ -th mode can be written:

$$m_j (\ddot{q}_j + 2\zeta_j \omega_j \dot{q}_j + \omega_j^2 q_j) = \int_0^H f_A(z,t) \phi_j(z) dz \quad (1)$$

where  $z$  is the vertical coordinate,  $f_A(z,t)$  is the aerodynamic force per unit height,  $q_j$  is the generalised

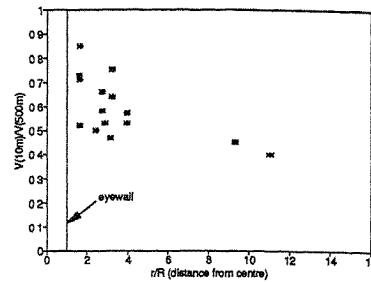


Figure 1: Ratio of Surface Wind Velocity to Upper Level Velocity, Hurricane Alicia

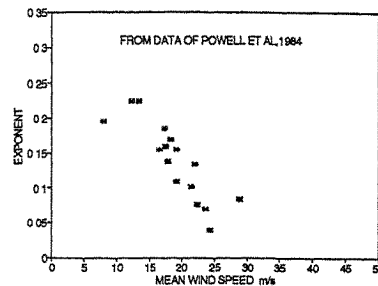


Figure 2: Relation between Power Law Exponent and Surface Wind Speed, Hurricane Alicia



deflection,  $\zeta_j$  is the damping ratio and  $\omega_j$  is the natural frequency. The mode shape  $\phi_j(z)$  can be split into three sub-vectors, i.e.

$$\phi_j(z) = \begin{pmatrix} \phi_{x_j}(z) \\ \phi_{y_j}(z) \\ \phi_{\theta_j}(z) \end{pmatrix} \quad (2)$$

Therefore the generalized mass of j-th mode becomes

$$m_j = \int_0^H (\mu(z) \phi_{x_j}^2(z) + \mu(z) \phi_{y_j}^2(z) + I(z) \phi_{\theta_j}^2(z)) dz \quad (3)$$

where

$\mu(z)$  is mass per unit height and  $I(z)$  mass moment of inertia per unit height about the z-axis

For the assumed case where the mode shapes vary linearly with height Equation 2 can be rewritten as

$$\phi_j(z) = \frac{z}{H} \begin{pmatrix} C_{x_j} \\ C_{y_j} \\ C_{\theta_j} \end{pmatrix} \quad (5)$$

where  $C_{x_j}$ ,  $C_{y_j}$  and  $C_{\theta_j}$  are participation factors for j-th mode x-sway component, y-sway component and  $\theta$ -twist component, respectively.

The right hand side of the Equation 1 may then be written as

$$F_j(t) = \int_0^H f_A(z,t) \phi_j(z) dz = \left(\frac{1}{H}\right) (C_{x_j} M_y(t) + C_{y_j} M_x(t) + C_{\theta_j} M_T(t)) \quad (6)$$

where

$F_j(t)$  generalized force of j-th mode

$M_x(t)$  instantaneous overturning moment of the aerodynamic forces about the x-axis on the base

$M_y(t)$  instantaneous overturning moment of the aerodynamic forces about the y-axis on the base

$M_T(t)$  generalized torque of the aerodynamic forces about the z-axis

The generalized torque cannot be determined with the same degree of completeness as the generalised forces using the force balance technique. This is because the only quantity that can be measured at the base is the overall torsional moment, i.e.

$$T(t) = \int_0^H f_{AT}(z,t) dz \quad (7)$$

where  $f_{AT}(z,t)$  is the aerodynamic torque per unit height, whereas ideally the measured quantity would be such that  $f_{AT}$  in the integral was multiplied by  $z/H$ . However, by assuming an appropriate vertical distribution of  $f_{AT}$  on the building, corrections can be derived in order to obtain more accurate results. A reasonable correction in many cases is to adjust the measured base torque  $T$  downwards by 30%. Note

that recently instantaneous pressure integration techniques have started to replace the force balance method in some studies, see Steckley et al<sup>[8]</sup>, which allows the product  $f_{AT}(z/H)$  to be measured and integrated directly using the same rigid model as built for pressure study of cladding loads. This then allows the true generalised aerodynamic torque to be measured making correction factors unnecessary.

The solution of Equation 1 may be expressed in terms of the power spectrum,  $S_{q_j}(\omega)$ , of  $q_j$  as follows:

$$S_{q_j}(\omega) = \frac{S_{F_j}(\omega)}{\omega^4 m_j^2 H^2 |\chi_j|^2} \quad (8)$$

where

$|\chi_j|^2$  reciprocal of the mechanical admittance

$S_{F_j}(\omega)$  power spectrum of the j-th generalized forces

$$S_{F_j}(\omega) = \left(\frac{1}{H}\right)^2 \left( C_{xj}^2 S_{My}(\omega) + C_{yj}^2 S_{Mx}(\omega) + C_{\theta j}^2 S_{MT}(\omega) \right) + 2 \left(\frac{1}{H}\right)^2 \left( C_{xj} C_{yj} \text{Re}[S_{MyMx}(\omega)] + C_{xj} C_{\theta j} \text{Re}[S_{MyMT}] + C_{yj} C_{\theta j} \text{Re}[S_{MxMT}] \right) \quad (9)$$

in which  $\text{Re}[\cdot]$  is the real part of the cross-spectrum.

Based on Equations 6 and 9, the generalized forces can be measured on a wind tunnel model designed to have very high natural frequency and its component spectra,  $S_{My}(\omega)$ ,  $S_{Mx}(\omega)$ ,  $S_T(\omega)$ ,  $S_{MyMx}(\omega)$ ,  $S_{MyT}(\omega)$  and  $S_{MxT}(\omega)$  can also be computed from measured time histories. Once  $S_{F_j}(\omega)$  has been determined, the response of the full-scale building is computed by means of Equation 8. In Equation 8, the building's generalized mass, natural frequency and damping ratio,  $\zeta_j$ , are required in order to calculate the reciprocal mechanical admittance term  $|\chi_j|^2$ .

From the spectrum of generalized deflection,  $S_{q_j}$ , the root-mean-square displacements and the root-mean-square accelerations,  $\sigma_a$ , at height  $z$  can be computed and the peak displacements and accelerations are calculated by multiplying the root-mean-square values by appropriate peak factors, typically in the range 3.5 to 4.0. The rms overturning moment,  $\sigma_{Mx}$ , can be computed from the relation:

$$\sigma_{Mx} = \sqrt{\sigma_{MxA}^2 + \sigma_{MxI}^2} \quad (10)$$

where the inertial contribution is

$$\sigma_{MxI} = \sqrt{\sum_j \left( \sigma_{q_j} \int_0^H \mu(z) \phi_{yj}(z) z dz \right)^2} \quad (11)$$

Similar expressions apply to the other moment and force components and, for lightly damped structures, the expression for generalized acceleration is

$$\sigma_q^2 = \int_0^\infty \omega^4 S_{q_j}(\omega) d\omega = \frac{\pi \omega_j S_{F_j}(\omega_j)}{4 m_j^2 H^2 \zeta_j} \quad (12)$$

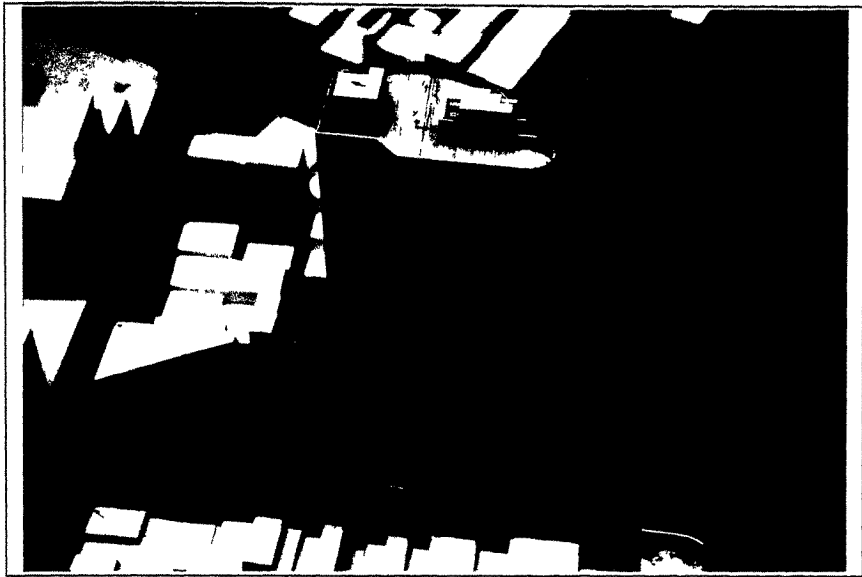


Figure 3: High-frequency Force-Balance Model of a 30 Storey Building

**Example**

Figure 3 shows a wind tunnel model of a 30 storey hotel building to be built in Taiwan. In the structural dynamic analysis, the mass centre was chosen as the origin and the x-axis was chosen as parallel to its longer side. Owing to its irregular shape, the building's sway motions and twist motions were structurally coupled. In the first x-sway dominated mode, the y-sway participation factor was about 20% and the twist participation factor was about 29% normalized by a typical radial distance. In the y-sway dominated mode, the x-sway participation factor was about 10% and the twist about 35%. In the first twist dominated mode, the x-sway participation factor was up to 84% and y-sway 64%.

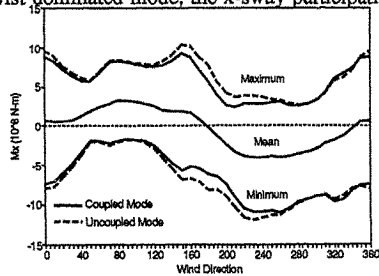


Figure 3: Base Moment  $M_x$

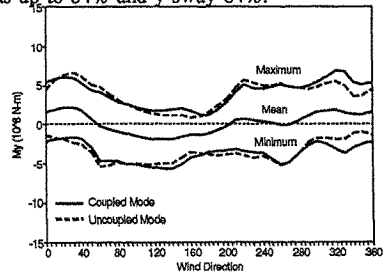


Figure 4: Base Moment  $M_y$

Figures 4 through 6 give the comparison of the predicted base moments using the above theory with those obtained by ignoring the structural coupling effects. Significant differences are evident

particularly for the base torque,  $M_z$ , because of strong coupling between all three components in the prime torsional mode.

#### 4. Motion Criteria

Motion criteria have been developed primarily in terms of acceleration limits. While other parameters such as angular velocity for torsional motions, or jerk for motions in general, have been proposed as possible supplements or replacements for acceleration, current practice is still to use acceleration. During the 1970's and 1980's in North America the procedure frequently adopted was to evaluate the acceleration corresponding to a 10 year recurrence interval and to try to keep peak accelerations below 2% to 2.5% of gravity for commercial buildings. More stringent criteria, in the range 1.0% to 1.5% were sometimes adopted for residential buildings and hotels. More recently there has been some re-appraisal of the choice of 10 years as the recurrence interval, particularly in areas frequented by Typhoons or Hurricanes where much of the current building development is taking place. With present day communication systems and abilities to track such storms, there is typically ample warning of their approach and, for a once-in-ten-years event, the great majority of occupants of commercial buildings may reasonably be expected to have gone home or evacuated the area. Those who remain in these circumstances, in either commercial or residential buildings, are going to be expecting to experience some motion. Therefore it appears more reasonable to select a shorter recurrence interval for the evaluation of motions and comfort, an interval corresponding to events of insufficient magnitude to trigger evacuation procedures. A recurrence interval of one year fits this purpose much better than ten years, and corresponding peak acceleration criteria in the range 1.0% to 1.3% of gravity appear reasonable for this interval, depending on the building's natural periods, its use and the owner's desire for quality. This range implies (see ISO Standard 6897-1983) that motions would typically be noticed, but not necessarily objected to, about once per year by occupants with average sensitivity to motion.

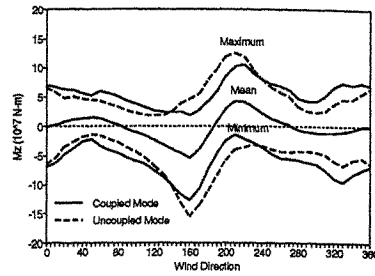


Figure 5: Base Torque  $M_z$

References:

1. Simiu, E., Variation of Mean Winds with Height in Hurricanes, *J. Eng. Mech., Proc. ASCE*, TN-100 EM4, pp. 833-837, Aug. 1974.
2. Powell, M.D., Marks, F.D., and Black, P.G., The Asymmetric Structure of Alicia's Wind Field at Landfall, *Proc. ASCE Specialty Conference, "Hurricane Alicia One Year Later"*, Galveston, Texas, 1983, pp.40 - 54.
3. Georgiou, P.N., Davenport, A.G., and Vickery, B.J., Design Wind Speeds in Regions Dominated by Tropical Cyclones, *J. Wind Engineering and Industrial Aero.*, **13**, 1983, 139 - 152.
4. Vickery, P.J., and Twisdale, L.A., Prediction of Hurricane Wind Speeds in the U.S., *Proc. of 7<sup>th</sup> U.S. National Conference on Wind Engineering*, July 27-30, 1993, Los Angeles.
5. Krayer, W.R., and Marshall, R.D., Gust Factors Applied to Hurricane Winds, *Bulletin American Meteorological Soc.*, **73**, No.5, May 1992.
6. Irwin, P.A., Pressure Model Techniques for Cladding Loads, *J. of Wind Engineering and Industrial Aerodynamics*, **29** (1988) 69-78.
7. Xie, J., Modified HFFB Technique for Structurally Coupled Buildings, *Proceedings of The 1st Chinese National Conference on Wind Engineering and Industrial Aerodynamics*, July, 1986
8. Steckley, A., Accardo, M., Gamble, S.L., and Irwin, P.A., The Use of Integrated Pressures to Determine Overall Wind-Induced Response, *J. of Wind Engineering and Industrial Aerodynamics*, **41-44** (1992) 1023-1034.

## Wind damage expert system for insurance industry

Kishor C. Mehta and Ronald H. Cheshire+

Department of Civil Engineering  
Texas Tech University, Lubbock, TX, USA  
+Florida Windstorm Underwriting Association  
Jacksonville, FL, USA

**Abstract:** Wind damage experiences can assist the insurance industry in assessing the relative wind resistance of individual buildings. The assessment is made through development of a knowledge-based expert system which consults the input data and provides a relative wind resistance grade. Building categories for wind damage and parameters affecting the wind resistance of buildings are identified by wind engineers in concert with insurance industry personnel. A damage experience knowledge base incorporated into a commercial expert system produces relative wind resistance grades. This grading system may be used by insurance companies to establish premiums, as well as assisting in collection of actuarial data on wind-induced property losses.

### 1. Introduction

Up to this point, the property insurance industry in the United States (U.S.) has maintained and fostered the idea that it is an intermediary--a *middleman*--in the process of paying wind-induced property losses and collecting premiums. That has worked well until recently [1]. The property loss experiences of Hurricane Hugo in 1989 (U.S. \$4 billion) and Hurricanes Andrew (estimate of U.S. \$15 billion) and Iniki of 1992 have strongly indicated that some mitigating measures to reduce losses are necessary.

The bar chart shown in Figure 1 indicates the number of catastrophe loss experiences recorded by the Property Claim Services (PCS) in the U.S. The PCS records an event as a catastrophe when there are numerous claims for property loss and the total claim amount exceeds 5 million U.S. dollars. The number of catastrophes between 1986 and 1992 averaged 31 per year, with a range between a low of 24 and a high of 36 [2]. Dollar losses in these catastrophes are shown in Figure 2; Figure 3 shows catastrophes by type. These figures clearly indicate that wind is a major factor in causing property losses. Close to 90 percent of catastrophe property losses are due to hurricanes, tornadoes and other windstorm events. The total dollar value of property losses due to windstorms are less than that for fire.

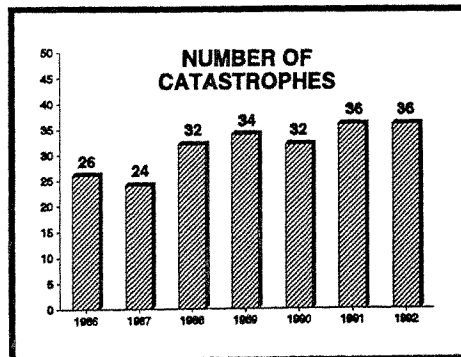


Figure 1. Number of designated catastrophes by Property Claim Services in each year [2]

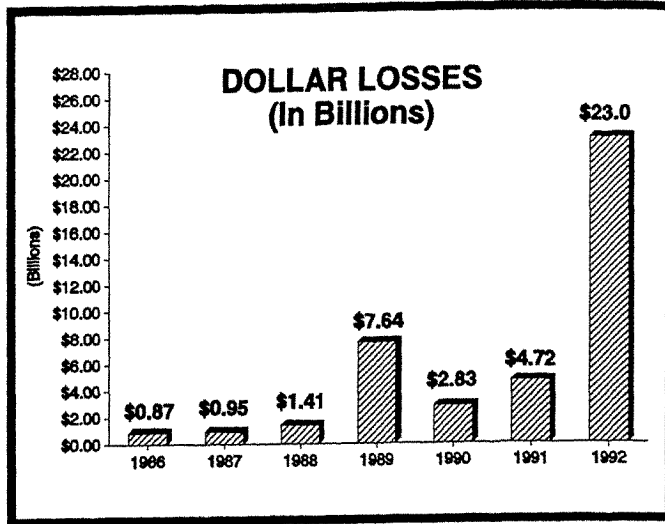


Figure 2. Annual property damage in catastrophes designated by Property Claim Services [2]

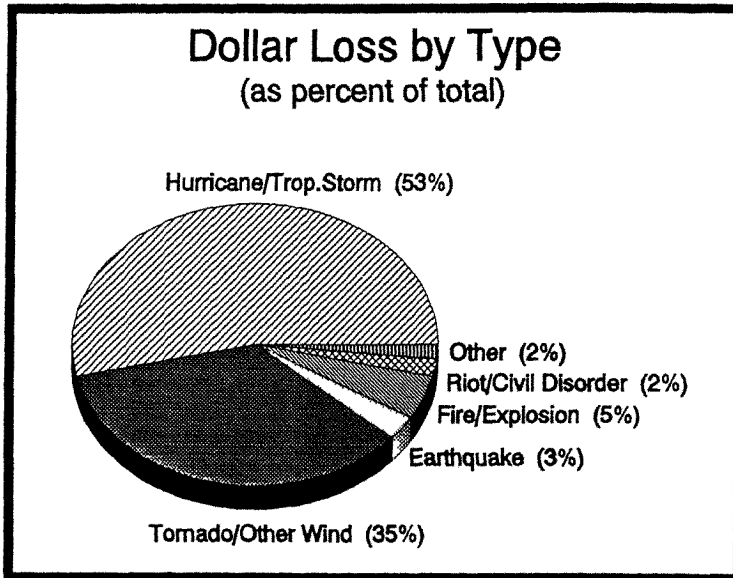


Figure 3. Percentage of property damage by type of designated catastrophes during 1986-1992 [2]

## **2. Background**

Personnel at Texas Tech University started documenting building damage caused by windstorms in 1970. Over the past 23 years, the group has documented more than 70 separate events all over the U.S., as well as in Australia and Mexico. Photographs, comments, newspaper clippings, maps and other material are catalogued for each event and are archived at Texas Tech University. Damage data are analyzed, reports are published, and conclusions are drawn for major events [3,4]. The damage data, along with the experiences by personnel, are a resource that can assist in predicting wind-induced damage to individual buildings. Admittedly, prediction of building damage is a complex problem because it depends on so many imprecise parameters. At the same time, use of an expert system and subjective weighting can provide a relative grade for building damage. The critical steps are to develop building classification and to formulate questions for building parameters that reflect wind resistance of buildings. These building classification and question terminology must be acceptable to the insurance industry if a technology transfer is to be achieved. The following paragraphs outline building classification, parameters and a relative grading system for building damage which the property insurance industry understands and uses.

## **3. Building Classification**

Buildings are divided into eight categories: (1) high rise (six stories or more); (2) reinforced concrete, (3) heavy steel, (4) reinforced masonry, (5) light steel, (6) timber, (7) unreinforced masonry, and (8) nonengineered. The categories are listed in descending order of potential structural damage caused by wind. Property damage is related to structural damage if the frame of the building collapses; it is also related to the wind resistance of the building envelope of roof and walls if the structural frame is not damaged. These building categories will assist the insurance industry in collecting property damage data in the future. The building classification developed for the insurance industry is a little different than the classification used by the engineers [5]. The reason for the difference is understanding and use of the classification by the nontechnical insurance industry personnel.

## **4. Parameters**

In order to develop the knowledge base for an expert system, the major parameters that relate to wind-induced building damage are identified as environmental, frame, roof envelope, wall envelope, and other. These parameters reflect wind effects, wind resistance, and engineering attention in the design process of a building. Wind effects relate to factors such as windstorms and debris potential. Wind and debris resistance of frame and roof and wall envelopes are considered with building dimensions, construction materials, and framing systems of a building. Engineering attention is reflected in the use of a specific building code or wind tunnel tests. The major parameters and factors are shown in Figure 4.

## **5. Expert System**

A commercial expert system software is used to manipulate building information that produces a relative grade for building damage. A key to the development of the system is the knowledge base. Building information is obtained through questions for each of the items shown in Figure 4. This information is manipulated using the knowledge base. Weighting functions based on damage investigation experiences are used for parameters; items in Figure 4 form the knowledge base. Since many items in Figure 4 are interrelated (e.g. debris exposure is not important if screens are provided in wall envelope, or type of roof structure is not critical if frame collapses), the system is nonlinear. The expert system is able to manipulate the logic of nonlinear interrelationship to produce a consistent answer. The system is only as good as the knowledge base incorporated into it.

The normal grade range for each building category is shown in Figure 5. The relative grades between building categories reflect structural damage (possibility of total property loss) potential for each building category. The median of each range is the target value; weighting of factors is adjusted during calibration to obtain target value. This goal of target value assures reasonableness of the subjective weighting.

One of the benefits of the knowledge-based software is that it can identify factors which are prominent in wind damage potential. For example, if window glazing is the most critical factor in

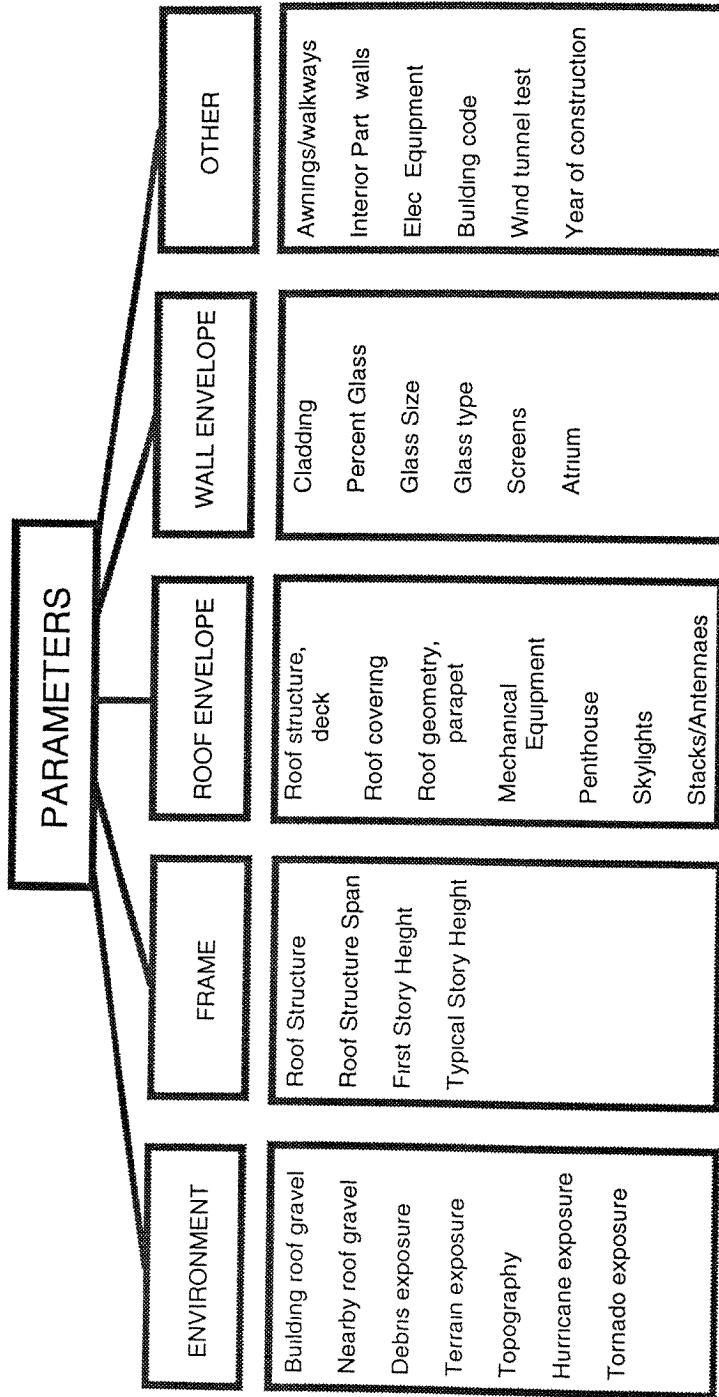


Figure 4 Building Parameters for Expert System



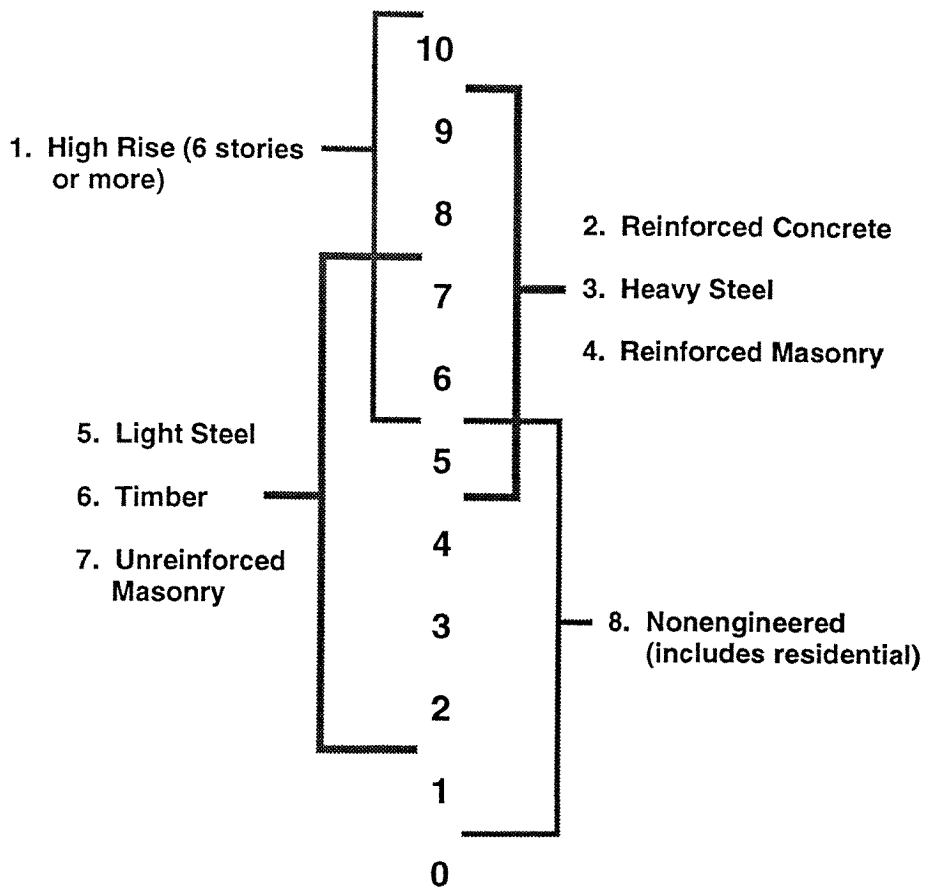


Figure 5 Grade range for each building category

wind damage potential for a specific building, the software can evaluate any improvement in relative grade with the installation of screens or shutters. This feature of *what if* scenarios by the software can allow the insurance underwriter to provide an economic incentive to the owner to improve the wind resistance of the building, i.e.: individual companies within the insurance industry may use these relative grades to establish insurance premiums when underwriting for wind damage.

## **6. Summary**

The knowledge-based expert system is under development at the time of preparation of this paper. When fully developed by wind engineers and implemented by the insurance industry, it has the potential to revolutionize the insurance underwriting procedure for wind damage in the U.S. The insurance premium can be based on wind resistance of building frame and its envelope. In addition, there will be an economic incentive for owners, architects and engineers to implement wind resistance construction.

## **7. Acknowledgements**

The National Committee on Property Insurance (NCPI), an industry organization, has established a steering committee: *Natural Disaster Loss Reduction*. One of the subcommittees under this steering committee is Wind Damage Mitigation (WDM), consisting of nine members and a liaison from NCPI. Both authors of this paper are members of the WDM subcommittee, with the second author being the chairperson. All members of the WDM subcommittee have actively participated in developing building classifications and formulating questions for wind damage parameters. Their input and support of the NCPI for this project is appreciated and acknowledged.

## **References:**

1. Texas Department of Insurance: HB 2 Report, Advisory Committee to Create Incentives to Depopulate the Cat Pool, R.H. Cheshire, Chairman, April 1992.
2. NCPI, Information distributed at the March 1993 meeting of the Wind Damage Mitigation Subcommittee of the National Committee on Property Insurance, Boston, MA (1993).
3. K.C. Mehta, Wind induced damage observations and their implications for design practice, *Eng. Struct.*, 6 (1984) 242-247.
4. J.E. Minor, K.C. Mehta and J.R. McDonald, Lessons learned from 20 years of windstorm damage investigations, presented at Structures Congress '92 (San Antonio, TX; April 15, 1992), American Society of Civil Engineers (1992).
5. K.C. Mehta, R.H. Cheshire and J.R. McDonald, Wind resistance categorization of buildings for insurance, *J. Wind Engrg. and Indus. Aero.*, 41-44 (1992) 2617-2628.

## Damage Assessment and Vulnerability Analysis Of Structures Subjected to Cyclones

T.L. Murlidharan ,J.Durga Prasad and T.V.S.R. Appa Rao

Structural Engineering Research Centre, Taramani, Madras-113, INDIA.

**Abstract:** Models for damage assessment and vulnerability analysis of structures subjected to cyclones are proposed. A mathematical model for vulnerability analysis using fuzzy sets is presented. The methodology developed in the paper can be used to determine the vulnerability of a typical industrial structure in a cyclone prone region of the east coast of India.

### 1.0 INTRODUCTION

East coast of India is frequently battered by intensive tropical cyclones. The states of Tamilnadu, Andhra Pradesh, Orissa and West Bengal suffer extensive damage due to cyclones. Assessment of damage is a very complex problem because of the number of aspects that are to be considered and also the fact that the data collected/made available is generally imprecise. Mostly good engineering judgement is used to assess the damage and to estimate the loss. There is considerable scope to improve upon the methodologies for accurate assessment of damage.

Another important area of interest to decision makers is the estimation of vulnerability of a region or a structure likely to be exposed to cyclonic storms. This again is a complex problem involving imprecise data and engineering judgement. Very little work has been reported in the literature dealing with vulnerability analysis of structures subjected to natural hazards such as earthquakes and cyclones. The basic uncertainties involved in cyclone vulnerability analysis relate to occurrence of cyclones of specific speed in a particular region, and uncertainties in structural performance and other equally important factors such as socio-economic aspects.

The rational methodology presented in this paper will enable one to make an estimation of the vulnerability of a structure in a cyclone prone region.

### 2.0 BASIC DEFINITIONS OF DAMAGE AND VULNERABILITY

#### 2.1 Damage

The term *damage* refers to any deficiency and/or deterioration of strength as caused by external loading and environmental conditions as well as human errors in design and construction. Therefore, a poorly designed and/or poorly constructed building can have an initial damage measure while it is still new without experiencing any severe loading conditions [Yao, 1985].

#### 2.2 Damage assessment

In general the current practice of damage assessment can be summarized as follows [Yao, 1985] :

(Field observations) --> (Analysis and interpretation by intuition and experience of select structural engineers) --> (Damage classification) --> (Quantitative Estimate of Damage)

### 2.3 Vulnerability

*Vulnerability* is defined as the sensitivity of the exposure (structure) to the hazards and the location relative to the hazards [Dong, 1986]. The location is defined as the position of the exposure relative to the hazard. Vulnerability index has also been defined as an indication of the 'state of health' of an existing building [Casati and Faravelli, 1991].

### 2.4 Vulnerability Analysis

Vulnerability analysis is the method of risk identification and evaluation based on past records of natural hazards and an analysis of the disaster susceptibility of structures.

A review of the current methods in seismic damage assessment and vulnerability analysis is given in [Appa Rao et.al. 1993].

### 3.0 DAMAGE ASSESSMENT MODEL

In a tropical cyclone high wind velocities are experienced. They affect large areas for periods of hours or days. Hence the wind damage due to a tropical cyclone can be considerable [Venkateswarlu et.al., 1978]. The model proposed herein operates at two levels, namely, global and structural levels. In the global model damage of whole regions affected by cyclones are assessed. At the structural level, damage of each structure in a particular region is assessed individually.

### 3.1 Global Damage Assessment

The information obtained from global assessment is necessary in order to understand the dimension of the task which faces the community after the disaster. Some of the questions to be answered are as follows:

i) How many people are injured ?, ii) How many structures have been destroyed ?, iii) What is the level of damage in these areas ?, iv) What is the social impact of this damage for future operation of the community, in other words, what is the extent of damage to essential service buildings - supply of water, gas, electricity, communication links, and v) What is the approximate cost of restoration ?

### 3.2 Damage Assessment of a Structure

Civil engineering structures in the coastal regions can be classified according to the construction materials, design and construction. The quality of different building materials used in coastal regions of India have significant influence in resisting severe cyclones. The damage to a structure can be assessed based on the severity of the cyclone, the damage to structure and its components, and the importance of the structure.

### 4.0 VULNERABILITY ANALYSIS MODEL

Experience from various damage surveys conducted by SERC, Madras [Venkateswarlu et.al., 1978] and others [Mehta, 1984] indicate that the major cause of loss induced by a cyclone is due to the collapse and failure of existing structures. To mitigate these losses, it is essential to identify hazardous existing structures and strengthen them to an appropriate level so that the future losses can be greatly reduced. Decisions have to be made about ranking these hazardous structures. This will help in making

decisions about allocation of limited funds to strengthen structures ranked as having the highest risk.

#### 4.1 Vulnerability of Regions

Any particular area in the coastal region of India will have a conglomeration of structures - some engineered and mostly non-engineered. To assess the vulnerability of such regions, data on past cyclone tracks/storms, rainfall particulars, and details regarding the nature of structures in the particular region are required. The "occupancy" and "type of construction" classification given in NBC, 1970, is used to obtain the data regarding the buildings. A qualitative vulnerability measure of each of the buildings is determined and a summation of these contributions along with other factors mentioned above determines the vulnerability of the region. The probability of occurrence of a cyclonic storm of given intensity can be arrived at by using a Poisson process model (Balaji Rao, et.al. 1991).

#### 4.2 Application of Fuzzy Sets to determine the overall vulnerability

The estimation of vulnerability of a structure in a cyclone prone region depends on a number of factors. The contribution of these factors are assessed in relative terms. A decision is made based on an assessment in terms of the chances of the structure being distressed by a cyclone. Vulnerability analysis is an ill-structured problem because : i) Vulnerability is not a physical measurement; ii) All the factors involved are uncertain either due to randomness or due to fuzziness; iii) The expertise about vulnerability analysis is mostly based upon judgemental knowledge and heuristics which have not been explicitly formulated; iv) Losses resulting from a cyclonic hazard can be categorized as: life and injury, property, business interruption, contents, etc. Vulnerability analysis therefore requires the identification of the losses as well as the identification of the hazards, exposures and their locations.

The factors that contribute to cyclonic vulnerability are organised in a hierarchical manner (Fig.1).

As can be seen from Fig. 1, some of the factors cannot be well defined quantitatively. Vulnerability analysis cannot be modelled by a simple mathematical expression. Expert judgement is required in performing this type of analysis. A mathematical model for vulnerability analysis using fuzzy sets is presented.

In practice, the determination of sets by means of linguistic definitions runs into difficulty because of the inherent ambiguity of the language. There are many classes of objects in which the transition from membership (belongingness) to non-membership (non-belongingness) is gradual. In order to model this kind of classes a fuzzy set [Zadeh, 1965] is necessary whose elements have various degrees of membership. The membership function  $\mu_A(x) \in [0,1]$  is used to express the grade of membership of  $x$  being in  $A$ . Formally, a fuzzy set is expressed by ordered pairs

$$A = \{(x, \mu_A(x)) \mid x \in X\} \quad (1)$$

A fuzzy matrix  $X$  is used to represent  $n$  variables each with  $m$  attributes where each row represents attributes of the variable. Typically,  $x_{i,j}$  means membership value of the  $i$ th variable. For the trapezoidal membership function, described later,  $m=4$  (see

Fig.2).

The weight/importance vector is also represented by a column vector with fuzzy elements :  $W = \{ w_1, w_2, \dots, w_m \}$

To convert the multi-fuzzy attributes to synthetic fuzzy evaluation of vulnerability, appropriate mapping functions have to be used, i.e.,  $y_i = f(x_i)$ , where  $f$  is the appropriate mapping function.

The Example given below illustrates how fuzzy sets can be used to determine the overall vulnerability of a building in a cyclone prone region.

## 5.0 EXAMPLE

### 5.1 Vulnerability Analysis of a Typical Industrial Structure

#### Problem Statement:

To estimate the overall vulnerability of a typical industrial building in a cyclone prone region. The grades or evaluation for the various variables that contribute towards the determination of overall vulnerability are given as initial guesses which are shown in the Table 1.

Few studies have addressed the problem of wind loads on low-rise buildings with a variety of parameters and configurations. The majority of studies have examined the loads on a single building of a particular configuration. Consequently, the effects of various parameters in assessing the damage or vulnerability of buildings can only be heuristically stated.

For determining the structural vulnerability, the linguistic guesses (evaluation) for each variable are given in Table 2. The structural vulnerability, and consequently the overall vulnerability for a building with *good construction quality* and *poor construction quality* have to be determined. For the present example the system reliability is classified as *high* (Balaji Rao et. al., 1993).

To estimate the value of the fuzzy Variable - structural vulnerability, the Table 3 is prepared. Trapezoidal membership functions are used to model the fuzzy attributes (given under the Grade column). Fig. 2 shows an example of trapezoidal membership function.

The structural vulnerability of a specific industrial building depends on five aspects given in the *variable* column of the Table 2. It is reasonable that the most severe consequence from these five variables will dominate the overall estimation of the structural vulnerability. Hence, the following mapping function (Min-Max function) is chosen

$$y_i = f(x_i) = \bigvee_{j=1}^m (w_j \wedge x_{i,j}), \quad i=1, \dots, n \quad \dots (2)$$

If construction quality is *very good*:

(For illustration,  $y$  values are calculated for memberships at levels 0 and 1.)

From the Table 3 ( $x_i$ ,  $i$  = variable number), at level 0:

$x_1 = [0, 0.1]$ ,  $x_2 = [0, 0.1]$ ,  $x_3 = [0, 0.3]$ ,  $x_4 = [0, 0.3]$ ,  $x_5 = [0, 0.3]$

$w_1 = [1, 1]$ ,  $w_2 = [1, 1]$ ,  $w_3 = [0.2, 0.5]$ ,  $w_4 = [0.5, 0.8]$ ,  $w_5 = [0.5, 0.8]$

Using the equation 2, at membership 0,

$$y = [0.0, 0.3]$$

Similarly, at membership 1,  $y = [0.0, 0.1]$

Therefore, structural vulnerability for *very good construction*

quality is low.

Similarly, assuming *poor construction* quality, the structural vulnerability is *high*.

at membership 0,  $y = [0.7, 1]$ , and at membership 1,  $y = [0.8, 1]$

Similarly the overall vulnerability of the building can be calculated by combining the attributes such as cyclone hazard, structural vulnerability, building importance, and building cost. Though, in this example linguistic evaluation for the variables such as cyclone hazard, building importance, and the building cost are assumed to be given, it is possible to evaluate them, using the procedure given for evaluating structural vulnerability. The factors that affect, say, building importance have been already explained in the text.

For estimation of the overall vulnerability of a building in a cyclone prone area, the following function may be used:

$$y_1 = f(x_1) = \frac{\sum_{j=1}^m w_{1,j} \cdot x_{1,j}}{\sum_{j=1}^m w_{1,j}} \quad \dots (3)$$

This example demonstrates how vague, imprecise, and verbal evaluations of the various attributes can be combined to quantitatively determine the total vulnerability of a building in a cyclone prone region. Based on this vulnerability measure, the buildings in a region can be ranked and priorities assigned as to which building should be strengthened first. It can also be used by surveyors to fix the premiums for insurance covers against cyclonic hazards.

## 6.0 CONCLUSION

The methodology presented in the above example is being incorporated into a knowledge-based system for damage assessment and vulnerability analysis of structures subjected to cyclones [Murlidharan et. al. 1992]. Such a system can be used by Government Departments, real-estate investment agencies, insurance underwriters and reinsurers, decision makers and portfolio managers, and structural engineers and appraisers in evaluating and revising investment strategies and insurance policies or premiums.

## REFERENCES

1. Yao J.T.P. "Safety and reliability of existing structures", Pitman Advanced Publishing Program, 1985.
2. Dong, W. Ph.D Thesis, Department of Civil Engineering, Stanford University, 1986.
3. Casciati, F and Faravelli, L., Micro. in Civil Engrg, Vol.6, 1991, pp.291-301.
4. Appa Rao, T.V.S.R., Murlidharan, T.L., and K.Balaji Rao, Research Report RD-39, Project Report No. STS-RR-93-2, March 1993.
5. Venkateswarulu, B., and Muralidharan K., Research Report, Structural Engineering Research Centre, Madras, 1978
6. Mehta, K.C., Engineering Structures, Vol.16, No.4, 1984, pp.242-247.
7. National Building Code of India, 1970, ISI, New Delhi.
8. Balaji Rao, K., Thomas, K.C and Appa Rao, T.V.S.R., Research Report RD-39, No.STS-RR-91-2, September 1991.
9. Zadeh, L.A., Information and Control, Vol.8, 1965, pp.338-353.
10. Murlidharan, T.L., Durgaprasad, J., and Appa Rao, T.V.S.R., Research Report RD-39, Project Report No. STS-RR-92-4, October 1992.

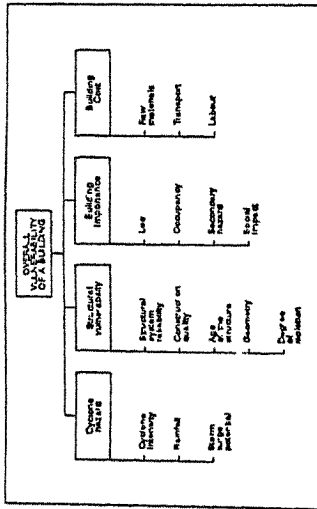
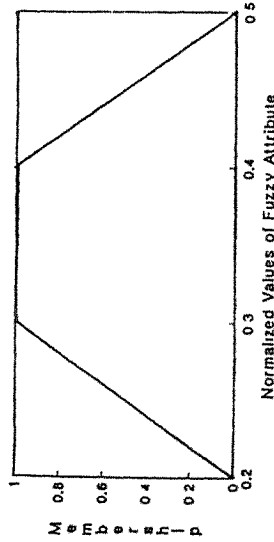


Fig.1 Overall vulnerability of a building

Fig.2 Membership function for *slightly important*



Series 1

TABLE 1: INITIAL GUESSES FOR THE VARIABLES FOR DETERMINING THE OVERALL VULNERABILITY

Variable	Linguistic Guess (Evaluation)
Cyclone Hazard	High
Structural Vulnerability	7
Building Importance	Medium
Building Cost	Medium

TABLE 2: LINGUISTIC GUESSES FOR VARIABLES DETERMINING STRUCTURAL VULNERABILITY

Variable	Linguistic Guesses (Evaluations)
System reliability	High
Construction Quality	1.Very Good 2.Poor
Date of Construction	Recent
Geometry (Aerodynamics)	Favourable (No adverse effect on structure)
Degree of Isolation	Favourable (No adverse effect on structure)

TABLE 3: DETERMINING STRUCTURAL VULNERABILITY

Variable	Linguistic Attribute/Grade	Weight/ Attribute/Grade Evaluations %	Significance %
System reliability	High	0,0,0,1,0,1	V.Important 1,1,1,1
Construction Quality	Very good	0,0,0,1,0,1	V.Important 1,1,1,1
Construction Quality	Poor	0,7,0,8,1,1	
Date of Construction	Recent	0,0,0,1,0,3	Slightly Important 0,2,0,3,0,4,0,5
Geometry	Favourable	0,0,1,0,3	Important 0,5,0,6,0,6,0,8
Degree of Isolation	Favourable	0,0,1,0,3	Important 0,5,0,6,0,6,0,8
Isolation	Favourable	0,0,1,0,3	Important 0,5,0,6,0,6,0,8

(The grades are adopted from Dong, 1986.)



**CYCLONE RESISTANT LOW COST HOUSES IN  
COASTAL REGIONS IN DEVELOPING COUNTRIES**

**G.C.Mathur (\*)**

**Former Director  
National Buildings Organisation  
Government of India**

**Abstract:** The damage and destruction of traditional types of low-cost houses, specially mud houses, due to cyclonic effects are indicated. Based on the experiences gained in the planning, design and construction of houses at low-cost in the coastal regions of India, innovative and appropriate techniques for building improved mud houses to resist cyclones and flooding to the extent possible, are presented as a case study. The need for international cooperation to mitigate the problem of homelessness due to natural disasters, is emphasised.

**1. Introduction**

The long coastal regions of India are prone to seasonal cyclonic effects causing heavy damage and destruction of traditional types of houses, specially mud-thatch roof houses, rendering large number of poor people homeless. Priority needs to be given to planning, design and construction of houses at low-cost using local materials like earth (mud) and thatch, bamboos, reeds, timber etc. so as to resist cyclones to the extent possible. The main objective is to minimise the sufferings of the poor families due to destruction of their homes, the final solution.

**2. Innovative and Appropriate Technology**

As a result of research and development work done in India and other developing countries, innovative and appropriate techniques of construction have been evolved to build houses at low-cost employing the use of mud for walling and thatch roofing of grass or leaves to resist cyclonic effects to the extent possible.

As a case study a comparison of traditional and improved construction techniques for building more durable mud-thatch houses at low-cost is given in the table below:

**Improved construction  
Techniques**

**Traditional Construction  
Techniques**

**CONSTRUCTION OF WALLS**

- |  |  |
|--|--|
| * Circular shape of huts is adopted as round shape of mud walls reduces wind pressure on walls.                                    | * The huts are of rectangular shape due to which greater wind pressure is exerted on the walls.                |
| * A foundation of at least 0.5m depth is provided for mud walls to improve their stability and strength to resist cyclonic effect. | * Often no foundation is provided to mud walls which makes them unstable and weak in resisting cyclonic winds. |

---

(\*) Consultant, Housing and Construction  
35, Mangla Apts, G-Block, Kalkaji, New Delhi 110 019

- \* The foundation is built in burnt brick or stone masonry so as to be durable and strong to resist strong winds and flooding.
- \* A plinth of 0.7m height built in burnt brick or stone masonry is provided for protection of walls in the event of flooding.
- \* The walls are constructed using sun-dried mud bricks or stabilised soil blocks which make them structurally stronger.
- \* Water-proof mud plaster with bitumen emulsion is applied on mud walls to protect them from erosion caused by rainfall and flooding.
- \* The height of the mud walls is kept low-upto 2.7m in single storey construction to minimise the effect of strong winds.
- \* The circular roof-thatch of grass or leaves is given an over-hang of 0.5m over the wall all round which protects the mud walls from rainfall.
- \* The foundation is built in mud construction which is weak to resist strong wind and flooding.
- \* The plinth is not provided to the walls as such rain or flood waters cause erosion to mud walls and their collapse.
- \* The mud walls are constructed with slods or lumps of mud due to which they lack adequate strength and durability.
- \* Ordinary mud plaster is applied to mud walls which does not offer much resistance to erosion caused by rainfall and flooding.
- \* The height of mud walls is often more than 2.7m, specially of the two side walls and some houses have attic floor on account of which the wind pressure is more.
- \* The thatch-roof overhang provides protection to only two walls on which the sloping roof rests, leaving the other two walls exposed to erosion caused by rainfall.

#### CONSTRUCTION OF ROOF

- \* Conical roof with a central wood post, over circular walls in a slope of 60° with pinnacle at the centre is provided to reduce wind pressure on the roof.
- \* The radial wood/bamboo rafters of the roof are placed securely on the walls and held there by cleats on to wooden planks to resist roof blowing off.
- \* Two-side sloping roof is generally constructed which receives greater wind pressure on the wind-ward and the lee-ward sides.
- \* The roof rafters of wood/ bamboo are either simply placed on the walls or embeded in it which does not adequately resist roof blowing off.

- \* Between the roof-thatch and the walls an air gap of 8 to 10 cm is provided for ventilation.
- \* A fire-retarding and preservative treatment for thatch is provided to minimise fire hazard and early decay of thatch. The treatment consists of dipping the thatch in casnut shell oil or application of water-proof mud plaster with bitumen emulsion on the top and underside of thatch-roof.
- \* The roof-thatch just sits on the two side walls, thereby providing very little ventilation space.
- \* The untreated thatch-roof is a great fire hazard and needs frequently renewal of thatch due to early decay.

### 3. Scope of Scientific Research

Scientific investigations and research need to be undertaken to build mud-thatch roof houses that offer more resistance to cyclonic effects in the coastal regions at the lowest possible cost using locally available materials and skills. Such houses also need to be protected from fire hazard and early decay of thatch roof.

During the International Decade for Natural Disaster Reduction, special attention should be given to construction of cyclone and flood resistant mud-thatch roof houses as these are most commonly built largely through self-help in the coastal areas at a cost affordable to the low-income and poor families.

### 4. Monograph on Disaster Resistant Housing

The author has been engaged in the planning, design and construction of disaster resistant low-cost houses and promotion of research in this field and application of results of research in practice. The work of preparing a monograph on this subject which has been sponsored by Department of Science and Technology Government of India is in hand and the author will welcome relevant details regarding disaster resistant low-cost houses in areas prone to cyclonic effects in particular and other types of natural disasters.

### References:

1. G.C.Mathur; Cyclone Damage and Rehabilitation with reference to Housing and Human settlements; Asian and Pacific Regional Symposium on Wind Engineering; Asian Institute of Technology and University of Roorkee, 1984.
2. G.C.Mathur and K.Mukarji; Building Materials and Construction Technologies for low-cost Housing in Developing countries; Building Technology series (twelve numbers); United Nations; ESCAP, Bangkok. 1989
3. G.C.Mathur; Improving Earth Houses; Building Research and Practice; Journal of International Council for Building Reserach (CIB), Rotterdam; 1985.

4. G.C.Mathur; Durable Mud Houses in Flood Affected Areas; International Conference on Flood Protection; International Commission on Floods; 1968.
5. G.C.Mathur; Wind Resistant low-cost Houses in Desert Regions in Developing countries; International Association of Wind Engineering 1st European and African Regional Conference; 1993.

## **Dampers and Active Control**



## Modelling of Tuned Mass Dampers for Wind Tunnel Tests on a Full-Bridge Aeroelastic Model

G. L. Larose, A. Larsen<sup>+</sup>, E. Svensson<sup>++</sup>

Danish Maritime Institute (DMI), Hjortekæsvej 99, Lyngby, Denmark

<sup>+</sup>COWIconsult A/S, Parallevej 15, Lyngby, Denmark

<sup>++</sup>Great Belt A/S, Vester Søgade 10, Copenhagen, Denmark

**Abstract:** A full-bridge aeroelastic model study of a multi-span approach bridge is reported in this paper. The objectives of the investigation were to study the vortex-shedding oscillations observed for the vertical bending modes during section model tests, and to determine the effectiveness of external means for reducing these oscillations. The effect of aerodynamic appendages such as guide vanes were studied as well as the effect of introducing additional damping to each of the seven 193m bridge spans using Tuned Mass Dampers. Model TMD's with adjustable frequency and damping were designed and their effect investigated on the aeroelastic model. The key to the model TMD's was the adjustable inherent damping provided by an electro-magnetic (eddy-current) mechanism. A detailed description of the TMD physical modelling is given and the use of a full-bridge aeroelastic model as a design tool for the deployment and tuning of TMD's is illustrated.

### 1. Introduction

The wind tunnel investigations for the Great Belt East Bridge included studies of the aerodynamic behaviour of the multi-span Approach Bridges through section model tests and full-bridge aeroelastic model tests. Parameters directly relevant to the design process were investigated, such as the effects of turbulence intensity, structural damping and wind screens on the aerodynamic performance of the deck cross-section. Particular attention was paid to the vortex-shedding induced oscillation phenomenon observed for the vertical bending modes in smooth and turbulent flow for various test conditions and especially for the deck fitted with wind screens.

The tests on the full-bridge aeroelastic model, conducted in DMI's 'Martin Jensen' Very Large Wind Tunnel, focussed on the study of wind induced oscillations in terms of amplitude of motion and energy input by the wind. The 13m long model, constructed at a geometric scale of 1:125, represented the 1556m long Western Approach Spans. This continuous steel box girder bridge is supported by 9 piers forming 10 spans, 7 of which are 193m long as seen on Fig. 1. A description of the prototype structure is given in Ref. [1].

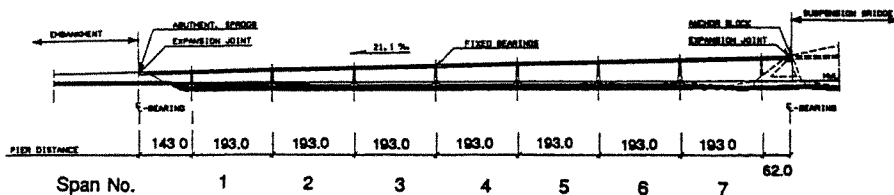


Fig. 1. Prototype Dimensions (m) of the Great Belt East Bridge, Western Approach Spans

The impetus for the use of a three dimensional representation of the bridge was found in a need to identify possible structural damping interaction between the first six vertical mode shapes that have very closely spaced natural frequencies.

This paper presents the main findings of the full-bridge aeroelastic model study and illustrates the use of a 3-D aeroelastic model as a design tool in conjunction with the mitigation of vortex-shedding excitation using Tuned Mass Dampers. The implications of the main conclusions of the wind tunnel tests on the design process are presented in a companion paper [1], along with comparisons with theoretical models for a deployment strategy of TMD's for a multi-span continuous beam bridge. To the authors knowledge, the only other aeroelastic modelling of a flexible multi-span bridge of more than three spans was done in the early '70's at BLWTL in Canada for the Northumberland Straits Crossing [2].

## 2. Experimental Procedures

### 2.1 Description of the Full-Bridge Aeroelastic Model

The model met the following requirements, given the objective of studying the vortex-shedding phenomenon:

- to model adequately the first six vertical bending modes and the first lateral mode;
- to provide a torsional stiffness large enough so that no coupling between vertical and torsional bending could occur as for the prototype structure;
- to obtain values of structural damping as low as possible, with the possibility of adjustment;
- to have the possibility of adding and removing wind screens and appendages to the model.

The aeroelastic model was made of a rectangular aluminium spine placed at the deck girder shear center, modelling the girder vertical and lateral stiffnesses. The spine was attached to the solid piers via leaf springs, modelling fixed restraints in all degrees of freedom except for the longitudinal motion and rotation around the lateral axis. The deck geometry and mass were modelled by 52 cladding segments made of a combination of foam, wood and brass. The length of the segments was 150 and 300mm separated by a 1-2 mm gap.

The model was designed to withstand large vertical oscillations for a long period of time based on the vortex-shedding excitation observed during section model tests. Table 1 presents the dynamic properties of the model and Fig.2 shows the model in the wind tunnel. The first two modes have very close natural frequencies, but have a maximum modal amplitude located at different spans along the bridge; this is true for the first six vertical modes [1].

Modes	Prototype $f(Hz)$	Model $f(Hz)$	Damping (log.dec.)
Vertical 1	0.476	5.2	1.5
Vertical 2	0.531	5.8	1.5
Vertical 3	0.612	6.7	1.4
Vertical 4	0.709	7.8	1.8
Vertical 5	0.814	9.1	1.6
Vertical 6	0.916	10.3	1.3
Lateral 1	1.145	12.5	-

Table 1. Dynamic Characteristics

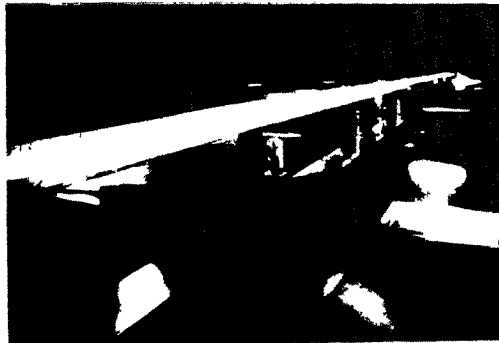


Fig. 2. View of Aeroelastic Model in 'Martin Jensen' Wind Tunnel



A nominal structural damping of approx. 1.5% (log.dec.) was measured for the first six vertical modes. A series of wind tunnel tests was conducted with this low damping level but the main part of the wind tunnel investigations was conducted with a more realistic structural damping level of 3%. Thin rubber pads cut in a 'bow-tie' shape and glued to the surface of the deck added damping between the segments. The damping obtained was practically constant with amplitude and stable throughout the tests. The damping was verified between each test series, since it strongly influenced the magnitude vortex-shedding oscillations.

## 2.2 Test Programme

The effect of the following parameters on the vortex-shedding response was investigated:

- i) structural damping, 1.5%, 3% and 6% log. dec.;
- ii) turbulence intensity, 1% and 6% at deck height;
- iii) continuous guide vanes, installed as shown on Fig.3., having full-scale dimensions of 1m x 1m;
- iv) tuned mass dampers, tuned to damp the first six vertical modes.

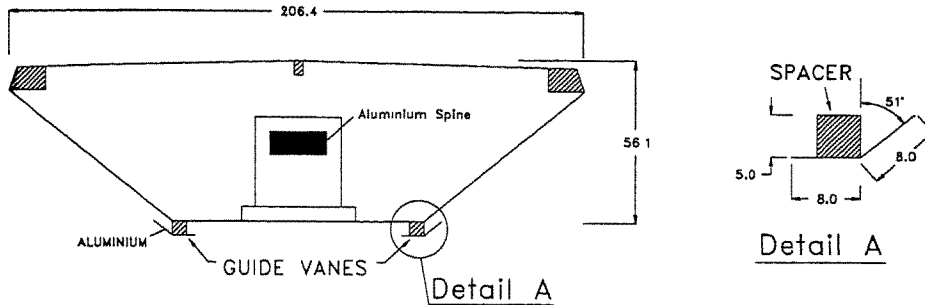


Fig. 3. Cross-section of Deck Segment with Guide Vane Arrangement in Model Scale (mm)

## 2.3 Physical Modelling of TMD

The modelling of the tuned mass dampers was based on specifications determined from the amplitude of vibrations observed during the section model tests and the conventional DenHartog linear theory for TMD design [3]. The model TMD's were constructed with an active mass of 1% of the generalized mass per mode of the deck. Each TMD unit had an equivalent full scale mass of 11t, an internal damping of 30-40% (log.dec.), a natural frequency set to 99% of the mode to be damped and a possible peak displacement equivalent to 1m full scale.

Fig. 4 gives the overall dimensions of the model TMD's, built with adjustable natural frequency and damping. They consisted of an active mass suspended at the end of an acrylic cantilever with adjustable length. Varying the length of the cantilever allowed precise tuning of the frequency of oscillations of the active mass. The active mass was a magnet, moving parallel to an aluminium plate. The disturbance of the magnetic field created by the aluminium plate induced electro-magnetic damping. The damping was adjusted by varying the gap between the aluminium plate and the magnet. The damping obtained was constant with amplitude, except for very large amplitudes, and was easily tuned to the desired level.

## 3. Experimental Results

### 3.1 Main Findings of Aeroelastic Model Study

Vortex-shedding induced oscillations of various amplitudes were observed for all the vertical bending modes of the model and for all the test conditions except for the tuned mass damper

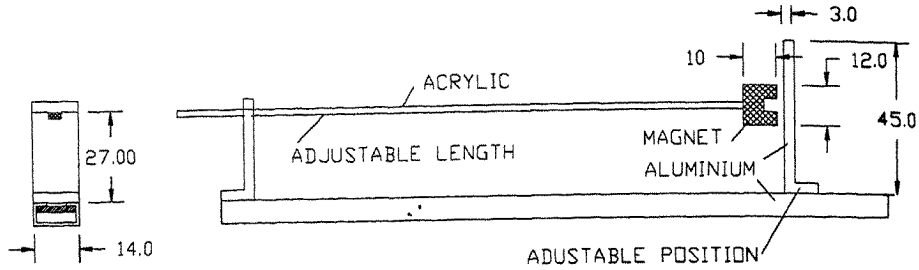


Fig. 4. Dimensions (mm) of the Model TMD

tests. Fig. 5 presents the maximum RMS response normalised by the depth of the girder  $D$  for the first six vertical modes, as a function of the reduced velocity,  $V/fB$ , where  $V$  is the mean wind speed at deck level,  $B$  is the deck width and  $f$  is the natural frequency of the given mode. These results are for the deck fitted with wind screens, in turbulent flow and 1.5% log.dec. structural damping. As expected, the vortex shedding responses collapsed around a reduced frequency of 1.6 to 1.75, corresponding to a Strouhal number of  $\approx 0.15 - 0.16$ .

No signs of damping interaction between the modes were observed that could have had a somewhat mitigating effect on the vortex-shedding excitation. In fact, it was observed that the presence of several modes with closely spaced natural frequencies had the effect of increasing the RMS response of the transition region between Strouhal velocities, that is the wind speed at which the onset of vortex-shedding lock-in occurs. It was observed for the transition period that more than one mode was excited. The RMS response for the transition region was, however, always smaller than the maximum response for adjacent modes during lock-in.

The investigation of the effect of the structural damping on the vortex-shedding response has verified that the RMS response is roughly inversely proportional to the structural damping. This is illustrated in Fig. 6 for the first vertical mode where the RMS response is plotted versus structural damping for two different flow conditions.

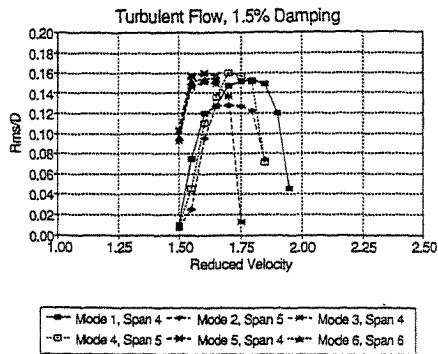


Fig. 5. Vertical RMS Response vs Reduced Velocity, Turb. Flow, 1.5% Damping

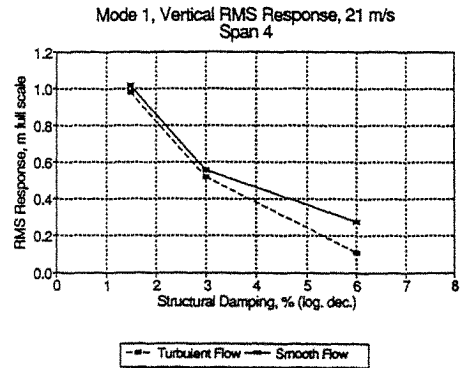


Fig. 6. Vertical RMS Response vs Structural Damping and Turbulence, Mode 1

shedding induced oscillations in smooth and turbulent flow for the first six vertical bending modes as shown by Fig. 8. This was achieved with a combination of 12 TMD's, 2 per mode, placed on 6 different spans. The preliminary tests in smooth flow have shown that a single TMD tuned to the first mode was sufficient to damp the vortex-shedding excitation of that span but not sufficient to damp the oscillations of the other span. In turbulent flow, one TMD, placed on the span of maximum modal amplitude, was sufficient to reduce strongly the oscillations of that mode for the entire bridge.

This led to a modification of the tuning and deployment schemes of the TMD's, originally based on the DenHartog linear theory [3], and the development of a new approach presented in Ref. [1]. The original schemes were defined from the results of section model tests and predicted that three 11t TMD's would be necessary to damp each mode. The results obtained here suggested that as little as one 11t TMD could be sufficient. Other researchers have obtained similar results for the applications of TMD's for wind induced vibrations of tall buildings [4], where the optimal tuning is greatly influenced by the character of the excitation, a narrow band excitation of the vortex-shedding type being the easiest to damp.

The effectiveness of the TMD's has proved to be sensitive to their location in relation to the mode to be damped, the active mass and their own structural damping but less sensitive to the tuned frequency and the lateral position of the TMD in relation to the longitudinal axis of the bridge. A deviation of  $\pm 5\%$  of the frequency of the TMD from the target frequency did not show any significant difference on their effectiveness. Reducing the internal damping of the TMD increased the displacement of the TMD's active mass and slightly reduced their effectiveness.

#### 4. Conclusions

The wind tunnel reported here on a multi-span continuous beam bridge have shown that a 3-D aeroelastic model could be used as a design tool in conjunction with the mitigation of vortex-shedding induced vibrations using tuned mass dampers or aerodynamic appendages. TMD's can be modelled elastically at small scale to optimize their tunings and their effectiveness can be demonstrated early in the design process on the full-bridge aeroelastic model.

#### 5. Acknowledgements

The permission of Great Belt A/S to publish the results of the wind tunnel tests on the East Bridge Approach Spans is gratefully acknowledged.

#### References

1. A. Larsen, E. Svensson and H. Andersen, "Design Aspects of Tuned Mass Dampers for the Great Belt East Bridge Approach Spans", in *Proc. of 3rd. APSOWE*, Hong Kong, Dec. '93.
2. A.G. Davenport, Personal Communication, May 1992.
3. E. Simiu and R. H. Scanlan, "*Wind Effects on Structures*", Wiley & Sons, 1986.
4. H. Tanaka and C.Y. Mak, "Effect of Tuned Mass Dampers on Wind Induced Response of Tall Buildings", *JWEIA*, 14 (1983) 357-368.

Fig. 6 also shows that the turbulence of the flow had the effect of reducing the amplitude of the vortex-shedding excitation. The effect of the turbulence appeared not only to be a function of the turbulence intensity but also a function of the structural damping. The turbulence mitigated the RMS response by more than 50% for the 6% damping case but only by 10% for the 1.5% damping case.

The wind screens, 50% porous and 3.2m high, had a large influence on the vortex-shedding excitation since they appeared to increase the amplitude of the oscillations by a factor of three (see Fig. 7). The decision to install them or not on the prototype structure has very important implications on the design [1]. However it was observed during section model tests that congested traffic had practically the same detrimental effect as the wind screens on the vortex-shedding response.

Guide vanes were investigated as aerodynamic appengages to reduce the vortex-shedding excitation. It was found that they provided a substantial reduction (see Fig. 7) of the RMS response for the deck fitted with wind screens for the higher modes of vibration, that is tests conducted at higher wind speeds. For tests at lower wind speeds, their effect appeared to be reduced. This discrepancy was attributed to local Reynold's number effects, where at lower wind speeds, there is not enough flow passing through the guide vanes to be injected into the wake to suppress the shedding of vortices. This was confirmed by subsequent section model tests where a parametric investigation of the effect of guide vanes was carried out with respect to Reynold's number and geometry.

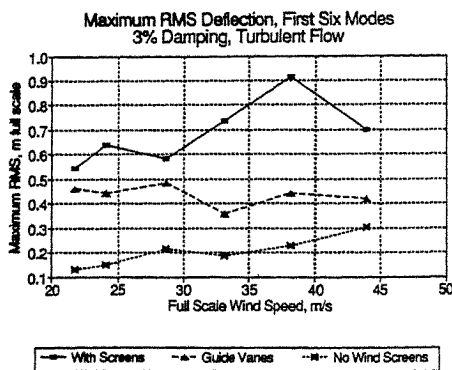


Fig. 7. Vertical RMS Response vs Wind Speed, 3% Damping, Turbulent Flow

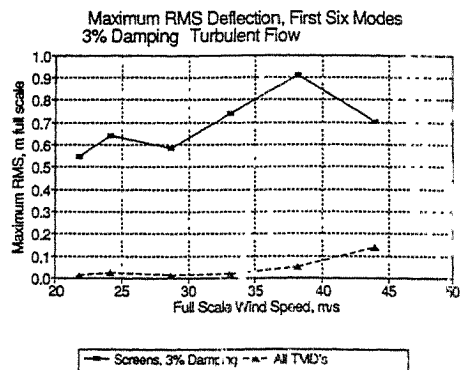


Fig. 8. Tuned Mass Damper Effect, 3% Damping, Turbulent Flow

### 3.2 Tuned Mass Damper Investigations

The test programme included a verification of the effectiveness of a combination of one to three TMD's placed on one to three different spans to damp the first vertical mode; tests with four TMD's to damp the first two modes, two per mode; and finally, given the results of the previous tests, to establish a strategy to damp the first six vertical modes with 12 TMD's, 2 per mode.

The TMD's were tuned and then simply glued on the model, typically at midspan of a given span. Their aerodynamic interference on the behaviour and the effect of their added mass were negligible.

The TMD tests have shown that it is possible to damp completely the strong vortex-

## Vibration control of wind-excited tall buildings with passive dampers

B. Samali and K.C.S. Kwok<sup>+</sup>

School of Civil Engineering, University of Technology, Sydney, Australia

<sup>+</sup> School of Civil and Mining Engineering, University of Sydney, Sydney, Australia

**Abstract :** The effectiveness of Tuned Liquid Column Dampers (TLCD) in reducing tall building vibrations induced by wind loads is investigated analytically. A numerical example pertaining to a 76-storey tall building is worked out to demonstrate the effectiveness of TLCD damper system. A thorough sensitivity analysis is performed in order to optimise the proposed damper system for maximum effectiveness and minimum mass. Top floor displacement reduction of up to 45 % was achieved with the inclusion of a TLCD system. This was achieved at a damper mass of only 0.7 % of the building mass. Other parameters such as tuning ratio and orifice opening ratio also affect the effectiveness of the proposed damper system. It is also concluded that higher modes of vibration affect the acceleration response of the building significantly.

### 1. Introduction

Excessive oscillations of tall buildings and towers in severe wind environments is of particular concern to engineers. Such excessive oscillations may cause perceptible motions or equipment malfunction. This is particularly true for modern tall buildings and towers as they are lighter, more slender and possess little natural damping, hence prone to excessive wind-induced oscillations. It is therefore important to search for effective and economical means of suppressing structural vibrations induced by wind gusts.

Tuned mass damper (TMD), as a passive damping device, is found to be effective in reducing wind-induced response of tall buildings and towers [e.g. 1,2]. Recently another type of damper system, namely, the Tuned Liquid Column Damper (TLCD) has been investigated [e.g. 3-8] which is particularly suited to high rise buildings, as the water of the damper system can be used for other requirements such as water supply and fire fighting.

In this paper, the effectiveness of TLCD system in suppressing wind-induced motions is investigated analytically using random vibration theory, and the parameters affecting the damper system and its performance are identified. The formulation of the problem utilises transfer matrices in the frequency domain for the analysis of wind-induced structure-damper interaction. In this study, the structure is modelled as a lumped mass multi-degree-of-freedom shear building with variable storey properties taking into account only shear (rotational degree of freedom is ignored). The results are compared with those obtained earlier using a cantilevered model [8]. Unlike force and displacement responses, it has been found that wind-induced acceleration response of tall and slender structures involve more than just the first vibration mode and neglecting higher modes may result in non-conservative errors. The transfer matrix approach allows the inclusion of any desired number of modes with no additional efforts.

Following the works of Saka'i [3], it has been established that the damping term in the governing equation for TLCD is non-linear. However, such nonlinearities are not significant and an equivalent linearisation technique may be utilised to linearise the governing equation for TLCD system. The stochastic response of tall buildings equipped with a damper system is determined following a random vibration analysis. The along-wind turbulence is modelled as a stochastic process which is stationary in time but non-

homogeneous in space. The power spectral density proposed by Davenport is utilised in the analyses. Due to space limitation however, the mathematical formulation of the problem is not included in this paper and only the results of the study are presented.

## 2. Numerical Example

A 76-storey building with floor masses lumped into ten masses was used to illustrate the effectiveness of TLCD system in suppressing wind-induced oscillations. The building has a total mass of 120162 tonnes. The results presented here pertain to a mean wind velocity of 16 m/s at 10 metres above ground. The first three natural frequencies of the building are 0.175, 0.336 and 0.509 Hz., respectively.

## 3. Summary of Findings

The performance of the TLCD system was compared with that of TMD (with identical mass). It is found that TLCD system is as effective as TMD system. TLCD system however, offers several practical advantages over TMD, including low cost and few maintenance requirements. A damper mass of only 0.7% was found to be able to suppress the response considerably. Tuning both the TLCD and the TMD to the first natural frequency of the building, it can be seen from Figure 1 that both damper systems are capable of reducing the first mode response significantly. However, the higher modes are unaffected. For acceleration response, the contribution of higher modes is quite significant as can be seen in Figure 1. The effectiveness of the TLCD system in comparison with the TMD system is summarised in Table 1. In determining the response of structures to wind forces, it is customary to neglect the effects of higher modes and only consider the first mode of vibration. This practice although acceptable for displacement and force type responses, can significantly underestimate the acceleration response and therefore is not recommended. This phenomenon can be clearly seen in Table 1. Furthermore, it can also be observed that by ignoring higher modes of vibration, the effectiveness of both the TLCD and TMD systems is exaggerated as these damper systems were tuned to the first mode only.

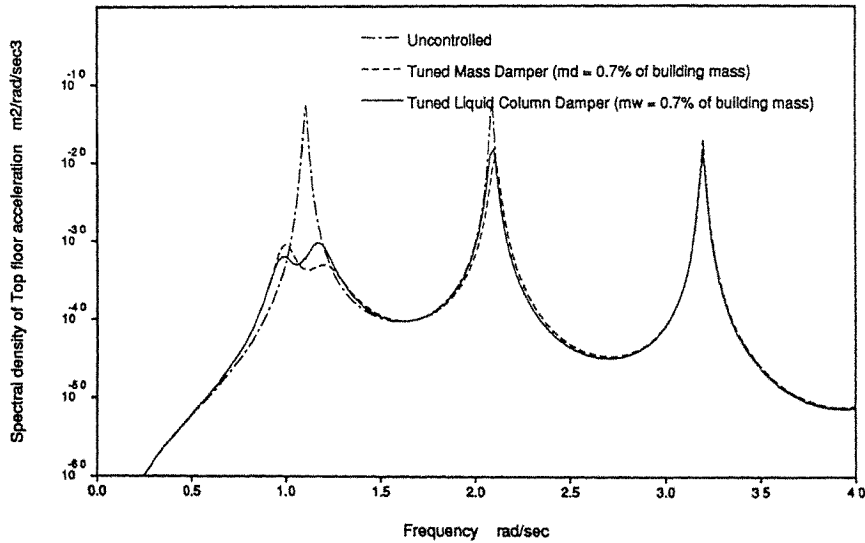


Fig. 1 Spectral density of top floor acceleration

Two salient characteristics affecting the performance of a TLCD system are the tuning ratio (denoted by T.R.) and the coefficient of head loss (denoted by CoHL). The coefficient of head loss is a function of orifice opening ratio, ie, the degree of flow obstruction as a result of installing an orifice plate with a cross section smaller than the main liquid tube. The results presented in Table 1 are for a few combinations of T.R. and CoHL. In Table 1, as well as in the subsequent graphs, the damping coefficient of the TMD system is denoted by Cd.

	$\sigma_{Q_0}$ kN	$\sigma_{Q_0}$ reductn %	$\sigma_{Y_N}$ mm	$\sigma_{Y_N}$ reductn %	$\sigma_{\ddot{Y}_N}$ mil.g	$\sigma_{\ddot{Y}_N}$ reductn %	$\sigma_{\ddot{Y}_N}$ mil.g	$\sigma_{\ddot{Y}_N}$ reductn %
Without Damping	2328.54		40.20		4.45		6.98	
TMD Cd optimised	1805.74	22.45	21.83	45.70	1.71	61.61	4.43	36.53
TLCD, CoHL & T.R optimised	1847.56	20.66	22.23	44.70	1.79	59.84	4.70	32.67
TLCD, CoHL=200 T.R optimised	1865.67	19.88	22.54	43.93	1.87	58.02	4.50	35.44
TLCD, T.R=100% CoHL optimised	1850.09	20.55	22.51	44.01	1.79	59.77	4.62	33.76

$\sigma_{Q_0}$  = Standard deviation of base shear force.

$\sigma_{Y_N}$  = Standard deviation of top floor displacement.

$\sigma_{\ddot{Y}_N}$  = Standard deviation of top floor acceleration (1st mode only).

$\sigma_{\ddot{Y}_N}$  = Standard deviation of top floor acceleration (with higher modes).

Table 1 Standard deviation responses of the 76-storey building with and without damper systems

Figures 2 and 3 represent the variation of top floor acceleration with damper mass. In Figure 2 only the first mode of vibration is included in the calculations, while in Figure 3 all modes of vibration are included. As can be seen from these figures, the variation of response with damper mass and its characteristics are quite different when only the first mode of vibration is considered in the analysis. These figures reveal that, the TMD system can offer marginally a better response reduction for the same damper mass. Figure 2 displays a sudden decrease in the acceleration response for mass ratios of up to about 0.2%. This sudden reduction in response, although apparent in Figure 3, is not as drastic. Figures 2 and 3, like Table 1, clearly indicate that considering only the first mode of vibration can lead to significant underestimation of the acceleration response.

The variation of optimum tuning ratio with damper mass is illustrated in Figure 4 for displacement and acceleration type response versus force type response. While the optimum tuning ratio decreases almost linearly with increasing mass ratio for displacement and acceleration responses, for base shear force it initially increases with mass ratio, flattens out and then starts to decrease with increasing damper mass. Similarly the optimum coefficient of head loss and its variation with damper mass is quite different for displacement (or acceleration) response versus base shear force as illustrated in Figure 5.

The variation of optimum tuning ratio with damper mass is illustrated in Figure 4 for displacement and acceleration type response versus force type response. While the optimum tuning ratio decreases almost linearly with increasing mass ratio for displacement and acceleration responses, for base shear force it initially increases with mass ratio, flattens out and then starts to decrease with increasing damper mass. Similarly the optimum coefficient of head loss and its variation with damper mass is quite different for displacement (or acceleration) response versus base shear force as illustrated in Figure 5.

As mention earlier, the structural model used here pertains to a shear building. To assess the sensitivity of the results to structural modelling, the results obtained here were compared with those obtained by Xu [8]. Xu used the same 76-storey building but modelled it as a cantilever taking into account both bending and shear. The results are

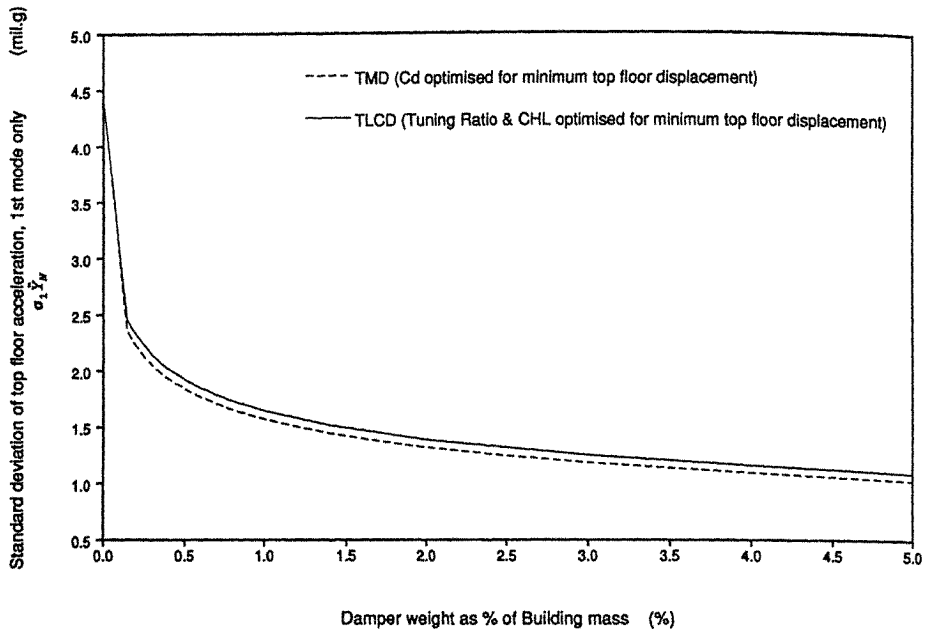


Fig. 2 Variation of top floor acceleration response with damper mass (first mode only)

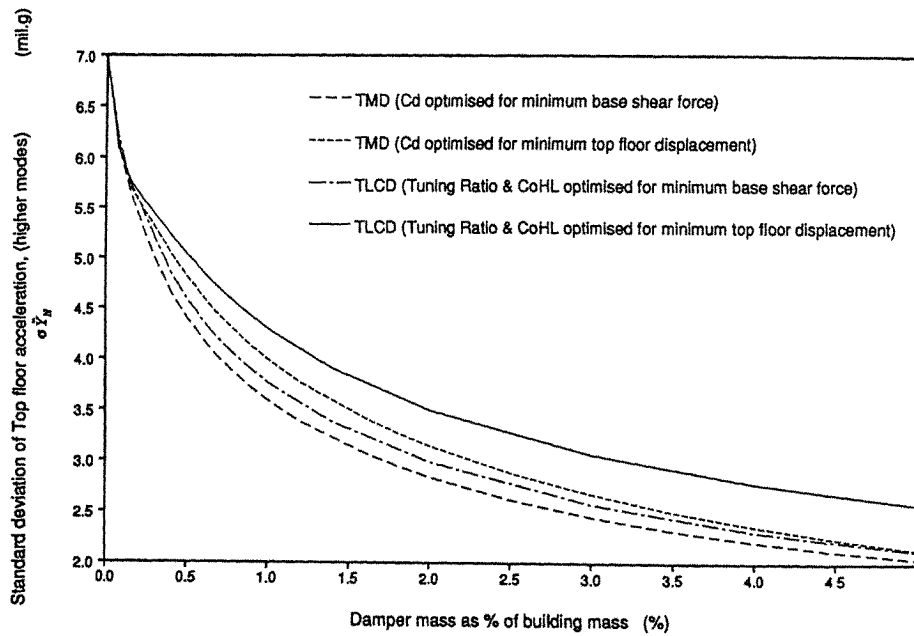


Fig. 3 Variation of top floor acceleration response with damper mass (all modes included)



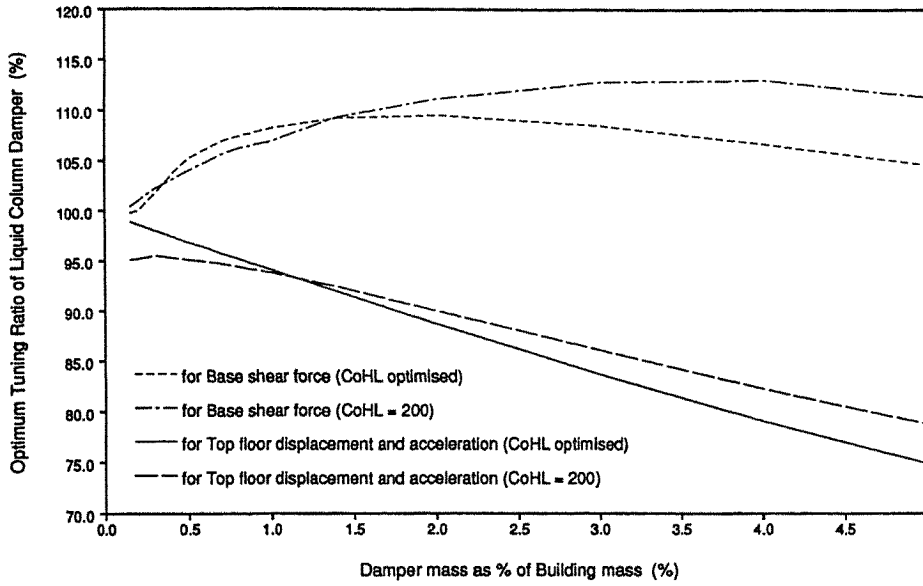


Fig. 4 Variation of optimum tuning ratio of TLCD with damper mass

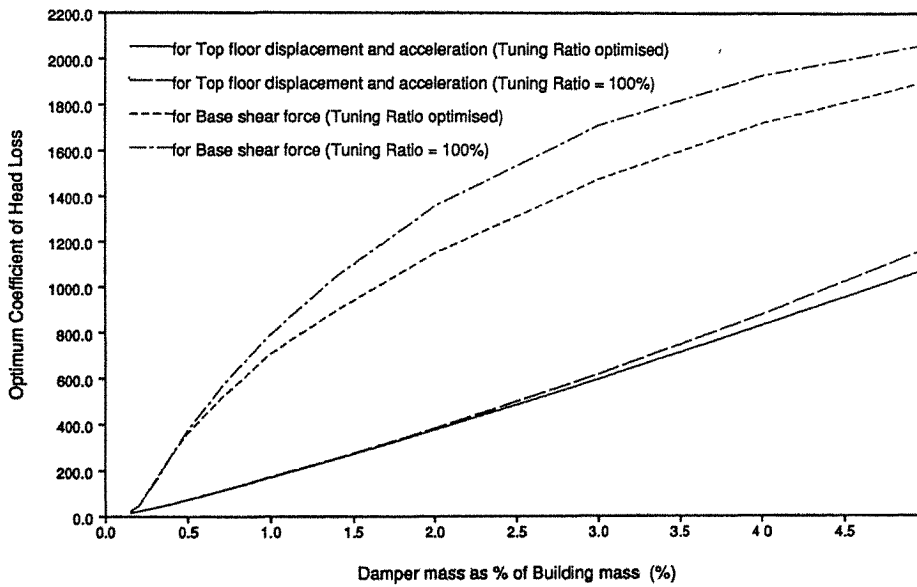


Fig. 5 Variation of optimum coefficient of head loss with damper mass

summarised in Table 2. From this Table it can be seen that with the exception of acceleration response, the maximum error is in the order of 6%.

Response Variable	model	WTD		TMD $m_d = 839 \text{ t}$		TLCD $m_d = 419.5 \text{ t}$		TLCD $m_d = 839 \text{ t}$	
			% error		% error		% error		% error
$Q_b$ (kN)	cantilever shear	2330	0.06	1895	2.62	1973	1.52	1883	2.97
		2328.5		1944.7		2002.9		1938.9	
$Y_N$ (mm)	cantilever shear	37.8	6.34	23.9	0.60	24.6	0.005	23.3	0.59
		40.2		23.8		24.6		23.2	
$\ddot{Y}_N$ (mil.g)	cantilever shear	7.7	9.35	6.0	14.83	6.3	14.13	5.9	15.93
		6.98		5.11		5.41		4.96	

WTD = With out any damper.  
TMD = Tuned Mass Damper  
TLCD = Tuned Liquid Column Damper.

Table 2 Effects of structural modelling on response

#### 4. Conclusions

TLCD system is a viable passive damper system capable of offering significant response reduction with only a small damper mass. From this study the following conclusions can be drawn:

1. In terms of response reduction and effectiveness, the TLCD system is almost at par with corresponding TMD system.
2. The contribution of higher modes of vibration to acceleration response is significant and cannot be ignored.
3. The effectiveness of the TLCD system in controlling acceleration response can be overemphasised if the higher modes of vibration are ignored.
4. The variation of optimum tuning ratio and optimum coefficient of head loss with damper mass is different for displacement (or acceleration) type response compared with force type response (eg base shear force).
5. Modelling of the structure (ie, shear building vs cantilever) has little effect on force and displacement responses, but moderately affects the acceleration response.

#### References

1. N.R. Peterson, ASCE Convention and Exposition, Boston, Mass. (1979), Preprint 3578.
2. R.W. Luft, J. Struct. Div., ASCE, Vol. 105, No. ST12 (1979), 2766.
3. F. Saka'i, S. Takaeda, S., T. Tamaki, Proc. International Conference on Highrise Building, Vol. 2, Nanjing, China (1989), 926.
4. B. Samali, Proc. of the Australian Vibration and Noise Conference, Melbourne, Australia (1990), 138.
5. B. Samali, K.C.S. Kwok, and Y.L. Xu, Proc. of Asia Pacific Vibration Conference, Melbourne, Australia (1991), 9.39.
6. B. Samali, P. Lee and K.C.S. Kwok, Proc. of First International Conference on Motion and Vibration Control, Yokohama, Japan (1992), 182.
7. R.D. Watkins and P.A. Hitchcock, Proc. of First International Conference on Motion and Vibration Control, Yokohama, Japan (1992), 1130.
8. Xu, Y. L., Samali, B., Kwok, K. C. S., J. Eng. Mech., ASCE, Vol. 118, No. 1 (1992), 20.

## Effect of Liquid Dampers on Along-Wind Response of Structures

Keming Sun, H.F. Cheong and T. Balendra

Dept. of Civil Engineering, National University of Singapore  
10 Kent Ridge Crescent, Singapore 0511

**Abstract:** A mathematical model for numerical analysis of wind induced stochastic response of structures with tuned liquid column dampers is proposed. An investigation is made for the possible application of tuned liquid column dampers in reducing the along-wind response of wind sensitive structures. The structure is modelled as a single-degree-of-freedom system and the wind turbulence is modelled as a stochastic process. The stochastic responses of structures and tuned liquid column dampers in terms of power spectrum and variance are evaluated. Furthermore, the effective damping of the system is determined. The numerical examples show that tuned liquid column dampers have significant practical advantages if the parameters of the liquid dampers are properly selected.

### 1. Introduction

Wind-excited vibration of tall or slender structures may cause structural failure, discomfort to occupants or malfunction of equipment. Therefore, the response analysis of tall buildings to wind loading has been the subject of numerous studies. An extensive review of the earlier work was provided by Simiu and Scanlan (1986), and Kareem and Sun (1987). The responses of buildings to random wind loading have been investigated by Yang and Lin (1981a,b), Kareem (1990), and Islam et al. (1990).

To reduce the response of wind loading, one of particular importance for this area is to search for an effective and practical device capable of suppressing structural vibrations induced by wind loading. Recently, some new devices which were referred to as nutation damper (Modi and Welt, 1988), tuned sloshing damper (Kareem, 1990), tuned liquid dampers (Fujino et al., 1988), and tuned liquid column dampers (Sakai et al., 1989) have been proposed. Some recent studies have demonstrated that sloshing fluid in a container if properly tuned will be very effective in reducing structural response (Kareem and Sun, 1987; Modi and Welt, 1988; Fujino, et al., 1988). Earlier studies have concluded that the containers partially filled with fluids and tuned liquid tube serve as vibration dampers if the parameters are properly selected. However, the detailed analysis quantifying the wind effects on structure and tuned liquid column damper (TLCD) systems, compared with the general analysis of the structures with traditional tuned mass dampers, is lacking.

It is the purpose of this study to propose a mathematical model for numerical analysis of the wind induced stochastic response of structures with TLCD and to investigate effectiveness of TLCD device for wind sensitive buildings. In this paper, a numerical analysis of the wind induced stochastic response of structures with TLCD is presented. The structure is modeled as a primary single-degree-of-freedom (SDOF) system and the TLCD is considered as a secondary system. The wind turbulence is modelled as a stochastic process with mean and random fluctuating parts, and the fluctuating part of the wind velocity is treated as a stationary Gaussian random process. The

nonlinear damping term in the fundamental equation of the TLCD is treated by an equivalent linearization technique. The typical responses including power spectrum, variance and equivalent damping, are statistically analyzed. Numerical examples are given to illustrate the effects of the mass ratio, frequency ratio and coefficient of head loss on dynamic behaviors of structure and TLCD system.

## 2. Equations of Tuned Liquid Column Dampers

A tuned liquid column damper is shown in Fig.1. The equation of motion of the liquid column is given by Saoka et al. (1988) and has been verified by a series of experiments (Sakai et al., 1989) as follows:

$$\rho AL\ddot{x} + \frac{1}{2}\rho A\delta|\dot{x}|\dot{x} + 2\rho Agx = -\rho AB\ddot{y} \quad (1)$$

where  $y$  and  $x$  are horizontal displacement of the tube and vertical elevation of the liquid, respectively;  $\rho$  and  $L$  are the density and the length of the liquid, respectively;  $B$  and  $A$  are, respectively, the width and cross-sectional area of the tube;  $\delta$  is the coefficient of head loss (constant) governed by the opening ratio of the orifice;  $g$  is the acceleration due to gravity; and the dot represents derivative with respect to time.

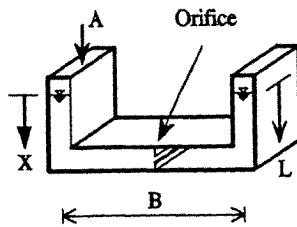


Fig.1 Tuned Liquid Damper

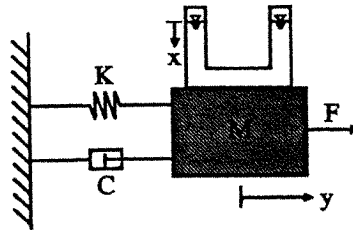


Fig.2 A SDOF System Fitted with a TLCD

The natural frequency  $\omega_d$  or the natural period  $T_d$  of the liquid column tube is given by the following equation:

$$\omega_d = \sqrt{\frac{2g}{L}} \quad \text{or} \quad T_d = 2\pi\sqrt{\frac{L}{2g}} \quad (2)$$

Eq.1 is nonlinear due to the presence of the liquid damping. In this study, wind excitation is modelled as a stationary Gaussian random process. The equivalent linearization technique may be independently applied to Eq.1 (Iwan and Yang, 1972; Spanos and Iwan, 1978). As a mean of obtaining an approximate solution of Eq.1, let us consider an auxiliary system which is described by a linear differential equation of the form:

$$m\ddot{x} + cm\ddot{y} + c_m\dot{x} + \omega_d^2 mx = 0 \quad (3)$$

where  $m = \rho AL$  is the total mass of the liquid,  $\alpha = B/L$  is the ratio between the tube width and liquid length, and  $c$  is the equivalent damping coefficient which can be expressed as:

$$c = \sqrt{\frac{2}{\pi}} \frac{\delta \sigma_x}{L} \quad (4)$$

where  $\sigma_x$  is the standard deviation of the liquid elevation velocity  $\dot{x}$ . In the derivation of Eq.4, it is assumed that the response is quasi-Gaussian with zero-mean velocities. Since Eq.4, for the equivalent damping, involves the yet-to-be-determined  $\sigma_x$ , an iteration solution procedure is required.

### 3. Stochastic Responses of Structures and TLCD System

Let us consider a SDOF system fitted with a tuned liquid column damper, as shown in Fig.2. Upon determination of the parameter  $c$ , the equations of motion of the resultant two-degree-of-freedom system subjected to a random fluctuation force,  $F(t)$ , can be written in the form:

$$\begin{bmatrix} m & m\alpha \\ m\alpha & M \end{bmatrix} \begin{Bmatrix} \ddot{x} \\ \ddot{y} \end{Bmatrix} + \begin{bmatrix} mc & 0 \\ 0 & C \end{bmatrix} \begin{Bmatrix} \dot{x} \\ \dot{y} \end{Bmatrix} + \begin{bmatrix} m\omega_d^2 & 0 \\ 0 & K \end{bmatrix} \begin{Bmatrix} x \\ y \end{Bmatrix} = \begin{Bmatrix} 0 \\ F \end{Bmatrix} \quad (5)$$

where  $M$  is the total mass of structure and liquid;  $C$  and  $K$  are the damping and stiffness coefficients of the primary structure, respectively.

The equivalent system given by Eq.5 is linear. Therefore, the spectral method may be used for evaluating the response statistics. Let  $\omega_p^2 = K/M$ ,  $C = 2\eta\omega_p M$ , and  $c = 2\xi\omega_d$ . Then the complex frequency response function can be obtained, from Eq.5, as:

$$H_y(i\omega) = \frac{1}{K} \frac{(1-\gamma^2) + 2i\xi\gamma}{[(1-\beta^2) + 2i\eta\beta][(1-\gamma^2) + 2i\xi\gamma] - (\alpha\mu\beta\gamma)^2} \quad (6a)$$

$$H_x(i\omega) = \frac{1}{K} \frac{\alpha\gamma^2}{[(1-\beta^2) + 2i\eta\beta][(1-\gamma^2) + 2i\xi\gamma] - (\alpha\mu\beta\gamma)^2} \quad (6b)$$

where  $\mu^2 = m/M$ ,  $\beta = \omega/\omega_p$ , and  $\gamma = \omega/\omega_d$ .

The power spectra of the displacement and velocity responses can be expressed as:

$$S_{yy}(\omega) = |H_y(i\omega)|^2 S_{FF}(\omega) \quad (7a)$$

$$S_{xx}(\omega) = |H_x(i\omega)|^2 S_{FF}(\omega) \quad (7b)$$

$$S_{\dot{x}\dot{x}}(\omega) = \omega^2 S_{xx}(\omega) \quad (7c)$$

where  $S_{FF}(\omega)$  is spectrum of wind loading which can be expressed as (Yang and Lin 1981a,b):

$$S_{FF}(\omega) = \frac{8k_0 F_0^2}{|\omega|} \frac{\lambda^2}{(1+\lambda^2)^{4/3}} \quad (8)$$

$$F_0 = \frac{1}{2} \rho_0 A_0 C_0 V_0^2 \quad (9a)$$

$$\lambda = \frac{600\omega}{\pi V_0} \quad (9b)$$

in which  $\rho_0$  is the air density;  $A_0$  is the frontal area of the building;  $C_0$  is the drag coefficient which can be different for different structural forms and should be experimentally determined,  $V_0$  is the mean wind velocity which can be selected as the average velocity at 10m above the ground and  $k_0$  is the ground-surface drag coefficient which is a constant.

The corresponding mean square responses are given by:

$$\sigma_y^2 = \frac{1}{2\pi} \int_{-\infty}^{\infty} S_{yy}(\omega) d\omega \quad (10a)$$

$$\sigma_x^2 = \frac{1}{2\pi} \int_{-\infty}^{\infty} S_{xx}(\omega) d\omega \quad (10b)$$

$$\sigma_z^2 = \frac{1}{2\pi} \int_{-\infty}^{\infty} S_{zz}(\omega) d\omega \quad (10c)$$

It should be mentioned that the integration of Eq.10 has to be evaluated numerically since the power spectra given in Eqs.6 are not easy to be calculated analytically. The evaluation of equivalent liquid damping,  $c$ , and the standard deviation of the liquid elevation velocity,  $\sigma_{\dot{x}}$ , should involve an iterative computational procedure for simultaneous solution of Eqs.4 and 10.

#### 4. Effective Damping

The effectiveness of the TLCD can be evaluated in terms of the effective damping, which can be defined as the viscous damping required to sustain the same magnitude of response under the same excitation. Therefore, the structure with TLCD system as shown in Fig.2 may be modeled as an equivalent SDOF system as shown in Fig.3.

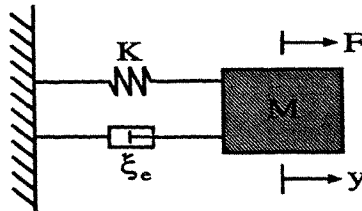


Fig.3 Equivalent SDOF System for a Primary Structure Fitted with a TLCD

In this model, the effect of the TLCD is defined as an effective viscous damping required by the primary structure to have the same magnitude of the response. Based on the equivalent SDOF model of Fig.3, the mean square response of the equivalent system, and the effective damping of the system can be determined under the excitation of wind loading. The variance response of the equivalent system is approximately given as:

$$\sigma_y^2 \approx \frac{\omega_p S_{FF}(\omega_p)}{4\xi_e K^2} \quad (11)$$

in which  $\xi_e$  is the ratio of effective damping. By equating Eqs.10a and 11, it becomes:

$$\xi_e \approx \pi \omega_p S_{FF}(\omega_p) / \left[ 2K^2 \int_{-\infty}^{\infty} |H_y(i\omega)|^2 S_{FF}(\omega) d\omega \right] \quad (12)$$

Therefore, the effective damping can be determined readily by using Eq.12.

### 5. Numerical Results

As an illustration of the analysis method, the variations of effective damping of a SDOF structure fitted with a liquid damper are presented. In this example, the wind loading of  $V_0 = 40m/s$ ;  $\rho_0 = 1.23kg/m^3$ ;  $k_0 = 0.03$  and  $C_0 = 1.2$  are used. In order to investigate the pure effect of TLCD on the system, the damping ratio of the primary structure  $\eta = 0$  is adopted. The structural parameters affecting the effective damping are the mass ratio,  $\mu$ , the frequency ratio,  $\Omega$ , and the head loss of TLCD,  $\delta$ . By varying these parameters, their significance on the effective damping can be observed.

The variations of effective damping with mass ratio,  $\mu^2$  are illustrated as a function of frequency ratio,  $\Omega$ , and the coefficient of head loss,  $\delta$ . The variations of effective damping for three values of frequency ratio  $\Omega = 0.95, 1.0, \text{ and } 1.05$  are illustrated in Fig.4. The variations of effective damping for four values of  $\delta = 5, 10, 20 \text{ and } 30$  are produced in Fig.5.

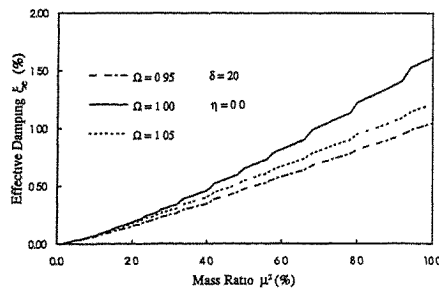


Fig.4 Effective Damping for Different  $\Omega$

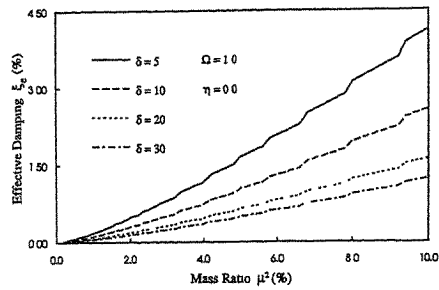


Fig.5 Effective Damping for Different  $\delta$

It is interesting to note that the TLCD will produce a maximal damping if the frequency ratio is  $\Omega = 1$  (see Fig.4). The results illustrated in Fig.5 demonstrated that the increase of the coefficient of head loss,  $\delta$ , will reduce the effective damping, which means that the dynamic response of primary structure will be increased. Therefore, smaller head loss is better than larger one for reducing the along-wind response of wind sensitive structures.

## 6. Conclusions and Remarks

For tall buildings and other large slender civil engineering structures, wind loads are usually the most significant dynamic loads in terms of design. While mass and stiffness of a structure play a role, the damping capacity of the structure is the most important factor in the control of vibrations induced by wind loads. On the basis of this study, it is found that the tuned liquid column damper device has great potential to increase the additional damping capacity and to reduce the deformation for the vibration control of tall building under wind loads.

The mathematical model and analytical expressions for numerical analysis of the wind induced stochastic response of structures with TLCD has been developed. The problem discussed and the results obtained in this paper are based on a primary structure modeled as a SDOF fitted with the TLCD system. However, it should be mentioned that the approach presented in this paper for estimating the effectiveness of a TLCD on the stochastic response of a SDOF system can be readily extended to continuous structures.

## References

1. Y. Fujino, B.M. Pacheco, P. Chaiseri, L.M. Sun, *Struct. Eng. Earthquake Eng.*, **5**(2),1988.
2. M.S. Islam, B. Ellingwood, and R.B. Corotis, *J. Eng. Mech.*, ASCE, **116**(7), 1990, 927.
3. W.D. Iwan, and I.M. Yang, *J. Appl. Mech.*, **39**, 1972, 545.
4. A. Kareem, *J. Wind Engrg. and Industrial Aerodynamics*, **36**, 1990, 725.
5. A. Kareem and W.J. Sun, *J. Sound and Vibration*, **119**(3), 1987.
6. V.J. Modi and F. Welt, *J. Wind Engrg. and Industrial Aerodynamics*, **30**, 1988, 85.
7. F. Sakai, S. Takaeda and T. Tamaki, *Proc., Int. Conf. on High Rise Buildings*, Vol.2, Nanjing, China, 1989, 926.
8. E. Simiu and R.H. Scanlan, *Wind Effects on Structures: An introduction to Wind Engineering*, 2nd Ed., Wiley-Interscience, New York, N.Y. 1986, 303.
9. P.T. Spanos and W.D. Iwan, *Int. J. Nonlinear Mech.*, **13**(2), 1978, 71.
10. J.N. Yang and Y.K. Lin, *J. Engrg. Mech. Div.*, ASCE, **107**(2), 1981a, 295.
11. J.N. Yang and Y.K. Lin, *J. Engrg. Mech. Div.*, ASCE, **107**(6), 1981b, 1209.



## Design Aspects of Tuned Mass Dampers for the Great Belt East Bridge Approach Spans

A. Larsen<sup>+</sup>, E. Svensson<sup>++</sup> and H. Andersen<sup>+</sup>

<sup>+</sup>COWiconsult A/S, Parallelsvej 15, Lyngby, Denmark

<sup>++</sup>Great Belt A/S, Vester Søgade 10, Copenhagen, Denmark

**Abstract:** The Great Belt East Bridge includes two approach bridges with steel girders designed as multi-span beams. The continuous long span design has led to flexible structures characterized by closely spaced eigenfrequencies for vertical vibration modes. Wind tunnel tests including section and full-bridge aeroelastic models have demonstrated that the approach bridge structures are prone to vortex shedding excitation at wind speeds encountered regularly at the bridge site. The present paper discusses design aspects of Tuned Mass Dampers for control of wind induced vibrations. A key point is the introduction of a new analysis model for assessment of TMD characteristics which acknowledges the non-linear motion dependent response observed in wind tunnel tests. Application of this model in design yields smaller TMD masses than obtained from conventional linear theory.

### 1. Introduction

The Great Belt East bridge currently under construction in Denmark consists of a 2694 m long, three-span suspension bridge, flanked by 2529 m and 1567 m long approach bridges. The Owner, Great Belt A/S, has entrusted the design work to a joint venture of COWiconsult and Rambøll Hannemann & Højlund.

The bridge will carry four lanes of motorway and two emergency lanes. Only four expansion joints are arranged for the full bridge length of 6.8 km: At the abutments and at the suspension bridge anchor blocks, resulting in expansion sections of 2529 m, 2694 m and 1567 m.

The approach bridges are designed as continuous beam bridges with a constant span length of 193 m between the concrete piers. The 25.8 m wide steel girder is designed as a closed trapezoidal box with a constant depth of 7.0 m (Fig. 1). The relatively long span length is obtained by using high yield strength steel (FE 460).

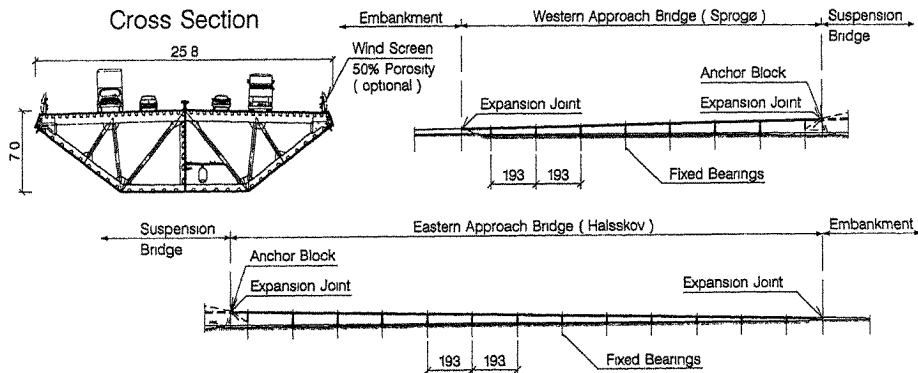


Fig. 1. Elevation and typical cross section for the Great Belt East Bridge Approach Spans

## 2. Preliminary Aerodynamic Evaluation

The fairly deep cross section of 7 m which was needed to meet demands on load carrying capacity was expected to make the girders appear "aerodynamically" bluff. Hence undesired wind induced vibrations due to lock-in between vortex shedding action and structural oscillations, vertical modes could not be ruled out during the early stages of design. Preliminary evaluation of the aerodynamic performance was obtained in terms of the critical wind speed  $U_c$  and maximum response amplitude  $\hat{y}$  from the following formulae given in the proposed British design rules for bridge aerodynamics [1]:

$$U_c = \frac{D f}{St} = (1.1 \frac{B}{D} + 1) f D, \quad \hat{y} = \frac{\rho B^{1/2} D^{5/2}}{8\pi M \zeta_s} \quad (1)$$

where  $St$  is Strouhal Number,  $B$ ,  $D$  are girder width and girder depth,  $f$  is the natural frequency for vertical oscillations and  $\rho$ ,  $M$ ,  $\zeta_s$  are air density, girder mass/unit length and structural damping relative to critical. As a rule of thumb  $f \approx 100 / \text{span length}$  for the first vertical mode of box girder steel beam bridges, i.e.  $f \approx 0.52$  Hz in the case of the East Bridge approach spans.

With an average superstructure weight  $M \approx 15.6 \cdot 10^3$  kg/m and an estimated structural lower bound for the damping  $\zeta_s = 0.005$  (relative to critical), a critical wind speed  $U_c = 18$  m/s and a vertical peak response  $\hat{y} = 0.34$  m are obtained from (1). Wind speeds of 18 m/s fall way below the design wind speed of 38 m/s adopted for the East Bridge and are encountered regularly during winter storms in the Great Belt region. The peak response  $\hat{y} = 0.34$  m exceeds the limiting dynamic response  $y_{\text{lim}} = 0.2$  m adopted in the design. A limiting dynamic amplitude of 0.2 m at 0.52 Hz corresponds to the ISO guidelines for user proficiency (ISO-2631 Addendum E, 1978) which yields a maximum acceptable acceleration RMS level of 1.5 m/s<sup>2</sup> for vertical vibrations at frequencies below 1 Hz. Based on this information it was decided to investigate the vortex shedding performance of the approach bridges in more detail.

## 3. Wind Tunnel Section Model Tests

Introductory wind tunnel tests of the approach bridge girders were carried out as 1:80 scale section model tests conducted in smooth and simulated turbulent flow at selected levels of structural damping. At a structural damping level  $\zeta_s = 0.005$  the vortex induced response was judged to be within acceptable limits for girders equipped with railings and open crash barriers only. Unacceptably large peak responses occurred if 3.5 m high wind screens of 50% porosity were added to the girders and/or if the approach bridges were congested by heavy traffic. Excessive responses at lock-in occurred at Strouhal Numbers in the range  $0.12 < St < 0.17$ . Maximum response  $\hat{y} = 0.8$  m (estimated full scale) occurred at  $St \approx 0.14$  and was found to be almost unaffected by the free stream turbulence but highly sensitive to structural damping.

Dynamic analyses of the approach bridges revealed that each of the continuous multi-span structures were characterized by a number of closely spaced eigen-modes of vertical vibration. A combination of section model tests results and structural analyses revealed that 5 respectively 7 vertical modes would receive unacceptably high vortex induced responses at wind speeds below 38 m/s in the cases of the western (Sprogø) and the eastern (Halsskov) approach bridges. This analysis is based on the assumptions that three dimensional aerodynamic effects are neglectible i.e. the nearness of the sea surface, interference from piers and abutments and possible modal coupling due to aerodynamic forces acting on the girders.

## 4. Full-Bridge Model Wind Tunnel Tests

Comprehensive wind tunnel tests were initiated using a 1:125 scale full aero-elastic model of the western (Sprogø) approach bridge in order to investigate the above mentioned assumptions and response predictions. The full-bridge model tests were also used for investigation of various concepts for damping of the vertical wind induced response, including addition of Tuned Mass Dampers (TMD's). Model tests and results are treated in more detail by Larose, Larsen and Svensson [2].

Four important conclusions relative to the TMD design were derived from the full-bridge model tests. 1) All vertical eigen-modes were excited by vortex shedding action at successively increasing wind speeds commencing at  $St \approx 0.16$  and peaking at  $St \approx 0.14$ . 2) The peak amplitude of recorded vortex induced responses was found to be in good agreement with results obtained from section model tests although slight variations were detected for the individual modes. 3) TMD's could be arranged to completely suppress vertical vortex induced girder response. 4) The TMD mass necessary to suppress vertical vortex induced responses amounted to approximately 1/3 of the TMD mass predicted from conventional linear forced oscillation theory given by DenHartog [3].

### 5. Assessment of Tuned Mass Damper Characteristics

Following the full-bridge model tests a decision was taken to provide TMD's for control of vortex induced vibrations of the East Bridge approach spans. It was considered important that the principles employed in the analysis and the design of the TMD's reflected the non-linear vortex excitation process. Values of structural damping in the bridges and TMD characteristics applied in the full-bridge tests (TMD mass, tuning and TMD eigen-damping) were not applied directly in the TMD design as it was deemed appropriate to be able to make allowances for possible variations in these parameters.

Larsen [4] has proposed a non-linear empirical model for assessment of characteristics of TMD's for control of vortex induced response of flexible bridge structures. An approximate expression for the critical mass ratio  $\mu_c = m^*/M^*$ , (mass ratio of the TMD to the bridge in generalized terms) necessary for complete suppression of the vortex induced response is given by:

$$\mu_c = 4(\eta - \zeta_s)\xi \left( \frac{(F^2 - 1)^2}{4\xi^2} + 1 \right) \quad (2)$$

where  $F = f_{TMD} / f_{bridge}$  is the TMD tuning and  $\xi$  is the TMD eigen-damping relative to critical. The parameter  $\eta$  corresponds to the apparent negative aerodynamic damping which drives the motion dependent vortex induced response.  $\eta$  and the two remaining aerodynamic parameters  $\epsilon$ ,  $\nu$  are obtained by least squares fit of the model response equation (3) to the steady state responses  $y_i$  inferred from wind tunnel tests conducted at varying values of the structural damping:

$$y = \left[ \frac{3\nu + 1}{\epsilon} \left( 1 - \frac{\zeta_s}{\eta} \right) \right]^{\frac{1}{2\nu}} \quad (3)$$

$\eta$  is particularly important as  $\zeta_s = \eta$  defines the numerical value of structural damping for which vortex induced structural responses will vanish. Fig. 2 illustrates the fit of (3) (full line) to response data obtained from the 4 lowest modes of the Sprogø full-bridge model tested at different damping levels and in faithfully scaled turbulent winds typical of the bridge site. It is noted that  $\zeta_s = 0.02$  indicates complete vanishing vortex induced response, hence  $\eta = 0.02$ . Numerical values of the remaining aerodynamic parameters were obtained as follows:  $\epsilon = 1.15$ ,  $\nu = 0.14$ .

At this point it might prove interesting to compare the relative TMD mass obtained from (2) to the relative TMD mass obtained from conventional linear theory [3]. The latter approach assumes that vortex shedding response of structures may be modelled as a linear oscillator driven at resonance by external forces independent of the structural motion. In this case  $\mu$  is obtained as:

$$\mu = 2\zeta_s \frac{y}{y_{lim}} \sqrt{\frac{(F^2 - 1)^2 + 4\xi^2}{F^4 + 4\xi^2}} \quad (4)$$

Assuming a structural damping  $\zeta_s = 0.005$  and that vortex induced response shall be reduced to 1/10 by means of TMD's with eigen-damping  $\xi = 0.05$  and perfect tuning  $F = 1.0$ , linear theory (4) yields  $\mu = 0.01$ . Non-linear theory (2) predicts  $\mu_c = 0.003$  for vanishing vortex response.

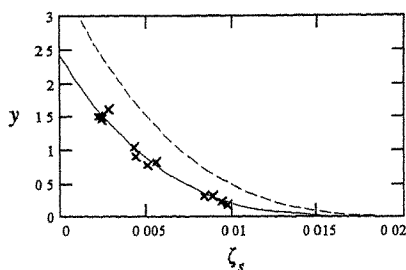


Fig. 2. Best fit (full) of response equation (3) to full-bridge model data. Response (dash) for 10% increase in aerodynamic parameters.

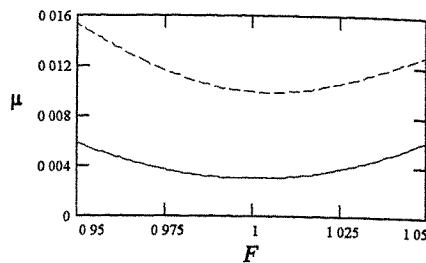


Fig. 3. TMD/bridge mass ratio as function of TMD tuning predicted from non-linear (2) (full) and linear (4) (dash) theory.

Hence  $\mu_c / \mu \approx 1/3$  as obtained from wind tunnel observations quoted in item 4) section 4. Fig. 3 compares predicted TMD mass ratios as function of the tuning given by (2) and (4).

### 6. Structural Damping of the East Bridge Approach Spans

The magnitude of vortex induced response is governed by the structural damping inherent in the approach bridges as demonstrated in Fig. 2. Available information on structural damping in continuous multi-span bridges in the literature is scarce. Hence field measurements on an existing structure of similar design were considered the most reliable way to acquire relevant data. On this basis it was decided to measure the inherent structural damping of the Sjælland-Farø Bridge, a 1600 m continuous steel box girder bridge designed by COWIconsult in 1986. The field tests yielded an inherent structural damping  $\zeta_s \approx 0.01$  for the Sjælland-Farø Bridge which is built with a 3.25 m deep box girder and a span length of 80 m between the piers. Allowances made for differences in girder depths and the mechanical properties of the road surfacings between the East Bridge and the Sjælland-Farø Bridge yielded an estimated inherent damping  $\zeta_s \approx 0.0065$  for the East Bridge approach spans.

### 7. TMD Characteristics for the East Bridge Approach Spans

TMD's designed according to linear theory are often chosen to be of the "optimum" type characterized by a fixed functional relationship between mass ratio and tuning  $F = 1 / (1 + \mu)$  and between mass ratio and TMD eigen-damping  $\xi = \sqrt{3\mu / 8(1 + \mu)^3}$ . For the East Bridge approach spans it was decided to adopt a "non-optimum" design strategy by allowing a  $\pm 2.5\%$  variation in tuning and a  $\pm 20\%$  variation in TMD eigen-damping relative to the nominal value  $\xi = 0.05$ . These allowances shall ensure that the TMD's remain efficient for changes in the bridge eigen-frequencies due to changing mass loadings, girder stiffness and support conditions (additional equipment, live loads, renewal of surfacing and changes in bearing slide) or in case of changing TMD eigen-damping due to temperature variations in the TMD dashpot elements.

Application of conservative estimates for tuning  $F = 1.025$  and TMD eigen-damping  $\xi = 0.06$  in (2) in conjunction with  $\zeta_s \approx 0.0065$  and  $\eta = 0.02$  yields a critical mass ratio  $\mu = 0.0038$  for suppression of vortex induced responses. Having approximately generalized masses  $M^* = 6500$  t and  $M^* = 10500$  t per vertical mode, the Sprogø and Halsskov bridges shall be equipped with TMD's having generalized seismic masses  $m^* = 25$  t and  $m^* = 40$  t for each vertical mode to be damped. Maximum allowable TMD deflections were set to 0.8 m in order to avoid excessive strain of spring elements.

### 8. Positioning and Tuning of TMD's

Svensson and Plum [5] have considered principles for positioning and tuning of TMD's in connection with damping of resonant response of continuous multi-span beams. The first and rather

obvious conclusion of this survey states that TMD's intended for damping of a certain mode should be located at positions where the particular mode displays maximum displacements. The second conclusion states that TMD's intended for damping of adjacent modes should not be located close together (at same spanwise position) because it will make the dampers work in opposite phases and therefore tend to cancel each other. Application of these principles to the Sprogø approach bridge is illustrated below

As a result of the full-bridge tests it was found appropriate to distribute the necessary TMD mass for damping of a particular mode in two or more individual spans. Furthermore in each span the TMD will be split in two separate units due to the heavy longitudinal plate bulkhead in the centre plane of the girder, Fig. 5. In Fig. 4, mode shapes and TMD positions are shown for the 5 lowest vertical modes likely to be excited by vortex shedding action in the wind speed range 18 m/s - 38 m/s. Each mode is damped by two pairs of TMD units located at the centre of the spans where maximum displacements occur. The accompanying Table 1 gives eigen-frequencies for the 5 vertical modes calculated under the assumption that piers and girder or alternatively the girder alone participates in the oscillatory motion.

Mode Number	Incl. Piers $f$ (Hz)	Excl. Piers $f$ (Hz)
1	0.496	0.469
2	0.549	0.521
3	0.621	0.599
4	0.707	0.692
5	0.802	0.793

Table 1. Eigen-frequencies for vertical modes 1 -5 including and excluding the participation of bridge piers in oscillatory motion.

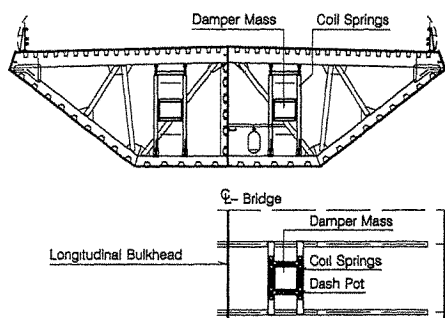


Fig. 5. Arrangement of TMD units in pairs located mid-span at either side of the heavy longitudinal plate bulkhead.

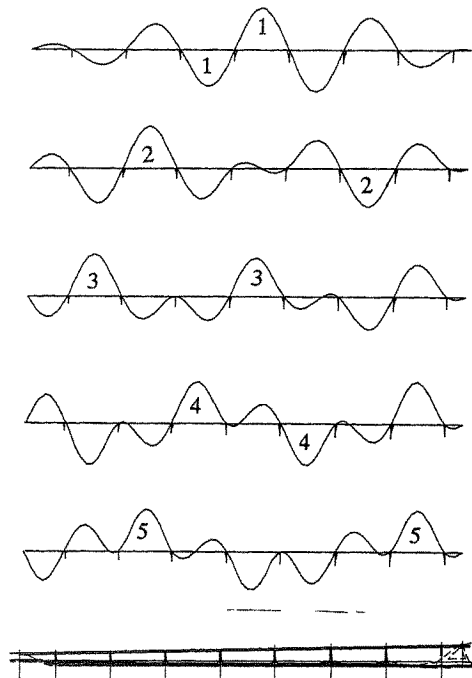


Fig. 4. Vertical mode shapes 1-5 and position of TMD's for suppression of vortex induced response in the wind speed range 18 - 38 m/s.

From Fig. 4 it is noted that it has been possible to distribute the TMD's almost evenly throughout the girder. Exceptions are spans no. 4 and 5 from the abutment which carry two TMD pairs each.

Table 1 reveals that the eigen-frequency of the vertical modes to be damped are dependent on whether or not the bridge piers participate in the oscillatory motion. The field tests on the Sjølland-Farø bridge demonstrated that the piers participated fully in oscillations as sliding in bearings did

not take place. Friction conditions in the bearings of the East Bridge approach spans are not known at the design stage. Hence the TMD design will allow for final tuning within the  $\pm 2.5\%$  frequency tolerance to be performed preferably upon measurement of the actual eigen-frequencies of the approach bridges.

### 9. Time-Domain Simulations of Vortex Induced Response

Time-domain simulations of the girder and TMD responses have been carried out using a Finite Element Model in order to study the effect of variations in the governing aerodynamic and structural parameters identified in (2). Motion dependent forces driving the vortex shedding process are modelled by means of a non-linear dashpot excreting negative damping. As an example Fig 6 presents transient girder and TMD decay traces for a structural damping  $\zeta_s = 0.005$  and assuming that the nominal aerodynamic parameters  $\eta$ ,  $\epsilon$ ,  $\nu$  are all increased by 10% (dashed line Fig. 2). Although a 10% increase in aerodynamic parameters leads to a drastic increase in the vortex induced response (above 50% at  $\zeta_s = 0.005$ ), steady state girder and TMD responses for this condition are observed to be around 0.03 m and 0.3 m respectively. Hence maximum allowable girder and TMD responses are not exceeded.

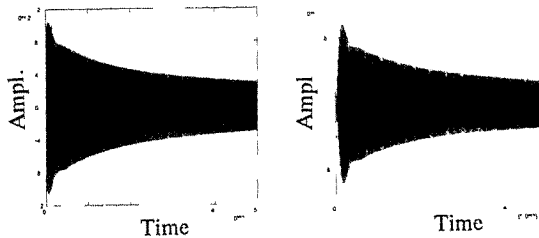


Fig. 6. Time-Domain Simulation of Girder (left) and TMD (right) response at off-design conditions.

### 10. Status on TMD Design and Acknowledgements

The TMD systems for the approach bridges are still under design during summer 1993. Current efforts includes tender design of mechanical systems and drafting of contractor specifications. Following detailed investigations of the wind climate at the bridge site, it has been decided that the East Bridge shall not be fitted with wind screens along the entire length when opened to traffic, but only if proven necessary by experience. Hence TMD's will only be provided for damping of vortex induced responses at wind speeds up to 25 m/s (2 modes for the Sprogø Bridge, 4 modes for the Halsskov Bridge), with the purpose of counteracting adverse aerodynamic effects of congested traffic. At wind speeds above 25 m/s the bridges are anticipated to be closed to traffic.

The authors would like to acknowledge the kind permission of Great Belt A/S to publish design considerations and wind tunnel test results obtained during execution of the project.

### References

1. Proposed British Design Rules for Bridge Aerodynamics, *Bridge Aerodynamics, Inst. of Civ. Ing.* Thomas Telford Ltd, London, 1981.
2. Larose, G.L., Larsen, A. and Svensson, E. Modelling of Tuned Mass Dampers for Wind Tunnel Tests on a Full-Bridge Aeroelastic Model, *3rd APSOWE Proc.*, Hong Kong, 1993.
3. DenHartog, J.P. *Mechanical Vibrations*, 4th ed. McGraw-Hill, New York.
4. Larsen, A. Vortex-Induced Response of Bridges and Control by Tuned Mass Dampers, *EURODYN'93 Proc.* Trondheim, 1993.
5. Svensson, E. and Plum, C.M. Tuned Mass Dampers for Continuous Beams, *IABSE Conf. Proc.*, Göteborg, 1993.

## Test and Research of Control for Alongwind and Acrosswind Responses of Tall Building by Cylindric Deep-Water Tank

W. L. Qu S. G. Liang<sup>+</sup> Z. Y. Li<sup>++</sup> K. S. Sheng<sup>+++</sup> G. Q. Li<sup>++++</sup>

Department of Building Engineering  
Wuhan University of Technology, Wuhan, China

<sup>+</sup>Department of Civil Engineering  
Wuhan Institute of Hydraulic and Electric Engineering, Wuhan, China

**Abstract:** On the basis of test analysis, this paper provides a calculation method of control for alongwind and acrosswind responses of tall building by cylindric deep-water tank. The calculation results of practical engineering examples show that the cylindric deep-water tank has obvious effect of suppressing vibration and does not need much more cost, as it can be combined with the living and fire fighting water tank which is necessary for tall buildings.

### 1. Introduction

Wind load is the main design load for tall buildings. With the increasment of the hight of tall building and the extension of steel structures, the stiffness and the damping of buildings are decreasing. Thereby, it is a new way to use the method of structural control for suppressing wind vibration responses of tall buildings. To make the method of structural control be widely used, it is necessary to find simple, cheap and effective control devices.

The cylindric deep-water tank is a kind of low cost and effective control device for wind vibration responses of tall building. Since it may be obtained by reforming the living and fire fighting water tank of tall building, it can be widely used in wind resistant design of tall buildings.

This paper presents a calculation method of control for alongwind and acrosswind responses of tall building by cylindric deep-water tank on the basis of test analysis. According to the principle of suppressing vibration of the cylindric deep-water tank, the paper establishes the controlled equations of structure in alongwind and acrosswind direction. After the calculating formulas of controlled wind vibration responses of structure is derived, the effect of control for wind vibration responses of a engineering example is calculated and analyzed.

### 2. Basic Principle of Vibration Control of Cylindric Deep-Water Tank

The cylindric deep-water tank is a kind of the water tank that ratio of water depth to diameter is greater than 1/8. When it is installed on building, it moves with the structure under wind load. This causes the water in the tank to slosh. In the case of reasonable design, the total dynamic pressures acting on the tank wall compose the control force suppressing vibration of the structure. Ref. Fig. 1.

According to the plinciple of engineering liquid mechanics, the potential function of velocity of water in the tank satisfies the following Lapelace equation:

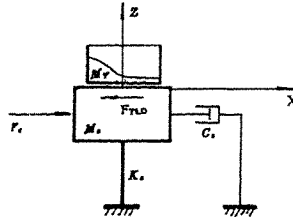


Fig. 1 basic principle of suppressing vibration of water tank

$$\nabla^2 \Phi = \frac{1}{r} \frac{\partial}{\partial r} \left( r \frac{\partial \Phi}{\partial r} \right) + \frac{1}{r^2} \frac{\partial^2 \Phi}{\partial \theta^2} + \frac{\partial^2 \Phi}{\partial z^2} = 0 \quad (1)$$

If the coordinate origin is assumed on the water surface, the boundary condition of the potential function can be described as:

$$\left. \begin{aligned} \frac{\partial \Phi}{\partial z} \Big|_{z=-h} &= 0 \\ \frac{\partial \Phi}{\partial t} \Big|_{z=0} + g\eta_0 &= 0 \\ \eta_0 &= \int_0^t \frac{\partial \Phi}{\partial z} \Big|_{z=0} dt \\ \frac{\partial \Phi}{\partial r} \Big|_{r=a} &= \dot{x}_k \cdot \sin \theta \\ \frac{\partial \Phi}{\partial \theta} \Big|_{\theta=\pm \frac{\pi}{2}} &= 0 \end{aligned} \right\} \quad (2)$$

The initial condition is

$$\Phi|_{t=0} = \dot{\Phi}|_{t=0} = 0 \quad (3)$$

Solving these equations, the following formulas can be derived.

The cyclic frequency of water sloshing in the tank is

$$\omega_L^{(n)} = \frac{g}{a} \sigma_n \tan k \left( \sigma_n \frac{h}{a} \right) \quad (4)$$

The control force of the water tank for the structure is

$$F_{TLB} = m_L [\ddot{X}_k(t) + \sum_{n=1,3,\dots}^{\infty} d_n F_n \ddot{W}_n(t)] \quad (5)$$

$W_n(t)$  in formula (5) can be treated as the generalized coordinates of water sloshing in the



tank. It satisfies the following equation:

$$\ddot{W}_n + 2\zeta_L^{(n)}\omega_L^{(n)}\dot{W}_n + (\omega_n^{(n)})^2W_n = -\ddot{X}_k(t) \quad (6)$$

If the water tank is installed on the  $k$ th floor of tall building, the controlled equation for structural wind vibration responses is

$$[M]\{\ddot{X}\} + [C]\{\dot{X}\} + [K]\{X\} = \{P(t)\} - \{H\}F_{TLD} \quad (7)$$

Applying the mode superposition method, Eq. (7) can be transformed as controlled equations of generalized coordinates  $q_i$ :

$$\begin{aligned} \ddot{q}_i + 2\zeta_i\omega_i q_i + \omega_i^2 q_i &= F_i^*(t) - \varphi_{i0} \frac{1}{m_i} F_{TLD} \\ (i = 1, 2, \dots, N) \end{aligned} \quad (8)$$

Combining Eq. (8) with Eq. (6) ( $n=1$ ), the equations of control for wind vibration responses of tall building are formed.

### 3. Test Analysis of Vibration Control of Cylindric Deep-water Tank

To understand the control effect of cylindric deep-water tank for structural wind vibration responses, a comparison test between installing and not installing the tank is done by a model of one-degree of freedom structure on vibration table. As the alongwind vibration of tall building is stochastic vibration caused by fluctuation wind and the acrosswind vibration is harmonic resonance responses mainly caused by the vortex cyclically shedding from wake in locked region, both artificial fluctuation wind excitation and harmonic excitation are inputted in the test to simulate the controlled structural vibration responses in alongwind and acrosswind direction.

For artificial fluctuation wind input, the test result is shown in Fig. 2. It can be seen that the coefficient of suppressing vibration of the water tank (in which the water mass is 1/100 of structural mass) in the stationary stage is 0.65. So, the cylindric deep-water tank is effective to reduce the alongwind fluctuation wind vibration responses of tall building.

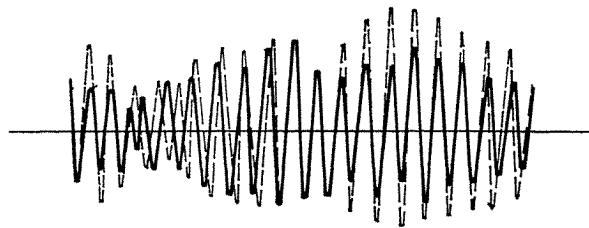


Fig. 2 test result of suppressing vibration

For harmonic input, the coefficient of suppressing vibration of the water tank is 0.6, this

indicate that the cylindrical deep-water tank is very effective to reduce the acrosswind harmonic resonance responses of tall building.

The test shows that the control of the cylindrical deep-water tank for alongwind and acrosswind vibration responses of tall building has following characteristics:

(1) The wave movement of the water surface in the water tank has the characteristic of standing wave.

(2) The control of the water tank can be made to be most effective by reasonably adjusting the damping of wave movement.

(3) When the frequency of water sloshing is near the natural frequency of structure, the control is most effective.

(4) In the case of same water mass, the less ratio of water depth  $h$  to radius  $a$ , the better effect of control is.

#### 4. Calculation Method of Control of Cylindrical Deep-water Tank for Fluctuation Wind Vibration Responses of Structure in Alongwind Direction

For fluctuation wind vibration responses of structure in alongwind direction,  $F_1^*(t)$  in Eq. (8) is generalized fluctuation wind load. Its power spectrum density function satisfies<sup>[1]</sup>:

$$S_{F_1^*}(\omega) = \frac{1}{(m_1^*)^2} \{\varphi\}_1^T [S_F] \{\varphi\}_1 S_f(\omega) \quad (9)$$

in which  $S_f(\omega)$  is the standardized Davenport spectrum density function. Therefore, from Eq. (8) and Eq. (6) ( $n=1$ ), the controlled vibration equations of structure in alongwind direction can be obtained as

$$\begin{aligned} \ddot{q}_i + 2\zeta_i \omega_i \dot{q}_i + \omega_i^2 q_i &= F_1^*(t) - \varphi_{ki} u_i \left( \sum_{j=1}^r \varphi_{kj} \ddot{q}_j + d_j F_1 \ddot{w}_j \right) \\ (i &= 1, \dots, r) \\ \ddot{w}_1 + 2\zeta_L \omega_L \dot{w}_1 + \omega_L^2 w_1 &= - \sum_{j=1}^r \varphi_{Lj} \ddot{q}_j \end{aligned} \quad (10)$$

Let  $\{Z\}^T = [q_1, \dots, q_r, w_1]$ , Eqs. (10) may be transformed as

$$[A]\{\ddot{z}\} + [B]\{\dot{z}\} + [C]\{z\} = \{F\} \quad (11)$$

According to definition of transfer function in the random vibration theory, the frequency response function matrix can be obtained as

$$[H(\omega)] = (-\omega^2[A] + j\omega[B] + [C])^{-1} \quad (12)$$

Therefore, the mean square errors of the controlled generalized responses of structure and the generalized response of the water sloshing in the tank are:

$$\left. \begin{aligned} \sigma_{qk}^2 &= \sum_{j=1}^r S_j \int_0^\infty |H_{qk_j}(\omega)|^2 S_f(\omega) d\omega \\ \sigma_{\dot{q}k}^2 &= \sum_{j=1}^r S_j \int_0^\infty \omega^4 |H_{qk_j}(\omega)|^2 S_f(\omega) d\omega \end{aligned} \right\} \quad (13)$$

and

$$\left. \begin{aligned} \sigma_{w_1}^2 &= \sum_{j=1}^r S_j \int_0^\infty |H_{w_1_j}(\omega)|^2 S_f(\omega) d\omega \\ \sigma_{\dot{w}_1}^2 &= \sum_{j=1}^r S_j \int_0^\infty \omega^2 |H_{w_1_j}(\omega)|^2 S_f(\omega) d\omega \end{aligned} \right\} \quad (14)$$

in which  $S_j = \frac{1}{(m_j^*)^2} \langle \varphi \rangle_j^T [S_p] \langle \varphi \rangle_j$ ,

Finally, the maximal responses of controlled structure can be obtained:

$$\left. \begin{aligned} (X_1)_{\max} &= \mu \cdot \sqrt{\sum_{k=1}^r \varphi_{1k}^2 \sigma_{qk}^2} \\ (\dot{X}_1)_{\max} &= \mu \cdot \sqrt{\sum_{k=1}^r \varphi_{1k}^2 \sigma_{\dot{q}k}^2} \end{aligned} \right\} \quad (15)$$

### 5. Calculation Method of Control of Cylindric Deep—Water Tank for Vortex—Induced Resonance Responses of Structure in Acrosswind Direction

The test shows that a locked region in acrosswind direction is produced above certain height of the tall building with circle shape section, at which the frequency  $\omega_s$  of wake-induced vortex shedding is equal to the natural frequency  $\omega_n$  of the structure, and a circular distribution force acts on the locked region. It will cause the vortex-induced resonance responses of the structure. In this case,  $\langle p(t) \rangle$  in acrosswind direction is the simple harmonic excitation with frequency  $\omega_1$ :

$$\langle p(t) \rangle = \langle p \rangle \sin \omega_1 t \quad (16)$$

In which the element of  $\langle p \rangle$  is expressed as follows when the location of disturbing forces is in the locked region. Conversely, it is 0 when the location of disturbing forces is out of the locked region.

$$p_j = \mu_s \cdot \mu_x(z_r) \cdot \mu_r \cdot \mu_L \cdot w_o \cdot \Delta A, \quad (17)$$

Therefore, the controlled wind vibration responses equation of the structure in acrosswind direction can be derived from Eqs. (8) and Eqs. (6)

$$\left. \begin{aligned} \ddot{q}_1 + 2\xi_1 \omega_1 \dot{q}_1 + \omega_1^2 q_1 &= F_1^* \sin \omega_1 t - \Phi_{k1} \mu_{L1} (\Phi_{k1} \ddot{q}_1 + d_1 F_1 \ddot{w}_1) \\ \ddot{w}_1 + 2\xi_L \omega_L \dot{w}_1 + \omega_L^2 w_1 &= -\Phi_{k1} \ddot{q}_1 \end{aligned} \right\} \quad (18)$$

Letting  $\{Y\}^T = [q_1, w_1]$ , Eqs. (18) can be added up as

$$[\bar{A}]\{\bar{Y}\} + [\bar{B}]\{\bar{Y}\} + [\bar{D}][\bar{Y}] = \{\bar{F}\}\sin\omega_1 t \quad (19)$$

The steady-state resonance response of above equation can be assumed as

$$\left. \begin{aligned} q_1 &= \bar{q}_1 \sin(\omega_1 t - \psi) \\ w_1 &= \bar{w}_1 \sin(\omega_1 t - \psi) \end{aligned} \right\} \quad (20)$$

Substituting Eq. (20) into Eq. (19), the elements of  $\{Y\}$  can be solved

$$\left. \begin{aligned} q_1 &= \bar{q}_{11} \sin(\omega_1 t - \psi_1) + \bar{q}_{12} \sin(\omega_1 t - \psi_2) \\ w_1 &= \bar{w}_{11} \sin(\omega_1 t - \psi_1) + \bar{w}_{12} \sin(\omega_1 t - \psi_2) \end{aligned} \right\} \quad (21)$$

So the vortex-induced resonance responses of the structure controlled by cylindrical deep-water tank are

$$\left. \begin{aligned} \{X\} &= \{\Phi\}_1 q_1 \\ \{\dot{X}\} &= -\omega_1^2 \{\Phi\}_1 q_1 \end{aligned} \right\} \quad (22)$$

## 6. Calculation Analysis of Practical Engineering Example

To understand the control effect of the water tank for wind vibration responses of tall building, the controlled wind vibration responses of Xiamen Jiuzhou Mansion are calculated by the computer program TLD3 which is edited based on the method provided in the paper.

Xiamen Jiuzhou Mansion is a steel frame structure with 28 stories. Its fundamental period is 2.984s. Thereby it is a relatively flexible and less damping structure. Since the wind load in that region is greater ( $w_0 = 0.75 \text{kn/m}^2$ ), the maximal fluctuation wind vibration acceleration at 25th storey of highest offices is  $0.61 \text{m/s}^2$ , which is greater than the critical value  $0.5 \text{m/s}^2$  of comfort degree for man. Thereby it must be controlled. Since the cylindrical water tank for living and fire-fighting are already designed at 28th storey of the structure, the size of the tank only need to be changed to radius 4.3m and height 2.6m (water depth is 1.29m, water mass is 1/300 of structural mass). The calculation result shows that the maximal acceleration at 25th storey under limit wind load is decreased to  $0.432 \text{m/s}^2$ , which satisfies the design requirement of comfort degree. As its coefficient of suppressing vibration is 0.71, the effect of suppressing vibration is very obvious. Thereby, the cylindrical deep-water tank is a kind of economical and effective device of suppressing wind vibration responses of tall buildings.

## References:

1. Qu Weilian, Control Design for Wind Vibration Responses of Highrise Structure and Tall Building, Publishing House of Wuhan Science Technical University of Survey and Drawing, (1991)
2. R. D. Blevins, Flow-Induced Vibration, Van Nostrand Reinhold Company, (1977)

## Wind Tunnel Investigation Of Active Vibration Control Of Tall Buildings

R.J.Facioni <sup>+</sup>, K.C.S.Kwok <sup>+</sup> and B.Samali <sup>++</sup>

<sup>+</sup> School of Civil & Mining Engineering  
The University of Sydney, N.S.W. 2006

<sup>++</sup> School of Civil Engineering  
University of Technology, Sydney, N.S.W. 2007

**Abstract:** *An Active Tuned Mass Damper (ATMD) installed in the top of a rectangular model building was tested in a wind tunnel for its effectiveness in suppressing cross-wind building vibrations. The ATMD was controlled using a sub-optimal control algorithm. Certain parameters critical to the operation of the ATMD were varied to observe how the ATMD's effectiveness would be altered. The ATMD was found to be effective in reducing cross-wind vibrations. The variation in design parameters of the ATMD resulted in different levels of reduction.*

### 1. INTRODUCTION

There have been numerous investigations, both analytical and experimental, into the area of passive vibration control of tall buildings. Passive vibration control devices such as Tuned Mass Dampers (TMD) have proven to be effective for certain applications but they are limited in the magnitude of motion reduction they can achieve. These limitations have led to the development of active control devices. These devices use a control algorithm which analyses the dynamic structural feedback to create a control force which drives a mass. The theory for active control has been extensively investigated for the past two decades and it has been found to be a superior method of vibration control. Experimental studies have been carried out to support these findings, but most have involved a shaking table to simulate earthquake loadings. To date there has been only one documented wind tunnel investigation (Soong and Skinner (1)) into the effectiveness of an active control system in suppressing wind induced vibrations. The lack of wind tunnel experiments to support the theoretical studies has arisen due to the complexities involved in developing an active control device which can be installed in a model building.

This paper describes the development of a scaled ATMD which is small enough to fit into a 1:100 scale model building without losing any of the integrity associated with active vibration control. The paper also reports on experiments conducted in a wind tunnel on the model building with the ATMD installed. The effect of changing certain parameters is also investigated. The effectiveness of the ATMD in suppressing wind induced vibration is discussed.

### 2. ACTIVE TUNED MASS DAMPER DEVELOPMENT

The initial intention was to develop an active control device which would be capable of operating in both an active and passive mode. This was required to

facilitate a direct comparison between active and passive vibration control. This concept required that the device be designed so that its parameters, such as mass, damping and frequency, could not only be measured but also modified for further research. To keep the design simple the ATMD model is only a one degree of freedom system.

Several attempts were made in developing an ATMD which was suitable for testing. Initially a 1:400 scale model was chosen for testing which proved to be a major problem for several reasons. The modelling requirements for 1:400 scale wind tunnel tests meant that the building chosen had dimensions of 0.45 x 0.115 x 0.075 with a natural frequency of approximately 7Hz and the damper mass could be no more than 10g. The high frequency of vibration and confined space, restricted the selection of possible actuators. It was found that only solenoids could be small in size and still operate at high speeds. High friction between the iron core of the solenoid and the plastic casing resulted in damping values in excess of what could be accepted. The restriction in the mass of the damper meant the iron core had to act as the damper mass itself. The light mass also resulted in a high natural frequency for the device in its passive mode. Attempts at creating a test model at this scale had to be aborted.

The decision was then made to move onto a scale of 1:100 for testing. Using the experience gained from the 1:400 attempts, the model building was designed to have a large working area and a low natural frequency. The larger scale also meant that a larger damper mass could be used. The new scale widened the range of actuators which could be chosen. Servo motors and stepper motors were both considered, but stepper motors were chosen because of their positional accuracy. A problem encountered with the stepper motors was that the torque of the motor dropped off as the speed of the motor increased. This problem was overcome by selecting the largest motor which could fit in the available space.

Many devices were developed at the larger scale, but problems were encountered in each attempt. High friction, high natural frequency and an effective driving method all linked to each other in some way. Overcoming one problem created another but eventually all the problems were conquered and a suitable system was developed.

All design criteria of the initial concept were satisfied in the final design which is illustrated in Fig.1. This was achieved by having an adjustable mass, with four roller bearings to guide the direction, suspended by four chains. Springs were attached to the ends of the mass via hooks and a paddle extending from the base of the mass to an oil container provided the damping. A shaft, with pivots at both ends, connecting one end of the mass to a lever arm on the stepper motor, was used to provide the drive force.

### **3. CONTROL THEORY**

The building model with the ATMD installed is a two degree of freedom system as shown in Fig.2 and the equations of motion for the system are;

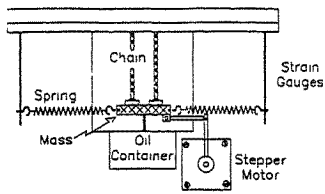


Fig.1. EXPERIMENTAL ATMD

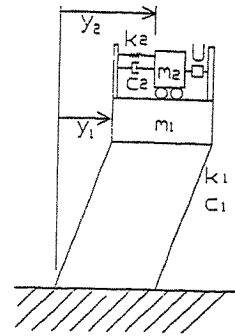


Fig.2. ANALYTICAL MODEL

PASSIVE MODE :

$$m_1 \ddot{y}_1 + c_1 \dot{y}_1 + k_1 y_1 - (\dot{y}_2 - \dot{y}_1) c_2 - (y_2 - y_1) k_2 = 0 \quad (1)$$

$$m_2 \ddot{y}_2 + (\dot{y}_2 - \dot{y}_1) c_2 + (y_2 - y_1) k_2 = 0 \quad (2)$$

ACTIVE MODE:

$$m_1 \ddot{y}_1 + c_1 \dot{y}_1 + k_1 y_1 - (\dot{y}_2 - \dot{y}_1) c_2 - (y_2 - y_1) k_2 + U = 0 \quad (3)$$

$$m_2 \ddot{y}_2 + (\dot{y}_2 - \dot{y}_1) c_2 + (y_2 - y_1) k_2 - U = 0 \quad (4)$$

where  $y_1$ ,  $m_1$ ,  $c_1$  and  $k_1$  are the top floor displacement, first mode generalised mass, damping constant and stiffness of the building model, respectively;  $y_2$ ,  $m_2$ ,  $c_2$  and  $k_2$  are the displacement, mass, damping and stiffness of the ATMD.  $U$  is the control force used when the ATMD is in active mode. A sub-optimal control algorithm which uses displacement feedback and drives the ATMD proportionally to the top floor displacement of the building is used to generate the control forces required to drive the mass. An equation to express the principle is;

$$U = y_1 k_2 R_F + \dot{y}_1 c_2 R_F \quad (5)$$

where  $R_F$  is the ratio of the mass displacement to the building displacement, and is set at 2.5 for the experiments described in this paper.

#### 4. EXPERIMENTAL PROGRAM

##### 4.1 Experimental Set-up

The ATMD was installed in the model building and tested in the No.1 Boundary Layer Wind Tunnel at the School of Civil and Mining Engineering, the University of Sydney. The wind tunnel used is of the open circuit type with a 2.4m x 1.8m working section. A Terrain Category 3 wind profile in accordance with AS1170.2-1989 (2) was generated by a combination of spires and roughness blocks. The model building used in the experimental program was a 1:100 scaled model with physical properties as listed in Table 1. The model was mounted on a single degree of freedom translational aeroelastic testing rig with strain gauges mounted to monitor the models dynamic behaviour. The system was designed so that the model would vibrate only in one translational mode with a constant mode shape. Fig.3 shows the experimental set-up.

Dimensions	0.2 x 0.3 x 1.1 (m)
Density ( $\rho_s$ )	228 (kg/m <sup>3</sup> )
Mass (M)	15.05 (kg)
Generalised Mass ( $m_1$ )	5.02 (kg)
Natural Frequency ( $f_n$ )	2.9 (Hz)
Structural Damping ( $\xi$ )	1.05% of critical
Generalised Stiffness ( $k_1$ )	1.67 KN/m

TABLE1. PROPERTIES OF MODEL BUILDING

### 4.2 Control System

Fig.4 is a schematic diagram of the control system used for the experiments. Strain gauges mounted at the base of the building have been calibrated to monitor the top floor displacement of the model. The displacement signal was then amplified and filtered. The signal was then passed through an analogue to digital (A/D) converter, and relayed to a 486 personal computer, where the control algorithm was executed. The control signal was subsequently transmitted via a digital to analogue (D/A) converter to the stepper motor controller, which in turn sends a signal to the stepper motor. A sampling rate of 300Hz was used for all experiments.

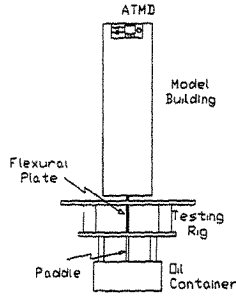


Fig.3. EXPERIMENTAL SET-UP

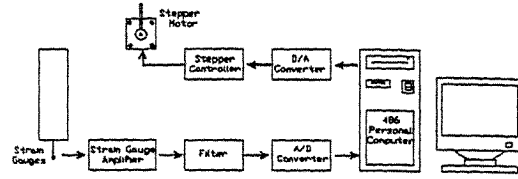


Fig. 4. CONTROL SYSTEM

### 4.3 Experimental Investigation

The normalised standard deviation cross-wind displacement at the top of the building model with and without the ATMD installed was measured at different reduced wind velocities. The ATMD was tested for five cases of varying parameters. The parameters varied were mass, damping and stiffness. The values used for each parameter were generalised mass ratio of 1.59% or 2.59%, damping of 6% or 18% of critical and stiffness ratio of 0.02 or 0.03. Table 2 lists the physical properties of the ATMD for each case tested. Table 3 lists the parameter changes pertinent to different ATMD's. A comprehensive parametric investigation will be carried out in future studies.

ATMD Type	ATMD 1	ATMD 2	ATMD 3	ATMD 4	ATMD 5
Mass ( $m_2$ )	0.08 kg	0.08 kg	0.13 kg	0.13 kg	0.08 kg
Frequency ( $f_2$ )	3.8 Hz	2.98 Hz	3.3 Hz	2.65 Hz	2.9 Hz
Damping ( $\zeta_2$ )	6%	6.8%	5.9%	6%	18%
Stiffness ( $k_2$ )	55.6 N/m	34.5 N/m	50.0 N/m	31.3 N/m	34.5 N/m
Mass Ratio ( $m_2/M$ )	0.53%	0.53%	0.86%	0.86%	0.53%
Generalised Mass Ratio ( $m_2/m_1$ )	1.59%	1.59%	2.59%	2.59%	1.59%
Stiffness Ratio ( $k_2/k_1$ )	0.03	0.02	0.03	0.02	0.02

TABLE2. PROPERTIES OF ATMD'S

ATMD'S	PARAMETER CHANGE
ATMD1-ATMD2	Decrease Stiffness Ratio 0.03 to 0.02.
ATMD1-ATMD3	Increase Generalised Mass 1.59% to 2.59%.
ATMD2-ATMD5	Increase Damping 6.8% to 18%.
ATMD2-ATMD4	Increase Generalised Mass 1.59% to 2.59%.
ATMD3-ATMD4	Decrease Stiffness Ratio 0.03 to 0.02.

TABLE3. ATMD COMPARISON



## 5. EXPERIMENTAL RESULTS

The normalised standard deviation cross-wind responses  $\sigma_y/b$  and  $\sigma_{y_{a3}}/\sigma_y$  are presented in Table 4 for the ATMD's in their active mode. Figure 5 is a plot of the normalised standard deviation cross-wind responses  $\sigma_y/b$  and  $\sigma_{y_{a3}}/b$  verses reduced velocity.  $\sigma_y$  represents the standard deviation cross-wind top floor displacement response of the structure,  $\sigma_{y_{a3}}$  represents the standard deviation cross-wind top floor displacement response of the structure with ATMD\* installed in it's active mode. The \* subscript represents the ATMD case number and b is the width of the structure normal to the wind.

Device Installed	Response	Reduced Velocity 4	Reduced Velocity 6	Reduced Velocity 8
None	$\sigma_y/b$	0.00150	0.00472	0.01395
ATMD1	$\sigma_{y_{a1}}/b$	0.00123	0.00334	0.00922
	$\sigma_{y_{a1}}/\sigma_y$	0.82	0.71	0.66
ATMD2	$\sigma_{y_{a2}}/b$	0.00125	0.00342	0.00962
	$\sigma_{y_{a2}}/\sigma_y$	0.83	0.72	0.69
ATMD3	$\sigma_{y_{a3}}/b$	0.00115	0.00307	0.00763
	$\sigma_{y_{a3}}/\sigma_y$	0.77	0.65	0.55
ATMD4	$\sigma_{y_{a4}}/b$	0.00117	0.00318	0.00828
	$\sigma_{y_{a4}}/\sigma_y$	0.78	0.67	0.59
ATMD5	$\sigma_{y_{a5}}/b$	0.00122	0.00329	0.00875
	$\sigma_{y_{a5}}/\sigma_y$	0.81	0.70	0.63

TABLE4. RMS CROSS-WIND RESPONSE ACTIVE MODE

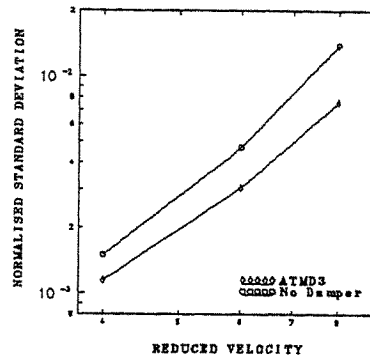


FIG.5. RMS RESPONSE

It can be seen from the results in Table 4 that the 1:100 scale active control device developed for wind tunnel testing is effective in reducing building vibrations. The control performance of the system is seen to be good for all the configurations tested. The performance is seen to improve with increasing reduced velocity, which is clearly seen in Fig.5. This is due to the fact that at low reduced velocities the building model vibrates with a broad range of frequencies, whereas at reduced velocity 8 the vibration tends to be around the natural frequency of the building. The nature of the ATMD developed is such that it operates more effectively when it is being driven in a regular manner, such as a sine wave, than a more random type vibration. A random vibration requires quicker operations from the stepper motor which are beyond the motors capabilities.

Looking at each reduced velocity individually, all the ATMD's can be seen to have reduction performance within a narrow range. This is due to the  $R_F$  ratio being set at 2.5, ensuring each ATMD case had a mass/building displacement ratio close to 2.5 as shown in Table5.  $\sigma_{ma}$  is the standard deviation mass displacement for the ATMD. Any difference in reduction performance was a direct result of the parameter configuration.

Device ATMD*	Active Mode $\sigma_{ma}/\sigma_{y_{a*}}$
ATMD1	2.45
ATMD2	2.52
ATMD3	2.38
ATMD4	2.57
ATMD5	2.48

TABLE5. MASS/BUILDING DISPLACEMENT RATIO

Looking at each ATMD independently and comparing it's active control performance, it can be seen how different parameters affect the system. The

parameters chosen for ATMD1 show a maximum active vibration control reduction of 34% for reduced velocity 8. For other velocities the system is still seen to be effective.

ATMD2 has the same parameters as ATMD1 except the stiffness has been lowered. The control performance of the system reduces the vibrational response of the building by 31% at reduced velocity 8. This is slightly lower than the reduction experienced for ATMD1. This trend is seen for all the reduced velocities tested. The effect of lowering the stiffness of the ATMD is a loss in its active vibration control performance.

The parameters of ATMD3 are the same as those for ATMD1 except the mass has been increased. With an increase in mass a noticeable increase in the control performance of the system was observed for all reduced velocities investigated. At reduced velocity 8 a reduction of 45% is achieved with active vibration control.

ATMD4 has the same parameters as ATMD2 and ATMD3 except for higher mass and lower stiffness, respectively. Comparing this system with ATMD3 which has higher stiffness, a loss of effectiveness is observed because of lowering the stiffness. Comparing this system with ATMD2, the increase in mass results in a more effective system. Both of these observations, support the previous findings.

ATMD5 is the same as ATMD2 but with an increased damping. The control performance of the system is a 37% reduction in vibrations at reduced velocity 8. The higher damping is seen to increase the active control performance for all the velocities tested.

It must be emphasised that for all ATMD's a better response reduction could be achieved if a larger  $R_f$  value is used. The performance of the control system can be further enhanced by adopting an optimal control algorithm rather than the sub-optimal one used here for these experiments. This will be investigated in further research.

## 7. CONCLUSION

An ATMD has been developed and successfully tested in a wind tunnel with significant reductions in building vibrations. The main conclusions from this investigation are:

1. Active vibration control can effectively be tested at a small scale in a wind tunnel while still maintaining its integrity.
2. Wind tunnel investigations offer a quick and much needed method of confirming the results of the theoretical studies conducted.
3. For an ATMD the active vibration control performance of the system can be seen to improve by simply modifying some parameters. Increasing parameters such as stiffness, mass and damping, increase the vibration control performance.

## References:

1. Soong, T.T and Skinner, G.T (1981). Experimental study of active structural control, *J. Eng. Mech., ASCE*, Vol. 107, No. EM6, Dec., pp.1057-1068.
2. AS1170.2 - 1989, Wind Loads. Standards Association of Australia.

**On control of along-wind and across-wind vibrations of structure  
by crossed dampers**

X.T. Zhang and R.C. Zhang\*

Department of Engineering Mechanics  
Tongji University, Shanghai, China

\*Department of Civil Engineering and Operations Research  
Princeton University, Princeton, New Jersey, USA

**Abstract:** Crossed tuned mass damper (TMD) and crossed tuned liquid damper (TLD) with tube-like container are proposed to be installed structures so that both along-wind and across-wind vibrations of structures may be suppressed. Dynamic response properties of the nonlinear structures are analyzed using a new version of linearization technique, which is, proposed by authors, based on energy equivalent criterion. Numerical example is carried out for illustration.

**1. Introduction**

The along-wind and across-wind structural vibrations may be excited to the wind loading at an arbitrary direction. It is noted that the across-wind vibration may also be triggered simultaneously as the along-wind vibration to the wind loading even at one principal axis. When the circular frequency of vortex shedding  $\omega_v$  is equal to natural circular frequency of structure  $\omega_n$  in the transcritical region (In general,  $Re > 3.5 \times 10^6$ ), the across-wind resonance occurs and the structural vibration may be amplified greatly and gone so far as to be collapsed. The requirement of human comfort has also a restriction to the large structural vibration. Therefore, it is important to control the structural vibration induced by wind loading. Among many structural control equipments, tuned mass damper (TMD) and tuned liquid damper (TLD) are often used. However, they are usually restricted in one direction.

In this paper, crossed TMD and/or TLD with tube-like container are proposed to be installed in the structures so that the structural vibration to the wind loading at an arbitrary direction may be efficiently suppressed. The liquid motion of crossed TLD is nonlinear, which is due to the orifices installed inside the tube-like container. The along-wind vibration is nonlinear and random due to random fluctuating wind while the across-wind vibration at resonance is nonlinear and determinate due to characteristics of period vortex shedding. To solve such nonlinear problems, equivalent linearization approach is used. In this paper, a new version, which is based on energy criterion, is applied in place of conventional method, which is based on governing equation. It has been verified [1-4] that new method provides much closer results for the response characteristics to the exact solution than the conventional one when the exact solution is available.

With the use of new approach, equivalent damping ratios for

crossed TLD are derived. The responses of both structure and damper are then obtained. The reduced vibration coefficients are also given for two kinds of vibrations. Finally an example is carried out for illustration.

## 2. Structural Vibration Under Control

Consider an  $n$ -storey structure subjected to wind loading at an principal axis. Crossed TMD or TLD with a tube like container, shown in Figs. 1 and 2 respectively, are assumed to be installed in the  $i$ -th floor, in which  $i$  may be  $1, 2, \dots, n$  but may not be all.

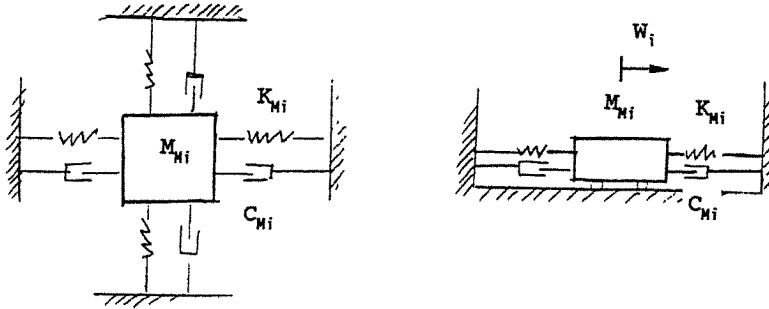


Fig. 1 Crossed TMD

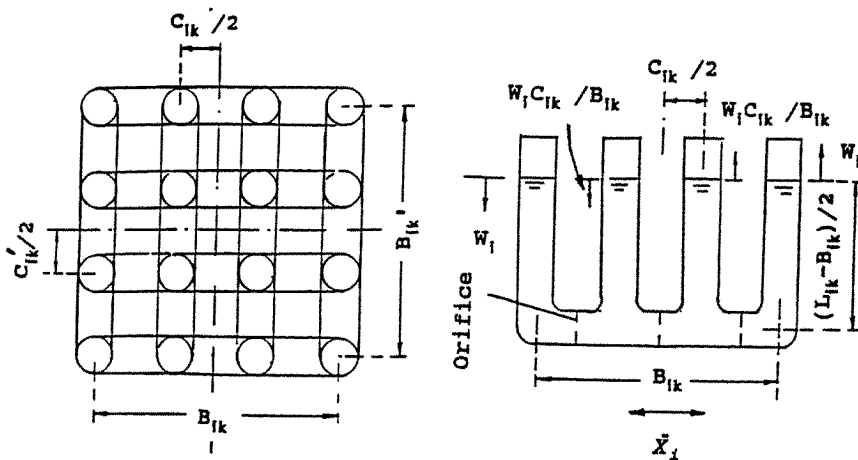


Fig. 2 Crossed TLD

The governing equations of motion for both the n-storey structure and the dampers are thus written in the following form, respectively,

$$[M]\ddot{X} + [C]\dot{X} + [K]X = P(t) - [M_{D1}]\ddot{W} - [M_{D2}]\dot{X} \quad (1)$$

$$[M_{D1}]\ddot{W} + F_D + [K_D]W = -[M_{D2}]\dot{X} \quad (2)$$

where matrices  $[M]$ ,  $[C]$  and  $[K]$  are respectively the  $n \times n$  matrices of mass, damping and stiffness of the n-storey structure;  $X$ ,  $P$  and  $W$  denote respectively the vectors of structural displacement, excitation and damper deviation along an axis direction which is either parallel or perpendicular to wind direction;  $F_D$  is the damping force vector,  $[M_{D1}]$ ,  $[M_{D2}]$ , and  $[K_D]$  are diagonal matrices, and their  $i$ -th element and  $i$ -th diagonal elements are respectively

$$M_{D1i} = \begin{cases} M_{Mi} & (TMD) \\ m_{Li}L_i & (TLD) \end{cases}, \quad M_{D2i} = \begin{cases} M_{Mi} & (TMD) \\ m_{Li}B_i & (TLD) \end{cases} \quad (3)$$

$$F_{D2i} = \begin{cases} C_{Mi}\dot{W} & (TMD) \\ \frac{1}{2}m_{Li}\zeta_{Li}|\dot{W}|\dot{W} & (TLD) \end{cases}, \quad K_{Di} = \begin{cases} K_{Mi} & (TMD) \\ 2m_{Li}g & (TLD) \end{cases} \quad (4)$$

in which  $M_{Mi}$ ,  $C_{Mi}$  and  $K_{Mi}$  are the tuned mass, damping coefficient and stiffness for the crossed TMD,  $m_{Li}$  is the mass per unit length of the liquid in the container,  $\zeta_{Li}$  is the coefficient of head loss, determined based on the ratio of areas of the opening orifice and the tube cross-section, the liquid length  $L_i$  and width  $B_i$  are

$$L_i = \sum_{k=1}^{S_i} L_{ik} + \sum_{k=1}^{S'_i} L'_{ik} \frac{C_{ik}}{B_{ik}}, \quad B_i = \sum_{k=1}^{S_i} B_{ik} + \sum_{k=1}^{S'_i} B'_{ik} \quad (5)$$

where  $S_i$  and  $S'_i$  denote the numbers of containers in the  $x$  and  $y$  directions, respectively.

Using equivalent linearization technique, equation (2) can be written as

$$[M_{D1}]\ddot{W} + [C_D]\dot{W} + [K_D]W = -[M_{D2}]\dot{X} \quad (6)$$

in which equivalent damping coefficient matrix  $[C_D]$  can be obtained using equivalent linearization technique, which will be shown in the next section.

Equations (1) and (6) may be solved by applying modal analysis approach. Introduce the following transformation

$$X = [\Phi]q \quad (7)$$

where  $q$  is the generalized coordinate vectors for the structure,  $[\Phi]$  is the vibration mode matrix. It has been shown [5] that the displacement responses of the structure subjected to the wind loading is primarily contributed by its first vibration mode. Therefore, equation (7) may be approximated to

$$X = \phi_1^T q \quad (8)$$

or

$$X_j(t) = \phi_{j1} q_1(t), \quad j = 1, 2, \dots, n \quad (9)$$

Similar to the form of equation (9), the damper motion  $W$  may also

be decomposed by

$$\dot{W}_i(t) = \dot{\phi}_{i1} q_{Di}(t) \quad , \quad i=1, 2, \dots, n \quad (10)$$

which is nothing but for ease in solving the problem at hand. Substituting equations (9) and (10) into equations (1) and (6), we obtain

$$\ddot{q}_1 + 2\zeta_1 \omega_1 \dot{q}_1 + \omega_1^2 q_1 = F_1^*(t) - \frac{\sum_{i=1}^n \dot{\phi}_{i1}^2 (M_{D1i} \ddot{q}_{Di} + M_{D2i} \dot{q}_{Di})}{M_1^*} \quad (11)$$

$$\ddot{q}_{Di} + 2\zeta_{Dei} \omega_{Di} \dot{q}_{Di} + \omega_{Di}^2 q_{Di} = -\frac{M_{D2i}}{M_{D1i}} \dot{q}_1 \quad , \quad i=1, 2, \dots, n \quad (12)$$

where the equivalent damping ratio  $\zeta_{Dei}$  can be obtained as shown in the next section and

$$\omega_{Di}^2 = \begin{cases} K_{Mi}/M_{Mi} & (TMD) \\ 2g/L_i & (TLD) \end{cases} \quad (13)$$

$$M_1^* = \{\phi_1\}^T [M] \{\phi_1\} \quad , \quad F_1^*(t) = \{\phi_1\}^T \{p(t)\}/M_1^* \quad (14)$$

For along-wind excitation, the structural vibration is random and  $F_1^*$  may be obtained according to fluctuating wind excitation [5]. The mean square of the displacement responses can then be expressed by

$$\sigma_{x_j}^2 = \phi_{j1}^2 \int_{-\infty}^{\infty} |H_{q_1}(\omega)|^2 S_p(\omega) d\omega \quad , \quad j=1, 2, \dots, n \quad (15)$$

$$\sigma_{\dot{w}_i}^2 = \phi_{i1}^2 \int_{-\infty}^{\infty} \omega^2 |H_{q_{Di}}(\omega)|^2 S_p(\omega) d\omega \quad (16)$$

where  $S_p(\omega)$  is the power spectral density function and

$$|H_{q_1}(\omega)|^2 = \frac{1}{D} \{ [\sum_i (\mu_{\omega_i}^2 - i \mu_{\omega'}^2)]^2 + [\sum_i 2\zeta_{Dei} \mu_{\omega_i} \mu_{\omega'}^2] \} \quad (17)$$

in which

$$D = \omega_1^4 \{ [\sum_i [i \mu_{\omega}^{\prime 4} + (i \sum_{i'} \mu_{mi'}) - \mu_{mi} - \sum_{i' \neq i} \mu_{mi} \mu_{Aii'}] \mu_{\omega}^{\prime 4} - (1 + \sum_{i'} \mu_{mi'}) \mu_{\omega_i}^2 + 4\zeta_1 \zeta_{Dei} \mu_{\omega_i} + i] (\mu_{\omega}^{\prime 2} + \mu_{\omega_i}^2) \}^2 + \omega_1 \{ [\sum_i [-\sum_{i' \neq i} \mu_{mi} \mu_{Bii'} \mu_{\omega'}^4 - 2(1 + \sum_{i'} \mu_{mi'}) \zeta_{Lei} \mu_{\omega_i} + i \zeta_i] \mu_{\omega}^{\prime 3} + 2(\zeta_1 \mu_{\omega_i}^2 + \zeta_{Dei} \mu_{\omega_i}) \mu_{\omega'}^2] \}^2 \quad (18)$$

$$\mu_{\omega_i} = \omega_{Di}/\omega_1 \quad , \quad \mu_{\omega'} = \omega/\omega_1 \quad , \quad \mu_{mi} = m_{D2i} \phi_{i1}^2 / M_1^* \quad , \quad \mu_{di} = B_i / L_i \quad (19)$$

$$\mu_{Aii'} = \frac{(\mu_{\omega_i}^2 - \mu_{\omega'}^2) (\mu_{\omega_i'}^2 - \mu_{\omega'}^2) + (2\zeta_{Di} \mu_{\omega_i} \mu_{\omega'}^2) (2\zeta_{Di'} \mu_{\omega_i'} \mu_{\omega'}^2)}{(\mu_{\omega_i}^2 - \mu_{\omega'}^2)^2 + (2\zeta_{Di} \mu_{\omega_i} \mu_{\omega'}^2)^2} \quad (20)$$

$$\mu_{Bii'} = \frac{(\mu_{\omega_i}^2 - \mu_{\omega'}^2) (2\zeta_{Di} \mu_{\omega_i} \mu_{\omega'}^2) - (\mu_{\omega_i'}^2 - \mu_{\omega'}^2) (2\zeta_{Di'} \mu_{\omega_i'} \mu_{\omega'}^2)}{(\mu_{\omega_i}^2 - \mu_{\omega'}^2)^2 + (2\zeta_{Di} \mu_{\omega_i} \mu_{\omega'}^2)^2} \quad (21)$$

For across-wind excitation, the resonance response, which is related to the region of  $Re > 3.5 \times 10^6$  and  $\omega_v = \omega_1$  (i.e.  $\mu_{\omega} = 1$ ), should be considered in design. The structural vibration in this region is determinate and the periodic  $F_1^*$  may be obtained according to wind-induced across-excitation [5]. The maximum displacement responses can then be expressed by

$$|H_{q1}(\omega)| = \sqrt{\frac{[\sum_i (\mu_{\omega i}^2 - i)]^2 + [\sum_i 2\zeta_{Dei} \mu_{\omega i}]^2}{D}} \quad (22)$$

### 3. Equivalent Damping Ratio

For along-wind nonlinear random vibration of structure with crossed TLD, the equivalent damping ratio is obtained using stochastic linearization technique, which is based on the following energy criterion, i.e. the difference of the generalized energies per unit time between original and equivalent systems be minimum,

$$E \left\{ [V(W_i, \dot{W}_i) - \frac{1}{2} C_{Lei} \dot{W}_i^2]^2 \right\} = \text{minimum} \quad (23)$$

where  $V$  is the energy of the original system,  $C_{Lei}$  is the equivalent damping coefficient. Equation (23) yields

$$C_{Lei} = \frac{2E[\dot{W}^2 V(W_i, \dot{W}_i)]}{E[\dot{W}^4]} \quad (24)$$

With the use of equation (4) the equivalent damping ratio may then be obtained

$$\zeta_{Lei} = \frac{4\zeta_{Li}\sigma_{\dot{W}_i}}{9\sqrt{\pi g L_i}} \quad (25)$$

For across-wind nonlinear determinate vibration of structure with crossed TLD, the energy criterion is that the difference of the generalized energies per unit time between original and equivalent systems be zero, i.e.

$$V(W_i, \dot{W}_i) = \frac{1}{2} C_{Lei} \dot{W}_i^2 \quad (26)$$

which results in

$$\zeta_{Lei} = \frac{\zeta_{Li} \dot{W}_i}{6\sqrt{g L_i}} \quad (27)$$

### 4. Reduced Vibration Coefficient

Reduced vibration coefficient  $\mu_r$  is defined as the ratio of the responses obtained with and without crossed TMD or TLD. For along-wind random vibration of structure,

$$\mu_r = \frac{\sigma_x}{\sigma_{x0}} = \frac{\sqrt{\int_{-\infty}^{\infty} |H_{q1}(\omega)|^2 S_F(\omega) d\omega}}{\sqrt{\int_{-\infty}^{\infty} |H_{q1}(\omega)|_0^2 S_F(\omega) d\omega}} \quad (28)$$

where  $\sigma_x$  and  $\sigma_{x0}$  denote the standard deviation of response with and

without crossed TMD or TLD and  $|H_{q2}(\omega)|^2$  is obtained as (17). For across-wind determinate vibration of structure in transcritical region

$$\mu_r = \frac{x}{x_0} = \frac{|H_{q1}(\omega)|}{|H_{q1}(\omega)|_0} \quad (29)$$

### 5. Simple Example

Consider a reinforced concrete tower structure. Only one damper is installed on  $i$ -th floor. Let  $\phi_{i1}=0.4$ ,  $\mu_{q1}=1$ ,  $M_1^*=1500$  t,  $M_{p2}=156.25$  t,  $\zeta_1=0.05$ ,  $\zeta_{pe}=0.1$ . The reduced vibration coefficient for across-wind vortex-shedding resonance response ( $\mu_u=1$ )  $\mu_r$  can be found as 0.54526, which indicates the across displacement response is approximately 50 percent reduced.

### 6. CONCLUDING REMARKS

Crossed TMD or TLD is proposed to be installed in the structures so that the structural vibration along arbitrary direction can be suppressed. Along-wind and across-wind formulae of reduced vibration coefficients have been derived. Equivalent damping ratio for nonlinear damping forces have also been obtained based on generalized energy criterion. All formulae presented are suitable to any kinds and any numbers of dampers.

### References

1. X.T. Zhang, Proceedings of International Conference on Applied Mechanics, Beijing, 1(1989) 236.
2. X.T. Zhang, I. Elishakoff and R.C. Zhang, Stochastic Structural Dynamics, Springer-Verlag, 1(1991) 327.
3. X.T. Zhang and R.C. Zhang, ASME-AMD 151, ASME-PVP 247 (1992) 211.
4. X.T. Zhang, R.C. Zhang and Y.L. Xu, J. Wind Engineering and Industrial Aerodynamics, (1993) (to appear).
5. X.T. Zhang, Theory of Wind-Loading of Structure and Applied Handbook, TJ Press, (in Chinese).



## Control for Turbulence Wind Vibration Responses of Nanjing TV Tower by Semi-Active TMD

W. L. QU and W. R. Cheng<sup>+</sup>

Department of Building Engineering  
Wuhan University of Technology, Wuhan, China

<sup>+</sup>Department of Civil Engineering  
Southeast University, Nanjing, China

**Abstract:** In the paper, the basic principle and the calculating method of semi-active control for fluctuation wind vibration responses of Nanjing TV tower by the hanging TMD are presented. And the effect of control for Nanjing TV tower is analyzed.

### 1. Introduction

Nanjing TV tower is built up at the west of Nanjing city. It is a highrise structure with 310.10m height. As the space cabin installed at the level of 240m is sightseeing, its wind vibration acceleration must satisfy the design requirement for degree of comfort. Considering that the requirement that sightseer on the space cabin is comfortable under 8 scale wind can not be satisfied (fluctuation wind vibration acceleration of the space cabin reaches  $0.29\text{m}/\text{sec}^2$ , which exceeds the limit value of  $0.15\text{m}/\text{sec}^2$ ), the control for fluctuation wind vibration responses of Nanjing TV tower is necessary.

According to the structural control plan of Nanjing TV tower under wind excitation, a set of the semi-active TMD system is installed in the reversed cone shell of the space cabin, and hanged on the floor of sightseeing room. The spring-dampers and adjustable dampers of TMD system are set along the circumference between ring-shape mass block and tube-shape structure. It is shown in Fig. 1.

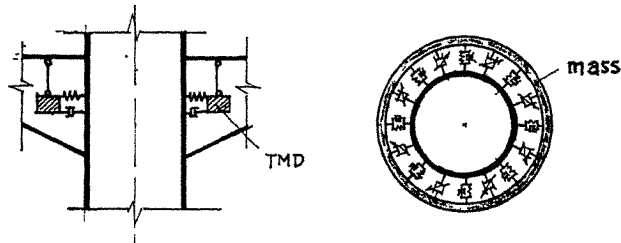


Fig. 1 Device of semi-Active TMD

In the paper, the basic principle and the design method of semi-active control of hanging TMD are presented, and the simulating calculation result for Nanjing TV tower are ob-

tained.

## 2. Basic Principle of Semi-Active Control for Wind Vibration Responses of Structure by Hanging TMD

As the hanging rods of TMD are very short, the restoring forces of the TMD vibration system is nonlinear, and its horizontal displacement is limited to that can not exceed length of the hanging rod. From this, the equations of the controlled responses of the hanging TMD and the structure are established as:

$$\left. \begin{aligned} [M]\{\ddot{X}\} + [C]\{\dot{X}\} + [K]\{X\} &= \{P(t)\} - \{H\}\{U^*(t) - C_T\dot{W} - K_T W\} \\ M_T\ddot{W} + C_T\dot{W} + K_T W + \frac{M_T \cdot g}{L} \cdot W \sqrt{1 - \left(\frac{W}{L}\right)^2} &= -M_T\ddot{X}_k + U^*(t) \end{aligned} \right\} \quad (1)$$

where:

$\{X\}, \{\dot{X}\}, \{\ddot{X}\}$  are vectors of horizontal displacement, velocity and acceleration of structural stories in direction of structural vibration;

$\{P(t)\}$  is vector of fluctuation wind load;

$\{H\}$  is location matrix of TMD;

$U^*(t)$  is semi-active control force provided by adjustable dampers in direction of structural vibration;

$W, \dot{W}, \ddot{W}$  are relative displacement, velocity and acceleration of the TMD system to installed storey of the structure;

$\ddot{X}_k$  is vibration acceleration of installed storey of the space cabin;

$M_T, C_T, K_T$  are mass, damping and stiffness coefficients in vibration direction of the TMD;

$L$  is length of hanging rod.

As spring-dampers and adjustable dampers are evenly installed along the circumference of TMD,  $C_T$  and  $K_T$  in vibration direction of the TMD are

$$\left. \begin{aligned} K_T &= \frac{2}{\pi} n \cdot k \\ C_T &= \frac{2}{\pi} n \cdot c \end{aligned} \right\} \quad (2)$$

and total control force in vibration direction of the TMD is:

$$U^*(t) = \frac{2}{\pi} \cdot n \cdot u(t) \quad (3)$$

where:  $n$  is total number of spring-dampers or adjustable dampers along the circumference;

$k, c$  and  $u(t)$  are the stiffness, damping coefficient of every spring-damper and the control force produced by every adjustable damper respectively.

Considering that  $u(t)$  is achieved by regulating the damping coefficient of the adjustable damper, its suppressing vibration effect may approach one of active control if change-law of the damping force of the adjustable damper approach optimal control force. Like this, the design and calculation of semi-active control for wind vibration responses of the structure by hanging TMD are to choose the parameter  $M_T, C_T, K_T$  of the TMD and rationally

to regulate the the damping parameter of adjustable damper for satisfying the requirement of wind resistant design of the structure.

### 3. Determination of Basic Parameters of TMD

Because passive control is realized by hanging TMD when the semi-active control device is closed, the parameters of TMD should be chose according to criterion that the effect of passive control of TMD is best.

As the equations (1) are nonlinear when  $U^*(t)$  is equal to 0, the control realized by passive TMD is a nonlinear control of the linear structure. For convenience, the equation of equivalent linear system of passive hanging TMD vibration system is assumed as

$$M_T \ddot{W} + C_T \dot{W} + (K_T + K_e)W = -M_T \ddot{X}_K \quad (4)$$

where  $K_e$  is equivalent linear stiffness coefficient of nonlinear restoring force of hanging TMD. Based on that the mean square value of the difference between equation (4) and (1-2) (in which  $U^*(t)=0$ ) is minimum, it can be found that

$$K_e = \frac{2}{\pi} \cdot \frac{M_T g}{L} \int_0^{L^{1/2} \sigma_w} \sqrt{y - \frac{2\sigma_w^2}{L^2} y^2} \cdot \exp(-y) dy \quad (5)$$

Then the equation (4) and (1-1) (in which  $U^*(t)=0$ ) describe passive control for wind vibration responses of the structure by the equivalent linear TMD, which may be solved by deriving they transferring function and using mode-superposition method.

According to linear control theory of passive TMD<sup>[1]</sup>, the greater  $M_T$ , the better control effect is, and the frequency  $\omega_T$  of linear TMD system is equal to the frequency  $\omega_c$  of controlled key vibration mode shape of the structure. From this, it is obtained that

$$K_T = M_T \omega_c^2 - K_e \quad (6)$$

The optimum value of  $C_T$  can be obtained by one-dimensional optimum design method minimizing the weighting value of the mean square deviation of random responses of the structure.

### 4. Realization of Semi-Active Control Force $U^*(t)$

Using mode superposition method, the equations (1) of control for wind vibration responses of the structure by hanging TMD may be transformed as

$$\left. \begin{aligned} \ddot{q}_i + 2\xi_i \omega_i \dot{q}_i + \omega_i^2 q_i &= F_i^*(t) - \mu_i \Phi_{ki} \left( \frac{1}{M_T} U^*(t) - 2\xi_T \omega_{Te} \dot{W} - \frac{K_T}{M_T} W \right) \\ (i = 1, 2, \dots, r) \\ \ddot{W} + 2\xi_T \omega_{Te} \dot{W} + \omega_{Te}^2 W &= - \sum_{j=1}^r \Phi_{kj} \ddot{q}_j + \frac{1}{M_T} U^*(t) \end{aligned} \right\} \quad (7)$$

where:  $\omega_{Te}^2 = \frac{K_T}{M_T} + \frac{g}{L} \sqrt{1 - \left(\frac{w}{L}\right)^2}$  is the function of time  $t$ ;

$2\xi_T \omega_{Te} = \frac{C_T}{M_T}$  is constant.

Let  $\{Z\}^T = [q_1 \dots q_r, W \dot{q}_1 \dots \dot{q}_r, W]$ , then the equations (7) may be combined as state equation,

$$\{\dot{Z}\} = [A]\{Z\} + \{B\}U^*(t) + [D]\{F(t)\} \quad (8)$$

Taking the evaluation function

$$J = \int_0^t \frac{1}{2} [\{Z\}^T [Q] \{Z\} + RU^2(t)] dt \quad (9)$$

the optimum active control force which minimizes above-mentioned J is

$$U(t) = -\frac{1}{R} \{B\}^T [P] \{Z\} \quad (10)$$

Where [P] is the solution of following Riccati equation:

$$[P] + [P][A] + [A]^T [P] - \frac{1}{R} [P]\{B\}\{B\}^T [P] + [Q] = [O] \quad (11)$$

it must be solved on-linear.

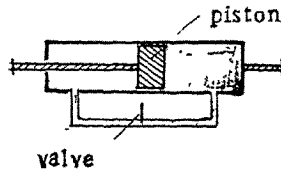


Fig. 2 adjustable damper

As the semi-active control force is realized by the adjustable damper shown in Fig. 2, which is regulated by the damping valve, it only provides the damping force in opposite direction to the speed  $W$  of TMD. Thereby, the adjustable damper can not provide active control force expressed by formula (10), and only can give the semi-active force which be expressed as

$$U^*(t) = \begin{cases} -C_u W & WU(t) < 0 \\ 0 & WU(t) \geq 0 \end{cases} \quad (12)$$

where the damping coefficient  $C_u$  of the adjustable damper should be regulated by following formula

$$C_u = \begin{cases} -U(t)/W & WU(t) < 0 \\ 0 & WU(t) \geq 0 \end{cases} \quad (13)$$

which may be realized by regulating the damping valve.

**5. Computer Simulation of Semi-Active Control for Wind Vibration Responses of Nanjing TV Tower by Hanging TMD.**

(1) Production of the Samples of Generalized Fluctuation Wind Loads

According to the basic principle of producing multi-dimensional random process<sup>[3]</sup>, the generalized fluctuation wind loads of Nanjing TV tower are simulated by following triangular series:

$$F_i^*(t) = \sum_{p=1}^i \sum_{k=1}^m \{a_{ip}(k) \cos[\omega_k t - \alpha_{ip}(k)] + b_{ip}(k) \sin[\omega_k t - \alpha_{ip}(k)]\} \quad (14)$$

(i=1, 2, ..., r)

(2) Calculation Result of Control for Wind Vibration Responses of Nanjing TV Tower.

As hanging TMD is limited by dimension of the reversed cone shell of the space cabin, the mass  $M_T$  of TMD is designed as 40t. When the fundamental wind pressure is taken as 0.35 kn/m<sup>2</sup> and the terrain kind is B, the controlled acceleration history response of the space cabin is calculated by the computer program SATMD on the basis of producing the samples of generalized fluctuation wind loads. The result is shown in Fig. 3, from which we may catch sight of that the maximum wind vibration acceleration response of the space cabin is from 0.29m/sec<sup>2</sup> to 0.18m/sec<sup>2</sup>.

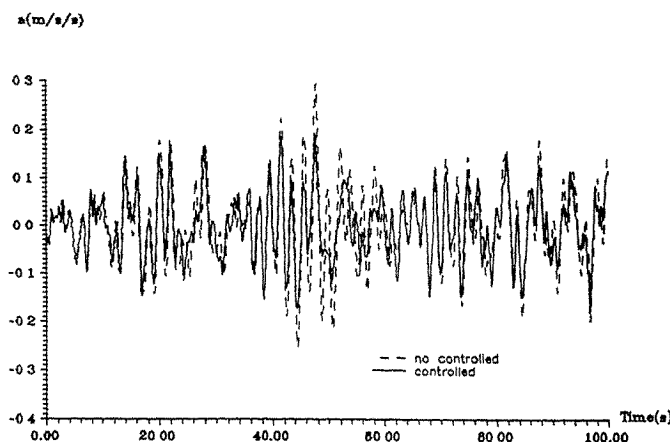


Fig. 3 controlled acceleration history response of space cabin

Obviously, its effect of suppressing vibration is very good. The history curve of the semi-active control force is shown in Fig 4, from which we may catch sight of that the maximum control force is only 34.0 kn and the history curve of the control force is not complete. It indicates that the semi-active TMD only can partly realize the optimum active control force, and its control effect is not optimal.

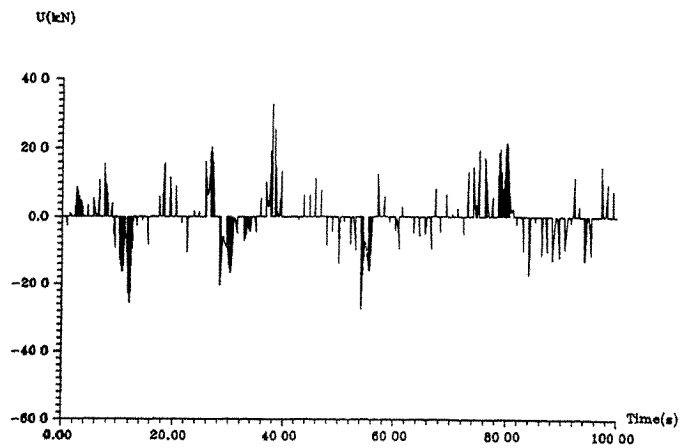


Fig. 4 history curve of semi-active control force

**References:**

1. Qu Weilian, Control Design for Wind Vibration Responses of Highrise Structure and Tall Building, Publishing House of Wuhan Science Technical University of Survey and Drawing, (1991).
2. D. Hrovat, P. Barak and M. Rabins, ASCE J. EM, (1986)
3. Xing Gusheng, Analysis of Random Vibration, Publishing House of Earthquake, (1977)

## **Wind Tunnel Techniques**





## Wind-tunnel modelling of the atmospheric surface layer

Jack E. Cermak, Leighton S. Cochran and Russ D. Leffler

Department of Civil Engineering  
Colorado State University, Fort Collins, CO USA

**Abstract:** Modelling of low-rise structures in the boundary-layer wind tunnel requires that the investigator focus on the lowest 100 m of the atmospheric boundary layer; the Atmospheric Surface Layer (ASL). Most of the key flow properties in this lowest portion of the Atmospheric Boundary Layer (ABL) have been successfully modelled in the wind tunnel for some time. However, this work demonstrates that two additional open-terrain flow properties may also be modelled with the wind tunnel: (i) the vertical distribution of Reynolds shear stress and; (ii) the lateral fluctuations of wind velocity and their power spectra.

### 1. Introduction

Wind-tunnel modelling of the Atmospheric Boundary Layer has allowed wind engineering to become a useful design tool for high-rise structures over the last thirty years (1). However, the financial losses due to wind are primarily the result of damage to low-rise buildings. Storms, such as Hurricane Andrew which hit Florida and Louisiana in August 1992, have placed further emphasis on the need to improve the design parameters for low-rise buildings and domestic dwellings. Recent research has been focused on low-rise structures occupying the lowest 50 m of the atmosphere (2,3,4). An arrangement placed in the wind tunnel of Fig. 1 is shown in Fig. 2 that provides a way of modelling the ASL (3) in the wind tunnel to a depth of over 1 m. This allows the useful scales of 1:100 and 1:50 to be used for low-rise buildings. For a scale of 1:100, the appropriate profiles of mean velocity, longitudinal turbulence intensity, lateral turbulence intensity, longitudinal integral length scale and Reynolds shear stress (3,5) can be achieved. However, at the 1:50 scale, the longitudinal integral length scale for model and prototype does not match as well as for the 1:100 scale.

In wind-tunnel flows the angular extremes in flow direction are significantly smaller than in nature (i.e. typically  $\pm 20^\circ$  in the wind tunnel and  $\pm 40^\circ$  in the field). An active set of vertically oriented, oscillating airfoils may be used to simulate this flow feature. Data are presented which

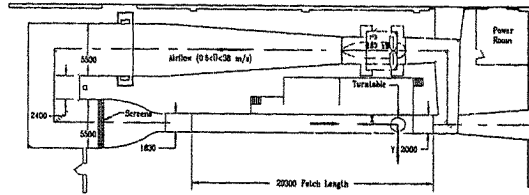


Fig. 1. The Meteorological Wind Tunnel at Colorado State University.

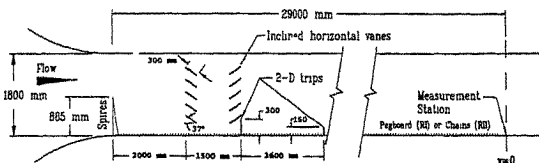


Fig. 2. Static flow modification devices used to generate a thickened atmospheric surface-layer flow (3).

show how this may be achieved with little impact on the more common referenced flow features noted above. A better understanding of these flows and their effects on low-rise buildings may lead to improved design codes for the common rectilinear low-rise buildings. In addition, the testing of complex shapes, such as tensile fabric structures, may become more commonplace in the future.

## 2. The Augmented ASL

Field data collected in neutral flow over uniformly flat terrain show that the principal Reynolds stress ( $-\rho\overline{uw}$ ) is approximately uniform with height in the ASL (5,6). Data from the Kansas field experiment is given in Fig. 3. More recently, the text by Stull (6) defines the surface layer as,

"...that part of the boundary layer where fluxes vary by less than 10% of their magnitude with height. To a first approximation, this layer is a constant flux layer."

In order to achieve this in the wind-tunnel modelling process one needs to consider the appropriate turbulence production term in the turbulent energy equation,

$(-\rho\overline{uw})\partial\overline{U}/\partial z$ . In the configuration shown in Fig. 2 the spires were inserted to create the mean vertical gradient and the horizontal vanes were added to generate a strong  $\overline{uw}$  correlation. With a long test section the shear-stress profile is able to reach an equilibrium condition in the flow. The resulting flow properties are shown in Fig. 4. At  $x = 0$  the shear stress is essentially constant with height which is in agreement with Fig. 3.

## 3. Enhancement of Low-frequency Lateral Turbulence

The constraint of the wind-tunnel walls results in lateral flow fluctuations that are restricted when compared to the field. The use of the randomly oscillating vertical airfoil sections (Fig. 5) may be used to "fill in" the low-frequency spectral content in the transverse velocity spectra. Longitudinal and lateral velocity time series were collected by cross-wire anemometers positioned at 40 mm and 80 mm above the centre of the turntable in the wind tunnel. The oscillating airfoils were installed 10 m upstream. By mechanically driving the five airfoils (two drive systems operating airfoils 1-3-5 and 2-4, respectively) with a low frequency random signal, a substantial increase in low-frequency lateral spectral energy occurs (Fig. 8), while the longitudinal energy spectrum remains virtually unchanged.

The field data in Figs. 6 to 8 are taken from the site near the Texas Tech University Experimental Building in Lubbock, Texas (3,4,7). A longer full-scale time series would be of value to give more data points at the low-frequency end of the velocity spectrum. Despite this observation, the longitudinal flow spectra are in good agreement between the model and full scale. A deficiency in the low-frequency lateral spectral content in the wind tunnel may be seen in Fig. 7. This feature may be corrected with the oscillating airfoils when used in a random mode. A cyclic motion only results in an isolated spike. In Fig. 8 the frequency range of the random motion should be increased by a factor of two to fully model the prototype flow spectrum. Work with this device is ongoing.

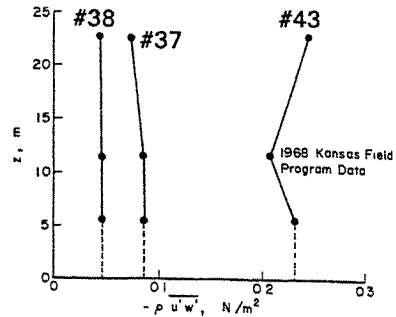


Fig. 3. Kansas field data for neutral flow run numbers 37, 38 and 43 (5).

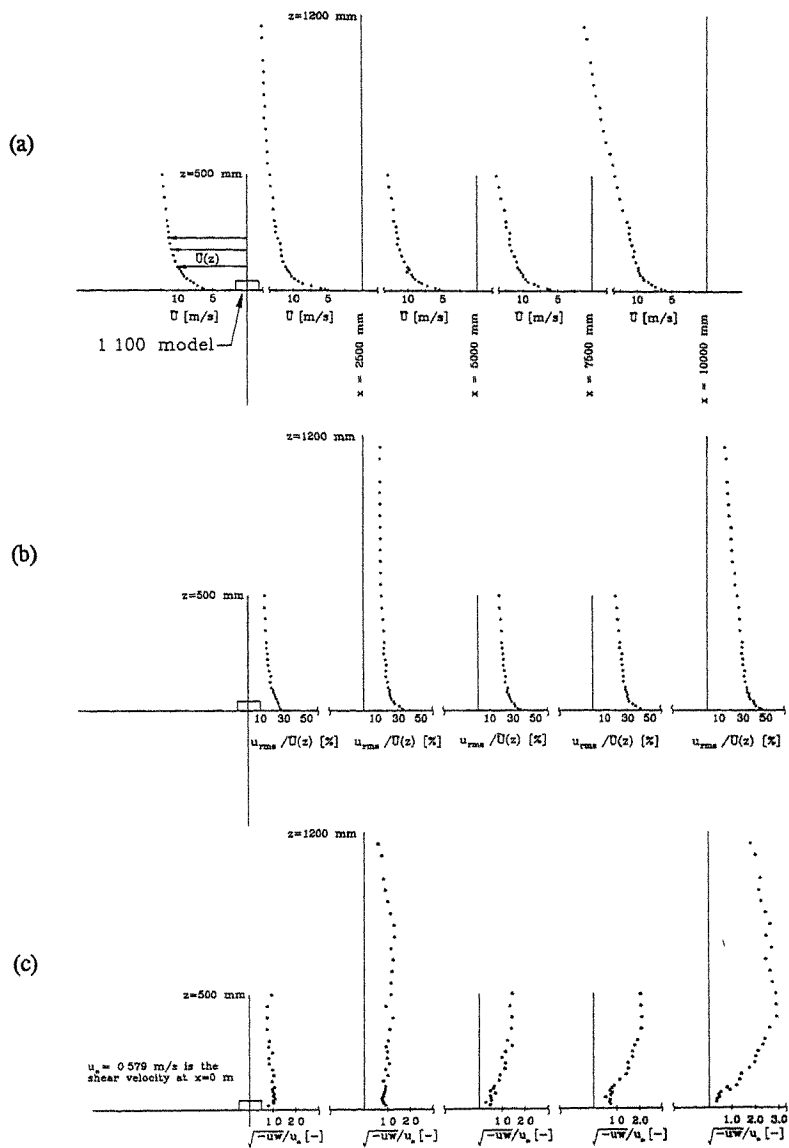


Fig. 4. Development of centerline (a) mean velocity, (b) turbulence intensity, and (c) non-dimensional shear stress in the approach flow ( $x = 0.0, 2.5, 5.0, 7.5$  and  $10.0$  m).

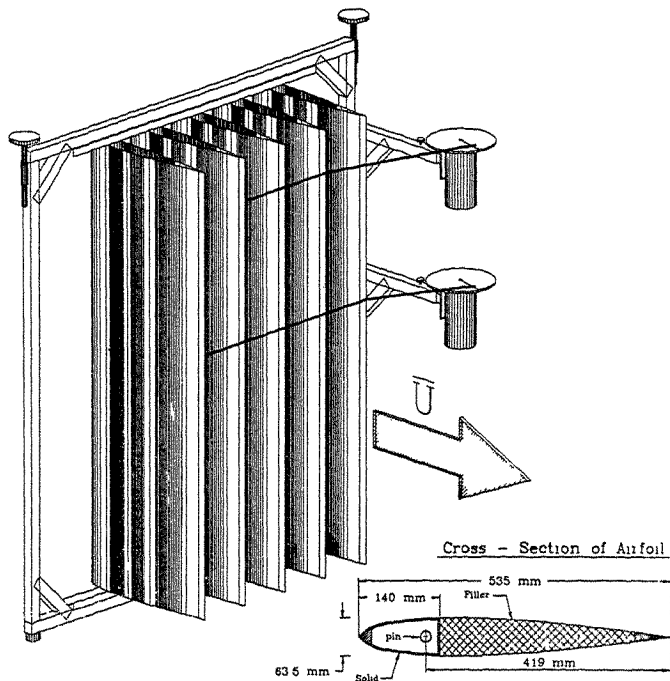


Fig. 5. Oscillating airfoil sections used to generate increased lateral length scales and the extreme directional fluctuations in the flow.

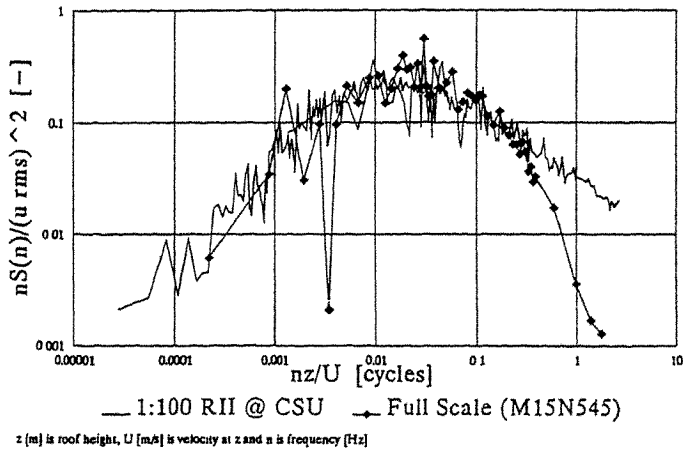


Fig. 6. Longitudinal velocity spectrum without the oscillating airfoils installed (i.e., using only the static devices on Fig. 2).

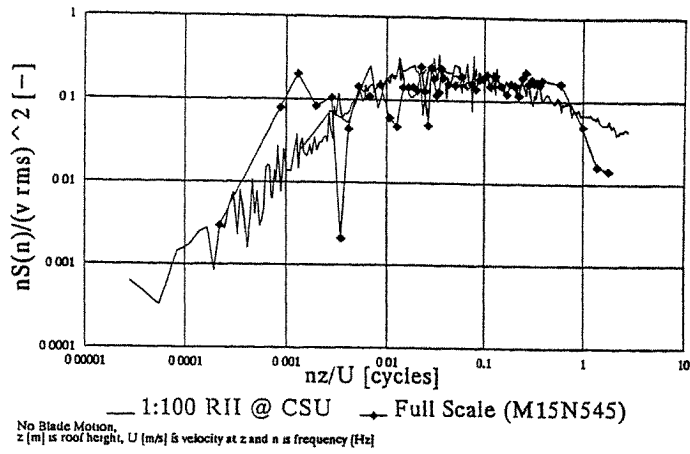


Fig. 7. Lateral velocity spectrum without the oscillating airfoils installed (i.e., using only the static devices of Fig. 2).

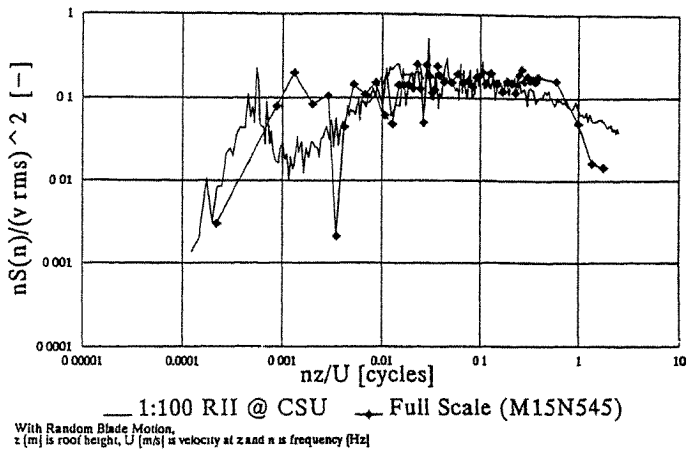


Fig. 8. Lateral velocity spectra with the oscillating airfoils in operation [7].

#### 4. Conclusions

A set of static wind-tunnel, flow-modification devices are presented which allows the ASL to be modelled at useful scales of 1:100 and 1:50. This has assisted researchers to pursue the recent interest in low-rise building studies. Additionally, a method is presented for reducing adverse effects of the flow-constraining wind-tunnel walls. The randomly oscillating airfoils make possible matching of the low-frequency component of the lateral velocity spectrum.

#### 5. Acknowledgements

This study was performed with the funding provided under the United States National Science Foundation Grants BCS-8821542 and BCS-8821163 for the Colorado State University/Texas Tech University Cooperative Program in Wind Engineering. The authors wish to thank Messrs. Byron Yeatts and George Thomas for their assistance in collecting and reducing the field data, as well as Ms. Gloria Garza for compiling this document.

#### References:

1. Cermak, J.E., "Application of Fluid Mechanics to Wind Engineering," A Freeman Scholar Lecture, Journal of Fluids Engineering, American Society of Mechanical Engineers, Volume 97, Number 1, March 1975.
2. Cermak, J.E., "Atmospheric Boundary Layer Modelling in Wind Tunnels," Proceedings of the International Symposium on the Experimental Determination of Wind Loads on Civil Engineering Structures, Oxford and IBH Publishers, University of Roorke, New Delhi, India, December 1990.
3. Cochran, L.S., "Wind-Tunnel Modelling of Low-Rise Structures," PhD Dissertation from Colorado State University, 509 pages, Fall 1992.
4. Chok, C.V., "Wind Parameters of the Texas Tech University Field Site," Master of Science Thesis, Civil Engineering Department, Texas Tech University, August, 1988.
5. Izumi, Y., "Kansas 1968 Field Program Data Report," United States Air Force Cambridge Research Laboratories, Massachusetts, Project Number 7655, December 1971.
6. Stull, R.B., "An Introduction to Boundary Layer Meteorology," Kluwer Academic Publishers, Second Edition, 1989.
7. Thomas, G., Cochran, L.S., Cermak, J.E. and Mehta, K.C., "Comparison of Full Scale and Wind-Tunnel Measured Spectra," 7th US Wind Engineering Conference, UCLA, June 1993.

## A Large Australian Dynamic Weather Testing Facility (DWTF)

David Paterson & Geoff Farrance

CSIRO Division of Building, Construction and Engineering  
PO Box 310 North Ryde NSW 2113  
AUSTRALIA

**Abstract:** Construction of the High Speed Dynamic Weather Test Facility at North Ryde is well underway. This facility will use the airflow of a turboprop engine from a Lockheed C 130 Hercules aircraft engine to produce cyclone (typhoon, hurricane) force winds. Samples up to eight metres high by eight metres across will be tested. A second smaller facility testing to various Australian Standards using a Pratt and Whitney R2800 18 cylinder 2400 Hp radial aircraft engine is already operating.

### 1. From Sea Fury to Hercules DWTF.

At the Experimental Building Station (EBS) at North Ryde as long ago as 1947, it was recognised that the effects of weather on buildings and their components needed to be shown as a performance criteria not just as a demonstration of its mechanical or physical properties. The EBS identified that the then present equipment could not replicate "Nature" either in power or in detail. The best solution was a high speed wind source and a series of combination sprays to give a demonstrable test regime. A Hawker Sea Fury aircraft was purchased and set up for the high speed wind source. The Sea Fury was a combat fighter used by the Australian Navy in the Korean War (Fig. 1). This aircraft had the outer section of the wings removed to remove the likelihood of flight, and the tail section held to the ground to maintain the flight angle of the fuselage for greatest efficiency of air flow. It was used for blowing air at building products and assemblies to see if they could withstand the wind forces with accompanying water spray to test their weather performance (Fig. 2). The aircraft was taken as a historic exhibit to the Australian War Memorial in 1987 after several serious mechanical problems developed and preparations for a replacement were begun.

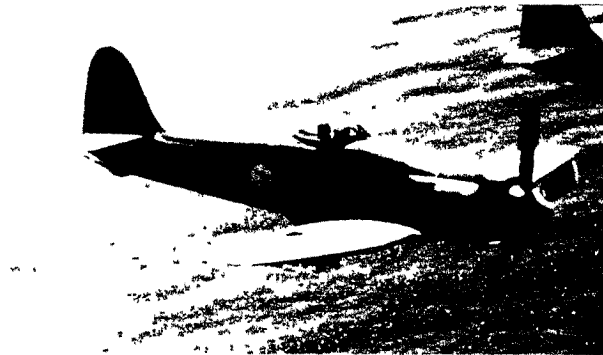


Fig. 1. The Hawker Sea Fury in flight.



Fig. 2. A water penetration test using the Sea Fury at the EBS.

The EBS became the National Building Technology Centre (NBTC) in 1982/83 and finally merged with the CSIRO Division of Building Research in 1989 becoming the CSIRO Division of Building, Construction and Engineering (DBCE). In 1984, the NBTC realised that a replacement was necessary and after exhaustive research and protracted discussions with various Government departments, an aircraft engine from a Lockheed C 130 Hercules transport was bought to give air volumes and wind speeds far in excess of that of the old Sea Fury (Fig. 3). This engine is an Allison T56-A11 turboprop engine of 3600 Hp available at the three bladed propeller. The facility is known as the Hercules DWTF.

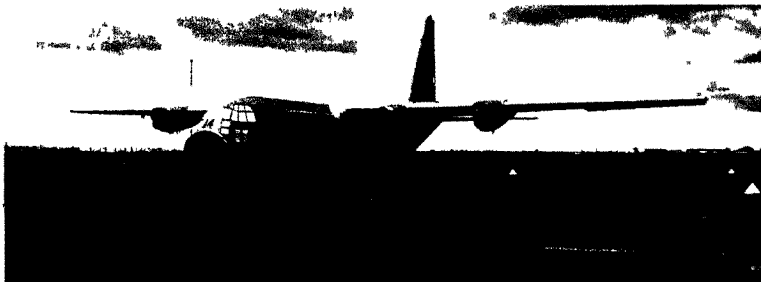


Fig. 3. The Lockheed C 130 Hercules transport aircraft.

With construction underway, we obtained a Pratt and Whitney R2800 piston driven aircraft engine on a cantilever test frame from the Perth office of the DBCE when it closed (Fig. 4) We are currently using this for air pressure, air flow and water penetration tests to test specifications, both Australian and other world test parameters. These tests have been performed on building components such as smoke and heat release ventilators, roofing hardware and awnings required under the Building Code of Australia (BCA).



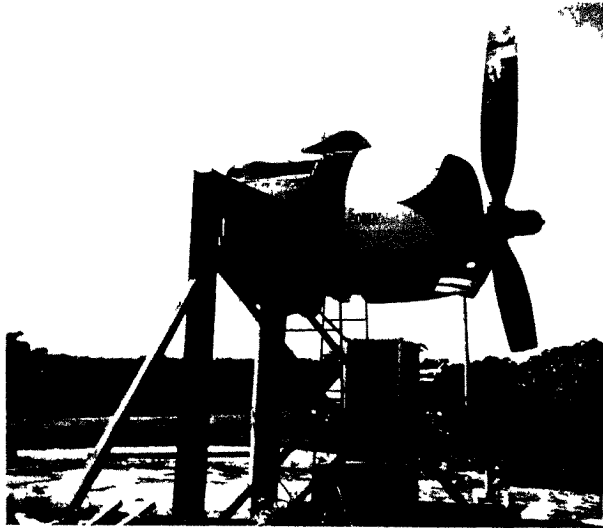


Fig. 4. The Pratt and Whitney R2800 aircraft engine ready for use.

## 2. Details

It was originally planned to construct a test building around the Allison engine from the Hercules. In later plans, the building was changed into a giant steel tube, with attached control room and cells for ancillary equipment (Figs. 5,6). The entire facility is mounted on rails to allow it to move sideways. This will allow some specimens to be tested in two or more places on one specimen and to allow others to be tested at the same time as others are being erected and dismantled.

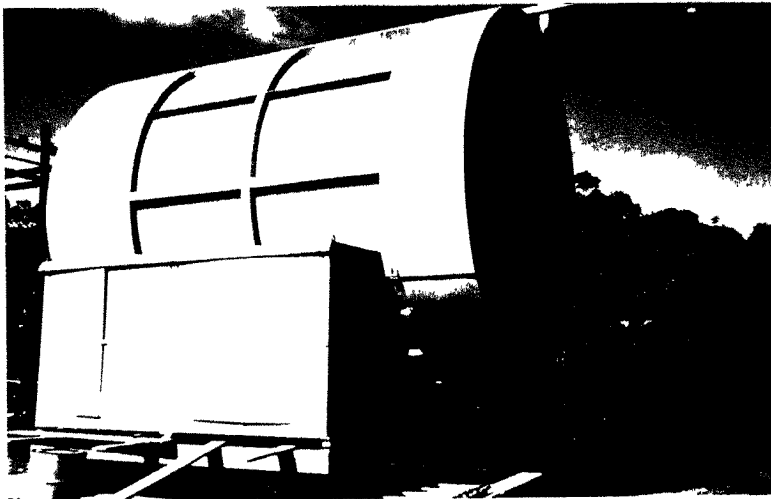


Fig. 5. A side view of the Hercules DWTF. Behind the doors are the Fuel and Electrical Bays.

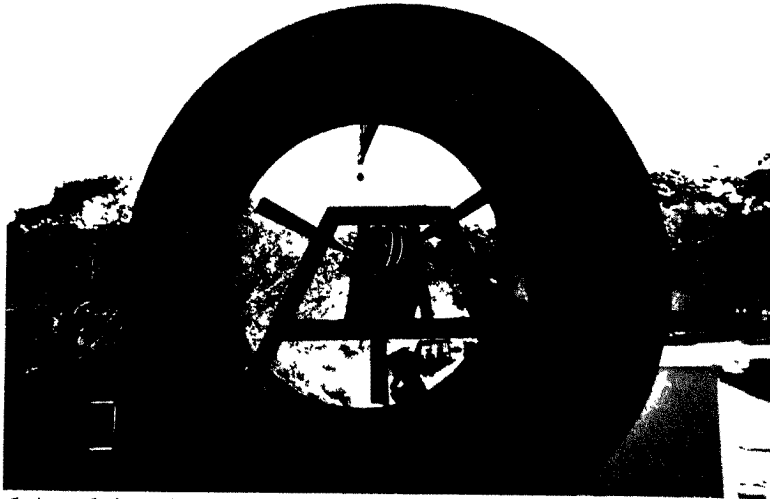


Fig. 6. An end view of the Hercules DWTF. The Control Room is on the left.



Fig. 7. The Allison engine inside the steel tube. A support frame for test specimens is behind.

Construction of the Hercules DWTF is nearing completion. The engine is in place. The fuel tank and compressed gas requirements are in place. The pipework for the engine is connected. The instrumentation and the fitting out of the control room is currently being installed by specialist aero engineers. All this work has been done by the DBCE without corporate sponsorship.

The six metre diameter steel casing around the engine and the A-Frame to which the engine is attached are very heavy. They are heavy in order to hold the engine rigidly in place when it runs.

Noise is a potential problem. There are two major sources of noise, the propellers and the exhaust. Original plans to build earth walls around the facility have been abandoned. Now, the steel casing is lined with noise absorbing foam within tuned cavities behind perforated steel sheet, and a tuned muffler is used on the exhaust. This will reduce the noise level to less than that of the less powerful Pratt and Whitney R2800 DWTF with a maximum sound output of 128 dBA at 10 metres.

There are four rooms/bays supported on the same frame that holds the Allison engine. These are the Control Room, Bottle Room, Fuel Bay and Electrical Bay. These sit on vibration dampers mounted in a cross plane alignment to negate most vibration and hysteresis from the engine (Fig. 8). The Control Room contains engine, fuel, electrical generation and compressed gas monitoring instruments and will have closed circuit remote television monitoring of the engine and test specimen. It is fully lined with sound absorbing materials. The Bottle Room contains air bottles which supply air to turn the engine over for starting until the fuel takes over. It also contains nitrogen bottles which feed nitrogen into the engine nacelle if a fire or overheat condition is detected internally and a CO<sub>2</sub> source for external fire fighting. The Fuel Bay contains a large tank of JET A fuel (a high quality kerosene) fuel and associated pipework. The Electrical Bay will contain the 3 phase 400 Hz generators needed for aviation equipment. The Fuel and Electrical Bays are separated by a fireproof wall.

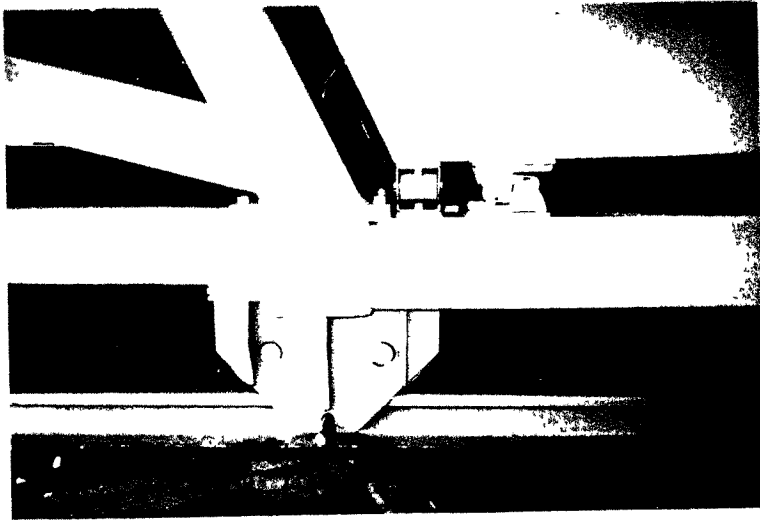


Fig. 8. The rails on which the Hercules DWTF rolls. The Bottle Room at upper right sits on vibration dampers.

There is a larger gap between the propeller and casing on the DWTF than those found in wind tunnels. This is because aeroplane engines are designed to run with no obstructions near the tips of the propellers. Obstructions can cause the reflection of pressure waves back onto the propellers which significantly reduces their lifespan.

The propeller of the Hercules DWTF is larger in diameter than that of the R2800 DWTF; typically 12ft 9 in on the R2800 and 15ft 2 in on the Allison engine. The turboprop of the Allison engine is more efficient than the piston engine of the R2800 and the propeller design is more advanced. This leads to much greater wind speeds being achieved using the Hercules DWTF. The Allison engine and propeller run at a constant rotational rate. The wind speed and power requirements are adjusted by changing the pitch of the blades.

The DWTF is made in sections so that it can be dismantled and moved to other sites. It is required to move it to another site in Sydney in the near future. The new site may be at Kemps Creek, near "Badgerys Creek" the planned site of Sydney's second international airport.

### **3. Conclusions**

The Hercules Hurricane DWTF is semi-enclosed. The jet of air from the engine spreads before hitting the sample to be tested. Test specimens up to eight metres high by eight metres across can be tested. This will allow, for example, the wind pressures on three storeys of a high rise building to be estimated.

The facility will be used for both research and commercial testing. There will be the ability to test full-scale vehicles and structural components in cyclone (typhoon, hurricane) force winds. It may even be possible to put complete houses in the test area. The wind speed generated will be able to match the design wind speed at any place on earth.

The ability to use large (full-scale) models in very strong winds makes this facility invaluable for research. The Reynolds numbers that can be generated are very large. The wind generated will not have low turbulence. Turbulence will be generated by the air passing over the A-Frame and past the aircraft exhaust. This could be an advantage. The resulting turbulence will have a very large length scale. Turbulence with length scales this large cannot be easily produced in wind tunnels. Large scale turbulence is a feature of atmospheric wind.

### **4. Acknowledgements**

This work has been paid for by the CSIRO DBCE. Much of the work has been done by present and former staff of the DBCE. Some people who have had a large part to play in the construction of this facility are as follows. Dr David Paterson and Dr Edmund Choi have had planning and supervisory roles. Mr Geoffrey Farrance and Mr Ron Bennett from QANTAS did all of the pre-design and procurement research and Michael Puak and Geoffrey Farrance have had design and detail supervisory roles. Roy Chapman and Greg Lofts from the Engineering Support Section have had a large part to play in the steelwork construction. Instrumentation is being installed with the help of specialists from the Historic Aircraft Restoration Society.

## Computer-controlled wind tunnel for wind-engineering applications

A. NISHI and H. Miyagi

Faculty of Engineering, Miyazaki University  
Miyazaki 889-21, JAPAN

**Abstract:** Many types of meteorological, environmental and boundary layer wind tunnels have been constructed to simulate atmospheric phenomena on buildings, structures and the transport of air pollutants. New types of 2- and 3-dimensional wind tunnels have been constructed in our laboratory, which has multi-fans controlled by a computer. To simulate the required wind structure in the wind tunnel, each fan is controlled independently to pile up turbulence characteristics on mean wind velocity profiles.

### 1. Introduction

Wind tunnels of many varieties have been used to investigate civil engineering problems for a long time. Reviews have been presented by Cermak and Peterka [1], Meroney [2] and Simiu and Scanlan [3]. In the conventional wind tunnels, it is easy to produce boundary layer mean wind profiles and corresponding turbulence intensities by using spires and roughness blocks on the floor. In general, however, it is difficult to produce desired turbulence length-scale profiles. Also it is difficult to change the profiles of these turbulence factors, since the rearrangement of blocks is required.

Recently new attempts have been reported by Cermak and Cochran [4] and Kobayashi and Hatanaka [5]. The latter tried to create large turbulence by using two rows of computer controlled blades in a conventional wind tunnel. This study revealed that a uniform mean velocity profile which involves the given power spectrum, integral scale of turbulence and turbulence intensities can be produced by several feed-back control trials.

Two new-type wind tunnels have been constructed in our laboratory. They have many fans, each of which can be controlled independently by a computer. This is an attempt to develop a new wind tunnel technique to simulate complicated wind characteristics only by changing computer programming. Two- and three-dimensional wind tunnels have been constructed. The experimental results mainly from the 2-dimensional tunnel are presented in this paper.

### 2. Experimental wind tunnels

The 2-dimensional wind tunnel has 11 fans arranged vertically, the 3-dimensional one has 6 rows of 11 fans horizontally, for a total of 66 fans. Each fan is connected to a personal computer through an inverter. The schematics of 2- and 3-dimensional tunnels are shown in Fig.1. Test-section dimensions (length, width, height) of the 2-dimensional and 3-dimensional tunnels are as follows; (3.8, 0.18, 1.0 m) and (5.7, 1.0, 1.0 m), respectively. The wind speed of each fan can be controlled from 0 to 11 m/s, by applying computer output voltages from 0 to 10 V. The contraction ratio of the fan inlet-channel cross-sectional area to the exit area is about 1:2. At the exit of all the channels, a honeycomb core, with each cell 10 mm in diameter and 100 mm in length, is installed to eliminate secondary

flow effect in the curved channels. To decrease the effect of the channel-wall boundary layer, 12 mm  $\phi$  cylindrical bars are inserted just after the honeycomb core. Each tunnel has a computer controlled traverse gear system to measure the mean velocity and turbulence distributions by hot-wire anemometers.

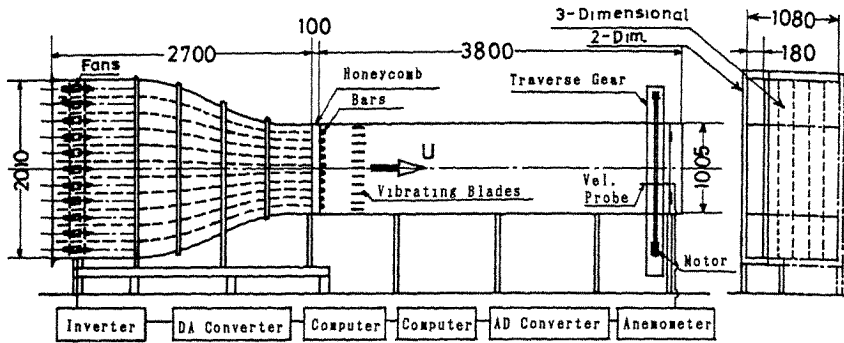


Fig.1. Schematics of the 2- and 3-dimensional experimental wind tunnels.

### 3. Control variables

To simulate atmospheric phenomena such as wind velocity distributions around buildings and structures, the velocity of the approach wind has to be exact, that is, it must have given turbulence characteristics. The important factors necessary to simulate atmospheric turbulence in a wind tunnel are as follows :

- (1) mean wind velocity profiles,
- (2) turbulence intensities,
- (3) integral length scales of turbulence, and
- (4) spectra of velocity fluctuations.

The major control variables of each fan necessary to produce a profile which involves an arbitrary combination of the above factors are as follows :

- (1) mean revolutionary speed of each fan,
- (2) fluctuation of the revolutionary speed of each fan, and
- (3) arrangement of mean revolutionary speed and fluctuation to produce the profile of turbulence factors.

As each fan has a time lag caused by motor inertia and aerodynamic load, a higher frequency response cannot be expected. An example of a frequency response is represented by the Bode-diagram shown in Fig.2.

### 4. Mean wind velocity profiles

At a position about 3 m downstream from the test-section entrance, the mean wind velocity profiles and turbulence intensities were measured in the 2-dimensional wind tunnel. In this case, each motor was driven without fluctuation of revolutionary speed, i.e., at a constant speed. Examples of uniform flow and boundary layer flow velocity profiles are presented in Fig.3 and Fig.4, respectively. Each profile was obtained by repeating feed-back trials up to the errors in wind velocity between given and measured values, until they became less than  $\pm 0.1$  m/s at the 11 points corresponding to each fan position. Four or five automatic

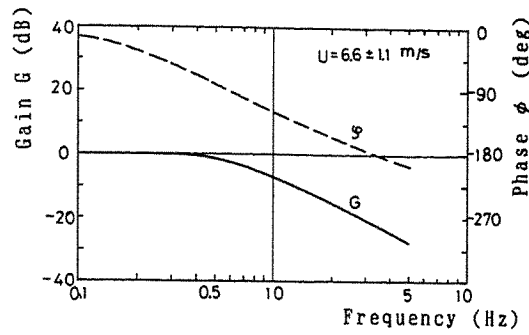


Fig.2. An example of the frequency response of each fan.

trials were required to obtain satisfactory results. Smooth curves on boundary layer profiles can be generated by adjusting the revolutionary speed of each fan.

The turbulence intensities are presented in the same figures. About 2 % of the intensities were obtained for uniform flow. This was an original value of the tunnel.

As an arbitrary boundary-layer velocity profile can be obtained on the floor, the same profiles can be produced easily under the ceiling. Many other complicated profiles could be produced by the same procedure [6].

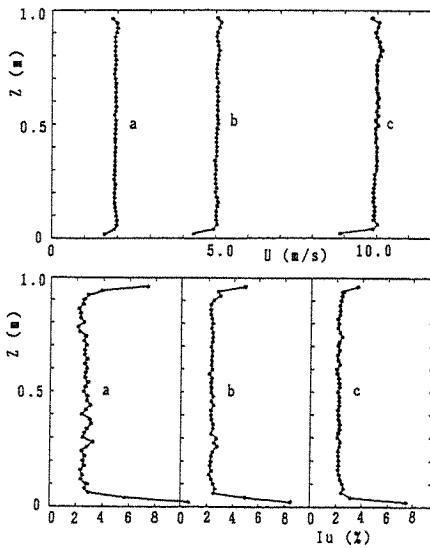


Fig.3. Profiles of mean wind velocities and turbulence intensities of the uniform flow.

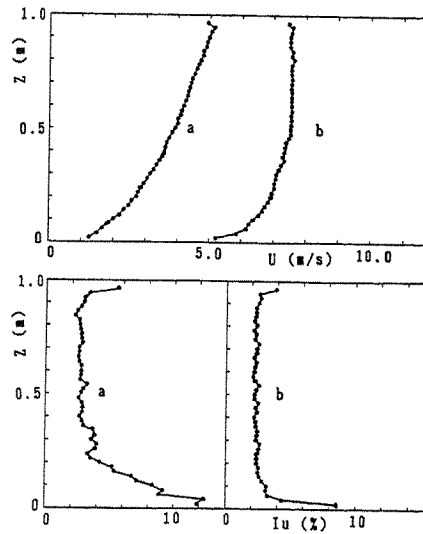


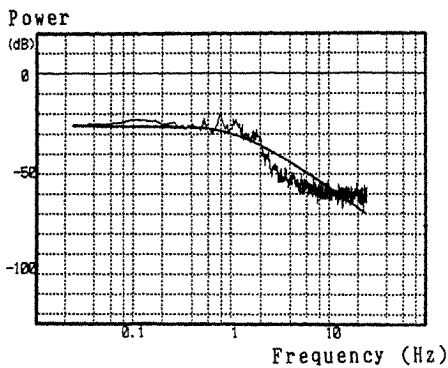
Fig.4. Profiles of mean wind velocities and turbulence intensities of the boundary layer flow.

## 5. Control of turbulence characteristics

### 5.1 Control method

The von Karman spectrum can be transformed into an expression which involves the mean wind velocity, turbulence intensity and turbulence scale [5]. First, the target spectrum is calculated by assuming the turbulence factors. Second, it is analyzed by using the inverse Fourier transform, and a time series of fluctuations is produced. This is given to all the fans, that is, all fans are driven by the same fluctuating input signals. An example of the comparison between the target spectrum and the observed one is presented in Fig.5. The difference of the power spectra at around 2~8 Hz depends on the time lag of the motor inertia and aerodynamic load. As an attempt to improve the differences in these power spectra, the odd-number fans were driven at high speed, and the even-number ones were stopped. The obtained spectra are presented in Fig.6. The lack of power does not appear in this case; however, a somewhat larger power can be obtained in high frequency region. There is a possibility improving the power spectrum by these trials.

The obtained turbulence factors corresponding to the target ones are given in these figures. The satisfactory values are obtained.



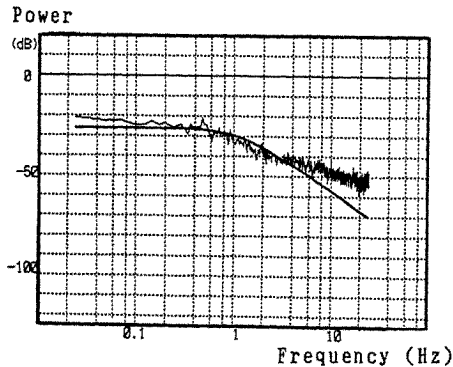
Target turbulence factors :

$U = 5$  m/s : mean velocity,  
 $I_u = 7$  % : turbulence intensity,  
 $L_u = 0.5$  m : length scale.

Measured values :

$U = 5.26$  m/s,  
 $I_u = 6.52$  %,  
 $L_u = 0.61$  m.

Fig.5. Comparison of target power spectrum and observed one.



Target turbulence factors :

$U = 5$  m/s : mean velocity,  
 $I_u = 7$  % : turbulence intensity,  
 $L_u = 0.5$  m : length scale.

Measured values :

$U = 5.05$  m/s,  
 $I_u = 7.9$  %,  
 $L_u = 0.43$  m.

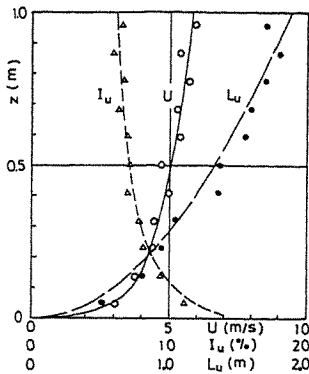
Fig.6. Comparison of power spectra for driving odd-number fans.



## 5.2 Profiles of turbulence factors

In a boundary layer wind tunnel, the mean velocity profile of logarithmic or power law is produced by using roughness blocks and/or spires. The desired turbulence intensity profile is also produced by adjusting the arrangement of the blocks. However, it is very difficult to get an arbitrary turbulence length scale profile by this method.

An attempt was carried out to produce the arbitrary profiles of these turbulence factors in the longitudinal direction of 2-dimensional tunnel. First, a different power spectrum was created for each fan by giving corresponding turbulence factors along the vertical direction. Second, the time series of fluctuations was produced by using an inverse FFT program. Moreover, the odd-number fans were driven in high speed and the even number ones were in low speed. The profiles of mean wind velocity, turbulence intensity and turbulence length scale were obtained by using feed-back control techniques. An example of these is shown in Fig.7. In this figure the boundary layer mean velocity profile, its turbulence intensity and turbulence length scale profiles are presented. The odd-number fans were driven by time series signals derived from the target spectrum. The even-number fans were driven by the values of 4/5 of corresponding time series.



The mean velocity target profile is given by,

$$U(z) = U_o (z/\delta)^{1/5}$$

where  $\delta = 0.5$  m,  $U_o = 5$  m/s at  $z = \delta$ .

The turbulence intensity target profile is assumed as,

$$I_u = I_o (z/\delta)^{-0.25}$$

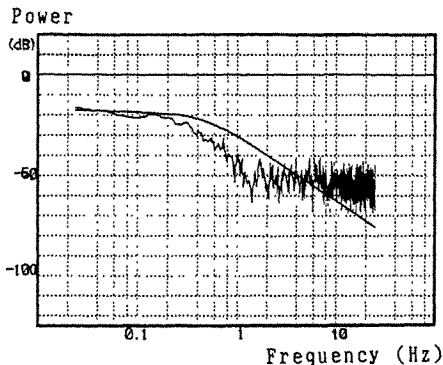
where  $I_o = 7$  %.

The turbulence length scale target profile is assumed as,

$$L_u = 100 [z / (30S)]^{0.5}$$

where  $S$  is the scale ratio of the model and prototype, 100 is used.

Fig.7. The profiles of turbulence factors.



Target turbulence factors at  $z = 0.5$  m :

$U = 5$  m/s : mean velocity at  $z = 0.5$  m,

$I_u = 7$  % : turbulence intensity,

$L_u = 1.3$  m : length scale.

Measured values :

$U = 4.5$  m/s,

$I_u = 6.94$  %,

$L_u = 1.34$  m.

Fig.8. Comparison of target and obtained spectra.

An example of the longitudinal power spectrum is shown in Fig.8. This spectrum was measured at the mid point of the test section in the 2-dimensional wind tunnel. The difference between the target spectrum and the obtained one around 1 Hz is larger than that in Fig.6. This should be improved by using a turbulence producer, such as a grid, vibrating blades, etc.. In addition, the excess power in the high frequency region should be decreased by using meshes, in the next stage of experiment.

## 6. Conclusion

Two-and three-dimensional wind tunnels with multi-fans were constructed. Each fan was connected to a computer through an inverter and could be controlled independently. These wind tunnels have many interesting characteristics. Some of them were tested in the 2-dimensional wind tunnel.

First, precise mean wind velocity profiles were produced by using the feed-back control technique, only giving target profiles to the computer. Second, trials were carried out to produce turbulence factors only by giving fluctuating signals to the fans. The target spectrum which involved target factors was analyzed by the inverse Fourier transform, and the time series of fluctuating signals was produced and given to the fans. Satisfactory results were obtained. Third, the profiles of turbulence factors were produced by using the same technique as above for each fan. In particular, it is of value that the turbulence length scale profile could be produced. This has been difficult in conventional boundary layer wind tunnels.

## References:

1. Cermak J.E. and Peterka J.A., Wind Engineering-Applications to Civil Engineering, ASCE Convention and Exposition, Chicago (1978).
2. Meroney R.N., Wind-Tunnel Modeling of the Flow about Bluff Bodies, Univ. of Karlsruhe (1986).
3. Simiu E. and Scanlan R.H., Wind Effects on Structures, 2nd Ed., John-Wiley & Sons (1986).
4. Cermak J.E. and Cockran L.S., Physical Modeling of the Atmospheric Surface Layer, Proc. 8th Intl. Conf. on Wind Engg., London, Ontario, Canada (1991), p.11-2.
5. Kobayasi H. and Hatanaka A., Active Generation of Wind Gust in Two Dimensional Wind Tunnel, Proc. 8th Intl. Conf. on Wind Engg., London, Ontario, Canada (1991), p.11-7.
6. Nishi A. et al., Computer Controlled Wind Tunnel, J. of Wind Engineering, No. 52,(1992), p. 406-411.

## On the Design of Wind Tunnel Inlet

Furman F.M. Fang and Kenny W.M. Gan

Department of Civil Engineering  
National Chung-Hsing University  
Taiwan, Republic of China

### Abstract

For an open-type wind tunnel, besides the designed shape and geometry of its inlet system, the pattern of the entrance flow is also an important factor in affecting the flow quality in the system. In many practical cases, since the distances between the inlet edge and the neighboring walls and ground are limited, an asymmetric entrance flow can be introduced, which may lead to degrade of the flow quality in the duct. A series of systematic studies were made to investigate numerically the wall and ground effects on the flow quality in a two-dimensional case, so as to gain additional insight into the design of wind tunnel inlet system.

### Introduction

Typically, the inlet system of an open, suction type of wind tunnel contains a flare, a setting chamber and a contraction, followed by a test section (see Fig. 1). From the design point of view, the bellmouth entrance is used to direct the flow into the tunnel system. Screens and honeycombs are usually set in the following straight chamber to eliminate large-scale vortices and to reduce the strength of turbulence in the flow. As the flow passes through the contraction, spatial irregularities carried by the accelerated stream can be smoothed out to produce a relatively more uniform flow with a lower relative turbulence level.

In general, the design of a tunnel inlet system requires consideration of the following two conditions:

- 1) maintenance of good contraction exit flow uniformity, and
- 2) avoidance of flow separation.

When designing a close-type wind tunnel system, the flow upstream of the contraction is usually assumed to be symmetric [1-9] along the centerline of the duct to simplify the analysis. However, for an open-type wind tunnel, the use of this assumption may result in a non-conservative design when the entrance flow is in an asymmetric manner.

### Design Consideration

A typical pressure distribution along the wall of the open-type tunnel (Referred to Fig. 1) is sketched in Fig. 2. Because there exist two adverse-pressure-gradient regions (one near the contraction inlet and the other one near the contraction exit), the boundary layer along the wall of the inlet system could separate. Previous studies [6,7] state that normally the separation near the contraction exit is less critical because the boundary layer near the pressure minimum is well energized after a long region of favorable pressure gradient and can better resist an adverse pressure gradient. However, Fang [9] argue that this may be true only if the developing turbulent boundary layer will not be relaminarized by the effect of a severe favorable pressure gradient in the contraction [10-12] since a laminar boundary layer is more prone to separate.

### Numerical Method

Because the boundary layer thickness is relatively thin compared with the dimensions of the tunnel sections, the inviscid solution can be regarded as the solution over the major portion of the flow with acceptable errors, when no separation occurs. Accordingly, a numerical method [13], based on Euler equations, is applied to obtain the steady, inviscid flow solutions in the system under various extents of ground and wall effects. The inviscid results along the wall of the inlet system and at the cross-section of the contraction exit in all cases are analyzed for further comparison.

### Parameters of Analysis

The parameters for the present analysis are given in the form of certain indicators which can be readily applied to evaluate the flow characteristics within the inlet system. Excluding the effects of screen and honeycomb temporarily, the study concentrate on certain criteria related to the flow quality, such as the extent of uniformity at the exit cross-section of the contraction, possibility of separation and turbulent boundary layer relaminarization.

#### 1) Contraction exit flow non-uniformity

$$u_2 = \frac{U_{\max} - U_{\min}}{U_{\infty}} \quad (1)$$

where  $U_{\max}$ ,  $U_{\min}$  and  $U_{\infty}$  represent respectively the maximum, minimum and mean velocities at the cross-section of the contraction exit.

#### 2) Relaminarization Parameter

Essentially, the boundary layer in the tunnel system is turbulent due to a high Reynolds number and the existence of screens and honeycombs. However, due to the previous arguments from [6,7,9], the occurrence of turbulent boundary layer relaminarization should be avoided. Kline[10] et al. proposed an acceleration parameter, defined as  $K = (\nu/U_x^2)(dU_x/dx)$ ; ( $U_x$  is the free-stream velocity), and stated that as the value of  $K$  exceeds about  $3.7 \times 10^{-6}$ , the turbulent boundary layer became relaminarized (Back et al.[12] used a value of  $2 \times 10^{-6}$ ). This acceleration parameter can be further normalized as

$$\kappa = Re_H \cdot K_{\max} = \frac{1}{(U_x/U_{\infty})^2} \frac{d(U_x/dU_{\infty})}{d(x/L)} \quad (2)$$

where  $Re_H = (U_{\infty}H/\nu)$ ;  $H$  is the width of the contraction inlet section;  $L$  is the contraction length;  $K_{\max}$  is the maximum  $K$  value along the wall of the contraction. The value of  $\kappa$  can be treated as an indicator in reflecting the possibility of the occurrence of relaminarization.

#### 3) Extreme Pressure Coefficient

As suggested by Fang [9] in his contraction design approach, the possible flow separation can be considered only in the first adverse pressure region (the one near the contraction inlet) provided that the possibility of relaminarization is eliminated. By utilizing this concept, a dimensionless coefficient corresponding to the extreme pressure near the separation is presented as

$$C_p = 1 - \left(\frac{U_x}{U_m}\right)^2 \quad (3)$$

where  $U_m$  is the velocity at the beginning of the first adverse pressure

gradient region. This coefficient is so defined that it can be directly applied into the Stratford separation criterion [14] as

$$C_p \left( X \cdot \frac{dC_p}{dx} \right)^{\frac{1}{2}} = A (10^{-6} R_x)^{0.1}, \quad (4)$$

where  $X$  : turbulent boundary layer growing distance, presumably starts from the last screen or honeycomb in the setting chamber

$$A = \begin{cases} 0.35, & d^2p/dx^2 < 0 \\ 0.39, & d^2p/dx^2 \geq 0 \end{cases}$$

$$R_x = U_m X / \nu \approx \text{order of } [10^6].$$

Examining Eq. (4) reveals that the  $C_p$  value is a weak function of  $R_x$ . Moreover, it is convenient to assume that the locations of the last screen or honeycomb (or the virtual origin of the boundary layer) in all cases are the same for better comparison. Accordingly, a new dimensionless parameter

$$C_s = C_p \cdot \left( \frac{dC_p}{d(x/L)} \right)^{\frac{1}{2}} \quad (5)$$

is used as indicative of the possibility of the occurrence of a flow separation in the study.

#### Numerical Study

Numerical calculations were carried out in a selected two-dimensional case (see Fig. 3). The flare is a half-circular arc with a radius equal to  $R$ . The length of the straight chamber is 0.375 time of the contraction length ( $L=1.25H$ ). The shape of the following contraction is taken as a combination of two matched cubics according to Morel [6,7] with a contraction area ratio ( $CR = H/h$ ) equal to 3.

The flow characteristics within the inlet system are evaluated based on the three selected parameters ( $u_2$ ,  $\kappa$  and  $C_s$ ). The effects from the wall and ground are obtained for discrete values of three geometric factors:

$$R/H = 0.0875, 0.125, 0.25$$

$$W/H = 0.5, 1.0, 2.0$$

$$G/H = 0.3, 0.5, 1.0,$$

where  $W$  and  $G$  are the distances between the inlet edge and the wall and ground, respectively.

#### Results

##### 1) Contraction exit flow non-Uniformity

Figures 4 to 6 depict the contours of  $u_2$  as functions of  $W/H$  and  $G/H$  at different values of  $R/H$ . It appears that when the wall and ground distances are fixed, the flow at the contraction exit becomes more uniform as the radius of the flare increases. In all three cases, the exit flow non-uniformity increases as the distances decrease. In addition, the wall and ground effects on the exit flow uniformity appears more significant as the wall and ground distances are less than about  $H$ .

##### 2) Relaminarization Parameter

When the ground distance ( $G$ ) is finite, an asymmetric pattern of flow will be introduced into the tunnel system. As a result, flow characteristics along the upper and lower walls are different. From the viewpoint of design, one should consider the more critical one. The

relaminarization parameter ( $\kappa$ ) contours are plotted in Figs. 7 to 9 versus  $W/H$  and  $G/H$  for all three  $R/H$  values. It is quite surprised to find out that as the wall and ground distances decrease, the possibility of the occurrence of relaminarization also decrease. In other words, the wall and ground effects contribute to avoidance of boundary layer relaminarization.

### 3) Extreme Pressure Coefficient

After comparing the  $C_s$  value corresponding to the upper and lower walls in all cases of study, one finds that as  $W$  is kept at a value larger than about  $0.7H$  the critical condition occurs at the upper wall. Figures 10 to 12 show the critical  $C_s$  contours as functions of  $R/H$ ,  $W/H$  and  $G/H$ . It can be seen that a larger radius of the flare results in a smaller value of  $C_s$  (or a less chance of separation). When  $R$  is fixed, large distances of  $W$  and  $G$  increase the possibility of separation. Also, it is important to point out that the wall and ground have roughly the same extent of influence on the separation indicator ( $C_s$ ) as  $G$  and  $W$  are less than about  $H$ ; when the two distances are kept at a value larger than  $H$ , the influence from  $G$  appears more significant.

### Conclusions

Flow characteristics in the inlet system of a two-dimensional open, suction type of wind tunnel were investigated numerically. The wall and ground effects as well as the radius of the half-circular-arc flare were discussed according to three parameters, which correspond respectively to contraction exit flow uniformity, possibility of turbulent boundary layer relaminarization and separation. Results show that if the inlet edge is kept at finite distances away from the wall and ground, it will degrade the contraction exit flow and increase the possibility of flow separation in the system on one hand. On the other hand, however, it leads to a less possibility of the occurrence of relaminarization.

### Acknowledgements

The work was supported by National Science Council in Taiwan under grants No. NSC 80-0410-E-005-04.

### References:

1. Cohen, M.J. and Ritchie, N.J.B.(1962), J. Royal Aeronautical Society, V. 66, 231.
2. Bussel, H.H. (1969), AIAA Journal, V. 7, No. 10, 2017.
3. Barger, R.L. and Bowen, J.T.(1972), " NASA TN D-6962.
4. Chmielewski, G E.(1974), J. Aircraft, V. 11, No. 8.
5. Mikhail, M.N. and Rainbird, W.J.(1978), Paper 78-819, AIAA Aerodynamic Testing Conference, 376.
6. Morel, T.(1975), J. Fluids Engg., ASME, 225.
7. Morel, T.(1977), J. Fluids Engg., ASME, 371.
8. Farell, C. and Fang, F.M.(1985), 5th U.S. Conference on Wind Engg.
9. Fang, F.M.(1989), Ph.D. Dissertation, University of Minnesota.
10. Kline, S.J., Reynolds, W.C., Schraub, F.A. and Runstadler, P.W.(1967), J. Fluid Mech., V 30, Part 4, 741.
11. Moretti, P.M. and Kays, W M.(1965), Int. J. Heat Mass Transfer, V. 8.
12. Back, L.H., Cuffel, R.F. and Massier, P.F.(1970), J. Heat Mass Transfer, V 92.
13. Song, C.C.S. and Yuan, M.(1990), J. Fluids Engg., ASME, V. 112, 155.
14. Stratford, B S (1959), J. Fluid Mech., V. 5, 1.

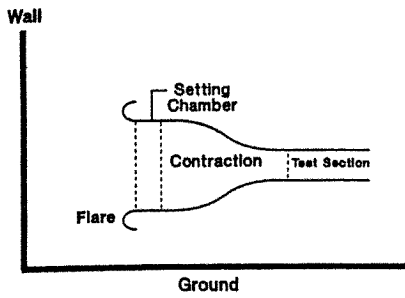


Fig. 1 Schematic of an open-type wind tunnel

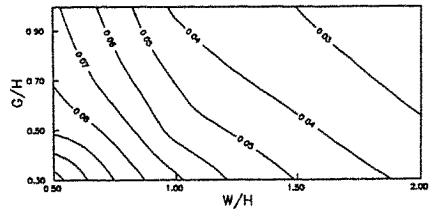


Fig. 4 Contraction exit flow non-uniformity ( $u_2$ ) as a function of  $W/H$  and  $G/H$  ( $R/H=0.0875$ )

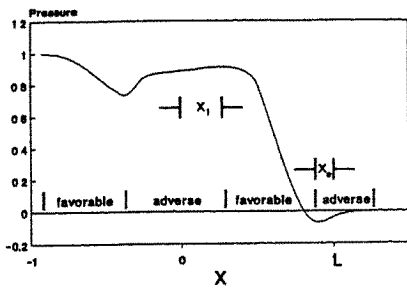


Fig. 2 Typical pressure distribution along wall in the inlet system

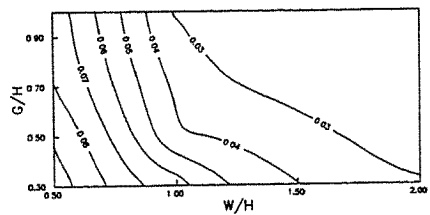


Fig. 5 Contraction exit flow non-uniformity ( $u_2$ ) as a function of  $W/H$  and  $G/H$  ( $R/H=0.125$ )

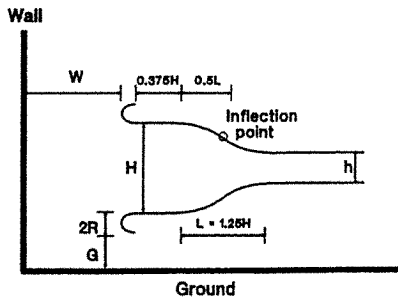


Fig. 3 Selected inlet system dimensions

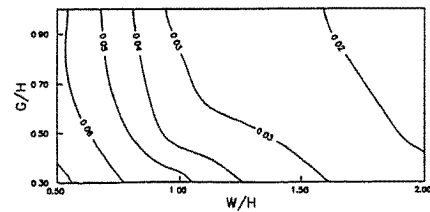


Fig. 6 Contraction exit flow non-uniformity ( $u_2$ ) as a function of  $W/H$  and  $G/H$  ( $R/H=0.25$ )

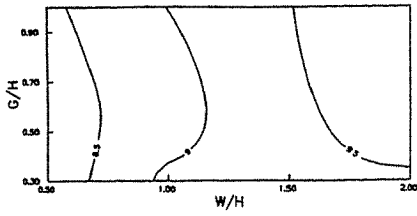


Fig. 7 Relaminarization parameter ( $\kappa$ ) as a function of  $W/H$  and  $G/H$  ( $R/H=0.0875$ )

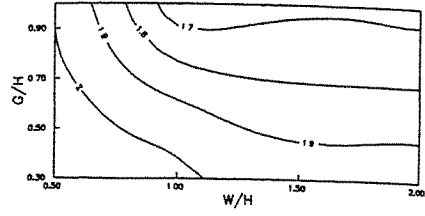


Fig. 10 Separation parameter ( $C_s$ ) as a function of  $W/H$  and  $G/H$  ( $R/H=0.0875$ )

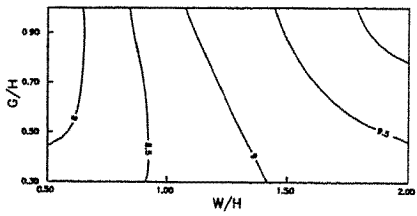


Fig. 8 Relaminarization parameter ( $\kappa$ ) as a function of  $W/H$  and  $G/H$  ( $R/H=0.125$ )

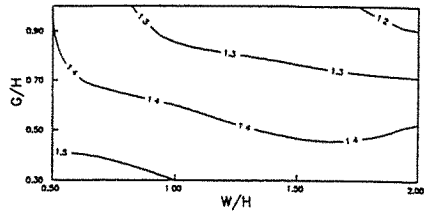


Fig. 11 Separation parameter ( $C_s$ ) as a function of  $W/H$  and  $G/H$  ( $R/H=0.125$ )

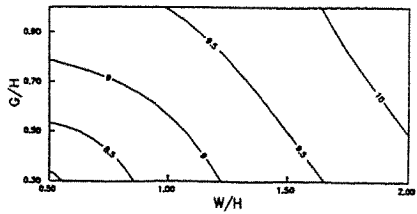


Fig. 9 Relaminarization parameter ( $\kappa$ ) as a function of  $W/H$  and  $G/H$  ( $R/H=0.25$ )

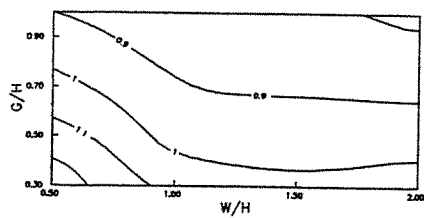


Fig. 12 Separation parameter ( $C_s$ ) as a function of  $W/H$  and  $G/H$  ( $R/H=0.25$ )



## Design of a low-cost stratified boundary layer wind tunnel

M. Schatzmann, J. Donat, S. Hendel  
Meteorological Institute  
University of Hamburg  
Hamburg, Germany

**Abstract:** A new stratified boundary layer wind tunnel has been developed and built. The tunnel is of closed circuit type with several layers, each of which insulated against the neighbouring layers, heated individually and driven by a separate fan.

The tunnel will be applied to solve environmental flow problems which are governed by stable atmospheric stability including elevated inversions.

### 1. Introduction

Atmospheric boundary layer wind tunnels play an important role in many meteorological and engineering applications. There are two main reasons for simulating the boundary layer in a wind tunnel. The first reason is to study the basic phenomena of micro-meteorological processes in the atmosphere. The second is to solve engineering problems of practical interest such as the dispersion of stack gases in complex terrain or in urban areas where buildings produce complex flow patterns.

In contrast to the many neutrally stratified wind tunnels which presently exist at several research institutions (for a survey see Hertig (1982)), wind tunnels which are able to generate thermally stratified layers are rather rare (worldwide about 15). This is certainly not due to a lack of interest in stratified flows since there exist many important applications for which stratification of the atmosphere is a key consideration. For example, air pollution problems are often critical in the presence of stable stratification or an inversion layer. Stratified boundary layer wind tunnels would be more widely used were it not for their high construction and operating costs.

### 2. Design of conventional stratified tunnels

As an example of the conventional type of stratified boundary layer wind tunnel, Fig. 1 shows the tunnel of the Military University of Munich, the only stratified boundary layer tunnel which was formerly available in Germany (Römer, 1989). This tunnel is equipped with a fan which sucks the air through a heating device and over a heated or cooled wind tunnel floor. To achieve a boundary layer of modest thickness with temperature, velocity and turbulence characteristics similar to nature, long tunnels are required (Cermak, 1993). The cost of the tunnel in Munich was about 8 Million DM, the power consumption of the fan, the heating section and the cooling section totals up to 1 MW.

### 3. Design of the multi-layer stratified tunnel

At Hamburg University, a new type of tunnel has been designed and built which is significantly cheaper than a comparable conventional tunnel and requires less laboratory space. The tunnel is based on an idea first introduced by Hertig (1982).

The tunnel is of closed circuit type. Fig. 2 shows a principal sketch of the tunnel. The return section is made up by 9 horizontal ducts of rectangular shape, the height and width of their cross sections is 12 cm and 2.3 m, respectively. The ducts are composed of 0.8 m long sheet metal boxes connected to one another and properly insulated against the wind tunnel hall and the neighbouring ducts by 2 cm

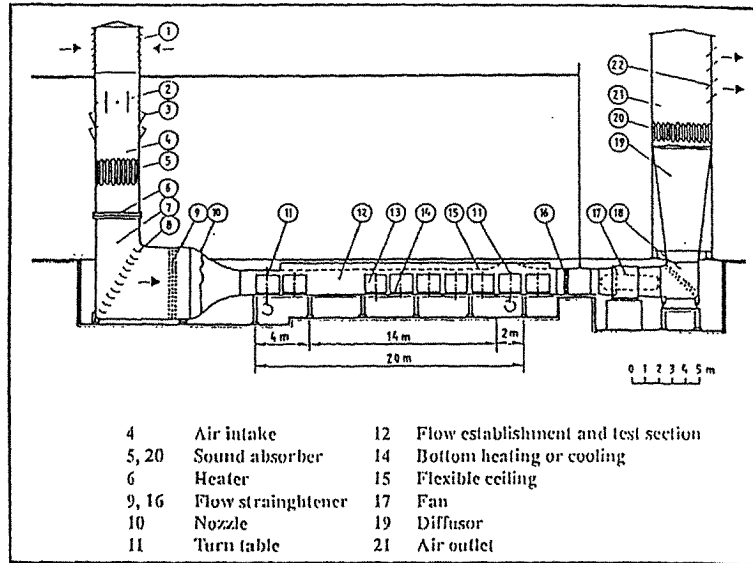


**Fig. 1:** Stratified boundary layer wind tunnel at Military University, Munich, Germany (from Römer, 1989).

thick sheets of insulation material. Small vertical pillars assure the accuracy to gauge and the stiffness of the boxes (Fig. 3).

In each of the ducts a separate fan and a bunch of 6 electrical heaters has been installed. The fans are driven by electromotors which are speed-controlled via microverters from a personal computer. Another PC controls the heaters and keeps the temperatures of the nine layers at pre-set values. Additional control mechanisms prevent the tunnel from being overheated.

The (tangential) fans, the motors, microverters and (tubular) heaters were all customary available and therefore inexpensive. The installed electric power is in total about 100 kW for the heating system and 20 kW for the electric motors.

The working section is made up by wood panels. It contains large double-glass windows in the side walls through which flow visualization experiments can be observed. The side walls are completely removable for periods when the tunnel is set up for a new experiment.

In the first 3.5 m of the working section floor a heat exchanger has been integrated which cools the floor down to about  $-20^{\circ}\text{C}$ . The coolant is supplied by a refrigerating machine as they are commonly used in the food processing industry. The wattage of the cooling system is about 15 kW. The subsequent test section floor is again wooden. It contains a turntable which is readily accessible from below the tunnel. The usable length of the test section is about 4.5 m. A 3-dimensional traversing system has been constructed which allows the remote-controlled transport of probes within the whole working section.

#### 4. Instrumentation of the tunnel

For the determination of boundary layer characteristics, temperature and velocity measurements have to be carried out. Continuous temperature registration is done by means of IC-temperature transducers (Analog Devices 592 CN) which work in the range  $-25^{\circ}\text{C} \leq T \leq 105^{\circ}\text{C}$  with about  $0.5^{\circ}\text{C}$  accuracy. The signals from the numerous sensors are processed by a personal computer equipped with an

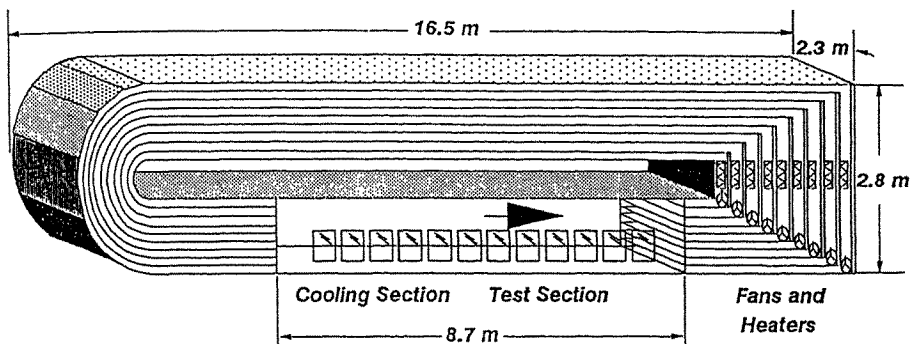


Fig. 2: Multi-layer stratified boundary layer wind tunnel of Hamburg University. Flow direction in the test section from left to right. Test and cooling section: length = 8.7 m, width = 2.3 m, height = 1.1 m.

A/D-card. The PC displays the actual vertical temperature profiles at the entrance and the exit of the test section.

Wind field and turbulence measurements are done with a DANTEC Laser-Doppler-Anemometer. The LDA used in Hamburg is equipped with a 300 mW Argon-Ion-Laser and a 2-dimensional fiber optic probe. The probe is as small as a cigar and can be moved with the traversing system. According to the manufacturer, the probe operates safely in environments with temperatures up to about 70°C.

### 5. Modes of tunnel operation

The tunnel operates in three distinct modes:

- (a) Neutral stratification: The mean velocity profile is generated by appropriate choice of the revolutions per minute of the nine tangential fans. In addition, roughness elements and, if necessary, vortex generators are employed to achieve turbulence characteristics which correspond to the real atmosphere.
- (b) Stable stratification: In addition to (a), the individual layers are heated and the bottom is cooled. The system installed provides temperature differences between the top layer and the ground up to 100°C which is sufficient to meet the Richardson number requirement for most dispersion problems.
- (c) Elevated inversion: Only a few layers at the top of the flow will be heated. The strength of the inversion can be modified by changing the temperature in these layers accordingly.

The convective boundary layer (which, however, prevails only a small percentage of the time of the year in central Europe) can not be simulated in our new tunnel. This is the domain of another multi-layer tunnel which is presently in the test phase at Karlsruhe University (Rau et al., 1991).

### 6. Boundary layer characteristics

In conventional stratified boundary layer wind tunnels (as well as in nature) the free stream velocity, the bottom roughness and the vertical heat flux determine the mean and fluctuating velocity and temperature field, provided the flow establishment section is sufficiently long that an equilibrium boundary layer can be achieved. This is different in a tunnel of multi-layer type. In such a tunnel arbitrary combinations of vertical velocity and temperature profiles are obtainable (at least within certain ranges), since the speed and temperature of the air in each layer are individually controlled. Only a small

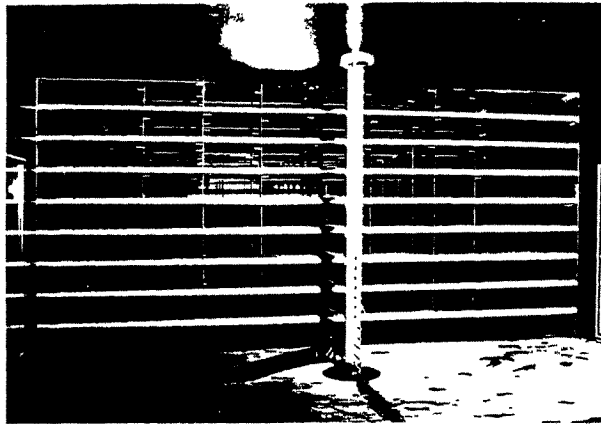


Fig. 3: View from the test section into the ducts. In front of the picture one of the rakes equipped with IC-temperature transducers can be seen.

number of possible combinations correspond to natural boundary layers and are of interest here.

At the begin of the test phase we started with neutral stratification and the same velocity in all layers. Neither vortex generators nor bottom roughness elements were in the tunnel. The vertical profiles of time averaged velocities and turbulence intensities at various test-section locations and at several velocities were measured. The situation was subsequently made more complex. A mean velocity profile was generated, vortex generators and roughness elements were added and, finally, the layers were heated and the bottom was cooled.

The results are too manifold to present them here in detail. Subsequently only a few examples will be given.

#### a) Neutral stratification, smooth floor

For three free stream velocities ( $u_\infty = 1.1$  m/s, 1.4 m/s and 2.9 m/s, measured at  $h = 52$  cm above ground) it was intended to generate a power-law profile with profile exponent  $n = 0.16$ . This value corresponds to boundary layers over smooth terrain. Fig. 4 shows the result at a position 3.6 m downwind from the entrance of the working section. Similar profiles were measured also further downwind. As can be seen, the desired mean velocity profile is easily achievable. The corresponding turbulence intensity profiles, however, are generally too low and not as smooth as expected. That means that much more time is needed until the turbulence characteristics adjust to the shear profile of the flow.

#### b) Neutral stratification, rough floor, vortex generators

In order to obtain a boundary layer of sufficient height ( $h \approx 50$  cm) and turbulence characteristics similar to nature, vortex generators in combination with sharp edged roughness elements (as they are used in our conventional unstratified boundary layer tunnel) were installed also in the multi-layer tunnel. Fig. 5 shows the result. The measurements from the conventional tunnel and from the multi-layer tunnel fall nearly on top of each other. Since the boundary layer characteristics from our conventional tunnel compare well with those known from field measurements (Schatzmann et al., 1988), this comparison can be interpreted as an indirect proof for the boundary-layer quality of also the multi-layer tunnel.

### c) Stable stratification

For a free-stream velocity of  $U(h) = 1 \text{ m/s}$  and mean and turbulence characteristics corresponding under neutral stratification to Fig. 5, tests have been carried out in order to determine the largest-obtainable, steady-state, linear, mean temperature gradient. Fig. 6 shows the result from different approaches. In each case both the heaters and the bottom cooling system were switched on. As can be seen, temperature gradients of about  $50 \text{ K/m}$  were generated. Since in undistorted models equal temperature differences over corresponding heights are required, this allows, e.g., small scale simulations

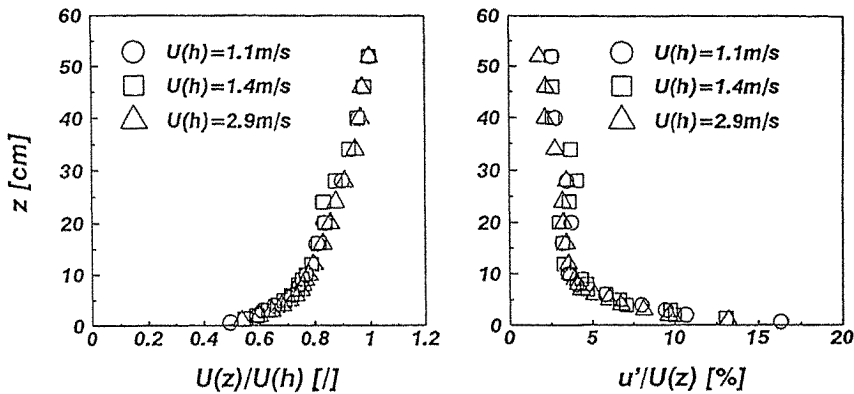


Fig. 4: Mean velocity and turbulence intensity profiles for various free stream velocities at the end of the cooling section. Smooth floor, neutral stratification.

in the scale 1:250 of up to  $20 \text{ K}/100 \text{ m}$  which is certainly more than needed.

It is remarkable that the temperature at the lowest probe position at  $z = 4.3 \text{ cm}$  above ground was already in the range of  $+30^\circ\text{C}$  although the coolant temperature was kept constant at  $-15^\circ\text{C}$ . Basing the stability parameters on the temperature difference between the free-stream temperature and the coolant temperature, as is sometimes done in literature, would, therefore, be extremely misleading.

### d) Elevated inversion

Finally, the potential of the new tunnel to generate an elevated inversion was investigated. The same basic set-up of the tunnel with vortex generators and bottom roughness elements was utilized but the free stream velocity was somewhat reduced to  $U(h) = 0.7 \text{ m/s}$ . Only the upmost three layers were heated. The heaters of all other layers as well as the bottom cooling system were switched off in order to keep the temperature profile in the mixed layer below the inversion as neutral as possible. Fig. 7 shows the development of the inversion layer as a function of time. The strongest inversion layer was obtained 105 min after the start of the experiment with a temperature gradient at the base of the layer in the order of  $100 \text{ K/m}$ .

## 7. Conclusions

The new multi-layer stratified boundary layer wind tunnel was built for about 0.5 Mio DM which is much less than a conventional tunnel would have cost. With a maximal electric power consumption of  $135 \text{ kW}$  also the operating costs appear to be reasonable.

The tunnel is able to produce stable stratification sufficient for most environmental applications.

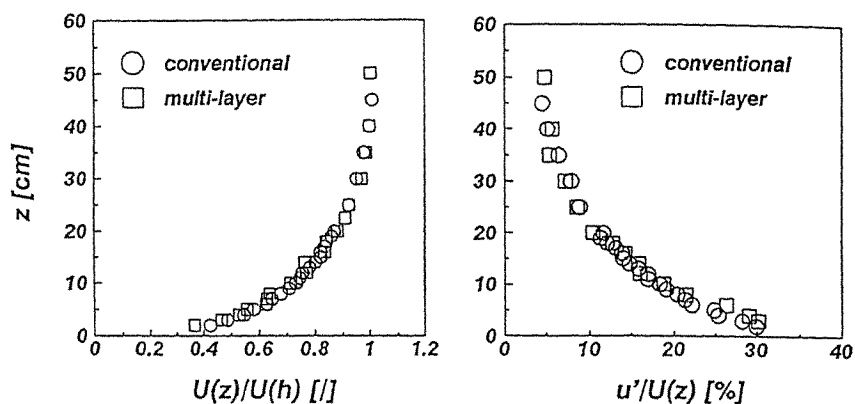


Fig. 5: Comparison of mean velocity and turbulence intensity profiles measured in a conventional boundary layer wind tunnel and in the new multi-layer tunnel. Vortex generators, rough flow, neutral stratification.

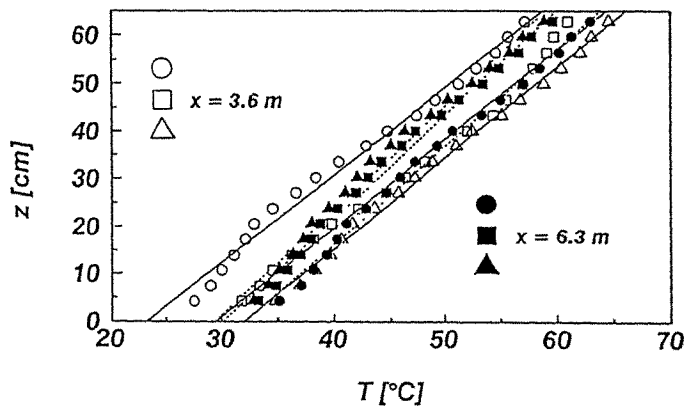


Fig. 6: Typical mean vertical temperature profiles realized in different tests at various locations of the test section.

There are, however, also disadvantages which should be noticed. As it was already mentioned in the text, a boundary-layer wind tunnel of multi-layer type has the potential of generating also such combinations of boundary layer parameters which are purely artificial and would never occur in reality. Thus, in comparison with a conventional tunnel, the simulation of a stratified boundary layer in the new tunnel requires more work until all major boundary layer characteristics are equal to pre-set values. Therefore, a very efficient control system for the temperature and velocity field is an essential necessity for such tunnels.

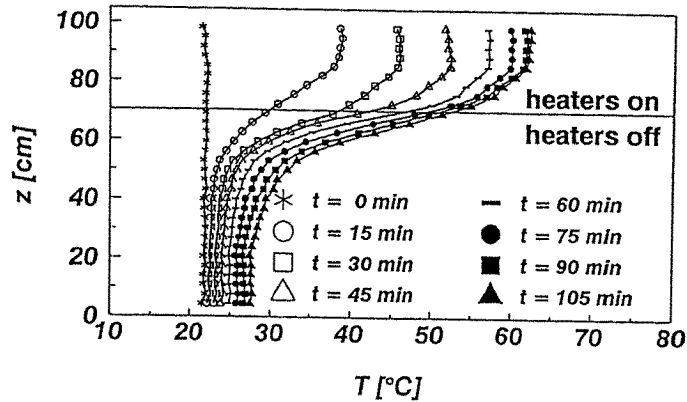


Fig. 7: Development of an elevated inversion as a function of time.

Since the length of the flow establishment section is usually not sufficiently long that equilibrium between mean and turbulent properties can be achieved, additional measures (increased bottom roughness, vortex generators) will mostly be necessary to adjust the turbulence to the mean field.

Other disadvantages are the fact that it takes substantial time until steady state conditions are obtained. As is the case with all recirculating tunnels, background concentrations increase rapidly when tracer experiments are carried out.

#### Acknowledgement

We are grateful to the German Ministry of Research and Technology (BMFT) for financial support.

#### References

1. Cermak, J.E. (1993) Physical modeling of flow and dispersion over urban areas. NATO Advanced Study Institute "Wind Climate in Cities", Waldbronn, Germany, July 5 to July 16.
2. Herig, J.A. (1982) A review of physical modeling of atmospheric air flows. Report, Ecole Polytechnique Fédérale de Lausanne, IENER, No. N 507.117.
3. Rau, M., W. Bächlin, and E.J. Plate (1991) Detailed design features of a new wind tunnel for studying the effects of thermal stratification. *Atmospheric Environment*, 26A, 1257-1263.
4. Römer, L. (1989) Simulation von Ausbreitungsvorgängen im Windkanal. In: *Ausbreitungsrechnung im Rahmen des Vollzugs der Störfall-Verordnung*, Texte des Umweltbundesamtes 1/89, Umweltbundesamt Berlin.
5. Schatzmann, M., and G. König-Langlo (1988) Application of scale modeling in environmental meteorology. *Proc. Int. Symp. on Scale Modeling Tokyo*, July 18-22.





## Basic Study on Blockage Effects in Turbulent Boundary Layer Flows

M. Noda, H. Utsunomiya and F. Nagao

Department of Civil Engineering  
University of Tokushima, Japan

**Abstract:** The blockage effects on the aerostatic forces such as the drag coefficient,  $C_D$  and the base pressure coefficient,  $C_{pb}$  were experimentally examined by using two dimensional rectangular cylinders,  $B/h=1.0$ , placed on the floor normal to flow direction in turbulent boundary layer flows (TBLF). At the same time, the effects of the wind characteristics of the TBLF on the aerostatic forces were investigated. It was shown that 1) the wind characteristics of the TBLF had little effect on the blockage constraint to the aerostatic forces, 2) the aerostatic forces were influenced by the wind characteristics of TBLF, in which the gradient of mean velocity profile at the height of model mainly controlled the flow properties around model.

### 1. INTRODUCTION

In wind tunnel measurements, the blockage effects is a very important problem to be solved. Many investigations on this problem have been carried out up to now. The easiest solution would be to use a huge wind tunnel or inversely a very small model, however either would be useless. Alternative positive procedures were summarized as follow; (1) To establish the blockage correction formula for bluff bodies; for example, Maskell proposed the correction equation for thin plates [1] and Awbi modified the Maskell's equation for two dimensional rectangular cylinders [2]. (2) To design the wind tunnel so that the requirement of corrections become negligibly small; for example, Parkinson [3] reproduced unconstrained flow patterns around the bluff body models by using the airfoil-slatted boundary configuration. Still more devices for a low-correction wind tunnel were also proposed such as flexible walls [4] and the longitudinal slats in these walls [5].

The correction of blockage constraint for the bluff bodies in uniform flows had already been achieved, however, the generalized correction formula for bluff bodies in TBLF has not yet been established.

In this study, the blockage effects for two dimensional rectangular cylinder placed on the floor normal to flow direction in TBLF are investigated (Case 1). Furthermore, the effects of the wind characteristics of TBLF on the aerostatic forces are also examined (Case 2).

### 2. EXPERIMENTAL CONDITION

#### 2.1 Models

In this study, two dimensional rectangular cylinders (the ratio of width  $B$  (parallel to flow direction) to height  $h$  (normal to the flow) of the cross section,  $B/h=1.0$ ) were used. The test model was placed on the floor normal to flow direction, as shown in Fig. 1. The drag force was calculated by the integration of the surface pressures. So the total drag force,  $D$  was able to separate into the upstream surface drag,  $D_u$  and the downstream surface drag,  $D_d$ . The total drag coefficient  $C_D$  can be written in the following form,

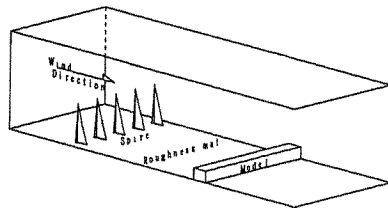


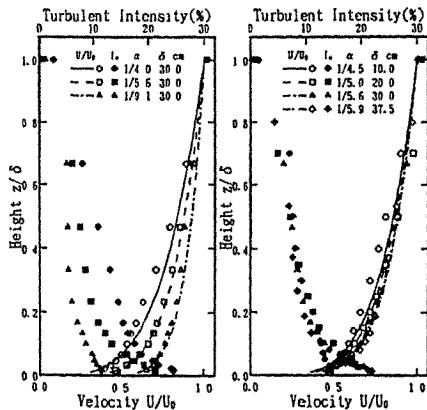
Fig. 1 Configuration of the wind tunnel test

$$C_D = C_{D_u} + C_{D_d} \quad \text{where } C_{D_u} = D_u / S q_h, \quad C_{D_d} = D_d / S q_h \quad (1)$$

where,  $q_h$  is dynamic pressure at the height of model, and  $S$  is the frontal area of the model.

## 2. 2 Turbulent boundary layer flows

Two groups of turbulent boundary layer flows (TBLF) were generated by using spires and roughness mats, and their flow properties are shown in Fig. 2. One group was three kinds of TBLF which had the different exponents of wind power law,  $\alpha=1/4, 1/5$  and  $1/9$  under the constant thickness of the boundary layer,  $\delta=30\text{cm}$ , to measure the effects of wind profile, as shown in Fig. 2 (a). Another group was four kinds of TBLF which had the different thickness of boundary layer,  $\delta=10, 20, 30$  and  $40\text{cm}$  under the constant exponent,  $\alpha=1/5$ , to examine the blockage effects, as shown in Fig. 2 (b). Furthermore, Fig. 3 represents the spectrum of fluctuating wind velocity which agrees with Von Karman's spectrum.



(a)  $\delta=30\text{cm}$   $\alpha=1/4, 1/5, 1/9$   
 (b)  $\alpha=1/5$   $\delta=10, 20, 30, 40\text{cm}$   
 Fig. 2 Properties of turbulent boundary layer flows

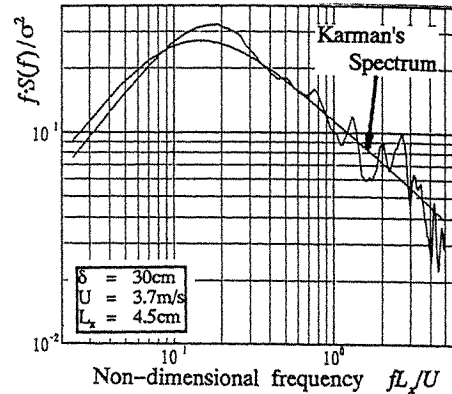


Fig. 3 Example of turbulent wind spectrum

## 2. 3 Details of experimental conditions

Table 1 (a) indicates the details of experimental conditions for Case 1. In this study, the ratio of the height of model,  $h$ , to the thickness of boundary layer,  $\delta$ ,  $h/\delta$  was kept 0.3 and 0.6. The blockage ratio ( $S/C$ ); the ratio of the frontal area of model,  $S$ , to the test section area,  $C$ ) was changed from 0.02 to 0.16 by altering the size of model.

Table 1 (b) indicates the details of experimental conditions for Case 2. One series of tests was carried out by changing the  $\alpha$  under the same  $\delta$ . (Case A~C,  $\alpha=1/4\sim 1/9$ ) Furthermore, the other test was also done by changing the  $\delta$  in constant  $\alpha$ . (Case D~G,  $\delta=10\sim 40\text{cm}$ )

Table 1 Details of experimental conditions

(a) for the test of blockage effects (Case 1)

Case	A	B	C	D	E	F	G	H
$\delta(\text{cm})$	10	20	30	40	10	20	30	40
$h(\text{cm})$	3	6	9	12	6	12	18	24
$h/\delta$	0.3	0.3	0.3	0.3	0.6	0.6	0.6	0.6
$S/C$	0.02	0.04	0.06	0.08	0.04	0.08	0.12	0.16

(b) for the effects of characteristics of TBLF (Case 2)

Case	A	B	C	D	E	F	G
$\alpha$	1/4	1/5	1/9	1/5			
$\delta(\text{cm})$	30			10	20	30	40
$h(\text{cm})$	6						
$h/\delta$	0.2			0.6	0.3	0.2	0.15

### 3. RESULTS AND DISCUSSION

#### 3.1 Blockage Effects in Turbulent Boundary Layer Flows (Case 1)

The pressure distributions measured by changing the blockage ratio for  $h/\delta=0.6$  are shown in Fig. 4. In this figure, the values of the pressures on the roof and downstream surface decrease with increase of the blockage ratio, however, the effects of the blockage ratio on the pressures on the upstream surface are almost negligible. Furthermore, the pressure distributions are almost same. Thus, it is found that the blockage effects are remarkable in the velocity of separated shear flow and the pressure in wake.

Fig. 5 shows the coefficients of the aerostatic force in  $h/\delta=0.6$ , due to the change in the blockage ratio. The coefficient of drag exerted on the downstream surface,  $C_{Dd}$ , and the total drag coefficient,  $C_D$  increase by the wall constraint. This result agrees with the behavior of the pressure distributions.

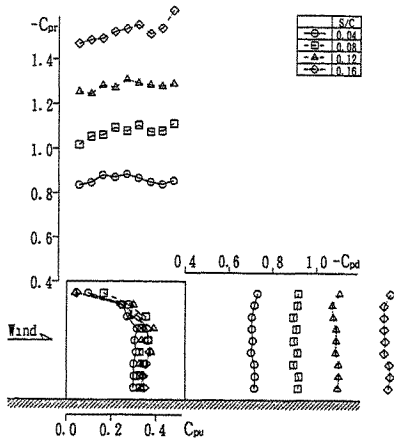


Fig. 4 Blockage effects on the pressure distributions ( $h/\delta=0.6$ )

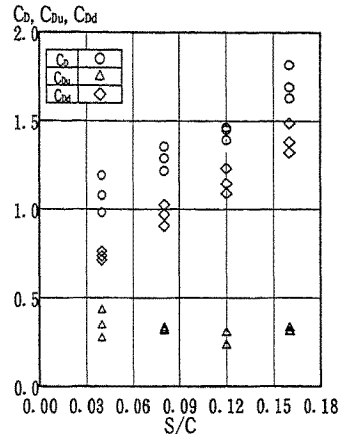


Fig. 5  $C_D, C_{Du}, C_{Dd}$  v.s.  $S/C$  ( $h/\delta=0.6$ )

Fig. 6 shows the relation between the drag coefficients and  $C_{Dd}S/C$  which is a modification of Maskell's equation by superseding the total drag coefficient,  $C_D$ , with the coefficient of the downstream surface drag,  $C_{Dd}$ . It is shown that each drag coefficients are increasing linearly with the  $C_{Dd}S/C$ , hence the relations between the drag coefficients and the  $C_{Dd}S/C$  can be represented by following equations;

$$C_{Du} = C_{Duc} + K_{Du} C_{Dd} S/C \quad (2)$$

$$C_{Dd} = C_{Ddc} + K_{Dd} C_{Dd} S/C \quad (3)$$

$$C_D = C_{Dc} + K_D C_{Dd} S/C \quad (4)$$

where,  $K_D, K_{Du}$  and  $K_{Dd}$ ; blockage factors for the total drag coefficient, for the coefficient of the upstream surface drag and for the coefficient of the downstream surface drag, respectively,

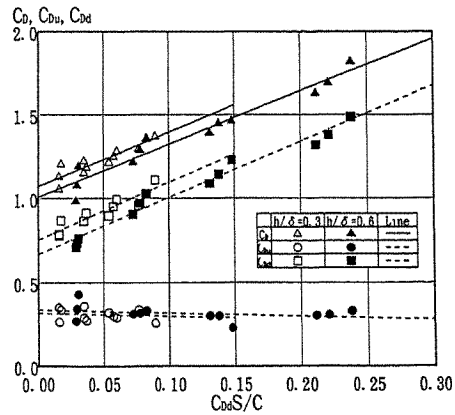


Fig. 6  $C_D, C_{Du}, C_{Dd}$  v.s.  $C_{Dd}S/C$

subscript 'c'; denoting the value undisturbed by the wall constraint. The values of  $K_D, K_{D_u}$  and  $K_{D_d}$  are given in Table 2. It is found that the blockage factors have the same values,  $K_D=3.2$ ,  $K_{D_u}=-0.2$  and  $K_{D_d}=3.4$ , being independent on the  $h/\delta$ . Thus, using  $C_{D_d}S/C$ , the blockage factors can be presented with constant values in TBLF. However, it seems that  $K_{D_u}$  is negligible, because  $K_{D_d}$  is small enough in comparison with other blockage factor.

Table 2 The measured blockage factor

$h/\delta$	$K_{D_u}$	$K_{D_d}$	$K_D$	$C_{D_{uc}}$	$C_{D_{dc}}$	$C_{D_c}$
0.3	-0.2	3.4	3.2	0.3	0.8	1.1
0.6	-0.2	3.4	3.2	0.3	0.7	1.0

### 3. 2 Blockage correction

The following blockage correction equations for two dimensional rectangular cylinders placed on the wind tunnel floor in TBLF can be derived by the equations (2), (3) and (4);

$$C_{D_{uc}} = C_{D_u} \quad (5)$$

$$C_{D_{dc}} = C_{D_d} - K_{D_d} C_{D_d} S/C \quad (6)$$

$$C_{D_c} = C_D - K_D C_{D_d} S/C \quad (7)$$

By using these blockage correction equations, the coefficients of the measured aerostatic force,  $C_D, C_{D_u}$  and  $C_{D_d}$  are corrected as shown in Fig. 7. The lines drawn in Fig. 7 indicate the measured values. The each corrected value successfully coincides for each  $h/\delta$ . In the practical wind tunnel measurement, the coefficient of the downstream surface drag,  $C_{D_d}$  will not be able to be measured easily.

Accordingly, it is to be desired that the base pressure coefficient,  $-C_{pb}$  is used in place of the coefficient of the downstream surface drag,  $C_{D_d}$ , because  $C_{D_d} = -C_{pb}$ , as follows;

$$C_{D_{dc}} = C_{D_d} - K_{D_d} C_{pb} S/C \quad (8)$$

$$C_{D_c} = C_D - K_D C_{pb} S/C \quad (9)$$

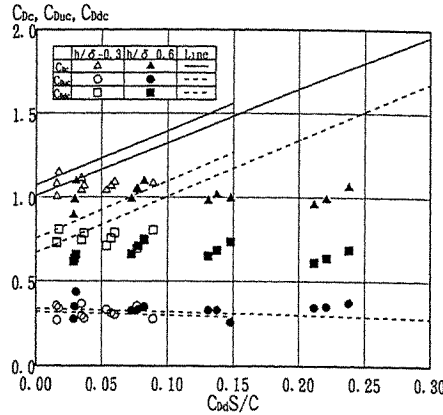
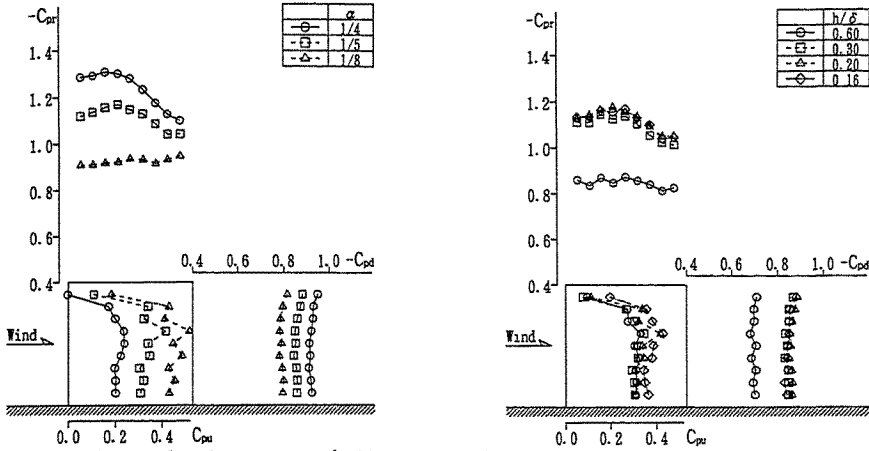


Fig. 7 The correction of  $C_D, C_{D_u}$  and  $C_{D_d}$

### 3. 3 Effects of the wind characteristics of TBLF on the aerostatic forces

The blockage corrections of the coefficient of the total drag,  $C_{D_c}$ , and the coefficient of the downstream surface drag,  $C_{D_{dc}}$  are given in Table 2 for  $h/\delta$ . The cause of this disparity can be inferred from the effects of the wind characteristics. Therefore, the effects of the wind characteristics on the aerostatic forces and the pressure distributions were experimentally examined by changing the exponent  $\alpha$  of wind profile and the thickness  $\delta$  of boundary layer.

The pressure distributions were measured in TBLF with three kinds of exponent,  $\alpha=1/4, 1/5$  and  $1/9$  under the constant thickness of boundary layer,  $\delta=30\text{cm}$ , as shown in Fig. 8 (a). The results of measurements by changing the thickness of boundary layer,  $\delta=10, 20, 30$  and  $40\text{cm}$ , under same wind profile, with exponent  $\alpha=1/5$  are shown in Fig. 8 (b). In Fig. 8 (a), the values of the upstream surface pressures decrease with increase of  $\alpha$ , and the pressures on the roof surface were changed from almost uniform distribution, which can be seen in the uniform flows, into the forms, which can be seen in the turbulent flows, by the increase of  $\alpha$ . In Fig. 8 (b), the pressure distributions on the upstream surface show almost the same shape. But the roof surface show the same change as given in Fig.8 (a), by the decrease of  $h/\delta$ .



(a) Effects of  $\alpha$  under the constant  $\delta=30\text{cm}$  (b) Effects of  $h/\delta$  under the constant  $\alpha=1/5$   
 Fig. 8 The effects of the wind characteristics of TBLF on the pressure distributions

Fig. 9 shows the relations between the aerostatic force coefficients and the exponent  $\alpha$  of wind power law. In Fig. 9, the total drag coefficient,  $C_D$ , decreases with increase in  $\alpha$ . This phenomenon is mainly caused by decrease in the coefficient of the upstream surface drag,  $C_{Du}$ . Inversely, the coefficient of the downstream surface drag,  $C_{Dd}$ , increases with increase in  $\alpha$ .

Fig. 10 shows the relations between the aerostatic force coefficients and  $h/\delta$ . In Fig. 10, it is found that the total drag coefficient,  $C_D$ , and the coefficient of the downstream surface drag,  $C_{Dd}$ , decrease with increase in  $h/\delta$ .

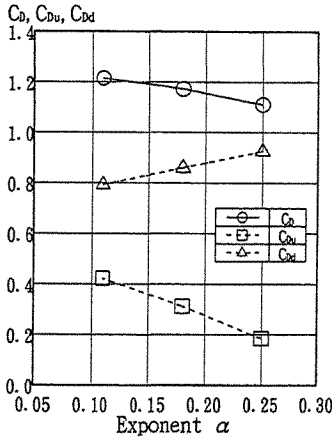


Fig. 9  $C_{Du}, C_{Dd}, C_D$  v.s.  $\alpha$

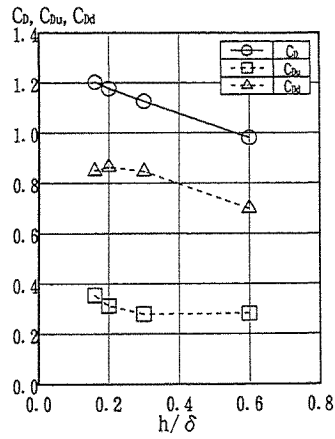


Fig. 10  $C_{Du}, C_{Dd}, C_D$  v.s.  $h/\delta$

From Fig. 9 and Fig. 10, it can be found that the coefficient of the downstream surface drag,  $C_{Dd}$ , increases with increase in the turbulence intensity at the height of model. However, it is said that the turbulent has the effect to recover the base pressure for the rectangular cylinder, in turbulent flows [6][7]. It is inferred that this phenomenon is caused by the wind

profile. Here, the non-dimensional gradient of wind velocity profile at the height of model is defined as follows;

$$\gamma = (d\bar{U}/d\bar{z})_{h/\delta} \quad \text{where } \bar{U} = U_z/U_G, \quad \bar{z} = z/\delta \quad (10)$$

The relation between the non-dimensional gradient and the coefficient of the downstream surface drag is shown in Fig. 11. It can be found that the wake pressure is strongly depended on the gradient of wind velocity profile at the height of model in TBLF and the coefficient of the downstream surface drag has a linear relation to the non-dimensional gradient  $\gamma$  at the height of model.

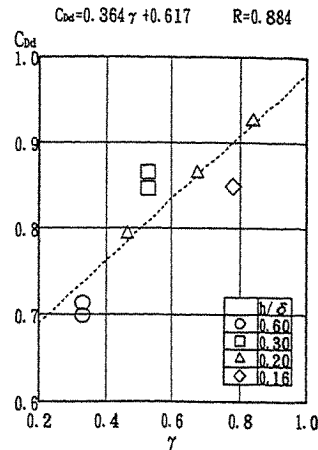


Fig. 11  $C_{Dd}$  v.s.  $\gamma$

#### 4. CONCLUSIONS

The following results are obtained:

- 1) The total drag coefficient,  $C_D$  for all models are increasing linearly with the  $C_{Dd}S/C$ . The increase of  $C_D$  due to the blockage effects is mainly caused by the increase of the coefficient of the downstream surface drag,  $C_{Dd}$ . Thus, the blockage constraint influences to the velocity of separated shear flow and the pressure in wake.
- 2) The blockage factor  $K_D$  became the constant value,  $K_D = 3.4$ , being independent on the  $h/\delta$ . By using this factor, the corrected value successfully coincides for each  $h/\delta$ .
- 3) The  $C_p$ -distribution and the downstream surface drag are influenced by the wind characteristics of TBLF. This phenomenon is mainly depended on the gradient of mean velocity profile at the height of model. The wake pressure has a linear relation to the non-dimensional gradient  $\gamma$  at the height of model.

#### 5. REFERENCE

- (1) E. C. Maskell, "A Theory of the Blockage effects on Bluff Bodies and Stalled Wings in a Closed Wind Tunnel", A.R.C.R. & M. 3400, (1963).
- (2) H. B. Awbi, "Wind-Tunnel-Wall Constraint on Two-Dimensional Rectangular-Section Prisms", J. Ind. Aerodyn., Vol. 3, (1978).
- (3) G. V. Parkinson and M. Hameury, "Performance of the Tolerant Tunnel for Bluff-Body Testing", Proc. BBAA, Kyoto, Japan, (1988).
- (4) U. Ganzer, "Wind Tunnel with Adaptive Walls for Reducing Wall Interface", Z. Flugwiss, Vol. 3, (1979).
- (5) S. Raimondo, P. J. F. Clark, "Slotted Wall Test Section for Automotive Aerodynamic Test Facilities", Proc. AIAA 12th Aero. Test. Conf., Williamsburg, (1982).
- (6) J. A. Roberson et al, "Turbulent Effects on Drag of Sharp-Edged Bodies", Proc. ASCE, HY7, (1972).
- (7) D. G. Petty, "The Effects of Turbulence Intensity and Scale on the Flow Past Square Prism", J. of Ind. Aerodyn., Vol. 4, (1979).

## **Optimization of pressure measurement system for wind tunnel experiments**

B. Bienkiewicz and Y. Sun

Department of Civil Engineering  
Colorado State University  
Fort Collins, Colorado 80523, USA

**Abstract:** This paper presents the experimental results of the optimization of the frequency response of pressure measurement systems used in wind-tunnel experiments. The major contribution of the present study is the idea of employing a restrictor at the output port of a scanivalve for point pressure measurement. As a result, only one restrictor is needed for one scanivalve channel. The measurement of the area-averaged pressure using pneumatic manifold is also addressed. The effects of the number and the non-symmetry of the manifold input channels on the system frequency response are discussed.

### **1. Introduction**

Typical pressure-measurement systems, used in wind tunnel experiments, consist of pressure transducers and tubing connecting the transducers with pressure taps on the surface of a model of a building or a structure. The wind pressures are time-dependent and they may be distorted due to the acoustic resonances and damping of the measurement system. Both the amplitude and the phase of the signal sensed by a pressure transducer may be altered. Since fluctuating wind pressures are of interest in physical modeling of wind loading on buildings and structures, it is desired to minimize the distortions of pressure signals.

The amplitudes and the positions of resonant peaks of the system depend on the length and the diameter of the tubing, Bergh & Tijdeman [1] and Gerstoft & Hansen [2]. The frequency at which the resonant peaks occur is lower for longer tubing, while the peak amplitudes are higher for tubing of a larger diameter. Therefore in order to minimize the distortion effects, short tubing with restrictors of small diameter have been frequently used by researchers (Holmes & Lewis [3, 4] and Holmes [5]). Alternative approaches employing numerical corrections (Irwin et al. [6]) and controlled leakage methods (Gerstoft & Hansen [2]) have been also reported.

The use of scanivalves to accommodate switching between pressure channels introduces further distortions in the pressure signal. To obtain the best frequency response for point pressure measurement, tubing systems incorporating restrictors placed at the input ports of a scanivalve have been used (Holmes & Lewis [3]). This configuration requires each input line to the scanivalve to have its own restrictor. Such arrangement is not convenient when many pressure taps are connected to a scanivalve.

The measurement of area-averaged pressure is typically accomplished through the use of pneumatic manifolds. Holmes and Lewis [4] investigated the effects of number of inputs on the frequency response for manifolds with parallel inputs. In the case of non-parallel inputs, such as star-shaped manifolds, the effects of the non-symmetry of the inputs have not yet been addressed.

This paper summarizes the experimental investigation of the frequency response of a point pressure measurement system with a scanivalve and an area-averaged pressure measurement system

with a star-shaped manifold. The optimal configuration of the scanivalve-tubing system is proposed. It employs a single restrictor placed at the output port of the scanivalve. As a result only one restrictor is required for each channel of a scanivalve. The effects of restrictor location are also investigated for such a scanivalve-tubing system. For the area-averaged pressure measurement system, studied are the effects of the number of manifold input ports and the input non-symmetry on the system frequency response.

## 2. Evaluation of Transfer Function

### 2.1 Experimental arrangement

The experimental set up for the measurement of the transfer function of a tubing system is shown in Fig.1. A Gaussian white noise voltage signal was used to drive a speaker. The speaker was sealed and a fluctuating pressure field was generated in the cavity of the speaker. The frequency range of the pressure was adjusted through the low-pass filtering of the input signal. A reference pressure transducer was attached to the speaker to measure directly (without a tubing) the pressure in the cavity. A second identical transducer was linked with the pressure source through a tubing system to be calibrated. The time series sensed by the two pressure transducers were collected using a microcomputer. The 1.59-mm internal diameter tubing was made of PVC. Restrictors used in the study were also made of PVC tubing and their internal diameter was about 0.4 mm.

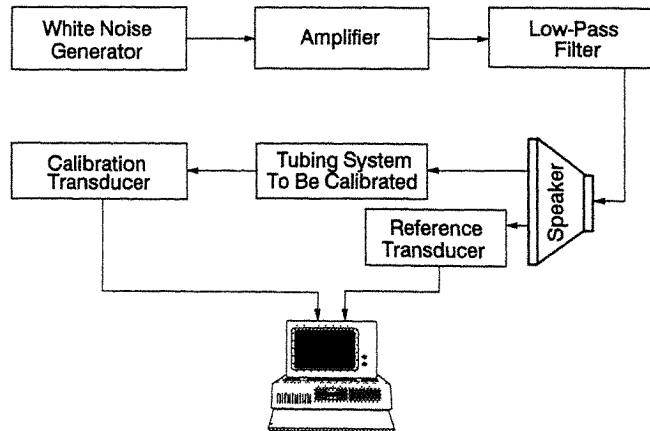


Fig.1. Experimental configuration

### 2.2 Transfer function

The transfer function of a tubing system,  $H(f)$ , is defined as

$$H(f) = \frac{G_{xy}(f)}{G_x(f)} \quad (1)$$

where  $G_{xy}(f)$  is the cross-spectrum of input ( $x$ --reference, undistorted) and output ( $y$ --calibration,



distorted) pressure signals, and  $G_p(f)$  is the power spectrum of the input pressure. The magnitude of  $H(f)$  represents the amplification/attenuation of the pressure signal by the tubing system, while the phase of  $H(f)$  represents the delay of the signal.

### 3. Results and Discussion

#### 3.1 Point pressure system with a scanivalve

The scanivalve (Scanivalve 48J9GM) used in the study had four channels driven by one stepping motor. Each channel of the scanivalve had 48 input ports and one output port. The experiments described in the paper were carried out for one of the channels of the scanivalve. The internal structure of the scanivalve involves right-angle bends of pressure paths. According to Holmes & Lewis [3], the effects of such paths on the scanivalve frequency response can not be modeled by an equivalent length of tubing.

The tested scanivalve-tubing system consisted of a tubing (between an input port of the scanivalve and a pressure tap) which was 280 mm long. The length of tubing connecting the output port of the scanivalve with the pressure transducer was 95 mm for the original configuration (before the system optimization), as indicated in Fig.2. The magnitude and the phase of the system transfer function of the original and the optimized scanivalve-tubing system are shown in Fig.2. The magnitude of the transfer function of the original system has a resonant peak around 120 Hz and a non-linear phase. After optimization, the system transfer function is nearly flat (close to unity with derivation less than  $\pm 5\%$ ) up to 200 Hz, and the phase (of the transfer function) is nearly linear within this frequency range. The optimized system employed a 80-mm long restrictor at the output port of the scanivalve, i.e., between the scanivalve and the pressure transducer. Compared with the conventional method, which uses restrictors at the input ports of a scanivalve, the current method is more practical because it requires only one restrictor for one scanivalve channel. Furthermore, since the restrictor in the present study is made of standard PVC tubing, it is easy to prepare restrictors of similar performance.

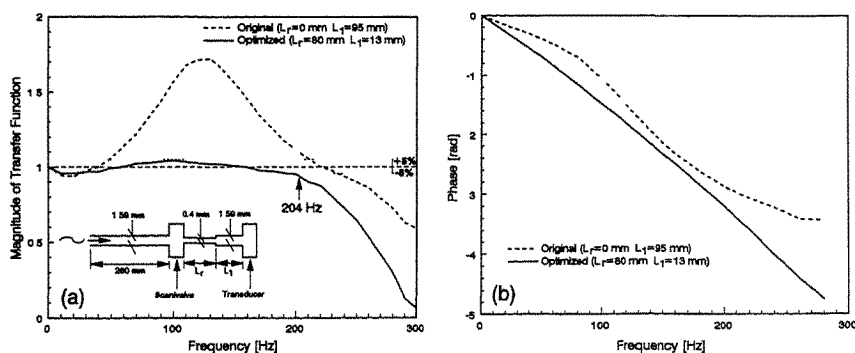


Fig.2. Transfer function of the original and the optimized scanivalve-tubing system: (a) magnitude; (b) phase

It was found that the frequency response of the scanivalve-tubing system was sensitive to the position of a restrictor relative to the pressure transducer, Fig.3a. As can be seen, as the restrictor is moved closer to the transducer, the attenuation of the resonant peak is reduced. However, the

phase of the transfer function does not change significantly. Although the total length of the tubing system was also altered (Configurations 1 through 4 in Fig.3), it was found that small changes in the total tubing length did not result in significant changes in the system frequency response. The main contribution to the change in the frequency response in Fig.3a came from the change in the restrictor position.

Figure 3b presents another example of the effects of the restrictor position. As described in the figure, the restrictor length was 70 mm. As the restrictor was moved away from the transducer (Configurations A and B), the resonant peak was attenuated. This trend is similar to that shown in Fig.3a. When the distance between the restrictor and the transducer was kept unchanged while the total tubing length was reduced (Configurations B and C), the resonant peak was reduced, due to the longer relative distance between the restrictor and the transducer. The results of Fig.3 are in agreement with findings reported by Holmes & Lewis [3].

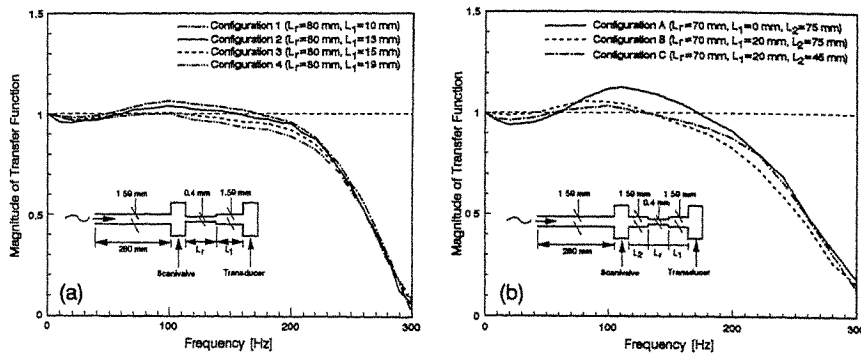


Fig.3. Effects of restrictor position

### 3.2 Area-averaged pressure system with a manifold

The star-shaped manifold used in the present study is shown in Fig.4. It has eight input ports and an output port. The input ports are connected with pressure taps and the output port transmits the pneumatically averaged pressure to a pressure transducer. Figure 5 depicts the frequency response of the original and the optimized manifold-tubing system. The resonant peak around 250 Hz of the original system was attenuated by a 63-mm long restrictor placed between the manifold and the transducer. This resulted in a transfer function with a constant magnitude and a linear phase up to 200 Hz.

The optimized manifold-tubing system was used to investigate the effects of the number and the non-symmetry of the manifold input ports. These effects are illustrated in Fig.6. It is seen that the number of input ports significantly affects the frequency response of the manifold-tubing system. When the number of input ports was increased, the frequency response of the system improved. This result is not in agreement with that of Holmes & Lewis [4], who concluded that the number of inputs of a manifold had small effects on the system frequency response. This discrepancy is probably due to differences in manifold geometry and configurations used in the studies.

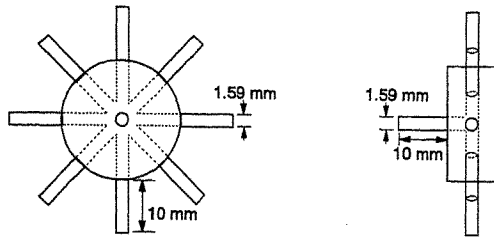


Fig. 4. Pneumatic manifold

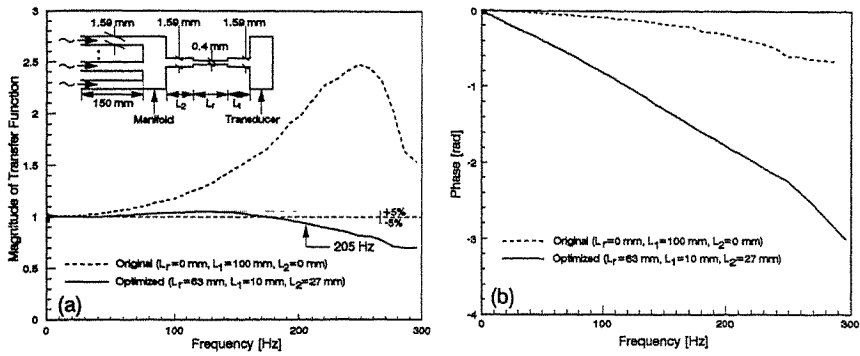


Fig. 5. Transfer function of the original and the optimized manifold-tubing system: (a) magnitude; (b) phase

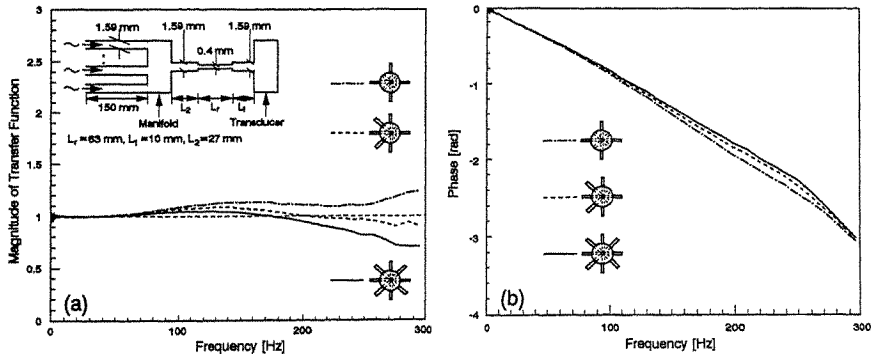


Fig. 6. Effects of number of manifold input ports on transfer function: (a) magnitude; (b) phase

The effects of the manifold input non-symmetry are shown in Fig.7 for two cases with four input ports, representing two extreme situations. As shown, the non-symmetry effects on the system frequency response are negligible.

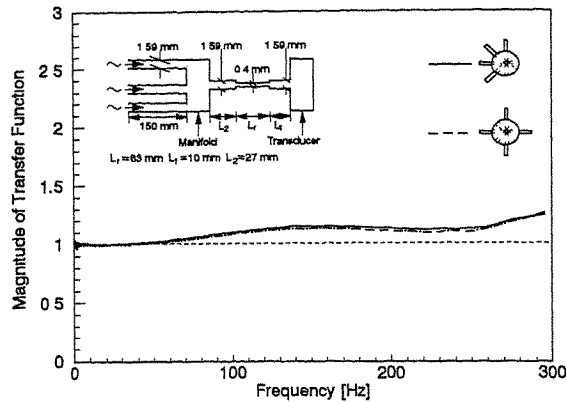


Fig.7. Effects of non-symmetry of manifold input ports on transfer function

#### 4. Conclusions

Point pressure measurement systems with scanivalves can be optimized using a restrictor at the output port of a scanivalve. This method is easy to implement. For such a tubing-scanivalve-restrictor system, the frequency response is sensitive to the restrictor location relative to the pressure transducer. Systems with pneumatic manifolds to measure area-averaged pressure can be optimized using a restrictor between a manifold and a pressure transducer. The number of input ports of a star-shaped manifold significantly affects the frequency response of the manifold-tubing system. The effects of non-symmetry of the manifold input are negligible.

#### References

1. Bergh, H. & H. Tijdeman, Theoretical and experimental results for the dynamic response of pressure measuring systems, Technical Report, National Aero- and Astronautical Research Institute, Amsterdam, Netherlands, No. NLR-TR-F238, January, 1965.
2. Gerstoft, P. & S.O. Hansen, A new tubing system for the measurement of fluctuating pressures, *J. Wind Eng. Ind. Aerodyn.*, 25 (1987) 335-354.
3. Holmes, J.D. and R.E. Lewis, Optimization of dynamic-pressure-measurement systems. I. Single point measurements, *J. Wind Eng. Ind. Aerodyn.*, 25 (1987) 249-273.
4. Holmes, J.D. and R.E. Lewis, Optimization of dynamic-pressure-measurement systems. II. Parallel tube-manifold systems, *J. Wind Eng. Ind. Aerodyn.*, 25 (1987) 275-290.
5. Holmes, J.D., A review of tubing techniques for measurement of fluctuating surface pressures, *Proceedings of the 2nd World Conference on Experimental Heat Transfer, Fluid Mechanics and Thermodynamics*, Dubrovnik, Croatia, June 23-28, 1991.
6. Irwin, H.P.A.H., K.R. Cooper & R. Girard, Correction of distortion effects caused by tubing systems in measurements of fluctuating pressures, *J. Wind Eng. Ind. Aerodyn.*, 5(1979)93-107.

## Geometric similitude applied to model and full-scale pressure tap sizes

Leighton S. Cochran, Marc L. Levitan<sup>+</sup>, Jack E. Cermak, and Byron B. Yeatts<sup>++</sup>

Department of Civil Engineering  
Colorado State University, Fort Collins, CO USA

<sup>+</sup>Department of Civil Engineering  
Louisiana State University, Baton Rouge, LA USA

<sup>++</sup>Department of Civil Engineering  
Texas Tech University, Lubbock, TX USA

**Abstract:** The collection of pressure data on low-rise building models in the wind tunnel has occasionally been compared to full-scale data. One of the few aspects of the geometric scaling process in the wind tunnel that is frequently not adhered to is the pressure tap size. On the prototype building surface it is common to use tap diameters of 8 mm or larger. This eases the practical problems of insect nesting and rain-water capillary action in the taps. Even at the relatively large scale of 1:100, the application of geometric similitude would require a model tap of 0.08 mm; an impractical diameter. In this discussion, mean and peak pressure coefficient data are presented for a larger tap at the full scale (diameter of 80 mm) to simulate a typical 0.8 mm diameter tap on the 1:100 model. The impact of this larger, area-averaging, full-scale pressure tap on the pressure coefficient data is presented and compared to the model-scale results.

### 1. Introduction

In recent years several comparisons of cladding pressures on low-rise structures have been made between wind-tunnel models and the corresponding full-scale building [1,2,3,4]. The most recent study [4,5,6] is the rotatable Texas Tech University (TTU) Test Building shown in Fig. 1.

In many flow situations the agreements between the model and full-scale mean and peak pressure coefficient data are good; regions of pure separation, reattachment and positive pressure. However, the peak minimum pressure coefficients under the roof corner vortices are underestimated by the wind-tunnel analysis by a factor of one and a half to two [4,5] for the cornering approach flow. It is demonstrated here that one contributing cause of this peak pressure coefficient mismatch under the corner vortices may be explained by the practice of not maintaining the correct geometrical scaling of the pressure taps themselves.

Some other phenomena that may be influencing the peak pressure coefficient mismatch under the corner vortices between the model on prototype include: (i) the large gusts and direction changes

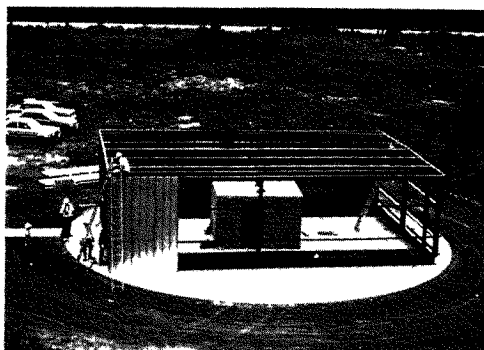


Fig. 1. The TTU Test Building under construction in Lubbock, Texas (1987). The fixed, internal blockwork room is where the data collection instrumentation are housed.

which wipe the vortices off the prototype roof are not modelled well in the wind tunnel [7,8]; (ii) full-scale atmospheric stability and solar insolation on the field site building; and (iii) the likely impact of the viscous stresses in the small vortices on the 1:100 model that seem disproportionately large (a vortex Reynolds number effect) [5]. Investigations of the Kolmogoroff length scales in the wind tunnel indicates that (iii) may be part of the answer, while the directional variation described in [5,7] appears to have little impact on the corner pressure coefficients. The atmospheric stability and surface heating issues have not been explored to date. As part of the ongoing investigation of this anomaly under the corner vortices the impact of mis-scaling the pressure tap itself is presented here using a full-scale device called the Super Pressure Tap (SPT).

## 2. The Super Pressure Tap (SPT)

A convenient pressure tap size that has been used on the TTU Test Building in Lubbock is a diameter of 8 mm. This size is comparable to that used by other researchers of prototype buildings [1,2,3]. Since the scale of the wind-tunnel models for low-rise pressure studies typically ranges from 1:50 to 1:250, the correct scaling of the tap size is not realistic. The smallest model tap size commonly used is in the range 0.5 mm to 1.0 mm. The value used in the Colorado State University (CSU) study was 0.8 mm [4,5]. Thus, the SPT was developed to explore this similitude anomaly between the model and full-scale pressure coefficients on the TTU Test Building.

Prior to the installation of the SPT onto the prototype building in Lubbock a series of tests were performed to judge whether the pneumatic averaging over the SPT was as expected. Fig. 3 shows the tap installed on a test stand (inclined at 20° from the horizontal) in the Industrial Wind Tunnel (IWT) at CSU. A variety of positive and negative pressure gradients were applied by rotating the test stand. Data were collected on both the individual 61 taps and with the area-averaging plug installed (Fig. 2) with one central tap. The tubing lengths were all 100 mm (with restrictor) and provided a flat frequency response to 250 Hz. A full description of the data collection system may be found in [4,5]. A summary of the results is presented in Table 1 and the contours of pressure coefficients over the SPT for the

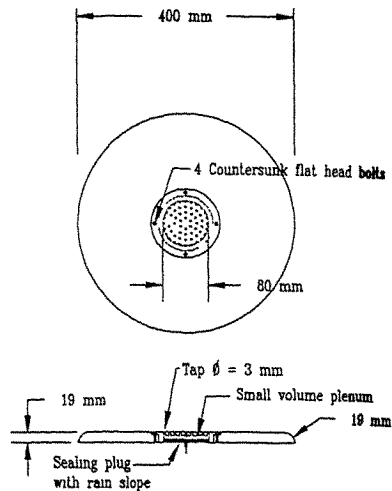


Fig. 2. Design sketch of the Super Pressure Tap (SPT) as installed on the prototype building in Lubbock.



Fig. 3. Initial testing of the SPT in the Industrial Wind Tunnel (IWT) at CSU. This orientation (0°) produces a positive pressure gradient since this view is from the upwind direction in the IWT.

steepest negative pressure gradient are in Fig. 4. The instantaneous pressure coefficient is defined as follows:

$$C_p = \frac{P - P_{ref}}{\frac{1}{2} \rho U_{ref}^2} \quad (1)$$

- P = pressure at a tap [Pa]
- P<sub>ref</sub> = reference static pressure [Pa]
- ρ = air density [kg/m<sup>3</sup>]
- U<sub>ref</sub> = mean velocity at eave level upwind of the test stand [m/s]

The tests in the IWT were only an indication of the SPT's performance. Obviously the flow scales and longitudinal turbulence intensities (14% at stand height) were not the same as the prototype flow, and the separated flow pressure gradient is steeper near the roof edge in full scale. However, as Table 1 indicates, the SPT gives representative average values of the individual pressures over the perforated surface; including a reduction in rms C<sub>p</sub> as one would expect.

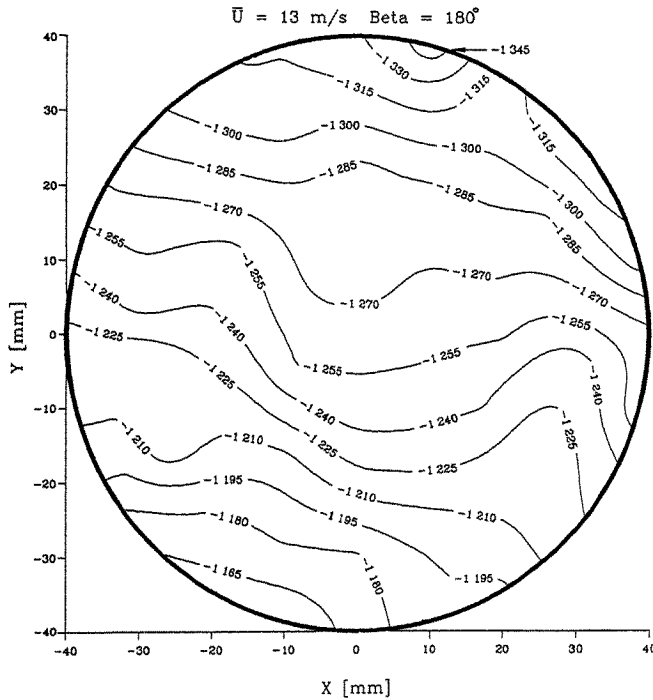
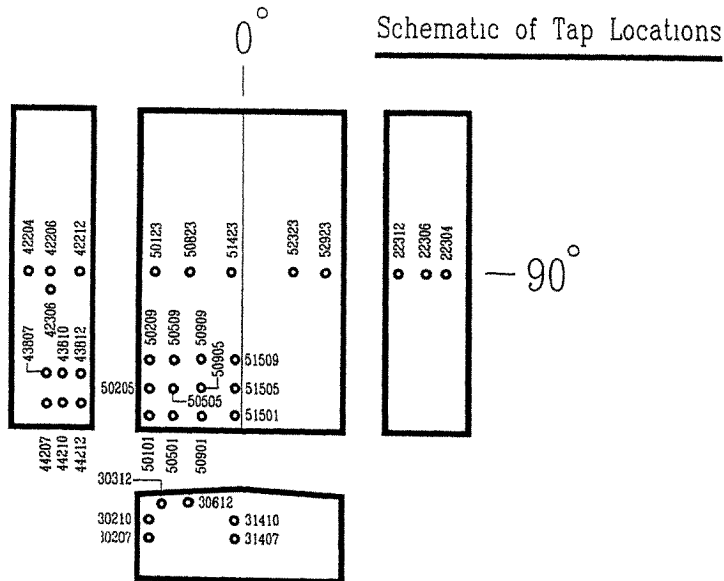


Fig. 4. Mean pressure coefficient variation over the 80 mm diameter of the SPT in separated flow collected at the IWT. This orientation had the largest pressure gradient and produced some reduction in the rms C<sub>p</sub> (Table 1).

	$\beta = 0^\circ$	$\beta = 45^\circ$	$\beta = 180^\circ$
<b>Individual Taps (Range)</b>			
Mean $C_p$	-0.026 to 0.012	-0.182 to -0.145	-1.349 to -1.151
Peak+ $C_p$	0.033 to 0.084	-0.128 to -0.084	-0.927 to -0.614
Peak- $C_p$	-0.136 to -0.056	-0.251 to -0.196	-1.840 to -1.544
rms $C_p$	0.017 to 0.019	0.014 to 0.016	0.103 to 0.126
<b>Area Averaged Tap</b>			
Mean $C_p$	-0.006	-0.147	-1.217
Peak+ $C_p$	0.067	-0.093	-0.787
Peak- $C_p$	-0.076	-0.204	-1.561
rms $C_p$	0.018	0.015	0.096

**Table 1:** Some statistical properties of the pressures on the SPT from data collected in the IWT.  $\beta$  is the orientation of the test stand from the position shown in Fig. 3.

After this preliminary testing the SPT was installed on the Texas Tech University Test Building at tap number 50501 (Fig. 5) and then moved to tap number 42206. This pneumatically averaged area is scaled to the tap size on the 1:100 wind-tunnel model (i.e. a 1:100 model tap diameter of 0.8 mm corresponds to a full-scale tap diameter of 80 mm).



**Fig. 5.** Schematic of tap locations on the TTU Test Building.



Data collected to date are presented in Figs. 6 and 7 (●) suggest that the peak pressure coefficient mismatch may be partially explained by the lack of tap similitude between the model and prototype. It seems that it is important to use the correct geometric tap size when the flow phenomenon is of a comparable scale to the tap itself. In this manner the peak pressure coefficients recorded in the field and recorded in the wind tunnel are averaged over the equivalently scaled area. However, a relaxation of this requirement may be valid when the flow scales are significantly larger than the tap size; as found under a separated shear layer or on the leeward/windward wall in Fig. 7.

### 3. Conclusions

These preliminary data on the use of the SPT to collect full-scale pressures indicate that the correct similitude is only necessary when the scale of the flow is comparable to the tap size. This situation is generally limited to corner vortex flows. In other flow regimes the more conventional 8 mm full-scale tap (which is not easily built into useful model scales) yields good agreement between model and prototype.

### 4. Acknowledgements

This study was performed with the funding provided under the United States National Science Foundation Grants BCS-8821542 and BCS-8821163 for the Colorado State University/Texas Tech University Cooperative Program in Wind Engineering. The authors wish to thank Mr. Russ Leffler for his assistance in collecting the wind-tunnel data and Ms. Gloria Garza for compiling this document.

### References:

1. Marshall, R.D., "A Study of Wind Pressures on a Single Family Dwelling in Model and Full Scale," *Journal of Industrial Aerodynamics*, Volume 1, No. 1, pp. 177-199, 1978.
2. Holmes, J.D., "Comparison of Model and Full-Scale Tests of the Aylesbury House," *Proceedings of the International Workshop on Wind Tunnel Modeling Criteria and Techniques in Civil Engineering Applications*, edited by Reinhold, T.A., pp. 605-618, Maryland, USA, 1982.
3. Hoxey, R.P., Robertson, A.P. and Richards, P.J., "Full Scale, Model Scale and Computational Comparisons of Wind Loads on the Silsoe Structures Building," *Proceedings of the Second Asia Pacific Symposium on Wind Engineering*, Beijing, China, pp. 477-484, June 1989.
4. Cochran, L.S. and Cermak, J.E., "Full-Scale and Model-Scale Cladding Pressures on the Texas Tech University Experimental Building," *Journal of Wind Engineering and Industrial Aerodynamics*, Volume 41-44, pp. 1589-1600, December 1992.
5. Cochran, L.S., "Wind-Tunnel Modelling of Low-Rise Structures," PhD Dissertation, Colorado State University, 509 p., Fall 1992.
6. Levitan, M.L., "Analysis of Reference Pressure Systems Used in Field Measurements of Wind Loads," PhD Dissertation, Texas Tech University, Fall 1992.
7. Cermak, J.E., Cochran, L.S. and Leffler, R., "Wind Tunnel Modelling of the Atmospheric Surface Layer," *Proceedings of the Third Asia Pacific Symposium on Wind Engineering*, Hong Kong, December 1993.
8. Parce, D., "Turbulent Dispersion About a Low Building with Emissions From a Short Stack," Master of Science Thesis, Colorado State University, Fall 1993.

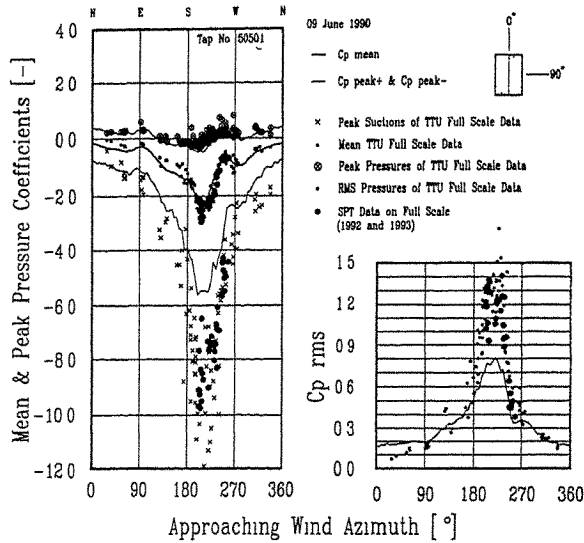


Fig. 6. Pressure coefficient data for tap number 50501 from the 1:100 model study (lines), the conventional full-scale 8 mm diameter tap and the 80 mm diameter SPT on the TTU full-scale building (roof vortex flow).

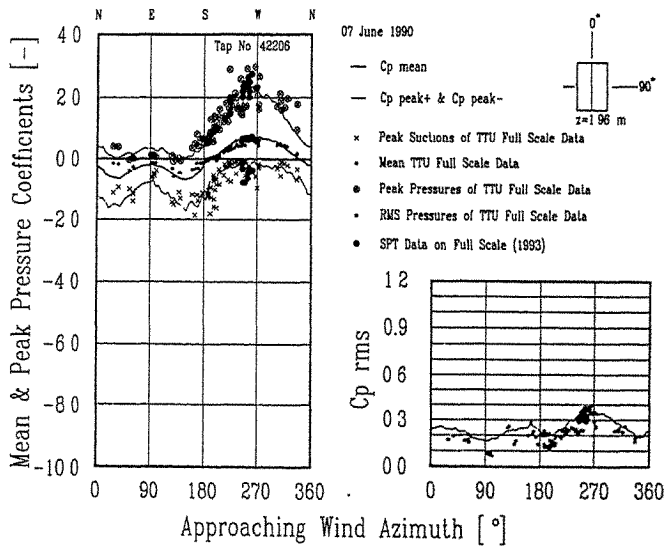


Fig. 7. Pressure coefficient data for tap number 44206 from the 1:100 model study (lines), the conventional full-scale 8 mm diameter tap and the 80 mm diameter SPT on the TTU full-scale building (leeward or windward mid-wall).

## Design and Calibration of High Frequency Base Balances Used for Dynamic Wind Load on Building Models

Chen Feng, Hu Guofeng and Lee, B. E. <sup>+</sup>  
China Aerodynamics Research & Development Center  
<sup>+</sup>University of Portsmouth, UK

**Abstract** High Frequency Base Balance technique is the most economical way to measure the dynamic loads on the entire building. Based on the practical experiences gained by China Aerodynamics Research and Development Center (CARD C) in recent years, this paper describes the design criterion and calibration method of such balances, and some typical test results, with high frequency balances designed and manufactured in CARD C, are presented.

### 1 Introduction

The trends towards lighter, more flexible and less damped structure has increased the importance of dynamic wind loads on tall buildings, which have to be determined experimentally in most cases. Although testing of an aeroelastic scale model in a boundary layer wind tunnel is accurately predicted, these tests are both expensive and time consuming. Since 1980's a high-frequency base balance (HFBB) technique has emerged and been in use in many wind engineering laboratories. The basis of the technique is the estimation of model wind loads on a building from overturning and torsional moments measured at the base of rigid model by using high frequency balance, which has been recognized as the most economical approaches. [1]

To establish the data base of dynamic wind loads on tall buildings, a parametric wind tunnel test program has been undertaken in CARD C under the China-UK joint project on "Assessment of Dynamic Wind Loads on Buildings"[2] and HFBB technique was utilized. In order to handle such a big test matrix, CARD C has designed and manufactured four balances of five-components to cover wide load range, including stem type and stem-plus-plate type. Those balances have either supported the joint project or provided to other wind engineering lab in China. The experiences in design and calibration of HFBB are summarised in this paper.

### 2 Design of High Frequency Balances

The critical point of HFBB technique is the estimation of power spectral density of mode generalized wind loads, which requires a balance to measure the complete time history. Therefore, the fundamental design criterion of the balance is to meet the requirement of high stiffness and good sensitivity.

The response measured during tests is greatly distorted near fundamental frequency of model-balance system. It is, hence, desirable for the balance to have high rigidity and flat frequency response over the range of frequencies of interest. The frequency also depends on the weight of the model which is therefore made as light as possible. The high natural frequency of balance-model combination would also reduce kinematic effects to meet the essential assumption of no aeroelastic feedback and would find the balance formula by static loading calibration. For most applications the frequency range above 100 Hz is desired since for the practical buildings it is necessary to measure the spectra for frequencies up to 30—40 Hz in wind tunnel.

The balance has to be sensitive enough to resolve much smaller fluctuating component from the wind

loads, since same balance has to measure the mean as well as the dynamic loads.

These are contradictory requirements and the appropriate compromise is necessary. The quality of the balance could primarily be assessed by a product of stiffness and strain output.

Other design requirements include uncoupled measurement of the orthogonal force components, stability and free of temperature and environment drift, good machinability, low cost and easy connection with the models.

Three different balance configurations have been used, stem-, plate- and stem-plus-plate type, and either foil strain gauges or piezoquartz may be employed as sensor elements. In order to achieve maximum rigidity, the measurement of normal forces was forgone, hence it is typical to measure five components of most interest in dynamic wind loads, both overturning moments, shear forces, and torque on the model base.

Since 1989, China Aerodynamics Research Development Center has designed and manufactured four 5-component high frequency base balances, covering wide load range and including both plate type and stem-plus-plate type.

Figure 1 schemes the configuration of two stem-plus-plate balances, JZW001 and JZW002. The building model is to be mounted on the central shear stem which is designed to sense the shear forces in two orthogonal direction and to transmit the wind loads into the cross girder sensing both overturning moments and torque at base.

The other two plate type balances, JZW003 and JZW004, are shown in Fig. 2. It simply consists of the moving frame and the earth frame. The former is a rigid cross girder, on which the models are to be attached. It is seen in the figure that to connect both frames there are six links. One of three vertical links, at the reference center O, supported the structure and restricted the motion in  $y$ -direction. The remaining five links, two vertical and three horizontal, transmitted the pull or push forces into corresponding load cells which were hinged at the link ends and fixed on the earth frame to measure the separate components of wind load. The hinges on both ends of the links were designed to mechanically resolve individual component and enable the simultaneous and independent measurement of all five components, since only the load along the link length would be transmitted.

The load cells were designed as bending beam or "s" beam with two holes. The miniature load cells, machined from hard aluminium alloy of high strength limit, have short length and great depth for lower modulus of elasticity. The quality of the balance was measured in a stiffness-strain product.

The strain gauges formed a full Wheatstone bridge. During the tests, the output from the bridge of each component was separated into static load (mean output) and dynamic load (filtered away the mean load and then amplified)

### 3 Calibration of High Frequency Balances

All the balances were statically calibrated in the Strain-Gauge Balance Calibration Rig, CARDC, by loading through standard weights and steel rope-pulley system. The balance output signals were put into IBM-PC/AT computer through amplifier, to obtain the balance formula and other parameters. The calibration results of four balances were given in Tab. 1. Also in calibration the fundamental natural frequencies of the balances were measured in hammer exciting way and by a dynamic analyzer SD-375. The natural frequencies are shown in Tab. 2 for three balances and five components.

### 4 Application of High Frequency Balances

Four 5-component high frequency base balances designed and made in CARDC have put into use in parametric test program in  $1.4\text{m} \times 1.4\text{m} \times 6.0\text{m}$  boundary layer test section, CARDC. According to the China-UK joint project "Assessment of Dynamic Wind Loads on Buildings", 12 different shapes of building models were tested to study the influences of model shape, wind direction, terrain and scaling. The

installation of the model-balance system in this wind tunnel is illustrated in Fig. 3, and the data acquisition and processing system is shown in Fig. 4.

The data on CAARC standard tall building model were compared with those from different wind tunnels around world,<sup>[3]</sup> the good agreement of which indicated the reliability of the balance.

The measurement precision of the balance has been examined in seven-run repeatability test and shown in Tab. 3.

## 5 References

- [1] Liu Shangpei, Dynamic Response of Tall Structure to Wind Action, CARDC Report, Nov. 1989.
- [2] Lee, B. E. , Liu Shangpei and Wang Qizhi, A Parametric Study of Dynamic Wind Loads on Buildings, Third Asia-Pacific Symposium on Wind Engineering, 13-15 Dec, 1993, Hong Kong.
- [3] Liu Shangpei, Wang Qizhi and Lee, B. E. , An Assessment of Dynamic Wind Loads on a Series of CAARC-Like Slender Buildings, Third Asia-Pacific Symposium on Wind Engineering, 13-15 Dec, 1993, Hong Kong.

Tab. 1 Specifications of four balances from static calibration

Balance	Configuration	Parameters	$F_z$	$F_z$	$M_z$	$M_x$	$M_y$
JZW001	Stem Plus Plate	Design load $\left(\frac{N}{N.m}\right)$	160	80	60	60	30
		Sensitivity $\left(\frac{N}{N.m}\right)$	0.5	0.5	0.1	0.1	0.6
		Precision (%)	0.07	0.14	0.07	0.03	0.55
JZW002	Stem Plus Plate	Design load $\left(\frac{N}{N.m}\right)$	100	100	50	50	50
		Sensitivity $\left(\frac{N}{N.m}\right)$	0.33	0.34	0.081	0.079	0.21
		Precision (%)	0.16	0.21	0.71	0.08	0.17
JZW003	Plate	Design load $\left(\frac{N}{N.m}\right)$	10	10	5	5	5
		Sensitivity $\left(\frac{N}{N.m}\right)$	0.022	0.019	0.0049	0.0048	0.002
		Precision (%)	0.092	0.167	0.153	0.232	0.325
JZW004	Plate	Design load $\left(\frac{N}{N.m}\right)$	100	75	35	35	4
		Sensitivity $\left(\frac{N}{N.m}\right)$	0.1	0.1	0.02	0.02	0.001
		Precision (%)	0.05	0.18	0.02	0.11	0.16

Tab. 2 Natural frequencies measured on three balance (Hz)

	$F_x$	$F_z$	$M_x$	$M_z$	$M_y$
JZW001	228	265	872	854	567
JZW003	90	126	232	340	142
JZW004	215	287	552	552	287

Tab. 3 Results for repeatability tests

	$C\sigma_{F_x}$	$C\sigma_{F_z}$	$C\sigma_{M_x}$	$C\sigma_{M_z}$	$C\sigma_{M_y}$
1st run	0.1552	0.1725	0.07617	0.04554	0.03678
2nd run	0.1550	0.1737	0.07452	0.04459	0.03598
3rd run	0.1577	0.1706	0.07675	0.04430	0.03587
4th run	0.1572	0.1727	0.07767	0.04521	0.03711
5th run	0.1528	0.1684	0.07436	0.04415	0.03666
6th run	0.1549	0.1729	0.07558	0.04612	0.03620
7th run	0.1546	0.1636	0.07622	0.04164	0.03645
mean $\bar{X}$	0.1553	0.1706	0.07589	0.04451	0.03643
rms $\sigma$	0.0017	0.0036	0.001184	0.00145	0.00045
relative error $\sigma/\bar{X}(\%)$	1.1	2.1	1.6	3.2	1.2

Model: 1/300 Yokohama building, Japan (F. S  $68 \times 48 \times 36$  m)

Simulated ABL:  $\alpha=0.40, V_R=18.80\text{m/s}, \beta=90^\circ$

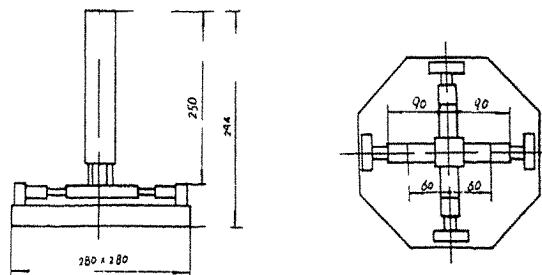


Fig. 1 Scheme of a stem-plus-plate balance JZW002

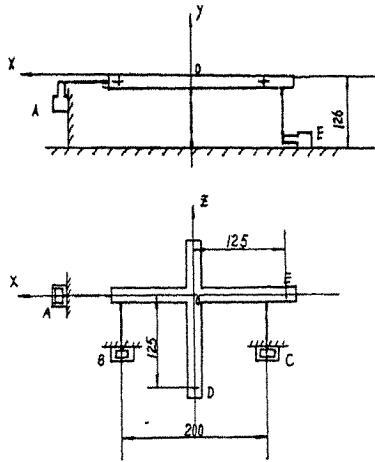


Fig. 2 Scheme of a plate balance JZW003

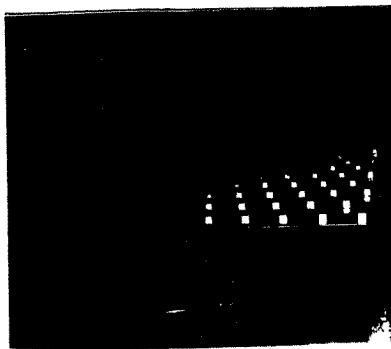


Fig. 3 Balance JZW003 with typical building model in wind tunnel

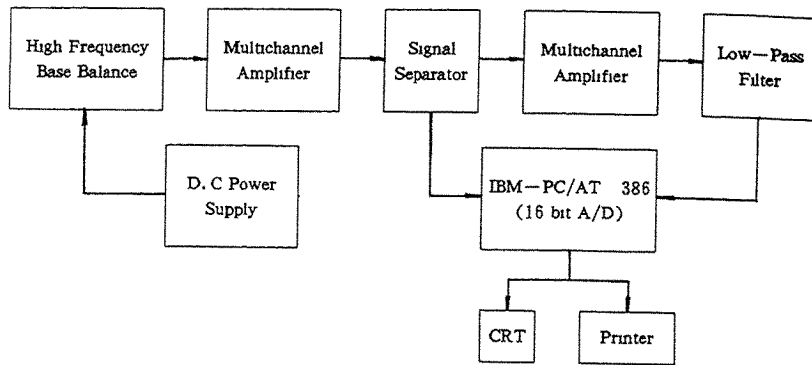


Fig. 4 Data acquisition system in HFBB tests



**A SIMPLE FIVE-COMPONENT BASE BALANCE FOR  
MEASUREMENT OF MEAN WIND LOADS ON BUILDING MODELS**

A.K.H. Kwan and K.M. Lam

Department of Civil & Structural Engineering  
University of Hong Kong, Hong Kong

**Abstract:** A plate type five-component base balance for the measurement of mean wind loads is developed. It is machined from a single piece of metal and does not require any expensive transducers. Calibration of the balance revealed that it is very stable and has a high sensitivity for the measurement of small wind loads. Its application is illustrated by using it to measure the overall wind loads on a tall building model.

**1. Introduction**

In spite of significant advances in wind loading codes, *ad-hoc* wind tunnel model tests are increasing being commissioned for building developments over the world. Necessity for an estimate of the dynamic behaviours of tall and flexible buildings is a main reason for model tests. Other principal reasons are quest for loading coefficients of unusual geometrical building forms and effects of complex topography.

For measurement of the dynamic behaviours of tall buildings, complicated and time consuming aeroelastic model testing methods have largely been replaced by the high frequency base balance technique which was first introduced in the 70s' [1-3] and subsequently developed to fruition by Tschanz in the 80s' [4,5]. This technique combines the dynamic loading components measured at the base of a rigid building model using a base balance with the dynamic properties of the structure to provide an estimate of the dynamic response. However, the base balance needed, which must have both high frequency response and high sensitivity at the same time, demand critical design and expensive investment because the two performance attributes impose contradictory requirements on the rigidity of the transducers.

Nevertheless, in less demanding situations, the dynamic wind loads may simply be estimated from the mean wind loads by using the quasi-steady equivalent-gust approach or more accurately the dynamic gust factor approach. The quasi-steady equivalent-gust method, though quite empirical, can still satisfy authorities in many countries as being adequate in estimating dynamic wind loads [6]. On the other hand, the dynamic gust factor method, which considers buffeting of wind turbulence by the building, has been well developed and included in the latest versions of some wind loading codes [7]. Hence, measurement of mean wind loads may already be adequate in many model tests for dynamic wind loads. In fact, some model tests are just to determine the static wind loads on buildings with unusual shapes and/or under the effects of complex topography, and for these applications, no dynamic measurements are required at all. A five-component base balance with the primary function to measure mean wind loads is much simpler to build than the high frequency base balance of Tschanz's type. As the requirement for high frequency response is less critical, the balance can be designed to have higher sensitivity for smaller scale model tests and more stable operation during the wind tunnel tests.

In this paper, the design of a simple five-component base balance for the measurement of mean wind loads on small scale building models is presented. The balance has been applied to the wind tunnel test of a tall building model and the results are compared to those obtained from pressure integration to illustrate the application of the device.

## 2. Description of the Balance

The five-component base balance developed is of the plate type. As shown in Fig.1, the whole balance is machined from an integral piece of aluminium block. It is purposely designed in such a way that there are no mechanical connections, bearings or hinges in order to totally eliminate any possible errors which may arise from loss of contact, friction or slip at mechanical interfaces. The structure of the balance consists of an attachment platform, an inner ring and an outer frame which are inter-connected together. The attachment platform is connected to the inner ring by four moment measuring links while the inner ring is connected to the outer frame by eight shear and torsion measuring links. All the moment/shear/torsion measuring links are strip elements with wide rectangular sections so that they have close to infinite stiffness in the in-plane directions of the strips. The base of the building model is fixed firmly onto the attachment platform with the centroidal axis of the model aligned with the centre of the balance. On the other hand, the outer frame serves as an earth frame for fixing the whole model-balance assembly onto the ground support.

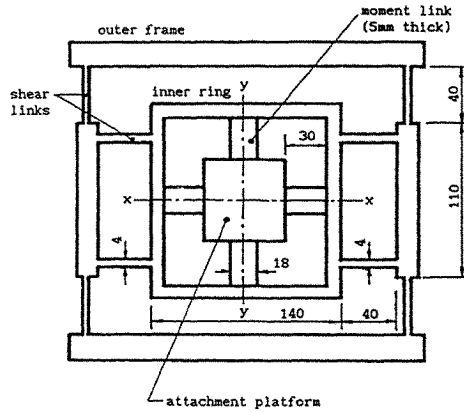


Fig.1 The plate type base balance.

The measuring principle of the balance is simple. All the strip elements are deformable in contraflexure about their minor principal axis which are parallel to the planes of the strips. The flexural deformations of the strip elements are proportional to the lateral shear forces acting on them. Hence, by measuring the flexural deformations of the strips, it is possible to determine the shear forces acting perpendicular to the planes of the strips. The four strip elements inside the inner ring are oriented with their planes horizontal for the measurement of vertical shear forces acting on them. From these vertical shear forces, the overturning moments acting on the building model may be determined by multiplying the vertical shear forces with their respective lever arms. On the other hand, the eight strip elements connecting

the inner ring to the outer frame are oriented with their planes vertical for the measurement of horizontal shear forces acting perpendicular to the planes of the strips. The lateral shear and torsional moment acting on the building model are determined from these horizontal shear forces.

The flexural deformations of the strip elements are measured by means of electrical resistance strain gauges glued at the ends of the strips where the bending strains are greatest, Fig.2(a). To compensate for temperature drift, the four strain gauges for the measurement of each force component are wired together to form a Wheatstone bridge, Fig.2(b). Note that the four strain gauges forming a Wheatstone bridge are all glued onto the same piece of metal and are symmetrically located on the balance. Hence, a very good compensation for any drift due to temperature or other effects can be achieved.

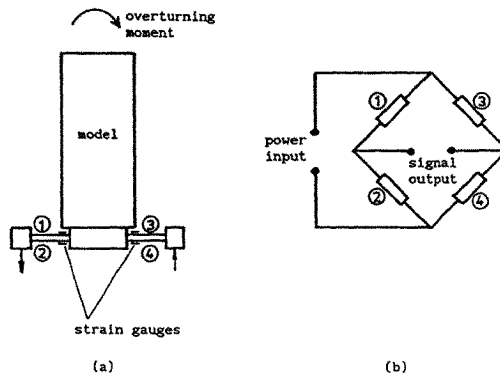


Fig.2 Arrangement of strain gauges.

The bridges are connected to a Tokyo Sokki Kenkyujo dynamic strainmeter model TML DC-1AF. Advanced electronic circuit design of the strainmeter ensures stable operation of the strain gauge measurements which used to be a problem for earlier base balances [1]. The five-channel outputs from the strainmeter are acquired with an analog-to-digital converter card in a 486 micro-computer which also performs necessary calculations to convert the measured strains into wind loads. All the wind load data are stored into a hard disk and can be retrieved when necessary for detailed analysis.

### 3. Calibration and Performance of the Balance

Static calibration of the balance was carried out by applying known loads with standard weights through a rope-pulley system. The loads were applied in each of the five loading directions successively and it was found that negligible cross-talk existed between the five output channels; in other words, the five orthogonal loading components were almost perfectly uncoupled in the five channels of strain measurement output.

The measuring sensitivities of the balance as obtained from the static calibration are shown in Table 1. Within the ranges calibrated, the balance demonstrated excellent linearity and repeatability with the error of measurement in each loading component being generally less than 0.3% of the respective maximum range.

channel no.	load component	range calibrated	sensitivity	strain at max. load
1	M <sub>x</sub>	0 - 4 Nm	1.099 v/Nm	110 $\mu\epsilon$
2	M <sub>y</sub>	0 - 4 Nm	1.241 v/Nm	124 $\mu\epsilon$
3	F <sub>x</sub>	0 - 10 N	0.152 v/N	38 $\mu\epsilon$
4	F <sub>y</sub>	0 - 10 N	0.143 v/N	36 $\mu\epsilon$
5	M <sub>z</sub>	0 - 2 Nm	0.873 v/Nm	44 $\mu\epsilon$

Table 1. Calibrated sensitivity of the plate type base balance.

However, as expected, the frequency response of the balance was rather low. The lowest natural frequency of the balance with a typical light weight building model attached to it was found by impacting and noting the spectral peak in the strain gauge signals to be 40 Hz. Therefore, the base balance is suitable only for the measurement of mean wind loads.

#### 4. Wind Load Measurement Using the Balance

The wind load measurements presented herein were obtained from the wind tunnel testing of a 160 m tall residential tower block located on a steep slope. Fig.3 shows the planform of the building which has a fairly complicated geometry. The external dimensions of the tower give a highly slender height-to-length-to-breadth ratio of 7.4:1.3:1.

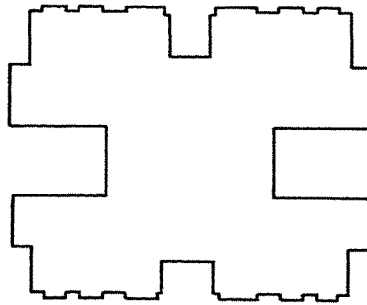


Fig.3 Planform of the building.

Two 1:350 scale models of the tower were constructed and tested in the boundary layer wind tunnel of the University of Hong Kong which has a working section of 3.0 m by 1.8 m and 12.0 m long. The model tests were carried out with the surrounding topography and under a velocity ratio of 1:4.

The first model (the base balance model) was made of a light weight but rigid foam material. It was fixed firmly onto the base balance for measurements of overall wind loads. The other model (the pressure model) was made of acrylic sheets with pressure tappings provided on seven levels of the tower. Readings of the pressure tappings were taken by using six sets of scanivalve plus pressure transducer assembly.

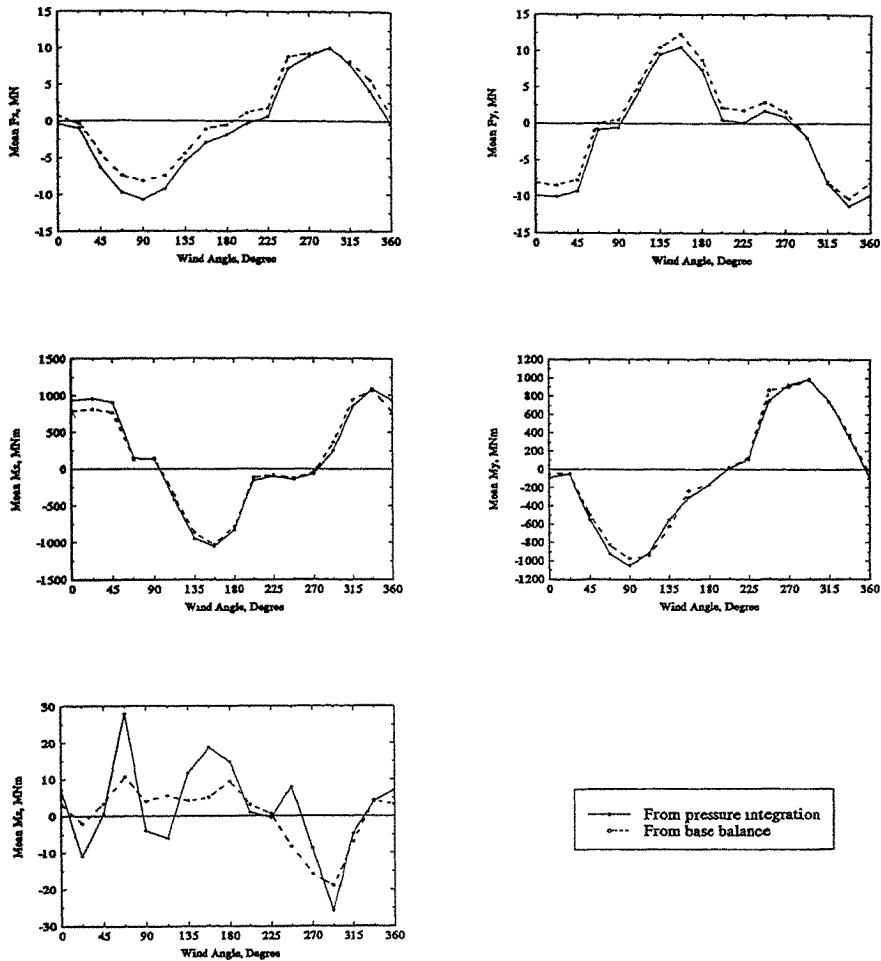


Fig.4 Measured mean wind loads on the building.

The five components of mean wind loads measured with the base balance are shown in Fig.4 where for comparison the mean wind loads computed by integration of the wind pressure profiles obtained with the pressure model are also plotted. Very good agreement between the two sets of data is obtained for the base overturning moments and shear forces. However, agreement for the base torsion is found to be poor, although the two sets of data show the same form of variation with the wind direction. The poor agreement is somewhat expected because the torsional moments were very small, being only about 1/40 of the overturning moments, and thus neither the base balance results nor the pressure model results can be expected to be accurate.

It is worth noting in Fig.4 the variations of the mean wind loads with the wind direction  $\theta$ . The variations of the shear forces and overturning moments with  $\theta$  exhibit a  $\sin \theta$  or  $\cos \theta$  form, which is typical for rectangular buildings. It seems that the present tower block with a planform essentially of a rectangle with several recessed bays does not possess any particular sensitivity to the wind direction. For the torsion  $M_z$ , the distribution roughly follows a  $\sin 4\theta$  form. Similar distributions have been reported for rectangular towers with near square planforms [8,9] but there have not been proposed any cause for this. The present departure of building planform from the uniform rectangle does not seem to alter the form of distribution.

## 5. Conclusions

A plate type balance for the measurement of mean wind loads is developed. It is machined from a single piece of metal and thus any possible errors due to lost of contact, friction and slip at mechanical interfaces are totally eliminated. Any drift due to temperature effects are also well compensated for by wiring the strain gauges, which are all on the same piece of metal and should therefore have the same temperatures, into Wheatstone bridges. The balance has been calibrated statically and it was found that there was negligible drift and the five orthogonal loading components were almost perfectly uncoupled in the output. It also showed excellent linearity and repeatability within the ranges calibrated. Application of the balance is demonstrated by using it to measure the overall wind loads on a building model and comparing the results to those obtained by pressure measurements.

## 6. Acknowledgement

The Authors wish to thank Mr. A. P. To for helping to carry out the calibration of the balance and the wind tunnel tests.

## 7. References

1. R.E. Whitbread, "The measurement of non-steady wind forces on small-scale building models", Proc. 4th Int. Conf. on Wind Effects on Buildings and Structures, Heathrow, (1975) 567-574.
2. E. English and F.H. Durgin, "A wind tunnel study of shielding effects on rectangular structures", Proc. 4th U.S. National Conf. on Wind Engineering Research, Seattle, (1981).
3. R.A. Evans and B.E. Lee, "The assessment of dynamic wind loads on a tall building: a comparison of model and full scale results", Proc. 4th U.S. National Conf. on Wind Engineering Research, Seattle, (1981).
4. T. Tschanz, "Measurement of total dynamic loads using elastic models with high natural frequencies", Wind Tunnel Modeling for Civil Engineering Applications, Ed:Reinhold T.A., Cambridge University Press, (1982) 296-312.
5. T. Tschanz and A.G. Davenport, "The base balance technique for the determination of dynamic wind loads", J. Wind Eng. Ind. Aerodyn., 13 (1983) 429-439.
6. N.J. Cook, The Designer's Guide to Wind Loading of Building Structures: Part 2: Static Structures, Butterworths Press, (1990).
7. Standards Association of Australia, SAA Loading Code: Part 2: Wind Loads: AS1170.2-1989, (1989).
8. R.E. Akins, J.A. Peterka and J.E. Cermak, "Mean force and moment coefficients for buildings in turbulent boundary layers", J. Wind Eng. Ind. Aerodyn., 2 (1977) 195-209.
9. N. Isyumov and M. Poole, "Wind induced torque on square and rectangular building shapes", J. Wind Eng. Ind. Aerodyn., 13 (1983) 183-196.

**A NUMERICAL INVESTIGATION OF A PROPOSED FORCE BALANCE TECHNIQUE TO IMPROVE  
THE WIND RESPONSE PREDICTIONS OF TALL BUILDINGS WITH COUPLED 3-D MODE SHAPES**

D.Y.N. Yip and R.G.J. Flay\*

Ove Arup & Partners (NZ)  
\*Mechanical Engineering Department  
University of Auckland, New Zealand

**Abstract:** The theory of the current force balance technique used to predict the wind-induced response of buildings with coupled 3-D modes is reviewed. For buildings of this type, the source of uncertainty of the technique's response predictions is not just with the errors of the mode shape corrections, but also with the limitations of not being able to allow for the coupled terms and higher mode effects in the response computation. An alternative force balance technique which is designed to overcome these limitations is presented in this paper. Numerical studies of the proposed method indicated the approach is reliable and always gives consistently accurate predictions of the numerically simulated 'exact' values of the loads and response.

### 1.0 Introduction

Studies of the wind-induced response of real buildings with coupled 3-D modes are limited. Work reported so far [e.g.1] were primarily concerned with studies of simple building cases which were isolated square prisms in homogeneous terrains, with hypothetical building properties and wind blowing normal to one face. Extrapolation of these results to buildings of complex shape, in real city wind environments where the building shape and surrounding buildings have a significant influence on the correlation and distribution of wind loads, is difficult and sometimes misleading. Fig.1 shows a building example and its coupled 3-D mode shapes.

During the past decade, the force balance technique remains one of the popular wind tunnel testing methods in routine tests of most commercial building projects. It has gained popularity for two main reasons : its relative low test cost, and most importantly, its ability to provide engineers with design information at the early design stage of a project. The approach has, however, some major limitations which are : (a) results are valid for buildings with linear sway mode shapes and analytical corrections are required for buildings with sway mode shapes that vary significantly from linear; (b) results are valid for buildings with a uniform torsional mode shape and analytical correction is always required for any type of real buildings. A reduction factor of 0.70 is commonly used, regardless of the actual mode shape which may not be linear, to approximate the modal torsional force from a uniform to a linear mode shape; (c) aeroelastic effects are not measured; (d) only fundamental modes of vibration in the two sway and one torsional modes are included in the response computation. Higher mode effects are neglected; (e) effects of the cross correlation of the wind forces or the modal forces are neglected; (f) it is nearly impossible to estimate full details of the modal forces for coupled 3-D mode shapes.

The method of using mode shape correction factors in (a) and (b) introduces a source of uncertainty to the response predictions of the force balance technique, as these factors are not actually derived from the measured data of a particular test. They do not reflect the site specific aspects of the actual test case, such as directional dependence of the wind climate or the influence of specific surrounding buildings, or terrain features etc. For buildings with complex shapes and coupled 3-D modes, all the other limitations may also significantly influence the accuracy of the technique's prediction. This paper presents an alternative force balance technique which attempts to overcome all the limitations of the conventional technique described above except (c).

## 2.0 Computation of Wind-Induced Dynamic Response

The response in terms of generalized coordinates can be solved for stationary random loads using methods of random vibration theory and spectral analysis. Assuming that the wind forces are stationary random loads, the spectral density matrix of the displacement response can be computed from

$$[S_d(z_1, z_2, f)] = [\Phi(z_1)][H(i2\pi f)][S_Q(f)][H^*(i2\pi f)]^T[\Phi(z_2)]^T = \begin{bmatrix} S_{dxx} & S_{dxy} & S_{d\theta\theta} \\ S_{dxy} & S_{dyy} & S_{d\theta\theta} \\ S_{d\theta x} & S_{d\theta y} & S_{d\theta\theta} \end{bmatrix} \quad (1)$$

where  $z_1, z_2$  are dummy space variables;  $f$  is frequency in Hz;  $N$  is number of modes included;

$[H(i2\pi f)] = N \times N$  diagonal matrix of frequency response function ;  $[H^*(i2\pi f)]$  its complex conjugate

$$[S_Q(f)] = N \times N \text{ complex matrix of the spectral densities of generalized wind forces} \\ = \int \int_0^H [\Phi(z_1)]^T [S_f(z_1, z_2, f)] [\Phi(z_2)] dz_1 dz_2 \quad (2)$$

$$[S_f(z_1, z_2, f)] = 3 \times 3 \text{ complex matrix of wind forces} = \begin{bmatrix} S_{fxx} & S_{fxy} & S_{f\theta\theta} \\ S_{fxy} & S_{fyy} & S_{f\theta\theta} \\ S_{f\theta x} & S_{f\theta y} & S_{f\theta\theta} \end{bmatrix} \quad (3)$$

$[\Phi(z_1)], [\Phi(z_2)] = 3 \times N$  mode shape

The elements of  $[S_Q(f)]$ , say the diagonal elements for the first three modes are given by

$$S_{Q11} = (\phi_1^x S_{fxx} + \phi_1^y S_{fxy} + \phi_1^{\theta} S_{f\theta\theta}) \phi_1^x + (\phi_1^x S_{fxy} + \phi_1^y S_{fyy} + \phi_1^{\theta} S_{f\theta\theta}) \phi_1^y + (\phi_1^x S_{f\theta\theta} + \phi_1^y S_{f\theta\theta} + \phi_1^{\theta} S_{f\theta\theta}) \phi_1^{\theta} \\ S_{Q22} = (\phi_2^x S_{fxx} + \phi_2^y S_{fxy} + \phi_2^{\theta} S_{f\theta\theta}) \phi_2^x + (\phi_2^x S_{fxy} + \phi_2^y S_{fyy} + \phi_2^{\theta} S_{f\theta\theta}) \phi_2^y + (\phi_2^x S_{f\theta\theta} + \phi_2^y S_{f\theta\theta} + \phi_2^{\theta} S_{f\theta\theta}) \phi_2^{\theta} \\ S_{Q33} = (\phi_3^x S_{fxx} + \phi_3^y S_{fxy} + \phi_3^{\theta} S_{f\theta\theta}) \phi_3^x + (\phi_3^x S_{fxy} + \phi_3^y S_{fyy} + \phi_3^{\theta} S_{f\theta\theta}) \phi_3^y + (\phi_3^x S_{f\theta\theta} + \phi_3^y S_{f\theta\theta} + \phi_3^{\theta} S_{f\theta\theta}) \phi_3^{\theta} \quad (4)$$

The covariance matrix of displacements and accelerations is given by

$$[\sigma_d^2(z_1, z_2)] = \int_0^{\infty} [S_d(z_1, z_2, f)] df \quad ; \quad [\sigma_a^2(z_1, z_2)] = \int_0^{\infty} [S_a(z_1, z_2, f)] df \quad (5)$$

The response such as the tip acceleration at the corner ( $r_x, r_y$ ) can be computed from

$$\sigma_{axx}^2(H, H) = \int_0^{\infty} S_{axx}(H, H, f) df = \sigma_{axx}^2(H, H) + r_y^2 \sigma_{a\theta\theta}^2(H, H) - 2r_y \sigma_{ax\theta}^2(H, H) \quad (6a)$$

$$\sigma_{ayc}^2(H, H) = \int_0^{\infty} S_{ayc}(H, H, f) df = \sigma_{ayc}^2(H, H) + r_x^2 \sigma_{a\theta\theta}^2(H, H) + 2r_x \sigma_{ay\theta}^2(H, H) \quad (6b)$$

## 2.1 Analytical Procedure Adopted by Current Force Balance Technique

The current technique computes Eqn.(1) and (4) by

$$[S_d(H, H, f)] = \begin{bmatrix} S_{dxx} & 0 & 0 \\ 0 & S_{dyy} & 0 \\ 0 & 0 & S_{d\theta\theta} \end{bmatrix} \text{ and } [S_Q(f)] = \begin{bmatrix} S_{Q11} & 0 & 0 \\ 0 & S_{Q22} & 0 \\ 0 & 0 & S_{Q33} \end{bmatrix} \quad (7)$$

where  $S_{dxx}(H, H, f) = \phi_1^x H_1 S_{Q11} H_1^* \phi_1^x + \phi_2^x H_2 S_{Q22} H_2^* \phi_2^x + \phi_3^x H_3 S_{Q33} H_3^* \phi_3^x$

$$S_{dyy}(H, H, f) = \phi_1^y H_1 S_{Q11} H_1^* \phi_1^y + \phi_2^y H_2 S_{Q22} H_2^* \phi_2^y + \phi_3^y H_3 S_{Q33} H_3^* \phi_3^y$$

$$S_{d\theta\theta}(H, H, f) = \phi_1^{\theta} H_1 S_{Q11} H_1^* \phi_1^{\theta} + \phi_2^{\theta} H_2 S_{Q22} H_2^* \phi_2^{\theta} + \phi_3^{\theta} H_3 S_{Q33} H_3^* \phi_3^{\theta}$$

$$S_{Q11} = \phi_1^x S_{fxx} \phi_1^x + \phi_1^y S_{fyy} \phi_1^y + \phi_1^{\theta} S_{f\theta\theta} \phi_1^{\theta} = \chi_1^x S_{Mxx} \chi_1^x + \chi_1^y S_{Myy} \chi_1^y + \chi_1^{\theta} S_{M\theta\theta} \chi_1^{\theta}$$

$$\text{and } S_{Q22} = \phi_2^x S_{fxx} \phi_2^x + \phi_2^y S_{fyy} \phi_2^y + \phi_2^{\theta} S_{f\theta\theta} \phi_2^{\theta} = \chi_2^x S_{Mxx} \chi_2^x + \chi_2^y S_{Myy} \chi_2^y + \chi_2^{\theta} S_{M\theta\theta} \chi_2^{\theta}$$

$$S_{Q33} = \phi_3^x S_{fxx} \phi_3^x + \phi_3^y S_{fyy} \phi_3^y + \phi_3^{\theta} S_{f\theta\theta} \phi_3^{\theta} = \chi_3^x S_{Mxx} \chi_3^x + \chi_3^y S_{Myy} \chi_3^y + \chi_3^{\theta} S_{M\theta\theta} \chi_3^{\theta}$$

$\chi_1^x, \chi_1^y, \chi_1^{\theta}, \chi_2^x, \chi_2^y, \chi_2^{\theta}, \chi_3^x, \chi_3^y, \chi_3^{\theta}$  are the mode shape correction factors;  $S_{Mxx}, S_{Myy}, S_{M\theta\theta}$  are the scaled spectra of the base overturning and torsional moments measured by the balance.

The corner response of Eqn (6) is computed by

$$\sigma_{axx}^2(H, H) = \int_0^{\infty} S_{axx}(H, H, f) df = \sigma_{axx}^2(H, H) + r_y^2 \sigma_{a\theta\theta}^2(H, H)$$

$$\sigma_{ayc}^2(H, H) = \int_0^{\infty} S_{ayc}(H, H, f) df = \sigma_{ayc}^2(H, H) + r_x^2 \sigma_{a\theta\theta}^2(H, H) \quad (8)$$

Comparing Eqn.(7) with Eqns.(1) and (4), or Eqn.(8) with (6) etc., it can be found that the approximations made in the current technique are not just a matter of applying mode shape correction factors to the balance base moments, but also involve neglecting all the cross terms in the wind force matrix  $[S_f]$ , the modal force matrix  $[S_Q]$  and the displacement response matrix  $[S_d]$ . These combined effects result in incomplete modelling



of both the diagonal and off-diagonal terms of all these matrices. For some building shapes, modal properties and wind directions, the cross terms in [Sf] and [SQ] are not necessarily small. Therefore the validity of using the results from the current technique in the design of these type of buildings, especially buildings with coupled 3-D mode shapes is fairly questionable.

### 2.2 Proposed Alternative Force Balance Technique

The basis of this method is briefly described here. During a balance test using a 5-component force balance, measurements of the time history of 2 base shears and 2 overturning moments at the base together with the total torsional moment about the balance vertical axis are made. From these 5 time history measurements, a total of 25 auto- and cross-spectra between the shear and moment components can be determined in the frequency domain. Instead of approximating the [SQ] directly from the balance base moments, an alternative method is to first approximate the integral function of the elements of the wind force matrix [Sf], then later compute the elements of [SQ] using the approximated [Sf]. In this method the co- and quad-spectra of the wind forces in each test wind direction are approximated by different frequency dependent, low order polynomial expressions similar to a power series expansion, with unknown coefficients. The expression takes the form of

$$S_{fd}(z_1, z_2, f) = c_{1kl}(f) \frac{z_1}{H} + c_{2kl}(f) \frac{z_2}{H} + c_{3kl}(f) \frac{z_1 z_2}{H^2} + \dots \quad (9)$$

where  $k, l = x, y, \theta$ ;  $c_{1kl}, c_{2kl}, c_{3kl}, c_{4kl}, \dots =$  unknown frequency dependent coefficients. To determine the unknown coefficients in Eqn.(9), the number of coefficients and the order of expression would have to match with the number of measured shear and moment spectra, taking any advantage of symmetry wherever applicable. For example, the unknown coefficients for  $S_{fxx}(z_1, z_2, f)$  can be obtained by the solving the following three simultaneous equations

$$\begin{aligned} S_{FXX}(f) &= \int_0^H \int_0^H S_{fxx}(z_1, z_2, f) dz_1 dz_2 = \int_0^H [c_{1xx}(f) + c_{4xx}(f) \left(\frac{z_1 z_2}{H^2}\right) + c_{7xx}(f) \left(\frac{z_1 z_2}{H^2}\right)^2] dz_1 dz_2 \\ S_{MXX}(f) &= \int_0^H \int_0^H S_{fxx}(z_1, z_2, f) z_1 z_2 dz_1 dz_2 = \int_0^H [c_{1xx}(f) + c_{4xx}(f) \left(\frac{z_1 z_2}{H^2}\right) + c_{7xx}(f) \left(\frac{z_1 z_2}{H^2}\right)^2] z_1 z_2 dz_1 dz_2 \\ S_{FXMX}(f) &= \int_0^H \int_0^H S_{fxx}(z_1, z_2, f) z_2 dz_1 dz_2 = \int_0^H [c_{1xx}(f) + c_{4xx}(f) \left(\frac{z_1 z_2}{H^2}\right) + c_{7xx}(f) \left(\frac{z_1 z_2}{H^2}\right)^2] z_2 dz_1 dz_2 \end{aligned}$$

where  $S_{FXX}(f)$ ,  $S_{MXX}(f)$ ,  $S_{FXMX}(f)$  are the auto-, co- or quad-spectra of the base shears and moments measured by the balance for the particular wind direction. Following similar calculations, 8 of the 9 elements of the wind force matrix [Sf] can be approximated from the measured spectra. They can then be used to compute the elements in [SQ]. While for  $S_{f\theta\theta}(z_1, z_2, f)$  which does not have sufficient measured information to derive an approximate expression, it is proposed that the modal force associated with this component be computed using  $\frac{\int_0^H \int_0^H \Phi_n^{\theta}(z_1) S_{f\theta\theta}(z_1, z_2, f) \Phi_n^{\theta}(z_2) dz_1 dz_2}{\int_0^H \int_0^H \Phi_n^{\theta}(z_1) S_{fxx}(z_1, z_2, f) \Phi_n^{\theta}(z_2) dz_1 dz_2} = \frac{\int_0^H \int_0^H \Phi_n^{\theta}(z_1) S_{f\theta\theta}(z_1, z_2, f) \Phi_n^{\theta}(z_2) dz_1 dz_2}{\int_0^H \int_0^H S_{fxx}(z_1, z_2, f) dz_1 dz_2} = \frac{\int_0^H \int_0^H \Phi_n^{\theta}(z_1) S_{f\theta\theta}(z_1, z_2, f) \Phi_n^{\theta}(z_2) dz_1 dz_2}{\int_0^H \int_0^H S_{f\theta\theta}(z_1, z_2, f) dz_1 dz_2} \quad (10)$

### 2.3 Use of a Multi-Segmented Model

A further refinement of the proposed force balance technique is to consider a multi-segmented model force balance test where the model is divided into several horizontal sections, and each section is connected simultaneously or in turn to the balance. The advantage of using a multi-segmented model in the test is two-folded : firstly it gives a more refined loading distribution, which also results a less significant variation of the actual mode shapes from the linear/uniform shape, and thus improves the response predictions as the number of segments increases; secondly it provides a means to conduct self-validation and to check convergence of the previous predictions using fewer segments. Extension of the previous proposed balance data analysis method from a single-piece model to a multi-segmented model is straightforward. The wind force approximation expressions and the measured balance force and moment spectra will simply be referring to individual segments and between segments. For example,  $S_{fxx}(z_1, z_2, f)$  will be  $S_{fxx}(z_1, z_2, f)$ , where  $i, j$  refers to the  $i$ th and  $j$ th segments, and  $z_1$  and  $z_2$  spans only the height of the  $i$ th and  $j$ th segments respectively.

### 3.0 Numerical Example

The effectiveness of the proposed force balance technique to predict wind-induced loads and response for buildings of coupled 3-D mode shapes has been extensively examined by the authors using numerically

simulated model tests. A mathematical 3-D wind force model developed from similar ones in the literature [2] was used to study the response of several real high-rise buildings using their actual structural properties. These numerical studies enabled full details of the 'exact' wind-induced loads and response of the buildings to be computed from the known wind load distribution and the complete set of the building properties. By simulating a force balance test using the same set of numerical data, details of the 'approximate' predicted response computed by the conventional and the proposed balance technique can also be obtained and compared with the 'exact' values. Some of the results obtained for the building shown in Fig.1 are presented here. The building was subject to the same approach wind characteristics ( $z_0=0.2\text{m}$ ,  $u_1=2.2\text{m/s}$ ) from 5 different wind directions.

The determination of the modal force spectra is only an intermediate step in the entire response computation process. In this study the total response, assuming 1% damping, was computed and compared against some 'exact' values in terms of their relative variations. 2 sets of mode shape correction factors had been assumed for the current balance technique: set(FBAC) assumed 0.7 for torsional mode and those suggested by Ref.[3] for sway modes, and set(FBTC) assumed 0.7 for torsional mode and 1.0 for sway modes. The 'exact' values of the response had been computed for 4 cases: case(6F) included 6 modes and all terms, case(6D) included 6 modes and only diagonal terms, case(3F) included 3 modes and all terms, and case(3D) included 3 modes and only diagonal terms. The last case is normally considered by today's practice to be accurate enough for design purposes. For case(6F) and (3F), the contribution of the quad-spectra of the cross terms had been ignored.

Fig.2(a) plots the modal force auto- and co-spectra of the first 3 modes, computed for the 60 degree wind case. The figure shows the covariance of the cross terms is comparable to that of the diagonal terms. Fig.2(b) compares the modal torsional force spectra for the same wind direction, between the 'exact', current balance technique approximations and the proposed balance technique approximation derived from 2 model segments. The proposed balance technique approximation agrees well with the 'exact' spectrum across the entire frequency range, while the 2 approximations by the current technique shows no consistent trend of agreement, although the FBTC spectrum agrees well over the frequency of interest (0.1-1 Hz). Fig.3(a)-(f) compare the relative values of the computed tip acceleration and displacement response of various cases, including the proposed method (NEWFB) with 1 model segment, against those of case(3D). From these figures, the following results can be derived: (a) case(3D) is not representative of all the other 'exact' cases and may grossly underestimate their values in excess of more than 50% in some wind directions, especially for the acceleration response; (b) there is no definite trend to show which 'exact' case dominates the design values for all 5 directions, although case(6F) generally appears to be more dominant in most cases; (c) both case(FBAC) and (FBTC) approximate the 'exact' values of the case(3D) reasonably well, usually within 15%, although case (FBTC) tends to overestimate while case(FBAC) tends to underestimate the 'exact' values; (d) the proposed balance data analysis method approximation derived from 1 model segment shows a similar order of accuracy, mostly within 10%. In these comparisons case (3D) is assumed to be the 'exact' case which obviously can not be correct in all situations. The 'exact' case will, in fact, vary from case to case. Fig.4 demonstrates the accuracy of the alternative method and the advantage of a multi-segmented model balance test concept, against the 'exact' values of the most complex case(6F). As the number of segments increases, the predicted response approaches the 'exact' values. Only 2 segments are required to keep the error to within less than 10%. Finally Fig.5 shows how the response values, computed by the 2 expressions of eqn.(10), converge to the 'exact' values of case (6F), with increasing number of model segments.

#### 4.0 Summary, Future Work and Acknowledgement

The accuracy, the reliability and the many other advantages of the proposed alternative force balance technique have been demonstrated in the above numerical example. Experimental work is being carried out to verify the numerical findings, the results of which will be published in the future.

The first author is grateful to Prof. Davenport and Ove Arup for the opportunity to complete the final part of the numerical studies, and the subsequent experimental work at the BLWTL of the University of Western Ontario under the sponsorship of the Ken Anthony Fellowship. Special thanks also to Prof. Vickery of BLWTL

who initiated this research direction and offered many helpful advice throughout the course.

**Reference**

[1] Tallin, A. and Ellingwood, B., Jr. *Str. Eng.*, Vol. 111, No.10, 1985, p2197-2213  
 [2] Solari, G., *Jn Eng. Mech.*, ASCE, Vol. 111, No.EM2, 1985  
 [3] Vickery, P.J., et al. *Proc. 5th U.S. Nat. Conf. on Wind Eng.*, Texas, 1985

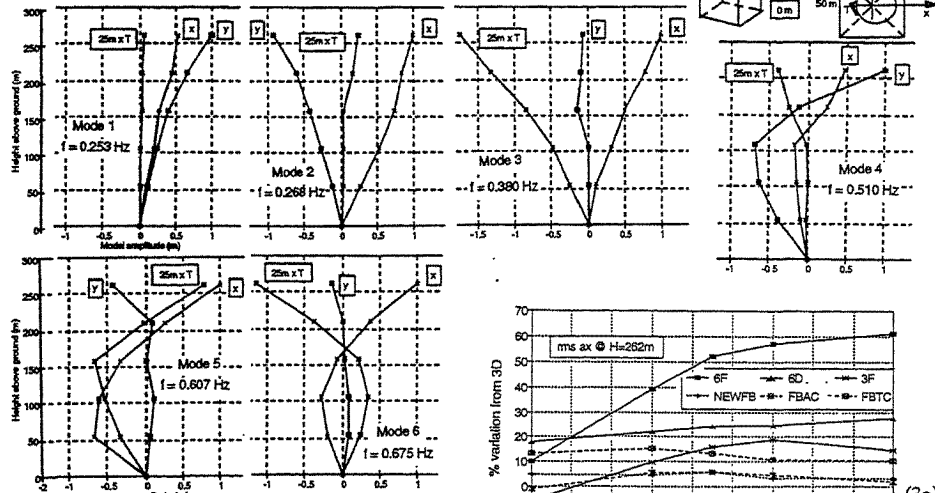


Fig. 1 Building model and its 3D modes

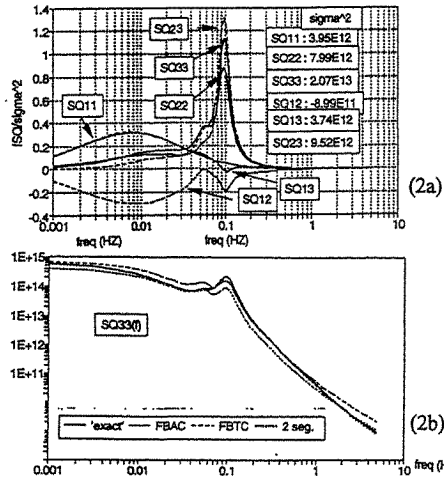


Fig.2 Modal force spectra (60° wind case)

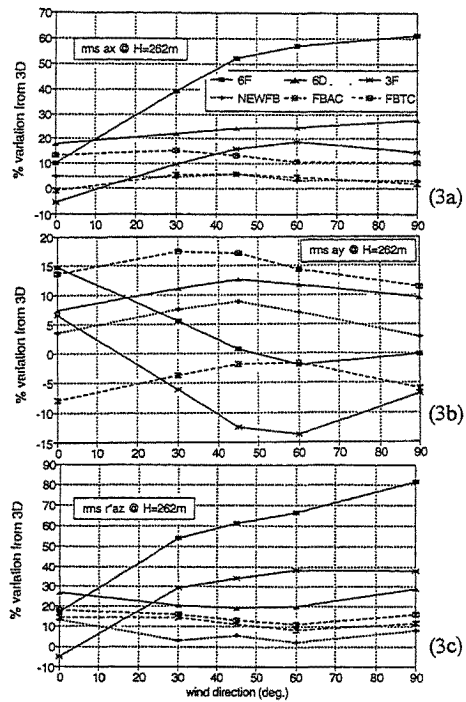


Fig.3 Tip acceleration response Vs case (3D)

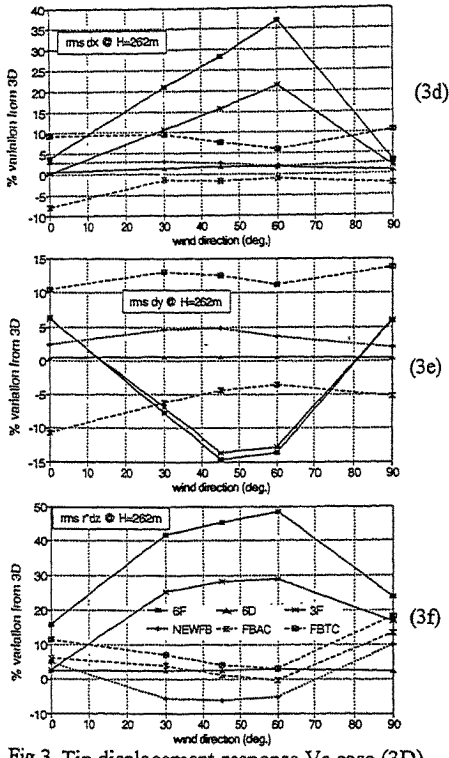


Fig.3 Tip displacement response Vs case (3D)

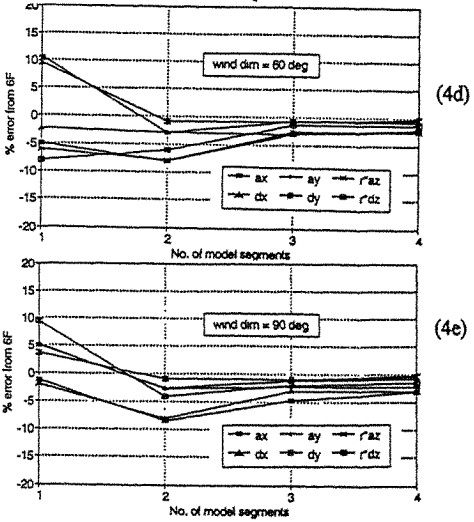
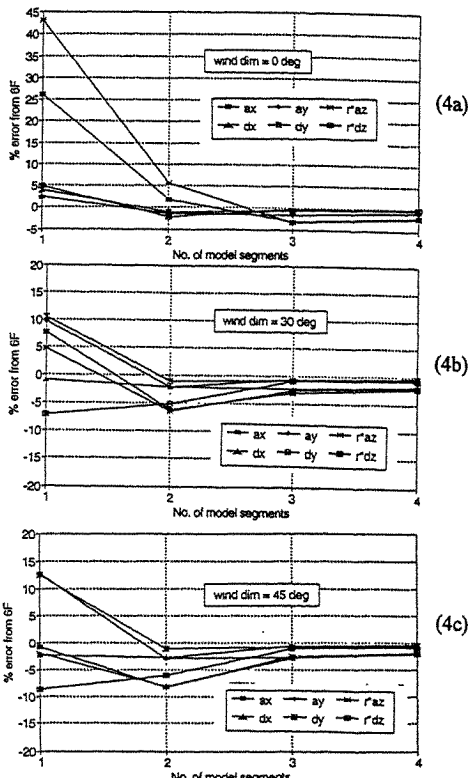


Fig.4 Computed response by new method

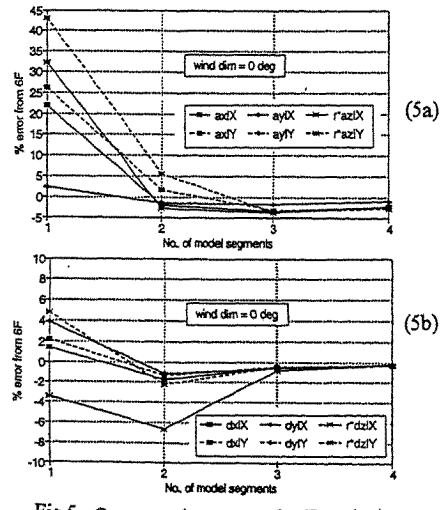


Fig.5 Computed response by Eqn.(12)

The Constant Temperature Hot—Wire(Film) Anemometer system  
 With Main Bridge Prephase—Shift Circuit

Sheng Senzhi & Zhuang Yongji

Department of Mechanics, Peking University  
 Beijing, 100871, China

**Abstract.** The authors, having analyzed the dynamic equation of the traditional constant—temperature hot—wire(film) anemometer, have advanced a new—type circuit model of the hot—wire(film) anemometer—main bridge prephase shift model, deduced the dynamic response equation of small disturbance under actual condition, and developed an entirely new IFV—900 hot—wire(film) anemometer. This anemometer abolishes three adjusting parameters of the traditional anemometer, it simplifies greatly the adjusting procedure; The apparent increase of the none self—excited oscillation range saves the operator a lot of trouble.

1. Introduction

The basic circuit mode of constant temperature HWFA (hot—wire/hot film anemometer) may be simplified as shown in fig 1. Here we assume the amplifier and bridge components are idealized, i. e. , there exists no electrophase shift.

The dynamic response equation is:

$$M_{ct}K(d/dt)(i_s/I_s) + (i_s/I_s) = h/2H$$

where  $M_{ct} = M_{ct}/2G(L-1)$  is the time constant;  $G$  is the gain;  $L$  is the overheat ratio;  $I_s$  is the current flowing through the hot wire (film); and  $H = \bar{H} + h(t) = A + B\sqrt{U}$  is the heat dissipation.

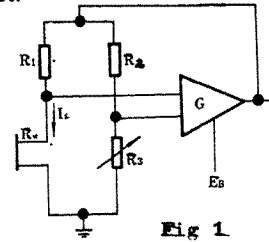


Fig 1

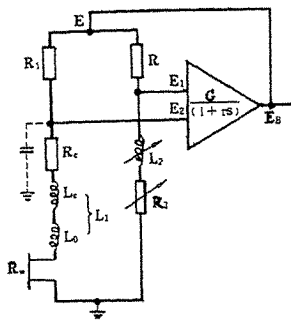
However, the actual situation is not so simple as shown in Fig 1, because the probe—lead cable has distributed capacitance  $C_c$  and inductance  $L_c$ , and the amplifier has time—lag, and the mainbridge component has distributed parameters, so the traditional HWFA have some problems; 1) There are three adjustment parameters which affect one another, causing

much trouble to the adjustment procedure. 2) The bandwidth is somewhat small, for the common 5 : 1 bridge it is 200 KHz, for the 1 : 1 bridge it is 500 KHz. 3) Once the velocity exceeds the corresponding adjustment point, the system becomes unworkable because of selfexcitation. So the traditional HWFA is not convenient to adjust and use.

## 2) The anemometer of main bridge prephase shift model

In order to overcome the above — mentioned shortcomings, we put forward the circuit model shown is Fig 2, where  $L_0$  is the fixed inductance in series with the probe arm,  $L_2$  is an adjustment component.

The following expressions are introduced:



$$\Delta_1 = \frac{L_1}{R_1 + R_c + \bar{R}_w}, \Delta_2 = \frac{L_2}{R_2 + R_3}, \Delta_3 = \frac{L_1 - \frac{R_1 L_2}{R_2}}{R_1 + R_c + \bar{R}_w}$$

$$g_1 = \frac{2(L-1)G}{(1 + \frac{R_3}{R_2})(1 + \frac{R_1 + R_c}{R_w})}, M'_{CT} = \frac{M_{CC}}{g_1} = M_{CT}(1 + \frac{R_3}{R_2})$$

$$\frac{e}{E} \left\{ 1 + \left( \frac{G}{g_1} \Delta_3 + M'_{CT} \frac{E_B}{E} \right) \frac{d}{dt} + \left[ \left( \frac{\Delta_1}{g_1} + M_{CT} \right) G \Delta_3 + M'_{CT} \left( \Delta_1 + \frac{E_B}{E} \Delta_1 + \tau + \Delta_2 \right) \right] \frac{d^2}{dt^2} + M'_{CT} \left[ 2\tau \Delta_1 + 2\Delta_1 \Delta_2 + \Delta_1^2 + \tau \Delta_2 + \frac{G \Delta_1 \Delta_2}{1 + R_3/R_2} \right] \frac{d^3}{dt^3} + M'_{CT} \left[ 2\tau \Delta_1 \Delta_2 + \tau \Delta_1^2 + \Delta_2 \Delta_1^2 \right] \frac{d^4}{dt^4} + M_{CC} \Delta_1^2 \Delta_2 \tau \frac{d^5}{dt^5} \right\}$$

$$= \frac{h}{2H} \left( 1 + \Delta_1 \frac{d}{dt} \right) + \frac{e_B}{E g_1} \left( 1 + \Delta_1 \frac{d}{dt} \right) \left[ 1 + M_{CC} \frac{d}{dt} + M_{CC} (\tau + \Delta_1 + \Delta_2) \frac{d^2}{dt^2} + M_{CC} (\tau \Delta_1 + \tau \Delta_2 + \Delta_1 \Delta_2) \frac{d^3}{dt^3} + M_{CC} \tau \Delta_1 \Delta_2 \frac{d^4}{dt^4} \right] \quad (1)$$

Fig 2

Apply Laplace transformation to equation (1). We take Butterworth lowpass response characteristics as target transfer function structure of equation (1), and assume

$$\eta = \frac{\epsilon_0}{\Delta_1}, \zeta = \frac{\epsilon_1}{\Delta_1}, f_{cut_0} = \frac{1}{2\pi\epsilon_0}, f_{cut_1} = \frac{1}{2\pi\epsilon_1} \quad (2)$$

We get:

$$(\eta^2 - \sqrt{2}\eta + 1)\xi^3 - (2\eta^2 - 2\sqrt{2}\eta + 2)\xi^2 + (2\eta^2 - 2\sqrt{2}\eta + 2)\xi - (\eta^2 - \sqrt{2}\eta) = 0 \quad (3)$$

From above equation we get the curve of relationship between  $M'_{CT}/\Delta_1$  and  $\eta$  (see Fig 3)

Notice that  $M'_{CT} > 0$  is the prerequisite condition for the physical realization. Therefore from Fig 3 we can obtain physically realizable proper solution region for equation.

Combining the above results we can write out a series of design formulas:

$$\begin{aligned}
 L_2 &= \frac{R_2}{R_1} L_1 \\
 \Delta_1 &= \frac{L_1}{R_1 + R_c + R_w} \\
 \eta &= \frac{\epsilon_0}{\Delta_1} \in (1.45, 2.95) \\
 \zeta &= \frac{\epsilon_1}{\Delta_1} \in (0.025, 0.782) \\
 \frac{M'_{CT}}{\Delta_1} &= \frac{\epsilon_0 \eta \zeta^3}{\tau} \in (0.0025, 0.153) \\
 G &= \frac{M_{CT}}{M'_{CT}} \left(1 + \frac{R_3}{R_2}\right) \left[1 + \frac{(R_1 + R_c)}{R_w}\right] \\
 \frac{\bar{E}_B}{E} &= \frac{\epsilon_0}{M_{CT}} \left(\sqrt{2} + \frac{2\zeta}{\eta}\right) \\
 \epsilon_1 &= \frac{\zeta}{\eta} \epsilon_0 \\
 L_1 &= L_0 + L_c \tag{4}
 \end{aligned}$$

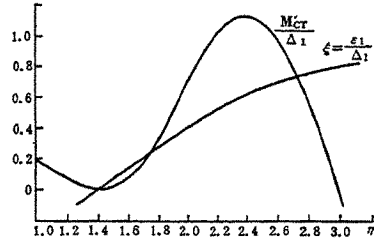
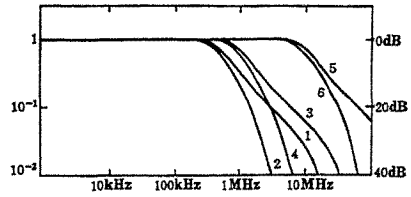


Fig 3



1	$f_{cut0} = 500\text{kHz}$	$\eta = 1.5$	$\zeta = 0.061$
2	500kHz	2.8	0.75
3	1MHz	1.5	0.061
4	1MHz	2.8	0.75
5	10MHz	1.5	0.061
6	10MHz	2.8	0.75

Fig 4

According to the formulas (4), we designed the IFV-900 anemometer and IFV-900 Intelligent flow-velocity measuring system (see Fig5).

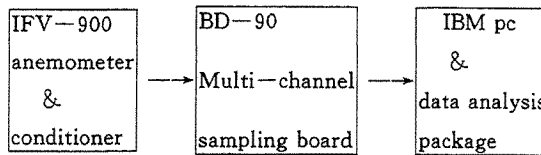


Fig 5

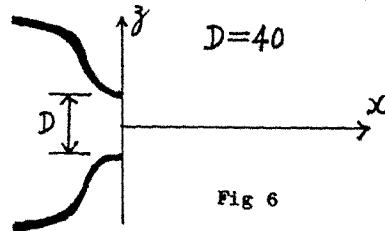
As compared with the traditional constant-temperature hot wire/film anemometer (HWFA), the IFV-900 system has the following characteristics:

### Performance Comparison

Model		IFV-900	Traditional HWFA
1	adjusting parameter	0	>3
2	square-wave test	optional	necessary
3	adjustment time	2 minutes	30 minutes
4	operation	convenient	not convenient
5	stability	very good	(self-excited)
6	bandwidth	0-700KHz	0-200KHz
7	typical equivalent input noise of amplifier (10m/s, 10khz)	(1nv/√ Hz ((0.006%, back-ground turbulence intensity)	≥ 1.6nv √ Hz (≥ 0.007%, back-ground turbulence intensity)
8	typical equivalent input drift	≤ 0.5μV/°C	≤ 3μV/°C
9	software function	very good	good(1984)
10	intelligent function	very good	good(1986)

### 3. The results of free-jet measurement.

The results of free-jet measurement is as following:





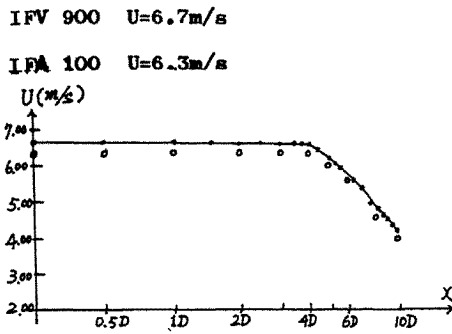


Fig 7

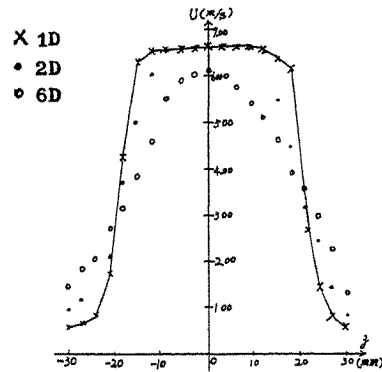


Fig 8

Fig 7 shown, the results of IFV—900 approach with the results of the IFA—100 intelligent flow analyzers (TSI INC.)

#### 4. Conclusion

- \* The main bridge prephase shift model has a fifth order dynamic equation.
- \* With the abolition of the three adjusting parameters for the traditional HWFA, it simplifies greatly the adjusting processs, the adjustment time is ten times shorter than the traditional HWFA.
- \* The apparently increased range of none self—excited oscillation saves the trouble of the square—wave test.
- \* The Software functions are better than the traditional ones.
- \* The degree of automation is raised greatly with the addition of the intelligent function.

#### References :

1. Sheng Senzhi, Shen Xiong and Shu Wei. "Flow velocity measuring technique" Beijing university press. 1987.
2. Freymuth, P. , J. phys. E. 10(1977), 705—710.
3. Freymuth, P. , Rev. Sci. Instrum, 1969. 40:258—262.
4. Freymuth, P. , Rev. Sci. Instrum, 1967, 38:677—681.

5. Zhuang Yongji & Sheng Sen—Zhi. Aerodynamic experiment and Measurement & control, Vol. 6, NO. 1, Mar. 1992.

6. Zhuang Yongji & Sheng Sen—Zhi. Aerodynamic experiment and measurement & control, Vol. 6, No. 3, sep, 1992.

#### Appendix: BT—90 Data analysis package

(1) The BT—90 software package is divided into eight programs. It is designed to simplify thermal anemometry measurements and analysis for 1—, 2—, and 3—sensor configurations. The eight programs incorporated in the software package are: data acquisition, statistical analysis, correlation and spectrum analysis, probe calibration, flow—field plotfile, digital filter, files management, and users interface.

(2) Statistics display: Mean velocity, Standard deviation, Turbulence intensity, Microscale, Skewness coefficient, Flatness coefficient, Shear stress, Correlation coefficient.

(3) The data acquisition program allows continuous acquisition it can be used as a data oscilloscope.

(4) It can display the velocity vector so that the user can observe directly the distributed pattern.

(5) It can display the data files so that the user can find the data.

(6) It can display the calibration curve so that the user can judge directly what is a “good probe” and what is a “bad probe”.

(7) It can process Multi—channel data directly.

(8) It uses the new calibration method of the X—probe.

(9) It has the digital filter function.

(10) It offers a user's software interface.

## Wind tunnel modeling test on mechanism of weakening Typhoon's damage to rubber forest by tea-rubber community

L.S.Lou and K.Zhao

Central Research Institute of Building and Construction  
of Ministry of Metallurgical Industry, Beijing, China

**Abstract:** In this paper, The wind velocity, turbulent structure and drag coefficient inside and above the tea-rubber artificial community were observed under the condition of neutral atmosphere. The best type of community for windbreak was decided through studying the mechanism of weakening Typhoon's damage to rubber forest. The experimental results show that wind velocity and kinetic energy (KE) reduced greatly due to friction with the tree canopy and leaves when Typhoon cross through the community. The larger scale Typhoon with higher kinetic energy and weaker turbulence turned into smaller scale eddies with weaker kinetic energy and higher turbulence, leading to the increment of attenuation rate of wind velocity and decrement of turbulent transference. As a result, damage of the rubber forest made by Typhoon was decreased remarkably. In different type of tea-rubber communities, the wind inside the community of two row in clumps has the maximum attenuation rate of wind velocity and minimum turbulence transference. Thus this type of the community has the best wind protection effect.

### 1. Background

The tea-rubber artificial community is a five row windbreak system. In center of the system are the Brazil rubber trees and tea-trees with large leaves that grow in Yunnan Province China. Each community occupies about 14000m<sup>2</sup> areas. Since the windbreak system provided good ecological and economic efficiency, more than 133million square meters of experimental sites have been established in Hainan Province, China.

Hainan province, However, is a region often stricken by Typhoon. every year more than 4 thousand million rubber trees were damaged. with direct economic loss over hundred millions RMB. For example 7 hundred millions RMB were lost in 1989 caused by three Typhoons. So it is importance of studying how to cut down the damage done by Typhoons.

Practices in Dongtai farm, Hainan province have proven that tea-rubber community has better effect than the pure rubber forest. According to the statistics, the tea-rubber community can lower damage about 17 percent. in

order to understand its mechanism and choose the best type We have studied, through the wind tunnel model test, the wind velocity, the turbulent structure and drag coefficient in the tea-rubber community.

## 2. Simulate method

In resent forest studies, wind tunnel model test are extensively used in researching meteorological effect of windbreak system. to make model test similar to actual situation, the following conditions must be met.

### 2.1 Geometrical similarity

Dimensions of modelling forest and tea-rubber artificial community should be proportional to the actual windbreak system.

### 2.2 Kinematic similarity

Wind velocity and turbulence intensity of points in modelling trial should be proportional to corresponding ones in actual flow, the wind permeability should be equal.

### 2.3 Dynamic similarity

The forces on the corresponding points of modeling and actual forest should be same, especially the Reynolds number, In wind tunnel trail, the actual Reynolds number ( $Re$  is 6million) is hardly reached. However, according to the research of Wudelafu etc, when  $Re$  is 25 thousands, the better results can be obtained. In our test, dynamic similarity is able to be reached at  $Re$  is 2thousands.

## 3. Experimental method

The model test was 100 times small than the actual size (based upon a 1/100th scale). the windbreak system and rubber forest had bamboo trunk, 3mm in diameters; and the plastic canopy. The tea trees were made of pins with cotton yarn wrapped on the top. The stunks were struck into a holey plate in shape of windbreak system.

During the test, Denmark DISA hot-wire instrument and IBM computer were used. the sampling and data pcessing, controled by the computer, and measured the average wind velocity, turbulent intensity and auto - power spectrum of turbulence. The drag coefficients of the tea-rubber artificial community and the rubber forest were taken by the force balance that consist of three component forces balances.

## 4. Results

4.1 Attenuation rate of wind velocity (windbreak effect) for the pure rubber forest, the forest-rubber community and the tea-rubber community.

Attenuation rate means the decreasing percentage of wind velocity of

one point, which is at Z the height and X distance behind the windbreak forest. compared with another point of the same height in the approaching flow.

The average attenuation rate of wind velocity at different height of the rubber forest and the tea-rubber community are shown in Figure 1. They were obtained by superimposing rate at same height and various down distance.

As shown in Fig. 1 the pure rubber forest had the poorest wind protecting effect. the maximum attenuation rate of wind velocity 0.62 appeared at 4m height over the largest canopy, but it decreased rapidly both above and lower the largest canopy. At the height of less than 10. the average attenuation rate only was 0.46. It went up considerably at the height of 4m -10m. After five rows of trees arranged in the way of 5. 4m times 2.7m were planted outside the rubber forest, and remained almost unchanged at 2 -4m. Within 10m height of the rubber forest, the average attenuation rate was up to 0.64. this means the windbreak efficiency was 46 percent higher than that of the pure rubber forest. When tea- rubber community was simulated, the attenuation rate of various tea- rubber communities increased greagly along the total height of the rubber forest. It is 13 percent higher in the tea-rubber community that were one row. 15 percent in two rows in belt. The average attenuation rate was 0.83 in the community that were in two row in clumps, increasing 23 percent in windbreak effect. the above facts suggest that the tea- rubber artificial community has better effect in windbreak than the forest-rubber community, and the type of two row in clumps are the best.

4.2 Turbulent structure inside the rubber forest, the forest- rubber community and the tea-rubber artificial community

Turbulent structure includes turbulence intensity and turrulence auto -power spectrtum. It reflects the degree of turbulence transfer that is the key factor for windbreak effect. The purpose of establishing Protecting forest is to break larger eddies into smaller ones when the flow pass the forest. The increment of the smaller eddies means a rise in turbulence intensity and a decrement in wind velocity, showing the weak transfer of longitudinal kineticenergy into vertical one. The weakness of turbulence transfer results in better protection effect.

4.2.1 Distrubution of turbulence intensity in the rubber ferest, the forest-rubber community and the tea-rubber artificial community

Fig.2. shows the average tubulent intensity throughout the heights of the community generated from various turbulent intensities at downward distances and heights. It evidents that in the pure rubber forest the

turbulent intensity reached to maximum 0.42 at the heights of 8m over the canopy and decreased at the heights more or less than 8m. With windbreak system, the turbulent intensity at the height of 8m went up to 0.45 and tended to go higher at points more 8m. with decreased intensity at point less than 8m. However the average turbulent intensity throughout the height of the rubber forest reached at 0.42, 20 percent higher than that of the pure rubber forest. It shows that there was 20 percent more decrease in wind kinetic energy in the forest-rubber community after windbreak forest had been established.

The average turbulent intensity were up 2.3 percent inside the tea-rubber community that were one row, rose 7.1 percent in community that were two row in belts, up 13 percent in community that were two row in clumps.

This reveal that the tea-rubber community in two row clumps has the maximum turbulent intensity and the largest wind kinetic energy loss so it can provide best wind protection.

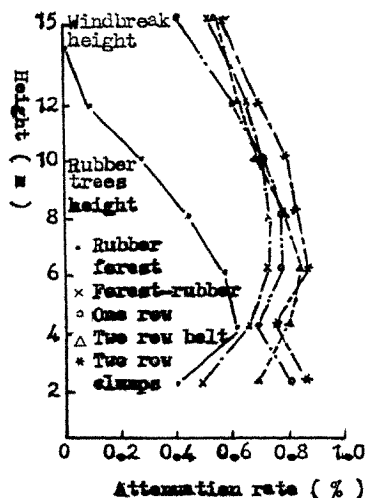


Fig1. Attenuation rate of wind velocity in community

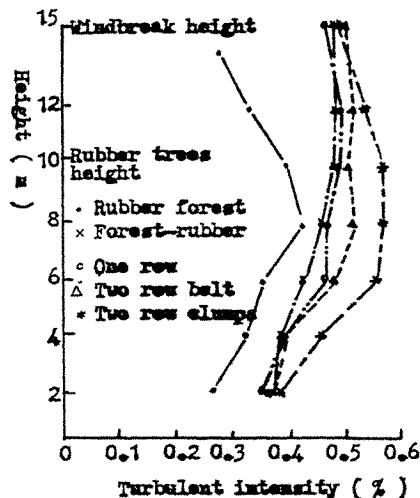


Fig2. Turbulence intensity in community

#### 4.2.2 Auto-power spectrum of turbulence in the tea-rubber community

Turbulent auto-power spectrum show the distribution of turbulent energy between different turbulent eddy scales. Table 1 gives out the maximum auto-power spectrums of the tea-rubber community measured when wind speed is 3m/s at the height of 10m. It is clear when turbulent intensity is

larger, so is the autopower spectrum, but the smallest the turbulent eddy. the tea -rubber community of two row in clumps has the maximum turbulent intensity (0.55) and maximum auto-power spectrum ( $1.34\text{m}^2/\text{s}^2$ ) with minimum eddy scale of 3.3m. this type of the community has up most efect in protection wind due to its maximum consumption of kinetic energy and reduction of velocity and the weakest turbulent transfer.

Table 1. Auto-power spectrum of turbulence in different type of tea-rubber community

Community type	Single low	Two row in belt	Two row inclumps
IX(%)	0.47	0.47	0.56
V(m/s)	0.64	0.90	0.71
nsu(n)( $\text{m}^2/\text{s}^2$ )	0.59	1.0	1.34
L(m)	21	16	3.3

Table 2. Drag coefficient measured in pure rubber forest forrest-rubber community and tea-rubber artificial community

Community type	Rubber forest	Forest-rubber community	Tea-rubber community				
			single	two row in belt	two row in clumps		
$\alpha$	0°	0°	0°	0°	90°	0°	90°
C	0.44	0.38	0.32	0.35	0.40	0.38	0.42
D	0.78	0.99	1.06	1.14	1.20	1.27	1.49

#### 4.3 Drag coefficient of the pure rubber forest, the forest- rubber community and the tea-rubber artificial community

Different drag coefficients in forest belt and in community can lead to various pressure distribution ( vertical and horizontal direction) , influencing the reduction of flow velocity and widbreak effect.

Drag coefficient is directlyh proportional to drag and inversely proportional to square of wind verlocity behind the forest. The community with smaller wind-leakage coefficient has larger drag and drag coefficiet.

The communities with the same drag coefficients have the same wind resisting effect. The drag coefficients of the pure rubber forest, the forest-rubber community and tea-rubber community measured in field are displayed in Table 2. As shown in Table 2, the minimum drag coefficient of 0.70 obtained in the pure rubber forest. It increased to 0.99 in the forest-rubber community, up 27 percent than in the pure rubber forest. However, compared with the forest-rubber community, the drag coefficient raised 7-12 percent in the tea-rubber community of one row type, up 15-21 percent in two row in belt type, and 20-50 percent in two in row clumps type. Obviously the tea-rubber community of two row in clumps has the best effect. Also seen from the Table 2. that when the angle between the approaching flow and the community is 90, the community has largest drag coefficient and the largest wind permeability there fore has better windbreak effect.

## 5. Conclusions

The wind tunnel test on decreasing the damage effect of Typhoon to the rubber forest by the tea-rubber artificial community has been successfully simulated, and the conclusions are as follows:

5.1 The tea-rubber community has better windbreak effect than both the pure rubber forest and the forest-rubber community

Due to, there are a great attenuation rate of the wind velocity. and there are little turbulence transfer. all reading to the better windbreak effect.

5.2 The angle between the tea-rubber artificial community and approaching flow be 90 degree when possible.

5.3 The tea-rubber communities, of two row in clumps is the optimum option of windbreak effect.

## References:

1. P.J.Richards, 2nd international phoenics user conference Meatcraw, London, Now 1987.
2. P.J.Mulhern, Boundary layer meterology, 10 (1976) 423-453.
3. B.D.Amiro, Boundary layer meterology, 51 1990 99-121.
4. Z.F.Wang, Meteorology forests, Jan. 1985.



## Physical modelling of natural wind and its guide in a large open pit mine

Peng Xi and Lu Guorong

Safety and Environmental Protection Research  
Institute, MIM, Wuhan, China

**Abstract:** This paper describes a wind tunnel modelling study of wind field and air pollutant concentration in a large open pit mine, and briefly introduces a preliminary study of guiding wind into the deep part of a pit. In this study, both the present pit and the projected final pit were modelled. Speed profiles and concentration profiles were obtained. Guiding wind test was studied in a 2D model. The effect of wind guide was compared. The expansion angle and the pollution problem were also discussed.

### 1. Introduction

In the field of open pit mine ventilation, much study was done in the Soviet Union. Russian scientists [1-3] published many specialized books and papers. In other countries study on this respect was seldom reported. Study on mine ventilation in China has been focused mostly on underground mines. This focus is due, in part, to the more serious consequences of air pollution underground and the greater ability to control underground ventilation parameters. As more and more surface mines go deeper and air quality problems in surface mines becomes more serious, more research efforts will be needed to improve air quality in surface mines. Since recent years, some work [4] on open pit mine ventilation have been done in China. In 1992, Chinese government authorized a key task entitled "Synthetical study on ventilation and dustproof in the large open pit mine". Safety and Environmental Protection Research Institute of MIM (SEPRI) is in charge of the task. This study is one of the task contents.

Surface mine ventilation can be classified into two categories: natural and controlled. Three types of research methods can be used to carry out this type of study: theoretical study, field test and wind tunnel modelling. Wind tunnel modelling has been widely used in aerosphere and industrial air pollution studies [5-18], but seldom has been used in mining research [19]. In this study, natural ventilation of a large open pit mine was modelled by using a wind tunnel [5] in the condition of neutral atmosphere. The wind tunnel is open circuit and suck-down type. The dimensions of the test section are 2.5 m wide, 1.25 m high and 7.0 m long. The speed in it can be continuously adjusted from 0.3 m/s to 6.1 m/s. Different from ordinary environment wind tunnel, the floor of the tunnel model area can be adjusted downward. The sunken part of the open pit mine model can be laid under the tunnel floor, so the model obstruction would be reduced.

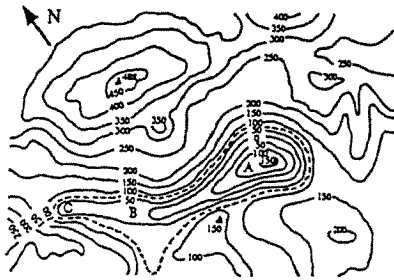


Fig. 1 The topographic map of the mine area.

## 2. Experimental Procedures and Discuss

The mine model was constructed based on a large surface mine located in southern China. The mine consists of 3 mining areas: A, B and C (Fig. 1) and is surrounded by complex mountainous topography. This study was conducted in Area A. At +72 m level, the mine turns from a hillside open pit to a sunken pit with a narrow entry. Currently, the mine operates at -36 m level or 108 m deep. The projected final pit is -168 m level or 240 m deep. Actually, the highest point of the pit is at +488 m level on the north-side of the pit. If measured from this point, the final pit depth would be 656 m. The area of the surface mine modelled was about 2.5 km × 2.5 km. The mine model dimensions are 2.5 m × 2.5 m at a 1:1000 scale.

### Wind Field Profile

The qualitative wind flow study was conducted under southeast wind. The wind direction in the pit was determined by hanging silk ribbons in the scale mine model. The waving direction of the silk ribbons is the wind direction. The results are presented in Fig. 2. It can be seen that the wind flow pattern for the projected final pit is a recirculatory type. According to two Russian scientists [1], recirculatory wind flow can be illustrated as shown in Fig. 3. The air above line OP1B directly moves out of the mine. The air below line OP1B keeps recirculating around the axis of line OP2C and hardly flows out of the pit. The expansion angle  $\alpha$  of the wind was treated as a constant (15 degrees) by the Russians.



Fig. 2 A typical vertical airflow profile.

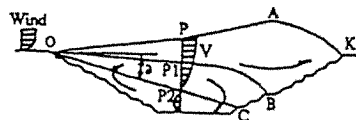


Fig. 3 A recirculatory airflow profile.

The quantitative study of wind flow was conducted under two wind directions: southeast and northwest. The wind speed was measured by using a hot-wire anemometer. The anemometer probe was equipped on a mobile 3D coordinate sys-

tem. By moving the probe horizontally and vertically, the results presented in Fig. 4 to Fig. 7 were obtained. As indicated in Fig. 4, when the wind entered the pit from the northwest direction, the air near the northwest side was in recirculation region. Similar results were obtained under southeast wind. Comparing Fig. 4 to Fig. 7, it can be found that more and more air joins the recirculating wake flow as the pit goes deeper. This could make the air pollution much worse.

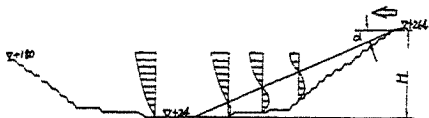


Fig. 4 Airflow velocity profile for the current pit under northwest wind.

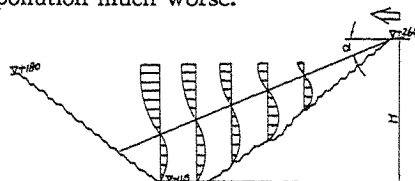


Fig. 5 Airflow velocity profile for the final pit under northwest wind.

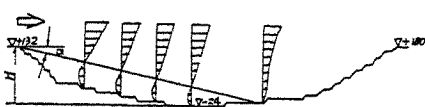


Fig. 6 Airflow velocity profile for the current pit under southeast wind.

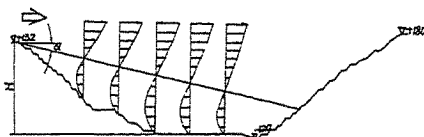


Fig. 7 Airflow velocity profile for the final pit under southeast wind.

### Expansion Angle $\alpha$

As mentioned previously, the wind expansion angle  $\alpha$  was treated as 15 degrees by the Russian scientists. Different results were obtained in this study. The angle  $\alpha$  obtained varied from 6 to 32 degrees. One reason is that their pit located in a plane area (no complex topography). In this study, it was found that the angle is not a constant and depends upon various factors such as the mine depth, slope and wind direction, furthermore, there was roughly a linear relationship between  $\alpha$  and the mine depth (Fig. 8). Therefore, when estimating the volume of the recirculatory air in a deep open pit, it is not appropriate to treat the angle  $\alpha$  as a constant of 15 degrees.

### Pollutant Concentration Profile

In this study, smoke was used to simulate air pollutant. A constant volume of smoke was released to the open pit model from a point source at the mine bottom. The smoke concentrations at various locations were measured using photo-electric sensor and typical results are shown in Fig. 9. It can be seen that the pollutant concentration generally increases from the top to the bottom of the pit. The concentration is significantly higher in the recirculation region. The air quality near the point source could be much worse than the upper areas.

Since it is possible to obtain the site measurement of the pollutant concentration at the current pit, profiles similar to Fig. 9 can be used to predict the air pollu-

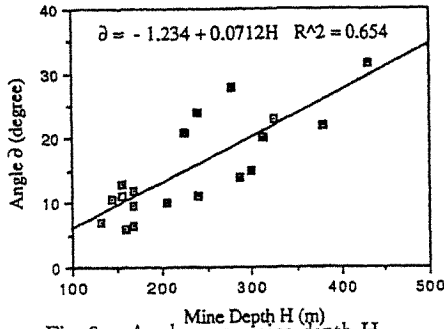


Fig. 8 Angle  $\alpha$  vs. mine depth H.

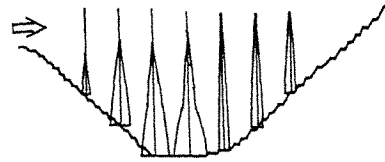


Fig. 9 Air pollutant concentration distribution profile.

tion for projected final pit. It was found that the pollutant concentration at the final pit bottom was about 3.2 times higher as that at the current pit bottom. The respirable dust concentration measured at the bottom of the mine site was  $2.62 \text{ mg/m}^3$ , and the other pollutant concentrations were much lower at the same standard. Therefore, under similar conditions, the respirable dust concentration at the final pit bottom is expected to be  $2.62 \times 3.2 = 8.4 \text{ mg/m}^3$ . It should not exceed the government health and safety standard of  $10 \text{ mg/m}^3$ . However, according to the site measurement and the modelling test, the air quality near the pollution source could easily exceed the government standard, especially under calm inversion pollution. At these locations special measures may be needed.

#### Natural Wind Guide

In surface mining, natural wind guide is an important step of overcoming ventilation problem. It may be realized through two methods as follow: (1) speeding up the coming wind with Venturi phenomenon or (2) changing the direction of the coming wind so as to add wind speed at some part in the pit.

Two walls shaped as a trumpet were laid near the lee slope top of a 2D pit model (Fig. 10). Wind passed between the walls and was speeded up. The wind speed in the pit center was increased. However, for the resistance of the walls, the total wind volume coming into the pit was decreased, and the space of wind circulation was not decreased. The effect of wind guide using the walls depends upon various factors such as the geometric shape, the relative location of the walls and the pit depth.

A plate and plates system were separately laid on the lee slope of the pit model (Fig. 11 and Fig. 12). In this test, it was found that the recirculation region at the pit bottom disappeared and was filled up by the wind flow with the same direction as that of the coming wind. The recirculation region was moved upward to the middle part of the pit space. If the space of a pit is not deep and big, the result similar to Fig. 11 would be obtained by rationally installing a big enough plate. When the pit goes deeper, better wind guide effect would be obtained by using the plate system similar to Fig. 12. Therefore, the pollution state at the pit bottom would be surely improved, provided the wind guide plate is rational designed and installed.

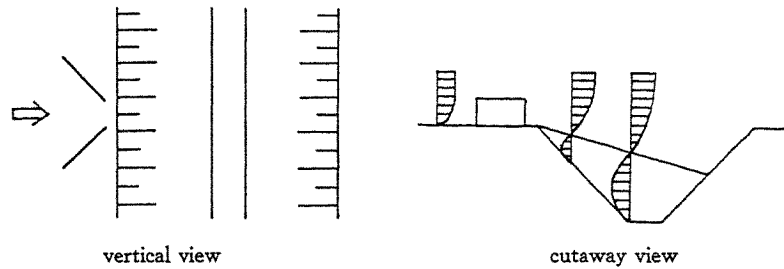


Fig. 10 Sketh of guiding wind by using the walls

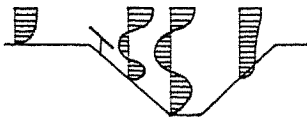


Fig. 11 Sketch of guiding wind by using a plate

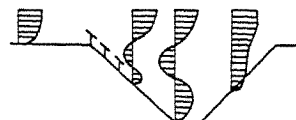


Fig. 12 Sketch of guiding wind by using a plates system

If the speed of avarage wind profile at different height is caculated according to the power law, that within 10 m high is ordinaryly less than half of that at 100 mhigh. In order to guide stronger wind into a pit, the mooring balloon may be used to hang the wind guide plate which easily lifts, falls and is changed the relative de-grees, furthermore, the problem about the structure strength and the project fare of the plate should be easily resolved too.

### 3. Conclusions

According to the modelling test, the following results and the conclusions were obtained.

(1) Wind tunnel modelling is a very effective and practical method for surface mine ventilation studies.

(2) The wind flow pattern in the test pit is generally recirculatory type. Most space of the pit depths is in the recirculation region. The condition of natural ventilation is bad.

(3) In the condition of neutral atmosphere, the average concentration of air pollutant in the test pit will not exceed the government standard.

(4) The mine ventilation condition can be obviously improved by using the wind guide plate or plates system to guide wind from the surface to the pit bottom.

The wind tunnel data is useful of the open pit mine to understand air pollution state of the pit and make the plan of prophylaxis and treatment. It is also useful of relevant numerical simulation studies.

### References:

1. НИКИТИН В. С. , БИТКОЛОВ Н. З. , ПРОВЕТРИВАНИЕ КАРЬЕРОВ, МОСКВА

- «НЕДРА», (1975).
2. НИКИТИН В. С., БИТКОЛОВ Н. З., ПРОВЕТРИВАНИЕ ВЕНТИЛЯЦИИ В КАРЬЕРАХ. МОСКВА «НЕДРА». (1980).
  3. НИКИТИН В. С., БИТКОЛОВ Н. З., ИВАНОВ И. И. БЕЗОПАСНОСТЬ ТРУДА В ПРОМЫШЛЕННОСТИ. СБОРНИК НАУЧНЫХ РАБОТ ИНСТИТУТОВ ОХРАНЫ ТРУДА ВЦСПС pp. 24-31. (1983).
  4. Cai, J. Y. and Lu, G. R., Occupational Health Conditions at Open Pit Work Posts and its Improvements, Proc. South-East Asian Ergonomics Society Second Conference, Malaysia. (1988).
  5. Sun, T. F., Cui, E. J. and Liu, S. P., Proc. APSOWE I, Beijing, pp. 89-102. (1989).
  6. Cermak, J. E., J. Fluids Engineering, Vol. 97, pp. 9-38, (1975).
  7. Hunt, J. C. and Fernholz, H., J. Fluid Mech., Vol. 70, part 3, pp. 543-559, (1975).
  8. Hunt, J. C., Puttock, J. S. and Snyder, W. H., J. Atm. Env., Vol. 13, pp. 1227-1239, (1979).
  9. Kitabayashi, K., J. Atm. Env., Vol. 25A, No. 7, pp. 1155-1161, (1991).
  10. Snyder, W. H., J. Atm. Env., Vol. 24A, No. 8, pp. 2071-2088, (1990).
  11. Bachlin, W., Theurer, W. and Plate, E. J., J. Atm. Env., Vol. 25A, No. 7, pp. 1135-1142, (1991).
  12. Konig-Langlo, G. and Schatzmann, M., J. Atm. Env., Vol. 25A, No. 7, pp. 1189-1198, (1991).
  13. Mccready, D. I., J. Aerosol Science and Tech., Vol. 5, pp. 301-312, (1986).
  14. Mcfarland, A. R., Ortiz, C. A., Cermak, J. E., Peterka, J. A. and Li, W. W., J. Aerosol Science and Tech., Vol. 12, pp. 422-430, (1990).
  15. Ranade, M. B., Woods, M. C., Chen, F. L., Purdue, L. J. and Rehme, K. A., J. Aerosol Science and Tech., Vol. 13, pp. 54-71, (1990).
  16. Visser, G. T., J. Atm. Env., Vol. 26A, No. 8, pp. 1453-1460, (1992).
  17. Lidin, C. D., Editor, Israel Programme for Scientific Translations, Jerusalem, pp. 8-26, (1966).
  18. Page, S. J. and Maksimovic, S. D., Proc. 3rd US Mine Ventilation Symposium, Pennsylvania, (1987).
  19. Stein, R. L., Breslin, J. A. and Strazisar, A. J., J. American Industrial Hygiene Association, No. 12, pp. 815-824, (1974).

## **Pedestrian Level Winds**





# **Pedestrian Comfort including Wind and Thermal Effects**

Michael J. Soligo, Peter A. Irwin, and Colin J. Williams

Rowan Williams Davies & Irwin Inc. (RWDI)  
650 Woodlawn Road West, Guelph, Ontario, Canada N1K 1B8

**Abstract:** The effects of wind force on pedestrians have been a concern since it was realized that tall buildings could greatly accelerate the wind at grade. The use of wind tunnels to assess pedestrian level winds has led to the development of criteria not only for safety but also for comfort. More recently there have been increasing attempts to develop more comprehensive criteria that include more of the overall microclimate rather than wind in isolation. This paper describes new methodology developed by the authors. It includes the effects of wind speed, temperature, relative humidity, clothing, activity, solar radiation, and exposure time. Thus not only is wind force considered but also the impact of wind chill on exposed skin and a person's thermal comfort. It is to be noted that thermal comfort depends to a significant extent on clothing levels and on the level of activity which affects a persons' metabolic rate.

## **1. Introduction**

In the 1990's and well into the 21st century, Urban Designers, Architects, Engineers, and Planners will be challenged to respond to society's growing concerns about the environment and the quality of urban life. The demands for "comfortable" living and a safe environment will be in the forefront. Comfort in the urban environment will refer to many aspects of the physical environment.

Through literature reviews, research, field studies and past experience, it has become apparent that pedestrian level comfort is not solely dependent on the force of the wind. However, the majority of pedestrian level comfort criteria have, in the past, been based solely or primarily on the wind force. Pedestrian level comfort is a combination of several components some of which include: wind force, thermal comfort, wind chill, noise levels, air quality, streetscape, aesthetics, etc.. While some of these components may be difficult to quantify, it is felt that the first three, namely wind force, thermal comfort and wind chill should be used to establish base criteria. Criteria based on these three components are by no means a final method of evaluation. However, they represent an advance and significant improvement over criteria based solely on wind force.

## **2. Components of a Pedestrian Level Comfort Study**

### **2.1 Wind Force Component**

In the analysis of wind force effects on pedestrians, it is necessary to consider the frequency of occurrence of various wind speeds. Wind direction may be of interest in some instances, but in general, it is only the magnitude of the wind velocity vector that is important. In terms of pedestrian level comfort, it is the wind force, resulting from the wind velocity, and its mechanical effects on people that are important. Mechanical effects include: blowing hair and flapping clothes in a moderate breeze; to more severe impacts such as impeding progress when walking, and affecting one's balance under high wind velocity conditions.

Many pedestrian level wind comfort criteria have been developed over the years. Typically these criteria categorize various wind velocity ranges as being appropriate for certain types of activity that can comfortably be performed. The criteria have also included acceptable frequencies of occurrence of the wind velocity values. Many past criteria have defined the comfort categories and their associated wind velocity patterns, in terms of infrequently occurring wind velocities, e.g. wind velocities occurring 1% of the time. However, our experience has been that criteria based on infrequent wind velocities are often too difficult to understand by those not knowledgeable in wind engineering. This represents the vast majority of end users of most pedestrian level comfort studies, namely; developers, architects, planners and the general public. A developer does not find it easy to understand why a project fails a comfort criterion at a certain location because a particular velocity is exceeded 1% of the time. The frequent reaction is "well this must mean it is comfortable for 99% of the time; so what's the problem?" To resolve this difficulty the authors have recast the criteria to answer the question "What will the wind conditions be like most of the time?" rather than "How high will the wind speed be for a small percentage of time?".

Note that the discussion in the preceding paragraph relates only to comfort criteria, not safety. When considering safety, it has generally been found that end users have not found it difficult to accept that unsafe conditions should be rare occurrences, e.g. not more than 3 or 4 times per year, or once per season.

The criteria presented here are based on the authors experience and practical application over the past two decades, plus results from previous researchers. Papers produced by Ratcliff and Peterka (1989)<sup>1</sup> and, Stathopoulos and Saathoff (1989)<sup>2</sup> compared the criteria of several well known researchers. Using these comparisons, the authors propose a wind force comfort criteria broadly consistent with those in the references cited. However, the format has been designed to reduce complexity and increase the practical approach to assessing pedestrian comfort.

**Table 2.2: Wind Force Criteria**

Category	Gust Wind Velocity	Frequency
sitting	0 - 17 km/h	≥80%
standing	0 - 25 km/h	≥80%
walking	0 - 32 km/h	≥80%
uncomfortable	>32 km/h	>20%
severe	≥88 km/h	0.15%

Note that in areas subject to frequent Hurricanes (or Typhoons as they are called in the Pacific region) some judgement may be required in applying the severe criterion. This is because present day warning systems are such that people are unlikely to be outside under these extreme conditions and so some relaxation of the severe criterion is reasonable, provided that the normal severe criterion is satisfied in non-hurricane winds.

The criteria consider two main aspects: 1) safety; and, 2) comfort levels for various pedestrian activities. Considering the safety aspect, unsafe conditions are those which would blow people over. Calculations by the authors, of the wind force on the projected area of a human being (as suggested by Penwarden (1972)<sup>3</sup>), and observations such as those of Melbourne

and Joubert (1971)<sup>4</sup> have shown that gust speeds in the range 80 to 100 km/h are sufficient to blow pedestrians over. The exact value depends on their weight, size, traction, clothing and other factors such as athletic ability. Therefore, the criterion for safety is set such that a location is categorized as severe if  $\dot{U} \geq 88$  km/h occurs more than 0.15% of the time or four (4) occurrences per year (assuming 3 hour events and 24 hours per day).

Considering comfort, the approach has been to first select a characteristic wind velocity range that is comfortable for a particular activity, (e.g. sitting) and then to require that this be satisfied for 80% of the time. This type of format is readily understood by end users, an important consideration in pedestrian wind comfort studies. The choice of 80% of the time, rather than some other percentage is, to some extent, flexible in that local planning authorities may wish to raise or lower the limit slightly, based on local experience. However, it is noteworthy that Penwarden and Wise (1975)<sup>5</sup> selected 80% based on discussions with developers and building managers. Also the American Society of Heating, Refrigeration and Air Conditioning Engineers (ASHRAE) has used 80% in indoor comfort applications.

## 2.2 Thermal Component

### 2.2.1 Background

The assessment of thermal comfort involves consideration of the heat balance of a human body to determine if excessive temperature change in the body is occurring after a certain exposure time to ambient conditions. The evaluation of thermal comfort is the most complex of the three comfort components and is affected by temperature, humidity, solar radiation, wind speed, clothing, activity, exposure time, and regulatory mechanisms that can maintain thermal comfort even under otherwise uncomfortable conditions.

These variables have been incorporated into various mathematical models of thermal comfort, two of the more well known being the Fanger<sup>6</sup> model and the Pierce Two-Node model (ASHRAE)<sup>7</sup>. The Fanger model is a steady state energy balance model which assumes a state of equilibrium has been reached. The Pierce model is a two-node model which evaluates the inner body temperature and skin temperature. It is a transient model that allows variation of exposure time. Both of these models were developed for indoor environments. However, a review of the research conducted by Arens, Gonzales and Berglund (1986)<sup>8</sup> and Doherty and Arens (1988)<sup>9</sup> indicated to the authors that the Pierce model has better validity over a wide range of outdoor environments and activity levels. Therefore, this model was chosen to evaluate outdoor thermal comfort.

### 2.3 Wind Chill Component

Wind chill combines wind velocity and air temperature to determine the chilling effect on exposed skin. Unlike the body heat balance, wind chill is generally not affected by clothing level in urban environments as the face, ears, and in many cases, the hands are exposed even when pedestrians are clothed in heavy winter apparel. Areas subject to seasonal temperatures less than 10°C should include a wind chill component when assessing pedestrian comfort. The wind chill index (WCI) provides an empirical estimate of wind chill<sup>8</sup> and is used to determine an equivalent wind chill temperature ( $T_{eq}$ ):

$$T_{eq} = -0.04544 (\text{WCI}) + 33^{\circ}\text{C}$$

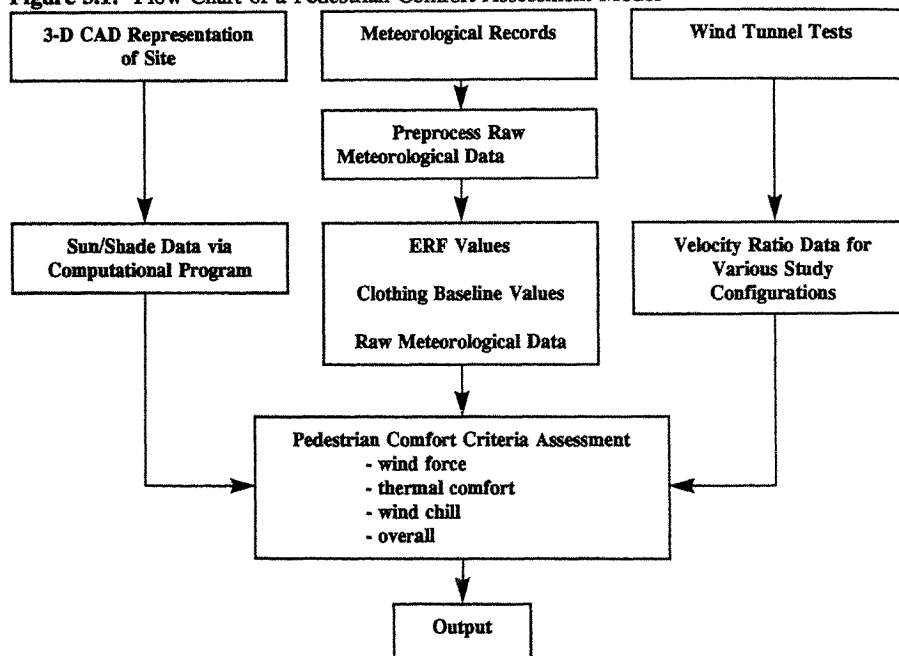
To determine if the wind chill criterion is met, a maximum allowable WCI value must be determined based on a minimum acceptable equivalent temperature. In this criterion, an equivalent temperature of  $-20^{\circ}\text{C}$ , translating to a maximum WCI of  $1166 \text{ kcal}/(\text{m}^2 \text{ h})$  is used.

### 3. Input Parameters for the Pedestrian Comfort Assessment Program

As previously discussed, pedestrian comfort involves three primary components: the mechanical force of wind; the combined effect of clothing, solar radiation, meteorological conditions, activity level and exposure time on the body's thermal comfort; and, wind chill effects on exposed skin resulting from wind velocity and ambient air temperature. If any combination of these "comfort components" is not satisfied to a particular level, then pedestrians will not be comfortable.

In order to assess the effect of urban developments on pedestrian comfort, the authors have developed a pedestrian comfort assessment computer program that evaluates the wind force, thermal comfort and wind chill levels. Various input parameters are acquired from three primary sources namely: a computerized sun/shade simulation; wind tunnel tests; and meteorological records. Predictions of pedestrian comfort for existing and proposed conditions are then obtained by combining parameters from these three sources. The evaluation takes place at pre-determined points, i.e. at locations where wind velocity measurements were taken in the wind tunnel tests. These points are referred to in this paper as sensor locations. The pedestrian assessment process is summarized by a flow chart as illustrated in Figure 3.1.

**Figure 3.1:** Flow Chart of a Pedestrian Comfort Assessment Model



#### 4. Pedestrian Comfort Assessment

For overall comfort, the three comfort components are combined into a single overall comfort evaluation for each of the three standard activities (sitting, standing, walking). In order to pass overall comfort in any given hour, all three individual comfort components must pass for that hour. For example, for an overall comfort level conducive to sitting to pass a particular hour of meteorological data (at a particular sensor location), the wind force (sitting), thermal (sitting), and wind chill components must all pass that hour. If any one of the three components fail, the overall comfort is categorized as failing that activity level for that hour.

The purpose of assessing these three comfort components individually is to identify which component or components cause a specific location to fail the overall pedestrian comfort analysis. By identifying the component(s), the type of mitigation required to improve conditions can be determined. Table 4.1 gives an example of results for the three different comfort components at two locations (sensors).

For the final output, only the overall pedestrian comfort assessment need be displayed for simplicity. The individual results of the wind force, thermal, and wind chill assessments may be listed in an appendix and used to isolate the source of discomfort, if required. A typical overall pedestrian comfort assessment may be displayed as shown in Table 4.2 which includes the safety criterion identified as the severe category.

**Table 4.1: RWDI Pedestrian Comfort Analysis Raw Data Output: Percentage**

Sensor	Wind Chill	Wind Force (Mechanical)				Thermal		
	Pass %	Sitting %	Standing %	Walking %	Uncomfort. %	Sitting cold/hot %	Standing cold/hot %	Walking cold/hot %
1	99.6	46.6	67.6	83.6	16.3	85.0 9.1/5.9	90.6 3.0/6.4	92.2 0.0/7.8
2	99.7	45.0	67.0	86.5	13.5	85.3 8.0/6.7	89.9 2.7/7.4	91.2 0.0/8.8

**Table 4.2: Overall Pedestrian Comfort Sample Output**

#### OVERALL COMFORT: SPRING SEASON

* Recommended Limit(%)		Sitting ≥80%	Standing ≥80%	Walking ≥90%	Uncomfort- able >20%	Severe ≥0.15%	
Location	Configuration	%	%	%	%	%	Comfort Category
1	A	38	60	77	23	0.19	severe walking
	B	57	73	66	14	0.00	
2	A	37	59	80	20	0.05	walking standing
	B	62	84	93	7	0.01	

Note: \* these percentages can be adjusted by individual municipalities depending upon existing conditions and the local planning objectives

The two locations listed in Table 4.2 are categorized according to the percentage of time a given pedestrian location is considered comfortable. The location is automatically considered severe if the 0.15% criteria is exceeded, as identified by Location 1 Configuration A. When more than one activity comfort limit is achieved, the most demanding condition is used to categorize the location. For example, at Location 2 Configuration B, conditions are comfortable for both standing and walking activities a minimum of 80% of the time. This location is categorized as comfortable for standing type activities as the standing level is more demanding to achieve than the walking level. The use of multiple configurations, defined as Configuration A and B in Table 5.1, is useful in identifying the impact at each location of, for example, a development. Configuration A could represent existing conditions and Configuration B represent conditions with the proposed development in place.

## 5. Conclusions

The comfort methodology described in this paper synthesizes the three major factors affecting pedestrians into a single model. The three factors are wind force (mechanical), thermal comfort, and wind chill. In our view, these three components should be studied concurrently to obtain a truly representative picture of the comfort conditions.

An assessment model must be flexible in order to reflect the varying meteorological conditions that occur regionally, and the different planning objectives of individual municipalities. The three input parameters of sun/shade simulation, wind tunnel tests, and meteorological records, which reflect specific characteristics of each location, aid in the customization of the assessment and comfort criteria.

A detailed paper on the various components comprising pedestrian comfort is currently being prepared by the authors. When published, this paper may be of interest to the reader.

## List of References

- [1] Ratcliff, M.A., and Peterka, J.A., "Comparison of Pedestrian Wind Acceptability Criteria", Cermak Peterka Peterson Inc., Fort Collins, Colorado.
- [2] Stathopoulos, T., and Saathoff, P.J., "Pedestrian Wind Environmental Criteria for the City of Montreal", Centre for Building Studies : Concordia University., 1989.
- [3] Penwarden, A.D., " Acceptable Wind Speeds in Towns ", Build. Sci. Vol. 8, pp. 259-267. Pergamon Press 1973.
- [4] W.H. Melbourne and P.N. Joubert, " Problems of Wind Flow at the Base of Tall Buildings". Paper presented at the International Conference on Wind Effects on Buildings and Structures, Toyko (1971). pp. 105-114.
- [5] Penwarden, A.D. and Wise, A.F.E., "Wind Environment Around Buildings", Building Research Establishment Report, HMSO, 1975.
- [6] Fanger, P.O., "Thermal Comfort Analysis and Applications in Environmental Engineering", Robert E. Krieger Publishing Company, Malabar, Florida, 1982.
- [7] ASHRAE 1989 Fundamentals Handbook, Chapter 8 : Physiological Principles, Comfort, and Health, 1989.
- [8] Arens, E., Gonzalez, R., and Berglund, L.G., " Thermal Comfort Under an Extended Range of Environmental Conditions", ASHRAE Trans, Vol.92, Pt.1, 1986.
- [9] Doherty, T.J., and Arens, E., " Evaluation of the Physiological Bases of Thermal Comfort Models ", ASHRAE Trans, Vol. 94, Pt. 2, 1988.
- [10] Williams, C.J.,and Soligo, M.J., RWDI, " A Discussion of the Components for a Comprehensive Pedestrian Level Comfort Criteria ", Eighth International Conference on Wind Engineering, London, Ontario, 1991.

## **Infrared-Thermography Technique for Pedestrian Wind Evaluation**

Hanqing Wu and Theodore Stathopoulos

Centre for Building Studies, Concordia University  
1455 de Maisonneuve Blvd. W., Montreal, Quebec, Canada H3G 1M8

**Abstract:** An infrared-thermography system has been developed for estimating the pedestrian-level wind conditions around buildings. Surface temperature variations have been attempted to relate to pedestrian-level wind speeds. Experiments were carried out in a boundary-layer wind tunnel for a variety of building models and the overall impact of building-induced winds was quantified via a parameter defined by the temperature distribution over the entire flow field. Details of the experimental setup, operational principles, calibration results and application examples are presented.

### **1. Introduction**

Wind environmental conditions at pedestrian level could be studied in laboratories by either point methods or area methods. Usually, point methods measure wind flows at selected positions, whereas area methods provide spatially continuous pictures for entire flow fields, though in less accurate patterns. Therefore, it is desirable to develop a technique that has the advantages of both point and area methods.

The application of infrared thermography for pedestrian wind measurements was first proposed in [1]. The methodology is based on the fact that heat transfer from a heated body to air flow is related to flow conditions near body surfaces. By using the infrared technique, wind-induced temperature variations on ground are detected and used as a measure of the wind impact at pedestrian level. The paper describes an infrared-thermography system recently developed at the Centre for Building Studies, Concordia University. Details are presented on the experimental setup, operational principles, calibration results and application examples of the technique.

### **2. Infrared-thermography System**

The infrared system consists of a heated plate as the ground where building models stand on, an infrared video camera with a floppy-disk driver for recording thermal images, and a microcomputer with software for data processing and presentation. These components are sketched in Fig. 1 with the wind tunnel, where flow features over a typical suburban terrain were simulated.

The heated plate is composed of four square flat pieces, each 60 cm wide. Electric circuits printed on a fiberglass sheet serve as controllable heat sources. An aluminum plate is sandwiched between the heater and the plexiglass to promote a uniform heat distribution. The top surface of plexiglass is sanded and grided to scale as the measuring plate. In order to minimize undesired heat leakage, the whole measuring plate is heat-insulated from the bottom and periphery. An infrared video camera, with a resolution of 0.1 °C, is installed on the wind-tunnel ceiling. Details of the camera and its operation are available in [2]. Thermal images are recorded as binary files in floppy disks for further processing. In an image file, the temperature distribution over a square area is digitized by 140 x 140 pixels, which can be displayed on a computer screen and printed in color or black-white. Considering the geometric scale of simulated wind flow, a pixel represents the information over a square of full-scale equivalent 2 m by 2 m in the current setup.

### 3. Performance of the Heated Plate

A series of pilot tests were carried out to examine the performance of the heated plate without building models in the tunnel. By using thermocouples, temperatures were measured at the centre of aluminum plate ( $T_h$ ), the top surface of plexiglass ( $T_s$ ) and the air flow in wind tunnel ( $T_a$ ) under different conditions, i.e. when (a) the heater is warmed up before the wind tunnel is started; (b) the tunnel is running full speed; and (c) the tunnel operates at different speeds.

Temperature measurements are shown in Fig. 2 for these three conditions. First,  $T_h$  and  $T_s$  increase with time while the heater is being warmed up. In the mean time,  $T_a$  may be affected by environmental factors such as the functioning of air conditioning systems in the laboratory. After the wind-tunnel is started, the wind flow cools down the measuring plate whereas the running motor heats up the environment. Due to heat accumulation, the plate temperatures may rebound with relatively low rates comparing with the significant temperature drops during the first few minutes. After a 20-minute stabilization for both

the wind tunnel and the plate, the final test was performed with the gradient wind speed changed every five minutes. For each time interval,  $T_h$  and  $T_s$  are found increasing when the wind speed decreases, and decreasing when the wind speed increases - this trend is essential for a quantitative evaluation of wind speeds by considering temperature variations.

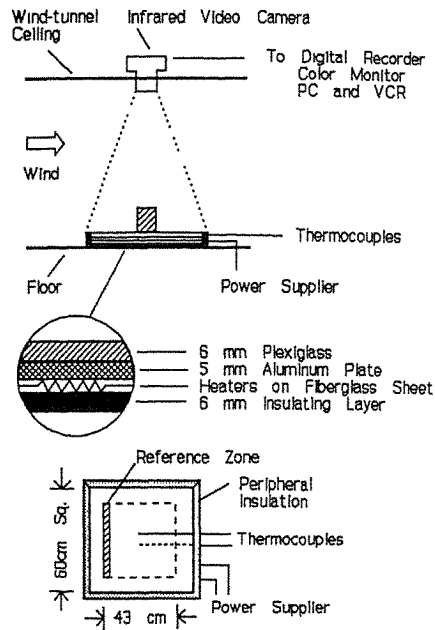


Fig. 1 Setup of the infrared-thermography system.

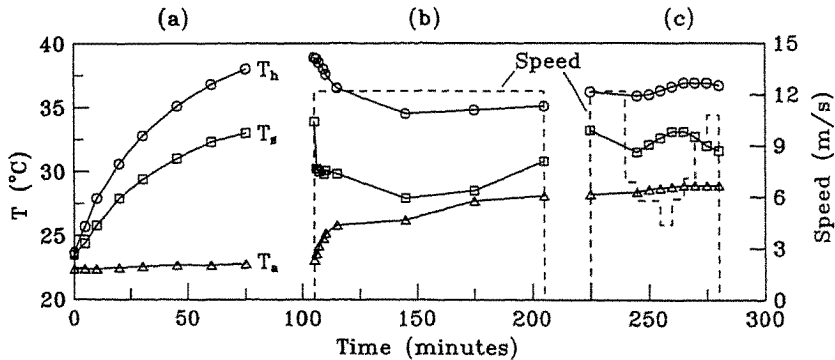


Fig. 2 Temperature variation under different conditions.



When the temperature distribution over the entire plate was examined, some cooling was detected along the perimeter even though insulation was provided. Hence, only data from the central part of the plate were selected for processing. The central part, enclosed by dash lines in Fig. 1, corresponds to a matrix of 101 x 101 pixels. A Reduced Temperature is defined as:

$$\delta T(x,y) = [T_o(x,y) - T_s(x,y)] - [t_o - t_s] \quad (1)$$

where  $T_o(x,y)$  and  $T_s(x,y)$  are temperature distributions on the measuring plate recorded in the absence and presence of buildings with a fixed time interval of five minutes between two recordings,  $t_o$  and  $t_s$  are averaged temperatures over the reference zone (Fig. 1) out of the influence of building models in order to compensate the temperature variation caused by changes of environmental parameters rather than wind speeds. This definition ensures  $\delta T=0$  over the unaffected region far from building models.

#### 4. Comparison of Wind Speed and Surface Temperature

Figure 3 displays three typical thermal images around isolated buildings with a height, a windward length and an along-wind width of (a) 30:30:30; (b) 60:30:30; and (c) 60:60:30 m, respectively. Original color images are smoothed and converted to the grey scale. Values of  $\delta T$  could be determined by checking the ruler beside, except in zones occupied by building models which are decorated. For these three models, reduced temperatures are found high in front and around corners of buildings and low in the wake area behind buildings.

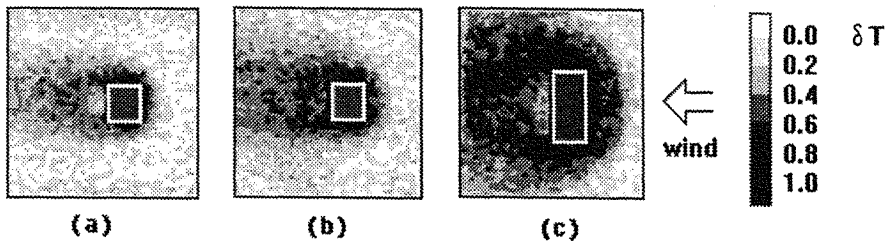


Fig. 3 Typical temperature distributions around tall buildings.

The wind speed variation induced by buildings can be described by an Overspeed Ratio ( $K$ ) of effective speeds ( $U_e$ ) when new buildings are present and absent:

$$K = \frac{(U_e)_{\text{present}}}{(U_e)_{\text{absent}}} , \quad U_e = \bar{U} + g U_{rms} \quad (2)$$

It was suggested in [1] that overspeed ratios with gust factor  $g=3$  are most appropriate for temperature variations. Contours of overspeed ratios ( $g=3$ ) and reduced temperatures ( $\delta T$ ) around a high-rise building are shown in Fig 4. An average temperature over a small area is considered to be more representative than the value at a single point. In this calibration,  $\delta T(x,y)$  is the average value over the selected point ( $x,y$ ) and its four adjacent points, an area of 20 m<sup>2</sup> in full scale. The overspeed ratios are measured by a vertically-installed hot-film anemometer at 2 meters from the ground.

Similar measurements have been performed for rectangular buildings of 30 to 120 m in height and 20 to 90 m in length. Data pairs of  $\delta T$  and  $K$  are selected at the same positions around

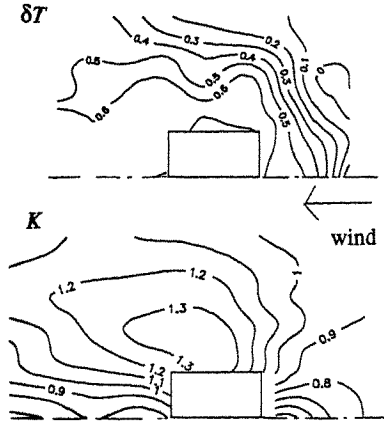


Fig. 4 Comparison of overspeed ratios and reduced temperatures around a tall building.

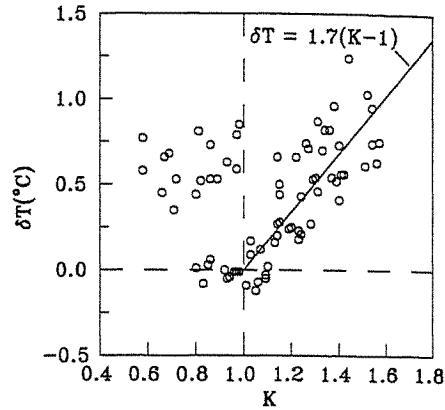


Fig. 5 Calibration of reduced temperatures by overspeed ratios at selected points.

similar buildings and compared in Fig. 5. Because of the clear difference in distributions of Fig. 4, data pairs scatter over the  $K$ - $\delta T$  plane. They could be characterized into three zones: (1)  $K > 1$  and  $\delta T > 0$ , corresponding to the corner-stream zone where the increase of wind speeds is indicated by both methods; (2)  $K < 1$  and  $\delta T > 0$ , the front-vortex zone where results are scattered; and (3)  $\delta T < 0$ , the wake-turbulence zone where sheltering effect is demonstrated to different extent.

In the corner-stream zone, where strong winds are most likely to happen, the reduced temperatures and Overspeed Ratios have comparable patterns in general (Figs. 4 and 5). A point-by-point calibration is performed for the data in this zone only. Ideally,  $\delta T$  should be zero when  $K=1$ . Thus, a linear function  $\delta T=1.7(K-1)$  is derived from data of corner streams. Other correlation functions could be attempted, but there might be little to be gained since data are quite scattered. The main deviation appears in front of the buildings probably because the vertical wind may induce cooling effects on the ground as strong as those due to the horizontal flow. However, a vertically-installed hot film can only detect the horizontal component of wind flows.

Other factors may also create errors in the calibration. These are as follows: (1) The selection of comparison points is subjective and maybe inaccurate; (2) The heat released from the plate may change the air temperature over other zones; and (3) Heat conduction exists within the plexiglass plate and from the plate to building models. At the current stage, a more practical and comprehensive approach for the infrared-thermography technique is to evaluate the wind impact over the entire wind field instead of a number of limited points.

### 5. Overall Impact of Wind Flow

A single parameter which quantifies the overall impact of wind flows may be defined by the area integration of reduced temperatures over influenced zones around buildings.

$$\Omega = \iint_{\delta T > 0} \delta T dA \quad (3)$$

The condition  $\delta T > 0$  specifies the integration only for the area with reduced surface temperatures excluding the region covered by building models. This definition estimates the total area of affected regions weighed by the reduced temperature. For rectangular building models, values of the overall impact are found directly related to buildings' windward dimensions. For

example, the models in Fig. 3 may induce overall impacts of (a) 6.3, (b) 9.6, and (c) 18.5  $k^{\circ}Cm^2$ , respectively. This integration applied to thermal images compromises the fluctuations in individual locations and provides an evaluation of wind impact in an average sense. The overall impact may be further compared with the hot film or LDA results for  $\delta T > t$ , where  $t$  may have any non-negative value, and may eventually establish the infrared thermography technique as a quantitative area method.

Flow patterns around low buildings are different from those around tall buildings and, sometimes, more complicated. The infrared thermography has been applied for several buildings 15 m high and 15 m wide. Results obtained are found similar with those from speed measurements under similar experimental conditions.

Figure 6 shows the reduced temperatures distributed around a long building (80 m) for two incident angles: (a) The normal wind creates windy zones downstream around both building corners symmetrically and the wake immediately behind the building is well protected; (b) For an oblique wind ( $22.5^{\circ}$ ), considerable wind disturbance is observed at one side behind the building. This is caused by the reattachment of jump-over flow with high mean speeds and strong fluctuations.

Thermal images around two identical low buildings (40 m in length) are displayed in Fig. 7(a)-(f). For buildings with a wide gap, 15 m in (a), the wind impact in the wake is partially alleviated by the gap jet. The flow pattern in (b) with a more narrow gap (10 m) is similar to that of the long building in Fig. 6(a). Figures 7(c) and 7(d) show less disturbances since these two models have smaller blockages to the coming wind comparing with other cases. Behind building models (e) and (f), the jump-over flow can be observed with relatively high disturbances. More specifically, configuration (e) is more critical in the wind environmental respect than (f), although the latter forms a funnel open to the oncoming wind. This is to be expected for low-rise buildings. The overall impact for all models in Figs. 6 and 7 is shown in Table 1.

## 6. Further Thoughts on the Infrared Technique

In experimental fluid dynamics, the heat-transfer method is used to measure the surface shear stress by placing a small heated plate on the surface to sense the temperature change [3]. For pedestrian-level wind measurements, the site surface under consideration can be modeled by a heated floor composed of a limited number of uniformly-heated small elements. The heat conduction between these elements is governed by their temperature differences. Thermal insulation between these elements or utilization of single-directional conductive materials may minimize the horizontal heat conduction. Then, each element can be treated individually as the sensor for shear stresses. Once the shear stress is obtained, wind speeds above the ground at corresponding locations can be estimated according to the law of the wall for shear flows.

More effort is needed to explore the relation between the heat loss and the effective wind speed since the wind flow at pedestrian level is not always parallel to the ground as constrained by the above model. An effective wind speed may be constituted to represent the combined effect of mean and fluctuating wind components in both horizontal and vertical directions. This may be studied numerically by simulating the heat transfer through the interface of air flow and plexiglass plate for different wind directions and turbulence intensities.

## 7. Concluding Remarks

In this paper, quantitative results derived from thermal images around different buildings are presented for both selected locations and overall affected regions. The infrared technique, at the current stage, is capable of visualizing surface flow fields through colour images; quantifying windy zones in terms of the reduced temperature; and evaluating the overall impact of pedestrian-level winds by additional calculations.

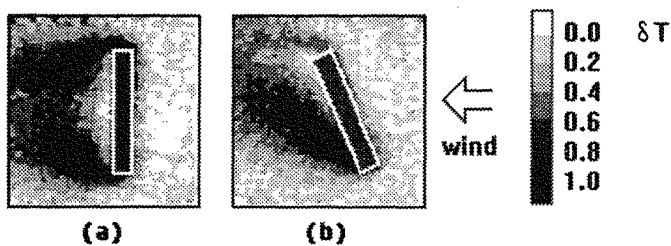


Fig. 6 Thermal images around long, low-rise buildings.

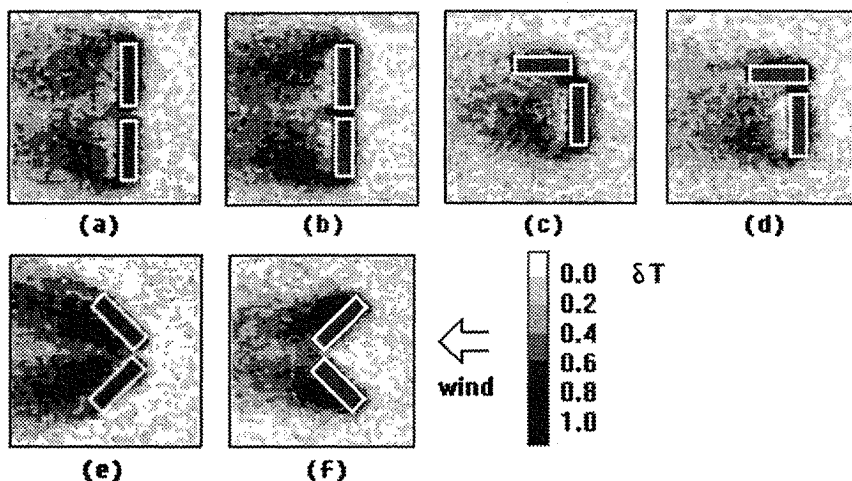


Fig. 7 Reduced temperatures distributed around models of two identical buildings.

Table 1. Overall impact around building models in Figures 6 and 7.

Model	Figure 6		Figure 7					
	a	b	a	b	c	d	e	f
$\Omega$ ( $^{\circ}\text{Cm}^2 \times 1000$ )	12.8	11.5	11.3	13.3	9.4	9.7	11.7	11.1

**References:**

1. Y. Uematsu, and M. Yamada, "Application of infrared thermography to the evaluation of pedestrian-level winds around buildings," *Int. Conf. on Exp. Fluid Mech.*, China, 1991.
2. Agema Infrared Systems, *Operating manuals for Thermovision<sup>®</sup> 400 series and CM-SOFT version 1.1*, Agema Infrared Systems AB, Sweden, 1991.
3. B.C. Bellhouse and D.L. Schultz, "Determination of mean and dynamic skin friction, separation and transition in low-speed flow with a thin-film heated element," *J. Fluid Mech.*, 24 (1966) 379-400.

## **Wind Environment Assessment: A case study in the Brisbane CBD.**

C.W. Letchford and J.D. Ginger

Department of Civil Engineering  
The University of Queensland  
Brisbane Queensland Australia 4072

### **Abstract**

Continuous full scale wind speed measurements at two locations on inner city footpaths are being undertaken in order to evaluate wind tunnel methods for predicting street level wind environment. Three years of data have been collected and analysed. This paper presents comparisons with predictions from wind tunnel tests.

### **1. Introduction**

The construction of exposed or tall buildings significantly alters the street level wind environment and many city authorities require wind tunnel testing of new developments to assess their impact on the local wind environment. Street level wind speeds are of concern for two reasons. Firstly, high gust wind speeds unbalance pedestrians which may lead to serious injury or death. Secondly, persistent lower strength winds causing a wind environment that is perceived as unpleasant can result in social and economic losses as people will avoid such areas. This particularly relevant in outdoor entertainment, shopping or eating areas.

The standard procedure for wind environment assessment combines the local wind climate information and an atmospheric boundary layer model to predict a reference wind speed for each global wind direction. Drawing on similarity, wind tunnel tests are then undertaken to establish ratios of street level winds to this reference wind speed for each global wind direction. The probability distribution of street level winds can then be predicted by integration over all wind directions. An assessment of the local wind environment can then be made using various criteria, eg. as suggested by Melbourne[1].

This paper describes a project that has been underway for approximately three years which specifically aims to obtain long-term street level wind data with the ultimate goal being to evaluate the performance of the current method of assessing the local wind environment. A preliminary report on this project is found in [2], since then significantly more full scale data has been analysed. In addition, 1:400 scale wind tunnel tests have been undertaken and this paper specifically presents comparisons between model and full scale.

## 2. Present study

Two locations within the heart of the Brisbane CBD have been instrumented with anemometers, wind vanes, data loggers and modems. Figure 1 gives an aerial schematic of the CBD showing the instrumented sites in George and Eagle Streets. These two sites were chosen to reflect the quite different wind conditions experienced in the city during summer and winter. The George Street site being exposed to winter westerlies and the Eagle Street site to summer northerlies and south-easterlies.

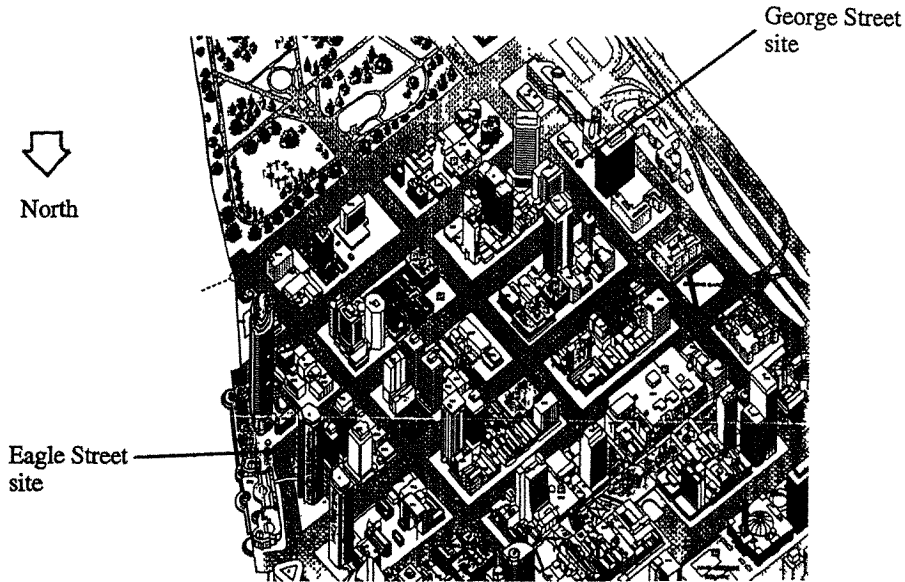


Figure 1. Aerial schematic of the Brisbane CBD showing the instrumented sites. (from JLW Metroscan)

Instrumentation and data acquisition details may be found in [2]. For each 10 minute period of the day the mean wind speed and direction were recorded together with the largest gust in that period and its direction. At the George Street site recording commenced in April 1990 and at the Eagle Street site in November 1990. Data has been analysed up to April 1993 and for the George Street site the down time amounted to 6% while for Eagle Street it was 10%. The maximum gust speeds measured to date have been 61km/hr (twice) in George Street and 71km/hr in Eagle Street, neither was associated with a thunderstorm.

The 10 minute mean wind speed and direction, at 10m height, recorded at half hourly intervals at the Brisbane Airport Meteorology Station have been digitized for correlation with the inner city sites. The meteorology station is located adjacent to Moreton Bay some 10km to the north-east of the CBD. Half hourly observations have

been taken at Brisbane Airport since the 1950's and a specific period from May 1961 until November 1987, employing the same anemometer, has been used to establish the long term wind climate of the region. Figure 2 shows the predicted 10 minute mean half hourly wind speed at Brisbane Airport with a probability of exceedance of 0.001. The prevailing northerlies, south easterlies and westerlies are in evidence.

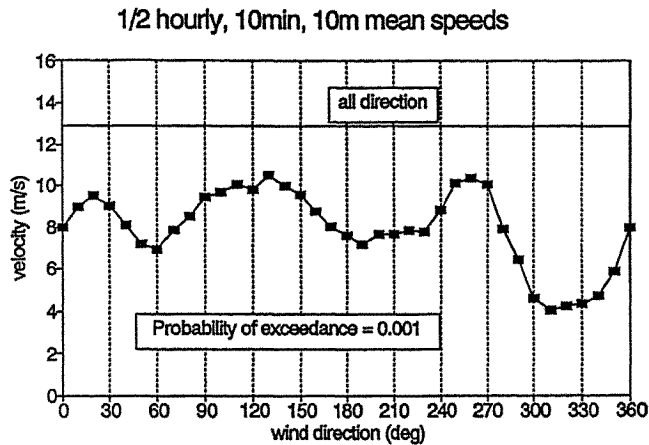


Figure 2. Brisbane Airport wind climate

### 3. Wind tunnel model tests

Wind tunnel model studies of the two locations were undertaken in the Department of Civil Engineering's boundary layer wind tunnel at a model scale of 1:400. The wind tunnel has a cross section of 2m by 3m and a working section of 12m for developing Atmospheric Boundary Layer simulations. A suitable simulation of an AS1170.2 [3] terrain category 3,  $z_0 = 0.2\text{m}$ , ABL was obtained with excellent matching of mean velocity and turbulence intensity profiles as well as the spectrum of the longitudinal component of velocity. Detailed modelling of the inner city for a radius of 550m from each site was situated on the wind tunnel turntable.

Street level velocity measurements were made with Irwin tubes [4] with some additional measurements made with DISA hot wire probes. The Irwin tubes were calibrated against a hot wire anemometer. During the experiment, the Irwin tube pressure measurements were non-dimensionalized by the mean dynamic pressure at 1.7m height in the wind tunnel away from the influence of the model. Final presentation of results were in the form of a ratio of street level wind speed to a wind speed located at 1.0m above the wind tunnel turntable centre without the model in place. By similarity this ratio would represent the full scale ratio of street level wind speed to that wind speed at 400m within a terrain category 3 boundary layer. Measurements were taken for 30° sectors and tests were undertaken with and without vegetation modelling to examine the effect of the screening.

#### 4. Results

The practically simultaneous 10minute mean wind speeds recorded at the airport and the city sites have been correlated to produce mean speed ratios for each 10° airport wind direction. Figure 3 shows these measured ratios for the Eagle Street site for two conditions of mean airport wind speed; all winds, ie.  $V_{\text{airport}} > 0.0\text{m/s}$  and only stronger winds, ie.  $V_{\text{airport}} > 5.0\text{m/s}$ . Also shown on Figure 3 are the predicted ratios from the 1:400 scale model test with vegetation. Somewhat incongruously, the measured ratios are sustained for both light and strong winds from the east while the stronger winds produce lower ratios for westerly winds. This is unusual because the more variable winds would be expected to be the easterly on-shore breezes whereas the westerly winds are generally stronger and more sustained. Smaller numbers of observations from the west may be masking the comparison.

The model test combined with the atmospheric boundary layer model in [3] lead to an overprediction of the city/airport ratios, particularly for easterly and south-westerly winds. These ratios were much larger when vegetation modelling was not included and thus emphasize the shielding that can be achieved.

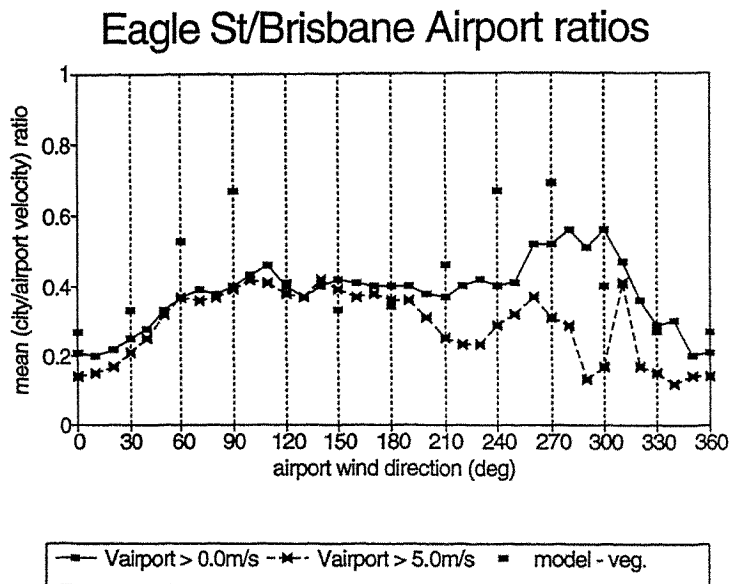


Figure 3. Measured and predicted mean (city/airport) velocity ratios at Eagle Street.



Figure 4 shows the measured all direction probability distribution of mean wind speed at the Eagle Street site compared with predictions obtained from a 1:400 scale model test. The full scale data points have been fitted to a Weibull probability distribution. As can be seen, the predicted wind speeds are significantly higher for a given probability, ie. a conservative result, which increases with mean wind speed. This overestimation is largely due to the larger ratios for the easterly and southwesterly directions shown in Figure 3. The effect of vegetation modelling is also clearly evident.

Possible reasons for the overprediction may include (1) inaccurate simulation of the street level environment, (2) the assumption of a neutrally stable atmospheric boundary layer for translating the airport wind climate some 10km inland to the city and (3) insufficient full scale data. The last point is unlikely to be the case as Williams and Wardlaw [5] suggest as little as 2800 hours of recording are needed to achieve stable street level to reference location speed ratios.

Figure 5 shows similar results for the 1:400 scale model test of the George Street site. However there is much better agreement between measured and predicted wind speed probability distributions in this case. Again the effect of modelling vegetation is significant.

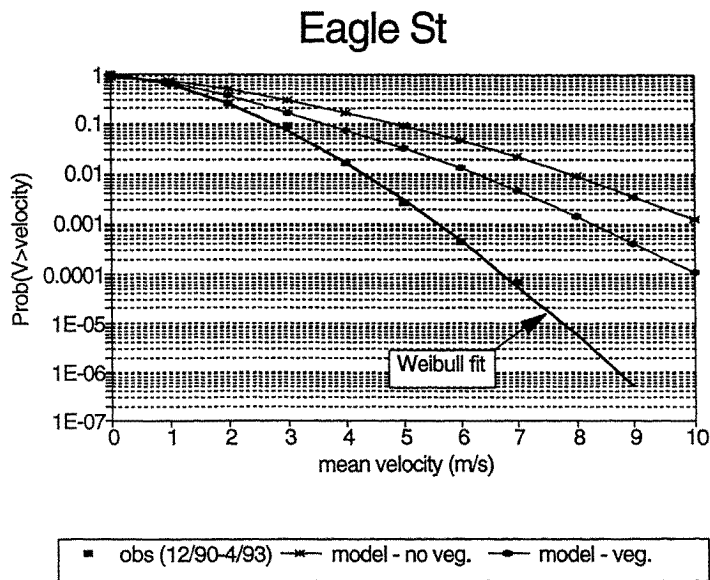


Figure 4. Comparison of measured and predicted (1:400 scale model) probability distribution of mean wind speed in Eagle Street, Brisbane.

## George St

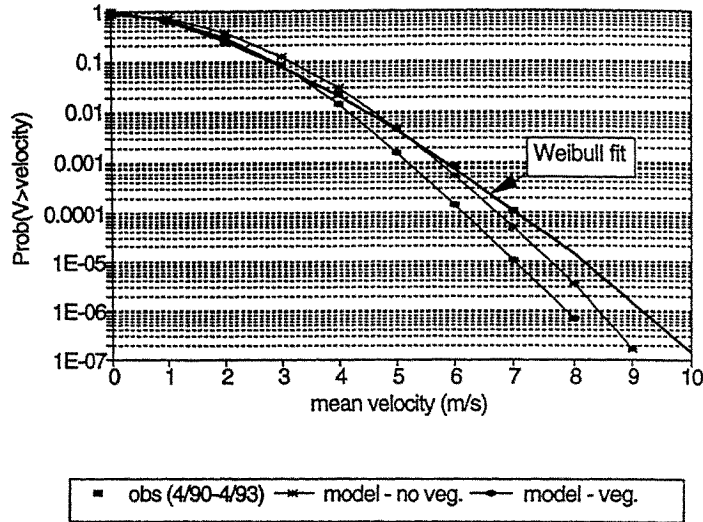


Figure 5. Comparison of measured and predicted (1:400 scale model) probability distribution of mean wind speed in George Street, Brisbane.

### 5. Conclusions

Three years of full scale wind speed data at two locations on inner city footpaths have been analysed and compared with predictions from 1:400 scale model tests. The results are inconsistent with the model test overpredicting the measured probability distribution at one site, while producing a good match at the other. Further analysis of the full scale data is underway and the model tests will be repeated with different measuring techniques to ascertain where the differences might lie.

### 6. Acknowledgements

This project was sponsored by the Australian Research Council and the University of Queensland Special Project Scheme. The authors also wish to thank the AMP Society's Property Management Division, Telecom Australia, the Brisbane City Council and Mr G. Illidge of the Department of Civil Engineering for their assistance.

### 7. References

1. W.H. Melbourne, Criteria for environmental wind conditions, *J. Wind Engng. & Ind. Aerodyn.*, 3 (1978) 241-249.
2. C.W. Letchford and L.T. Isaacs, Full scale measurements of wind speed in an inner city, *J. Wind Engng. & Ind. Aerodyn.*, 44 (1992) 2331-2341.
3. Australian Standards, SAA Loading Code Part 2: Wind Loads AS1170.2 (1989)
4. H.P.A.H Irwin, A simple omni-directional sensor for wind tunnel studies of pedestrian winds, *J. Wind Engng. & Ind. Aerodyn.*, 7 (1981) 219-239.
5. C.D. Williams and R.L. Wardlaw, Determination of the pedestrian wind environment in the City of Ottawa using wind tunnel and field measurements, *J. Wind Engng. & Ind. Aerodyn.*, 41 (1992) 255-266.

## Generic Models for Pedestrian-level Winds in Built-up Regions

Theodore Stathopoulos and Hanqing Wu

Centre for Building Studies, Concordia University  
1455 de Maisonneuve Blvd. W., Montreal, Quebec, Canada H3G 1M8

**Abstract:** Wind conditions around buildings in built-up regions were studied in a boundary-layer wind tunnel. The effects of spatial densities of street blocks, building heights over their surroundings, directions of the approaching wind and relative locations of buildings on wind speeds are presented in this paper. Generic building models have been established with empirical relations derived from the literature information and the current findings. These models can be applied for estimating the wind environmental conditions around buildings with the assistance of other relevant knowledge.

### 1. Objective

Wind conditions around buildings in a built-up area may be determined by weather records, upstream terrains, surrounding blocks, adjacent buildings and the geometry of the main buildings under consideration. Wind-tunnel experiments have been carried out for simplified models such as isolated buildings, twin buildings and more complex building combinations [1]. Parametric relations have been established between wind speeds and building configurations including dimensions, geometries and relative positions. However, those relations cannot directly apply for practical situations unless the influence of surroundings and other impact parameters is properly taken into consideration.

The effects of surroundings were studied via uniformly distributed square blocks by Murakami et al [2] and Jamieson et al [3]. In order to generalize the knowledge of wind conditions around buildings, the current research has progressed in three ways: (1) measurement of wind speeds along streets between uniform blocks; (2) investigation of wind effects of tall buildings surrounded by uniform street blocks; and (3) analysis of the results from generic models simulating actual city configurations. This paper presents details of the evaluation of wind conditions around buildings, particularly on the effects of wind direction and building location.

### 2. Experimental Set-up

Experiments were conducted in a boundary-layer wind tunnel designed for building aerodynamics applications [4]. Suburban wind conditions were simulated with a velocity profile of power law exponent equal to 0.25 and a geometric scale of 1:500. Building models were made of wood pieces with the same dimensions of 19 x 100 x 200 mm, corresponding to full-scale street blocks 9.5 m high and 50 m x 100 m in plan size. The block height could easily be increased by piling up wood pieces. In a typical model arrangement, there were usually five rows of blocks upstream of the main building which was located at the centre of the turntable of wind tunnel.

Wind speeds were measured by Irwin's surface wind sensors [5] at a height of 4 mm (2 m in full scale) above the ground. For detecting horizontal wind speeds on streets, 37 sensors were distributed as shown on the top-left plot in Fig. 1. The sensors were installed in the centre of streets and at distances of 5 mm (2.5 m in full scale) from buildings, mainly on sidewalks and crosswalks

of streets where both high-speed winds and pedestrian activities take place. While most attention was paid to the along-wind street, wind speeds on cross streets were also measured on crosswalks, and in front of and behind the main building. The least distance between sensors was 20 mm to avoid any potential interference.

Only mean wind speeds ( $U$ ) are presented in this paper and they are normalized by two reference speeds, namely,  $U_o$ , the mean wind speed at each measured point when no building models are present and  $U_s$ , the wind speed on streets between uniform blocks when all buildings are of the same height ( $h=H$ ). The ratios  $U/U_o$  and  $U/U_s$ , therefore, indicate variations of wind speeds relative to the approaching wind with no surrounding buildings and with the existing built surroundings, respectively. By definition,  $U/U_s=1$  at all measured points when  $H/h=1$ . For the same configuration, values of  $U/U_o$  are usually lower than one due to the shelter effect caused by buildings. The street-level wind patterns become different when the height of main building increases, as indicated in Fig. 1 - note that the three building models have not been plotted to scale. In the following sections, the wind conditions over uniform street blocks are studied first. Then the wind effect of the height of main building relative to its surroundings is examined. Finally, the impact of wind direction and building location within a block is discussed.

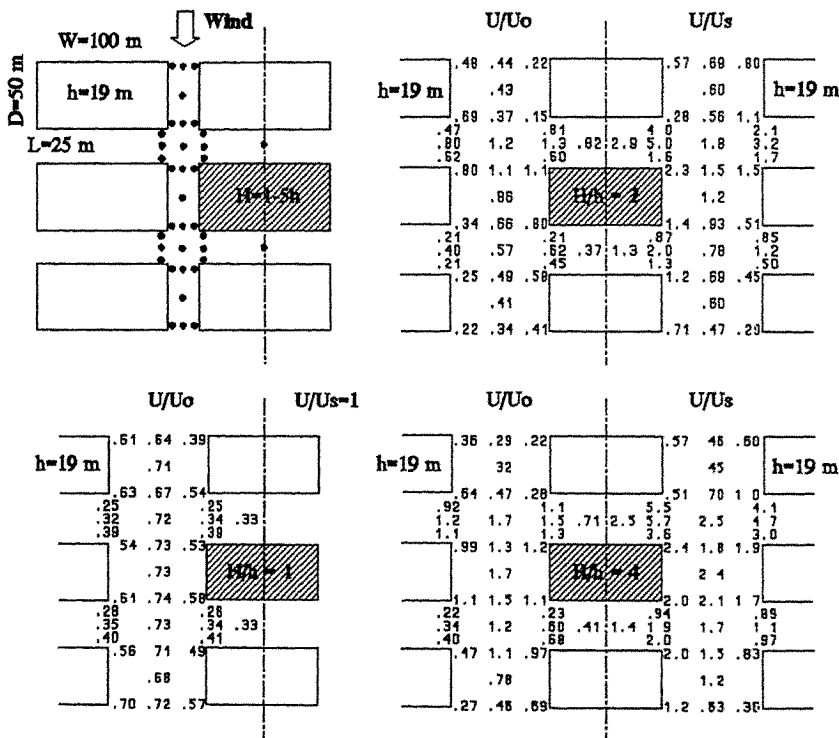


Fig. 1 Wind speeds around tall buildings surrounded by uniform street blocks.

### 3. Blockage Ratio and Along-street Speed

For uniform surroundings, the wind speed along streets is mainly dependent upon the distribution of densities of street blocks. If buildings on a street block are typified by a single cuboid as in Fig. 2, the following two area ratios can be defined: the plan density,  $R_p$ , which is the ratio of the roof area of building ( $A_r$ ) over that of the building lot ( $A_l$ ); and the blockage ratio,  $R_b$ , describing the percentage of approaching air flow 'seen' by the building ( $A_f/A_f$ ). These ratios can be expressed as follows:

$$R_p = \frac{A_r}{A_l} = \frac{W \times D}{(W+L)(D+L)}, \quad R_b = \frac{A_f}{A_f} = \frac{W \times h}{(W+L)^2} \quad (1)$$

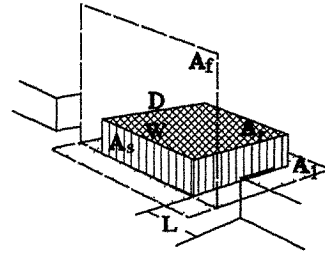


Fig. 2 Building density and blockage.

where  $W$  and  $D$  are cross and along-wind lengths of a street block,  $L$  is the street width that may have different values around the same block, and  $h$  is the average height of obstacles on the block. The blockage ratio  $R_b$  is related not only to the plan dimensions ( $W$  and  $L$ ), but also to the building height and it is found more indicative than the plan density  $R_p$  for the wind conditions on streets.

In the current study,  $h$  is a multiple of 9.5 m,  $W$  and  $D$  are either 100 m or 50 m depending on the wind direction, the width of along-wind street ( $L$ ) is 25 m or 15 m whereas that of cross-wind street is kept constant at 25 m. Wind speeds on streets vary with block dimensions and street widths. An average wind speed  $\bar{U}_s$  is taken over all measured points on the along-wind street, excluding 14 points on cross-wind streets (see the top-left plot in Fig. 1). Figure 3 displays the value of  $\bar{U}_s$  decreasing when the block height increases and when the width of along-wind street decreases.

Statistical analyses were performed for data from the literature [2 and 3] and the current study in order to relate  $\bar{U}_s$  to the building ratios. When wind flow comes over terrains with a power law exponent  $\alpha$  from 0.15 to 0.25, the average wind speed at the pedestrian level along streets is found only dependent on the blockage ratio  $R_b$ . An empirical relation could be expressed as:

$$\bar{U}_s/U_o = 1 - 0.9R_b^{0.4} \quad (2)$$

The agreement of such a relation with the wind-tunnel results is demonstrated in Fig. 4.

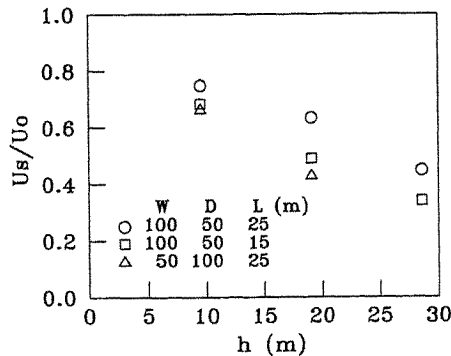


Fig. 3 Variation of averaged speed on along-wind street.

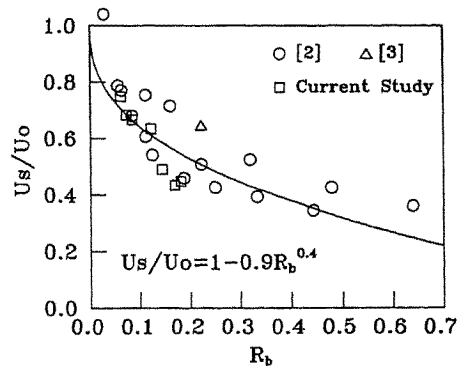


Fig. 4 Empirical relation between wind speed and blockage ratio.

According to this relation, wind speeds along streets decrease with increasing blockage ratio. For example, suburban terrains with low  $R_b$  values cannot provide shelter for street winds. On the other hand, wind flows may skim over downtown cores of large cities with high  $R_b$  values, without disturbing pedestrians on streets. However, this is true only for buildings with comparable heights. If a building is well taller than its surroundings, wind speeds on streets around the building may change dramatically.

#### 4. Tall Buildings above Uniform Surroundings

As shown in Fig. 1, the maximum values of  $U/U_o$  are 0.74, 1.2 and 1.7 for  $H/h=1, 2$  and 4. The speed variation may be attributed to several geometric factors such as  $H, h, W$  and  $L$ , but the most direct cause is the relative height ( $H-h$ ). For a tall building in a built-up region, only the building surface above surroundings obstructs and deflects air flow down to the street level. For a number of building configurations, the maximum speeds ( $U_m/U_o$ ) are plotted against the relative height ( $H-h$ ) in Fig. 5. These maximum values increase with increasing relative height. The blockage ratio of surroundings, thus the average speeds  $\bar{U}_s$ , may also contribute to the magnitude of maximum wind speeds, especially when  $H$  approaches to  $h$ , but no clear dependence could be found from the current experiment.

The highest wind speed normally takes place around the windward corners of a tall building. The vortex flow in front of the tall building, however, is also critical for pedestrian comfort, but the speed varies in a different pattern. The speed ratio  $U_f/U_o$  at the central point in front of the main buildings is 0.33, 0.82 and 0.71 for  $H/h=1, 2$  and 4, as indicated in Fig. 1. The speed ratio jumps from its lowest value at  $H=h$  to the maximum at  $H/h=2$  to 3. After reaching the maximum, the speed decreases slightly for any further increase in building height for all cases tested as shown in Fig. 6. One possible explanation to this phenomenon is that the intensity, size and position of front vortices depend not only on the tall building height, but also on the height of surroundings and the distance between buildings. These parameters may contribute in a complex way to the flow reversal at the bottom of front vortices [1].

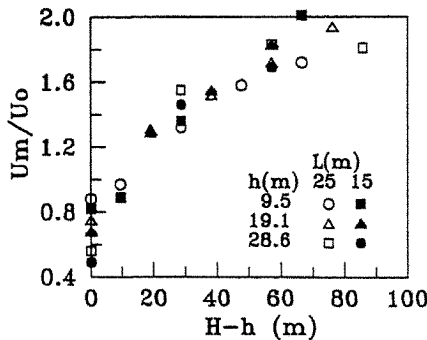


Fig. 5 Variation of maximum wind speed amplification with relative height.

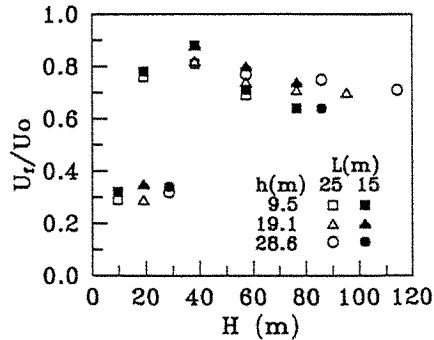


Fig. 6 Wind speed variation in front of buildings.

#### 5. Other Considerations

In all building models discussed so far, the wind flow is parallel (or perpendicular) to streets. Actual winds, however, may come from any direction. For oblique wind directions, the blockage

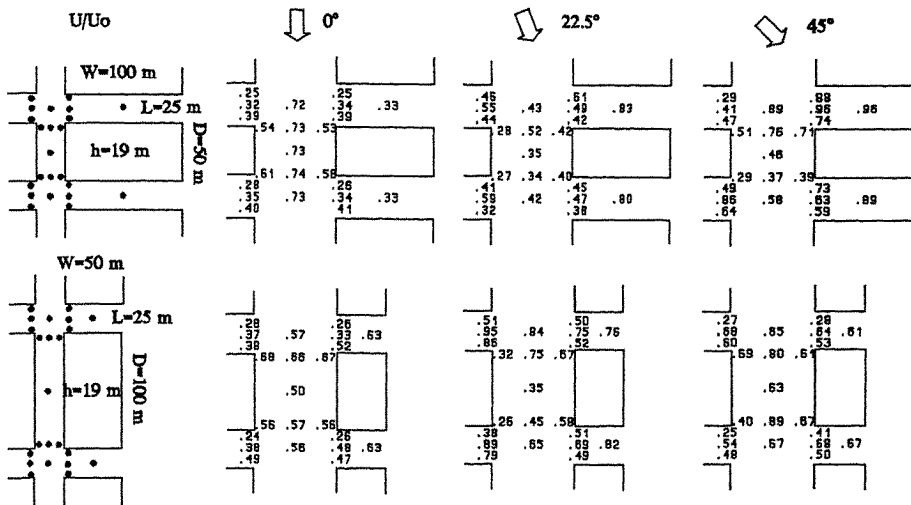


Fig. 7 Effect of wind direction on wind amplification factors.

ratio, hence the wind speed, is expected to change. Figure 7 shows the distributions of speed ratios  $U/U_0$  around uniform street blocks ( $h=H=19\text{m}$  and  $L=25\text{m}$ ) for three wind directions. For street blocks with  $W=100\text{ m}$  and  $D=50\text{ m}$ , wind speeds along vertical streets decrease from about 0.7 to 0.4 when the wind direction changes from  $0^\circ$  to  $22.5^\circ$ . At the same time, wind speeds along the horizontal streets do not change much, except at the centre of streets where wind speeds are more than doubled. When the wind angle becomes  $45^\circ$ , wind speeds on both streets are higher than those for  $22.5^\circ$ . This is also true for the street arrangement with  $W=50\text{ m}$  and  $D=100\text{ m}$ , for which, oblique winds provide higher speeds in general. This appears contradictory to the well-known guidelines that street blocks should be oriented diagonally to prevailing winds for the best protection of pedestrians. However, this is limited to uniform blocks with buildings of low heights. More measurements are required to study the speed variation with the incident angle for different configurations of street blocks.

In built-up cities, a tall building may be located at the corner or midway of a block, instead of occupying an entire block. Consequently, its impact on the wind environment may be different on nearby streets. Figure 8 provides an example of wind speed distribution along the central line of a nearby street when the tested tall building has different dimensions and locations. The building height of surroundings is  $9.5\text{ m}$  and the street width is  $25\text{ m}$  for all three cases. The main building tested is equally divided into two parts with heights  $H_1$  and  $H_2$ . When the two parts have the same height  $H_1/h=H_2/h=8$ , i.e. a single building covering the entire block, both speed ratios get values higher than other cases. If the tall building with a half width of the block is located nearer the street where the measurements occur ( $H_1/h=8$  and  $H_2/h=1$ ), the speed ratios decrease slightly in comparison to the previous case. When such a building is moved to the far side of the block ( $H_1/h=1$  and  $H_2/h=8$ ), the speed ratios drop significantly. The maximum values of  $(U/U_0, U/U_0)$  for these three cases are  $(1.7, 2.3)$ ,  $(1.7, 2.0)$  and  $(1.1, 1.3)$ , respectively.

In practical cases, the approaching wind flow may be modified by terrains far upstream of

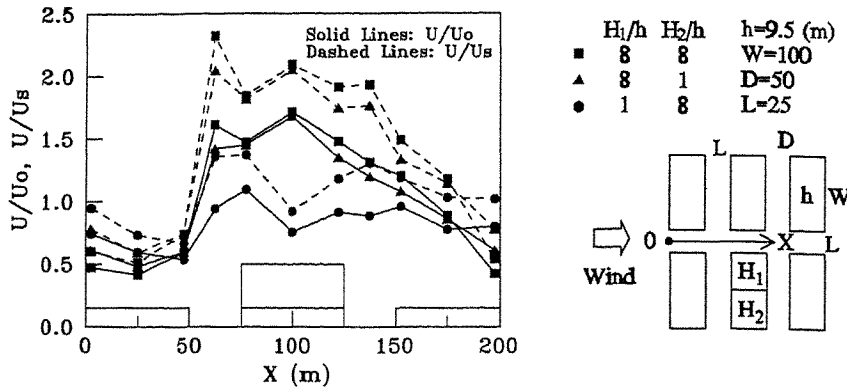


Fig. 8 Effect of building location on wind amplification factors.

the construction site. The oncoming wind flow will be further adjusted within several blocks away from the projected site by surrounding buildings of different distribution densities. Buildings adjacent to the main building may have an even more direct impact if they constitute a variety of configurations aerodynamically active for pedestrian winds. Finally, the most important factor is the main building itself. Strong wind flows may be created in the vicinity of a tall building, most likely on streets immediately adjacent to the building.

## 6. Conclusions

The conclusions of this paper can be summarized as follows: (1) The average wind speed along streets between building blocks can be estimated by using an empirical relation associated with the blockage ratio of surroundings; (2) For a tall building in a uniformly built region, it is the relative height of the building over its surroundings that determines the wind conditions on streets; (3) The effect of wind direction is complex and the variation of wind speeds with wind angles is dependent upon block dimensions and their arrangement. For the uniform blocks tested, oblique winds are found creating higher wind speeds on streets than normal winds; and (4) The location of a slender building inside a street block has a significant influence on the wind conditions on the adjacent streets.

## References:

1. T. Stathopoulos, H. Wu and C. Bedard, "Pedestrian-level winds around buildings: a knowledge-based approach," *J. Wind Engng. and Indust. Aerodyn.*, 41-44 (1992) 2377-2388.
2. S. Murakami, K. Uehara and H. Komine, "Amplification of wind speed at ground level due to construction of high-rise building in urban area," *Proc. 3rd Colloq. on Indust. Aerodyn.*, Aachen, West Germany, 1979, 55-77.
3. N.J. Jamieson, P. Carpenter and P.D. Cenek, "The effect of architectural details on pedestrian-level wind speeds," *J. Wind Engng. and Indust. Aerodyn.*, 41-44 (1992) 2301-2312.
4. T. Stathopoulos, "Design and fabrication of a wind tunnel for building aerodynamics," *J. Wind Engng. and Indust. Aerodyn.*, 16 (1984) 361-376.
5. P. Irwin, "A simple omnidirectional sensor for wind-tunnel studies of pedestrian-level winds," *J. Wind Engng. and Indust. Aerodyn.*, 7 (1981) 219-239.



## Evaluation of pedestrian level wind environment around a row of tall buildings

A.P. To, K.M. Lam and D.K.T. Thung

Department of Civil and Structural Engineering  
The University of Hong Kong, Pokfulam Road, Hong Kong

**Abstract:** Wind-tunnel experiments were carried out on the wind environment around the base of a row of identical tall buildings. Distributions of mean and rms wind speeds as well as wind angles were measured by a split-fiber probe for various wind directions at the pedestrian level. The wind environment was evaluated using two different pedestrian level wind descriptors, namely a quantile level wind speed descriptor and an "effective wind speed". The results showed the effect on the pedestrian level winds around a tall building being located in a group of identical buildings. It is also suggested that the quantile level wind speed descriptor is a more efficient means to evaluate the wind environmental conditions.

### 1. Introduction

It is well known that unpleasant and sometimes dangerous windy conditions often occur at the pedestrian level around the base of tall buildings. Wind environment around tall buildings has become an important technological and social problem. For important building development projects, the best available solution to this problem remains, to date, expensive ad-hoc wind tunnel studies. There have been a number of more fundamental studies aiming at obtaining quantitative data on the wind environmental effect around tall building of particular geometries and arrangements [1,2].

In highly populated cities like Hong Kong, there is a trend towards large residential estates which comprise a number of identical tall residential towers located together with shopping and recreational facilities. In many cases of achieving the most pleasant exposure, the group of tall buildings are arranged in a row along a lake side, a beach or other scenic features. Since the towers normally rise higher than 100 m and are erected closely together at about one building breadth apart, it becomes important to investigate the wind environmental conditions around their base, a region which is sometimes used for leisure activities. This paper presents a part of a series of wind tunnel experiments to explore the pedestrian level winds of a row of identical tall buildings. The configuration presented is the side-by-side arrangement. Configuration of the diamond arrangement is being studied.

### 2. Experimental Set-up

The experiments were carried out in the boundary layer wind tunnel of the Department of Civil and Structural Engineering at the University of Hong Kong. The wind tunnel is of the recirculating type with a working section of 3 m wide by 1.8 m high and 12 m long. A simulated atmospheric boundary layer were provided at the model location with spires and fetch of roughness elements. A power-law of exponent 0.15 best fits the mean speed profile which corresponds to the open exposure terrain in a 1:200 scale.

The configuration reported here is a row of four identical tall buildings in the side-by-side arrangement. The building models were square in plan-form with a breadth of 15 cm. The height-to-breadth ratio is 2.5:1. The separation between buildings was one building breadth. The mean wind speed at the roof height was set to 11.0 m/s in the wind tunnel. This speed will be used as the reference wind speed  $\bar{U}_R$ .

used as the reference wind speed  $\bar{U}_H$ .

Pedestrian level winds were measured by a split-fiber probe (Dantec 55R57) at a height of 10 mm above the wind tunnel floor which corresponds to 2 m height in full scale. We choose to use a split-fiber probe because this miniature sensor can measure both the instantaneous wind speed and wind direction in a two dimensional flow. The probe is made of a quartz cylinder (0.2 mm diameter) coated with two thin nickel films. The two films are separated by two gaps along the axis of the cylinder. The sum of the heat transfer from the two sensors depends only on velocity, while the difference depends on both the velocity and angle. The probe was operated with two channels of a constant temperature anemometer.

The probe was calibrated in a uniform flow where the probe was rotated between  $-90^\circ$  to  $+90^\circ$  around the fiber axis at step of  $10^\circ$ . At each step, the uniform flow was adjusted from 1.2 m/s to 24.0 m/s. The flow speed and angle characteristics were obtained as follows. Flow speed was first related to the sum of the squared output voltages by the usual King's law. Difference of the squared output voltages was plotted against flow angle for the same flow speed on which we performed a fourth-order-polynomial fit. Hence, we had a set of four coefficients to calculate flow angle from the difference of the squared voltages for every 0.1 m/s velocity step ranging from 1.2 m/s to 24.0 m/s. Acquisition of anemometer output voltages was performed with an analog-to-digital convertor in a 486 computer. The computer also carried out probe calibration and analysis of the wind tunnel data.

### 3. Results and Discussion

In this paper we only present the results of the side-by-side configuration. Three cases were tested. Case I, isolated building; Case II, four buildings arranged in a row, and wind flow perpendicular to the row; Case III, wind flow along the row of four buildings.

#### 3.1 Mean and rms wind speed

Distributions of mean wind speed  $\bar{U}$  for Case I,II,III are shown as contour maps in Figure 1. The contours of rms wind speed  $\sigma_u$  are shown in Figure 2. Both values are normalized by the mean reference wind speed  $\bar{U}_H$  of the approach flow at the building roof height.

For the isolated building, Case I, a region of high pedestrian level winds is observed extending from the upwind corners. This is often reported in previous studies [3]. In Fig. 1a, the maximum value of  $\bar{U}/\bar{U}_H \approx 1.2$  is found at the contour close to the upwind corners. The upwind corners have a large velocity fluctuation  $\sigma_u/\bar{U}_H \approx 0.33$  as shown in the Fig. 2a. We also observe the closely packed contour line of  $\sigma_u$  near the downwind corners. This may due to vortex shedding from rear side of the building. Large velocity gradients in those downwind corners may cause discomfort to the pedestrians.

For Case II, wind flow perpendicular to the row of buildings, the most windy conditions also occur in the upwind corners with  $\bar{U}/\bar{U}_H \approx 1.3$ , (Fig. 1b). However, high speed is found in the entire area bounded by the two building's side wall with average  $\bar{U}/\bar{U}_H \approx 1.2$ . This is clearly due to the channelling effect of the two buildings which results in wind speed increase and flow angle parallel to the side of the buildings as we shall see in the flow angle discussion part later. Velocity fluctuations  $\sigma_u/\bar{U}_H \approx 0.12$  is found at the middle of the two buildings (Fig. 2b). Suppression of velocity fluctuations again shows the channelling effect in this configuration as compared with the  $\sigma_u$  contours in Case I (Fig. 2a).

For Case III, wind flow along the row of four buildings (Fig. 1c), the wind patterns for the first building do not differ much from those of the isolated building. For the second and other downwind buildings (not shown in the figure), the most windy conditions do not occur in the upwind corners of the blocks. Instead, a smaller value  $\bar{U}/\bar{U}_H \approx 0.5$  is found in the downwind corners. This is due to the sheltering of the first block so that separation at the upwind corners is not vigorous. However, large velocity gradients are still found in all buildings in the downwind corners. In regions behind the buildings, low pedestrian wind speeds are found.

### 3.2 Quantile level Descriptor

Most acceptability criteria for environmental wind conditions are based either on some gust wind speed values or on the long-term probability of exceedance of certain mean wind speed values [4,5]. The former descriptor of gust wind speed or "effective wind speed"  $U_{\text{eff}}$  as quoted in some literature is usually estimated from the mean wind speed  $\bar{U}$  and the standard deviation  $\sigma_u$  as  $U_{\text{eff}} = \bar{U} + K\sigma_u$  [3].  $K$  is a parameter representing the degree of the wind speed fluctuations. Though simpler to use than the other criteria involving probability analysis, the choice of this peak factor  $K$  presents problems and it is not possible to use one fixed value of  $K$  at all locations of interest.

The most reliable choice of  $K$  requires the knowledge of the probability density function (p.d.f.) of the wind speed time history. A more direct and reliable way to estimate the gust wind speed would be to use a quantile level if we can have the p.d.f. available [6].

It is the authors' opinion that a value of  $U_{10}$  will be another suitable descriptor for environmental wind conditions.  $U_{10}$  is defined as the wind speed that is being exceeded for 10% of the observation time. The adoption of  $U_{10}$  will avoid the problem of choosing  $K$  in formulation of  $U_{\text{eff}}$ .

For Cases I,II,III, results on the distributions of  $U_{10}$  normalized by  $\bar{U}_H$  are shown in Figure 3. Comparing these figures with mean speed distributions, the high speed region lies closer to the building's side wall.

We have computed the value of  $K$  which will give an effective wind speed  $U_{\text{eff}}$  equal to  $U_{10}$ . Variations of  $K$  are presented in Figure 4. It is shown that  $K$  cannot have the same value for the entire flow region.

In Case I (Fig. 4a), the maximum value of  $K \approx 1.6$  is found at the upwind corners. The value of  $K$  then decreases as one goes away from the building's side wall. In Case II (Fig. 4b), due to the channelling effect of the buildings, surprisingly small values of  $K$  nearly unity are found in the upwind corners of the buildings. In Case III (Fig. 4c), the value of  $K$  attain its maximum value of 1.5 at the upwind corners of the first block.  $K \approx 1.4$  are found near the building's side wall for all downwind buildings. In general,  $K \approx 1.3$  are normally found for the outside regions. This exercise clearly rejects the feasibility of using a fixed value of  $K$  for all geometries and arrangements of building developments.

### 3.3 Effective wind angle

As we have obtained the real time history of wind speed and wind angle, we could select those wind flow angles with wind speed exceeding  $U_{10}$ . The mean value of those angles are defined as gust wind angle ( $\theta_{U>U_{10}}$ ). Results of mean flow vectors and gust flow vectors ( $U_{10}, \theta_{U>U_{10}}$ ) are shown in Figure 5.

For Case I (Fig. 5a), all mean flow vectors point away from the building. However, gust flow vectors pointing towards the side wall are found near the upwind wind corners of the building. This shows that high velocities may be associated with vortices separation from the upwind corners. In the downwind corners, gust wind vectors pointing towards the wake region are found, suggesting that the high velocities always flow towards the region behind the buildings. For Case II (Fig. 5b), wind flow vectors are almost parallel to the buildings's side wall except in the upwind corners. Negligible difference is observed for the two vector patterns as a result of the channelling effect of the buildings. For Case III (Fig. 5c), the pattern around the first building resembles that of the isolated one. For other downwind buildings, the flow angles are normally parallel to the side walls.

## 4. Concluding Remarks

Pedestrian level wind environment around a row of tall buildings has been experimentally investigated in the wind tunnel use a split-fiber probe. Distributions of mean and rms wind speed,  $\bar{U}$  and  $\sigma_u$ , were found to be affected by the presence of neighbouring buildings. Comparison of

the results of effective wind speed  $U_{eff} = \bar{U} + K\sigma_u$  and  $U_{10}$  suggested that the latter quantile level wind speed descriptor is a more efficient means to evaluate the wind environmental conditions. Contour maps of value of  $K$  suggested different values for different locations. This clearly rejected the feasibility of using a fixed value of  $K$  for all geometries and arrangements of building developments. Results of wind vector measurement show that high velocities may be associated with vortices separation from both the upwind and downwind corners of the buildings.

**Acknowledgement**

The investigation is supported by a research grant of the University of Hong Kong.

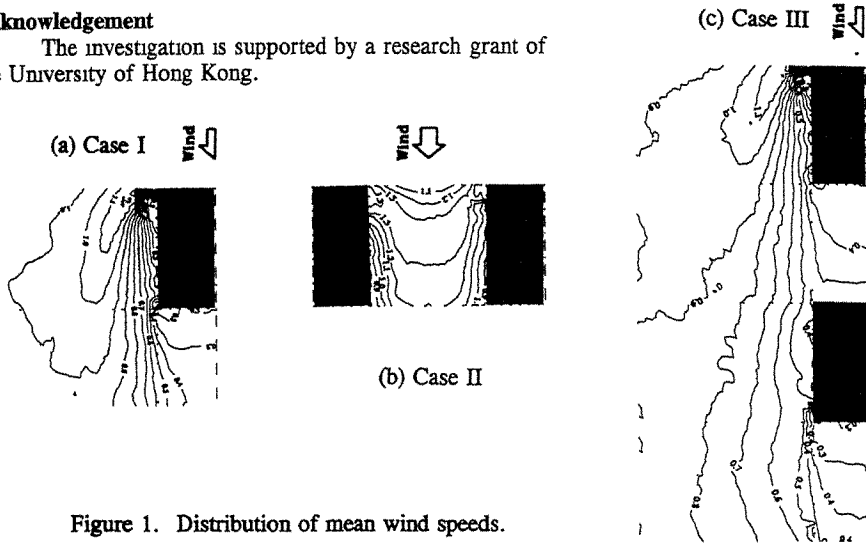


Figure 1. Distribution of mean wind speeds.

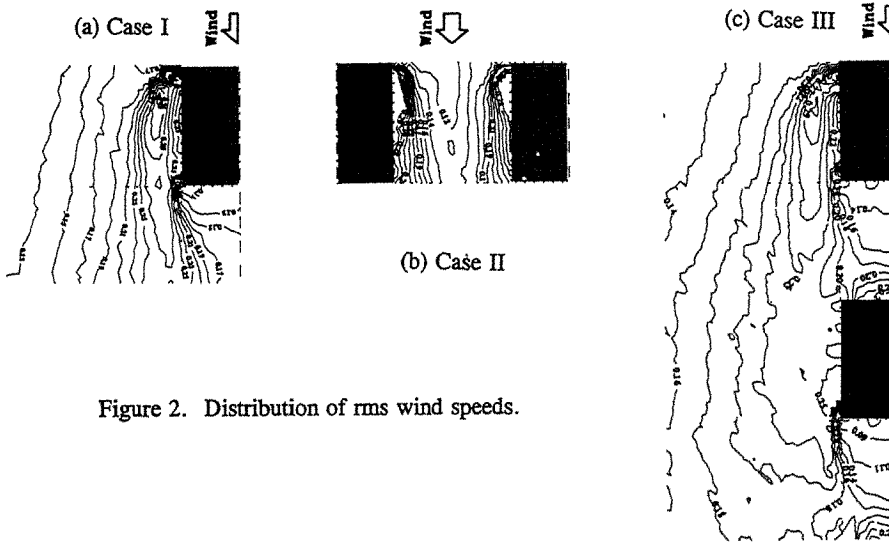


Figure 2. Distribution of rms wind speeds.

**References:**

1. W.H. Melbourne and P.N. Jourbert, Proc. 3rd Int. Conf on Wind Effects, Toyko (1971).
2. T. Stathopoulos and R. Storms, J Wind Eng Ind. Aerodyn., 24 (1986) 19-31.
3. Y Uematsu et al., J Wind Eng Ind. Aerodyn , 44 (1992) 2289-2300.
4. A G. Davenport, Colloquium on Building Climatology, Stockholm (1972).
5. W.H. Melbourne, J.Ind Aerodyn., 3 (1978) 301-307
6. K M. Lam, J Wind Eng Ind. Aerodyn , 44 (1992) 2313-2314

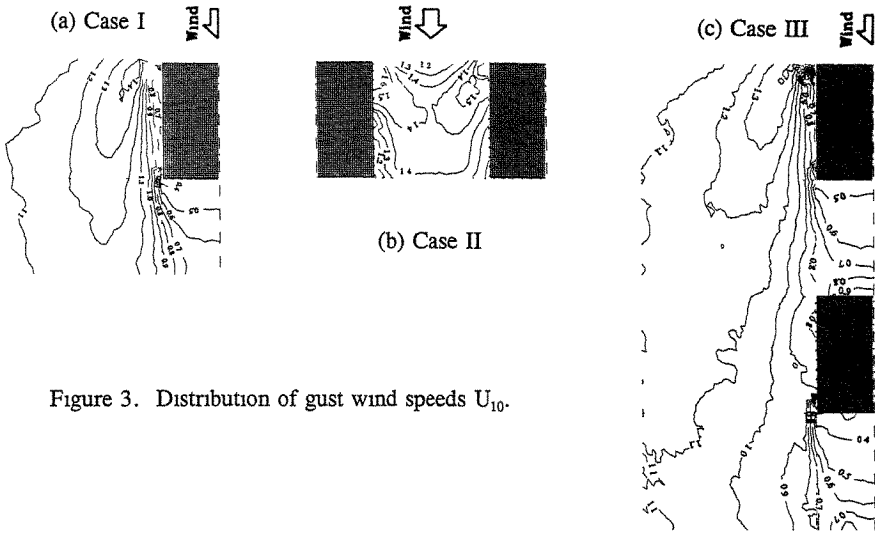


Figure 3. Distribution of gust wind speeds  $U_{10}$ .

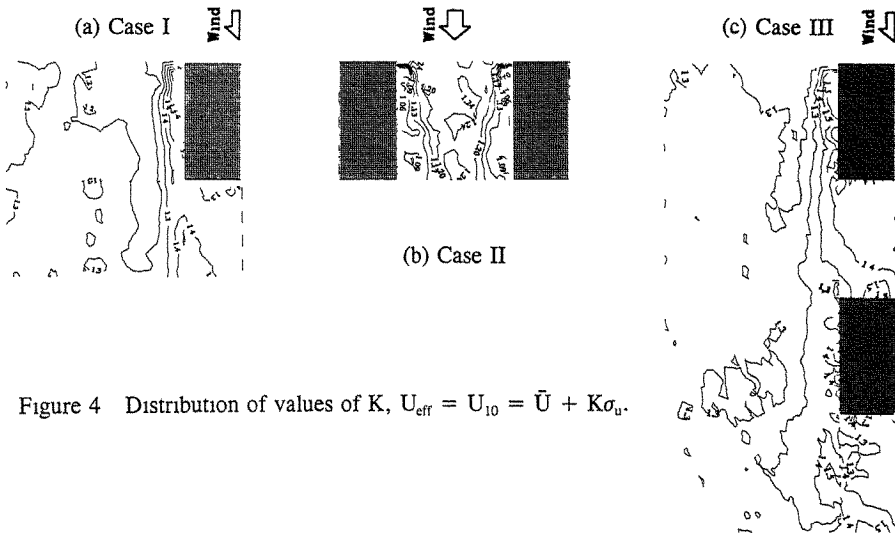
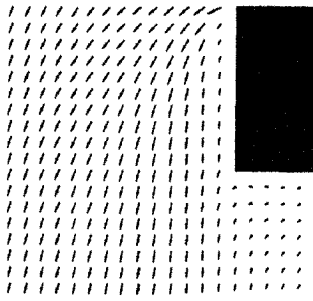
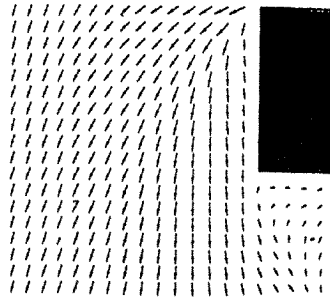


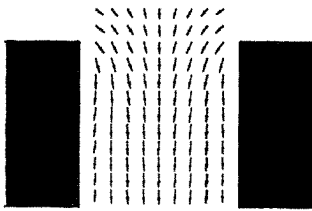
Figure 4 Distribution of values of  $K$ ,  $U_{\text{eff}} = U_{10} = \bar{U} + K\sigma_u$ .



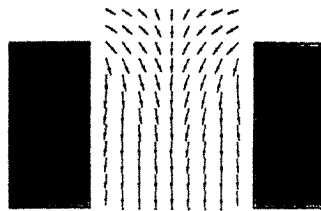
(a) Case I, mean flow vectors



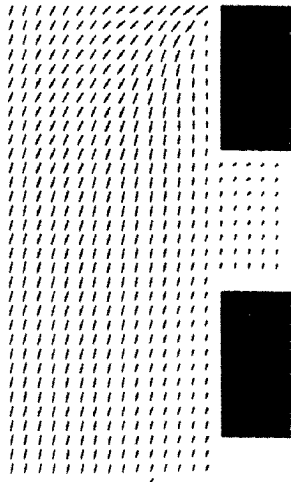
(a) Case I, gust flow vectors



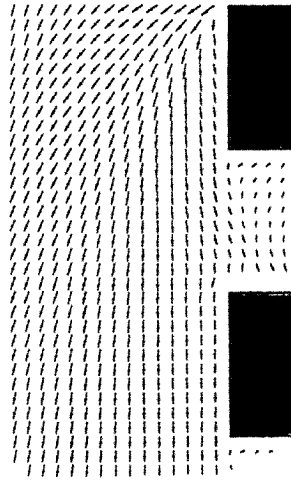
(b) Case II, mean flow vectors



(b) Case II, gust flow vectors



(c) Case III, mean flow vectors



(c) Case III, gust flow vectors

Figure 5 Distribution of mean flow vectors and gust flow vectors

## **Atmospheric Dispersion**





## Computational atmospheric dispersion of a pollutant over a complex-shaped terrain

M.J.S. Morais and L.A. Oliveira

Department of Mechanical Engineering  
University of Coimbra, 3000 Coimbra, Portugal

**Abstract:** A calculation procedure based on a control-volume approach with a staggered grid arrangement in a generalized nonorthogonal coordinate system is described, validated and subsequently applied to the two-dimensional, turbulent wind dispersion of an atmospheric pollutant over an irregularly-shaped terrain. Numerical diffusion is minimized by using the physical covariant velocity components as the dependent variables in the momentum equations. The dispersion analysis shows the importance of the dynamic conditions as well as the point source height, relative to the terrain geometry.

### 1. Introduction

Over the past few years, numerical predictions have been increasingly used, in conjunction with experimental approaches, as an important tool for the study of wind engineering flow problems.

Compared to finite element methods, the use of curvilinear, boundary conforming coordinate systems is the price one has to pay in order to apply control-volume formulations to flows that are bounded by irregular geometries.

In current applications of computational wind engineering, like the atmospheric dispersion of pollutants or the propagation of a forest fire, numerical (false) diffusion may arise as a major problem. This is often the case when cartesian velocity components are adopted as the dependent variables in the momentum equations. In those situations the alternative selection of velocity components that are mainly aligned with the flow may be a crucial choice.

In the present contribution a calculation procedure for wind engineering flow problems is briefly described, validated and subsequently applied to a practical situation: the two-dimensional, turbulent wind dispersion of an atmospheric pollutant over an irregularly-shaped terrain. A system of nonorthogonal curvilinear coordinates is used, together with a control-volume approach in a staggered grid arrangement. The physical covariant velocity components are selected as the dependent variables in the momentum equations, thus providing an important reduction of false diffusion. Mass conservation is indirectly ensured through the SIMPLEC algorithm. Turbulent transport is represented by use of a two-equation, low Reynolds number model.

### 2. Mathematical Model

In the presence of an isothermal velocity field  $\bar{u}$ , the transport of a chemical species of mass fraction  $m_s$  is governed by a set of differential equations expressing, on a unit-volume basis, the conservation of mass  $\rho$ , momentum  $\rho\bar{u}$ , and mass of the species  $\rho m_s$ . If turbulent flow conditions are present and modelled through a  $k$ - $\epsilon$  type approach, two additional equations are required for the conservation of both the turbulence kinetic energy  $\rho k$  and its rate of dissipation  $\rho \epsilon$ .

As particular statements of a generalized conservation principle, all those equations can be cast into a common form. If the dependent variable is denoted by  $\phi$ , the steady-state general differential equation, written in Cartesian tensor notation, is as follows [1]

$$\frac{\partial}{\partial x_i} \left( \rho u_i \phi - \Gamma_\phi \frac{\partial \phi}{\partial x_i} \right) = S_\phi \quad (\phi \equiv 1, u_i, m_s, k, \epsilon) \quad (i = 1, 2, 3) \quad (1)$$

where the diffusion coefficient  $\Gamma_\phi$  and the source term  $S_\phi$  are specific to a particular signification of  $\phi$  and the remaining variables have the commonly accepted meaning.

The conservation equations (1) for a general dependent variable  $\phi$  can now be written in a generalized coordinate system  $(\xi^1, \xi^2, \xi^3)$ , thus yielding [2]

$$\frac{1}{\sqrt{g}} \sum_{i=1}^3 \frac{\partial}{\partial \xi^i} \left[ \rho (\sqrt{g} U^i) \phi - \sqrt{g} g^{ii} \Gamma_\phi \frac{\partial \phi}{\partial \xi^i} \right] = \frac{1}{\sqrt{g}} \sum_{i=1}^3 \frac{\partial}{\partial \xi^i} \left( \sqrt{g} \Gamma_\phi \sum_{\substack{l=1 \\ l \neq i}}^3 g^{il} \frac{\partial \phi}{\partial \xi^l} \right) + S_\phi \quad (2)$$

where  $\sqrt{g}$  denotes the Jacobian of the transformation,  $U^i$  ( $i=1,2,3$ ) is the  $i^{\text{th}}$  contravariant velocity component and  $g^{il}$  ( $i,l=1,2,3$ ) is the  $(i,l)$  element of the contravariant metric tensor. These latter quantities are related to the covariant  $\bar{a}_i$  and contravariant  $\bar{a}^i$  base vectors, defined as  $\bar{a}_i = \partial \bar{x} / \partial \xi^i$ ,  $\bar{a}^i = \nabla \xi^i$  ( $i=1,2,3$ ), through the following expressions

$$\begin{aligned} \sqrt{g} &= \bar{a}_i \cdot (\bar{a}_j \times \bar{a}_k), \quad U^i = \bar{a}^i \cdot \bar{u}, \quad g^{il} = \bar{a}^i \cdot \bar{a}^l = g^{li} \\ (i &= 1,2,3) \quad (i,j,k \text{ cyclic}) \quad (l = 1,2,3) \end{aligned} \quad (3.a,b,c)$$

The term  $S_\phi(\xi^1, \xi^2, \xi^3)$  in equation (2) is the transformed version of  $S_\phi(x_1, x_2, x_3)$  in equation (1).

The transformed equation (2) can now be numerically integrated in a rectangular domain with uniform control-volumes.

### 3. Numerical Integration

The procedure for obtaining nodal, algebraic approaches of the differential governing equations has been described in detail by Karki and Patankar [3]. The discretization is performed in the physical space by an averaging procedure over small, contiguous quadrilateral control-volumes surrounding the nodal points.

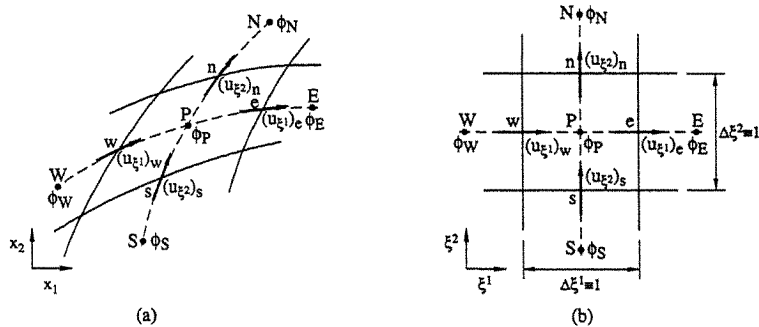


Fig. 1. A typical control-volume in the physical space (a) and in the transformed space (b).

A typical control-volume, in both the cartesian and nonorthogonal grid (physical and transformed space, respectively), is shown in the  $\xi^3 = \text{constant}$  coordinate surface of figure 1. A staggered grid arrangement is used in which all scalar variables are located at the geometrical centers of the control-volumes while the velocity components are displaced along the coordinate directions to lie at the center of the control-volume faces.

The integration of the general transformed equation (2) is now performed in the numerical space (complete details are available in [4]), thus leading to

$$\sum_{i=1}^3 \left[ \rho(\sqrt{g} U^i) \phi - \sqrt{g} g^{ii} \Gamma_\phi \frac{\partial \phi}{\partial \xi^i} \right]_{\text{inf}^i}^{\text{sup}^i} = \sum_{i=1}^3 \left[ \sqrt{g} \Gamma_\phi \sum_{\substack{l=1 \\ l \neq i}}^3 g^{il} \frac{\partial \phi}{\partial \xi^l} \right]_{\text{inf}^i}^{\text{sup}^i} + \sqrt{g} S_\phi \quad (4)$$

where the bounding surfaces lying between the control-volume of figure 1 and its neighbours are specified according to table 1.

Index	Boundary sup <sub>i</sub>	Boundary inf <sub>i</sub>	Node I+1	Node I-1
1	e	w	E (East)	W (West)
2	n	s	N (North)	S (South)
3	t	b	T (Top)	B (Bottom)

Table 1. Control-volumes and control-surfaces identification, as referred to figure 1.

The terms in the left-hand side of equation (4) are treated implicitly, using the power-law differencing scheme [1]. The cross-diffusion terms involving  $g^{il}$  ( $i \neq l$ ) are calculated explicitly and treated as source terms, together with  $S_\phi$ . The resulting general discretized equation has the form

$$a_P \phi_P = \sum_{i=1}^3 (a_{I+1} \phi_{I+1} + a_{I-1} \phi_{I-1}) + b_\phi \quad (5)$$

where  $a_{I+1}$  and  $a_{I-1}$  are the combined convection-diffusion coefficients and  $b_\phi$  lumps all the terms that must be calculated explicitly:  $S_\phi$ , cross-derivatives, pressure gradients and curvature source terms, if any.

The physical covariant velocity components  $u_{\xi^i}$  ( $i=1,2,3$ ) are chosen as the dependent variables of the momentum equation. Only one velocity component is stored at a control-volume face. The velocity components along the face are treated explicitly and estimated by interpolation of the neighbouring values that are actually calculated.

Following Karki and Patankar [3], the definition of  $u_{\xi^i}$

$$u_{\xi^i} = \bar{u} \cdot \frac{\bar{a}_i}{|\bar{a}_i|} = \sum_{j=1}^3 \frac{a_{ij}}{|\bar{a}_i|} u_j \quad (i = 1, 2, 3) \quad (6)$$

is used in combination with the discretized momentum equations for the Cartesian velocity components ( $\phi \equiv u_j$  in eqn. (4)) to obtain

$$a_P (u_{\xi^i})_P = \sum_{s=1}^3 \left[ a_{S+1} (u_{\xi^i})_{S+1} + a_{S-1} (u_{\xi^i})_{S-1} \right] + \left( \frac{\sqrt{g}}{|\bar{a}_i|} \right)_P [p]_{\text{sup}^i}^{\text{inf}^i} + b_{u_{\xi^i}} \quad (i = 1, 2, 3) \quad (7)$$

where the pressure difference and the source term (which includes the effect of curvature) are both treated explicitly.

The contravariant velocity components can be expressed in terms of the covariant ones as follows [4]

$$U^i = \sum_{r=1}^3 g^{ir} |\bar{a}_r| u_{\xi^r} \quad (i = 1, 2, 3) \quad (8)$$

thus giving, for the continuity equation ( $\phi \equiv 1$ ,  $S_\phi = 0$  in eqn. (4))

$$\sum_{i=1}^3 \left[ \rho g^{ii} \bar{a}_i |u_{g_i}| \right]_{\text{inf}_i}^{\text{sup}_i} = - \sum_{i=1}^3 \left[ \rho \sum_{\substack{r=1 \\ r \neq i}}^3 g^{ir} \bar{a}_r |u_{g_r}| \right]_{\text{inf}_i}^{\text{sup}_i} \quad (9)$$

Numerical integration of the conservation equations was performed with a modified version of the "Teach" program developed by Gosman and Ideriah [5].

The velocities and pressures were calculated using the SIMPLEC algorithm described in the work of van Doormal and Raithby [6] (again, details may be found in [4]). In this sequential (iterative) approach, the equation for pressure correction is obtained by combining the discretized continuity and momentum equations. Turbulence calculations were performed using the k- $\epsilon$  type, low Reynolds number model prescribed by Nagano and Tagawa [7], with some modifications [4].

The algebraic equations for all grid nodes, associated with the general variable  $\phi$ , were solved line-by-line via a tri-diagonal matrix algorithm (TDMA). An algebraically generated, nonuniform grid was used, as shown in the physical plane of figure 2.a. A distribution of 42 $\times$ 32 nodes along the horizontal and vertical directions respectively was adopted, though negligible differences were observed between the solutions obtained with this grid and one of 52 $\times$ 42 nodes.

#### 4. Results and Discussion

The two-dimensional, turbulent wind dispersion of an atmospheric pollutant ( $\text{SO}_2$ ) over a cossinus type shaped terrain configuration with amplitude  $H$  and period  $L$  was analysed (fig. 2.a). The boundary layer thickness of the approaching flow was  $\delta=2H$  and the fluid velocity  $U$  at that level was used to define the Reynolds number  $Re=U\delta/\nu$ . The North and East side boundary conditions for the velocity field were based on global mass conservation. These boundaries were located far enough from the curved zone to ensure that they did not significantly affect the flow in the region of interest. For the remaining variables, North and East boundary conditions were defined by vanishing second order variations.

Only forced convection conditions were considered in this work. Thus, the transport equation for the pollutant was only solved when convergence of both the pressure and velocity fields had already been achieved.

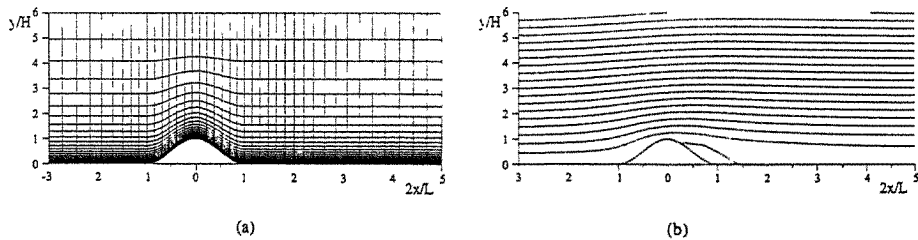


Fig. 2. The problem considered. (a): grid configuration; (b): streamline pattern for  $Re=8.66 \times 10^4$ .

Validation tests were performed through comparison of the present predictions obtained for the dynamic and pressure fields with the corresponding measurements reported for identical conditions in reference [8]. A very satisfactory agreement was seen to hold in those tests [4]. A sample of streamline configuration calculated for  $Re=8.66 \times 10^4$  is shown in figure 2.b.

A virtual point source of pollutant was added to the inflow dynamic conditions. Several tests were conducted in order to evaluate the influence of its vertical position  $h$ , compared to the relative terrain geometry, on the pollutant concentration distribution.

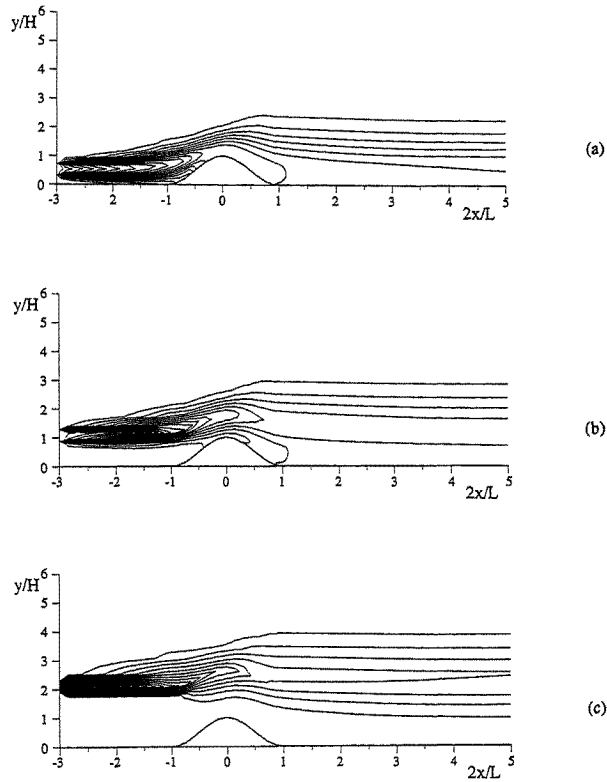


Fig. 3.  $\text{SO}_2$  mass fraction distributions for  $\text{Re}=8.66 \times 10^4$  and different source locations: (a)  $h/H=0.5$ , (b) 1 and (c) 2.

Predicted results are shown in figure 3 for  $\text{Re}=8.66 \times 10^4$  and  $h/H=0.5, 1$  and 2. For the lowest values of the point source height, the concentration distribution is highly influenced by the recirculation region that is originated by flow separation downstream of the obstacle. This influence is however seen to decrease with increasing values of  $h/H$ . Actually, it becomes negligible and vertical symmetry of the plume is recovered for  $h/H > 4$ .

As long as the flow is turbulent, the extent of the recirculation region slightly tends to diminish as the Reynolds number is increased beyond a certain level. The same behaviour was correspondingly observed in its influence on the pollutant concentration distribution (not shown).

The influence of the horizontal distance that separates the source from the obstacle is also shown in figure 4 through the comparison of two horizontal source locations:  $x=-(3/2)L$  and  $x=-L$  ( $\text{Re}=8.66 \times 10^4$  and  $h/H=1$  in both cases). In the former case the plume dispersion is more

pronounced than in the latter. This is also valid for other source heights, but tends to become less apparent as the ratio  $h/H$  is increased, as would be expected from observation of figure 3.

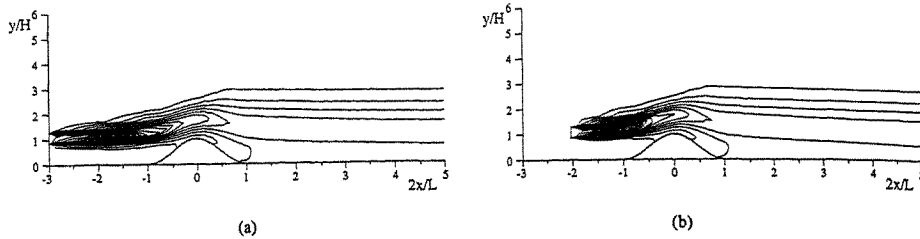


Fig. 4. Influence of horizontal source location on concentration distribution ( $Re=8.66 \times 10^4$ ,  $h/H=1$ ).  $x/L=-3/2$  (a) and  $-1$  (b).

## 5. Conclusion

A calculation method for wind engineering flow problems, based on a control-volume formulation with a staggered grid arrangement was described, validated and subsequently applied to a practical situation: the two-dimensional wind dispersion of an atmospheric pollutant over an irregularly-shaped terrain. The discretized equations for the covariant velocity components were obtained by an algebraic manipulation of those for the Cartesian velocity components rather than by integrating their own differential equations. This formulation renders the present procedure quite easy to implement and also tends to eliminate numerical diffusion errors.

The forced convection transport in an atmospheric environment of a pollutant ( $SO_2$ ) originated by a virtual source located upstream of a cossinus type shaped ground configuration was analysed for different geometric and dynamic conditions.

For a given Reynolds number value, the influence of the ground configuration upon the pollutant concentration distribution tends to decrease with increasing values of the source height and to increase as the source is horizontally approached to the obstacle.

This preliminary analysis was conducted with the aim of verifying that such type of calculations, with irregular boundaries and covariant velocity components as dependent values of the momentum equations, performed satisfactorily well in pollutant transport turbulent conditions. A more accurate and systematic analysis of the physical problem involved is foreseen for a near future work.

## References

1. S.V. Patankar, Numerical Heat Transfer and Fluid Flow, Hemisphere Publ. Corp., Washington D.C., (1980).
2. J.F. Thompson, Z.U. Warsi and C.W. Mastin, Numerical Grid Generation - Foundations and Applications, North-Holland, Amsterdam, (1985).
3. K.C. Karki and S.V. Patankar, Num. Heat Transfer, 14 (1988) 295.
4. M.J. Morais, Master Dissertation, Coimbra (Portugal), (1993).
5. A.D. Gosman and F.J.K. Ideriah, Dep. of Mech. Eng. Report, Imperial College (London), (1976).
6. J.P. Van Doormal and G.D. Raithby, Num. Heat Transfer, 7 (1984) 147.
7. Y. Nagano and M. Tagawa, ASME J. Fluids Eng., 112 (1990) 33.
8. A.D. Ferreira, J.P. Monteiro and D.X. Viegas, Proc. Int. Conf. Forest Fire Research (1990), B.09-1.

## Field study of Roof Top Dispersion in Urban Area

K.S. Lam and S.C.Kot<sup>+</sup>

Department of Civil & Structural Engineering  
Hong Kong Polytechnic

<sup>+</sup>Department of Mechanical Engineering  
Hong Kong University of Science & Technology

**Abstract:** A non buoyant plume of SF<sub>6</sub> was released continuously from an exhaust in Chemistry Building for two months. Grab samples of SF<sub>6</sub> was measured once every 15 minutes on the roof of a neighbour building (distance: 71 m, height: 6 m above exhaust). Four minimum dilution formulae were validated using the field data collected. Chiu & Wilson formula has the best fit for the one hourly averaged field data. It accomodates over 99% of the field data.

### 1. Introduction

In a metropolitan area, the proximity of high rise buildings creates air pollution problems. Unwanted gases are created by many processes. Discharged gases in many situations are able to re-enter its own building or its neighbours buildings, thus lowering indoor air quality. Recycled air may be a nuisance or could be hazardous to health. Due to insufficient guidelines in near building dispersion study, in many new buildings remedial actions were necessary in response to complaints from new building occupants. On the other hand in many other cases, fume exhausts were unnecessarily oversized. Official guidelines on near building dispersion have been published ASHRAE 1989 [1], and HHSC handbook no. 4 [2]. Both guidelines were derived from wind tunnel studies on isolated rectangular blocks. It is controversial to apply these guidelines to irregular building topography. Furthermore, the guidelines are not comprehensive, many uncertainties exist and discretion needed when one comes to field application. Successful application of guidelines developed by wind tunnel studies requires a lot of field validation. However, field studies on near building dispersion were scarce e.g. Halitsky 1962 [3], Drivas & Shair 1974 [4], Lamb et. al. 1980, 1988 [5] [6]. The main objective of this study was to validate existing wind tunnel empirical formulae and to estimate the level of impact of Chemistry Building exhausts on its neighbour buildings. These objectives were met by conducting a tracer gas experiments.

### 2. The Site

Chemistry Building is one of the buildings located in the main campus of the University of Hong Kong. The main campus is at the western side of Hong Kong Island. The island is mountainous with flat terrain on the coastal area. The island experiences strong North to Easterly Monsoon in winter time, whereas the summer monsoon is the more gentle south to westerly wind. The prevailing wind is the East wind which contributes over 40% annually. The campus is located on a slope. The elevation is about 100 meters above sea level. The slope is to the southern side of the Chemistry Building. As the campus is located on a slope, the Chemistry Building is surrounded by buildings on the east, south and west side which form a natural barrier. The distances between buildings are of the order of 30 meters. The size of

Chemistry Building is 16m in width, 57m in length and 19m in height. The building has a pitched roof. The topography and the facilities provided in the Chemistry Department together form an ideal site for the impact study of an exhaust stack on its neighbouring buildings.

### 3. The experiment

The plan view of the exhaust vent and the receptor location is shown in figure 1. The tracer gas SF<sub>6</sub> was emitted continuously from a selected exhaust vent located approximately at the edge on the roof of Chemistry Building. The SF<sub>6</sub> concentration was measured once every fifteen minutes continually at a fixed location on the roof of the flyover for 2 months. The monitoring commenced in March 1989 and completed in April 1989.

The tracer gas SF<sub>6</sub> was supplied from a compressed gas cylinder. Flow rate was kept constant by maintaining 24 hours continuous flow through a fine metering stainless steel valve. Stainless steel tube of  $\phi 1/8$ " was used throughout the line for gas delivery and discharge. The discharge point was placed approximately in the middle and 250mm above the work surface inside the selected fume cupboard. The height of the sash was adjusted to 500mm which is the optimum working condition of the fume cupboard. The tracer gas was drawn into the exhaust duct and discharged into the atmosphere through the fan and the exhaust stack. The height of the exhaust stack was about 350mm above roof level. SF<sub>6</sub> was discharged at 2.85 ppm concentration at ambient temperature at the exhaust vents.

Flow rate of SF<sub>6</sub> was 65 ml/min. Owing to the low discharge concentration, the difference between the density of the discharge gas and the ambient air was negligible. The discharge gas had no buoyancy. The height of the receptor is 6 m above the exhaust vent. The azimuth direction of the receptor was 10 degree north from the exhaust vent. The flow rate was monitored twice everyday at 9:00am and 5:00pm. Gas samples were taken once per week in the exhaust duct for calibration purposes. Since the flow was continuous, the flow was very stable. The constant discharge rate was easily maintained within 5% error by the fine metering needle valve. The errors were only due to variation of ambient temperature, the uncertainty of soap bubble meter and timing devices.

A portable field tracer gas monitor (215AUP, System Science and Software) was installed for the measurement of SF<sub>6</sub>. Its internal components consist of a sampling valve, a sample loop, a sample injector for manual sampling, an internal pump, a column, and an electron capture detector. The carrier gas flow rate was maintained at 50ml/min. Since backflush facility was not

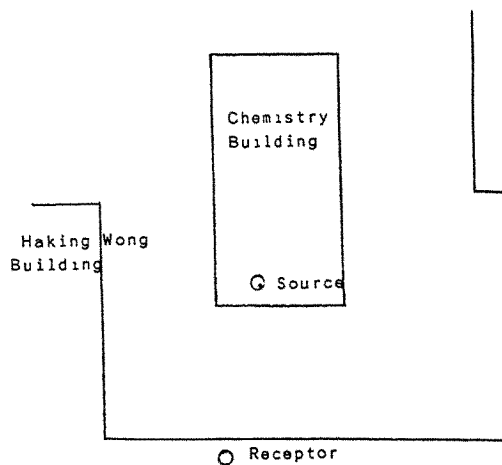


Figure 1: Layout of Chemistry Building



available during the experiment, sampling was done only once every fifteen minutes to allow all interfering gases to elude before taking a new sample. The samples collected were grab sample. The primary calibration of the gas monitor was carried out by the manufacturer. The secondary calibration of the gas monitor was carried out twice daily. Standard gas was prepared using static dilution method. The calibration curve obtained compared very well with the calibration curve supplied by the manufacturer ( $\pm 10\%$ ).

The wind direction over the roof of Chemistry Building was measured by a wind vane. The output voltage varies between 0 and 5 volts in proportion to the 0 to 540 degree rotation of the wind vane. Wind speed over Chemistry Building was measured by a 3-cup anemometer. The wind speed range was adjusted to 0 - 25m/s. The time constant was adjusted to 9 seconds. The anemometer was tested in a wind tunnel before installed on site. 3 minutes average of wind speed and direction were then computed for gas dispersion analysis.

## 5. Results

Instantaneous dilution factors D obtained were studied in relation to wind direction, wind speed, and averaging time. The ensemble of D were sorted in 8 different sectors. All the instantaneous dilution factors were plotted against the 3 minute averaged horizontal wind speeds  $\bar{u}$  which are measured over the roof of chemistry building. The 3 minute averaged wind speed was taken right before a gas sample was taken (figure 2). Four minimum dilution factor ( $D_{MIN}$ ) criteria were superimposed onto the graphs for evaluation: (1) Halitsky 1963 [8] (Clinical Centre Test):

$$D_{min} = 4.44[3.16 + 0.1r]^2 \left(\frac{u}{v_e}\right) \quad (1)$$

(2) Wilson 1977 [9] (Wind Tunnel Modelling)

$$D_{min} = \frac{0.11ur^2}{Q_e} \quad (2)$$

(3) Chiu and Wilson 1988 [10] (Wind Tunnel Modelling)

$$D_{MIN} = \left[ (1 + 7M^2)^{0.5} + \frac{0.2 \left(\frac{U_T^2}{Q_e}\right)^{0.5}}{1 + \left(\frac{1.7\theta}{1+\theta}\right) \exp(-3.5M)} \right]^2 \quad (3)$$

put  $\theta = \pi/4$ ,  $M = V_c/U_H$

(4) Li & Meroney 1983 [11] (Wind Tunnel Modelling)

$$D_{min} = \frac{0.11 f(\theta)ur^2}{Q_e} \quad (4)$$

$$f(\theta) = \frac{1}{1 + \frac{4\theta}{\pi}} \quad (5)$$

Time averaging were carried out both for the dilution factors and  $\bar{u}$ . One hour, six hour and twenty four hour time averaged dilution factors were plotted against one hour, six hours and twenty four hours time averaged  $\bar{u}$  respectively (figure 3 to figure 5).

## 6. Discussion

From figure 2 it can be observed that: There is no relationship at all between the dilution factor and the horizontal wind speed. The dilution factors scatter wildly for all sites in the field study. A lack of correlation of D with u indicates that wind speed is not a sole parameter affecting the dispersion mechanism, there are other parameters contributing to the dilution of air contaminants. Different combinations of pertinent parameters at constant wind speed lead to different dilution capability. All four minimum dilution factor criteria cannot accommodate all field instantaneous data. Even the most conservative Halitsky criteria was exceeded in many occasions. This is not surprising at all because all the criteria were developed by wind tunnel experiments and they represent time mean values equivalent to about 10 minutes time weighted average. Therefore time averaging is necessary for their evaluation. The lowest instantaneous D recorded was 750. The lowest one hour averaged D recorded was 1550. From figure 3 to 5, it can be observed that dilution factors increase with averaging time. This is a characteristic of atmospheric dispersion due to the wide range of eddy motions in the atmosphere. The minimum dilution criteria proposed by Chiu & Wilson is the best estimate out of the four for one hour averaged dilution factors. It successfully accommodates over 99% of the gas samples. Chiu and Wilson formula accounts for the dilution created by exhaust jet entrainment which is very prominent at very low wind speed. The field study suggests that this dilution effect might have been caused by the domination of thermal turbulence. All four minimum dilution criteria are satisfied under all conditions for both the 6 hour and 24 hourly averaging.

## 7. Conclusion

The field study is successful in the validation of empirical formulae. Chiu and Wilson formula has the best fit for one hour averaged field data. All four formulae were obtained using physical modelling methods. Although the field data might be site specific, it can be concluded that wind tunnel modelling method is appropriate and conservative for near building dispersion analysis. Their results are compatible to field data.

## References:

- 1 ASHRAE - Airflow Around Building. ASHRAE Handbook and Product Directory, Fundamental, Chapter 14, 1985.
- 2 Huges D. - Discharging to Atmosphere From Laboratory Scale Processes. HHSC Handbook No.4, 1989.
- 3 Halitsky J. - Gas Diffusion near Buildings. ASHRAE Transactions, 69, pg464-484, 1963.
- 4 Drivas P.J. & Shair F.H. - Probing the Air Flow within the Wake downwind of a Building by means of a Tracer Technique. Atmospheric Environment, vol., pg.1165-1175, 1974.
- 5 Lamb B.K., Vitols V., Skogvold O. - Atmospheric Tracer Techniques and Gas Transport in the primary Aluminium Industry. Journal of the Air Pollution Control Associations,

- vol.30, 5, pg.558-566, 1980.
- 6 Lamb B.K., Cronn D.R. - Fume Hood Exhaust Re-entry into a Chemistry Building. Journal of American Industrial Hygiene Association. 47(2), pg.115-123, 1986.
- 7 Ogawa Yasushi, Oikawa Susumu, Uehara Kiyoshi - Field and Wind Tunnel study of the Flow and Diffusion Around a Model Cube-Part I & II. Atmospheric Environment, vol.17, pg.1145-1171, 1983.
- 8 Halitsky J. - Diffusion of Vented gas around Buildings. Journal of Air Pollution Control Association, vol.12, pg74-80, 1962.
- 9 Wilson D.J. - Contamination of Air Intakes from Roof Exhaust Vents. ASHRAE Transaction: 82 partI, pg.1024-1038, 1976.
- 10 Li W.W. & Meroney R.N. - Gas Dispersion Near a Cubical Model Building Part I & II. Journal of Wind Engineering and Industrial Aerodynamics, vol.12, pg.15-47, 1983.
- 11 Chiu E.H. and Wilson D.J. - Effect of varying Wind Direction or Exhaust Gas Dilution. Journal of Wind Engineering and Industrial Aerodynamics, vol.31, pg.87-104, 1988.

\* D — Wilson — Hallitsky - - Li & Meroney — Chiu & Wilson

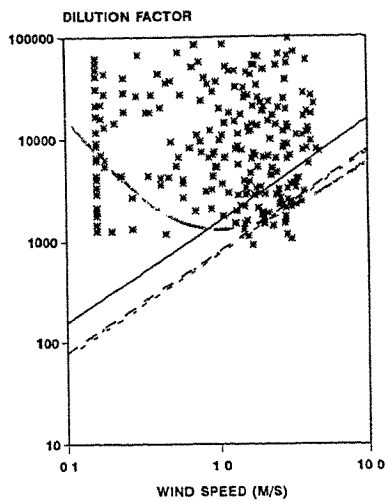


Figure 2 Instantaneous D vs 3 minutes averaged u

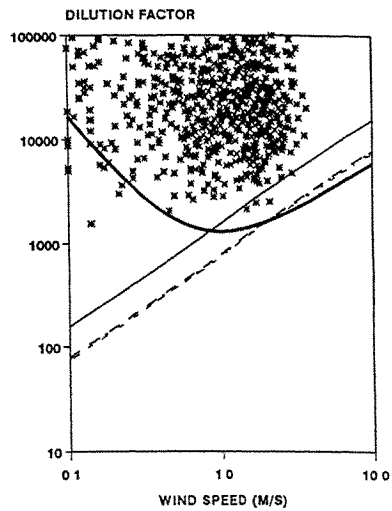


Figure 3 1 hour averaged D vs 1 hour averaged u

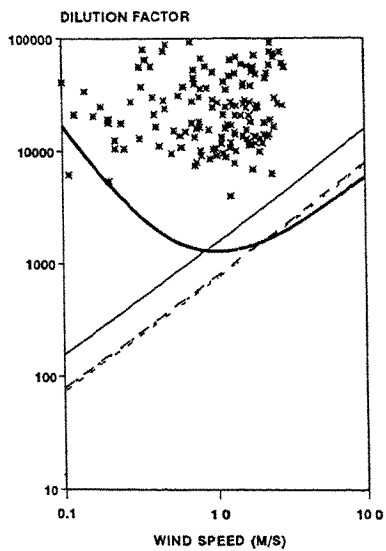


Figure 4 6 hour averaged vs 6 hour averaged u

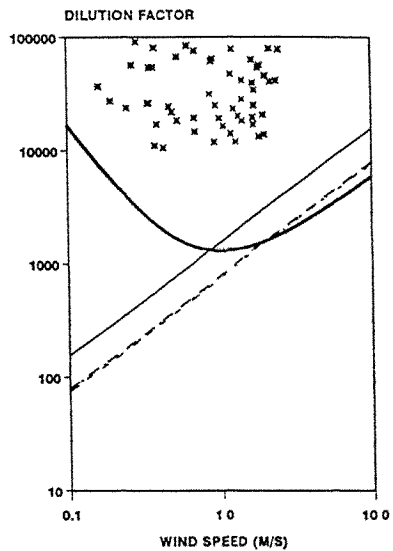


Figure 5: 24 hour averaged D vs 24 hour averaged u

# Effects of Model Scale in Estimating Pollutant Dispersion near Buildings

P.J. Saathoff, T. Stathopoulos and M. Dobrescu

Centre for Building Studies  
Concordia University  
Montreal, Quebec, Canada

**Abstract:** Wind tunnel experiments were performed to measure tracer gas concentrations on the surface of model cubes. The tracer gas was emitted with low exhaust momentum from a flush vent at the center of the roof. Three building models were constructed at scales of 1:500, 1:250 and 1:125. Data were obtained for open country, suburban and urban exposures. The results indicate that a 4 to 1 mismatch of model and boundary layer scales does not significantly affect estimates of pollutant concentration on building surfaces.

## 1. Introduction

Emissions of exhaust gases from rooftop vents and stacks can lead to air quality problems. Depending on the wind conditions and the quantities of chemicals released, high concentrations of toxic and odorous chemicals can occur at air intakes of the building or surrounding buildings. Exceedances of health or odor criteria may also occur at ground level receptors near the building.

Empirical formulas have been developed to estimate plume dilution in the vicinity of rooftop stacks [1]. However, because of the complexity of the wind flow around buildings, these formulas can only provide rough estimates of minimum plume dilution at a receptor. Errors of an order of magnitude in dilution estimates using ASHRAE formulas have been reported [2].

Wind tunnel modeling can provide more accurate estimates of plume dilution near buildings, given that the important modeling criteria are satisfied. One of the criteria for dispersion modeling is the matching of the model scale to the scale of the simulated atmospheric boundary layer. However, if the boundary layer scale is of the order of 1:500, this criterion may require the use of very small building models and thus may make it difficult to meet other modeling criteria. For example, the generally accepted criterion for building Reynolds number is  $Re_b > 11000$  where  $Re_b = U_h D / \nu$ ,  $U_h$  is the mean wind speed at building height,  $D$  is the minimum building side dimension, and  $\nu$  is kinematic viscosity [3]. If  $D$  is small, the value of  $Re_b$  may be well below 11000.

Another criterion that is difficult to satisfy using small models is ensuring that exhaust flow from stacks is turbulent. The stack Reynolds number should exceed 2000 and if this cannot be achieved, a trip should be placed in the stack to create exhaust turbulence [3]. It is usually not possible to satisfy the stack Reynolds number criterion for small diameter stacks and it is also difficult to trip the flow for such stacks.

The use of large-scale models of 1:200 or 1:100 can eliminate these problems and also allow greater spatial resolution of concentration data. Although the scale of the boundary layer simulation should match the model scale, previous studies have shown that pressure distributions on low-rise buildings are relatively insensitive to the boundary layer scale. A model that is twice the correct

size produces errors in mean pressure distributions on the roof and sides of less than 20% [4,5]. It is therefore of interest to determine whether a mismatch of scales by a factor of two or four significantly affects estimates of mean pollutant concentration in the vicinity of buildings.

If the building model is too large for the boundary layer simulation, the turbulence intensity at the building height will be less than that for the full-scale building. Wilson and Chui [6] have shown that the absence of upstream turbulence can decrease the dilution of exhaust from rooftop stacks by as much as a factor of 10, depending on the building shape and stack location. On the other hand, a recent study by Huber [7] has shown that characteristics of the upstream boundary layer do not significantly affect the dispersion of a tracer gas emitted at ground level in the near wake of a block-shaped building.

Distorting the model scale by increasing the model dimensions also reduces the relative scale of turbulence,  $L_x/D$ , where  $L_x$  is the integral scale of the longitudinal velocity component. Studies of two-dimensional flow over long flat plates have shown that the mean flow is not significantly affected by turbulence scale for  $0.5 < L_x/D < 2.0$  [8,9]. However, the influence of  $L_x/D$  on the mean flow around buildings is not well understood.

The purpose of the present study is to determine whether distortions of model scale by as much as a factor of four will significantly affect mean concentrations of a tracer gas emitted from a rooftop source. The paper presents dispersion data which have been obtained with an isolated cubical building at three scales.

## 2. Experimental Procedure

The study was performed in the boundary layer wind tunnel at the Centre for Building Studies (CBS), Concordia University. The wind tunnel is 12.2 m long and has a cross-section of 1.8 m by 1.8 m. Open country, suburban and urban exposures having power law exponents ( $\alpha$ ) of 0.15, 0.25 and 0.38, respectively, were simulated.

Three cubical models with side dimension,  $D$ , of 30 mm, 60 mm and 120 mm were constructed out of aluminum. These correspond to a full-scale building with a height of 15 m at scale reductions of 1:500, 1:250 and 1:125, respectively. Each model had 40 brass tappings (0.8 mm diam.) on the roof and sides which were used to obtain tracer gas samples via a SCANIVALVE system. Concentrations very close to model edges were measured with a movable probe which was placed 0.2 mm from the roof surface. The tracer gas was emitted from a flush vent located at the center of the roof. The vent had an internal diameter ( $D_v$ ) of 0.1D.

Sulfur hexafluoride ( $SF_6$ ) was used as the tracer gas. The mean concentration of  $SF_6$  at air intakes was measured using a Varian gas chromatograph which has a measurement resolution of 1 ppb. Samples of air were collected via plastic tubes which had an inside diameter of 1.6 mm. At each tapping, ten samples were collected over a period of 2 minutes to obtain stable estimates of mean concentration. The measurements correspond to full-scale concentrations obtained over 10 or 15 minutes [3]. The background  $SF_6$  concentration in the wind tunnel was measured upstream of the model and subtracted from the measured intake concentrations to obtain the actual concentration at the receptor. Repeatability checks were carried out for selected tappings and the uncertainty of the data was found to be less than 20%.

Flow parameters for the three models are shown in Table I. Because  $D$  varied by a factor of 4, it was not possible to have the same building Reynolds number for each model. However, it is assumed that the results are independent of  $Re_b$ , since  $Re_b > 11000$  for each model. Effects of wind tunnel blockage are insignificant; the blockage ratio for the largest model was only 0.5%.

The exhaust flow rate was adjusted so that the momentum ratio ( $M = \lambda(U_e/U_p)^2$ ) was the same for each model, where  $\lambda$  is the ratio of exhaust gas density to the ambient air density and  $U_e$  is the exhaust velocity. The value of  $M$  was very low ( $M = 0.07$ ) and thus, the plume was completely

trapped in the recirculation zone of each model. This value of  $M$  was also chosen so that measurements could be compared to results of Li and Meroney [10]. Values of Reynolds number at the outlet ( $Re_o$ ) were 110, 90 and 190 for the 30mm, 60mm and 120 mm cubes, respectively.

### 3. Results and Discussion

Profiles of rooftop concentration for the three models in the open country terrain are shown in Figure 1 for wind direction  $\theta=0^\circ$ . Also shown are data obtained by Li and Meroney [10]. The data are expressed in terms of the nondimensional concentration coefficient  $K=CH^2U_w/Q$ , where  $C$  is the tracer gas concentration and  $Q$  is the release rate of the tracer gas. The value of  $K$  at the outlet,  $K_o$ , was 1780 for each model.

Distributions of  $K$  on the roof show little dependence on model scale. Maximum concentration occurs upstream of the vent, indicating that the flow has reattached downstream of the vent, trapping the effluent in the separation bubble. Results obtained by Li and Meroney are also shown and are generally similar to the measured data except near the leading edge. Significantly higher values of  $K$  were measured at  $x/H=0.05$  in the present study, where  $x$  is the distance from the leading edge. The discrepancy may be due to the interpolation scheme used to obtain  $K$  contours in [10]. A movable probe was used in the present study to measure tracer gas concentrations close to the leading edge. Values of  $K$  were less than 0.1 at  $x/H<0.01$ , in agreement with Li and Meroney's results.

Concentration distributions for  $\theta=45^\circ$  are shown in Figure 2. In this case the tracer gas is immediately transported downstream as it exits the vent. Consequently, the maximum concentration for each cube occurs downstream of the vent. The contour plots for the three models are generally similar, although the data show greater variability than those for  $\theta=0^\circ$  because of increased instability of the flow for  $\theta=45^\circ$ .

Profiles of concentration along the center line of the three cubes for  $\theta=0^\circ$  are shown in Figure 3 for open country terrain. Data obtained by Li and Meroney [10] are also shown. The results indicate that, for this building shape and exhaust location, effects of mismatching the boundary layer and model scales are small.

The influence of freestream turbulence on values of  $K$  is shown in Figure 4 where data for the 1:250 cube are presented. Values of turbulence intensity,  $\sigma_w/U_w$ , at roof height for open country, suburban and urban exposures are 0.14, 0.19, 0.30, respectively. As  $\sigma_w/U_w$  increases,  $K$  decreases upstream of the vent and increases downstream of the vent. This is probably caused by the reduction in size of the inner recirculation zone over the roof as  $\sigma_w/U_w$  increases. As the recirculation region fluctuates in size, emissions will be alternately transported upstream and downstream.

Also shown in Figure 4 are data of Ogawa et al [11] obtained in a smooth boundary layer and a rough boundary layer. Values of  $\sigma_w/U_w$  at building height were 0.07 and 0.27, respectively. In the rough boundary layer, the maximum value of  $K$  occurred downstream of the vent. This result agreed qualitatively with field results presented in [11] for a model cubical building ( $H=1.8$  m).

### 4. Conclusions

The results of this study indicate that a four to one difference in model and boundary layer scales does not significantly affect measurements of concentration on building surfaces. Measurements obtained with the 1:125 scale cubical model were very similar to those obtained with the 1:500 scale model which was the correct size for the boundary layer simulation. These results indicate that errors in concentration measurements resulting from scale mismatching are small, provided that wind tunnel blockage is not significant. However, further work should investigate whether this conclusion is valid for rooftop stacks with different heights and exhaust momentum.

**References:**

1. American Society of Heating, Refrigeration and Air Conditioning Engineers, ASHRAE Handbook -- 1989 Fundamentals, Chap. 14 (1989)
2. R. Petersen and D. Wilson, "Analytical Versus Wind Tunnel Determined Concentrations Due to Laboratory Exhaust," ASHRAE Transactions Vol. 89, Part 2 (1989) 729.
3. W.H. Snyder, "Guideline for Fluid Modeling of Atmospheric Diffusion," USEPA, Research Triangle Park, NC, Report No. EPA600/8-81-009, (1981).
4. A. Hunt, "Wind Tunnel Measurements of Surface Pressures On Cubic Building Models at Several Scales," Journal of Wind Engineering, Vol. 10, (1982) 137-168.
5. T. Stathopoulos and D. Surry, "Scale Effects in Wind Tunnel Testing of Low Buildings," Journal of Wind Engineering, Vol. 13, (1983) 313-326.
6. D. Wilson and E.H. Chui "Effect of Turbulence from Upwind Buildings on Dilution of Exhaust Gases," ASHRAE Transactions, Vol. 93, Part 2, (1987) 2186-2197.
7. A. Huber "Wind Tunnel and Gaussian Plume Modeling of Building Wake Dispersion," Atmospheric Environment, Vol. 25A, No. 7, (1991) 1237-1249.
8. P. Saathoff and W.H. Melbourne, "The Generation of Peak Pressures in Separated-Reattaching Flows," Journal of Wind Engineering, Vol. 32, (1989) 121-134.
9. R. Hillier and N. Cherry, "The Effects of Stream Turbulence on Separation Bubbles," Journal of Wind Engineering, Vol. 8, (1981) 49-58.
10. W.W. Li and R.N. Meroney, "Gas Dispersion Near a Cubical Model Building. Part I. Mean Concentration Measurements," Journal of Wind Engineering, Vol. 12, (1983) 15-33.
11. Y. Ogawa, S. Oikawa, and K. Uehara, "Field and Wind Tunnel Study of the Flow and Diffusion Around a Model Cube -- Part II. Nearfield and Cube Surface Flow and Concentration Patterns," Atmospheric Environment, Vol. 17, No. 6, (1983) 1161-1171.

Parameter	1:500 Cube	1:250 Cube	1:125 Cube
H (mm)	30	60	120
$U_h$ (m/s)	7.8	3.3	3.3
$Re_b$	15,600	13,200	26,400
$D_o$ (mm)	3	6	12
$U_o$ (m/s)	0.55	0.23	0.24
$Re_o$	110	90	190
M	0.07	0.07	0.07

Table 1. Modeling parameters used in the study



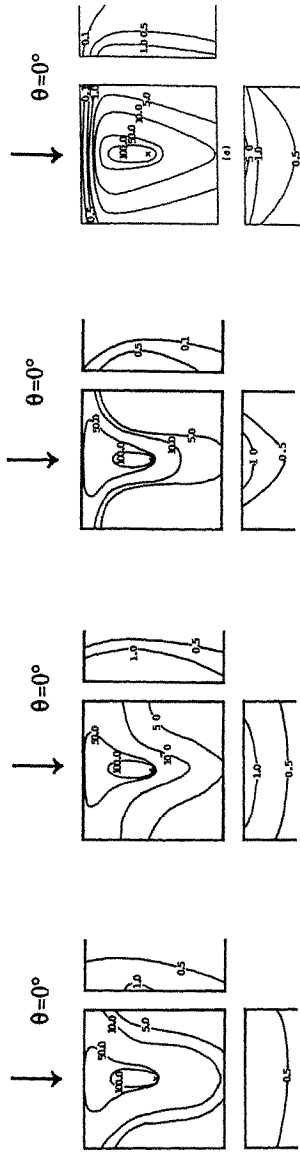


Figure 1. Concentration coefficient contours obtained in open country terrain for  $\theta=0^\circ$

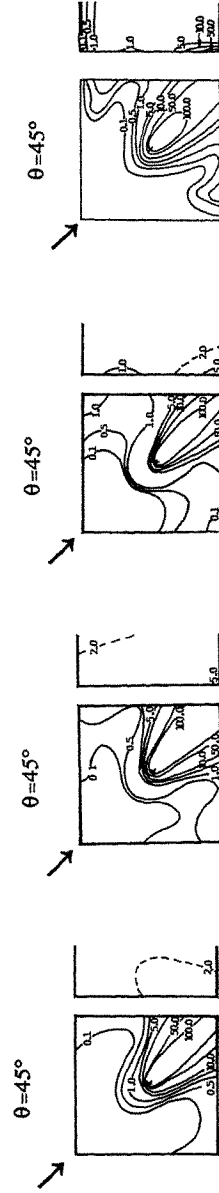


Figure 2. Concentration coefficient contours obtained in open country terrain for  $\theta=45^\circ$

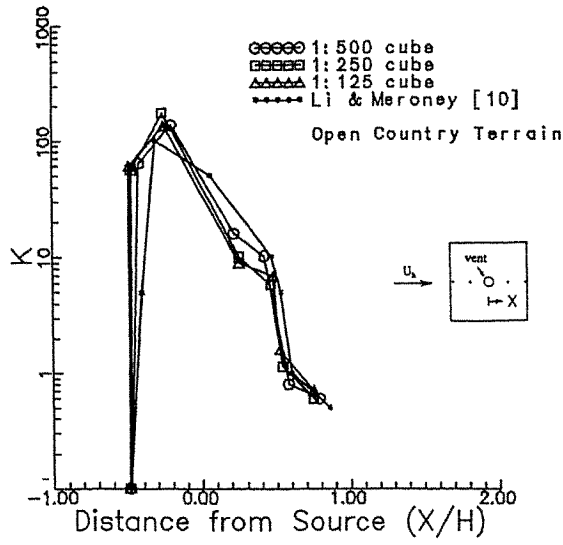


Figure 3. Concentration coefficient profiles along model center line for  $\theta=0^\circ$

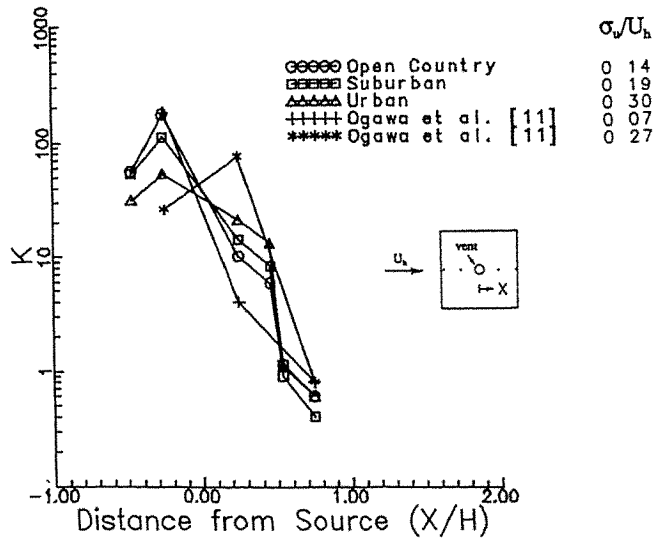


Figure 4. Effect of turbulence intensity on concentration profiles for 1:250 cube ( $\theta=0^\circ$ )

## Building downwash of plumes and plume interactions

J.C.K. Cheung and W.H. Melbourne

Department of Mechanical Engineering  
Monash University, Clayton, Vic 3168, Australia

**Abstract:** This paper presents a number of wind tunnel measurements of building induced downwash effects on the plume in a neutrally stable boundary layer. Vertical and horizontal profiles of mass concentrations of the exhausts from stacks on a rectangular model building were measured downwind of the buoyant source in the near wake. These experiments were conducted in a simulated natural wind over open country terrain for various freestream wind speeds with different stack and building configurations. Significant downwash effects from the building below the stack were observed in all tested configurations. In this preliminary study, only mean concentrations were evaluated and are presented in non-dimensional form.

### 1. Introduction

Wind tunnel modelling of buoyant plumes has been undertaken in Monash University in both neutrally stable [1] and convective [2] wind flows. Although thermal stratification may significantly alter the flow around the building, dispersion studies in neutrally stable conditions are still essential to provide a database for further investigations into this already complicated problem dominated by the complex, unsteady flow in the building wake.

When the momentum and buoyancy of the exhausts discharged from the stacks are insufficient to overcome the low pressure suction in the wake, the plume is entrained rapidly downward into the low pressure wake region. This aerodynamic downwash of plume in the immediate lee of the stack has been studied for neutrally buoyant plumes [3]. This stack-tip downwash generally does not occur if the stack exit velocity is more than 1.5 times the wind speed at stack height. The downwash due to the building wake has been shown not to occur if the stack height is more than 2 to  $2\frac{1}{2}$  times the building height. Detailed measurements of the building downwash were made [4], but with the effluent source mainly at ground level. The intent of this paper is to present an initial measurement of the building downwash of plumes from stacks on the roof of the building. Also, the interaction effects of one plume on another nearby plume were investigated. The results can then be used for mathematical model development and guidance in similar situations.

### 2. Experimental Design

The experiments were carried out in the 4x3m working section of the 450 kW close-return type Boundary Layer Wind Tunnel at Monash University. The basic model of a rectangular building, 240mm by 80mm by 62mm high, was tested in a 1/200 scale model of the natural wind flow over open country terrain. The natural wind boundary layer model was generated using roughness elements and vorticity generators upstream of the model, which accurately simulated the turbulent wind characteristics of neutral conditions with a freestream vertical profile of mean velocity followed a power law with an exponent of 0.15 and a longitudinal turbulence intensity of 0.18 at building height.

The short stream-wise length of the building was oriented parallel to the freestream flow so that no re-attachment occurred. Four stacks were located at the centre of the building roof, with the stack separation width 5m side by side and 6m in tandem full scale. The stack height above the roof tested ranges from  $\frac{1}{2}$  to 2 times building height, such that building downwash always occurs. The full scale stack exit temperature is 90°C, the exit diameter is 1.3m, the exit velocity is 8.7 m/s and thus the stack-tip downwash would be less than one stack diameter below the top of the stack.

A helium and air mixture was used to model the buoyancy and momentum of the discharge gas in the measurements.

Density of discharge gas at full scale temperature

$$= a \times \text{Density of helium at model temperature} \\ + (1 - a) \text{ Density of air at model temperature}$$

where  $a$  is the percentage of helium in the mixture.

For undistorted geometric, kinematic and dynamic similarity, i.e. strict Froude scaling, it follows that the velocity scaling, model to full scale ratio

$$V_r = \sqrt{L_r}$$

where  $L_r$  = model length scale = 1/200

∴ the discharge flow rate ratio

$$Q_r = V_r L_r^2 = L_r^{2.5}$$

The helium and air flow rates were metered to a plenum from where the gas mixture was discharged through the stacks. Helium in this type of experiment is used as a tracer and for scaling of the buoyant discharge. The concentration of helium, and hence discharge gas, in a downstream air sample was measured by a mass spectrometer tuned to helium.

$$\begin{aligned} \text{Mass concentration} &= \frac{\text{Density of discharge at full scale temperature}}{\text{Density of air at model temperature}} \\ &\times \text{Volume concentration measured} \\ &= \frac{1}{a} \times \frac{\text{Density of discharge at full scale temperature}}{\text{Density of air at model temperature}} \\ &\times \text{Volume concentration of helium measured} \end{aligned}$$

The spectrometer output was sampled at 1000 Hz over a model scale period of 250 seconds (equivalent to approximately an hour in full scale time) and low-pass filtered at 30 Hz i.e. approximately 2 Hz equivalent in full scale. This modelling technique is accurate in the near-field where the dispersion of exhaust gases is dominated by large scale turbulent motions generated by the topographical boundary layer and building wake flows. The procedure used to obtain each data point was to set the model to the desired configuration and then to measure the concentration of exhaust gas in ambient air, at various locations on a horizontal plane traverse at ground level and a vertical plane traverse at the centre downstream of the discharge. In full scale terms the hourly mean, standard deviation and peak of exhaust gas concentrations in ambient air by mass ratio, were determined. The mean mass concentrations are presented in this paper in the following non-dimensionalised form.

$$\text{Concentration coefficient} \quad \chi = \frac{\rho C_M U H B}{\rho_s \omega A_s}$$

where	$C_M$	=	mass concentration
	$\rho$	=	air density
	$\rho_s$	=	stack exhaust density
	$U$	=	freestream wind velocity
	$\omega$	=	stack exit velocity
	$H$	=	height of building
	$B$	=	width of building
	$A_s$	=	area of stack

### 3. Results and Discussion

High concentrations are seen to occur at wind speeds approximately 10.7 m/s at heights up to at least 2 to 3 buildings heights above the stack heights, 2 to 3 buildings widths wide and 5 to 50 building widths downstream. Plume interactions, where the plume buoyancy of the downstream stack raises the upstream plume, are seen to reduce the highest ground level concentration by 40% near the building and by 10% farther away 5 buildings widths downstream. A small air gap under the building is seen to decrease the high ground level concentrations behind the building, but only moves the high concentrations due to downwash further away from the building. The addition of downstream buildings increases entrainment and is seen to increase the downwash effect. As the stack height increases to 2 building heights, the downwash effect decreases and the highest ground level concentration is reduced by 50%.

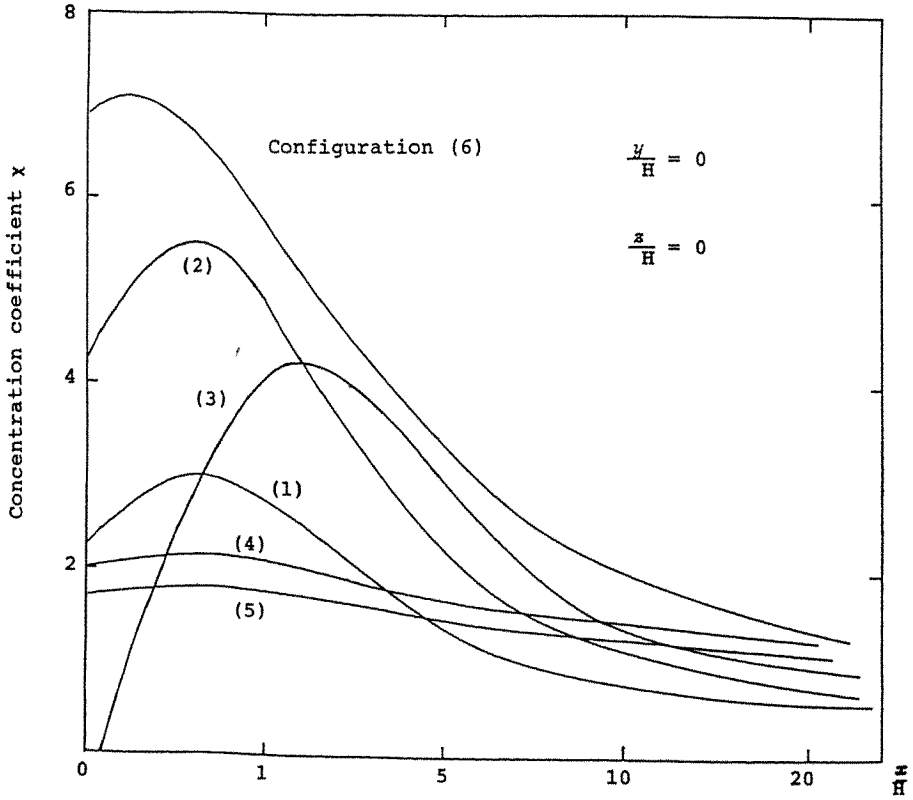
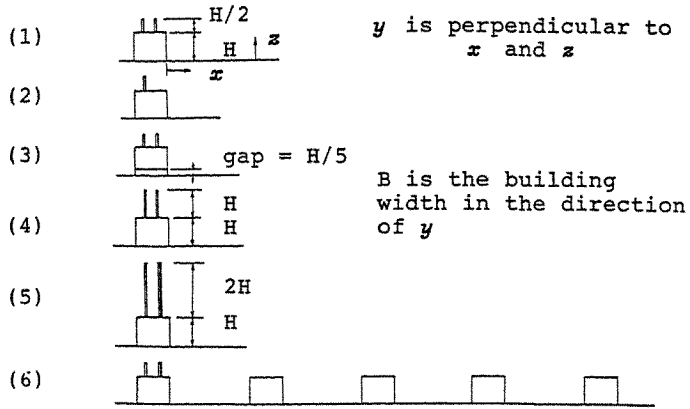
### Acknowledgements

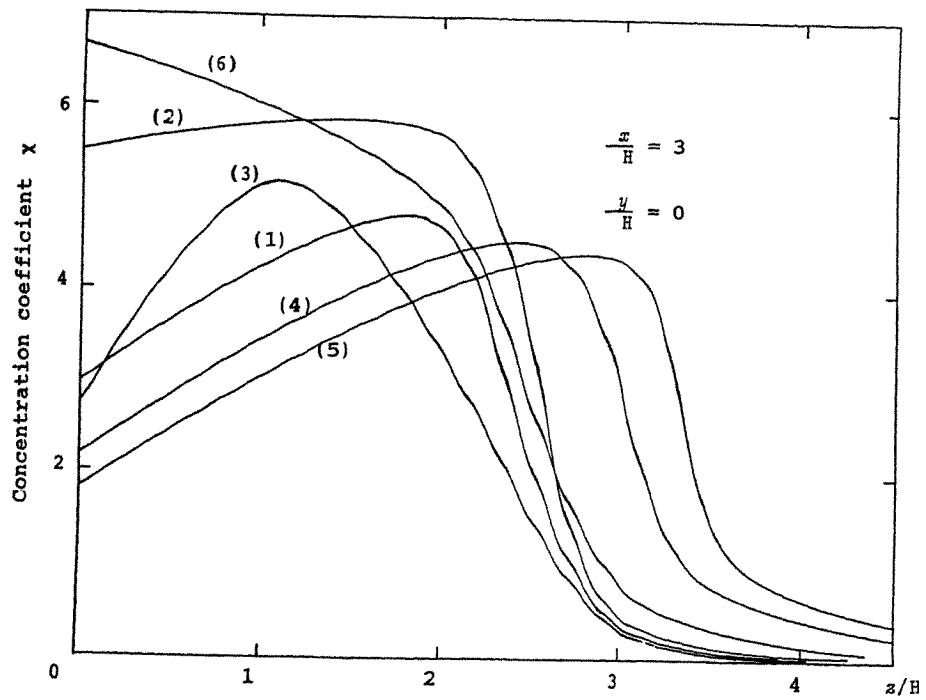
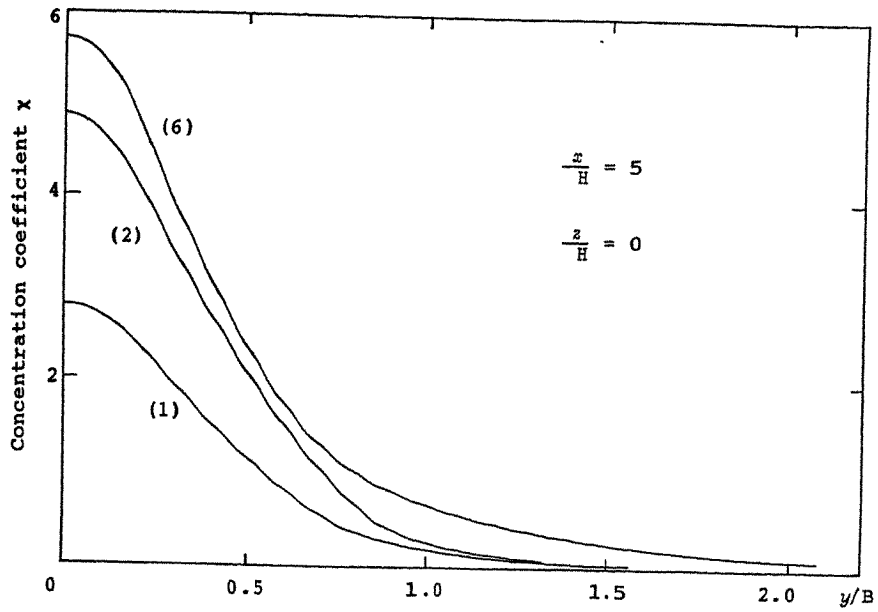
This research was supported by Alcoa of Australia Limited. The authors also wish to thank Mr D Collins of Alcoa Port Henry Works for permission to include in this paper some experimental data from a more comprehensive study previously sponsored by Alcoa.

### References:

1. W H Melbourne (1968) "Wind tunnel modelling of buoyant chimney plumes", Proc. 3rd Australasian Conf. on Hydraulics and Fluid Mechanics, Inst. of Engineers, Australia, pp 81-85.
2. W H Melbourne, T J Taylor and C F Grainger (1993) "Dispersion modelling in convective wind flows", Prepared for submission to Atmospheric Environment.
3. W H Snyder and R E Lawson (1991) "Fluid modelling simulation of stack-tip downwash for neutrally buoyant plumes", Atmospheric Environment, Vol 25A, No.12, pp 2837-2850.
4. A H Huber (1991) "Wind tunnel and Gaussian plume modelling of building wake dispersion", Atmospheric Environment, Vol 25A, No.7, pp 1237-1249.

Configuration









## Models of urban air diffusion and their application

wang shu—fang

Centre of Environmental Sciences  
Peking University, P. R. China

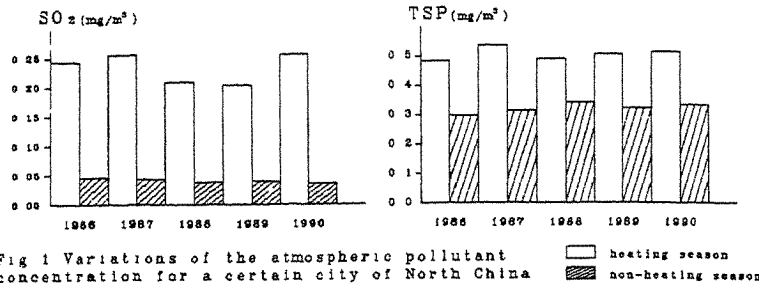
**Abstract:** In this paper, a set of air quality models used to calculate the concentration distribution of SO<sub>2</sub> and dust particulates in urban areas is developed. The models are particularly designed for those cities where coal is the main energy sources in winter season and the pollutions of SO<sub>2</sub> and TSP are very serious, for example, most cities in North China. This set of models has been put in practical use in cities like Beijing, Mudanjiang and shijingshan district (a large steel industry area in Beijing) with satisfied results and is going to apply in shijiazhuang city.

### 1. Introduction

Based on the research works the author took part in since 1973 about the approaches of anti—air pollution against SO<sub>2</sub> and TSP, and the prediction method of atmospheric pollution, also considering the special condition of the cities in North China, we summarized a set of models for the calculation of SO<sub>2</sub> and dust pollution for urban areas. In recent two years, those models have been applied in Mudanjiang (in the North East of China) and one district of Beijing for the control of total amount of SO<sub>2</sub> and TSP with quite satisfied results.

The North China cities are in mid—latitudes, belonging to the temperate continental monsoon climate. There is a heating season lasting for about 5—6 months each year. During This heating period, coal consumption increases considerably and most of the emissions are not from elevated chimneys, but from distributed small boilers with chimney heights only about 10—20 meters and southands of family coal stoves with very low emission heights. Thus, the air pollution during this period exceeds seriously over the standard. Fig. 1 shows the annual variation of average concentrations of SO<sub>2</sub> and TPS for the heating and non—heating seasons for a North China city.

TSP and SO<sub>2</sub> pollutions have different properties in: (1)the difference of average concentration between heating and non—heating seasons for SO<sub>2</sub> is larger than that for TSP, (2)daily variation of the average concentration of SO<sub>2</sub> during the heating seasons is larger than that of TSP, (3)over a distance of 50km from the city center, TSP is still with a quite high average concentration (0.2—0.3mg/m<sup>3</sup>), while for SO<sub>2</sub>, this concentration is already very low even at a distance of 10km (0.02—0.03mg/m<sup>3</sup>). Thus, in calculating TSP, one must consider the city



TSP background [1] as well as the resuspended surface dust, this is different from the situation in some developed countries where city air pollution is less serious and these two factors can be ignored.

After detailed investigations, measurements, data analyses for the sources of SO<sub>2</sub> and dust emission, also through collecting and analysing the actual monitored data and local meteorology data, we designed multi-source diffusion models for SO<sub>2</sub> and dust which are suitable for different cities, practical, convenient in routine applications, The calculation results of these models could be used well in improving air quality, selecting city plan and so on.

## 2. Fundamentals of the models

### 2.1 Model for SO<sub>2</sub> point source

Assume that at a downwind distance  $x$  from the point source, concentration is uniformly distributed within  $22.5^\circ$  (a wind azimuth unit), then the surface concentration at  $x$  is:

$$K = \sqrt{\frac{2}{\pi}} \frac{Q}{\bar{u} \left(\frac{\pi x}{8}\right) \sigma_y} \exp\left(-\frac{H_e^2}{2\sigma_z^2}\right) \exp(-\psi x / \bar{u}) \quad (1)$$

where  $Q$  is the point source intensity;  $H_e$  is the effective height of the plume with  $H_e = H_s + \Delta H$  and  $H_s$  is the geometrical height of chimney,  $\Delta H$  is the plume rise, this formula is recommended by Chinese EPA.  $\bar{u}$  is the average wind speed at the exit height of chimney,  $x$  is the downwind distance of receptor from source,  $\sigma_z$  is a vertical diffusion coefficient and also measured values for each city are used,  $\exp(-\psi x / \bar{u})$  is a damping term of the pollutants due to certain physical or chemical processes,  $\psi = \ln 2 / T_{1/2}$  is a damping constant, where  $T_{1/2}$  is the half life-time of pollutants, for SO<sub>2</sub>  $T_{1/2}$  takes 2-4 hours for heating seasons, 0.5 hour for non-heating seasons.

In a calm-wind situation, we take a wind speed of 0.4-0.5m/s and assume the concentrations uniformly distributed over all the 16 azimuth units.

## 2.2 Model for SO<sub>2</sub> area source

Our area source model is based on the ATDL model [2, 3] with a revision for source height. In a situation of relatively uniform source intensity, the pollutant concentration at certain position is mainly determined by intensities of area sources in upwind directions. Wind path grids are designed for different wind directions and in each wind path grid the paths for 16 wind azimuth are fixed.

Under certain wind direction at a receptor the pollutant concentration affected by all area sources upwind can be expressed as:

$$k = \frac{1}{u} (C_0 Q_0 + C_1 Q_1 + C_2 Q_2 + \dots) \quad (2)$$

where  $Q_i$  is the intensity of the  $i$ th area source upwind with annual and diurnal variations.

$$C_0 = \sqrt{\frac{\pi}{2}} \int_0^L \frac{1}{\sigma_x} \exp\left(-\frac{H_s^2}{2\sigma_x^2}\right) dx \quad (3)$$

$$C_i = \sqrt{\frac{\pi}{2}} \int_{(-\frac{1}{2})L}^{(+\frac{1}{2})L} \frac{1}{\sigma_x} \exp\left(-\frac{H_s^2}{2\sigma_x^2}\right) dx \quad i = 1, 2, \dots \quad (4)$$

where  $L$  is the length scale of area source grids,  $C_0, C_1, C_2, \dots$  are called area source grid coefficients, in general  $i \leq 8$ .

## 2.3 Model for particle point source

Calculations of concentration for dust particles adopt a model of partial reflection combined with tilted plume model:

$$K = \frac{1 + \alpha}{2} \sqrt{\frac{2}{\pi}} \frac{Q}{u \left(\frac{\pi}{8} x\right) \sigma_x} \exp\left[-\frac{(Vg \frac{x}{u} - H_s)^2}{2\sigma_x^2}\right] \quad (5)$$

where  $Vg$  is the deposition speed of dust particles under gravity calculated from Stokes' formula, it could be divided into several classes according to the particle diameter in calculation,  $\alpha$  is the reflectivity of dust particles,  $\alpha = 1$  (for  $d \leq 10 \mu\text{m}$ ) and  $\alpha = 0$  (for  $d = 100 \mu\text{m}$ ), between 10 and  $100 \mu\text{m}$ ,  $\alpha$  decreases as particle diameter increases.

## 2.4 Model for dust area sources

Similar to dust point source, pollutant concentration is calculated in several classes according to particle diameters, the concentration is expressed as:

$$K = \frac{1+\alpha}{u} (C_0Q_0 + C_1Q_1 + C_2Q_2 + \dots) \quad (6)$$

where 
$$C_0 = \int_0^{L/2} \frac{1}{\sqrt{2\pi}} \frac{1}{\sigma_x} \exp\left[-\frac{1}{2} \frac{\left(Vg \frac{x}{u} - H_s\right)^2}{\sigma_x^2}\right] dx \quad (7)$$

$$C_i = \int_{(-\frac{1}{2})L}^{(+\frac{1}{2})L} \frac{1}{\sqrt{2\pi}} \frac{1}{\sigma_x} \exp\left[-\frac{1}{2} \frac{\left(Vg \frac{x}{u} - H_s\right)^2}{\sigma_x^2}\right] dx \quad i = 1, 2, \dots \quad (8)$$

### 2.5 Long term average concentrations

Multiply the above calculated values by a combined occurring frequency, that is the occurrence frequency at a fixed month (season or year) for a given wind direction, wind speed and atmospheric stability, and then the product is a representation of long term average concentration. Such a result is reasonable generally for point source, because the emissions from point source is relatively uniform for one day or one season. As for the area source emissions from sources of different type in one day are less uniform, so the calculated results are multiplied by a stability-weighted factor, which is different for different type of sources. This factor is expressed as

$$CW_{i,s} = \frac{1}{N_s} \sum_{t=1}^{24} CE_{i,t} \cdot n_{s,t} \quad (9)$$

where  $i$  is the number of types of sources,  $s$  is the number of classes of the stability,  $t$  is the time in which the statistics is taking (1 to 24 hour),  $CE$  is the emission coefficient for given type of area source in a whole day (unity for average over 24 hours),  $n_{s,t}$  is the occurrence frequency for  $s$  class of the stability at time moment  $t$ , and finally,  $N_s$  is the total occurrence times for  $s$  class of the stability in one day, both  $n_{s,t}$  and  $N_s$  are statistics over one month, one season or one year.

### 2.6 Calculation of TSP

At each monitoring station, the sampling of background dust, surface dust, coal smoke dust and other industrial dust is taking simultaneously and contents of about 20 chemical elements in those samples are analyzed so that according to the relation of these contents with the spectra of the chemical composition of source particles, the ratio of the origin of environmental particles can be determined, and thus, percentage of surface dust in TSP is obtained for each monitoring station. Finally, TSP of each monitoring station is calculated by

$$\text{TSP (calculation)} = (\text{dust calculation} + \text{city background}) / (1 - \text{percentage of surface dust}) \quad (10)$$

where the city background is the average TSP for different seasons taking 50km away from city center.

## 2.7 Calculations of industrial dust from non—chemney emission.

Those dusts from steelworks, cooking plants, lime fields, cement factories are all treated as from area sources . The concentration formed by them is calculated by using vertual point source formula.

## 3. results of calculation

Fig. 2 and Fig. 3 show the calculation of  $SO_2$  and TSP in shijingshan district of Beijing for Dec. 1988 and Sept. 1988, using the models discribed in this paper. For  $SO_2$  most of the values lower than the measured are in general near the boundary of this district, this is because that source data outside the district are those before 1985, new pollution sources after 1985 are not taking into account, meanwhile, most of the values higher than the measured concentration in downwind direction of large steelworks, non—chemney emission of iron particles from those steelworks, makes  $SO_2$  convert quickly to  $SO_3$  and alkaline dusts from lime—kiln nearby neutralize part of the  $SO_2$ , this results in a lower values of measured  $SO_2$ . The error of TSP calculation comes partly due to lack of source data outside the district for 1988, partly due to some errors in estimating percentage of surface dust.

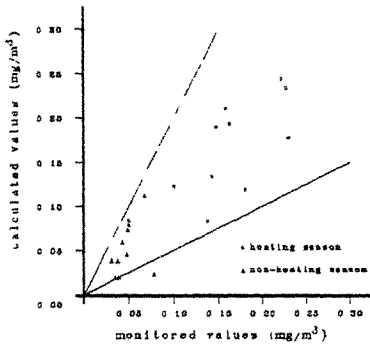


Fig 2 Comparison of the calculated  $SO_2$  values with the monitored values

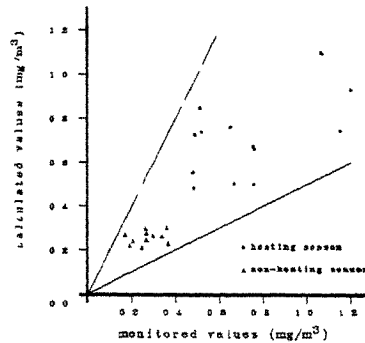


Fig 3 Comparison of the calculated TSP values with the monitored values

## 4. Application of the models

A special detailed menu in chinese characters was designed for situations in different cities, so that there is a wide selection for atmospheric environmental management or study at different cities.

Before applying these models one must use the data of pollution sources (spatial distribution and temporal variation), pollution meteorological data and monitored data of the concentration of the pollutants for a certain reference year for each city to do many pre—calculations, so that one can adjust model parameters, in order to obtain a better correlation between calculations and

monitored data.

These models can be applied to the following aspects:

(1) To calculate the daily averaged concentration of  $\text{SO}_2$  and particulates at several receptors ( $\leq 60$ ) under various meteorological condition.

(2) To predict the pollutants monthly (or seasonal) averaged concentration distributions of planning years in the future.

(3) To calculate and predict percentage contribution of concentration at several receptors for different sort of sources.

(4) To check whether the desired air quality is reached or not at several receptors.

(5) To make comparison of various pollution control schemes to choose a best one.

This set of models has been put in practical use in cities like Beijing, Mudanjiang and Shijingshan district with satisfied results and is going to apply in Shijiazhuang city.

The models require relatively simple parameters for input and take shorter time in calculation. With PC-386, it takes about two minutes for the case of points sources less than 50, as for area sources, the results will be displayed immediately. The total computing time is within one hour. It is especially suitable for middle and small cities where are lack of specialized experts.

#### References:

1. Wang Shu-fang etc. , Journal of Environmental Sciences Vol. 7 No. 2 (1987).
2. F. A. Gifford and S. R. Hanna, Power Generation: Air Pollution Monitoring and Control. (1971)71.
3. F. A. Gifford and S. R. Hanna, Atmos. Environ. 7 (1973) 131.

## Plume diffusion model of internal boundary layer

*Jie Xuan, Wenhui Ye and Tianfeng Sun\**

Environment Science Center, Peking University, Beijing 100871, China

\*Department of Mechanics, Peking University, Beijing 100871, China

**Abstract:** This paper deals with the plume diffusion model of internal boundary layer proposed by the authors. Since it concerns mainly the response of plume diffusion parameters  $\sigma_z$  and  $\sigma_y$  to an internal boundary layer (shortened as IBL) formed from the step change in surface roughness, the model is simple enough to understand and to apply. From results of the computation examples of the model, the phenomenon of the jumping of the diffusion parameters  $\sigma_z$  and  $\sigma_y$ , where the plume enters IBL, successfully reappears. The phenomenon was firstly revealed by scientists of Peking University in both field investigation and wind tunnel modeling in later seventies.

### 1. Introduction

When wind blows from sea to land, or from rural area to a city, the roughness length of the ground surface  $z_0$  changes rapidly and an IBL develops from the step change in roughness. It is well known that plume dispersion from a plant chimney is seriously affected by IBL and most of dangerous fumigation style pollution events occur in coast area in the situation (Fig.1).

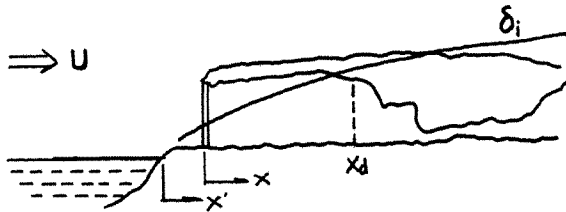


Fig.1 Plume diffusion affected by IBL

However, the wind tunnel experiments conducted by both Pendergrass and Arya [1] and present authors (unpublished) detected no fumigation

episodes in neutral IBL after the step change in surface roughness. Still, the maximum ground concentration  $c'_{gmax}$  and its distance from source  $x_{gmax}$  showed no difference in IBL case compared with uniform surface roughness case in the experiments. The meaning of the results is that the fumigation is caused mainly by vertical thermal convection of TIBL (thermal internal boundary layer). On the other hand, it is well known that the turbulence vortices which scale is similar to the width of the plume much contribute to the diffusion of the plume, but the ratio of plume width to IBL height,  $d/\delta_i$ , in the experiments was so large that the effect of IBL on plume diffusion might be minimized.

Late in seventies, scientists of Peking University did a comprehensive investigation on plume diffusion on coast of Bohai Sea. It was discovered in field investigation that a jump in plume diffusion parameters  $\sigma_x$  and  $\sigma_y$  occurs where the plume enters IBL [ 2]. Wind tunnel modeling experiment conducted later in a bigger tunnel which testing section is 1.5 m wide and 1 m heigh showed the same phenomenon (Fig.2).

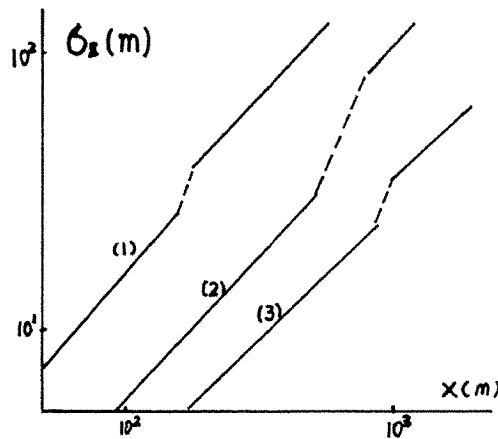


Fig.2 Tested curves of  $\sigma_x$ , smooth - rough IBL  
(1,2): field, (3): wind tunnel

It showed us a way to model plume diffusion affected by IBL with only the response of diffusion parameters  $\sigma_x$  and  $\sigma_y$ . Based on the basic research of IBL [3], present authors proposed the IBL plume diffusion model which is simple to understand and easy to apply. Computation results of the model are in good accordance with the jumping phenomenon of both the field and the wind tunnel investigations.



## 2. IBL plume diffusion model

Plume diffusion parameters  $\sigma_x$  and  $\sigma_y$  are defined as

$$\sigma_y^2 = \frac{\iint_{-\infty}^{\infty} c' y^2 dy dz}{\iint_{-\infty}^{\infty} c' dy dz} \quad (1)$$

$$\sigma_z^2 = \frac{\iint_{-\infty}^{\infty} c' z^2 dy dz}{\iint_{-\infty}^{\infty} c' dy dz} \quad (2)$$

Here  $c'$  is the pollutant concentration at the coordinate point  $(x, y, z)$  of the plume. We will discuss only  $\sigma_z$  hereafter, but it will be the same for  $\sigma_y$ .

Taylor(1921) deduced a well known equation which can be referred to square deviation of plume diffusion in steady and homogeneous turbulence[4]

$$\sigma_z^2 = 2\bar{w}'^2 \int_0^{t_1} \int_0^{t_1} R(\xi) d\xi dt_1 \quad (3)$$

Here  $\bar{w}'^2$  denotes the mean square of the vertical turbulence velocity and the  $R(\xi)$  the Eulerian auto-correlation coefficient of it.

Also, Townsend (1976) pointed out a universal relation of  $\bar{w}'^2 \propto \overline{u'w'}$   $\propto u_*^2$ , which is still true in turbulent boundary layer [5], here  $\overline{u'w'} = \tau / \rho$ ,  $\tau$  denotes the shear stress, and  $u_*$  the friction velocity. So, a simple formula is suggested

$$\sigma_z^2 = u_*^2 F(t) \quad (4)$$

Equation (4) has meaning of significance, i. e., the diffusion square deviation  $\sigma_z^2$  of the plume is not only dependent on local turbulence ( $u_*$ ) but also relative to its historical accumulation ( $F(t)$ ). The equation can also be deduced with similarity consideration as

$$\frac{\sigma_z^2}{u_*^2 F(t)} = 1 \quad (5)$$

Equation (5) suggested us that the dimension of  $F(t)$  is  $[T^2]$ .

Furthermore, we suppose that, in short distance after the plume enters IBL, the varying rate of  $\sigma_z$  with fetch  $x$  is mainly dependent on the violent changing of the local turbulence structure ( $u_*$ ) whilst the function  $F(t)$  changes little, i.e.

$$\frac{d}{dx} \sigma_z^2 \propto u_* \quad (6)$$

With combination of equations (4) and (6), we deduced following differential equation for  $\sigma_z$  (for  $\sigma_y$  the same)

$$\frac{d}{dx} \sigma_z^2 = \frac{u_*}{u_*} \Big|_{x'=0^-}^{x'=x-x_d} \left( \frac{d}{dx} \sigma_z^2 \right)_{x=x_d} \quad (7)$$

Here  $x$  denotes the downwind distance from chimney,  $x'$  the downwind distance from the step change in surface roughness (coastline) and  $x_d$  the distance at which the plume enters IBL. It is required by equation (7) to know the friction velocity  $u_*$  ( $u_* = \sqrt{\tau_w / \rho}$ , here  $\rho$  is the density of the air and  $\tau_w$  the surface friction stress) just before the step change in surface roughness and in short distance after it.

The IBL model divides the dispersive process of the plume affected by IBL into three stages:

Stage 1,  $x < x_d$  (outside IBL). According to the stability category of atmosphere, corresponding Briggs' formula of  $\sigma_z = \sigma_z(x)$  in Tab.1 is suggested to use [6].

Category	Parameter $\sigma_z$ (m)
A	$\sigma_z = 0.20x$
B	$\sigma_z = 0.12x$
C	$\sigma_z = 0.08x / \sqrt{1+0.0002x}$
D	$\sigma_z = 0.06x / \sqrt{1+0.0015x}$
E	$\sigma_z = 0.03x / (1+0.0003x)$
F	$\sigma_z = 0.016x / (1+0.0003x)$

Tab.1 Briggs' diffusion parameter  $\sigma_z$  of plume in rural area ( $10^2 < x < 10^4$  m)

Stage 2,  $x > x_d$ , in short distance. With the value of  $u_*$ , just before and after the step, equation (7) is suggested to calculate the relation of  $\sigma_z = \sigma_z(x)$ . Usually, a jump in the diffusion parameter  $\sigma_z$  appears in the stage.

Stage 3,  $x \gg x_d$ . An interpolation curve of Briggs' formulas of different stability categories, which passes the end point of the second stage, is suggested.

As to the parameter  $\sigma_y$ , procedure is just the same.

It may be helpful to notice that the value of  $u_*$ , just before and in short distance after the step, can be measurement data or calculation results of the IBL response model proposed by present authors [3].

### 3. Computation examples of the model

Few input parameters of the model are atmospheric stability category, mean distance  $x_a$  at which plume enters IBL and friction velocity  $u_*$  just before and in short distance after the step change in surface roughness.

In Stage 1, the curve of  $\sigma_z = \sigma_z(x)$  is drawn with one of the Briggs' formulas, and the value of  $(\frac{d}{dx} \sigma_z)_{x=x_a}$  can then be obtained.

In Stage 2, Simpson numerical integration is used to solve equation (7).

Value of  $\frac{d}{dx} \sigma_z$  should be calculated as well as that of  $\frac{d}{dx} \sigma_z$ . As soon as the value of  $\sigma_z$  reaches the slope of one of the interpolation curves of Briggs' formulas at the point, the Stage 2 ends. And, the interpolation curve which passes the point gives the relation of  $\sigma_z = \sigma_z(x)$  in Stage 3.

Figs 3 and 4 show the computation results of the model. Dashed lines B, C, D, E and F are Briggs' curves of different atmospheric stability categories. The value of  $u_*$  used in the computation was drawn from the classical wind tunnel experiments of Antonia and Luxton [7, 8] with supposing scale ratio of 1/20000. The plume was always supposed to enter IBL at the distance of  $x_a = 1000$  m. It can be seen by comparing the figures with Fig.2 that the jump in diffusion parameter  $\sigma_z$  reappears and its magnitude is of the same level with that from the field investigation and from the wind tunnel experiment. The good agreement of the model computation with the experiment data implies success of the model.

### 4. Analyses and conclusions

Where a plume enters IBL, its diffusion parameters  $\sigma_z$  and  $\sigma_y$  show a jump in short distance. The jump is positive and steeper for smooth-to-rough IBL, e.g., IBL from sea to land. It is negative and gentler for rough-to-smooth case.

### References:

1. W.R.Pendergrass and S.P.S.Arya, Proc. 3rd Conf.on Application of Air Pollution Meteorology, San Antonio, (1982) 248.
2. A.C.Zhang and W.H.Ye, China Environment Science, 5(1983) 54.
3. J.Xuan and T.F.Sun, Recent Advances in Wind Engineering ( edited by T.F.Sun), Pergamon press, Beijing (1989) 210.
4. D.H.Slade, Meteorology and Atomic Energy, U.S. AEC (1968).
5. A.A.Townsend, The structure of turbulent shear flow ( 2nd edition), Lodon, (1976).
6. S.R.Hanna, G.A.Briggs and R.P.Hosker Jr. , Handbook on atmospheric diffusion, U.S. Department of Energy (1982).
7. R.A.Antonia and R.E.Luxton, J.Fluid Mech., 48(1971) 721.

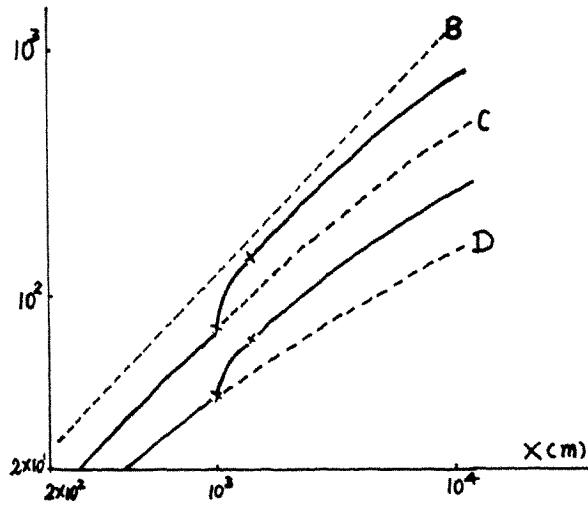


Fig.3 Computed curves of  $\sigma_z$ , smooth - rough IBL

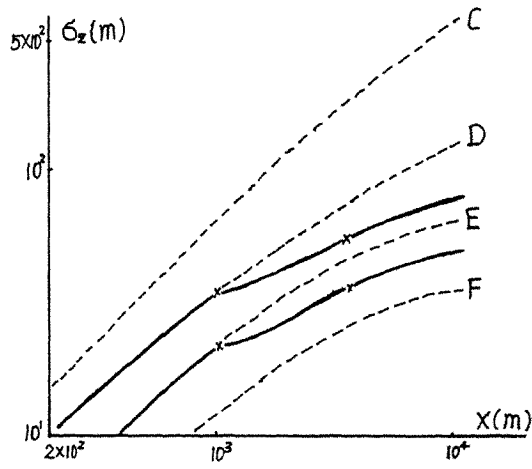


Fig.4 Computed curves of  $\sigma_z$ , rough - smooth IBL

## **A new research method of atmospheric environmental capacity**

**Liu BaoZhang**

(Centre of Environmental Sciences, Peking University, Beijing, China)

### **1. Abstract**

The atmospheric environmental capacity is an important concept. The linear planning method was used to calculate atmospheric environmental capacity. In the method, the pollutant concentration is proportioned to the amount of emitted pollutant. The effect of transport and dispersion of pollutant substance is not considered in the method.

We think that the atmospheric environmental capacity depends on meteorological conditions, emission styles of pollutants and underlying surface of local area, i.e., the atmospheric environmental capacity should include effect of pollutant transport, dispersion and underlying surface character. On this consideration, We suggest a new method to calculate atmospheric environmental capacity.

First, calculating the difference between objective value of local environmental quality and existing concentration, and then calculating permitted emission amounts by a developed Gauss dispersion model. In the method, the information of pollution source, wind direction, wind speeds and joint frequency of atmospheric stability, emission styles of pollutants is included.

### **2. Principle**

The earth atmosphere accept pollutants from nature and artificial process, on the other hand, it continuously clean and transform pollutants. When this dynamical balance was maintained, the pollutants in air will keep under some level, if the level is under the objective value of atmospheric quality, then the pollutant in air will do not harm human health and biological environment. Thus, we can say that the air has certain capacity for pollutant. For local atmospheric environment, the pollutant continuously transports and exchanges on the boundary. A part of pollutant transports to the upper air through the upper boundary layer, air is not an isolated system. Moreover, it is related to the meteorological conditions, emission styles of pollutants and underlying surface of local areas that whether the pollutant substance can reach a harm level in an area. Therefore, for an area, the atmospheric environmental capacity is an embodiment of air transport, dispersion and emission styles of pollutant.

In China, since 1980, the local atmospheric environmental capacity has been studied in Shenyang, Taiyuan, Beijing, Tianjing, etc.. In Shenyang the control-day method is adopted to confirm the environmental objective value. In Beijing a various of models were established to study the law of pollutant transport and emission. In Tianjing, from the energy planning and by the means of mathematics model, the environmental goal is confirmed to make the pollution treatment plan. All the methods above have their characteristics.

According to the concept described above, this paper adopts a new method to calculate the atmospheric environmental capacity. At first, using combination model of advection flow diffusion model and the plume trajectory model to calculate the local existing concentration. And then its difference with the objective concentration value is calculated. At last, the atmospheric environmental capacity is calculated.

The downwind concentration of pollutant emitted from elevated point source can be expressed as follow.

$$C(m,n) = \frac{\alpha Q(k,1)}{u} X^{-\gamma} \exp(-\beta_1 H^2 X^{-\beta_2}) \exp(-\beta_3 Y^2 X^{-\beta_4})$$

Where parameter  $\alpha, \beta_1, \beta_2, \beta_3, \beta_4, \gamma$  depend on air transport and diffusion capability;

$C(m,n)$  the pollutant concentration at the point  $(m,n)$ ;

$X$  the downwind distance from source point  $(k,1)$  to point  $(m,n)$ ;

$u$  the mean wind velocity;

$H$  the plume height from surface;

$Y$  the lateral horizontal distance;

$Q(k,1)$  the source emission strength at the point  $(k,1)$ .

For simplicity, this paper adopt traditional Gauss Puff Dispersion Model to calculate the mean concentration. The downwind concentration,  $C(m,n)$ , on the point  $(m,n)$  can be expressed by following formula:

$$C(m,n) = \left(\frac{2}{\pi}\right)^{1/2} \sum_{i=1}^6 \sum_{j=1}^7 \sum_{k=1}^N \frac{8f_{ij}Q_k}{\pi u_i \sigma_{z_i}} \exp\left(-\frac{H_i^2}{2\sigma_{z_i}^2}\right) \quad \text{-----(1)}$$

here

$f_{ij}$  the joint frequency of stability category  $i(i=1,2,\dots,6)$ , wind direction and wind grade  $j(j=1,2,\dots,7)$ ;

$Q_k$  the emission strength of source  $n$   $k(k=1,2,\dots,N)$ ;

$\sigma_{z_i}$  the vertical diffusion parameter of category  $i$ ;

$H_i$  the effective plume height at wind grade  $j$ .

This formula is just suited for one direction.

Equation (1) can be reversibly used to calculate the emission strength,  $Q_k$ , with the known pollutant concentration,  $C(m,n)$ . But it is very difficult.

We deduce an equation from (1), which is used to calculate the emission strength of source  $Q(L,k)$

$$Q(M,N) = \sum_{l=1}^{16} \sum_{k=1}^M \frac{F_{lk} C(m,n) X_k}{AB_1} \quad \text{-----(2)}$$

Here  $l$  denote wind direction (1,2,3,.....16);

$f_{lk}$  the factor which shows the effect of the source  $Q(l,k)$  on concentration  $C(m,n)$

$X$  the distance between the point  $(l,k)$  and point  $(m,n)$

$M$  the total step number of distance  $X$ ;

$A$  a constant, it is can writes  $A = \left(\frac{2}{\pi}\right)^{1/2} \frac{8}{\pi}$

$B_1$  a parameter depending on wind velocity, diffusion parameter and emission styles of pollutants;

$$B_1 = \frac{1}{u_1 \sigma_{z1}^2} \left( -\frac{H_1^2}{2\sigma_{z1}^2} \right)$$

$\sigma_{z1}$ ;  $H_1$  mean vertical diffusion parameter and mean effective height in the direction. Come back equation (1) from equation (2).

$$C(m, n) = A \sum_{k=1}^M \frac{Q(1, k) B_1 f_{1k}}{X_k} \quad \text{-----(3)}$$

Here  $\Sigma$  denote the effect of the emission source.  $Q(1, k)$ , at different distance on summation of the concentration  $C(m, n)$ .

$$C(m, n) = \sum_{i=1}^{16} C_i(m, n) \quad \text{-----(4)}$$

substitute equation (3) into the equation (4)

$$C(m, n) = \sum_{i=1}^{16} A \sum_{k=1}^M \frac{Q(1, k) B_1 f_{1k}}{X_k} \quad \text{-----(5)}$$

$$\sum_{i=1}^{16} \sum_{k=1}^M \frac{Q(1, k) B_1 f_{1k}}{X_k} = \frac{C(m, n)}{A} \quad \text{-----(6)}$$

Equation (6) shows pollutant concentration at fix grid from various direction and distance.

Now, we are concerned about allowance of emission amount, . In equation (6),  $Q(1, k)$  is able to be written as follow:

$$Q(1, k) = \frac{C(1, k) X_k}{A B_1 f_{1k}} \quad \text{-----(7)}$$

and

$$C(1, k) = f_{1k} C(m, n) F_{1k} \quad \text{-----(8)}$$

Then

$$Q(1, k) = \frac{F_{1k} C(m, n) X_k}{A B_1} \quad \text{-----(9)}$$

Here  $F_{1k}$  is the ratio that shows the contribution of emission source to the concentration in different distance. The function,  $F_{1k}$  is attainable beforehand. Generally the downwind distance,  $X_k$  can be taken as twenty kilometer. If the step length is one kilometer.  $M$  equals to twenty. Usually  $M$  depends on the distance and step length.

The equation (9) is a basic formula for solving the atmospheric environmental capacity. In

the form of a summation formula:

$$Q = \sum_{l=1}^{16} \sum_{k=1}^M Q(l, k) = \sum_{l=1}^{16} \sum_{k=1}^M \frac{F_{l,k} C(m, n) X_k}{AB_l} \quad \text{-----(10)}$$

The equation (10) is a complete formula for solving the atmospheric environmental capacity. All variables on the right side of the formula are knowable. With equation (10), it is easy to solve atmospheric environmental capacity.

Previously, a statistics method called linear planning was used to solve atmospheric environmental capacity, in which pollutant concentration proportions to emission strength of pollutant source. Statistical formula:

$$\left. \begin{aligned} \text{Max } F(Q) &= \sum_{t=1}^N Q_t \\ A_{st} Q_t &\leq C_s \\ Q_t &\geq 0 \end{aligned} \right\} \quad \text{-----(11)}$$

An example is shown in the Figure 1, with concentration data of 25 grid points and corresponding emission strength data of 5 sources.

5 *	10	15	20 *	25
4	9	14	19	24
3	8	13 *	18	23
2	7	12	17	* 22
1 *	6	11	16	21

Figure 1.

In equation (11), the matrix  $A_{s,t}$  is regarded as constant matrix. Practically speaking, the coefficient matrix  $A_{s,t}$  is not constant. It is a variable function of the meteorological conditions, emission style change and so on.

In our work, large amounts of statistics are avoided and at same time the process of the pollutant transport, diffusion and pollutant emission styles are included. the atmospheric environmental capacity is calculated directly from the pollutant concentration. The method bases on the physical understanding of atmospheric process, the work are much better than previous linear planning method. In practice, it gives quantitative results and needs less computation task.

### 3. Result

The author has used the new method to calculate the atmospheric environmental capacities in the environmental planning projects of Ningbo area, Zhejiang province, and Haikou area, Hainan province (both in China) with meteorological data, pollutant source data and known diffusion condition. The results are in accordance with the field practical situation and will be used to quantitative management of environment protection of the areas.

We assume three stack height: fifty meter, one hundred meter and two hundred meter. The



annual diurnal-average concentration is used as goal of environmental quality. This value subtract existing concentration is the remainder concentration.

Substitute remainder concentration into equation (10) and three stack heights are used to calculate the atmospheric environmental capacity separately. The results show the amount of emission for two hundred meter stack is larger than for one hundred meter stack, and the amount of emission for one hundred stack emission is larger than for fifty meter stack.

In a common city, when calculating atmospheric environmental capacity, we think it is reasonable to adopt fifty meter stack emission.

#### 4. Conclusion

According to the air pollutant source and the information of wind direction, wind velocity and stability joint frequency, we choose connection method of advection flow diffusion model and trajectory plume model to calculate the difference between the existing concentration and the objective value of environment quality of sulphur dioxide, which we call the allowable emitting concentration of the atmospheric environment. And upon this base, we adopt simple and easy new model to obtain average allowable emitting quantity of sulphur dioxide in per unit area. The mean allowable emission quality is called atmospheric environmental capacity of sulphur dioxide. The method is simple and instinct, the results can be quantitatively shown. The results are excellently agree with Ningbo and Haikou real condition. This new method include transport, diffusion and emission styles of pollutant.

In the future, the method is available to be used directly in the work, that is, the environmental protect quantitative management.

#### 5. References

- (1) Liu Baozhang, "Research of Atmospheric Environmental Assessment and Planning in the Ningbo Area", 1990.11.
- (2) Wang Huadong, "Environmental Planning Method and Example", Chemical Industry Press, 1989.10.
- (3) Wang Huadong, "Environmental Impact Assessment", Higher Education Press, 1989.6.



## Study on the Thermal Internal Boundary Layer and Dispersion of Air Pollutant in Coastal Area by Numerical Simulation<sup>Ⓞ</sup>

W.M. Jiang and H.B. Yu

Department of Atmospheric Sciences, Nanjing University, Nanjing, China

**Abstract:** In this paper, a scheme on the mesoscale dispersion modeling system was set up. The modeling system was used to study the turbulence structure of TIBL and dispersion features during shoreline fumigation situation. The modeling has solved successfully the problem of meteorological input of the stochastic dispersion model and exploited a new approach for comprehensive applications of this kind of the dispersion model.

### 1. Introduction

Many power plants, industrial complexes, nuclear reactors, and other potentially polluting installations are located in coastal zones. The coastal thermal internal boundary layer (TIBL) is one of the most important and interesting atmospheric processes in shoreline area, because it has some distinct turbulent features that has a major influence on dispersion of contaminants.

The dispersion model should handle the unique meteorological conditions present in the coastal environment. Most of fumigation models are Gaussian and assume smooth growth of the TIBL and the instantaneous perfect vertical mixing of an entraining plume. The validity of these assumptions has been questioned. The Lagrangian particle dispersion model avoids the above assumptions and has some advantages over the other dispersion model. Recently, it was demonstrated by some researchers that the Lagrangian particle dispersion model was suitable to the simulation of fumigation dispersion (Luhar et al., 1990; Hurley et al., 1991).

Firstly, the Lagrangian stochastic model has been set up and applied to the fumigation phenomenon over the shoreline area in this paper. The irregular shape of the TIBL profile was considered. Secondly, a mesoscale dispersion modeling system during shoreline fumigation was set up. A second-order closure model provides meteorological wind and turbulence fields, as well as the TIBL profile, for input of the Lagrangian particle dispersion model. Finally, some sensitivity tests were performed.

### 2. An application of Lagrangian stochastic modeling to dispersion during shoreline fumigation

Lagrangian stochastic modelling has become popular in recent years to simulate atmospheric diffusion particularly in complex flows where many other techniques are inappropriate or invalid. The model is simplicity in concept and application, and limited programming and computer resource requirements are required.

In the Lagrangian particle dispersion model developed and applied to dispersion during shoreline fumigation, a number of particles was released from source continuously. When a particle intersect with TIBL interface, it was entrained into TIBL and was carried to the ground via convection. Then, it was reflected between the ground surface and the TIBL

---

<sup>Ⓞ</sup>Sponsored by National Foundation of the Natural Sciences No. 491315110

interface continuously. The particle trajectory equations are as follows:

$$X_i(t + \Delta t) = X_i(t) + (v_i + v'_i) \Delta t \quad (i = 1, 2, 3) \quad (1)$$

where  $v_i$  denotes mean wind velocities;  $\Delta t$  is the time step;  $v'_i$  denotes the turbulence fluctuation velocities which may be obtained from Markov Chain simulation, i.e. :

$$v'_i(t + \Delta t) = v'_i(t) R_i + (1 - R_i^2)^{1/2} \sigma_i \gamma + (1 - R_i) T_{ii} \frac{\partial \sigma_i^2}{\partial z} \delta_{3i} \quad (i = 1, 2, 3) \quad (2)$$

where  $R_i$  ( $i = u, v, w$ ) is auto-correlation coefficient and it is taken simply as exponential form;  $\sigma_i$  is the standard deviation of the fluctuation velocities;  $\gamma$  is a Gaussian random number,  $T_{ii}$  is the Lagrangian time scale. The last term is a term of drift correction to the vertical velocity (Legg and Raupach, 1982).  $\delta_{3i}$  is Kronecker denotation.

The TIBL interface generally increases parabolically to inland from the shoreline until an equilibrium height is reached. However, it was found in the experiment that the TIBL interface presented local fluctuation. So that this feature would have important influence on dispersion. According to Deardorff and Willis (1982), the variation of  $Z_i$  (the top of the TIBL) is:

$$\Delta Z_i = \left( 0.2 + 4 \frac{W_e}{W_*} \right) Z_i \quad (3)$$

where  $W_e$  is entrainment rate and  $W_*$  is the scale of convection velocity. It was assumed that the particles intersected with variable TIBL interface in an equal probability during the modeling.

The parameterizations of  $\sigma_i$  and  $T_{ii}$  ( $i = u, v, w$ ) are one of the key problems in the random walk model. Out of the TIBL, stable stratification was assumed; within TIBL, air is in convective state. The different fitting formula (Hanna, 1982) was used in the model. The variable time step  $\Delta t = 0.1 T_{iw}$  was used and then the statistical numbers of the particles in the different grid cells were calculated to obtain the pollutant concentration. Complete reflection on ground surface and at the top of the TIBL was imposed.

Some relevant data of Nanticoke Shoreline Fumigation Project on the Northern shore of Lake Erie (1978, 6, 6, 16:00) was inputted to presented model. The distribution of ground level centerline concentration of  $SO_2$  was simulated (see Fig. 1). The figure also shows the field observations [1] and results of some fumigation dispersion model, such as the Misra model [2], the modified Misra model [3] and Deardorff and Willis model [4]. It showed that the maximum was in accordance with observation, except for the location of the maximum. The performance of the model is superior to the other fumigation dispersion models, so that the Lagrangian stochastic approach is suitable for simulation of fumigation dispersion on shoreline regions.

### 3. A mesoscale simulation system for fumigation dispersion over shoreline area

#### 3.1 Controlling experiment and its validation

In section 2, a set of fitting formula of  $\sigma_i$  ( $i = u, v, w$ ) were used as input to the Lagrangian stochastic model. However, these fitting formula were inappropriate in complex terrain. One of the most feasible approaches is to use a prognostic PBL model for simulating the flow fields and the TIBL structure under the sea-breeze condition. Meanwhile, the PBL model can offer the wind and turbulence parameters needed for a dispersion model. In the past decades, a mesoscale atmospheric dispersion modeling system has been used successfully (Segal et al., 1988a,b; Jiang et al., 1990). However, the use of a K-model to study the turbulence structure and dispersion would be inappropriate due to the complication on the turbulence features under the TIBL condition and somewhat coarse resolution.

Our modeling system is composed of two numerical codes, a second-order closure PBL model and a Lagrangian particle dispersion model. Detailed discussion of the formulation and preliminary applications of the PBL model may be found in author's paper (Jiang et al., 1992, 1993). The meteorological wind and turbulence fields are provided by the PBL model. Referencing Kao and Yamada (1988), the standard deviations of the fluctuation velocities were presented as follows:

$$\sigma_u = (\overline{u'^2})^{\frac{1}{2}} + C_H \Delta X \left| \frac{\partial u}{\partial x} \right| \quad (4a)$$

$$\sigma_v = (\overline{v'^2})^{\frac{1}{2}} \quad (4b)$$

$$\sigma_w = (\overline{w'^2})^{\frac{1}{2}} \quad (4c)$$

where  $C_H = 3$  is an experimental constant. Height of the TIBL profile was determined by calculated potential temperature field from the prognostic model.

The dispersion modeling system has been run to the estimation of pollutant concentrations from an elevated point source posited on the shoreline during fumigation situation under typical onshore flow condition.

Simulated results from the PBL model showed that there are obvious fluctuation and changing slope on the top of the TIBL (Jiang et al., 1992). It is in accordance with some observed profiles (Fritts, 1980). It is believed that the spread of the particles in the TIBL will be under the influence of this feature seriously. Fig. 2 presents the profiles of  $\overline{u'^2}$ ,  $\overline{v'^2}$ ,  $\overline{w'^2}$  at 20km inland. It was seen that  $\overline{u'^2}$  and  $\overline{v'^2}$  reached the maximum near the surface, due to stronger wind shear; however,  $\overline{w'^2}$  reached the maximum at the height of 300m or so, resulting mainly from buoyancy effect. Below 500m,  $\overline{u'^2} > \overline{v'^2} > \overline{w'^2}$  and over 500m,  $\overline{u'^2}$  and  $\overline{v'^2}$  tended to be equivalent, however  $\overline{w'^2}$  is greater than  $\overline{u'^2}$  and  $\overline{v'^2}$  obviously because it is in convective boundary layer condition (Wyngaard et al., 1974)

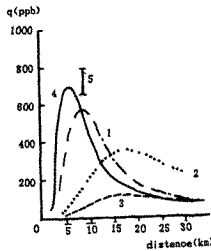


Fig.1. The distribution of surface centerline concentration (1978, 6, 6, 16:00)

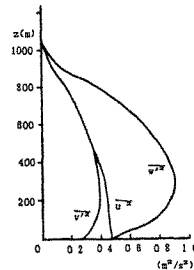


Fig.2. The distribution of  $\overline{u'^2}$ ,  $\overline{v'^2}$  and  $\overline{w'^2}$  at 20km from shoreline

Some dispersion features during developing course of the TIBL on shore was revealed by the particles distribution in X-Z plane. At the beginning, the particles traveled in stable layer and its dispersion in vertical was very weak (see Fig. 3). Late, the particle cluster was intersected by the TIBL and mixed perfectly in the TIBL. At the 5km (11:00) and 6km (14:00) from

the source, it fall on the ground surface. Generally, the distances of intersection and falling on the ground surface at 14:00 is closer to shoreline than those at 11:00. But, the calculated TIBL profile has obvious fluctuation and changing slope which result in this local singularity.

Despite the limitation in applying a Gaussian model based evaluation in this study, it is worth comparing the magnitude of the concentrations predicted using a modified Gaussian dispersion model, such as Lyons et al. (1975), with those obtained using the more refined approach developed in this paper. Fig. 4 illustrates the comparative result on the distributions of surface centerline concentration. It shows that both values of the maximum surface concentration are very closed but both locations of the maximum surface concentration are different. This is probably due to unreasonable assumptions in the Lyons model, such as instantaneous perfect mixing.

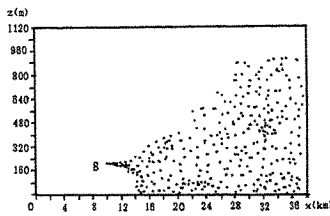


Fig.3. Calculated particle distribution projected on the X-Z plane(14:00)

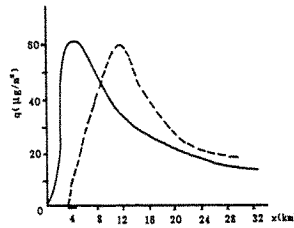


Fig.4. Distribution of surface centerline concentrations at 14:00 (solid line: Lyons model; dashed line: present model)

### 3.2 Sensitivity analysis of the modeling system

#### 3.2.1 Test 1

When the releasing height of the particle cluster was different, the position of the intersecting points between the plume and the TIBL profile may be different so that the influence on the surface concentration will be different also. Fig. 5 presents the ground-level centerline concentration for different releasing heights. It was seen that when the releasing height increased from 200m to 400m, the maximum of surface concentration was on the decrease in  $80\mu\text{g}/\text{m}^3$  to  $59\mu\text{g}/\text{m}^3$  and the distance of the maximum from the shore was farther (6.2km and 12.4km respectively). This analysis supported that the height of plume relative to TIBL is an important factor affecting the dispersion in coastal area.

#### 3.2.2 Test 2

The presence of large scale background wind is an important factor affecting sea-land breeze circulation. In this part, a synoptic scale wind along shoreline was taken. Under this condition, the front of sea-breeze extends to nearer inland, but the vertical extent is greater. The obvious recirculation was revealed. Fig. 6(a),(b) showed the distributions of particles projected on X-Y plane under different synoptic flow conditions. It is seen that, during alongshore flow situation, the horizontal spread of the particles is greater than those during onshore flow. This is due to stronger veering of wind during alongshore flow. However, the displacement that the particles travelled in stable layer is smaller. Meanwhile the position falling on ground level is nearer (see Fig. 7 and 3). So it was concluded that the pollutant would

accumulate near the shore during alongshore flow situation.

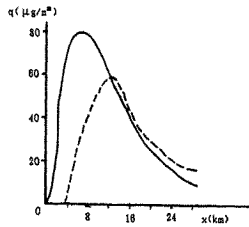


Fig.5. Distribution of surface centerline concentrations(14:00)  
(solid line:  $H_e = 200\text{m}$ ; dashed line:  $H_e = 400\text{m}$ )

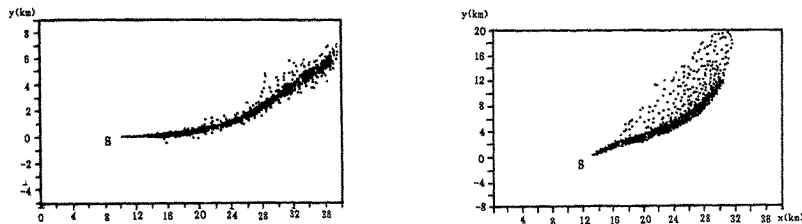


Fig. 6. The distribution of particles projected on X-Y plane  
at 14:00 (a: onshore flow; b: alongshore flow)

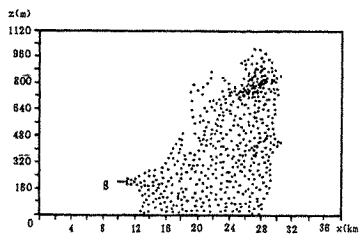


Fig. 7. The distribution of particles projected on X-Z plane  
during alongshore flow condition

#### 4. Discussion and conclusions

A scheme on the mesoscale fumigation dispersion modeling system has been designed and discussed in this paper. The system consisted of a second-order closure PBL model and a Lagrangian particle dispersion model and it has been employed to make the estimation of a realistic fumigation condition. The modeling has solved successfully the problem of meteorological input of the stochastic dispersion model and exploited a new approach for

comprehensive applications of this kind of the model.

It is clear from this work that the scientific significances of this scheme for mesoscale modeling system developed in this paper are that (1)The temporal and spatial variation of the TIBL structure and the PBL meteorological fields were simulated with the higher-order closure PBL model. (2) because of the complexity of the atmospheric dynamic, thermodynamic,PBL structure under sea- breeze and TIBL conditions, it is demonstrated that the modeling system methodology described in this paper may be a suitable approach for assessments of mesoscale dispersion; (3) the particle dispersion model is Lagrangian type and don't need more assumptions so that it is more reasonable than other models based on the Gaussian type. Preliminary results and numerical tests indicate that the performance of the modeling system was well. The field experiments over mesoscale areas are necessary to assess quantitatively its ability to predict concentration field.

#### References:

1. T.W. Fritts, Preprint, Second Conf. on Coastal Meteorology, AMS,1980,147.
2. S.R. Hanna, in Atmospheric Turbulence and Air Pollution Modeling, chapter 7, (edited by F.T.M. Nieuwstadt and H. Van dop), Reidel, Dordrecht, 1982,275.
3. P. Hurley et al., Atmos. Environ., 25a(1991),1313.
4. W.M. Jiang et al., Boundary-Layer Meteorology, 53(1990),43.
5. W.M. Jiang et al., Boundary-Layer Meteorology, 61(1992),301.
6. W.M. Jiang et al., China Environmental Sciences(in Chinese ) 13(1993), 28.
7. C-Y.J. Kao et al., Mon. Wea. Rev. 116(1988),293.
8. B.J. Legg et al., Boundary-Layer Meteorology, 24(1982).
9. A.K. Luhar et al., Atmos. Environ., 24a(1990),871.
10. W.A. Lyons et al., in Lectures on Air Pollution and Environmental Impact Analysis. Chapter 5(1975),136.
11. M. Segal et al., Atmos. Environ. 22(1988a), 1319.
12. M. Segal et al., Atmos. Environ. 22(1988b), 471.
13. M. Stunder et al., Boundary-Layer Meteorology, 34(1986),177.
14. J.C. Wyngaard et al., Adv. Geophys. 18a(1974),193.



## **A puff model under changing meteorological condition used in a real time dose assessment system for Qinshan nuclear power plant**

**Erbang Hu and Han Wang**

**China Institute for Radiation Protection, China**

**Abstract:** A puff model under changing meteorological condition is adopted in a real time dose assessment system for Qinshan nuclear power plant. In the model a correction for dry and wet deposition, physical decay and partial plume penetration of an elevated inversion and a deviation of puff centreline caused by complex terrain have been taken into account. This system is able to provide a contour of concentration within about 10 minutes after acquisition of input data.

### **1. Introduction**

At present, the accident consequence assessment of nuclear facilities includes following categories: ACA, PCA, Real-time and over-event<sup>[1]</sup>. "Real-time assessment", also known as the name of Emergency Response Assisting Systems, is mainly used for assessing consequences of a release that has actually taken place, and the assessment is more or less carried out simultaneously with the development of accident situation.

Qinshan Nuclear Power Plant (QNPP) is the first nuclear power plant which was designed and constructed by ourself in china. It was into operation in the end of 1991. It is PWR type and the total nuclear net capacity installed is 300 MW (e). It is located at the foot of Qinshan mountain, Haiyan County, Zhejiang province. The site is 87 km south-west of Shanghai and 67km north-east of Hangzhou. It is near hills and by the sea. It has a complex topography.

The real time dose assessment system (RTDAS) plays an important role in the emergency planning of accident for NPP. It must be established and into operation before getting the licence. The RTDAS-QNPP consists of the following three parts: real-time data acquisition system, system of assessment computer and code system of calculation and assessment. The atmospheric diffusion model is the one of

the most important code. Based on the recommendation of IAEA<sup>[2]</sup> and the fact that the terrain of QNPP site is neither smooth nor very complex, a puff model under changing meteorological condition is adopted.

## 2. Model And Parameters<sup>[3]</sup>

### 2. 1 Gaussian puff Model

A Gaussian puff model under changing meteorological condition is adopted to predict the concentration distribution withing 80 km from reactor.

The surface concentration at grid point (x, y, 0) for ith puff at the end of K time step can be expressed by the following formula which has taken into account the dry and wet deposition depletion, physical decay and the factor of partial plume penetration of an elevated inversion.

$$C_k^{(i)}(x, y, 0) = \frac{2Q^{(i)}F_{d,k}^{(i)}F_{w,k}^{(i)}F_{R,k}^{(i)}}{(2\pi)^{3/2}\sigma_{x,e,k}^{(i)}\sigma_{y,e,k}^{(i)}\sigma_{z,e,k}^{(i)}} \exp\left[-\frac{(x-x_{0,k}^{(i)})^2}{2\sigma_{x,e,k}^{(i)2}}\right] \exp\left[-\frac{(y-y_{0,k}^{(i)})^2}{2\sigma_{y,e,k}^{(i)2}}\right] \\ \left\{ \exp\left[-\frac{(Z_0^{(i)})^2}{2\sigma_{z,e,k}^{(i)2}}\right] + F_{P,k}^{(i)} \exp\left[-\frac{(2L-Z_0^{(i)})^2}{2\sigma_{z,e,k}^{(i)2}}\right] \right. \\ \left. + F_{P,k}^{(i)} \exp\left[-\frac{(2L+Z_0^{(i)})^2}{2\sigma_{z,e,k}^{(i)2}}\right] \right\} \quad (1)$$

where

- x, y, z is the rectilineal axes
- Q is the total amount of material in the ith puff
- $\sigma_{x,e,k}\sigma_{y,e,k}\sigma_{z,e,k}$  is the effective diffusion parameter in the x, y and z direction at kth time step
- $x_{0,k}^{(i)} y_{0,k}^{(i)} z_{0,k}^{(i)}$  is the position of ith puff center in the x, y and z direction at the end of kth time step.
- $F_{d,k}^{(i)}, F_{w,k}^{(i)}, F_{R,k}^{(i)}$  is the factor of dry deposition depletion, wet deposition depletion and radioactive decay respectively at kth time step for ith puff
- L is the height of mixing layer
- $F_{P,k}^{(i)}$  is the factor of partial plume penetration of an elevated inversion, its definition is given as follows:

$$F_{P,k}^{(i)} = \int_0^L \exp\left[-\frac{(Z-Z_0^{(i)})^2}{2\sigma_{z,e,k}^{(i)2}}\right] dz / \int_0^\infty \exp\left[-\frac{(Z-Z_0^{(i)})^2}{2\sigma_{z,e,k}^{(i)2}}\right] dz \quad (2)$$

## 2. 2 Grids

The calculation domain is divided into three square grid areas with a sideline 10 Km, 40 Km and 160 Km and a grid interval 0. 5 Km, 2. 0 Km, 8. 0 Km respectively.

## 2. 3 Wind field

An automatic meteorology station transmits meteorological data to Micro VAX II in the form of real time on line. In case of accident the meteorological data will be acquired by specific wireless telephone from 11 surface meteorological stations around QNNP. wind field are determined by a mass consistent three dimension diagnosis model.

## 2. 4 Puff release

The duration of release for PWR1—9 accident could be changed from half hour up to 10 hours. Different time intervals between successive puffs should be selected for different type of accident in order to ensure a enough number of puff released within a certain duration of release which is required for a proper accuracy. In addition, a certain amount of puffs should be released during early stage of accident (such as first 30 min) in order to obtain a fairly accuracy of predicting consequences for early stage. A set of puff release with different time interval at different stage are developed to simulate the release of various type of accident.

## 2. 5 Puff trajectory

The trajectory of puff transportation is changed with the time. Supposing the length of time step  $dt=t_k-t_{k-1}$ , the coordinate of ith puff center at end of wth time step is given by following:

$$X_{o,w}^{(i)} = \sum_{k=1}^w U_{x,k}(t_k - t_{k-1}) \quad (2)$$

$$Y_{o,w}^{(i)} = \sum_{k=1}^w U_{y,k}(t_k - t_{k-1}) \quad (3)$$

where

$$U_{x,k} = V_k \sin \alpha_k, \quad U_{y,k} = V_k \cos \alpha_k, \quad \alpha_k = 180 + D_k (\text{Degree}),$$

$D_k$ ,  $V_k$  are wind direction and wind speed of ith puff at point of  $(X_{o,k}^{(i)}, Y_{o,k}^{(i)}, Z_{o,k}^{(i)})$  in

kth time step.

## 2. 6 Deviation of puff centreline

Simulation experiment in wind tunnel demonstrates that plume axis near source point is subjected to a certain degree of deviation at 4 wind directions (SE, E, ESE, NE) of interest under the condition of neutral stability. The deviation DY (m) can be expressed as the function of downwind distance.

## 2. 7 Puff rise

Briggs formula is adopted to calculate the puff rise.

## 2. 8 Diffusion parameter

The effective diffusion parameter for ith puff at the end of wth time step under varying meteorological conditions can be expressed as follows:

$$[\sigma_{j,e,w}^{(i)}]^2 = \sum_{k=1}^w [\sigma_{j,k}^{(i)}]^2 \quad (j = x, y, z) \quad (4)$$

where

$$[\sigma_{j,k}^{(i)}]^2 = \sigma_{j,k}^{(i)2}(t_k) - \sigma_{j,k}^{(i)2}(t_{k-1}) \quad (5)$$

if using the form of power function, then

$$[\sigma_{j,k}^{(i)2}] = P_j \{ [\sum_{m=1}^k (U_m^{(i)}(t_m - t_{m-1}))^{2\alpha_j}]^{2\alpha_j} - [\sum_{m=1}^{k-1} U_m^{(i)}(t_m - t_{m-1})]^{2\alpha_j} \} \quad (6)$$

where supposing

$$\sigma_{x,k} = \sigma_{y,k} \quad (7)$$

In RTDAS—QNPP four sets of diffusion parameters are provided for choice such as observed values (default) of field tracer experiment on site of QNPP which was obtained in a set of SF<sub>6</sub> tracer field atmosphere experiment in 1984—1985 (see table 1), P—G curves, IAEA parameter, Briggs' diffusion parameter suitable for city. In addition, anisotropic diffusion parameter of wind tunnel experiment is also adopted.

Atmospheric stability	Diffusion parameter	
	$\sigma_y, m$	$\sigma_z, m$
B	$0.160x^{1.00}$	$0.139 (x-27.5)^{0.999}$
D	$0.907x^{0.73}$	$1.208 (x-77.5)^{0.556}$
E-F	$1.670x^{0.60}$	$2.157 (x-90.5)^{0.385}$

Table 1. Diffusion parameter from SF<sub>6</sub> tracer experiment in QNPP

## 2. 9 Atmosphere stability

Atmosphere stability is determined by an apparatus of stability classifications, which should be input into MV I by pressing terminal key.

## 3. Results

The system can display the contour graph of the following calculation results for any nuclide with a background of site map for three calculation areas (small, intermediate, large) within about 10 minutes after acquisition of input data: time-integrated concentrations in air, surface deposition amount, external exposure dose from passing plume, external exposure dose from surface deposition, inhalation dose, thyroid dose for iodine, effective dose. As an example, suppose the duration of an accident is 30 minutes, release amount of I-131 is 7.46E17Bq, release height is 25m, the meteorological condition during the accident is as given by table 2. Then table 3 gives the time-integrated concentration in air for I-131 at several point.

Time step	0-10min	10-20min	20-30min
Wind direction	S, 180°	SSE, 157.5°	SSW, 202.5°
Wind speed m/s	1.0	2.0	3.0
Atmospheric stability	D	D	D

Table 2. Meteorological condition during accident

Position	x, km	y, km	Time-integrated concentration, Bq · s/m <sup>3</sup>
Point 1	0. 0	0. 5	5. 74E12
Point 2	0. 0	1. 0	5. 64E11
Point 3	0. 0	1. 5	4. 14E11

Table 3. Time-integrated concentration in air for I-131

References:

1. Ulf Tveten (edited), Environmental Consequences of Release from Nuclear Accident, Norway, (1990).
2. IAEA, Techniques and Decision Making in the Assessment of Off-Site Consequences of An Accident in A Nuclear Facility, Safety Series No. 86, (1987)
3. F. Desiato, et al., Sequential Puff for Atmospheric Dispersion Evaluation, DISP/ARA/MVT, Italy, (1986).

## **Wind-tunnel Simulation on the Thermal Buoyancy Plume Rise and Dispersion from Multipipe Stack**

G.L.Xie and W.M.Jiang

Department of atmospheric sciences,  
Nanjing University, Nanjing, China

**Abstract:**The tests of the plume rise and dispersion from multi-pipe stack were performed in NJU wind tunnel at Nanjing University. A series of tests was separately conducted with just single-pipe stack and with double- and four-pipe stack. According to the similarity principle of speed ratio, i.e., exit speed over environmental wind speed and smoke buoyancy. The ethene-air mixture smoke was used and the smoke made by heating system and vacuum pump was introduced into the model stack. The main results from a series of tests are: (1) the trajectories and height of plume rise; (2) the concentration distributions in vertical and horizontal of the tracer gas. And then the environment benefit can be analysed from this information on plume rise height and ground level concentration. The synthetic results show that under the combined stack by a four-pipe there is obviously increasing effect for plume rise of the value of 18% in average.

### **1. Introduction**

There are major effects on the atmospheric environment because of the buoyant plume and air pollutants emitted from a stack at a large power station. Since the maximum ground surface concentration of pollutants emitted from a chimney is inversely proportional to the square of the effective source height, there is practical interest in the plume rise. At modern power station and at many large industrial, there is usually a stack combined by two or more separate pipes. If the plume from this kind of stack merges as it rises, it has frequently been assumed that the combined plume will have a higher rise height than the individual plume as to decreasing the maximum ground surface concentration. The problem is that of this enhance rise does occur and how much is the practical environment benefit. Now there is no enough and effective experiment basis for this. It is difficult and expensive for performing the field experiment so that it is usually to do some simulation tests in wind tunnel. In this paper some experiments were performed in wind tunnel to explore the practical significant of multi-pipe stack.

### **2. Experimental facility and procedure**

## 2.1 Meteorological wind tunnel

The experiments of this project were performed in NJU meteorological wind tunnel for atmospheric environment simulation at Nanjing University. NJU meteorological wind tunnel is a low speed open return tunnel with a bit of positive pressure and with a long and rectangular test section: 1.4 by 2.0m cross section, and a 16m long. Figure 1 show an overview of the NJU meteorological wind tunnel and provides a aerodynamic layout and showing the major dimension and labeling various sections.

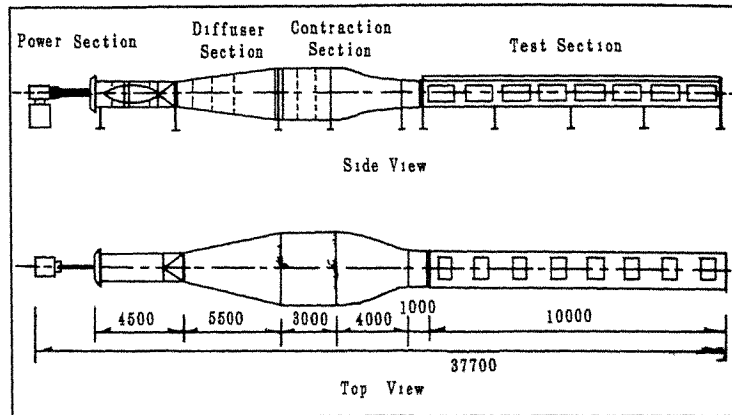


Fig.1 NJU meteorological wind tunnel

A carriage system is available which permits remote placement in three coordinate directions and it provides the capability of positing a probe of instruments and samplers for the sampling of tracer. Instrumentation associated with the facility consists of a complete system for sensing, analyzing and recording turbulence statistics and mean velocity and the positing, control and readout are effected remotely for the individual operative console.

## 2.2 Emitting and sampling system for the plume rise tests

The model stacks were 15cm tall, 0.6cm diameter copper tubes and it was heated by a heating belt. It is 150m height with a diameter 6m in full scale according to scale ratio of 1:1000. To ensure that the flow at the stack exit would be turbulent, a coiling wire in the stack below the exit. A ethene ( $C_2H_2$ )–air mixture was used to simulate the buoyant stack gases. Smoke made by heating box was added to the stack to allow the sampling



and detecting the concentrations of the tracer gas in the sampling emitted from the stack. The emitting and sampling system was showed in the Figure 2.

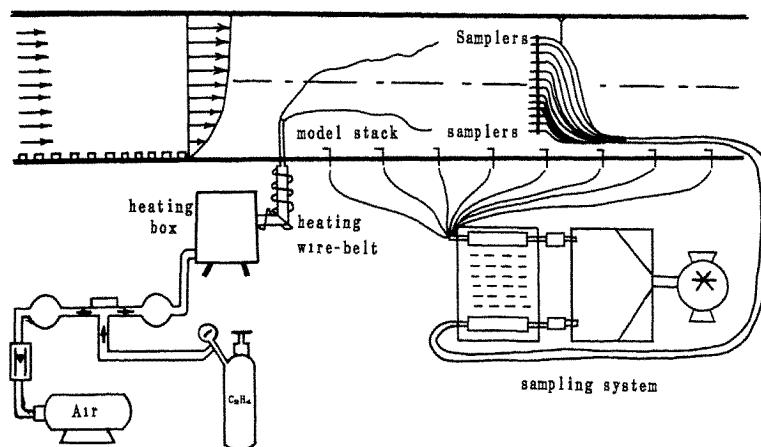


Fig.2 Emitting and Sampling System

### 2.3 Experimental procedure

A series of tests was performed with two- and four- pipe stack to determine the plume rise height. Tests were performed at following conditions. The emitting parameters from single model stack are: rate of smoke flow is 440 l/h; exit speed is 2.4m / s; smoke temperature is over than 100° C in average and the environmental temperature in average is 27° C, and a series of tests was also conducted with just one- pipe to determine the plume rise height under the same condition and to provide a reference set of data on single stack rise for comparison with the multipipe stack data.

A series of tests with a model stack separately with double- and four- pipe under various wind speed conditions was conducted. Sampling the samples of ethene-air mixture gas by the sampling system in vertical arrangement and in horizontal centreline arrangement and analyzing the concentrations of  $C_2H_4$  by gas-chromatograph method, the plume rise trajectories, rise height and the ground surface centreline concentrations of tracer gas can be determined. For each test condition 5-8 set of sampling data of the plume rise and centreline contraction were taken.

Tests were conducted at various wind speeds at the source height, i.e., various speed

ratio:  $R = 4.8, 2.4$  (exit speed over mean wind speed). Tests were performed under the upstream air flow conditions in wind tunnel of: (1) at the upstream end of test section, mean wind speed profile with index  $p = 0.14$ ; (2) the profile of turbulence intensity and the turbulence intensity of  $i_x = 0.10$  at the source height (see fig.3).

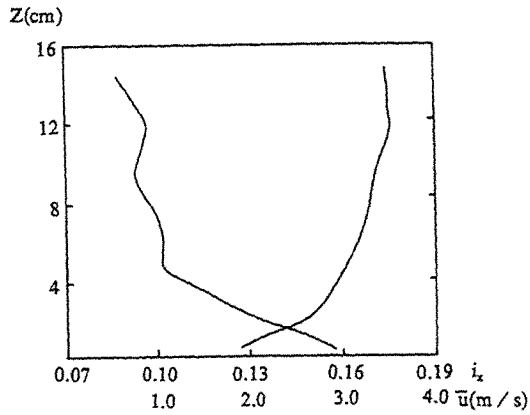


Fig.3 Profiles of the mean wind speed and turbulence intensity at the upstream end of test section.

### 3. Data analysis

#### 3.1 Comparison between a single- and four-pipe stacks

Table 1(a) and (b) list separately the data of the measuring concentrations in average under the single and four-pipe conditions in wind tunnel and Figure 4 presents the plume rise trajectories in average results.

The ratios of the plume rise heights between a single- and four-pipe stacks are: 1.05, 1.11, 1.10, 1.16 and 1.48 and the results show that under the combined stack by a four-pipe there is obviously increasing effect for the plume rise of the value of 18% in average.

#### 3.2 Vertical distribution at the centreline of the tracer concentrations

Figure 5 presents the vertical distributions at the centreline of the tracer concentrations and the plume rise in average under various speed ratios ( $R = 4.8$  and  $2.4$ ) and different pipes conditions.

So it is obviously that the plume rise height is with four-pipe than it is with two-pipe and single pipe also. And the ratios of the plume rise height are

1.45, 1.15 and 1.21, 1.08 under the different speed ratios.

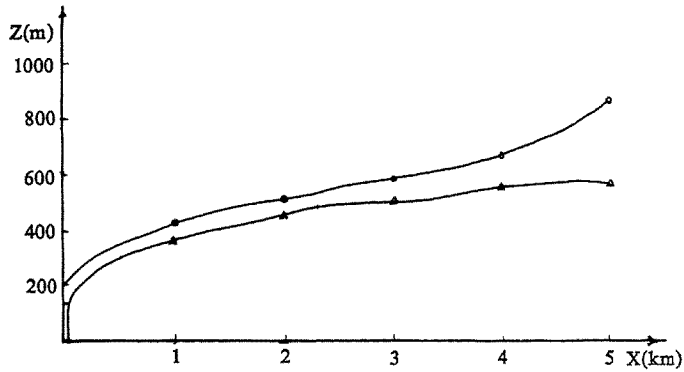


Fig.4 Simulated plume rise trajectories in average

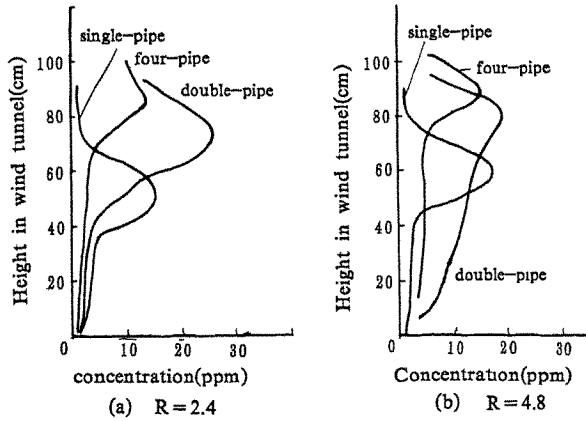


Fig.5 Vertical distributions of measuring tracer concentrations in wind tunnel (a)R = 2.4; (b)R = 4.8

#### 4. Conclusion

The test results demonstrated that the experimental method of the buoyant plume rise and dispersion is effective. And the environmental benefit can be analysed from the informations and it is about 18–22% in a synthetic results.

Table 1 Data of the measuring concentrations(ppm) in wind tunnel

(a)

Heights (cm)	Distance from the stack(m)				
	1.0	2.0	3.0	4.0	5.0
23	0.808	0.065	0.102	0.607	0.007
31	1.442	0.332	0.350	0.272	0.009
37	1.382	0.810	0.561	0.207	0.009
43	2.178	0.053	0.202	0.458	0.067
49	0.993	0.741	0.053	0.384	0.008
55	1.304	0.233	0.229	0.221	0.038
61	0.845	0.010	0.021	0.446	0.243
67	0.520	0.340	0.009	0.239	0.086
71	0.408	0.0	0.078	0.325	0.086
76	0.803	0.0	0.009	0.344	0.068
81	0.008	0.0	0.009	0.296	0.024
86	0.006	0.059	0.061	0.226	0.134
96	0.007	0.023	0.009	0.0	0.134
111	0.006	0.006	0.005	0.0	0.008

(b)

Heights (cm)	Distance from the stack(m)						
	0.5	1.0	2.0	3.0	4.0	5.0	6.0
13	0.433	0.571	0.541	0.869	0.717	0.093	0.102
21	6.491	5.199	0.941	0.829	0.641	0.431	0.350
27	26.930	8.086	1.315	1.016	0.624	0.373	0.713
33	33.017	14.339	2.006	1.499	0.834	0.646	0.829
39	25.149	6.768	2.444	1.557	0.719	0.563	0.860
45	13.727	11.631	2.985	1.543	0.941	0.820	0.920
51	3.402	10.896	3.277	1.529	0.833	0.909	0.975
57	0.313	2.218	2.867	1.695	0.993	0.893	0.872
61	0.848	2.834	2.458	0.887	0.930	0.877	0.931
66	0.088	0.685	1.597	1.372	0.879	1.071	1.060
71	0.278	0.278	0.975	1.294	0.979	1.074	1.428
76	0.009	0.009	0.847	1.084	0.950	1.337	1.728
86	0.007	0.007	0.436	0.826	0.942	1.609	1.277
101	0.008	0.007	0.035	0.446	0.873	0.993	1.777

## Wind tunnel modeling of dust emission and deposition in lower atmosphere: similarity principles

*Jie Xuan and Wenhui Ye*

Environment Science Center, Peking University, Beijing 100871, China

**Abstract:** Wind tunnel modeling is probably the most effective means of investigating dust emission and deposition in lower atmosphere. The authors proposed an extensive system of similarity principles, which was used in wind tunnel experiments studying the emission and deposition process and the shelter effect of windbreaks on dust emitting surface. Since complex terrain and turbulence in lower atmosphere were modeled, the experiments produced many new results of significance, e.g., affected by terrain and turbulence, the emission rate is higher than previous estimates and the threshold wind speed is lower than previous estimates, and the shelter effect of trees of enough thickness is better than thin screens [1,2].

### 1. Introduction

The dust pollution of the air is serious in Northern and Western China. High levels of total suspended particulates (TSP) are significantly contributed by fugitive dust from sources such as storage piles, materials transfer points, unpaved road, bare ground, and agricultural tilling, etc.. Sometimes in spring, yellow dust and minute sand coming from huge desert area of Western China fall down to the ground in the eastern regions, and even down to the East China Sea.

The emission rate of particulates from coal (sand, ash, etc.) piles into the air depends on many factors, e.g., the emitting material's texture, its bulk density, surface consolidation, moisture content and particle size distribution, storage pile geometry, and wind velocity near the pile surface, etc.. What we know about the emission process is that the mean wind velocity is the primary factor affecting particle uptake and a cubic power law exists [3]

$$Q_e \propto u^3 \quad (1)$$

Here  $Q_e$  denotes the dust emission rate ( $\text{mg}/\text{cm}^2 \cdot \text{min}$ ) and  $u$  the mean velocity ( $\text{m}/\text{s}$ ). The power exponent tested in wind tunnel ranges 2 - 6 [4]. The deviation reflects the effect of the other factors. So, it is very difficult to model the emission process exactly because the process is little understood.

The particle motion induced by wind is of three types: the largest moving particles simply tumble or roll along the surface (surface creep), much smaller ones are carried by turbulence and suspended in the air (suspension), whereas intermediate sized particles travel by injection into the air followed by subsequent fall back to the surface (saltation). Since the particle size distribution of real sources such as coal piles ranges widely, e.g.,  $10^{-4}$  -  $10^2$  cm, the particle emission is a very complex process. Finally, present authors are concerned about the motion of suspended particulates which pollute the air. So, some technical measures are needed to exclude creeping and saltating particles from dust emission rate tested.

Some previous authors simulated the emission from a flat dust surface in flow of low turbulence intensity without modeling of complex terrain and turbulence in lower atmosphere. Some others studied the effectiveness of windbreaks (screen, etc.) on reduction of dust emission from piles with the model piles made of wood or plastic block. Since no dust emission was simulated, only mean velocity or surface shear stress, near or on the pile surface, were tested to estimate the effectiveness.

In following sections, we are to discuss the importance of modeling terrain, turbulence, pile shape and screen aperture, and to introduce an extensive system of similarity principles, which was proposed by present authors and successfully used in wind tunnel modeling experiments.

## 2. Effect of terrain and turbulence

The wind forces acting on the upper part of individual solid particles in a pile are due to random turbulent fluctuations. This means that energy from the mean air flow is transported to the solid particles mainly by turbulence. As a consequence, some particles are able to overcome the surface resistance forces and enter into the air stream. Their subsequent motion also depends on the turbulence in the air flow. It seems most unlikely that similarity between model and prototype processes affecting dust emission and dust deposition from piles can be achieved without adequate modeling of the turbulence structure in the lower atmosphere.

Complex terrain, including buildings and piles, produces wake vortices which greatly enhance the energy transport from mean flows to the solid particles. Additionally, aerodynamic deformation of the mean flow, induced by complex terrain, increases the magnitude of the vertical component of the mean wind. This can play a major role in promoting the emission of particles. Finally, buildings and terrain produce unequal distributions of horizontal wind velocity, which causes spatial differences in the erosion of coal piles.

Undulations in ground topography induce changes in the effectiveness with which dust is deposited and retained at the surface. This is another route by which surface dust depositions are affected by terrain.

Most of previous authors did not model the turbulence and the terrain in experiments. However, present authors obtained the equal results with theirs when modeling dust emission process with no turbulence and no terrain modeled. Nevertheless, results of our other experiments in which we modeled turbulence and terrain were obviously different. Few examples are given as follows[1,2].

Threshold wind speed  $V_c$  at which large particles begin to creep is tested 2.6 m/s in flow of high turbulence intensity  $i = 36 \%$ , where  $i = \sqrt{u'^2 + v'^2 + w'^2}$ , whilst it is 4.3 m/s in flow of  $i = 6 \%$  with all the other conditions unchanged. Also, dust emission  $Q_e$  and deposition  $Q_d$  in the flow of strong turbulence increase by two or three times over those in the flow of weak turbulence.

When a row of model buildings of 3 cm height (corresponding to 10.5 m field height) is constructed along south wall of a coal plant, the dust emission  $Q_e$  increases by 10 % (in north wind) or 37 % (in south wind) with all the other conditions unchanged.

The decaying of dust deposition rate  $Q_d$  with fetch  $x$  along central line is often expressed as

$$Q_d \propto x^{-\alpha} \quad (1)$$

The exponent  $\alpha$  equals 0.75 in the flow of strong turbulence and 1.32 in the flow of weak turbulence. This means that, in wind tunnel flow of weak turbulence, the deposition rate decreases with fetch faster than it really does.

### 3. Porosity and aperture of windbreaks

Screens are often used to reduce the mean wind speed onto the piles so as to decrease the dust emission. Porosity  $r$ , the ratio of the area of openings to the total area of the screen, is a primary parameter. Since scale model screens are tested in wind tunnel, its mean opening aperture  $d$  should be considered as well as the porosity  $r$ . Two dimensional parameters,  $h/d$  and  $du/\nu$ , have been studied, where  $h$  denotes the height of the screen and  $\nu$  the kinematic viscosity of the air. The value of  $h/d$  for prototype screens lies in range  $10^3 - 10^5$ . There should be a critical value for the parameter, which is the least requirement in modeling experiments to ensure the similarity of the flows. The situation is similar for the aperture Reynolds number  $Rd = du/\nu$ , i.e., a critical value of  $Rd$  exists. Fig.1 shows profiles of turbulence intensity  $i$ , upwind and downwind two screens. Both screens have equal porosity of  $r = 45 \%$  and different aperture Reynolds number of  $Rd = 63$  (Fig.1 (a)) and 1450 (Fig.1 (b)), where  $u$  is taken as the velocity at the upwind location of  $x = -10 h$  and at the height corresponding that in field of 10 m. Omitting detailed discussions, we now point out that, in short distance downwind the screen, the

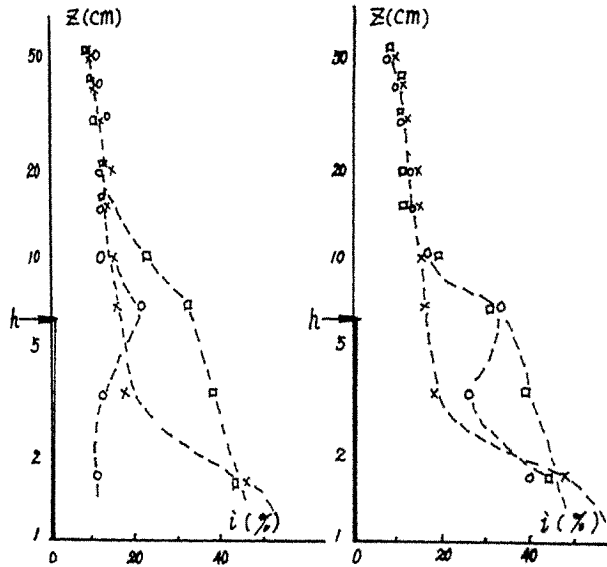


Fig.1 Profiles of turbulence intensity, upwind and downwind  
 (a):  $r = 45\%$ ,  $d = .019$  cm; (b):  $r = 45\%$ ,  $d = .44$  cm  
 $\times$ :  $x = -10$  h,  $\circ$ :  $x = 1.3$  h;  $\square$ :  $x = 8$  h

turbulence intensity  $i$  turns to be obviously weakened and restored its original strength before the distance of  $x = 9$  h. The situation of larger aperture shown in Fig.1 (b) is different, no this kind of weakening-restoring process of turbulence intensity exists. However, dust emission rate  $Q_0$  in the latter case is 50 % larger than that in the former case whilst the reductions of mean wind velocity downwind screens in the two cases are nearly the same. This means that the aperture Reynolds number of  $Rd = 63$  is below the critical value.

#### 4. Modeling criteria of creeping and saltating particles

There has been a system of similarity principles, which was successfully used in modeling of creeping and saltating particles of plane sand surface [5,6]. It includes:

- 1)  $(\gamma/\rho)_m = (\gamma/\rho)_p$  or, at least,  $(\gamma/\rho)_m > 600$ , where  $\gamma$  is the bulk density of solid particles, and  $\rho$  the density of the air, foot notes  $m$  and  $p$  denote model and prototype quantities, respectively;
- 2)  $(u_* / u_{*c})_m = (u_* / u_{*c})_p$ , where  $u_{*c}$  is the threshold friction velocity;



- 3)  $(U_f/u_w)_{\text{m}} = (U_f/u_w)_{\text{p}}$ , where  $U_f$  is the terminal velocity of particles falling in the air;
- 4)  $(u_w^3/2g\nu)_{\text{m}} = (u_w^3/2g\nu)_{\text{p}}$  or, at least,  $(u_w^3/2g\nu)_{\text{m}} > 30$ , where  $g$  is the gravitational acceleration, and  $u_w^3/2g\nu = \text{Rp}$  is the particle Reynolds number.

Four further criteria arise when it is necessary to model a block body projecting from sand surface, i.e. [7]

- 1)  $(U/u_w)_{\text{m}} = (U/u_w)_{\text{p}}$ , where reference velocity  $U$  is that at block body's height  $h'$ :  $U = u|_{z=h'}$ ;
- 2)  $(U^2/gh')_{\text{m}} = (U^2/gh')_{\text{p}}$ , where  $U^2/gh' = \text{Fr}$  is Froude number which can hardly be modeled in wind tunnel;
- 3)  $(u_w T/h')_{\text{m}} = (u_w T/h')_{\text{p}}$ , where  $T$  is the character time;
- 4)  $(h'/l')_{\text{m}} = (h'/l')_{\text{p}}$ , where  $l'$  is the width of the projecting body.

This system does not concern the modeling of turbulence in lower atmosphere, and the dust emitting surface is considered a plane. Still, the dimensional parameters are composed with friction velocity  $u_w = \sqrt{\tau_w/\rho}$ , but the surface friction stress  $\tau_w$  can hardly be measured on dust surfaces. Nevertheless, the system has laid us a base to develop our similarity system of modeling dust emission and deposition under conditions of atmospheric turbulence and complex terrain.

### 5. Modeling criteria of dust emission and deposition

In this extensive system of similarity principles, the turbulence structure and the mean wind profiles of the lower atmosphere are modeled, so the well known relationship of  $u \propto u_w$  enables us to compose the dimensional parameters with reference velocity  $U$ , instead of friction velocity  $u_w$ . Still, to model the emission of dust, we make up the model piles with real coal (sand, ash, etc.) powder and ensure the wind forces on the model surface, the normal pressure and the friction stress, equal to those of prototype. The system is composed with following items:

- 1) Geometrical similarity of complex terrain, buildings, and configuration of piles;
- 2)  $(U)_{\text{m}} = (U)_{\text{p}}$ , in this system, we take the reference velocity  $U = u_1 = u|_{z=z_1}$ , with  $z_1$  corresponds to 10 m field height;
- 3)  $(UL/\nu)_{\text{m}} > 5 \times 10^4$ , where  $UL/\nu = \text{Re}$  is the Reynolds number with  $L$  the length of piles;
- 4)  $(z_0/L)_{\text{m}} = (z_0/L)_{\text{p}}$ , where  $z_0$  is the surface roughness length;
- 5)  $(z_0 u_w/\nu)_{\text{m}} > 2.5$ , where  $z_0 u_w/\nu = \text{Rr}$  is the roughness Reynolds number;

(Items 4 and 5 can easily be satisfied if the terrain is "complex enough", and the  $u_w$  and the  $z_0$  are not needed to test.)

- 6)  $(n)_{\text{m}} = (n)_{\text{p}}$ , where  $n$  is the exponent of the wind profile power law

$$u/u_1 = (z/z_1)^n \quad (2)$$

- 7)  $(i_1)_{\text{m}} \approx (i_1)_{\text{p}}$ , where  $i_1 = i|_{z=z_1}$ ;

- 8)  $(\gamma)_m = (\gamma)_p$ , and to manufacture model piles with real dust powder (coal, ash, sand, etc.);
- 9) To stop creeping and saltating particles in 1 - 5 m downwind distance, and to collect them;

10)  $(r)_m = (r)_p$ ;

11)  $(h/d)_m > 15$ ;

12)  $(dU/v)_m > 300$ ;

(The critical values of 15 and 300 in above two items are suggestion amounts roughly estimated, further testings are needed to make them more definite.)

13)  $(UT/L)_m = (UT/L)_p$ .

### References

1. J.Xuan, W.P.An, J.F.Yin, X.Y.Wang, H.Huo and J.L.Wang, China Environment Science, 12(1992)261.
2. J.Xuan, G.M.Lin, R.T.Ding, H.Huo, Q.Gu, Y.Q.Peng and B.L.Quan, China Environment Science, 13(1993).
3. R.A.Bagnold, The physics of blown sand and desert dunes, London (1941).
4. Q.Ma, G.Quan, L.Shi, B.Wang, M.Qi and Y.Xu, J. Wuhan Institute of Water Transportation Engineering, no.1(1985)17.
5. J.D.Iversen, Cold Regions Science and Technology, 9(1984)259.
6. R.J.Kind, Cold Regions Science and Technology, 12(1986)217.
7. J.D.Iversen, W.P.Wang, K.R.Rasmussen, H.E.Mikkeisen, J.F.Hasiuk and R.N.Leach, J.Wind Engineering, 36(1990)345.

## Experimental studies of dispersion near building complex

Zhang Maoshuan, Yao Rentai  
Liu Jinfeng and Tao Shuwang

China Institute for Radiation Protection, Shanxi, China

**Abstract:** The effect of a building complex and groups of building on the mean flow and turbulence structure and plume diffusion is investigated through experiments conducted in a environmental wind tunnel. Based on the results of the experiments, an improved plume diffusion model considering the effects of buildings and emission conditions on plume dispersion is presented.

### 1. Introduction

The characteristics of pollutant transport and diffusion are evidently influenced by geometry and arrangement of buildings and release conditions. up to now, a large number of studies have been reported on flow and dispersion near a collection of buildings such as nuclear reactors (Halitsky, 1975; Hatch et al, 1977; Martin, 1965; Cagnetti, 1975; Allwine et al., 1978; Start, 1977). The Gaussian plume model and the associated diffusion parameters are often used to estimate pollutant concentrations close to building complex or groups of buildings. Cagnetti (1975) pointed out that the diffusion behavior near nuclear reactors remarkably changed with wind directions, but the models previously used assumed that modified plume heights not keep changing and the diffusion parameters unchange with emission height and wind direction.

In this paper the flow structure and diffusion behavior near building complex are studied in details. In accordance with the results obtained from the wind tunnel test and by comparison with the data gained from field experiments, an improved model suitable for plume dispersion near building complex is proposed.

### 2. Modelling theory

The purpose of wind tunnel experiments is to reproduce the flow and diffusion of atmosphere in a small scale flow field according to similarity theory. The basic requirements summarized by J. E. Cermak are to satisfy equivalences of a group of non-dimensional parameters for atmospheric and modelling flow besides similarity of geometry and boundary conditions. For simulating neutral wind, S. Nemoto proposed that equivalence of the turbulent Reynolds numbers and consistence of turbulence distributions should be ensured. Supposing that the ratio of model scale  $L_M$  to prototype  $L_P$  was proportional to the ratio of mean turbulence scales of model to prototype and that the flow structures of model and prototype was similar, the ratio of modelling velocity  $U_M$  to field velocity  $U_P$  would be expressed as follows.

$$\frac{U_M}{U_P} = \left(\frac{L_M}{L_P}\right)^{1/3}$$

### 3. Experimental facilities and procedure

The modelling experiments were carried out in the CIRP wind tunnel, which has a 1.5m wide, 1.4m high and 10m long test section with 0.2—9m/s velocity. The wind tunnel ceiling was adjusted to minimize the longitudinal pressure gradient. The velocity profile and the turbulence intensity distributions of the modelling flow can be controlled by a velocity carriage at the entrance to the test section and roughness elements on the tunnel floor. The experimental model must be strictly made with a 1 : 500 scale and has a suitable roughness on its surface.

In the experiment, four approaches, i. e., hot—wire anemometer surveying, marker observation, the ethylene trace and plume photography, were used to investigate the local wind field and pollutant concentration distribution. The flow measurements were made with a DANTEC hot—wire anemometer and 2— and 3—dimension probes, which were calibrated in the range of very low speed on an improved DANTEC 55D90 calibration equipment with a high precision pressure transducer. The pictures of flow visualization by using the smoke trace technique were also taken by the cameras. The cavity region was roughly determined by the marker, a tiny fluff, fastened on the tip of the support and indicating the flow direction. Meanwhile, the diffusion parameters of plume, ground concentrations and vertically inclining and horizontally deflecting angles of the plume axis were obtained by the ethylene trace method.

In the experiments, the observations and measurements for two kinds of reactors (see Fig. 1) were carried out by surveying typically about 1300 vertical profiles in 17 wind directions (7 for A, 10 for B), and more than 32000 data were obtained. The ethylene tracer was released from the scaled model chimney for 7 stack locations at 3—4 typical emission heights and was sampled horizontally and vertically in air and on ground downwind in 10 typical wind directions (6 for A, 4 for B), respectively.

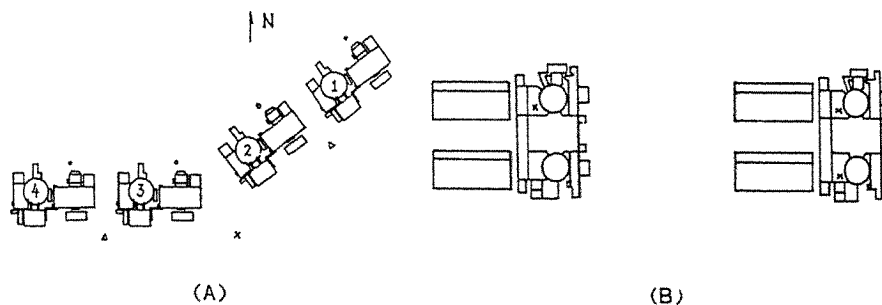


Fig. 1. The configuration and arrangement of nuclear reactor building complex

On the other hand, the hourly meteorological measurements were conducted on a 100m high tower (no building influence) from NOV. 1991 to OCT. 1992. The anemometers were installed on the tower at heights of 10m, 20m, 50m, 70m and 100m. Besides, the wind field and the turbulence observation were made with the pilot balloon and the triple—axis anemometers installed on the tower at heights of 10m and 100m in AUG. —SEP. 1992. The full—scale experiments provided much valuable information for the modelling test. Comparisons of the incoming velocity and the turbulence intensity profiles in the wind tunnel test with those of the field experiments are shown in Fig. 2.

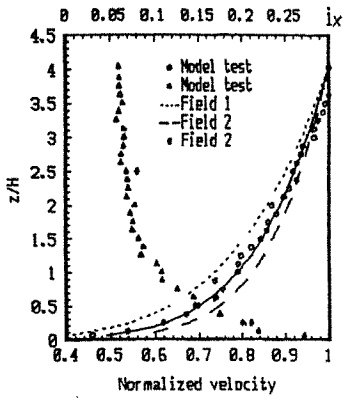


Fig. 2. Velocity and turbulence intensity profiles of incoming flow.

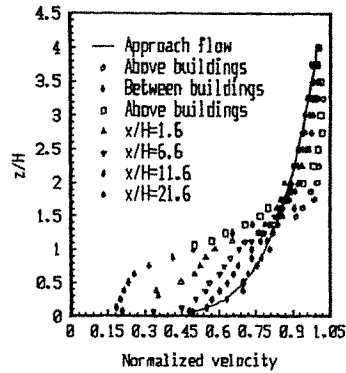


Fig. 3. Normalized longitudinal mean velocity profiles.

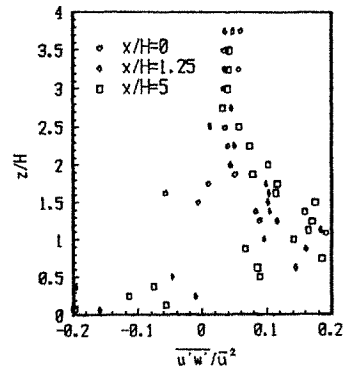
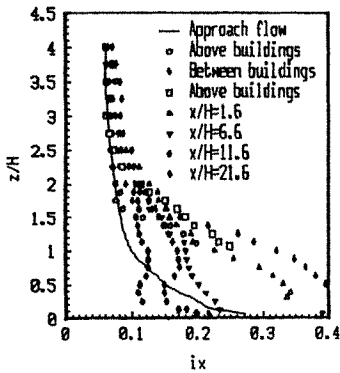


Fig. 4. Distributions of longitudinal turbulence intensity and shear stress

#### 4. Results and discussion

##### 4.1 Flow structure

In general, the aerodynamic distortion field caused by the existence of building complex is divided into displacement zone, wake and cavity according to the classical classification. M. S. Zhang et al. studied the wake structure of mountain body and its effects on the plume diffusion. The wake structure of building complex is similar to that of mountain, but it becomes more complex and is related to building geometry, building arrangement and wind directions. The vertical profiles of normalized mean velocity and longitudinal turbulence intensity at various positions above the building complex and in the wake are presented in Fig. 3 and Fig. 4. For comparison, the profile of the undisturbed flow is also included.

Flow over building complex creates a positive pressure zone on the upstream side and negative pressure zones on the roof, lee and lateral sides. The zones of pressure induce bending of mean streamline, secondary flow motions, separation and re-attachment. Apart

from a large cavity on the lee, several small return regions on the roof and lateral sides are formed. As expected, the flow speeds up over the building complex, and the velocity profiles become nearly uniform with very little vertical wind shear. The flow in the cavity region is characterized by reduced mean velocities and increased turbulence intensities. Note that the reduction in velocity is confined to about  $2H$  in vertical (where,  $H$  denotes the mean height of building complex), but extends to  $15-20H$  downwind distance, and the perturbations in the longitudinal turbulence intensity extend to  $2.5H$  in vertical and downwind distances of more than  $30H$ .

It can be found that there is a strong turbulence region behind the cavity as a continuation of the cavity. The upper boundary of the strong turbulence region is tangential to that of the cavity region and tends to incline downwards. In addition, under the action of both the "pressure zone" and the "sharp corner", a very complex vortex system is formed around building complex, especially horseshoe vortices that obviously affect pollutant transport and diffusion.

The flow characteristics mentioned above strongly affect the vertical inclinations and horizontal deflections of the plume axis, diffusion parameters and the maximum concentration on ground and its downwind distance.

#### 4.2 Diffusion Parameters

As mentioned above, because the characteristics of mean flow and turbulence of the background field change due to the presence of building complex, a series of special pollution processes occur frequently and are hardly calculated quantitatively. For this reason, some means were used in the experiments, such as arranging more measuring points, increasing the number of sampling and prolonging the sampling time.

In the near wake of buildings, the diffusion parameters were greatly enhanced, especially for lower sources, as clearly shown in Fig. 5. Thus, the effects of building complex on the diffusion parameters can be summed up to increase an initial spread in near field. It is also shown that the lateral diffusion parameters  $\sigma_y$  is strongly influenced by the release height and the vertical diffusion parameters  $\sigma_z$  weakly. The experiments also indicated that there are different diffusion parameters at the same emission height but in different wind directions

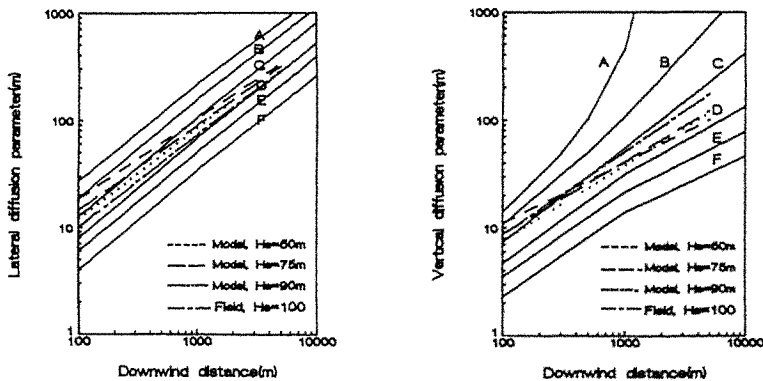


Fig. 5. Comparisons of diffusion parameters obtained from modelling test with P-G curves and field experiment results.

In order to confirm rationality of the results obtained from the wind tunnel test, we compared the diffusion parameters weighted by wind frequency with those of the field experiments. It can be seen that the diffusion parameters from the modelling test are larger than those from the field measurements in short distance because of the influence of the building complex.  $\sigma_y$  is smaller in long distance due to the restricting effects of the horseshoe vortices behind buildings. Generally speaking, the results would be reasonable.

#### 4.3 Diffusion model

Recently a great deal of field observation, numerical modelling and wind tunnel test have been carried out to develop many plume diffusion models near buildings, but no model can exactly predict the concentration distributions on ground level for various kinds of building complex. In attempting to formulate physical models of the processes relating to the dispersal of pollutants near buildings, a simple model was found to adequately account for the effects of geometry and arrangement of buildings, emission height, source location and wind direction on the diffusion parameters and the vertical inclinations and horizontal deflections of the plume centerline.

The ground concentrations near building complex can be expressed by the following equation.

$$C = \frac{Q}{\pi u \sigma_y \sigma_z} \text{EXP}\left(-\frac{y^2}{2\sigma_y^2}\right) \times \text{EXP}\left[-\frac{(B \times H_e)^2}{2\sigma_z^2}\right]$$

Where  $B$ , a modified building factor, depends on geometry and arrangement of buildings, emission height, source location and wind direction, and is given by the experiments (see Table 1). We also took the horizontal deflections of the plume axis into account by using this model. The results predicted by the model are very consistent with those of ground sampling (Fig. 6). The entrainment of the plume into the wake of buildings can result in maximum ground level concentrations that are significantly greater than those found for similar sources in the absence of buildings. The general effects of the building complex on ground level concentrations are clearly shown in Fig. 7.

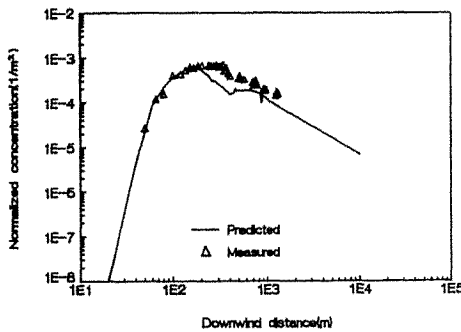


Fig. 6. Comparisons of longitudinal ground level concentration profile from model with that from test

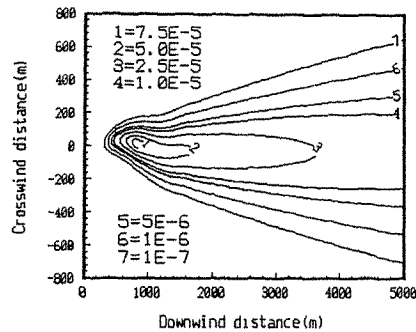


Fig. 7. The ground concentration contours

#### 5. Conclusions

1. An improved Gaussian plume model was developed on the basis of the wind tunnel

test. In this model, the enhanced diffusion in the wake of building complex, the building geometry and arrangement, source location and emission height are taken into account. The forecasted results from the model are consistent with those from ground sampling. The method proposed in this paper can be applied to various kinds of building complex through experiments.

2. The diffusion parameters are influenced by geometry of buildings, source location, emission height and wind direction, especially for lower sources.  $\sigma_y$  increases with decreasing the release height remarkably, but  $\sigma_z$  changes weakly. The diffusion parameters from the wind tunnel and field experiments are essentially in agreement.

3. The horizontal deflections of the plume centerline should be taken into account if the ground concentrations of contaminants emitted near or on building complex were computed, otherwise, there would be greater deviations of the concentration in the near field.

4. In the scope discussed in this paper, the source location upwind of building complex may be of advantage for preventing short-lived periods of high ground level concentration.

#### References:

1. J. E. Cermak, AIAA, 9 (1971), 9, 1746-1754.
2. S. Nemoto, Met. Geophys., 12 (1961), 30-52.
3. M. S. Zhang et al., J. Environ. Sci., 12 (1991), 1, 12-18. (in Chinese)
4. M. S. Zhang et al., Proceedings of the 1st International Conference on Experimental Fluid Mechanics, 1991, 327-332.

Table 1 Calculation of the modified B, considering the effect of buildings on the plume axis.

Source location	Effective emission height	Formula	Angle between building face & wind direction	$K_T = H_T/H_a$	$K_M = H_M/H_a$	$X_M$ (m)
Source located upwind of buildings	$h_a > H_b + 1.5l_b$	$B=1$				
	$h_a \leq H_b + 1.5l_b$	$B = \frac{1 + (K_T - 1)X}{X_T} \quad (X \leq X_T)$	90°	1.146-1.583	1-1.3	490 ( $H_a = 60m$ ) 760 ( $H_a = 80m$ ) 980 ( $H_a = 100m$ )
		$B = \frac{K_T - (K_T - K_M)(X - X_T)}{(X_M - X_T)} \quad (X_T < X < X_M)$				
		$B = K_M \quad (X > X_M)$	45°	1.145-1.5	0.5-0.8	
Source located downwind of buildings	$h_a > H_b + 1.5l_b$	$B=1$				
	$h_a \leq H_b + 1.5l_b$	$B = \frac{1 - (1 - K_M)X}{X_M} \quad (X \leq X_M)$	90°	1	0.667-0.75	380-460 ( $H_a = 100m$ ) 1005-1050 ( $H_a = 120m$ )
		$B = K_M \quad (X > X_M)$				
			45°	1	0.438-0.8	

where  $X_T$  and  $H_T$  is downwind distance and height at the maximum height of the plume axis;  $X_M$  downwind distance at the maximum ground concentration;  $H_M$  height of the plume axis when  $X \geq X_M$ , the length  $l_b$  is assumed to be the smaller of building height  $H_b$  and with  $W_b$



## **Low-altitude wind structure and atmospheric pollutant diffusion**

**Zheng Xiong**

Liuzhou Environment Protection Research Institute  
Guangxi, China

**Abstract:** Based on the synchronous monitoring result on low-altitude wind field and terrestrial concentration field of atmospheric pollutants, which was taken three winters continuously, the paper studies the interrelation between low-altitude structural change and atmospheric pollutant diffusion in Liuzhou city.

### **1. Introduction**

As the motive power of the transportation and diffusion of atmospheric pollutant, the wind has pollutants gained a pulse speed from multi-dimensional spaces to move and possessed a mobility, overlap and directionality. The pollution of atmospheric effluent resources to a city concerns people seriously. On the basis of the cooperative research with the China Institute for Environmental Science, the paper analyzes the materials of pollutional meteorological observation and atmospheric pollutants monitoring in three winters continuously, studies the low-altitude wind structure and pollutant diffusion in many ways, thus the interrelation between local low-altitude wind field and the transportation of atmospheric pollutants is elementally made clear.

### **2. The Wind Field Structure of Atmospheric Boundary Layer**

#### **2.1 The Turbulence Feature of Atmospheric Boundary Layer**

The research monitored the feature of atmospheric turbulence structure by means of M-2000 Doppler Sonic Radar and Three-Component Turbulence Detector, and determined atmospheric diffusion parameters by measuring turbulence characteristic quantity.

Experiment indicated that the turbulence intensity increases with increasing instability in Liuzhou district, while longitudinal turbulence intensity is much higher than transverse and plumb ones. However, the average lifetime of low-altitude turbulence eddies is very short, normally it disappears 1 or 2 minutes after a new one generates. The average spacious dimension of a turbulence eddy is about 400 m. The lower limit of time of the Gauss diffusion mode applied in Liuzhou is around 2 minutes. Analysis of turbulent spectral characteristics shows that along with the

increase of atmospheric stability , peak of spectrum shifts to low frequency, while that of high frequency has no much relationship with the stability. In rough-grounded area, moreover, mechanical turbulence develops rapidly with increasing wind speed and makes peak of turbulence spectrum shifted to high-frequency . So the change of wind speed is the main factor causing a amplitude change of high frequency spectrum.

## 2.2 The Characteristics of Wind Field Structure

Based on a continuative synchronous observation ,the ground current field is studied in an area of 82.5 km<sup>2</sup> scattered with 10 EL electrical automatic recorders of wind direction and speed. According to the analysis of ground current diagram (Fig.1), the horizontal wind structure apparently featured south-north convergence current field with its central as the convergence area and south-north direction as the divergence one.

Wind direction is one of the important parameters to study atmospheric diffusion. Fig.2 is a stereo rose diagram which represents the wind direction frequency in various altitudes within 1000m. It shows that wind rotates clockwise along with increasing altitude (from lower to upper) within 100 to 400 m , i.e., the principal wind moves in a direction of NNW→N→NNE , a confrontation between the south wind group and the north one occurs within 500 to 800 m ; in the altitude of 900 m there mainly exists NE wind; while in 1000 m, the principal wind rotates anticlockwise with SSW as priority .

## 2.3 Determination of Atmosphere Diffusion Parameter

This research obtains ground diffusion parameters by three-components turbulence measurer , gets diffusion parameters in various altitudes by M-2000 Sonic Radar . So a series of complete atmospheric parameters are gained. The results are as follows:

1) On conditions of the same altitude and stability, the wind diffusion parameter  $\delta_y$  in transverse direction is larger than that of  $\delta_x$  in vertical direction , which suggests that local diffusion ability in horizontal direction is stronger than that in vertical direction.

2) Upon the condition of a same stability , horizontal diffusion parameters  $\delta_y$  in various altitude layers are different in a sequence of 210 m > 60 m > 90 m , But  $\delta_x$  in altitude of 210 m increases on the contrary , the main reason is that  $\delta_y$  is not only a function of strength of turbulent current but also that of wind speed  $u$ .

3) On unstable and neutral stability conditions , vertical diffusion parameters in lower layer is not much different from those in higher layer, only that in 210 m is a bit larger. Upon stable condition, however, there are no much differences between those in altitude of 90 M and 210 M , while it is a bit smaller in 60 m.

### 3. Pollution Sources and Pollutant Characteristics

#### 3.1 Distribution Feature of Pollution Resources

The research area is divided into 598 meshed investigation units with the same square of 1×1 km, among which 456 units are point resources and 142 ones are surface resources. So as to the distribution of pollution resources, there are 128 point resources scattered in upwind side of the city. Annual effluent amount of SO<sub>2</sub> and dust occupies 28.1% of total amount of investigated point resources, and effluent amount of SO<sub>2</sub> and dust is 50.8% and 63.9% separately. According to a statistics of effluent altitude of pollution resources, there are only 2 chimneys in a height over 100 m; 20 between 45 to 100 m; 102 between 25 to 45 m. Among which, effluent amount of chimneys lower than 25 m occupy 68% of all point pollution resources. The direct-view stereo Fig.3 and 4 show the annual effluent amount of SO<sub>2</sub> and dust, with most as effluent units. The two figures indicate that pollution resources have a feature of colonization distribution and low effluent altitude.

#### 3.2 Pollution Effluent Characteristics

Coal is the main local fuel, the amount of waste gas, SO<sub>2</sub> and dust producing from coal's burning occupy 84%, 94% and 78% (does not include drifting dust) of total related pollutant effluent amount. In this district, it is obvious a coal smoke pollution. SO<sub>2</sub> and dust are two main atmospheric pollutants in investigated area. According to a sequence of the strength of pollution resources, the effluent amount SO<sub>2</sub> and dust of the first 50 places strong resources occupy 72.6% and 83.6% of total effluent amount separately.

#### 3.3 Characteristics of Atmospheric Pollutant

A ripe calculating mode of the diffusion and transport of the gas pollutant SO<sub>2</sub> has been formed. It will not go into details here. The research mainly goes into a deep study on aerosol.

We take aerosol sample by an American Doul-Channel Sampler and classify suspending granules into 3 grades according to their sizes, i.e., those smaller than 2.5 μ, between 2.5 to 15 μ and those between 15 to 200 μ. An analysis on results from various observation spots in winter and autumn suggests that mass density of drifting dust in investigated area occupies 52 to 57% of the TSP mass density. The proportion of shifting dust is high, this is an important characteristics of local aerosol pollutant.

The number, surface and volume densities are three basic physical magnitudes characterizing aerosol. According to many important studies in China and other countries, the granule of atmospheric aerosol can be classified into three kinds of mode according to their sizes, that is, the Aiken Nucleus mode (<0.1 μ), accumulative mode (0.1 to 2.0 μ) and coarse mode (>2.0 μ). Table 1 is physical magnitude densities in three natural modes based on a statistics of observation result.

**Table 1 A Statistics Table of Physical Magnitude Densities of Aerosol Granules**

Physical Magnitude Mode	Number Density		Surface Density		Volume Density	
	Density (article/cm <sup>3</sup> )	Content (%)	Density (μm <sup>3</sup> /cm <sup>3</sup> )	Content (%)	Density (μm <sup>3</sup> /cm <sup>3</sup> )	Content (%)
Aiken Nuclear	49183.03	68.82	236.25	26.09	2.25	4.47
Accumulative	7464.09	13.18	637.83	70.74	23.76	47.16
Coarse Granule	0.419	0.000007	28.53	3.17	24.36	48.37
Totally	56647.54	100	901.61	100	50.36	100

A density analysis over 21 elements, 6 cations and 4 anions for 31 items totally on samples was made. Then the principal factor PFA and the target transfer factor TTFA were analysed to decide the main resource of aerosol.

#### 4. Low-altitude Structure and Atmospheric Pollutant Diffusion

##### 4.1 Horizontal Wind Field and the Distribution Law of Ground Density of Atmospheric Pollutants

According to atmospheric pollution feature of coal smoke, we did a monitoring over ground density of atmospheric pollutants in three winters (1988, 1989 and 1990) continuously in investigated area. Fig.5 and Fig.6 are ground density distribution charts, which suggested conclusions as follows:

1) In the winter of investigated area, distribution laws of surface density of SO<sub>2</sub> and TSP were obvious. During the observation, three high density peak areas of these two pollutants were observed almost every day, their covering areas changed only with meteorological condition while their position oscillated in south-north direction along with principal wind axis but had no much oscillation in east-west direction.

2) Meteorological condition determined azimuth and distance of high density area appearing in colonization pollution resources. In investigated area, yearly still wind frequency was 39% and wind direction frequency of the south-north group is 36%; north wind, the principal wind, appeared at a frequency of 12% while east-west wind appeared at a very low frequency. Therefore, high density areas all appeared in a certain distance away from downwind direction of colonization pollution resources and two sides of east and west were relative stable low density area of atmospheric pollutants.

3) Under the influence of the geographical condition, channel effect of the

river and flap of Karst peak forests, wind direction of surface wind field had an obvious convergence effect. Surface density field of atmospheric pollutants corresponded with surface wind field, pollutants were transported to the lowest, relieved south central area and accumulated to form a high density area.

#### 4.2 Low-altitude Wind Structure and Pollutant Diffusion

We divide actually monitored average wind speeds in every altitude into 10 classes and 3 stabilities of unstable, neutral and stable ones. A law brought from statistics indicates that strong wind frequency increases with increasing altitude and weak wind frequency decreases with increasing altitude. So point resource effluence in high altitude is in favour of long-distance transport of atmospheric pollutants.

An analysis on typical wind contour under different stability in atmospheric boundary layer in winter is made, which suggests that under stability conditions B and C, exchange ability of upper and lower turbulences is strong, no much change of wind speed occurs when altitude changes. Vertical shear of wind speed is small, this is beneficial to the diffusion of pollutant. Under condition D, vertical gradient of wind speed obviously becomes higher. The average wind speed in low-altitude, however, is by far smaller than that in common plain area; i.e., wind speed in altitude of 100 m is 3.6 m/s, it is up to 5.8 m/s in 300 m and 7.4 m/s in 900 m. In condition E and F the exchange of atmospheric turbulent currents is weaker, and the change of wind speed along with altitude is also greater than that in B and C.

### 5. Conclusion

5.1 Low-altitude wind structure in investigated area is affected by complex geographic features considerably. Horizontal wind field forms obviously a convergence wind field in a direction of south-north along the axis of the city. While vertical wind field changes with altitude, and its wind direction has somewhat distortion and shear.

5.2 The low-altitude diffusion transfer of atmospheric pollutants of coal smoke atmospheric corresponds with current direction of horizontal wind field. Because the action of horizontal wind field, atmospheric pollutants in an angle of  $180^\circ$  of upwind side in the city are collected to convergence area, and a stationary density peak value area is formed under the influence of mixed current from other places.

5.3 Result of the study shows that research on irrationality of local industrial distribution can provide scientific basis for city programme and the development of city ecology and local industry.

References: (omitted)

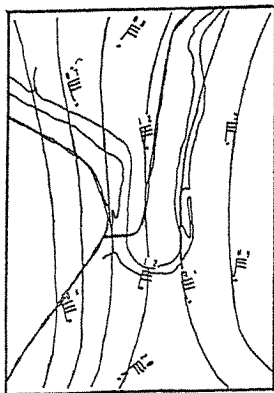


Fig. 1. Current direction of ground wind field

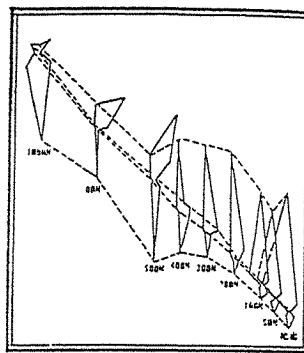


Fig. 2. Stereo rose diagram of wind direction frequency in various altitudes

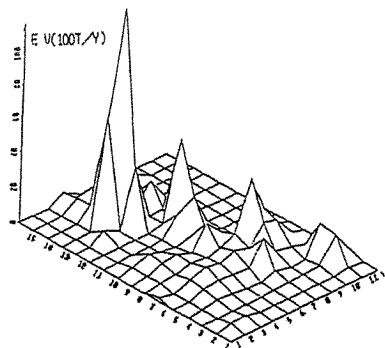


Fig. 3. Annual effluence amount of  $SO_2$  in 1990

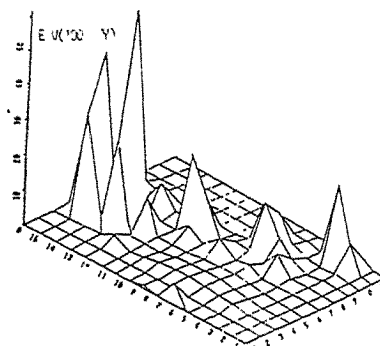


Fig. 4. Annual effluence amount of TSP in 1990

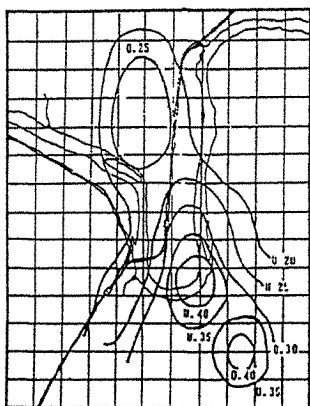


Fig. 5. Ground density field of  $SO_2$

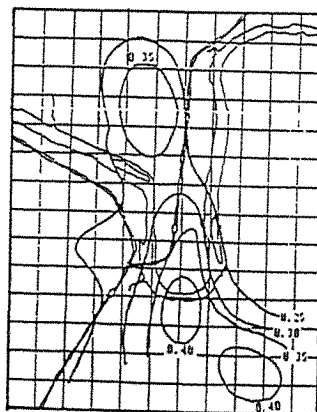


Fig. 6. Ground density field of TSP

## **Transportation**





## Drag reduction of trucks through boundary-layer control

V.J. Modi, S. St. Hill and T. Yokomizo<sup>†</sup>

Department of Mechanical Engineering  
The University of British Columbia  
Vancouver, B.C., Canada V6T 1Z4

<sup>†</sup>Department of Mechanical Engineering  
Kanto Gakuin University  
Mutsuura, Kanazawa, Yokohama, Japan 236

**Abstract:** The paper presents results of an organized and extensive wind tunnel test-program, complemented by flow visualization and full-scale road tests, aimed at assessing the effectiveness of a boundary-layer control procedure for the drag reduction of a cube-van. Wind tunnel results, obtained using 1/6 scale model, at a subcritical Reynolds number of  $10^5$ , suggest that tripping of the boundary-layer using fences reduce the pressure drag coefficient. The entirely passive character of the procedure is quite attractive from the economic consideration as well as the ease of implementation. The road tests with a full-size cube-van substantiated the trends indicated by the fence data.

### 1. Introduction

The present investigation is directed at energy conservation through an effective reduction in aerodynamic resistance of a typical truck configuration. Recognizing that: (a) two-thirds of all the goods in North America are transported by trucks; (b) on an average a truck covers around 130,000-150,000 km/year; (c) 50-70% of the truck's power (at 70-100 km/h speed) is consumed in overcoming aerodynamic resistance, compared to around 20-30% for rolling friction and 10-15% lost in the transmission system; a simple analysis of this set of data suggests that even 1% reduction in the aerodynamic drag can amount to a significant saving in the fuel cost [1-5]. With this as background, the paper studies, through an extensive set of: (a) wind tunnel experiments with 1/6 scale models of a cube truck configuration; (b) flow visualization studies in a water channel; (c) full-scale prototype road tests; effectiveness of the fence-type boundary-layer tripping device in reducing the drag. The variables of interest are the fence width and height ( $b_f$ ,  $h_f$ , respectively), and their geometric locations. These parameters were systematically varied during the test-program conducted in the smooth flow condition.

### 2. Wind Tunnel Experiments and Results

A 1/6 scale cube truck model was constructed using Plexiglas. The model is based on a mid 1980's GMC truck, with the van-body mounted on it. It has a hydraulic diameter of 469.2 mm. Figure 1 schematically shows the two configurations studied and details of the fences. The models were tested in the boundary-layer wind tunnel at the University of British Columbia. The models were suspended from the ceiling by four wires to minimize the effect of friction. The aerodynamic resistance was monitored using a strain gage transducer with a sensitivity of 4N/V.

The amount of information obtained is somewhat extensive however, to facilitate understanding, only more important results useful in establishing trends are recorded here [5]. To get some preliminary information about the optimum dimensions of the fences and their locations, it was decided to conduct tests with a three-dimensional rectangular prism first ( $H = 22.8\text{cm}$ ,  $B = 21.5\text{cm}$ ,  $L = 101.5\text{cm}$ ,  $d = 25.4\text{cm}$ ). Four fences were mounted on the front face of the prism to form a square about its geometric center. The results suggested an optimum height as well as width of the fences. The maximum reduction in  $C_D$  obtained was from 1.24 to 0.85 ( $\approx 31\%$ ) for  $h_f/d = 0.13$  and  $b_f/d = 0.5$ .

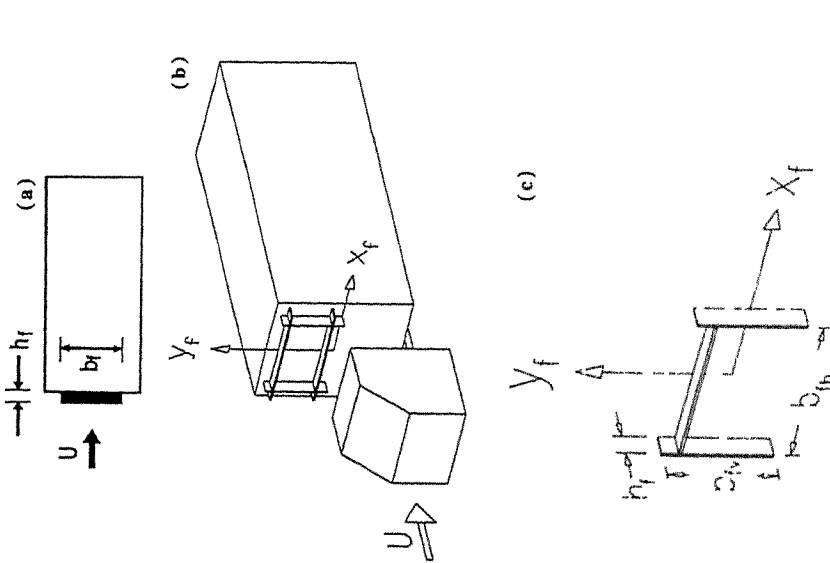


Fig. 1 Configurations used during the fence based boundary-layer control study in a wind tunnel: (a) three dimensional rectangular prism; (b) 1/6 scale model of a cube-truck; (c) geometry of fences.

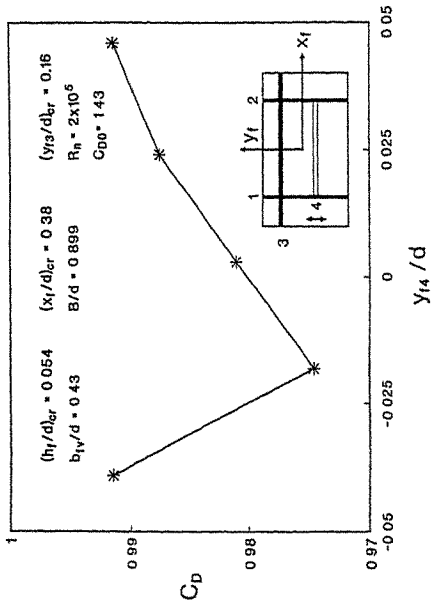


Fig. 2 Wind tunnel test results for the cube-van model with two horizontal and two vertical fences.

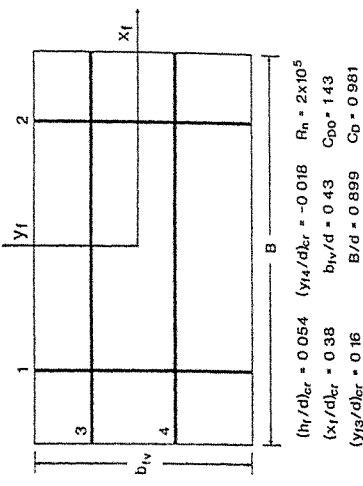


Fig. 3 Wind tunnel test results for the cube-van model showing optimum four fence configuration

The truck model was now tested with various arrays of fences. The model had a baseline drag coefficient  $C_{D0} = 1.43$ . Initially only vertical fences were installed on the model, which gave a drag reduction of 12.5% for an optimal height ( $h_f/d$ ) of 0.054. When a horizontal fence is added to the two vertical fence configuration the drag coefficient decreased to 1.03, a 28.0% reduction based on the reference case. Extensions were then added to the horizontal fence, so that it reached the full truck width, and again there was an improvement in the performance ( $C_D$  of 0.999, a total reduction from the baseline of 30.1%). A second horizontal fence continued the trend and further reduced the drag slightly, to 0.981, i.e. a decrease of 31.4% (Figures 2, 3)!

### 3. Flow Visualization Study

A flow visualization program was undertaken concurrently with the wind tunnel tests to obtain better physical understanding of the complex flow. The study proved to be invaluable in planning the wind tunnel tests judiciously to arrive at configurations likely to be most successful in reducing the drag. It provided fundamental information concerning stagnation, separation, reattachment and wake conditions associated with the boundary-layer.

The tests were carried out in a water channel using slit lighting with polyvinyl chloride particles serving as tracers. The pictures were taken over a range of model and fence geometries as well as orientations. The test Reynolds number, based on the free-stream speed and bluff body width ( $H$ ) was around  $4 \times 10^4$  which is quite different from the prototype situation. Hence the results should be considered only qualitative in character, however, they do show effectiveness of the boundary-layer control procedure (Figure 4).

### 4. Full-Scale Road Tests

The truck tested was a 1991 Chevy, one tonne Cube-Van. This type of vehicle is generally used for small deliveries, and transport around town. It was selected for its bluff character, ease of operation and economy. The test were conducted over a wide range of speeds.

Four different configurations of the truck were used during the road tests : the plain cube-van as purchased ; the one with the extended roof ; the extended roof truck with a horizontal fence, and the fourth set of tests with one horizontal and two vertical fences installed. The extended roof configuration served as the baseline reference. Each of the configurations was subjected to extensive road tests to ensure repeatability and accuracy of data. Figure 5 shows the extended box configuration with a horizontal - vertical fence combination.

The data monitoring instrumentation consisted of two transducers : a torquemeter and a fuel meter. They were connected to a Dycor DA/M100 analog to digital converter, which in turn was interfaced with a 386 SX lap top computer. The computer logged data from each transducer, sampled at a rate of 1 Hz, and displayed it in real-time. The on-screen output was designed to indicate the drive train force versus vehicle speed. The steady state torque method permits an accurate determination of the drag coefficient and its variation as a function of speed. This resulted in the precise estimate of drag reduction, effectively incorporating the yaw angle sensitivity and the Reynolds number variations in a polynomial representation of the force as a function of speed.

A procedure was developed to ensure that the results obtained during the road-tests were accurate and repeatable. Several computer codes were developed for efficient acquisition and processing of the data [5]. The tests were carried out on highway 99 between Vancouver and the U.S. border. It was found that the repeatability and accuracy were far improved when the tests were performed at night. It gave the advantage of both lower wind levels and reduced road vehicle interference.

### 5. Results and Discussion

The truck without its extended roof had a  $C_D$  of 0.40. However, once the extension was placed on the vehicle, the  $C_D$  increased to 0.62. This represented 75.25% of the total force exerted by the engine to propel the truck at 100 kph. With a horizontal fence installed there was only a small

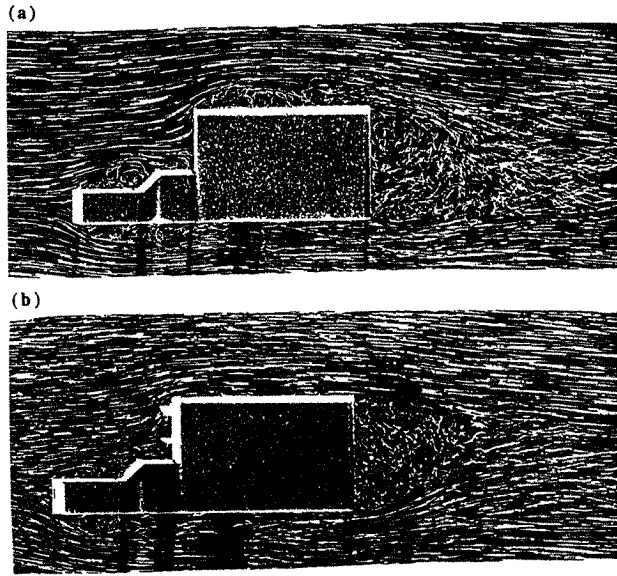


Fig. 4 Typical flow visualization photographs showing effectiveness of the fence based tripping of the boundary-layer: (a) model of the cube-truck without fences; (b) the model with two horizontal fences.

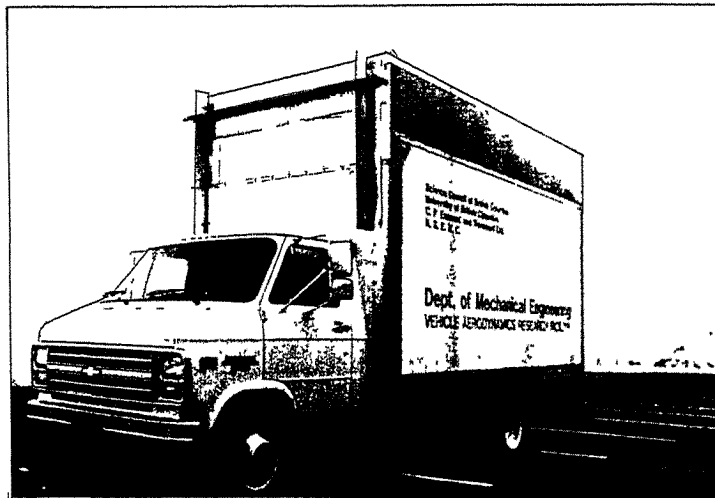


Fig. 5 The prototype extended roof truck with a horizontal and two vertical fences.

change in the drag coefficient ( $C_D = 0.616$ ). Note, this represents a decrease of drag by only 0.65%. However, the situation changed dramatically with the addition of two vertical fences (Figure 6). Now the  $C_D$  reduced to 0.517, a decrease of aerodynamic resistance by 16.6%.

It is of interest to recognize that the benefit resulting from the application of the fences diminishes at lower speeds (<30kph, Figure 7). This would suggest that, at a lower speed, the fluid is unable to clear the fences, i.e. the stagnation condition is created resulting in an increase in pressure and a corresponding increase in drag. Fortunately, the increase in fuel consumption is rather small as the nominal demand itself is low at lower speeds.

## 6. Concluding Remarks

Based on a rather fundamental study with a cube-van model, aimed at the boundary-layer control through application of trip-fences, the following general conclusions can be made:

### Wind Tunnel Model Tests

- (i) Trip fences are successful at reducing the pressure drag when applied to a cube-van model. With the fences, the drag reductions were 31.4% for model with sharp edges and 24.8% for the one with rounded edges. This suggested considerable promise for the concept and need for full-scale tests.
- (ii) The entirely passive character of the fences, their simplicity and ease of application are indeed quite attractive features conducive to full-scale application.

### Full Scale Tests

- (i) In general, the full-scale tests with the fences substantiate the positive influence of the fences in reducing drag. A decrease in drag coefficient by 16.6% with two vertical and one horizontal fences is indeed impressive. It represents a reduction in the power demand by 11.1% with a decrease in fuel consumption of around 9.6%, the average over the speed range used during the tests.
- (ii) As the fuel consumption would depend on the speed of operation, the 11.1% reduction in power with the application of fences would now permit use of the overdrive instead of the 3rd gear. For the truck negotiating a flat terrain at 100 kph, with overdrive, the reduction in fuel consumption amounts to around 39.6%. Of course, in actual practice, the net benefit would be smaller due to energy expended during acceleration, braking, negotiation of the gradient, decent, etc.
- (iii) The tests account for the yaw effect only in an average fashion. Performance of the fences at various yaw orientation has not been established systematically. Fortunately, as pointed out by Drollinger [6], most trucks spend a large portion of their time at yaw angles of less than  $4^\circ$  (only a 10% probability of yaw angles greater than  $4^\circ$  for commercial trucks). Hence the results are not likely to be affected significantly by the presence of yaw.
- (iv) Due to differences between the prototype and the model, the fence geometry and orientations are not yet optimum. Hence, there is a scope for further improvement in the performance.

### **References:**

1. D. Simanaitis, Road and Truck, (1980) 88.
2. B. Ying, M.A.Sc. Thesis, University of B.C., Vancouver, (1991).
3. G. Sovaran, T. Morel and T.W. Mason, Jr., Proc. Symp. General Motors Research Laboratories, Warren, (1978).

4. P.W. Bearman, Trans. ASME, J, Fluids Engg., 102 (1980) 265.
5. S. St. Hill, M.A.Sc., Thesis, University of B.C., Vancouver, (1992).
6. R.A. Drollinger, SAE Paper No. 870001 (1987).

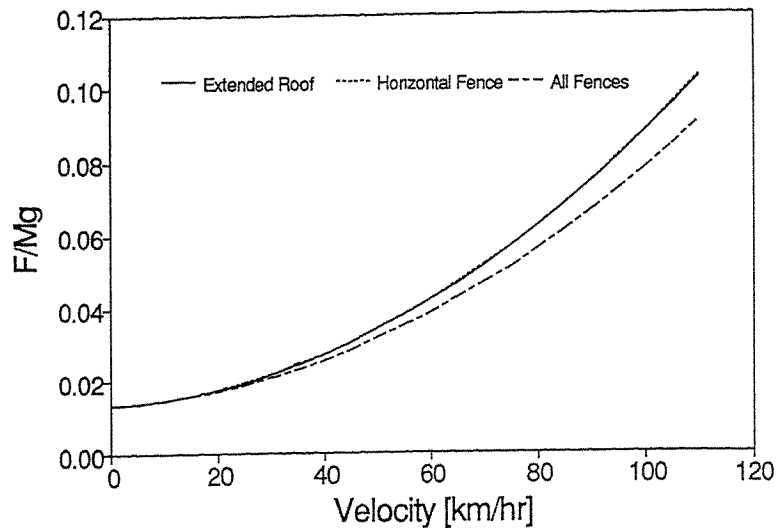


Fig. 6 Comparative regression analysis showing the effect of fences. The resistance force nondimensionalized with respect to weight.

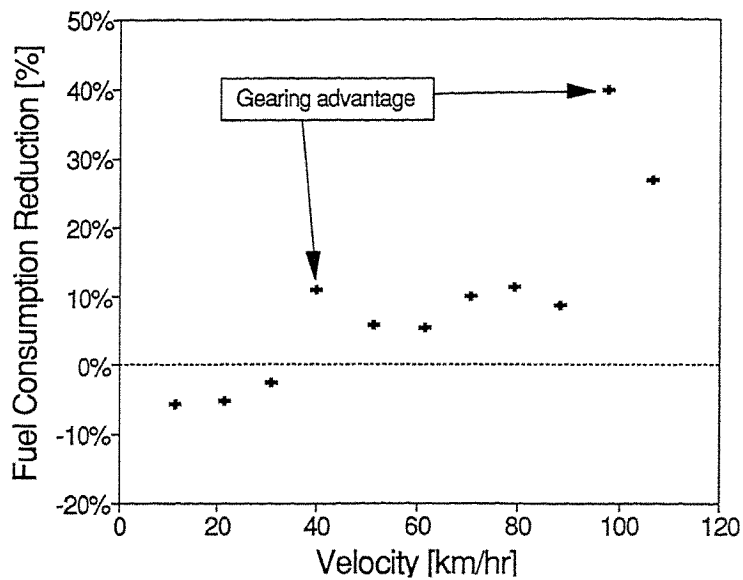


Fig. 7 Effect of fences on the fuel consumption over a range of truck speed.

## Environment over Helideck of Offshore Platform

Qiang Chen, Zhifu Gu, Tianfeng Sun and San Song<sup>+</sup>

Dept. of Mechanics, Peking university  
Beijing, china (100871)  
CNOOC, Tanggu, Tianjin , China

**Abstract:** Testing of wind environment over helideck of a model jack-up offshore platform was carried out in an atmospheric boundary layer wind tunnel. Hot-wire anemometer was used to measure velocity distribution over the helideck at five different wind directions. The results show that the mean velocities and root-mean-square values of fluctuating velocity are quite different under various wind directions. Flow visualization by smoke-wire technique was also presented.

### 1. Introduction

Helidecks are often equipped on offshore platforms for helicopters to take off and land. The wind environment over helideck is rather important to safe operation of helicopters. The flow field over the helideck is similar to that over a three-dimensional flat-plate flow in atmospheric boundary layer stream, but it is also effected by the gas launcher, truss and other structures of platform. So far as present authors aware, the relevant data is rather limited [1, 2].

This paper gives the results of wind tunnel study of the wind environment of helideck of a certain offshore platform in Behai Sea. It may give some insight to flow mechanism over helideck and provide some data for designers.

### 2. Experimental Equipments and Model

The test was carried out in an atmospheric boundary layer wind tunnel of Peking University, with a test section of 1.2m wide, 1.0m high and 8.0m long. To produce a velocity profile and turbulence intensity similar to that over open ocean, roughness elements over floor of test section were employed. The exponential index of power law velocity profile of simulated stream at model station was 0.11 (Fig. 3).

Model of platform used was 1/100 of the full size one (Fig. 1 & 2).

The velocities over helideck were measured by hot-wire anemometer TSI 1050 for five different directions (ie. five  $\beta$ 's as defined in Fig. 2). There were 800 measurement points for each directions. Wind is generally a random variable with time. As in usual practice, the instantaneous velocity measured at any point was decomposed into a time-mean velocity  $U$  and a fluctuating part. The later should be

described by statistical quantities, of which the most important one is its root-mean-square value, denoted as  $V'$  here.

In this paper the oncoming velocity  $V_r$  at the reference height  $Z_r$  will be used as the characteristic velocity and the length of helideck  $L$ , as the characteristic length. The test Reynold number  $Re$ , based on  $V_r$  and  $L$ , is  $2.7 \times 10^5$ .

Flow visualization by smoke-wire equipment BD S-2 was also conducted to show the features of the flow field.

### 3. Test Results

Fig. 4 gives the distributions of  $U$  and  $V'$  over helideck at  $\beta = 90^\circ$ . On the upstream front edge of helideck, mean velocities are quite large (maximum  $U$  attaining  $1.4V_r$ ) though  $V'$  are rather small. This is owing to that the oncoming flow, rising up due to blockage of the platform, separates from the front edge and the separated shear layer has larger mean velocity and smaller fluctuation. In the region between front edge and center part of deck,  $V'$  increases significantly. The maximum fluctuating velocities reach  $0.4V_r$  because the flow field is effected by separated eddies under the shear layer. The measured shedding frequency is 16HZ. In the center region of helideck, mean velocities have turn-points which may mean unstability[3]. In the rear part of deck,  $U$  is much smaller while  $V'$  is larger.

Fig. 5 gives isotaches of  $U$  on a horizontal section of  $Z/Z_r = 0.1$ . It shows a feature of district in distribution. Near the front edge of deck, closely-spaced isotaches indicate there is a big gradient along horizontal direction and the separated shear layer rises rapidly. There are two closed regions on the left and right sides of deck where  $U/V_r$  have the values of 0.8 and 1.0 respectively. Flow reattachments result at these two regions. The difference of these two values is probably owing to that gas launcher lies on the left side of deck along wind direction. The center region of deck is the separating region with small  $U$ . The isotaches of 0.6 between center region and other regions may represent the separating lines.

Fig. 6, 7, 8 are distributions of  $U$  and  $V'$  over the helideck at  $\beta = 0^\circ, 104^\circ, 270^\circ$  respectively. When  $\beta = 0^\circ$ , the gas launcher is located ahead of the helideck and the flow field behind is effected. Except  $\beta = 0^\circ$ ,  $U$  have turn-points in the center region which has different size for different wind directions. It is related to the shedding eddies. At  $\beta = 104^\circ$  which is the prevailing wind direction at the site of the platform, the flow arrives at helideck from both the front edge and the side edge. Near these two edges,  $V'$  is much small, and the region where turn-points occur moves away from center and toward the other side of the helideck. There maybe a big separated bubble in the region closed by isotach of value 1.06 (showed in Fig. 9).

Fig. 10 is a picture by smoke visualization over helideck at  $\beta = 90^\circ$ . It shows that flow separates from the front edge and creates shedding eddies. Other pictures of visualizations show that there are reattachments near the left and right sides of



helideck at  $\beta = 90^\circ$  and the flow features conform with that measured by hot-wire at other directions.

#### 4. Conclusions

From the wind tunnel testing, we have found that the distributions of mean velocities and fluctuating velocities are quite different at different wind angles.

1. Flow generally separates at the front edge of the helideck.
2. Fluctuating velocities are quite large in a certain region between the upstream edge and the center part of helideck.
3. In the center part of helideck, mean velocity  $U$  sometimes has turn-points which mean instability.

#### Reference:

1. W. H. Melbourne, "Turbulence Bluff Body Aerodynamics and Wind Engineering" 7th Australian Hydraulics and Fluid Mech. Conference, Brisbane, 18-22 August.
2. Akins, R. E., J. A. Petaka and J. E. Cermak Averaged Pressure Coefficients for Rectangular Buildings, Wind Engineering, ed. by J. E. Cermak, (1979) 369-386.
3. Willmarth, W. W., and S. S. Lu: J. Fluid Mech. 55, 65(1972).

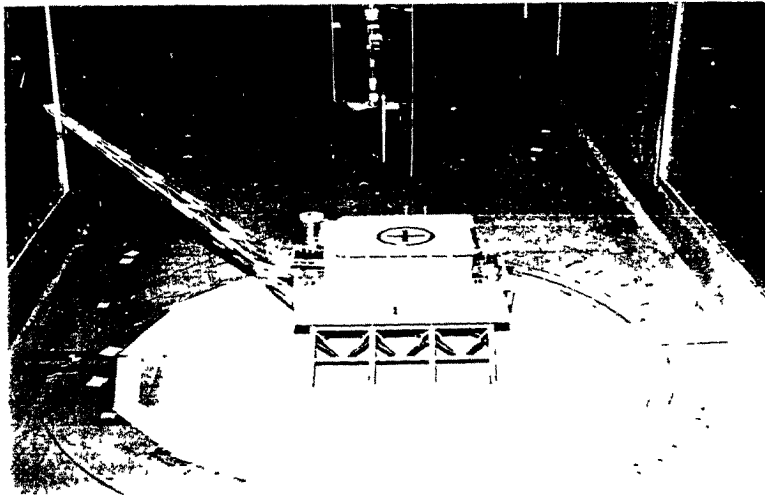
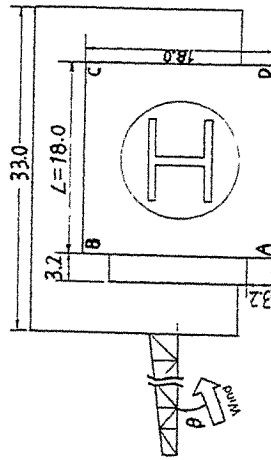
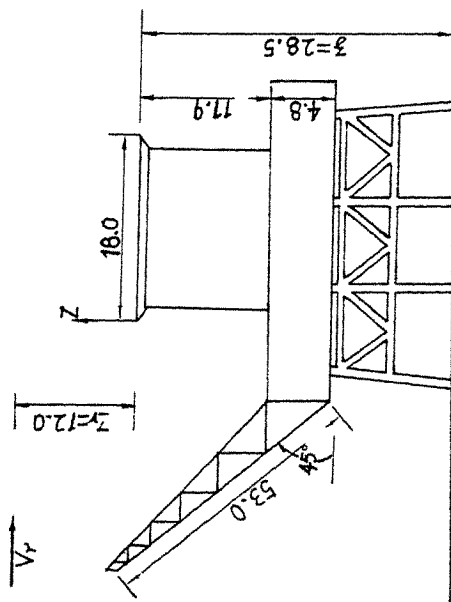
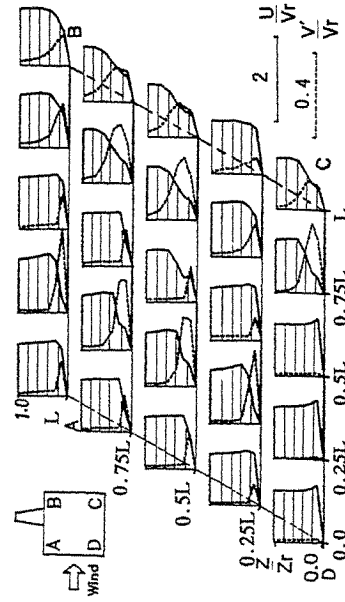
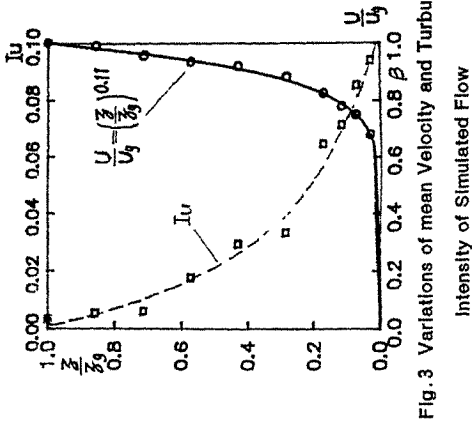


Fig 1: Model Positioned in Wind Tunnel



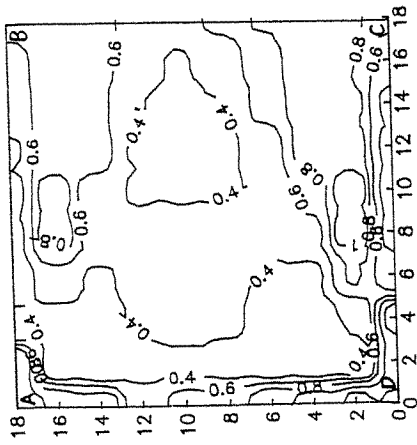


Fig. 5: Isotach for  $\beta=90^\circ$ ,  $Z/Z_r=0.1$

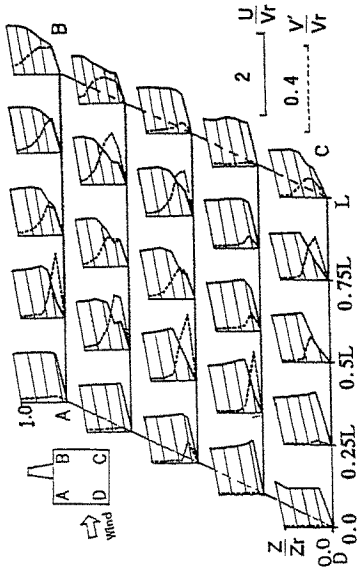


Fig. 7: Velocity Profiles at  $\beta=104^\circ$

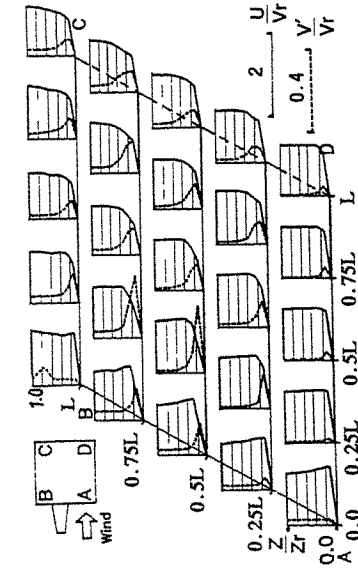


Fig. 6: Velocity Profiles at  $\beta=0^\circ$

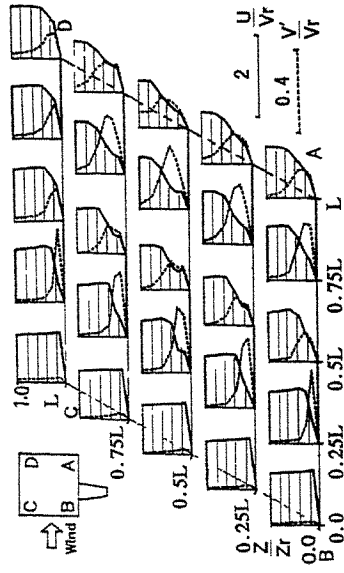


Fig. 8: Velocity Profiles at  $\beta=270^\circ$

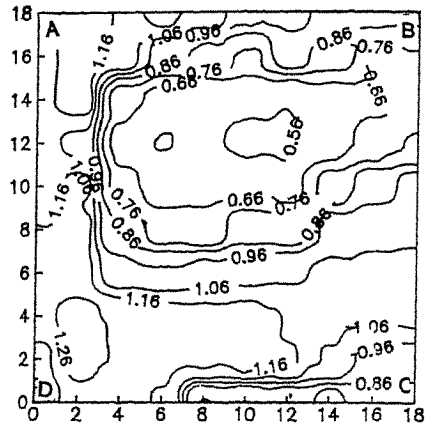


Fig.9 : Isotach for  $\beta=104^\circ$ ,  $Z / Z_r=0.17$



Fig 10:Smoke Visualization at  $\beta=90^\circ$ ,  $U=2\text{m/s}$ ,  $t=120\text{ms}$

## Some Wind Tunnel Experiments on Three-dimensional effects of Circulation Control Sail Wing\*

Pan Weiming Wang Xianfu Zhang Shaoqing  
Department of Marine Engineering  
Wuhan University of Water Transportation Engineering  
Wuhan, Hubei, China 430063

**Abstract:** A small aspect ratio Circulation Control Sail Wing ( $\lambda=1$ ) has been studied experimentally in wind tunnel. The results show: there are strong three-dimensional effects on small aspect ratio CCSW. Unless the strong three-dimensional effects of small aspect ratio CCSW are effectively reduced, the excellent high-lift characteristics of CCSW will not be realized on sail assisted ship. Some three-dimensional wind tunnel experiments of a small aspect ratio CCSW have been performed with the purpose of reducing three-dimensional effects of CCSW. And an effective method of reducing three-dimensional effects of CCSW is also discussed and recommended in this paper.

**Key Words:** CCSW (Circulation Control Sail Wing); tangential wall jet; three-dimensional effects; wind tunnel experiment

### 1. Introduction

As a new type of high-lift wing which is simple in construction and convenient in control, the Circulation Control Wing (CCW) has been paid more and more attention recently. The CCW utilizes a tangential wall jet blowing over the upper surface of the wing near the trailing edge to increase and control the circulation and hence the lift of the wing. This technique has been considered an effective method to obtain high-lift wing in aeronautical engineering. There are many data on the two-dimensional experiments and computations of CCW. But, comparatively speaking, few data are available on the three-dimensional research.

Since 1988, a project on CCW and its application on marine engineering has been carried out in Wuhan University of Water Transportation Engineering. One of the purposes of the project is to utilize the excellent high-lift characteristics of CCW on sail assisted ship, that is, to apply CCW as the wing of sail.

From our three-dimensional experiments and the few data available on three-dimensional research, it is found that there are large differences between the aerodynamic characteristics of three-dimensional CCW and two-dimensional CCW, and these differences are larger than those of general wing. For sail assisted ship, because of the small aspect ratio of its sail, the three-dimensional effects of Circulation Control Sail Wing (CCSW) will be strong. Unless the three-dimensional effects are reduced or restricted, the excellent high-lift characteristics of CCSW will not be realized on sail assisted ship.

McLachlan [1] has done some two-dimensional experiments of a CCW with 20% thickness/chord ratio elliptical section and single trailing slot. His results (Fig. 1) show that, under the condition of zero attack angle and jet blowing momentum coefficient  $C_{\mu} = 0.1$ , the lift coefficient  $C_L$  is as high as 2.2. But, in the three-dimensional experiments of Trainor [2], he could only get  $C_L=0.515$  under the condition

\* The Project Supported by FOK YING TUNG EDUCATION FOUNDATION

of zero attack angle and  $C_{L\alpha} = 0.12$  (Fig. 2.). The authors [3] had also done some three-dimensional experiments of CCSW. The results showed that there are large differences between our three-dimensional experimental results and McLachlan's two-dimensional experimental results although our results are better than those of Trainer's. It is because the strong three-dimensional effects of small aspect ratio CCW that there are large differences between the experimental results of three-dimensional CCW and two-dimensional CCW. Moreover, the three-dimensional effects of CCW is different from that of general wing because of the different way in which lift is produced. In order to investigate the three-dimensional effects of CCSW and the way of reducing the three-dimensional effects of CCSW, we have done some three-dimensional wind tunnel experiments of a small aspect ratio CCSW.

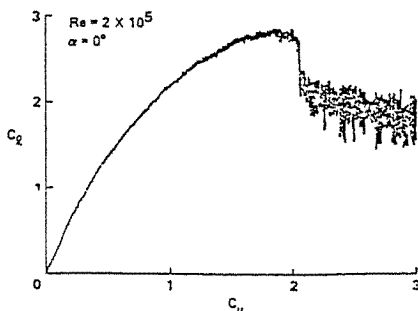


Fig. 1. 2-D experimental results of Malachlan

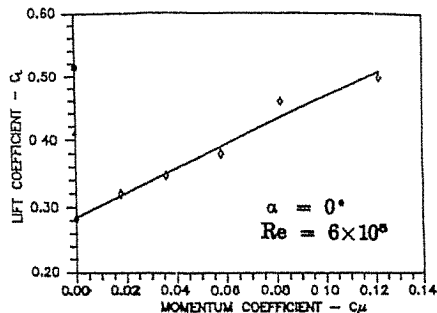
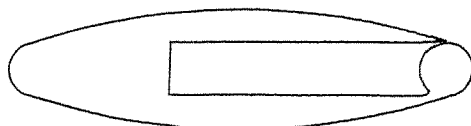


Fig. 2. 3-D experimental results of Trainer

## 2. Description of Experiment

The model CCSW is of elliptical section (25% thickness/chord ratio) with circular-arc leading and trailing edges, upper-surface trailing-edge jet slot, and plenum chamber. The model is 300mm in chord and 300mm in span, that is, its aspect ratio is 1.0. The model section is shown in Fig. 3.



### WING PARAMETERS

Chord :  $C = 300\text{mm}$       Thickness :  $0.25C$   
 Jet slot height:  $h$       Jet slot position :  $94.2\%C$

Fig. 3. Wing geometry and parameters

$$C_L = L/qA \quad (1)$$

$$C_D = D/qA \quad (2)$$

$$C_M = M/qAC \quad (3)$$

where,  $L$  — lift  $D$  — drag  $M$  — pitching moment  $A$  — projected area of model

The experiments were performed in the No. 2 wind tunnel of Wuhan University of Water Transportation Engineering. The wind tunnel has an experimental section of  $\Phi 1.0\text{m} \times 1.5\text{m}$  and a maximum speed of 60m/s.

The lift, drag and pitching moment measured were expressed in general lift coefficient  $C_L$ , drag coefficient  $C_D$  and pitching moment coefficient  $C_M$ .

$C$  — chord of model  $q$  — free stream dynamic pressure,  $q = \rho_{\infty} U_{\infty}^2 / 2$   
 $U_{\infty}$  — mean free stream velocity  $\rho_{\infty}$  — free stream air density

The amount of jet blowing was expressed in jet blowing momentum coefficient  $C_{\mu}$  which was

$$C_{\mu} = \frac{\dot{m} U_j}{qA} = \frac{2}{\rho_{\infty} \rho_j A a} \left( \frac{\dot{m}}{U_{\infty}} \right)^2 \quad (4)$$

where,  $\dot{m}$  — jet flow rate  $a$  — jet slot area  $U_j$  — jet exit velocity  
 $\rho_j$  — jet exit density (calculated based on isentropic expansion)

By measuring the mass flow rate  $\dot{m}$ , station parameters ( $p_0$ ,  $\rho_0$  or  $T_0$ ) of jet and the velocity and density of free stream  $U_{\infty}$ ,  $\rho_{\infty}$ , the jet blowing momentum coefficient  $C_{\mu}$  could be determined by formulate (4).

### 3. Experimental Results and Discussion

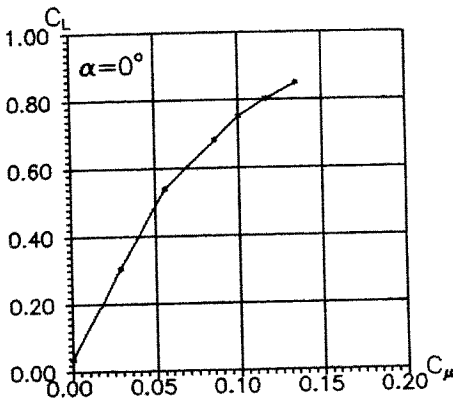


Fig. 4. 3-D experimental results of our CCSW model

Fig. 4. is the  $C_L$ - $C_{\mu}$  curve of our CCSW model. From the experimental curve shown in fig. 4., it is evident that the effect of circulation control (by means of tangential wall jet blowing) is very effective. At zero attack angle, a small value of  $C_{\mu}$  can bring about quite large value of  $C_L$ . The ratio of  $C_L / C_{\mu}$  can be as high as 10 or higher at the small value of  $C_{\mu}$ . But, compared with 2-D experimental results, our 3-D experimental results are still unsatisfactory although our results are better than Trainor's results. It is owing to the strong 3-D effects of the small aspect ratio CCSW that there are large differences between 2-D and 3-D results.

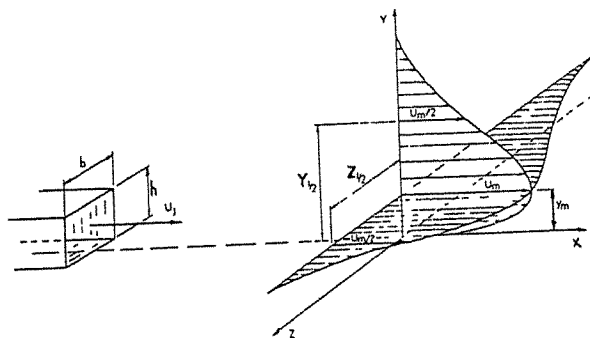


Fig. 5. The three-dimensional wall jet

For general wing with limited span, its 3-D effects are caused mainly by its tip free vortex. But for small aspect ratio CCSW, there is 3-D spread in its high velocity trailing wall jet besides the 3-D effects of general wing described above. Consider three-dimensional wall jet in the coordinate

shown in Fig. 5. Supposing the velocity components as  $(u, v, w)$  and the vorticity components as  $(\Omega_x, \Omega_y, \Omega_z)$  ( $\Omega$  is positive in clockwise rotation), from vorticity equation we have

$$\frac{D\Omega_x}{Dt} = \Omega_x \frac{\partial u}{\partial x} + v \nabla^2 \Omega_x \quad (5)$$

Investigate the change rate of vorticity  $\Omega_x$  in thin boundary of wall jet:

$$\frac{D\Omega_x}{Dt} = \Omega_x \frac{\partial u}{\partial x} + \Omega_y \frac{\partial v}{\partial y} + \Omega_z \frac{\partial w}{\partial z} + v \nabla^2 \Omega_x \quad (6)$$

The second and third term in Equation (6) represents vorticity change rate caused by vortex-line-bending. They have obviously different effects according to dimensions of the flow. We can see this clearly from Equation (7)

$$\Omega_y \frac{\partial v}{\partial y} + \Omega_z \frac{\partial w}{\partial z} = \frac{\partial w \partial u}{\partial x \partial y} - \frac{\partial v \partial u}{\partial x \partial z} \quad (7)$$

For two-dimensional flow ( $w = 0, \partial u / \partial z = 0$ ), the right of Equation (7) is identically equal to zero. But, in three-dimensional flow (supposing plane  $y = 0$  is solid wall), from the view point of physics, we consider that:  $|\partial w / \partial x| > |\partial v / \partial x|$ ,  $|\partial u / \partial y| > |\partial u / \partial z|$ , thus the first term on the right of Equation (7) will be dominant in the change rate of  $\Omega_x$ . Since  $\partial w / \partial x < 0$  over the whole flow region,  $\partial u / \partial y > 0$  over the inner region of the boundary layer of jet ( $y < y_m$ ) and  $\partial u / \partial y < 0$  over the outer region of the boundary layer of jet ( $y > y_m$ ), the increment of  $\Omega_x$  is thus negative in inner region and positive in outer region. A lateral velocity profile will be formed finally (shown in Fig. 6). Compared with two-dimensional wall jet, the increase of  $\Omega_x$  change rate caused by vortex-line-bending will bring about an increase of  $z$  component velocity in three-dimensional wall jet. This is why the lateral spreading rate (in parallel with solid wall) is greater than the normal spreading rate (perpendicular to solid wall) in three-dimensional jet. From reference [4], we can see that the ratio of lateral spreading rate to normal spreading rate is as high as 5.5:1 in three-dimensional wall jet.

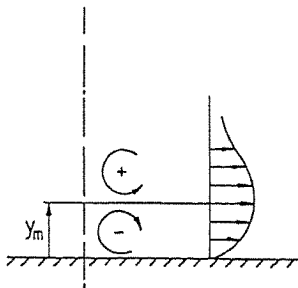


Fig. 6. lateral velocity profile of jet

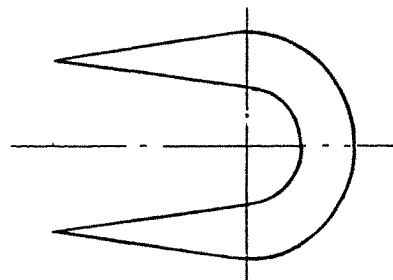


Fig. 7. small partial end plate

For circulation control wing, there is also a lateral spreading mentioned above in its high velocity wall jet near trailing edge. From the view point of lift producing, we do not hope the wall jet has lateral spreading, because the lateral spreading not only fails to produce lift but also lowers the main velocity of jet blowing and



finally lowers the benefit of lift producing by wall jet blowing. In order to weaken the three-dimensional effects, three types of end plates have been designed:

1. End plate A: 1.33C in length, 0.5C in width, placed at the tip of the wing.
2. End plate B: the size is the same as end plate A, placed at the end of jet slot.
3. End plate C: a small partial end plate ( shown as Fig. 7. ), placed at the end of jet slot.

Fig. 8. is the  $C_L$ - $C_{\mu}$  curves of our model with end plates and without end plates as well as the result of Trainor's 3-D experiment and McLanchlan's 2-D experiment.

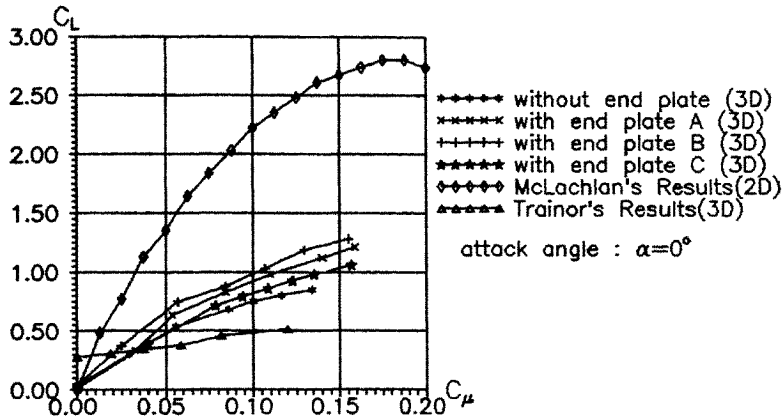


Fig. 8. the  $C_L$ - $C_{\mu}$  curves of our model with end plates and without end plates as well as the result of Trainor's 3-D experiment and McLanchlan's 2-D experiment.

From Fig. 8. we can see that the lift characteristics has been improved by placing end plate A. Since the jet slot of our model is 280mm and there is still 20mm between each end of slot and wing ends, the end plate A placed at the tip of the wing can only control the tip free vortex, but it has not any effect on controlling lateral spreading of the wall jet. To control the lateral spreading of the wall jet, end plate B is used, that is, two end plates (the same size as end plate A) are placed at the ends of jet slot. In this way, the effect of three-dimensional effects controlling is improved. Under the condition of  $C_{\mu}=0.1$ , the  $C_L$  of model with end plate B is as high as 0.986. Compared with the  $C_L$  of model without end plate ( $C_L=0.762$ ) and with end plate A ( $C_L=0.922$ ), the is increased 31% and 7%. To investigate the influence of lateral spreading control on lift characteristics, two small partial end plates (end plate C) are placed at each end of the jet slot (the  $C_L$ - $C_{\mu}$  curve is shown in Fig. 8. ). Under the condition of  $C_{\mu}=0.1$ , the  $C_L$  of model with end plate C is still as high as 0.822. This indicates that satisfactory benefit of lift increasing could be obtained only by controlling lateral spreading of the wall jet. Table 1. is the  $C_{L_{max}}$  ( $C_{\mu}=0$ ,  $\alpha \neq 0$ ) and the  $C_L$  ( $C_{\mu}=0.1$ ,  $\alpha=0$ ) of the same model with different end plates

From table 1. we can see that the  $C_L$  ( $C_{\mu}=0.1$ ,  $\alpha=0$ ) of the model with end plate B and C is greater than its own  $C_{L_{max}}$  ( $C_{\mu}=0$ ,  $\alpha \neq 0$ ), but, the  $C_L$  ( $C_{\mu}=0.1$ ,  $\alpha=0$ ) of the model with end plate A and without end plate is smaller than its own  $C_{L_{max}}$  ( $C_{\mu}=0$ ,  $\alpha \neq 0$ ). This indicates that the end plates placed at the tip of the wing can only

End plate	A	B	C	without end plate
$C_{Lmax}(C_{\mu}=0, \alpha \neq 0)$	1.0428	0.8486	0.8047	0.8117
$C_L(C_{\mu}=0.1, \alpha=0)$	0.922	0.986	0.822	0.752

Table 1. the  $C_{Lmax}(C_{\mu}=0, \alpha \neq 0)$  and the  $C_L(C_{\mu}=0.1, \alpha=0)$  of the same model with diferent end plates

control the tip free vortex but can not control the lateral spreading of jet blowing if there are some distances between jet slot ends and wing tips. The closer to jet slot end the end plates are placed, the more effective the control of lateral spreading of jet blowing, and thus the more efficient generation of lift by means of wall jet blowing.

Comparing the  $C_L$  values of table 1., it is evident that, as long as suitable method is applied to control its three-dimensional effects, the  $C_L$  of small aspect ratio CCSW can be as high as its  $C_{Lmax}(C_{\mu}=0, \alpha \neq 0)$  under the condition of  $C_{\mu}=0.1, \alpha=0$ . That is, without attack angle the CCSW can also provide the thrust as large as the maxium thrust of general sail, and can provide more thrust than that of general sail if the attack angle is greater than zero. For more details about the application of CCSW on sail assisted ship, see referenc [3] please.

#### 4. Conclusion

From our experimental research of small aspect ratio CCSW, we can conclude as follows:

1. There are strong three-dimensional effects on small aspect ratio CCSW. Unless the strong three-dimensional effects of small aspect ratio CCSW are effectively reduced, the excellent high-lift characteristics of CCSW will not be realized on sail assisted ship.
2. The three-dimensional effects of CCSW are more complex than that of general wing. Besides the three-dimensional effects of general wing, there are also three-dimensional effects in the jet flow of the wall jet of CCSW. All of these have reduced the high-lift characteristics of CCSW.
3. The three-dimensional effect can be effectively reduced by applying end plates. Moreover, in order to effectively reduce the three-dimensional effects, the end plates should be placed close to the ends of slot.
4. The small partial end plates placed at the end of CCSW can also achieve satisfactory effect of reducing three-dimensional effects. This is good for the situation where the whole end plates are not suitable.

#### Reference:

1. B. G. McLachlan, Study of a Circulation Control Airfoil with Leading/Trailing-Edge Blowing, J. AIRCRAFT, Vol. 26, No. 9, Sept. 1989, pp 817-821
2. John W. Trainor, A Wind Tunnel Study of of a Sting-Mounted Circulation Control Wing, AD-A216248
3. Pan Weiming & Wang Xianfu, A Study of the Application of Circulation Control Wing on Sail Assisted Ship, Eighth Internatuinal Conference on Wind Engineering, 8-12 July 1991, London, Canada
4. B. E. Launder & W. Rodi, The Turbulent Wall Jet — Measurements and Modeling, Ann. Rev. Fluid Mech. 1983. 15, pp 429-457

## Wake Survey and Analysis on the Scaled Car Models

Wang Maoxun, Zhou Yuping and Zhu Wei

China Aerodynamics Research and Development Center

**Abstract:** In last decades, a great advance has been reached in vehicle aerodynamic drag reduction. The further effective reduction of drag, however, will be increasingly difficult if only conventional methods were used. The technique using vehicle wake measurement to reduce its aerodynamic drag is a quantitative flow diagnosis tool without destruction of models, which may find the drag origins and assist the performance improvement. In this paper were described the tests on a series of scaled car models in  $4\text{m} \times 3\text{m}$  low speed wind tunnel, CARDC, including wake survey and balance measurement. The drag data from wake integration were compared with those from balance tests, and good agreement was obtained. Some problems in test technique seem needed to improve.

### 1. Introduction

In last decades, a great achievement has been reached in the drag reduction of cars. Due to earlier less pressure on fuel consumption, the aerodynamic drag coefficient of the conventional cars was up to 0.55~0.66 till 60's. Then the energy crisis stimulated car aerodynamics studies. The great efforts on drag reduction led to the lowered drag coefficient 0.35~0.45 for commercial cars, and even 0.15~0.20 for advanced prototypes. Note that the earlier efforts in drag reduction were mainly based on trial-and-error methodology, using conventional tools such as force, pressure and flow visualization tests. Due to lack of detail study on flow mechanism, the study on drag was getting difficult.

Since 80's the investigation on car aerodynamics has focused attention on the wake structure behind car, resulting in new progress in drag reduction. Betz first calculated the aerodynamic drag of body through wake survey and integration based on the momentum theorem. Betz's formula required an integration on entire field and were impracticable in three-dimensional separation cases. A correction was developed by Maskell, reducing the integration range from entire field to difinited wake area and including wall effects. Although the accuracy was much improved, it was still impracticable in engineering because of the limited tunnel length. J. C. Wu and J. E. Hackett rededuced Maskell's formula, that the limitation on integration in far wake was removed into near-wake. In last decade, the refinement of CAFV technique (Computer Aid Flow Visualization) assissted the study method by wake measurement behind car in-to engineering practice.

Recently, the wake measurements behind a series of  $1/3$  scaled car models were carried out in  $4\text{m} \times 3\text{m}$  low speed wind tunnel, CARDC, using CAFV system and seven-hole probe. Analysis and drag integration were made on measured results. A good agreement with balance data on drag was obtained with correlation factor 1.01.

### 2. Facility and Model

CARDC  $4\text{m} \times 3\text{m}$  low speed wind tunnel is a single return, closed circuit and closed jet tunnel, with a test section of 4m wide, 3m high and 8m long, and maximum wind speed 100m/s.

The wake survey was completed by a computerbased six degree-of-freedom traversing system,

(Fig. 1), of precisions up to 0.02mm in linear displacement and 0.1 deg. in angular movement, respectively. Either single- or multi-DOF composed movement modes were available under the computer control. A seven-hole probe of 3mm diameter was mounted on the sting tip, to measure total pressure, static pressure and velocity vector. Through scanivalve and sensors, the data measured were input into computer to automatically acquire and process, and on-line display the vectors and pressure at points on a colour CRT.

The 1/3 scaled models of shape-simplified Japanese COROLLA car were tested. Three different rear configurations were designed, fastback, notchback and squareback (see Fig. 2). The positions of model and survey sections in the test section were indicated in the Fig. 2. The ground was simulated by tunnel floor and the wheels were mounted at 8mm above floor. In force tests, the wheels were fixed on the traylets which were connected with six-component strain-gage balance and above the floor. The earth-frame of balance was mounted under the floor.

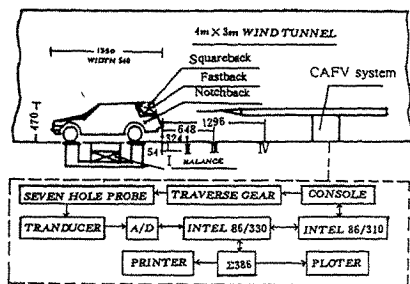


Fig. 1 Experimental system  
(all dimensions in mm)

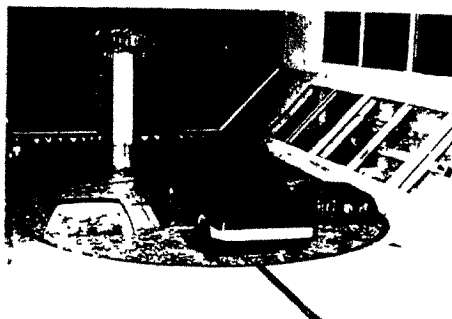


Fig. 2 Models in 4m x 3m Wind Tunnel

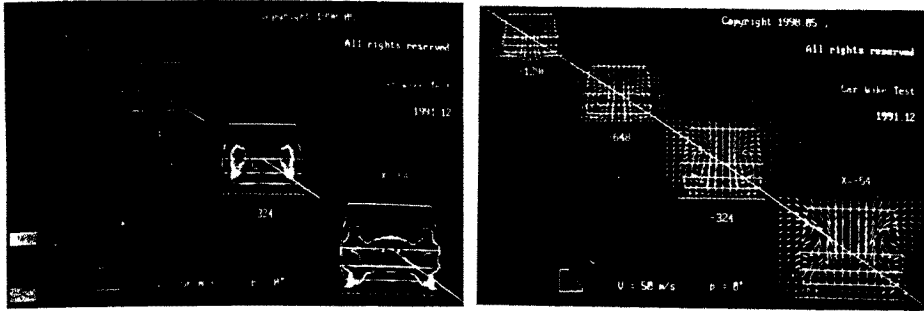
### 3. Test Results and Analysis

Four survey sections were selected at 54mm, 324mm, 648mm and 1296mm behind car rear end, respectively, and the section bottoms were 40mm above the floor. Wind speed of 50m/s and yaw angles of  $0^\circ$ ,  $\pm 4^\circ$  and  $8^\circ$  were tested.

#### 3.1 Wake Survey Results

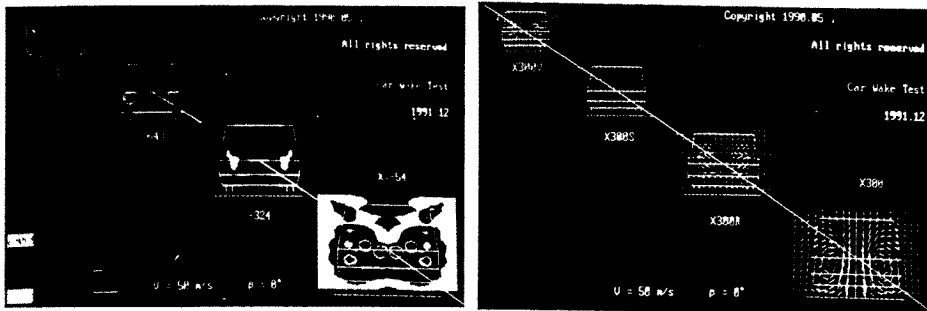
Some typical results for different configurations at each survey stations were presented in Fig. 3~6. The flow characteristics in the wake of various configurations were seen from those and briefed as following.

**FASTBACK** The total pressure deficit and cross-flow vectors at various stations for yawing  $\beta = 0^\circ$  and  $8^\circ$  were shown in Figs. 3~4. The source/vortex induced vectors at station II were presented in Fig. 3(d). It was seen from Figs. 3(a) and (b) that two pairs of vortex had been generated at station I, among which upper one was much stronger than lower one, and then at station II were merged into single pair of tail vortex moving downstream. The potential flow effect resulted in the middle of wake close to the floor, while the vortex flow effect resulted in the pressure gradient decaying from inside to outside due to cross-flow extrusion. In the area with maximum pressure gradient, the cross-flow extrusion increased towards outside. The vortex centers were near the lower pressure area, where the source-sink effect was mainly considered. Even at station IV, the tail vortex remained recognized, but their cores further moved toward outside and floor. It was expected that they would break-down and disappear far downstream.



(a) Total pressure deficit

(b) Crossflow vectors



(c) static pressure distribution

(d) source and vortex-induced vectors at section II

Fig. 3 Wake measurements of fastback model at  $\beta=0^\circ$

In the case with yawing, shown in Fig. 4, two tail vortices were still clearly seen. The significant differences between them, however, occurred in vortex strength, core position, velocity vector, and total pressure deficit, and much more obvious as yawing angle increased.

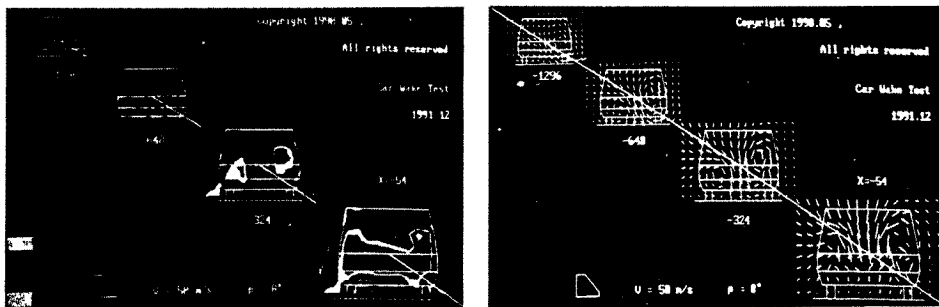


Fig. 4 Total pressure deficit and crossflow vectors at  $\beta=8^\circ$  for fastback model

NOTCHBACK The total pressure deficit and velocity vectors at various stations were shown in Fig. 5 for  $\beta=0^\circ$  and  $8^\circ$ . Similar to fastback, a pair of tail vortex was seen in the wake behind notchback car, moving downstream, but with vortex core closer to ground due to larger angle of C-column. It may be expected that its tail vortex would be broken and disappear earlier and move shorter distance than in fastback case.

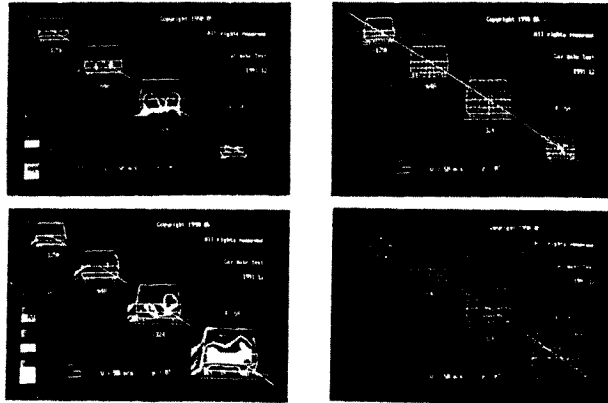


Fig. 5 Total pressure deficit and crossflow vectors at  $\beta=0^\circ, 8^\circ$  for Notchback Model

SQUAREBACK The total pressure deficit and velocity vectors at various stations were shown in Fig. 6 for  $\beta=0^\circ$  and  $8^\circ$ . Because of the induced upwash along the section centerline by the potential flow downstream, the total pressure contour was expanded in vertical direction and contracted at lower portion. No strong vortex pair was observed and the area with uniform flow was rather larger, which indicated the full separation of flow.

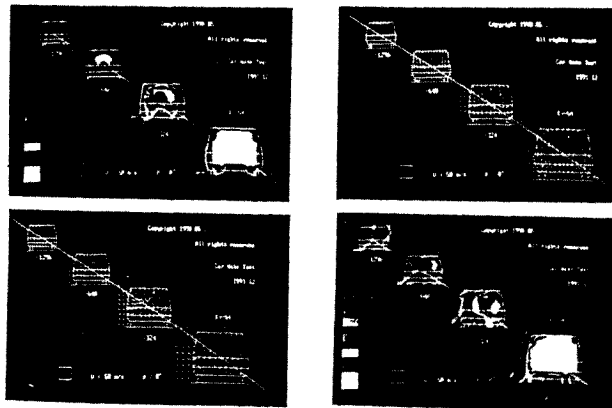


Fig. 6 Total pressure deficit and crossflow vectors at  $\beta=0^\circ, 8^\circ$  for Squareback Model

### 3.2 Drag by Wake Integration

Using the wake survey results for three models, the drags were calculated by following integration formula:

$$D = \iint_{\text{wake}} [(H_0 - H_2) + \frac{\rho}{2}(U_2^2 - U_1^2)(U_2^2 + U_1^2 - 2U_0^2)] ds - 2\rho AU_0^2 + \frac{\rho}{2} \iint_{\text{wake}} \psi_2^2 ds \quad (1)$$

where the total aerodynamic drag consisted of three parts, viscous drag, wake blockage and vortex drag. Some typical calculation results were presented in Table 1. The blockage ratios of present models were about 1%, and wall interferences were ignored in calculation.

Table 1. Correlation Between drags by wake integration and balance

Model	$\beta^\circ$	Wake integrated Drag				Drag by Balance $C_{D_b}$	$\frac{C_{D_w}}{C_{D_b}}$
		Viscous Drag	Wake blockage	Vortex Drag	Total Drag		
Fastback		0.370	-0.0015	0.0055	0.374	0.372	1.0
		99	-0.4	1.4	100	100/100	
Squareback		0.375	-0.0026	0.0026	0.375	0.383	0.98
		97.9	-0.7	0.7	98	100/100	
Notchback		0.391	-0.0021	0.0107	0.399	0.376	1.06
		103	-0.6	2.8	106	100/100	
Fastback	8	0.383	-0.0020	0.0177	0.399	0.427	0.93
Squareback		0.491	-0.0032	0.0185	0.434	0.450	0.96
Notchback		0.400	-0.0023	0.0171	0.415	0.438	0.94

### 3.3 Analysis on Correlation

In Fig. 7 were shown the drag coefficients with yawing angles for three configurations obtained from balance tests, indicating  $C_{D_{\text{fastback}}} = 0.372$ ,  $C_{D_{\text{notchback}}} = 0.376$  and  $C_{D_{\text{squareback}}} = 0.383$ , respectively. The wake survey showed that in squareback case, the largest integrated area and highest total pressure deficit  $C_{p_{\text{min}}} = 0.990$  resulted in higher viscous drag and hence the highest total drag ( $C_D = 0.383$ ). The situation in fastback case is opposite ( $C_{p_{\text{min}}} = 0.992$ ), so that the total drag  $C_D = 0.372$  is the lowest, which agreed with balance results.

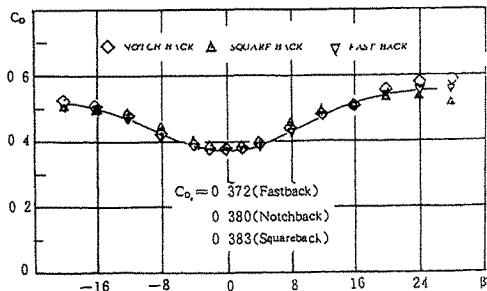


Fig. 7 Drag coefficient from Balance Tests

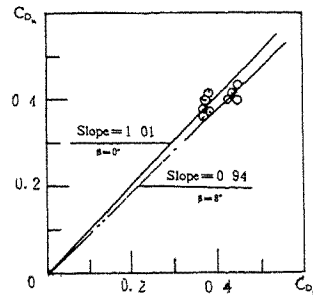


Fig. 8 Correlation Between drags by wake integration and Balance

Table 1 and Fig. 8 indicated that better correlation was obtained at  $\beta=0^\circ$  between the drag from wake integration and balance tests, with slope 1.01. At  $\beta=8^\circ$ , however, the correlation was worse with slope 0.94 because of limited survey range in yawing case with expanded separation area and wider wake. The data in the Table showed that the wake integration at station III described the flow characteristics in the wake well.

It was also found in Table 1 that due to clean aerodynamic shape of simplified car models vortex and source/sink drag was very lower comparing to viscous drag. The wake integration at station III when  $\beta=0^\circ$  showed the ratio of vortex drag to total drag was the lowest in squareback (0.7%) and the highest in notchback (2.7%).

The influence of floor boundary layer could be seen in the wake survey results, though the models had been raised above the floor. The refinement in the selection of the quantity and range of survey points was need in future.

#### 4. Conclusions

1. The wake survey technology used in present study has well described the basic characteristics of wake generation, development and decay behind the car models.
2. A good agreement of drag from wake integration and balance test was obtained, with correlation factor near 1.0. The drag component resolution from wake integration indicated that the viscous drag (or form drag) was primary, and vortex and source drag were lower. All source drags were lower than 1% total drag.
3. Some further improvements are needed for more accurate wake measurement, such as use of multi-probe rake, expand the survey range in wake, increase measurement points and ground modeling, and so on.

#### References

1. J. C. Wu, AIAA J. Vol. 14, No. 8 (1976).
2. J. C. Wu, J. C. Hackett and D. E. Lilley, AIAA 79-0279.
3. J. E. Hackett and A. Sugavanam, SAE 840577(1984).



## Numerical Simulation and Characteristic Analysis of Flow around Embankment of Railway Line

Zhang Jianbo, Cui Erjie, Fu Guangming

Beijing Institute of the Aerodynamics , China

**Abstract:** Starting from N-S equations, employing SIMPLE algorithm in the computational plane, we have simulated the flow field around the railway embankment in windy district. The influences of the Re number and shear intensity of the incoming wind and the profile of the embankment on the flow field can be easily seen from the computation results. By introducing K - ε turbulence model, we have calculated the distribution of the pressure and the friction velocity on the wall along the surface of the standard and the eroded embankment at high Re number. The peak value of the negative pressure and the friction velocity at the shoulder part of the eroded embankment reduces, its distribution becomes smooth, which indicates that the aerodynamic characteristics of the eroded embankment becomes much better. We have also set up an effective procedure to generate orthogonal and body-fitted coordinates.

**Key words:** embankment, wind-induced erosion, grid generation, SIMPLE, K - ε model

### 1. Introduction

The wind induced erosion and deposit of the railway embankment are common disasters for the railway lines in windy district. It severely endangers the safety of the train operation. Clarifying the underlying mechanism of the erosion and deposit is conducive to the reduction of the expenses of the protection engineering . The properties of the flow field and the composition materials of the embankment are the most important factors dominating the problem . The development of the embankment profile in the erosion process has been observed and measured on site by a number of investigators . Wind tunnel experiment and water tunnel visualization have found out some main characteristics of the flow field . Since it is difficult in the experiment to simulate the Reynolds number over  $10^5$ , which is still much lower than that in reality, it is necessary to study the problem through numerical approach . Up to now, the pressure distribution along the surface of the embankment has been obtained by others through the solution of the Euler equation . But the viscous effect , which has serious influences on the flow field , hasn't been taken into consideration.

In this paper , starting from the N-S equation , employing the SIMPLE algorithm in the computational plane , we have set up a code which can be used to solve this problem and which is also effective to other relevant engineering problems . Using this code , we have investigated the influences of the inflow Reynolds number and the inflow shear intensity on the flow field . And by introducing the K-ε turbulence model , we have calculated the distribution of pressure and friction velocity along the surface of the standard and the eroded embankment at high Reynolds number .

### 2. Numerical Simulation

#### 2.1 Governing Equations

For steady-mean flow, the continuity equation and the N-S equation are written in a Cartesian tensor form

$$\frac{\partial}{\partial x_i} \rho u_i = 0 \tag{1}$$

$$\frac{\partial}{\partial x_i} \rho u_i u_j = -\frac{\partial p}{\partial x_j} + \frac{\partial}{\partial x_i} [(\mu + \mu_t) (\frac{\partial u_i}{\partial x_j} + \frac{\partial u_j}{\partial x_i})] - \frac{2}{3} \rho K \delta_{ij} \tag{2}$$

$$\begin{aligned}\alpha &= x_{\eta}^2 + y_{\eta}^2 & \beta &= x_{\xi}x_{\eta} + y_{\xi}y_{\eta} \\ r &= x_{\xi}^2 + y_{\xi}^2 & J &= x_{\xi}y_{\eta} - x_{\eta}y_{\xi}\end{aligned}$$

The last term on the right side of Eqn(12) includes the 2rd order cross derivative of variable  $\phi$ . If this term is treated as the source term in the new coordinate system, Eqn(12) bears the same form with Eqn(11), therefore, the SIMPLE solution procedure, which has been successfully used for flow calculation in the Cartesian system, can be extended to the body-fitted system after some modifications.

### 2.3 Grid Generation

The body-fitted orthogonal coordinate system is generated in two steps:

(1) Nonorthogonal body-fitted coordinate  $(\mu, \nu)$  is obtained by solving the elliptic equations [4]

$$\nabla^2 \mu = (g_{22}/g) P(\mu) \quad \nabla^2 \nu = (g_{11}/g) Q(\nu) \quad (13)$$

where  $P(\mu) = -f_1''/f_1'$ ,  $Q(\nu) = -f_2''/f_2'$ ,  $f_1, f_2$  are the grid point distribution along the boundaries  $\mu, \nu$  respectively. The metrics  $g_{11}, g_{22}$  and  $g$  are evaluated in the coordinates  $(\mu, \nu)$ . The right hand side of Eqn(13) can effectively propagate the grid point distribution along the boundaries into the inner region.

(2) The orthogonal systems is constructed by orthogonal trajectories method. Keep  $\nu = \text{constant}$  curves unchanged (let  $\eta = \nu$ ), the  $\xi = \text{constant}$  curves which is orthogonal to the  $\eta$  lines is obtained by integrating the following ordinary differential equation [5]:

$$\frac{d\mu}{d\nu} \Big|_{\xi=\text{constant}} = - \left( \frac{\partial x}{\partial \nu} \frac{\partial x}{\partial \mu} + \frac{\partial y}{\partial \nu} \frac{\partial y}{\partial \mu} \right) / \left( \frac{\partial x}{\partial \mu} \right)^2 + \left( \frac{\partial y}{\partial \mu} \right)^2 \quad (14)$$

The grid generation process are demonstrated in Fig 1.

### 2.4 Boundary Conditions

The computation domain is shown in Fig 2. The boundary conditions are set as follows:

(1) Inlet: The velocity profile is prescribed.

$$u = \left( \frac{y}{z_s} \right)^\alpha u_s \quad (15)$$

where  $z_s, u_s$  are reference height and reference velocity respectively,  $\alpha$  is the index of shear intensity. The turbulence kinetic energy  $K$  is given as measured in the experiment. The turbulence energy dissipation  $\epsilon$  is given differently in the inner and outer layers

$$\begin{cases} \epsilon = u^{*3}/(ky) & (y^+ \leq 500) \\ \epsilon = C_\mu \rho K^2/\mu_t \Big|_{y^+=500} & (y^+ > 500) \end{cases} \quad (16)$$

where  $u^*$  is wall friction velocity,  $k$  is von Karman constant,  $y^+ = y(C_\mu^{1/4} K^{1/2})/\nu$ ,  $\mu_t \Big|_{y^+=500}$  is the turbulent viscosity at  $y^+=500$ .

(2) Outlet:  $\frac{\partial \phi}{\partial \xi} = 0$

(3) Upper side:  $\frac{\partial \phi}{\partial \eta} = 0$

(4) Wall:  $u = v = 0$

where  $\rho$  is the mean density,  $u_j$  the mean velocity, and  $p$  the mean pressure. From the  $K - \epsilon$  turbulence model, the turbulent viscosity  $\mu_t$  is given by

$$\mu_t = C_\mu \rho K^2 / \epsilon \quad (3)$$

where  $K$  is the turbulence kinetic energy and  $\epsilon$  is the turbulence energy dissipation. The equations for  $K$  and  $\epsilon$  present as follows:

$$\frac{\partial}{\partial x_i} \rho u_i K = \frac{\partial}{\partial x_i} \left( \frac{\mu_t}{\sigma_k} \frac{\partial K}{\partial x_i} \right) + P - \rho \epsilon \quad (4)$$

$$\frac{\partial}{\partial x_i} \rho u_i \epsilon = \frac{\partial}{\partial x_i} \left( \frac{\mu_t}{\sigma_\epsilon} \frac{\partial \epsilon}{\partial x_i} \right) + \frac{\epsilon}{K} (C_1 P - C_2 \rho \epsilon) \quad (5)$$

where  $P = \overline{-\rho u_i u_j} \partial u_j / \partial x_i$  is the rate of production of turbulence kinetic energy. The five empirical constants assume the following values:

$$C_\mu = 0.09, C_1 = 1.45, C_2 = 1.90, \sigma_k = 1.0, \sigma_\epsilon = 1.3 \quad (6)$$

Equations(4) and (5) are only valid for fully turbulent regions. The wall function method is often used to bridge the near-wall region: The first computation point  $p$  is located within the region in which the logarithmic law is valid, i.e.  $11.3 \leq y_p^+ \leq 400$ , where

$$y_p^+ = \rho (K_p C_\mu^{0.5})^{0.5} y_p / \mu \quad (7)$$

$$\epsilon_p = (C_\mu^{0.5} K_p)^{1.5} / k y_p \quad (8)$$

$$\left. \frac{dK}{dy} \right|_w = 0 \quad (9)$$

$$\mu_t = \frac{\mu y_p^+}{\ln(E y_p^+) / k} \quad (10)$$

where  $k=0.4$ ,  $E=8.8$

## 2.2 SIMPLE algorithm on body-fitted system

The set of conservation equations typically can be written in the Cartesian system of coordinates for a general dependent variable  $\phi$  :

$$\frac{\partial}{\partial x} (\rho u \phi) + \frac{\partial}{\partial y} (\rho v \phi) = \frac{\partial}{\partial x} \left( \Gamma \frac{\partial \phi}{\partial x} \right) + \frac{\partial}{\partial y} \left( \Gamma \frac{\partial \phi}{\partial y} \right) + S \quad (11)$$

where  $\Gamma$  is an effective diffusion coefficient and  $S$  denotes the source term. When body-fitted coordinates system  $\xi = \xi(x, y)$ ,  $\eta = \eta(x, y)$  is introduced, Eqn(11) is transformed to :

$$\begin{aligned} \frac{\partial}{\partial \xi} (\rho U \phi) + \frac{\partial}{\partial \eta} (\rho V \phi) &= \frac{\partial}{\partial \xi} \left( \frac{\Gamma}{J} \alpha \phi_\xi \right) + \frac{\partial}{\partial \eta} \left( \frac{\Gamma}{J} r \phi_\eta \right) \\ &+ [J S(\xi, \eta) - \frac{\partial}{\partial \xi} \left( \frac{\Gamma}{J} \beta \phi_\eta \right) - \frac{\partial}{\partial \eta} \left( \frac{\Gamma}{J} \beta \phi_\xi \right)] \end{aligned} \quad (12)$$

where

$$U = u y_\eta - v x_\eta \quad V = v x_\xi - u y_\xi$$

## 2.5 Characteristic of the Flow Field

By varying the Re number ( $Re=U_z z_r/\nu$ ) and the shear intensity of the incoming flow, the paper investigated the flow patterns around the railway line embankment. By introducing K -  $\epsilon$  model, the paper calculated the distribution of friction velocity ( $u^*=\sqrt{\frac{\tau_w}{\rho}}$ ) and pressure coefficient ( $C_p=(p_1-p_a)/\rho U_z^2/2$ ,  $P_a$  is the static atmospheric pressure) along the surface of the standard and the eroded embankment at high Re number.

From the numerical results obtained in this paper, we got the following conclusions:

- (1) The influences of the incoming flow Reynolds number on the flow field around the embankment are quite obvious. The recirculating zone behind the embankment enlarges with the increase of the Reynolds number, and the flow pattern in it becomes more and more complicated. The negative pressure and the friction velocity on the wall of the windward side increase accordingly. Therefore, the Reynolds simulation in the experiment should be satisfied as well as possible. See Fig 3,4,5.
- (2) The flow field tends to be unstable as the shear intensity of the incoming flow increased, accompanied with the occurrence of the complicated vortex structure. The distribution and the amplitude of the pressure and friction velocity on the wall are quite different at varied shear intensity. Therefore, care should be taken to simulate the shear intensity of the incoming flow in the experiment. See Fig 6,7.
- (3) The aerodynamic characteristics of eroded embankment becomes much better than that of the standard one. The recirculating zone near the foot of windward side disappears. There is a sharp peak area of negative pressure coefficient and friction velocity on the shoulder of the windward side of the embankment. It indicates that the shoulder part is more susceptible to erosion and the shoulder part is the major place for protection in the engineering. When the incoming wind speed is about 20m/s ( $Re = 10^7$ ), for the standard embankment,  $C_{p_{min}}=-2.85$ ,  $u_{max}^*=2.46$ . As for the eroded embankment, the distribution of the pressure and shear stress becomes smooth and even.  $C_{p_{min}}=-1.96$ ,  $u_{max}^*=1.91$ , the maximum negative pressure and friction velocity near the shoulder reduce approximately by 30% and 20% compared with that of the standard one. This explains partly why the erosion-starting wind speed increases for the eroded embankment. See Fig 8,9.

## 3. Conclusion

Starting from the Reynolds-averaged N-S equation, closed with the K -  $\epsilon$  model for turbulent case, the paper investigated the properties of the flow field at different Re number and shear intensity  $\alpha$  of the incoming flow. As the Re and  $\alpha$  increase, the flow patterns become quite different. Therefore, the Re number and the value of  $\alpha$  should be simulated as well as possible in the experiment. The aerodynamic characteristic of the eroded embankment becomes much better than that of the standard one.

An effective two-step procedure to generate orthogonal body-fitted coordinate systems is proposed in this paper.

With the aid of the analysis of the mechanism of the wind-induced erosion [6], the present work forms the basis for the determination of the erosion-starting wind speed, for the determination of the protection region, and for the prediction of the stable erosion profile from the properties of the flow field.

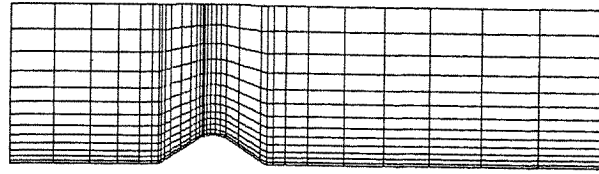
## Acknowledgements

This work was supported in part by the National Natural Science Foundation of China.

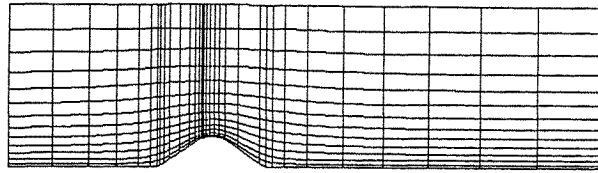
## References

1. Zhao Hongbin, Zhang Boyin, Wan Hou Xong, Nie Xongyuan etc., Investigation of the Mechanism of Wind-Induced Erosion and Deposit of Railway line Embankment in Windy and Sandy District, Beijing, 1992.
2. S. V. Patankar, Numerical Heat Transfer and Fluid Flow, Hemisphere, Washington, D. C. 1980.
3. W. Shyy, S. S. Tong, and S. M. Corra, Numerical Recirculating Flow Calculation Using A Body-Fitted Coordinate System, Numerical Heat Transfer, Vol.8, PP.99-113, 1985.

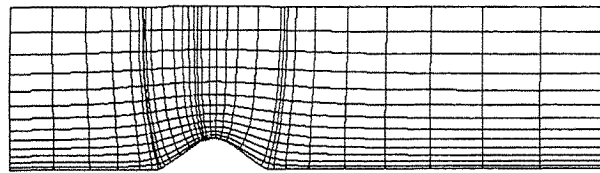
4. Z.U. A. Warsi and J. F. Thompson, Mssu-EIRS-ASE-77-1, Mississippi State Univ., 1976.
5. R. A. Graves and H. H. Hamilton II, AIAA J. 19(1981), 2
6. Zhang Jianbo, Cui Erjie, Fu Guangming, Investigation of the Mechanism of Wind-Induced Erosion and Deposit of Railway line Embankment in Windy District, <<Development and Application of the Research in Structural Wind Engineering>>, 1993.



1-a Initial grid



1-b Body-fitted grid



1-c Orthogonal grid

Fig.1 Grid generation process

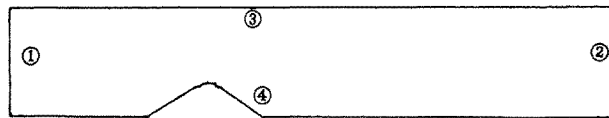


Fig.2 Computation domain

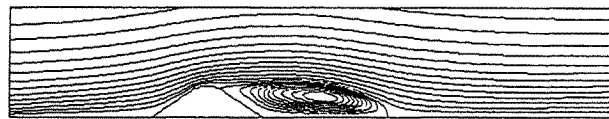


Fig.3 Streamline for the standard embankment  
 $Re=10^2$ ,  $\alpha=0.113$



Fig.4 Streamline for the standard embankment  
 $Re=10^3$ ,  $\alpha=0.113$



Fig.5 Streamline for the standard embankment  
 $Re=5 \times 10^3$ ,  $\alpha=0.113$



Fig.6 Streamline for the standard embankment  
 $Re=10^3$ ,  $\alpha=0.0$



Fig.7 Streamline for the standard embankment  
 $Re=10^3$ ,  $\alpha=0.2$

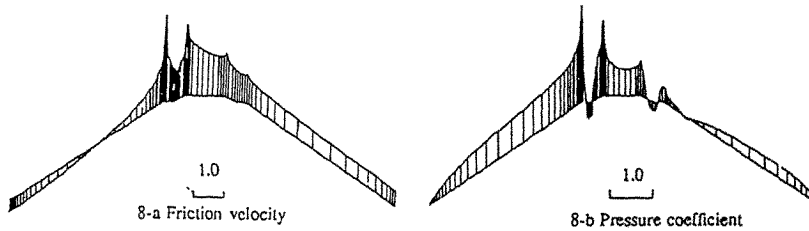


Fig.8 Standard embankment  
 $Re=10^7$ ,  $\alpha=0.113$

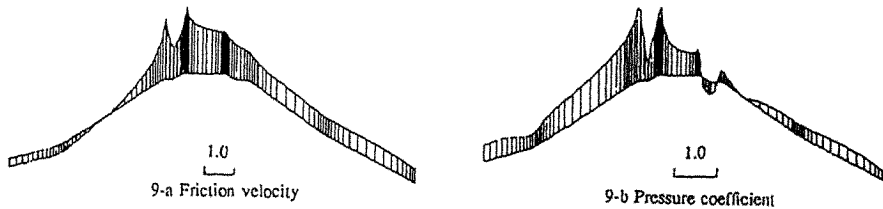


Fig.9 Eroded embankment  
 $Re=10^7$ ,  $\alpha=0.113$

## **Study on the numerical method for surrounding flow field of coaches**

**G. Y. Gong; Y. S. Chen; Q. F. Li and L. Gao**

**Xi'an Highway Transportation University**

**Abstract:** In order to better the aerodynamic performances of China — made coaches and reduce their air resistance, we, while conducting aeronautical wind — tunnel experiments, have studied the numerical method for surrounding flow field of coaches. With the help of the theory of potential flow, we have established an analog numerical method for coach surface pressure distribution — first order panel method. The comparison of the calculation and experiments indicates that the two results can go well with each other in the area where no air draft division takes place.

### **1. Introduction**

With the rapid development of high — grade highway construction in China in recent years, the running conditions for China — made vehicles have been greatly improved, and consequently their speed has also been raised. The air resistance, undoubtedly, has become greater in this process. We have studied the numerical method for surrounding flow field of coaches. On the basis of the above studies, we have set up an estimation method for evaluating the partial changes of coach contour on the influence of aerodynamic performances. This method is very useful for sampling work at the early stage of plastic design of coach bodies.

### **2. The calculation for the surface pressure distribution of coach bodies**

#### **2.1 The simplification of flow field**

As coaches do not run at very high speed, since they have a gentle contour and their air draft division is small, the air flow on the most surface can be taken as laminar flow and the smaller amount of displacement thickness of the approaching surface can be neglected. Therefore, the surrounding flow field can be approximately used as displacement flow, and the mirror — image method is

used as ground effect imitation. Here, the very thin box—like shape covering the wake vortex takes the place of the wake and the body length is taken from its basic point.

## 2.2 The steps of calculation

On the basis of the potential flow theory, this study has established an analog numerical method for coach surface pressure distribution—first order panel method. This numerical method is used to work out the equation “Laplace”,

eg. 
$$\frac{\partial^2 \varphi}{\partial x^2} + \frac{\partial^2 \varphi}{\partial y^2} + \frac{\partial^2 \varphi}{\partial z^2} = 0 \quad (1)$$

That is, we divide the surface into definite panels. On each panel, the first order panel approximately replaces the original surface and singular points are arranged on each panel ( source, vortex and dipol ). The iteration of interference flow field from the singular points and the flow from the distant front approximately imitates the actual flow field. After the singular point intensity has been obtained through a set of boundary conditions, we can get the distribution of velocity flow field and pressure distribution and then the resultant forces and its matrix exerted on the object.

There are five steps in the calculation:

Paneling of the coach body surface;

Calculating the geometric quantity of all the panels;

Calculating the induced velocity potential from each source intensity and setting up influence coefficient matrix formula through boundary conditions

Working out influence coefficient matrix formula to get source intensity

Calculating aerodynamic parameter of the coach body, e. g. pressure intensity coefficient  $C_p$ , velocity  $V$ , resultant force  $F$  and resultant force matrix  $M$

## 2.3 The establishment of mathematical model of coach body surface

The coach body is simple in contour. On the basis of the three—dimensional formation of coach body contour and surface division put forward by Tang Zi—qing, we have established another convenient and method for rapidly imitating three—dimensional coach body contour. With this method we ensure a high precision of imitation only through a proper division of longitudinal spline. The longitudinal spline line is imitated by the least—squares method of cubic spline, and the cross section is imitated by the mixture of circular arc, ellipse arc and straight lines.

## 2.4 The formation of aerodynamic influence coefficient matrix

In this study we choose source singular point as the basic method to solve the equation. So (1) becomes:



$$\bar{V}_\infty \bar{n}(q) + grad[-\frac{1}{\pi} \oint_{S_B} \frac{\sigma(S_B)}{r} ds_B] \cdot \bar{n}(q) = 0 \quad (2)$$

In this equation,  $\sigma(S_B)$  is the partial source intensity on the coach body surface.

$q$  is the arbitrary point of the coach body surface.  
 $\bar{n}(q)$  is the outer normal line vector of Q point.

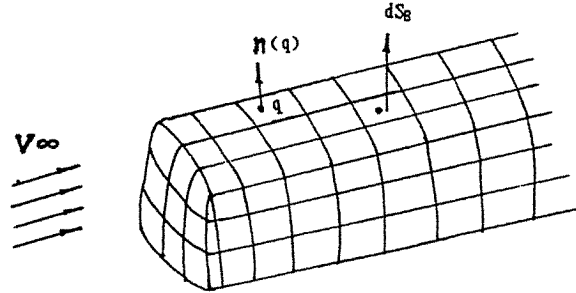


Fig. 1 Dispersion of Body Surface

If there are M quadrilateral panels that can replace the body surface ( Fig. 1 ) and the source on each panel has a constant distribution, ( 2 ) becomes:

$$\sum_{j=1}^m \frac{\sigma_j}{4\pi V_\infty} [(- grad \oint_{S_B} \frac{1}{r} ds_j) \cdot \bar{n}(q)] = \frac{V_\infty \bar{n}(q)}{V_\infty} \quad (3)$$

We can introduce:

$$X_j = \frac{\sigma_j}{4\pi V_\infty}$$

$$A_{qj} = (- grad \oint_{S_j} \frac{1}{r} ds_j) \cdot \bar{n}(q)$$

$$R_q = \frac{V_\infty \bar{n}(q)}{V_\infty}$$

Here ( 3 ) can be rewritten:

$$\sum_{j=1}^m X_j A_{qj} = R_q \quad (4)$$

If we can repeatedly use the controlling point of M panels, we can get a linear equation of -m:

$$AX = R \quad (5)$$

which will influence coefficient matrix equation.

2.5 The solution of influence coefficient matrix equation and the calculation of aerodynamic performances

The quantity of influence coefficient matrix equation completely depends on the number of panels that replaces the coach body surface. As the number

of panels should not be smaller than 500 on such a complex surface of coach bodies, it is better to use the iteration method suggested by Gauss when we work out matrix equation.

By working out influence coefficient matrix equation, we can get the source intensity of all the panels. Here is the formula for calculating air flow velocity on any point of the body surface:

$$\bar{V}_i = \bar{V}_i \infty + \sum_{k=1}^m V_{ij} \sigma_j \quad (6)$$

The pressure intensity coefficient is:

$$C_{p_i} = 1 - V_i^2 \quad (7)$$

If the pressure intensity on each panel is constant, it is:

$$F_i = \bar{n}_i C_{p_i} S_i \quad \bar{F} = \sum_{i=1}^m \bar{F}_i \quad (8)$$

Here  $\bar{n}_i$  is the unit vector of the panel, and  $S_i$  is the area of the panel.

### 3. The wind—tunnel experiment of coach models

#### 3.1 The design of coach modls

In order to testify the correctness and application scope of the calculated models of the surface pressure distribution for the three—dimensional coach body, we have divided two ideal models 1#k and 2#k with differnt front plastics. Only the coach body part has been designed for the two models, no other parts. We have also made use of JS6120 coach designed and produced by Yang Zhou Coach Factory for further testification. All these models were used to carry out force and pressure tests in the low—speed wind—tunnel lab.

The model is installed on the wind—tunnel support. There is a fixed board with an opening—seam sucking air device, which can imitates the ground effect. ( The support interference is eleminated by “Separating Support Method”). During the experiment, we mainly tested aerodynamics and aerodynamic matrix of the model coach JS6120 and also made pressure testing experiments on some other ideal models, in which 184 pressure testing points were arranged on the surface of these models.

3.3 The comparison of results between the experiments and calculation medium—sized computer Seimen—7507C in my university. Through the comparison of the results between the calculation and wind—tunnel test of the ideal models 1#k and 2#k, we can find that most areas studied go well with one another except the front corner and tail part on the 1#k model's longitudinal section. On the horizational section and the cross section, the error area mainly appears on the surrounding corners ( Fig. 2 ). The final results of the idel models 2#k and 1

#k are basically the same but 1#k is, on the whole, better than 2#k.

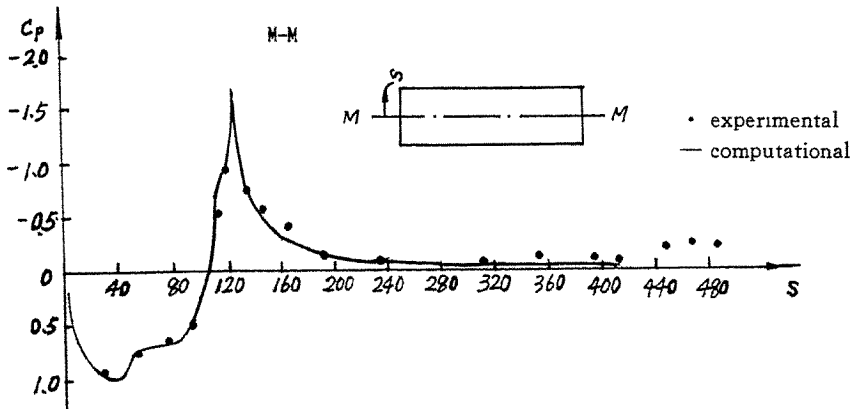


Fig. 2

#### 4. The approximate estimation of aerodynamic resistance of coaches

In order to compare the different front plastics with its influence on the aerodynamic performances during the early stage of plastic design, we have simplified the surrounding flow field to two-dimensional flow and set up an estimation method for evaluating the changes between the inclination angle  $\theta$  of the front wind screen and angularity  $R$  from the front wind screen to the front top of the coach. This method was developed on the following thoughts. First we take the pressure value that approaches the rear part of body surface as rear pressure value. Second, we can correct the pressure value on the longitudinally symmetric surfaces which is obtained from the theoretical calculation. That is, the pressure coefficient from the front part is multiplied by the corrected coefficient  $C_T$  ( $C_T$  can be got with the experiential formula). By formula (8), we can work out the approximate resistance of the coaches.

$C_T$  is the function of inclination angle of the front wind screen and angularity  $R$  from the front wind screen to the front top of the coach. According to the results of the theoretical calculation and experiment done, we can get the following formulas through imitation:

$$C_T = C(R) \cdot C(\theta) \quad (9)$$

Here:

$$C(R) = a_0 + a_1R + a_2R^2 + a_3R^3 \quad (10)$$

$$C(R) = b_0 + b_1R + b_2R^2 \quad (11)$$

$$C(\theta) = C_0 + C_1\theta + C_2\theta^2 \quad (12)$$

(10) is only used when  $R < 50\text{mm}$  or  $R > 100\text{mm}$

(11) is only used when  $50 \leq R \leq 100$

The coefficients of the above formulas are:

$$a_0 = 0.3586 \quad a_1 = -1.7024\text{E}-3 \quad a_2 = 2.8165\text{E}-5 \quad a_3 = -6.822\text{E}$$

-8

$$b_0 = 0.2154 \quad b_1 = 2.5364\text{E}-3 \quad b_2 = -3.464\text{E}-4$$

$$c_0 = 0.5992 \quad c_1 = 4.1392\text{E}-2 \quad C_2 = -8.2107\text{E}-4$$

## 5. Conclusion

5.1 With the development of high-grade highway, especially the construction and wide use of freeway in China, it is high time we studied automobile aerodynamics, but the present conditions of wind-tunnel experiments in China are still poor. So it is necessary for us to carry out the research for calculating automobile surrounding flow field.

5.2 According to the calculation model established by potential flow theory, we can work out the pressure distribution of three-dimensional coach body surface, and this calculation is comparatively correct even to most of the surfaces of no air draft division.

5.3 Our method still has its shortcomings as we cannot imitate air draft division in the front part, surrounding corners, the rear part and the part where wind cannot approach.

5.4 The coach JS6120 manufactured by Yang Zhou Coach Factory is the typical model for city touring (box-like shape, plane wind-screen glass). Therefore, the numerical method for the aerodynamic performances from the wind-tunnel experiments of this kind of coach can be used at the early stage of coach plastic design for the similar ones. By it, we can estimate the changes of inclination angle  $\theta$  of the front wind screen and angularity  $R$  from the front wind screen to the front top on the influence of aerodynamic performances.

## References:

1. C. Bertar, T. Tacea and A. Zucchelli, Aerodynamic study on Vehicle shape with the "Panel Method" SAE 801401.
2. Harijono Djodjodindjo, Development of Aerodynamic computation Routine for Road Vehicles Using Panel Method, SAE 830891.
3. C. Y. Gong, Q. F. Li, Reseach and Development of Atomotive Air Dynamics numerical methods Autotive Researching Vol 11 No3 sep 1992.

## 100 PASSENGER AIR FOIL CRAFT TYPE AF-2

Hu An-ding

Marine Design & Research Institute of  
China, China

**Abstract:** Based on using wing energy to develop the aerodynamic transport systems, an air foil craft is a new-type of amphibian wing-in-ground effect (WIG) craft with a powered air cushion as the take off/landing system. Since the powered air cushion system provides wonderful amphibious and manoeuvrable capability, it can be operated on shallow waterways, frozen surface as well as on uneven ground and grassland. With high lift drag ratios and a rather high cruising speed, these new vehicle should be possible to accomplish the desired mission with good transport efficiency and high productivity. It is characterized by its safe, high speed, energy-saving and comfort in riding. This kind of high speed vehicle will find its wide and prospective applications both in military and civil use.

Following the success of the two-seat air foil craft type 750 in 1987, a larger 20 passenger air foil craft type AF-1 is being built since 1991. This craft can be widely used as a passenger fast ferry, tourist craft, coastal rescue craft, revenue cutter etc. This paper presents a project of 100 passenger air foil craft type AF-2 with its aerodynamic configuration, main technical performance, take-off performance, model test results in wind-tunnel and power plant.

### 1. Introduction

In the mid of 70's, on the basis of the WIG and PAR concepts, the authors of this paper made many of theoretical calculations, wind-tunnel model tests and radio controlled model tests. A two-seat amphibian WIG craft called "air foil craft type 750" was completed and tested in 1987. The technical key problems such as the take-off and landing system, the transition phase from hull borne operation to cushion borne operation and thus to WIG flying operation,

longitudinal and transverse stability on WIG operation, jetstream source used for creating a powered air cushion, an extra-light fuselage and wing structure had be solved. The air foil craft type 750 was operated successfully on uneven grassland at low speed (Fig 1). A larger 20 passenger air foil craft type AF-1 was produced since June 1991.

With its high speed, energy-saving, safe and comfortable performance, the 100 passenger air foil craft type AF-2 (Fig 2) should be possible to operate with good transport efficiency and high productivity.

## 2. Aerodynamic Configuration

A special configuration for the air foil craft type AF-2 has been used, which is composed of two air tunnels mounted at the ends of the main wing and a high trail wing. A reasonable arrangement of main wing, air tunnel, trail wing, ducted thruster and the centre of gravity of the craft is most important for the longitudinal stability of the craft flying on WIG mode. A restoring moment offered by two air tunnels gave the craft a good transverse stability. Figure 5 shows the running attitude of the air foil craft type AF-2.

## 3. Main Technical Performance

### (1) Dimensions

Length overall	32.0 m
Beam overall	18.0 m
Height overall	8.0 m

### (2) Weight

Max. take-off wight	45 t
---------------------	------

### (3) Performance

Speed max.	240 km/h
Range	800 km

Seakeeping capability. This craft can be operated stably in force seven gust wind and a wave height  $H_{1/3}$  of 2.5 m.

Amphibious capability

The craft can:

- . Take-off on ground and then run onto water surface.
- . Land from water surface and then run onto ground.
- . Operate on rough ground surface and grassland.

#### Anti-capsizing capability

It can meet the requirement of one compartment floodability.

(4) Passengers 100

(5) Hull

A major proportion of the air foil craft structure will be in aluminium alloys with aircraft construction technology.

#### 4. Take-off Performance

The air foil craft type AF-2 is equipped by a powered air cushion as the take-off/landing system. While manoeuvring at low speeds, during take-off and while operating through hump speed, two forward ducted-thrusters are installed to direct their efflux downward into the air duct formed by the top wing under-surface, floats, trailing edge flaps and the water or other supporting surfaces. They create a powered air cushion, so that within a short distance the air foil craft will be lifted out of the water. The craft can take-off/land at low speeds. The take-off speed is about 80 km/h with take-off time about 30 sec, take-off distance about 560 m. Figure 3 shows the take-off course of the air foil craft type AF-2.

Operation state	Time (sec)	Engine operation		Flap angle ( $\theta_f$ )	Speed (km/h)	Distance (m)
		forward	rear			
float	/	/	/	0	0	/
static hover	0	rated power	/	$[\theta_f]_{max}$	0	0
hump speed	10	rated power	rated power	$[\theta_f]_{max}$	50	80
take-off	30	rated power	rated power	$\frac{1}{2} \theta_f$	80	560
cruising	100	0.5 rated power	0.85 rated power	0	210	2700

Table 1. The take-off performance of the craft

#### 5. The Craft Model Test Results in Wing-Tunnel

Wind-tunnel tests have been carried out to determine the aerodynamic characteristics of the air foil craft type AF-2. The test models were of wood with coating paint. The model tests were carried out at the Wind-tunnel Laboratory of MARIC. Figure 4 shows the model test at wind-tunnel. Figure 5 shows lift coefficient

versus the angle of attack of craft model. Figure 6 shows the drag coefficient versus the angle of attack of craft model. Figure 7 shows the pitch moment coefficient versus the angle of attack of craft model. Figure 8 shows the lift coefficient versus the flying height of craft model. Figure 9 shows the pressure distribution on the main wing at several flying heights of craft model. Figure 10 shows the comparison of the pressure distribution of test QY14-15 wing profile with Clark-y wing profile.

## 6. Conclusion

The air foil craft with a powered air cushion as the take off/landing system has been under research and development by the author of this paper for nearly a quarter of a century. During this time the author of this paper has carried out a lot of theoretical computations, wind-tunnel tests and radio-controlled model tests. The two-seat air foil craft type 750 was completed in 1985, and over the period March 1985 to June 1987 over 40 trial flights were performed, exploring various operating conditions. The twenty passenger air foil craft type AF-1 as produced since June 1991. Single air duct tests of static cushion lift was carried out in July 1992.

The project of 100 passenger air foil craft type AF-2 satisfies a few of the essential design requirements:

- \* High aerodynamic efficiency both during the take-off mode and during cruise.
- \* Stability throughout the whole range of the air foil craft operation modes: in floating, transient or flight conditions.
- \* Ensuring the required seakeeping qualities.
- \* Marvellous amphibility.

The 100 passenger air foil craft can be used as a high speed passenger transportation in and around the Pearl River Delta in South China. The time for travelling from Shekou to Hong Kong is only about 0.3 hour.

## References

1. Hu An-ding: A Study on the Powered Air Cushion, Journal of Shipbuilding of China, No.1, 1982.
2. Hu An-ding: Development of An Amphibian Wing in Ground Effect Craft, International High-Performance Vehicle



Conference, November 1988 at Shanghai, China.

3. Hu An-ding: On the Aerodynamic Characteristics of Thicker Wings in Ground Effect with End Plates, Journal of Ship-building of China, No.4, 1980.
4. Hu An-ding: Aerodynamic Characteristics of Amphibian Wing-in-Ground Effect Craft, Proceedings of the Second Asia-Pacific Symposium on Wind Engineering, Beijing, China, June 26-29, 1989.
5. Hu An-ding: Pressure distribution on a wing closed to the supporting surface, Proceedings of the third Symposium on Wind Engineering, Nanking, China, August, 1990.



Fig.1 The air foil craft type 750 was running on grassland

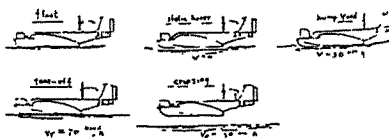


Fig.3 The take-off course of the air foil craft type AF-2

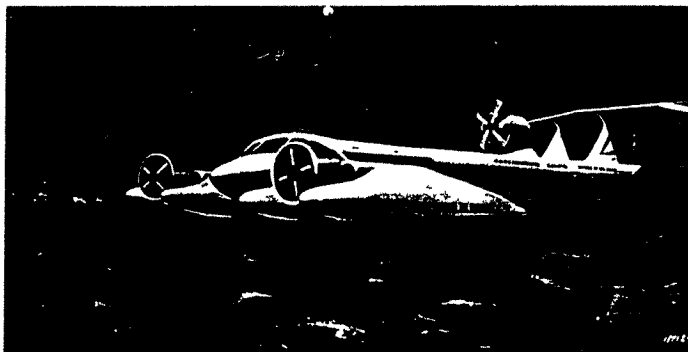


Fig.2 The running attitude of the air foil craft type AF-2

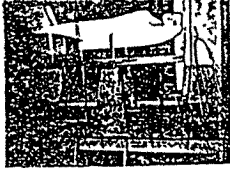


Fig 4 The model test at wind-tunnel

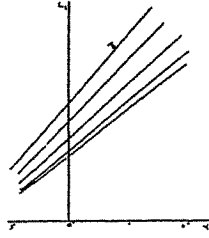


Fig 5 Lift coefficient versus the angle of attack of craft model

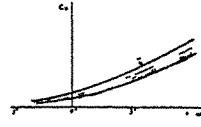


Fig 6 Drag coefficient versus the angle of attack of craft model

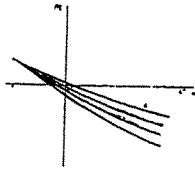


Fig 7 Pitch moment coefficient versus the angle of attack of craft model

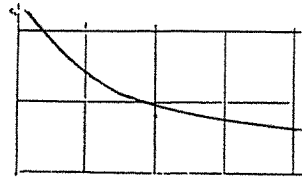


Fig 8 Lift coefficient versus flying height of craft model

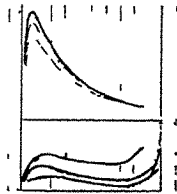


Fig 9 Pressure distribution on the main wing at several flying height

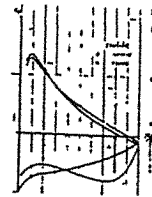


Fig 10 Comparison of test QY14-15 wing profile with clark-y wing profile

## **Wind Breaks, Wind Power and Others**



## Full-scale measurements of the effect of a porous windbreak on wind spectra

G.M. Richardson<sup>†</sup> and P.J. Richards<sup>\*</sup>

<sup>†</sup>Silsoe Research Institute  
Wrest Park, Silsoe, Bedford MK45 4HS U.K.  
<sup>\*</sup>Department of Mechanical Engineering  
University of Auckland  
Private Bag 92019  
Auckland, N.Z.

**Abstract:** Streamwise turbulence spectra in the vicinity of a porous windbreak are presented. These clearly illustrate the effect of a windbreak which reduces the low frequency turbulence in the flow passing through the windbreak but also results in the generation of high frequency turbulence in the flow passing over the windbreak. It is suggested that the frequencies of the generated turbulence are related to the velocity gradients in the region where generation occurs.

### 1. Introduction

Porous windbreaks are used throughout the world to modify the micro-environment. It is generally accepted that such windbreaks can significantly reduce the mean windspeeds but much less is known about their effect on the wind spectra. With some applications, such as the protection of horticultural crops e.g. kiwifruit, there is no benefit in reducing the mean wind if the turbulence is simultaneously increased.

Previously published spectra both from wind-tunnel studies [1] and from the experiments covered by this paper [2] have illustrated the variations in spectra at different streamwise positions but at a common height. This paper will show that greater insight can be obtained by comparing spectra at a range of heights at the same streamwise location.

### 2. Experimental Procedures

As described in greater detail by Richardson [2,3] a 50 m long windbreak was purpose-built for wind pressure and drag measurements on an exposed site at the Silsoe Research Institute. There were no obstructions within 600 m of the face exposed to the prevailing wind.

The windbreak material consisted of vertically spaced 50 mm wide webbing with vertical ties at 1 m intervals resulting in an approximate geometric porosity of 46%. A 1.83 x 1.05 m sample of the webbing was tested in a closed duct manner in the University of Auckland wind-tunnel. The mean velocity in the duct and the pressure drop across the webbing were measured and a pressure loss coefficient  $k = 5.2$  deduced. This relatively high loss coefficient would also be obtained from a round wire mesh screen with a geometric porosity of only 28% [4].

The depth of webbing was 2 m in all experiments but this was positioned between 1 m and 3 m for some tests and between 0 m and 2 m for the remainder. The guyed fence posts were spaced at 4 m intervals with two adjacent posts in the centre of the windbreak equipped with guys connected to load cells for drag measurement. The reference wind total pressure was sensed by a directional pitot tube held into the flow by a vane. The sensor was mounted 15 m to windward of the windbreak with the pitot tube at a height of 3 m and the static pressure sensor 0.3 m higher.

Identical pitot and static sensors were mounted on a mobile mast and measurement made at heights of 3.0, 2.0 and 1.0 m at positions 15 m windward and 10 m and 20 m leeward of the windbreak. Continuous records of one hour duration were made for power spectral analysis. During all tests the mean wind direction was within 30° of perpendicular to the fence.

Continuous recordings of four channels were made simultaneously using a four-channel frequency modulated instrumentation tape recorder. In all cases channels 3 and 4 recorded the electrical analogue of the wind dynamic pressure and reference wind direction respectively.

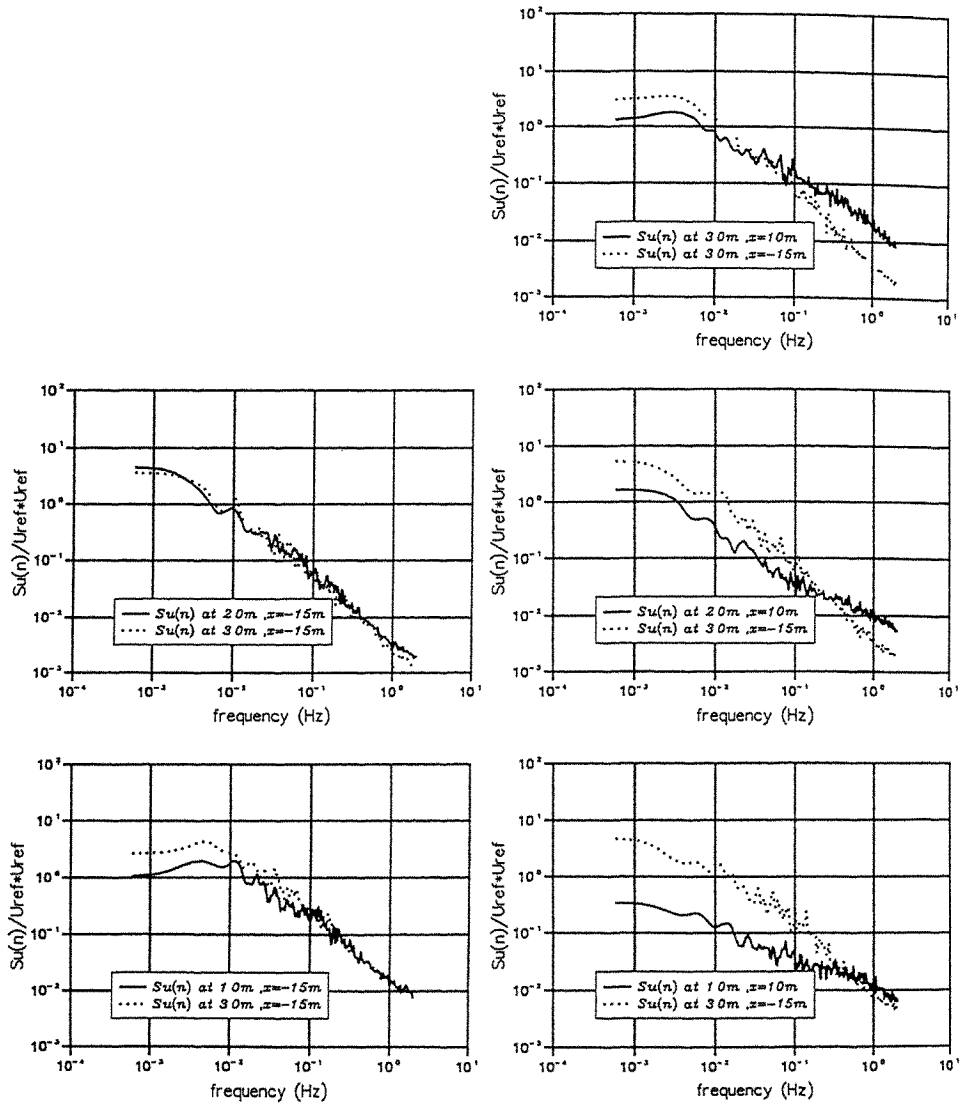


Fig. 1. Streamwise turbulence spectra in the vicinity of a 3m high windbreak (1m gap below the webbing) at positions 15m upstream and 10m downstream of the fence.

Channels 1 and 2 recorded electrical analogues of either drag or local pressure measurements. All these analogue records were later low pass filtered at 10 Hz and digitised at 20 Hz for computer analysis.

Additional measurements of the wind spectra at various heights on the same site but without the windbreak have been made using directional pitot tubes [5] and ultrasonic 3-component anemometers [6].

### 3. Results and Discussion

Fig. 1 shows the streamwise wind spectra 15 m upstream and 10 m downstream of the windbreak in its higher position. In each sub-figure the spectrum at a particular location is shown together with the simultaneously recorded spectrum at the reference point ( $x = -15$  m,  $z = 3.0$  m). For the upstream cases the only noticeable feature is the slightly lower low frequency content at the lowest height ( $z = 1.0$  m). These and other results tend to suggest that the low frequency end of the

spectra scales in proportion to  $\bar{V}(z)^2$ , ie the low frequency components of turbulence are also affected by ground roughness. In contrast the high frequency end of the upstream spectra show little variation with height.

On the right hand side of Fig. 1 the downstream spectra show significant reductions in the low frequency turbulence at all three heights. This reduction is to be expected since as shown in Fig. 2 the spectrum of the drag force on the fence  $S_D(n)$  is closely related to the reference dynamic

pressure spectrum  $S_q(n) \approx \rho^2 \bar{U}^2 S_u(n)$  up to a frequency of approximately 0.1 Hz. The ratio of these spectra (Fig. 2 dashed line) is expected to be related by

$$\frac{S_D(n)}{S_q(n)} = C_D^2 \chi^2(n)$$

where  $C_D$  is the drag coefficient which was measured as 0.93 [3] and  $\chi^2(n)$  is the aerodynamic admittance function.

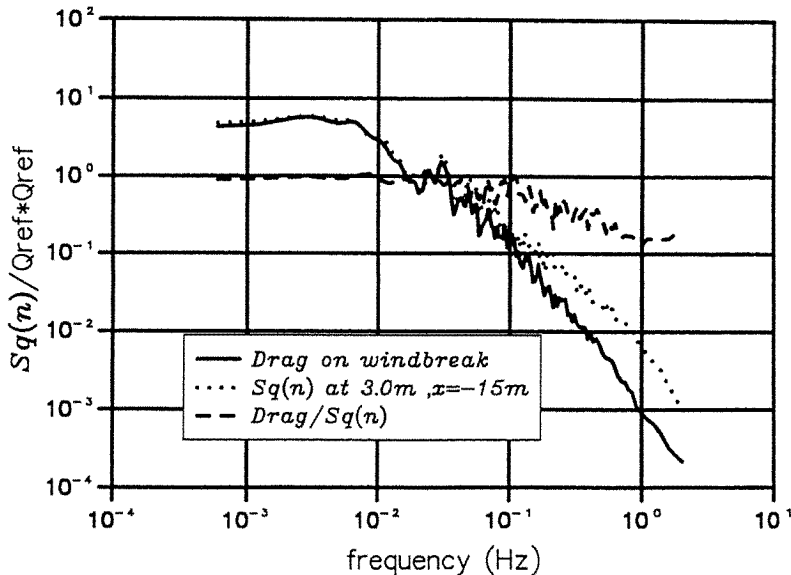


Fig. 2. Windbreak drag and dynamic pressure spectra.

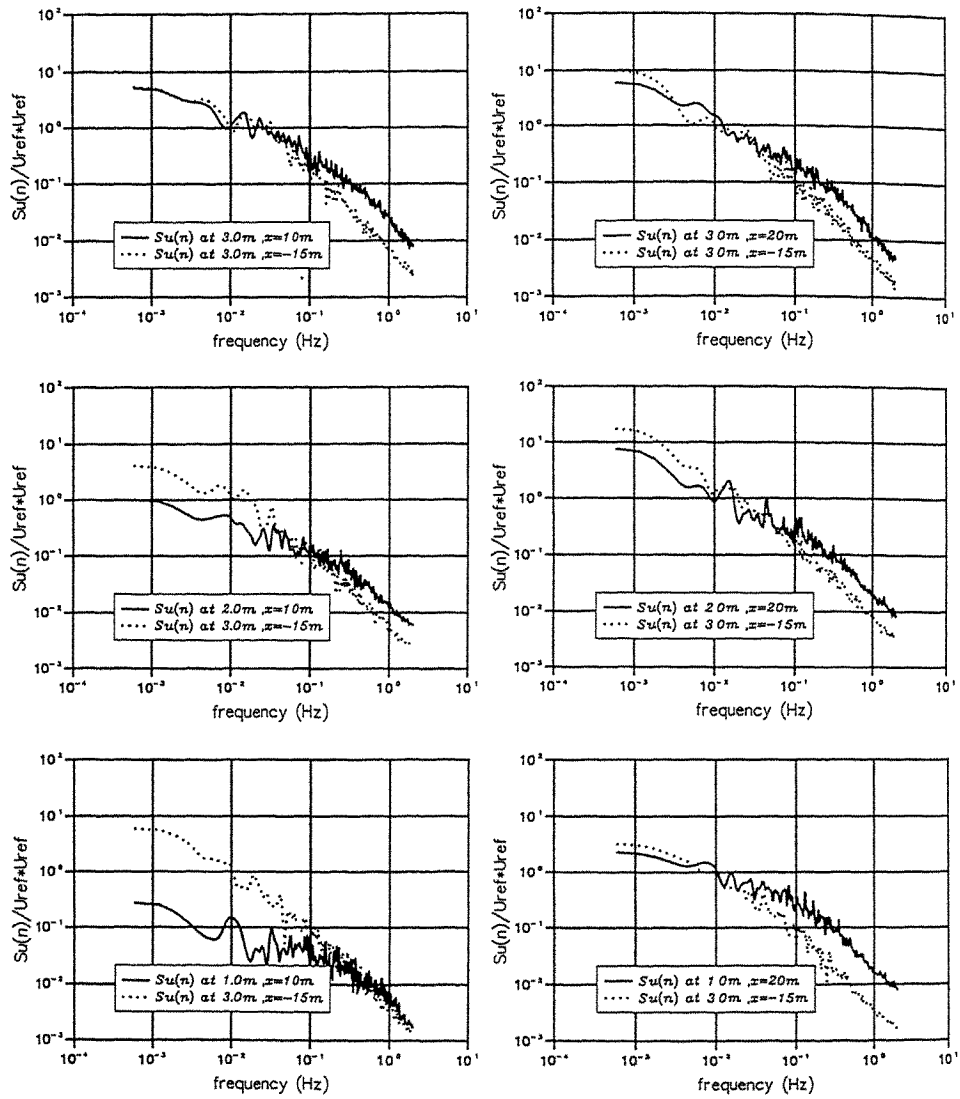


Fig.3. Streamwise turbulence spectra in the vicinity of a 2m high porous windbreak (no gap) at positions 10m and 20m downstream from the fence.



The results of Vickery and Davenport [7] suggest that the admittance function has a value of approximately unity for  $n < \frac{0.2 \bar{U}}{\sqrt{A}}$  and decreasing thereafter. For the windbreak this corresponds to  $n < 0.32$  Hz which is only slightly greater than that observed.

Hence it is not surprising that the fence has reduced the energy in the low frequency fluctuation in a manner similar to its effect on the mean windspeed. However it may also be observed that the presence of the fence has resulted in an increase in the high frequency end of the spectrum, especially at the highest height.

The contrasting effects on the two ends of the spectrum are even clearer in the spectra at 10 m behind the windbreak in its lower position (Fig. 3 left hand side). At the lowest height (half fence height) the low frequency end is significantly reduced while the high frequency end is relatively unaffected. While the inverse effects are observed at the highest height ( $1\frac{1}{2}$  fence heights). Both effects are observed to a certain extent at 2 m which is level with the top of the fence.

The generation of turbulence in the region above the fence can be observed to be most significant at frequencies above 0.03 Hz. Ultra-sonic anemometer measurement of the atmospheric boundary layer on the same site [6] have shown that the Reynolds stress spectrum exhibits the most significant interaction between the mean velocity gradient and the turbulence at a frequency

$$n = 0.15 \frac{d\bar{U}}{dz}$$

and with interactions decreasing to almost nothing at frequencies two orders of magnitude higher or lower than this. This is illustrated in Fig.4 which shows the normalised cospectrum

$$-C_{uw}(n)/(S_u(n) S_w(n))^{1/2}$$

obtained at a height of 1.01 m using an ultra-sonic anemometer. This curve represents the contribution to the Reynolds stress which exists as a proportion of that which could possibly occur with the particular level of turbulence.

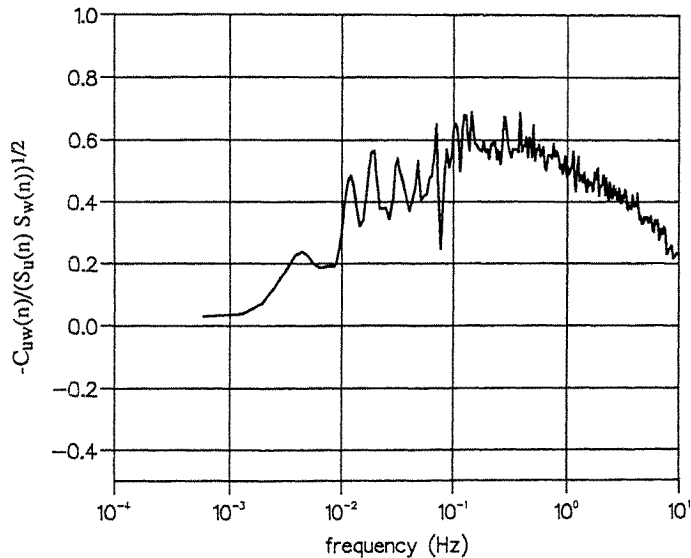


Fig.4. Normalised co-spectrum at a height of 1.01m.

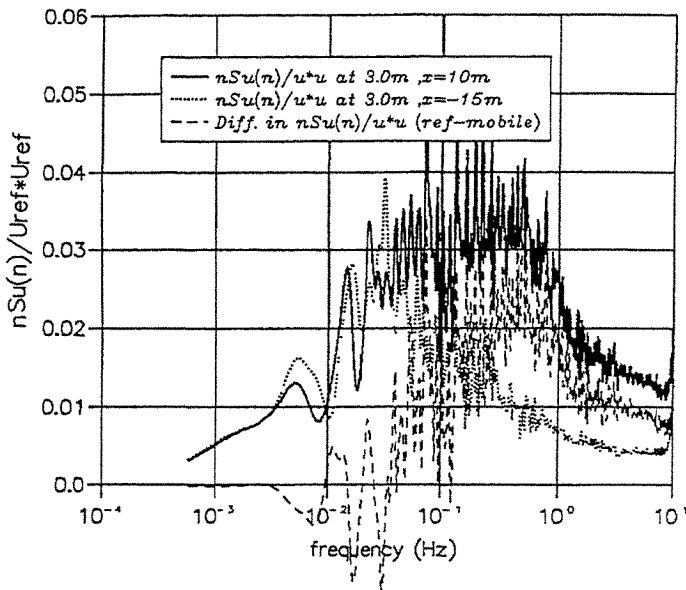


Fig.5. The differences between spectra at a height of 3m.

Applying this concept to the flow over the windbreak we might anticipate that with velocity gradients of the order of 4 m/s/m that generation would occur between frequencies of .006 and 60 Hz with a peak around 0.6 Hz. This general concept is borne out by Fig. 5 which shows the additional energy present at  $z = 3$  m and  $x = 10$  m in comparison to the reference point.

The spectra in the right hand side of Fig. 3 show that further downstream the high frequency turbulence generated in the shear flow above the fence has spread to all levels.

#### 4. Conclusions

The effect of a porous windbreak on the streamwise turbulence spectra has been shown to exhibit two major features. At low level the low frequency end of the spectrum is reduced in a manner related to the reduction in mean velocity. At the same time the shear flow above the fence results in the generation of high frequency turbulence which has a characteristic frequency related to the velocity gradient.

#### References:

1. J.K. Raine and D.C. Stevenson, *J. Wind Eng. Ind. Aerodyn.* 2 (1977) 159-180.
2. G.M. Richardson, *J. Wind Eng. Ind. Aerodyn.* 32 (1989) 101-110.
3. G.M. Richardson, *J. Agric. Eng. Res.* 38 (1987) 65-76.
4. Engineering Sciences Data Unit, ESDU Data Item 72009.
5. R.P. Hoxey and P.J. Richards, *J. Wind Eng. Ind. Aerodyn.* 41-44 (1992) 317-327.
6. R.P. Hoxey and P.J. Richards, *UK Wind Engineering Conf. Cambridge* (1992)
7. B.J. Vickery and A.G. Davenport, *Proc. Int. Res. Sem. on Wind Effects on Buildings and Structures, Ottawa, Canada* (1967) 705-738.

Measurement of the Reynolds Stress structure behind  
the multiple windbreaks across-wind

Bao-Shi Shiau \*,\*\*

\* Department of Harbor and River Engineering  
National Taiwan Ocean University  
Keelung, 20224  
TAIWAN

\*\* Institute of Physics  
Academia Sinica  
Taipei, 11529  
TAIWAN

**Abstract:** In this paper the Reynolds stress structure behind the multiple windbreaks across-wind was measured and investigated. The measurement was carried out in wind tunnel which had a test section of 3 m wide, 2.2 m high and 18.5 m long. A cross-type hot wire was used to obtain the time series of Reynolds stress  $u'w'$  for the flow field behind windbreak. Here  $u'$  and  $w'$  are the streamwise and transversewise velocity fluctuation, respectively. The quadrant analysis theory was applied to analyze the data. By partitioning the stress into ejections, sweeps, inward, and outward interactions, the results show that the Reynolds stress behind the multiple windbreaks across-wind is mostly contributed by the sweep and ejection events. The contributions to the Reynolds stress by the inward and outward interaction events are less and even negative.

### 1. Introduction

In recent decades, many researchers studied the aerodynamics of flow over windbreak or fence [1-6]. Their studies are focused on the flow past solid single windbreak and fence. In reality, multiple windbreaks aligned across-wind is a practical engineering design for wind protection [7].

The turbulence intensity structure behind the multiple windbreaks across-wind has been investigated by Shiau [8]. It is known that the Reynolds stress plays an important role in momentum transport in the flow field. Therefore, in order to understand the flow momentum transport phenomenon behind the windbreak, it is necessary to investigate and analyze the Reynolds stress thoroughly. Shiau [7] indicates that from economic point of view, the selection of 50 % opening ratio arrangement of the multiple windbreak across-wind is preferable. Therefore, in present study, we study the case of opening ratio 50 %. The time series of turbulent velocity behind the windbreak was measured and a quadrant analysis theory is applied to investigate the Reynolds stress structure.

### 2. Experimental Procedures

The experiments were conducted in the boundary layer wind tunnel of the Institute of Physics, Academia Sinica. The tunnel

is an open suction type, which has a free stream velocity range 1-18 m/s. The air passes through a honeycomb and four fine-mesh screens, then goes through a nozzle with 4:1 contraction ratio into the 3 m x 2.2 m test section, and exits through the 16-blade axial fan to the atmosphere. The test section is 18.5 m long.

Measurement of the turbulent velocity was made by using the Kanomax cross-type hot wires (each wire has a length of 2 mm, and a diameter of 5  $\mu\text{m}$ ) in conjunction with a DANTEC 56C01/C17 constant temperature anemometer. The hot wires were calibrated by the use of the TSI 1125 calibrator. The output of the hot wire anemometer was analog signal. The analog signal was digitized through a Metra-Byte DAS-16 12-bit analog-to-digital converter. The digitized data were processed on personal computer.

The windbreak model is a thin rectangular type which has 10 cm high and 7.2 cm wide. They are arranged across-wind with equal space of 7.2 cm. Fig.1 is the schematic diagram of the arrangement of the windbreaks.

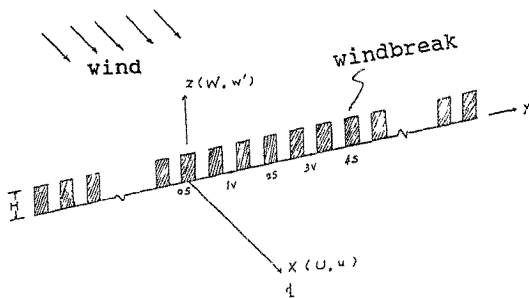


Fig.1 Schematic diagram of the arrangement of the windbreaks

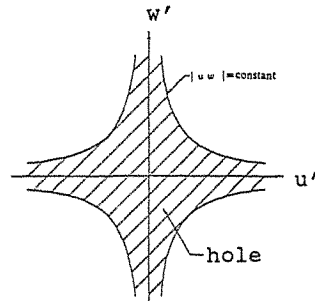


Fig.2 Sketch of the 'hole' region and four quadrants in the  $u'$ ,  $w'$  plane

### 3. Quadrant Analysis Theory

The time averaged value of total Reynolds stress  $\overline{u'w'}$  at a single point can be defined as the sum of contributions from different types of events. The measurements were made with cross-type hot wire at various distance from the wall and different downstream stations from center of windbreak. The  $u'$ ,  $w'$  plane was divided into five regions as shown in Fig.2 [9]. Here  $u'$  and  $w'$  are streamwise and transverswise velocity fluctuations, respectively. In the figure, the cross-hatched region is called a 'hole', and is bounded by the curves  $|u'w'| = \text{constant}$ . The four quadrants excluding the 'hole' are the other four regions. We label the events defined by the four quadrants  $i$  as (1) outward interactions ( $i=1$ ;  $u'>0$ ,  $w'>0$ ), (2) ejections ( $i=2$ ;  $u'<0$ ,  $w'>0$ ), (3) inward interactions ( $i=3$ ,  $u'<0$ ,  $w'<0$ ), and (4) sweeps ( $i=4$ ,  $u'>0$ ,  $w'<0$ ), respectively. The contribution of each event can be calculated by a stress fraction which is defined as:

$$S_{i,H_S} = \left[ \lim_{\tau \rightarrow \infty} \frac{1}{\tau} \left( \int_0^\tau u'(t)w'(t) I_{i,H_S} dt \right) \right] / \overline{u'w'} \quad (1)$$

where the index  $I_{i,H_S}$  is 1 if  $(u',w')$  is in quadrant  $i$  and if

$|u'w'| > H_S |\overline{u'w'}|$ ; otherwise it is 0. Here  $H_S$  is the hole size.

The contribution to Reynolds stress from the 'hole' region is the same definition as equation (1) with  $i=0$  and index  $I_{i,H_S}$  is 1 if  $|u'w'| \leq H_S |\overline{u'w'}|$ ; otherwise it is zero.

The total sum of the stress fraction for four events and hole region equals one. Furthermore,

$$S_{1,0} + S_{2,0} + S_{3,0} + S_{4,0} = 1 \quad (2)$$

since the hole region vanished when  $H_S=0$ .

#### 4. Results and Discussion

##### (1) Correlation coefficient distribution

The correlation coefficient is defined as

$$R = \frac{\overline{-u'w'}}{(\tilde{u} \tilde{w})} \quad (3)$$

where  $\overline{-u'w'}$  is the total Reynolds stress and  $\tilde{u}$ , and  $\tilde{w}$  are the root square of streamwise and transverse velocity fluctuation, respectively. The correlation coefficients at various heights and different downstream locations are show in Fig.3. The coefficients are in the range of 0.3 to 0.55. Lu & Willmarth [9] studied the whole turbulent boundary layer and obtained an averaged value of 0.44. And Raupach [10] get a value in the range of 0.4 to 0.53 for smooth-wall to rough-wall turbulent boundary layers. The turbulent boundary layer over a windbreak had be disturbed, therefore, the correlation coefficient of the Reynolds stress of present study is somewhat different from that of the undisturbed turbulent boundary layer.

##### (2) Joint probability density distribution

The joint probability density function of the product  $u'w'$  is

$$P(u_1, u_2) = \frac{1}{2(1-R^2)^{1/2}} \exp\left\{ \frac{-1}{2(1-R^2)} (u_1^2 - 2R u_1 u_2 + u_2^2) \right\} \quad (4)$$

where  $u_1 = u'/\tilde{u}$ ,  $u_2 = w'/\tilde{w}$  and  $R$  is correlation coefficient. The probability density distribution of the normalized  $u'w'/\tilde{u}\tilde{w}$  for

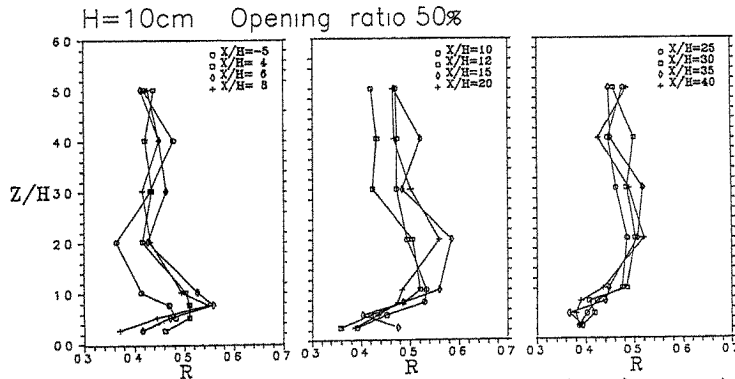


Fig.3 The correlation coefficient distributions at various downstream stations

a turbulent boundary layer is derived by Lu & Willmarth [11] which is shown as

$$\beta(u'w'/\tilde{u}'\tilde{w}') = \frac{1}{\pi} \frac{R}{(1-R^2)^{1/2}} \exp\left(\frac{R^2 u'w'/\tilde{u}'\tilde{w}'}{1-R^2}\right) K_0\left(\frac{R u'w'/\tilde{u}'\tilde{w}'}{1-R^2}\right) \quad (5)$$

where  $K_0$  is the zero-order K Bessel function.

Fig.4 shows the probability distribution of the  $u'w'$  signals at  $Z/H=0.5, 1.0$ , and  $X/H=6, 10, 20$ . Here  $Z$  is the distance from the ground;  $H$  is the windbreak height;  $X$  is the downstream distance from the windbreak. The equation (5) is also included in Fig.4. Due to windbreaks which disturb the turbulent boundary layer, the measured results has a deviation from equation (5).

### (3) Contributions to Reynolds stress from different events

By using the quadrant analysis theory, we can understand better the nature of contributions to Reynolds stress from different events. The Reynolds stress fraction profiles for hole size  $H_S=0$  at various downstream stations are plotted and shown in Fig.5. The results clearly exhibit that sweep events ( $S_4$ ) and ejection events ( $S_2$ ) are dominant contributions to the Reynolds stress. Since  $S_4 + S_2$  exceeds one, and according to equation (2), the excess of the Reynolds stress leaves for  $S_1$  and  $S_3$ . The inward and outward interaction events ( $S_3$  and  $S_1$ ) thereafter become negative contributors to the Reynolds stress. The stress fraction difference between the sweep and ejection events ( $S_4-S_1$ ) for  $Z/H < 1$  is larger at near downstream station and become small at a far downstream station. This implies that sweep events dominate the Reynolds stress at a location near the windbreak.

The stress fraction versus hole size at  $Z/H=0.5, 1.0$  for various downstream stations are shown in Fig.6. We can see that  $S_2, S_4$  are large and  $S_1, S_3$  are negative, when  $H_S=0$ . But with the increase of hole size, stress fraction,  $S_1, S_2, S_3$ , and  $S_4$ , would

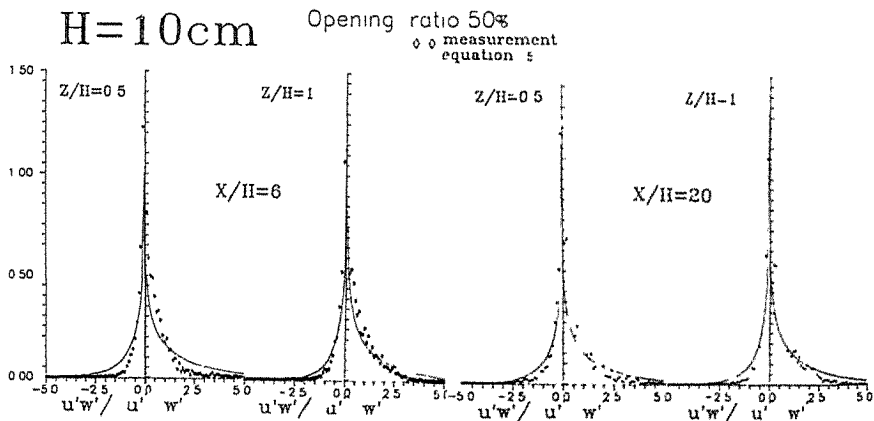


Fig.4 The probability distribution of  $u'w'$

be decreased; and hole region stress fraction,  $S_0$ , increases. It is seen that at near location of windbreak ( $Z/H=0.5$ ,  $X/H=6$ ), when hole size becomes large (e.g.  $H_s=3.0$ ), the stress fractions  $S_1$ ,  $S_2$ , and  $S_3$  approach zero; but the hole region and sweep events fraction,  $S_0$ , and  $S_4$  still dominate the contributions to the local Reynolds stress.

The above results and discussions exhibit that the ejection and sweep events are the most dominant contributors to the

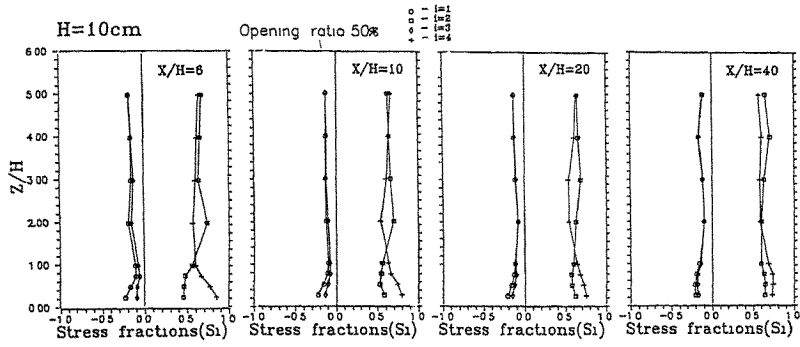


Fig.5 The Reynolds stress fraction profiles at various downstream stations

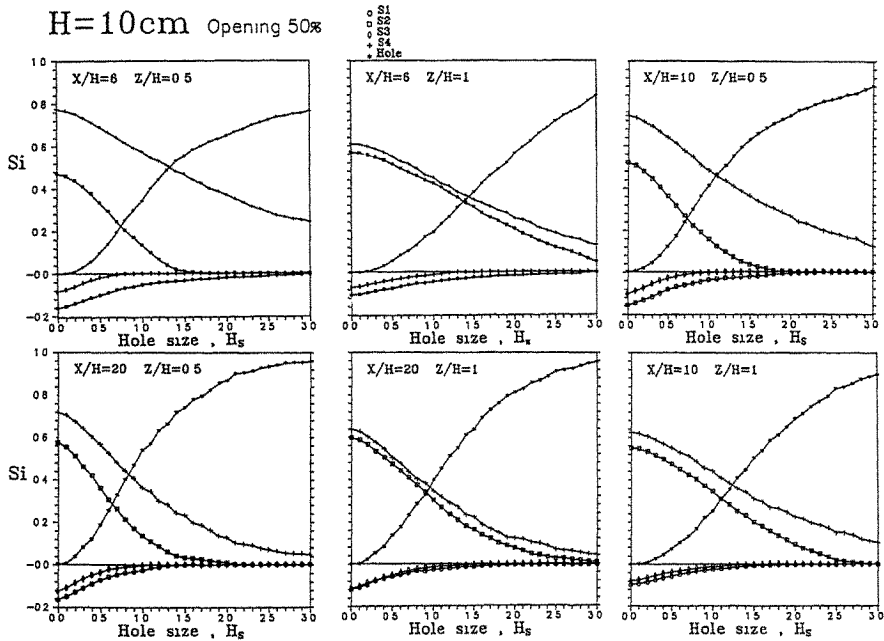


Fig.6 The Reynolds stress fraction versus hole size

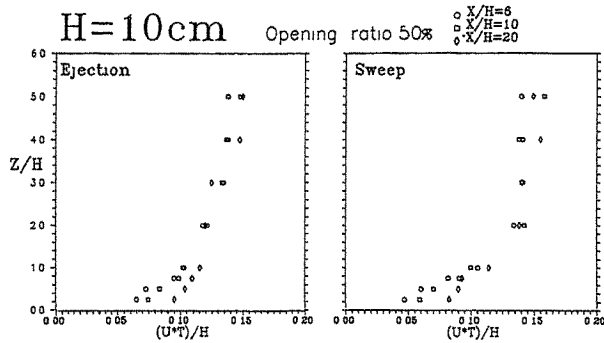


Fig.7 The mean period profiles of ejection and sweep events

Reynolds stress. And the mean period,  $T$ , of the occurrence of these events for  $H_g=1$  at various distance and downstream stations are shown in Fig.7. The mean period of time of sweep and ejection events increase for a far downstream station at  $Z/H < 1$ . When  $Z/H > 4$ , the mean period of sweep and ejection events,  $UT/H$  is about 0.15. Here  $U$  is the local mean wind speed.

### 5. Conclusion

The Reynolds stress structure behind the multiple windbreaks across-wind with 50 % opening ratio is investigated. The quadrant analysis theory is applied to analyze the measured Reynolds stress time series. The contributions to Reynolds stress is partitioning into outward interaction, ejection, inward interaction, and sweep events. The results indicate that the sweep and ejection events contribute mostly to the Reynolds stress behind the windbreak. And the inward and outward interaction events are negative contributions to the Reynolds stress. Also at a near location behind the windbreak, sweep events play an dominant role in the contribution of the Reynolds stress.

### References:

1. E.J. Plate, *Agricultural Meteorology*, 8 (1971) 203.
2. J.D. Wilson, *J. Wind Eng. Ind. Aerodyn.*, 21 (1985) 119.
3. I.P. Castro, *J. Fluid Mech.*, 93 (1979) 631.
4. J. Counihan, J.C.R. Hunt, and P.S. Jackson, *J. Fluid Mech.*, 64 (1974) 529
5. A.R. Borges and D.X. Viegas, *J. Wind Eng. Ind. Aerodyn.*, 29 (1988) 145
6. I. Seginer, *Boundary layer Meteorology*, 9 (1975) 133.
7. B.S. Shiau, *J. Wind Eng. Ind. Aerodyn.*, (1993). (In Press)
8. B.S. Shiau, *J. Wind Eng. Ind. Aerodyn.*, 41 (1992) 461.
9. S.S. Lu and W.W. Willmarth, *J. Fluid Mech.*, 60 (1973) 481.
10. M. R. Raupach, *J. Fluid Mech.*, 108 (1981) 363.
11. S.S. Lu and W.W. Willmarth, Dept. Aerospace Eng., University of Michigan, ORA Rept. 021490-2-T, (1972)



**MODELLING THE FLOW FIELD AROUND WINDBREAKS  
WITH SURFACE VORTICITY METHOD**

C R. Chou, John Z Yim and C C Yu+

Department of River & Harbour Engineering  
National Taiwan Ocean University  
Keelung, Taiwan R O C  
+Bureau of Harbour Administration  
Taichung Harbour, Taichung  
Taiwan, R O C

**Abstract:** Stability of a mooring ship in harbour can be greatly endangered by wind action. Warehouses, when properly designed, could be used as windbreaks which shelter marine vehicles efficiently. The velocity distributions at the rear of a windbreak were studied both numerically and experimentally. Qualitative agreements could be demonstrated. Based upon the results, the optimum height and location of a windbreak that reduces ship motions most effectively were inferred, and tentative suggestions for planning future facilities of a wharf were made.

**1. Introduction**

Mooring ships in harbour for loading and unloading are subjected to actions of both wind and waves. Motions induced by wind can sometimes exceed those due to waves. In Taiwan, harbours are exposed to seasonal winds which usually last for more than half of a year, for which the Taichung Harbour is an excellent example. In an attempt to reduce wind-induced action and to ensure safety within the harbour, a variety of possibilities has been considered by the Bureau of Administration. Windbreaks, or tall warehouses, if properly designed, are the most favourable candidates, among all other alternatives.

Windbreaks and fences have always played an important role in the history of human endeavor in fighting against the malicious nature environments. In an attempt to find the most efficient sheltering effects, intensive studies have been carried out experimentally as well as analytically by many researchers in the last fifty years [1,2,3,4,5]. However, judging from the fact that, turbulent separations are involved both in front and behind such a device [6,7], it is questionable that if such a phenomenon could ever be modelled exactly, either numerically or experimentally [8,9]. Nevertheless, it seems plausible that, by applying one of the present available numerical methods, flow fields behind a windbreak can be studied qualitatively, at least for engineering practice.

To find the optimum windbreak with the lowest construction and maintenance cost, which yet yields maximum protection for marine vehicle on downwind side, studies were carried out for both numerically and experimentally. Numerically, flow field behind a windbreak is simulated using surface vorticity method. This method has been applied by Lewis and his coworkers to model separated flows from bluff bodies [10,11]. Satisfactory results were reported by them. To verify numerical predictions, contemporary experiments were carried out in a wind tunnel. With these results, tentative suggestions for the most suitable height and location of a windbreak were made.

The layout of this paper is as follows: A short description of the theoretical backgrounds of the numerical method is given in section 2. Experimental procedures are described in section 3. Results from both calculated and measured velocity distributions are presented in section 4, together with short discussions. Section 5 then concludes this paper.

## 2. Theoretical backgrounds

Surface vorticity method is used to model the body flow, together with vorticity generation, shedding and convection, the regime of separation behind a windbreak can then be simulated. Detailed descriptions of the method are given in the references mentioned earlier [10,11]. Only the essentials of the method are outlined here.

Basically, the surface vorticity method consists of representing the inviscid, incompressible flow by distributed discrete vorticity elements on the surface. Consider an inviscid flow at the surface of any two-dimensional body, (Fig. 1). Assuming an infinitely thin vorticity sheet of strength  $\gamma(s)$  in contact with the body surface, it can then be shown that the local surface velocity at location  $s$  can be expressed as:

$$\gamma(s) = v_s \quad \text{-----(1)}$$

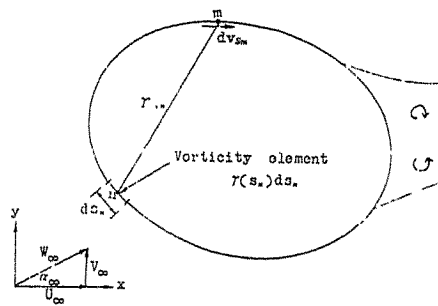


Fig. 1 Surface vorticity model for potential flow past a two-dimensional body

The potential flow problem is now reduced to the selection of a  $\gamma(s)$  distribution such that the resulting flow is parallel to the body surface at all points.

When the Dirichlet boundary condition is applied to a point  $m$  on the body in a uniform flow  $W_\infty$ , the following non-singular Fredholm integral equation then results:

$$\int \gamma(s_n) K(m,n) ds_n - \frac{1}{2} \gamma(s_m) = -W_\infty \left( \frac{dx_m}{ds} \cos \alpha_\infty + \frac{dy_m}{ds} \sin \alpha_\infty \right) \quad \text{-----(2)}$$

Where  $\alpha_\infty$  is the angle of inclination of  $W_\infty$  with respect to the x-axis and  $K(m,n)$  is a coupling coefficient.

For the case in which  $Z$  vortices  $\Gamma_N$  are scattered throughout the outer flow field, (Fig. 2), equation (2) may be expanded in a very simple manner, as follows:

$$\int \gamma(s_n) k(m,n) ds_n - \frac{1}{2} \gamma(s_m) = -W_\infty \left( \frac{dx_m}{ds} \cos \alpha_\infty + \frac{dy_m}{ds} \sin \alpha_\infty \right) - \sum_{N=1}^Z \Gamma_N L(m,N) \quad \text{-----(3)}$$

Where  $L(m,n)$ , similar as  $K(m,n)$  in Eq. (2), is the coupling coefficient which gives the velocity at  $m$  parallel to the surface due to a unit vortex at position  $N$ . The integral equation (3) provides a complete description of the generalized two-dimensional potential flow past bodies with flow separation regimes.

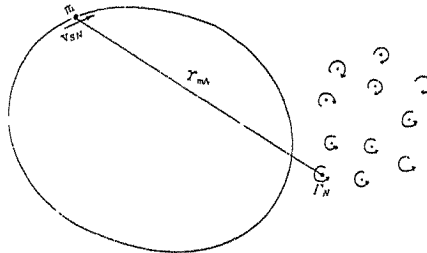


Fig. 2 Influence of shed vortices in the wake.

Vorticity shedding from sharp edges and convection in the wake is then considered. In each time step a new vorticity element of the strength  $\Delta\Gamma_n$  is shed into the flow field, where

$$\Delta\Gamma_n = \gamma(sp)v_{sp}\Delta t = \frac{1}{2}v_{sp}^2\Delta t \quad \text{-----(4)}$$

The velocity components  $u, v$  at  $m$  due to a unit clockwise vortex located at  $n$  are given by:

$$u = U(m,n) = \frac{1}{2\pi} \left\{ \frac{(y_m - y_n)}{(x_m - x_n)^2 + (y_m - y_n)^2} \right\} \quad \text{-----(5)}$$

$$v = V(m,n) = \frac{1}{2\pi} \left\{ \frac{-(x_m - x_n)}{(x_m - x_n)^2 + (y_m - y_n)^2} \right\}$$

Now, the free vortex element in the wake  $\Delta\Gamma_n$  will be subjected to the convection velocities induced by all other vortex elements in the field, together with the uniform stream  $W_\infty$ . The components of the convection velocity of the vortex element  $\Delta\Gamma_n$  may be computed from:

$$u_{CN} = \sum_{n=1}^M \gamma(s_n)\Delta s_n U(m,n) + \sum_{\substack{n=1 \\ n \neq N}}^Z \Delta\Gamma_n U(m,n) + U_\infty \quad \text{-----(6)}$$

$$v_{CN} = \sum_{n=1}^M \gamma(s_n)\Delta s_n V(m,n) + \sum_{\substack{n=1 \\ n \neq N}}^Z \Delta\Gamma_n V(m,n) + V_\infty$$

Equations (6) may be used to calculate streaklines at any point in the flow field for the time step  $\Delta t$ .

### 3. Experiments

Experiments were conducted in a wind-wave tunnel. The tunnel is located in the Laboratory for Ocean Engineering of the Department. Descriptions of the wind-wave tunnel are given in a paper by Yim et al. of this Conference. The experimental setups are shown schematically in Fig. 3

Experiments were carried out using a prototype wind speeds of 5, 10, and 15 m/s, with three windbreak heights of 3, 6, and 9 metres, located at 15, 21, and 27 metres away from the wharf.

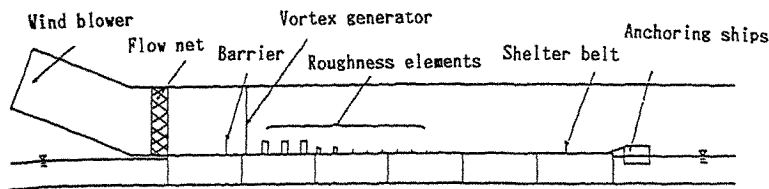


Fig. 3 Experimental setups.

#### 4. Results and comparison

Calculations were carried out for the cases described above. Only two cases will be discussed here. Fig. 4 shows simulated velocity distributions of a windbreak of 3-meter high with a 5 m/s wind. Shown in the figure are calculations for the 10-th, and 30-th time steps. As the vortex is swept downstream from the windbreak with increasing time steps, more and more areas behind the fence were seen to be affected. Similar results were obtained for cases with higher wind speeds. With the increase of wind speed and windbreak height, however, the vortex will become disintegrated (Fig. 5). This seems to be associated with the neglect of viscous effects in the model, as discussed by Lewis & Porthouse [11]. Without viscosity to diffuse it out of the wake, the shedding and loss rate of vorticity can not be held in balance, and the wake will continue to grow.

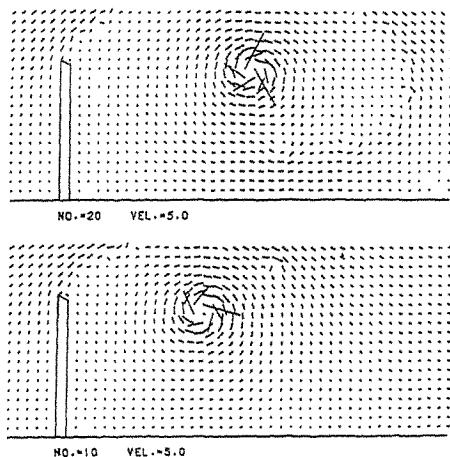


Fig. 4 Velocity distributions around a 3-meter windbreak. Wind velocity is 5 m/sec. 10-th (a), and 20-th (b) time step.

Fig. 6 shows compares calculated and measured velocity distributions for the 3-meter windbreak. Shown in the figure are for cases with wind velocities of 5 and 15 m/sec. Results

obtained from measurements are drawn with unbroken lines, whereby simulated are drawn with broken. As can be seen, calculated results deviate from measured for stronger wind. Fig. 7 are the results for a 9-meter windbreak. Comparing with Fig. 6, the deviations between these calculated and measured results are less pronounced.

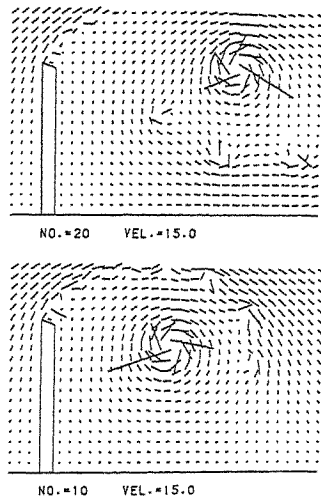


Fig. 5 Velocity distributions around a 9-meter windbreak. The wind velocity is 15 m/sec. 10-th (a), and 20-th (b) time step.

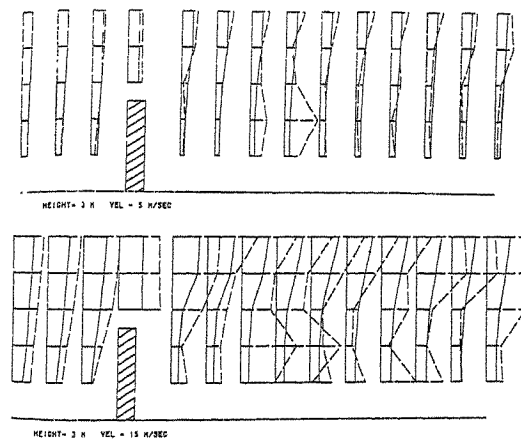


Fig. 6 Measured (unbroken lines) and calculated (broken lines) velocity distributions for a 3 meter windbreak. Wind speed: 5 m/sec (a) and 15 m/sec (b).

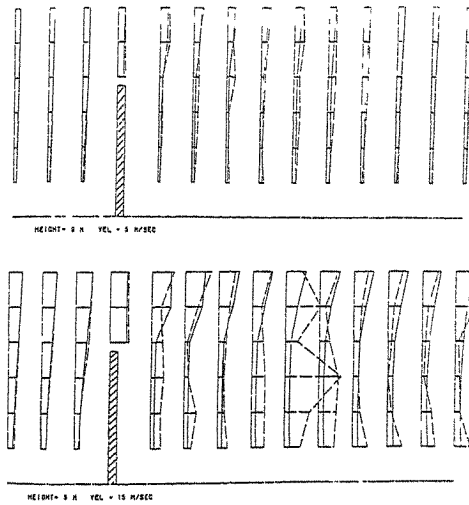


Fig. 7 Measured (unbroken lines) and calculated (broken lines) velocity distributions for a 9 meter windbreak  
Wind speed: 5 m/sec (a) and 15 m/sec (b).

## 5. Conclusion

Velocity distributions at the rear of a windbreak were simulated using surface vorticity method. Calculated results are then compared with measurements taken in a wind-wave tunnel. From results presented here in this paper, it is clear that, viscous effects are important for a more realistic simulation of flow fields behind a windbreak. Improved algorithms, which take these effects into consideration, are now being considered.

As for the wind-induced ship motions are concerned, our experimental results (not shown here) indicate that, for the dimensionless ratios of  $X/H$ , where  $X$  is the distance between windbreak and quay, and  $H$  is the windbreak height, between 2.5 and 4.5, the motions can be reduced drastically.

## References

1. R.Baltaxe, *Archiv Meteor. Geophysik, Bioklim.*, B15(1967) 287
2. I.Seginer and R.Sagi, *Agric. Meteorol.*, 9(1971/72) 323
3. J. van Eimern, R.Karschon, L.A.Razumova and G.W.Robertson, *World Meteorol Organization, WMO-No.147.TP.70(1964)* pp. 188
4. J.W.Sturrock, *New-Zealand J. Sci.*, 12(1969) 754
5. J.W.Sturrock, *New-Zealand J. Sci.*, 15(1972) 113
6. E.J.Plate, *Agr. Meteorol.*, 8(1971) 203
7. P.K.Pande, R.Prakash and M.L.Agarwal, *J. Hydraulics Div. ASCE*, 106(1980) 191
8. J.L.Lumley, *Phys. Fluids*, A4(1992) 203
9. P.Tengel and H.H.Fernholz, *J. Fluid Mech.*, 212(1990) 615
10. R.I.Lewis, *J. Mech. Engng. Sci.*, 23(1981) 1
11. R.I.Lewis and D.T.Porthouse, *J. Mech. Engng. Sci.*, 26(1984) 157

## THE DEPOSITION OF SAND PARTICLES ON AND AROUND STRUCTURES WITH DOMED ROOFS

A AROUSSI

Department of Mechanical Engineering, University of Nottingham,  
Nottingham, NG7 2RD

**Abstract:** The wind environment of structures with domed roofs is investigated experimentally and numerically. The experimental work consists of non-intrusive velocity measurements made on scaled models of buildings (1:240), placed in an open circuit wind tunnel which simulates natural wind. The computer predictions of the measured flow fields are obtained with a two equations model of turbulence. The measured velocity values are used to validate the numerical solution.

### 1. Introduction

Sirocco winds and sand storms frequently occur in the African sahara desert; particularly in the spring season. Similar events occur elsewhere at other times of the year. As a consequence, large amounts of sand are shifted locally whilst small amounts are transported over longer distances. For example, sand from the Sahara desert can be carried as far north as the United Kingdom. The locally shifted sands result in serious disruption to the daily life of the inhabitants of the area. For instance, roads are often closed by sand dunes rapidly forming on them. Flat roofs require regular cleaning to avoid their collapse under the load of the sand. To eliminate the latter problem, roofs of dwellings in the sahara region have evolved from flat to their present domed shapes. These shapes also promote cooling in the summer heat.

The interaction of wind with buildings results in turbulent, separated and recirculating flows of theoretical and practical importance. The wind environment generated from such an interaction includes regions of well defined eddies and is characterised by big fluctuations of velocity and pressure in the vicinity of the structure. This fluid behaviour affects the distribution of pressure, sand particles and rain water on the surfaces of the building, the energy consumption of the structure, the comfort of pedestrians at ground level, the dispersal of smoke and other effluents and in severe cases can result in structural damage.

The present paper consists of an experimental and computational study of the deposition of sand particles on and around building models with domed roofs. The experimental work consists of non-intrusive velocity measurements made on scaled models of buildings (1:240), placed in an open circuit wind tunnel which simulates the flow characteristics of natural wind. The anemometers used are a Laser Doppler Anemometer (LDA) and a Digital Particle Imaging Velocimeter (DPIV).

### 2. Experimental measurements

The experimental programme determines the velocity fields using two optical

numerical simulation, requires a fine grid; consequently the computer time and storage become disproportionately large. Simplifying assumptions are therefore made to obtain a practicable solution.

Since it is impracticable to solve equations repeatedly on a micro-scale, the approach is to use "time averaged" equations on a coarse grid. However, the formulation of these time-averaged equations results in the introduction of additional terms which are essential to the description of flow behaviour; namely the Reynolds stresses and the turbulent mass flux.

Turbulence models of varying complexities are used to define these terms and are classified by the number of additional differential equations they contain. The choice of a particular model depends on its accuracy, economy of computations, but most important on the nature of the flow to be simulated. This study uses the two equation  $K\epsilon$  model with its standard empirical constants (Launder and Spalding 1972).

A solution of a closed system of differential transport equations, that make a mathematical model, is only possible when the boundary and initial conditions are specified. The fluid motions, in this study, are of an elliptic nature where perturbations at any point in the flow can influence conditions anywhere in the solution domain. Therefore it is necessary to specify the flow variables at all the boundaries, these can be a solid wall or a free boundary. Close to solid boundaries a viscous sublayer exists because the mean velocity components and the turbulent viscosity fall to zero, due to the no-slip condition. The models of turbulence do not take this into account and consequently an alternative approach is required in the near wall region. This means the use of the "wall function" method which connects the sublayer with special functions which bridge the conditions at its outer edge to those at the wall, thus avoiding this low Reynolds number region (Launder and Spalding 1972). A universal logarithmic law is therefore applied near solid walls where the values of  $K$  and  $\epsilon$  are obtained from the friction velocity  $U_*$  to give

$$K_{wall} = \frac{U_*^2}{C_\mu^{1/2}}$$

$$\epsilon_{wall} = \frac{U_*^3}{\kappa y}$$

The other boundary conditions are set as follows:

Solid walls All the dependent variables  $U$ ,  $V$ ,  $K$  and  $\epsilon$  are set to zero.

Outlet A fixed zero pressure is prescribed.

Inlet The flow properties prescribed are those profiles measured with the laser Doppler anemometer.

The grids used for the solution are body fitted and non-uniform with a fine mesh in areas of steep gradients.

#### 4. Results and discussion

The important features of the flows investigated (Fig 2) are the zones of re-circulation upstream and downstream of each model where there is a high degree of mixing.

In this two dimensional representation, the approach flow is brought to rest by the



anemometers - namely an LDA and a DPIV system- and models of buildings placed a wind tunnel. This has a cross-section 0.5x0.5m and a velocity range 0-10m/s. The models are made of wood (scale 1:240), with a smooth finish and mounted on the floor of the test section.

The wind incident on the models has the velocity profile and the turbulence characteristics of a semi-rough terrain; both are obtained using a slatted screen technique. This screen generates a power law velocity profile of index 0.28. To minimise the blockage effect, the front area of the biggest model is less than 12% of the working cross-section. This ratio is acceptably small and allows direct comparison to the computational results. The air flow is seeded with smoke generated from the vaporisation of a light mineral oil. To obtain an even distribution of smoke particles in the working section, the mist generator is placed 2 metres away from the inlet and therefore the mist is completely diffused when it reaches the bellmouth.

The laser anemometer is a digital correlator based system used in the backscatter mode; the optics are mounted on an XYZ traversing mechanism. The three dimensional flow field is mapped by a series of discrete measurements at intervals of 5 to 10mm; the size of the model and the rate of change of the flow properties determine the steps. At each point the longitudinal and the vertical components of the mean velocity are obtained.

DPIV like PIV involves the recording of multiple images of scattering particles on a single picture. However, this picture is captured directly via a CCD camera rather than by still photographs. From the displacement of separate scattering particles and the time between consecutive exposures, the velocity of the flow local to each such particle is calculated. The only restriction on the use of DPIV is the small size (2cmx2cm) of the flow area investigated. The Light source for the DPIV system is an 18W, continuous wave, Argon Ion laser. The arrangement used is such that the beam passes through a mechanical chopper which allows the generation of the required discrete images, and then a glass rod to produce a light sheet, 2mm thick (Fig 1).

The flow field around and over two buildings at various separations are obtained. The dimensions of the buildings are Height/Width/Depth = 1/1/1. The separations investigated are H, H/2 and H/4.

### 3. Computational study

The aim of this study is to simulate the flows generated within the selected geometries and to validate these predictions by comparison with the measurements obtained using the LDA and DPIV systems. An assessment of the accuracy of the mathematical model used is then conducted.

The fluid motion resulting from the interaction of a free stream and a bluff body is turbulent, recirculating and governed by equations elliptic in nature. The primary eddy is formed when the shear layer separates at the curved top of the geometry and reattaches further downstream.

The Navier-Stokes and the continuity equations describe all laminar and some simple cases of turbulent flows (for example, flow in pipes). The randomness and complexity of re-circulating flows, consisting of a cascade of eddies, cannot be dealt with satisfactorily by these two equations; the computation time makes a solution impracticable, although possible. To resolve the smallest area of turbulence, in a

model and its kinetic energy is converted into dynamic pressure; this longitudinal deceleration and the subsequent vertical acceleration result in the fluid escaping radially from the stagnation point at the front face. Most of the flow passes over the roof and around the sides with the rest of the fluid trapped between the front wall and the floor forming a windward re-circulation zone.

Predicted velocity values of air flow over the building models are presented in vectorial form (Figs 3-5). The patterns show the acceleration of the wind deflected past the buildings, the slowing down of the fluid due to the blockage effects of the model and the subsequent formation of the upstream eddy. For the primary obstacle the separation of the fluid at roof level depends on the radius of curvature of the roof and on the Reynolds number (Fig 3). The zone between the two structures acts as a cavity and is filled by a large vortex, whose shape and strength depends on the size of the separation (Fig 4). For narrow separations ( $H/4$ ), this recirculation zone is made up of a large primary vortex and a weaker secondary eddy (Fig 5).

The above phenomena are clearly identified in the vertical profiles of the longitudinal velocity (Fig 6). The flow deflected over the building increases in speed relative to the free stream. For example on the roof of the first building a velocity of  $1.77U_{\infty}$  is measured (Fig 6) and  $1.53U_{\infty}$  is predicted with the  $K\epsilon$  model. This rise in velocity causes suction on the roof and in severe cases results in structural damage.

High values of turbulence energy are calculated in the shear layer over the roofs and downstream of the buildings which is the result of the mixing in the shear layer (Fig 7).

A comparison of vertical profiles of the longitudinal velocity, at  $X/H=1.0$  downstream of the second building, shows good agreement between the three sets of results (Fig 8). However, the  $K\epsilon$  model slightly overpredicts the strength of the flow in the recirculation area.

## 5. Conclusions

The turbulent fluid motion resulting from the interaction of wind with dome roofed buildings has been investigated using LDA, DPIV and numerical predictive methods and the following conclusions can be drawn.

All the measured flow features such as the flow deceleration upstream of the facade, the acceleration of the deflected fluid, the separation point at the edge of the roof and the associated eddy downstream have been reproduced by the model of turbulence. The recirculation areas are the zones where sand particles are deposited. The size and therefore the weight of the particles dictate the pattern of deposition and subsequent build up. Furthermore, these patterns are dependent on the orientation of the buildings with respect to the approaching wind as well as the neighbouring structures. The only safe way of reducing or eliminating such depositions is to project the sand particle in the free stream and hence away from the dwellings or to slow them down sufficiently prior to reaching the buildings. The latter technique is the one often adopted in practice, whilst the former is difficult to implement but is more efficient.

## REFERENCES

Launder B E and Spalding D B (1972), Academic Press.

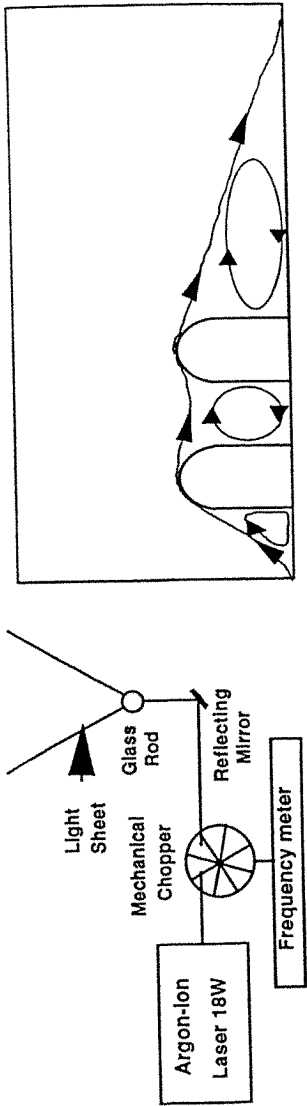


**Fig 1: DPIV arrangement** **Fig 2: Flow geometry examined**

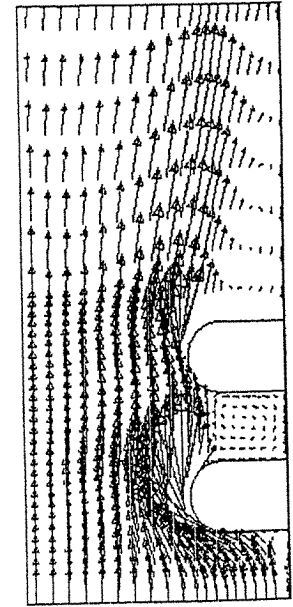


**Fig 3: Predicted velocity field**  
(separation = H)

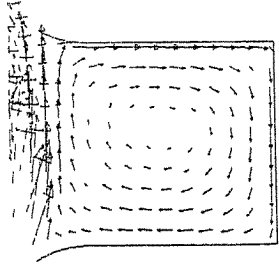


**Fig 4: Fluid flow between the structures**

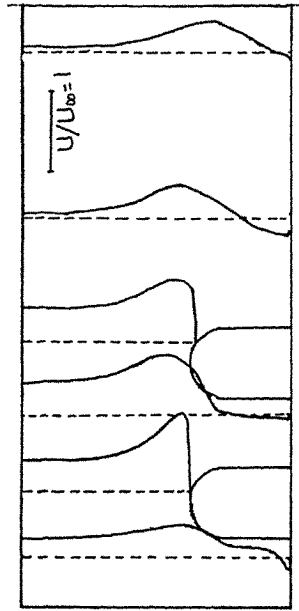


Fig 6: U velocity profiles

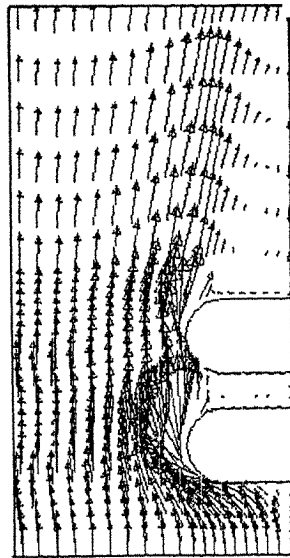


Fig 5: Predicted velocity field  
(separation = H/4)

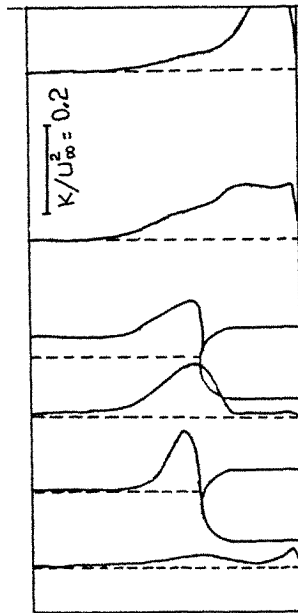


Fig 7: Turbulence energy profiles

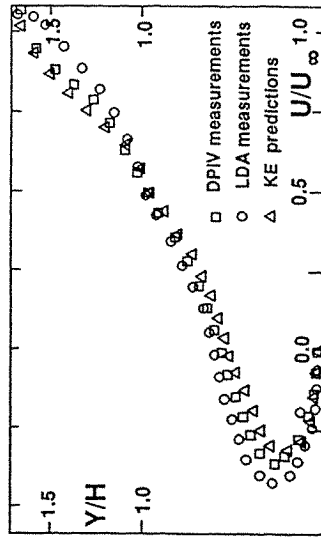


Fig 8: Comparison of longitudinal velocities

## Wind powered treatment of waste water - FRED's 'WATER' process

J S Shrimpton, D A Janes & N H Thomas +

FRED Ltd, Research Park, University of Birmingham B15 2SQ, England  
+ For all correspondence; also FAST Team, School of Chemical Engineering

**Abstract:** The notion is ecologically ideal: namely, directly harvesting wind power as a 'pure' natural resource to cleanse man's contamination of another- and, most especially, without introducing any of the secondary pollution associated with all conventionally powered treatment plant. Conceptually, the notion is not only feasible but extraordinarily apt, at least in principle. ie mean winds in excess of 5m/s or so should suffice to meet the aeration demands of practicable aerobic systems. The key issue here is viability, both technical and commercial. The former hinges on integration of aeronautical, mechanical and biochemical engineering skills to deliver a processing operation resilient enough to tolerate the considerable excursions in energy supply, most notably prolonged absence of aeration during slack periods. The latter is defined by accepted thresholds for competitiveness with conventional plant, say £1-2K/kW installed cost. This short paper describes our inspiration and achievements.

### 1. Introduction

Following concept propositions to the UK Department of Trade and Industry (DTI) under their Small firms Merit Award in Research & Technology (SMART) scheme, FRED won DTI SMART1 sponsorship in 1990 to execute a feasibility evaluation followed by SMART2 sponsorship in 1991 to assess scale-up viability and prospects for product delivery. Whereas the title notion is ecologically attractive, its implementation as realisable technology has proved to be a daunting multidisciplinary exercise and a stern financial challenge for a small company with core business formerly restricted to technical advisory services and no prior experience of proto-product work-up. Without subsidy since February, we are presently persevering with pilot plant field trialling and prototype product definition exercises augmented by continuing basic studies pursued on campus as PhD projects part-sponsored by FRED.

Whilst proprietary specification for our 'WATER' (Wind Assisted Treatment for Environmental Recovery) process is the subject of continuing patent application upgrades, the underlying rationale and basic principles, also first evaluations as small-scale model tests, have already been reported in previous papers (Janes & Thomas, 1992, 1993; Thomas & Janes, 1992). Here we provide a short account of the project work-up and an indication of our first results from field trialling in 1992 using a 2m pilot plant sited at a sewage treatment plant in mid-Wales, courtesy of Severn Trent Water. Although the biological performance was not especially exciting, these results provided valuable diagnostic guidance on configurational and operational limitations which have since been largely rectified. We now have two 2m pilot trialling machines, one located in a large slurry waste storage tank (1Km<sup>3</sup>) at a local pig farm, the other on campus at Birmingham University. The first of these units has served to identify such 'field-truth' operational problems as crust formation in hot weather! The second unit is driven by windtunnel outflow for ongoing evaluation of strategies remediating biological inhibition associated with wind intermittency.

Our immediate future goal is to introduce a 4m unit as pre-production plant subjected to cost-constrained fabrication as a commercial viability exercise and implemented as an integrated multi-stage fed-batch system for longterm

field demonstration. Envisaged target markets include municipal/ domestic sewage treatment for small and remote rural communities (especially as an augmentation of lagoon storage to meet improved sanitation expectations in poorer countries), farm waste control for odour suppression prior to land-spreading or even treatment to discharge quality where land availability is minimal, process industry effluents, municipal solid waste leachates and environmental recovery of polluted waters.

## 2. Conceptual context

Rough calculations suffice to indicate that energy availability from wind environments with annual mean speeds in excess of 5 m/s or so might suffice in principle for practicable exploitation in aerobic treatment of municipal and domestic waste waters. Typically possessing Biological Oxygen Deficits (BOD's) of up to 500 mg/L or so and Ammoniacal Nitrogen (Amm-N) loadings of perhaps 50 mg/L, such effluents can be effectively bio-oxidised in 10-20 hours using conventional agitator-aerators with Oxygen Dissolution (DO<sub>2</sub>) efficiencies in the order of 1kg/kWh, consistent with the rule-of-thumb minimum power density demand of 30w/m<sup>3</sup> to sustain aerobic activity. For a process tank of 1m depth, this requirement translates into a wind capture area equal to the process platform area. ie based on 1kWh/m<sup>2</sup> availability at 10m/s with cubic scaling of power on windspeed and supposing an overall recovery factor of 1/2 or so. Whilst 5m/s mean wind thus represents the threshold for viability on this basis, 7m/s would deliver a respectable operating margin, in principle capable of delivering power densities of about 100w/m<sup>3</sup> over 1m depth or, equivalently, accommodating aerobic oxygen demand of treatment tanks to about 3m depth.

Admittedly simple, perhaps appropriately so in view of the complex uncertainties involved, these plausibly attractive estimates provided the background rationale for FRED's SMART WATER initiative. Indeed, at first sight the processing demand here is exceedingly well-matched to the wind supply available in many coastal and upland areas worldwide. In the UK, for example, 7m/s annual mean wind is delivered over most western regions including many remoter rural communities in the major farming counties of SW and NW England, throughout Wales and extending well inland for hillier areas like the Peak District and throughout Scotland.

Beyond this favourable context, serious technical challenges were foreseen concerning biological resilience to oxygen depletion during slack periods and mechanical realisation not just combining minimal maintenance ruggedness with adequate responsiveness for energy capture even from light breezes (ie sufficient circulation to maintain oxygenation by surface renewal) but also feasibly deliverable as a viably priced product. For the UK at least, this last constraint is absolutely crucial as it translates to a point-of-sale cost no more than £1-2K/kWh or so, a break-even figure that obviously depends on local environmental subsidy which is currently as much as 50% for farm waste treatment facilities in the UK. Recalling that £1-1.5K/kWh has been regarded as a guideline measure for private sector interest in wind-powered electricity generating machines, we don't anticipate 'windfall' profit margins from this venture. Indeed, future success of our prospective WATER products will depend critically on continuing buoyancy of the 'green niche' market sector.

As an immediate technical consequence of this bottom-line constraint we judged that cost viability alone demanded the mechanical simplicity of uni-axial transmission and so adopted Vertical Axis Wind Turbine (VAWT) technology as the best prospect. An outline of the project history and its evolution to current status is given in the following sections.

## 3. Modelling work-up

VAWT We sought to combine the low speed cut-in and high torque benefits

of Savonius rotors with the high speed efficiency of Darrius rotors by using pivoted windfoils whose adaptive attitude is controlled by spring reaction and centrifugal forces. Thus low speed cross-flowing wind causes each blade in turn to flap inwards thereby generating drag-induced rotor torque whilst at higher speeds the blades are confined centrifugally against outer stop pins. Cut-in windspeeds as low as 2m/s (light breeze) were thereby achieved, with transition to high speed operation (nonflapping blades) occurring at windspeeds exceeding 5 m/s or so. More complicated mechanical arrangements were explored, including coupling the flapping motions of diametrically opposed blades by means of belts and lost-motion tie-rods as a way of delivering simultaneously increased efficiency and stiffness, but these ideas were eventually abandoned in the interests of fabrication simplicity and running reliability: ie, ultimately to reduce cost and maintenance.

The present configuration (figure 1), a four-bladed medium solidity (0.6) VAWT with 1.1 height-to-diameter ratio, has been broadly fixed since completion of our wind tunnel tests early in 1991. Using a 1/4m model for these studies, the maximum measured power coefficient was only about 0.2, disappointingly low but inevitably so with the extremely crude tube-and-fin blade sections we used here; ie drag factor of perhaps 0.5 or more, effectively confining the VAWT to Savonius operation (tip-speed envelope less than unity). The 2m pilot machine in figure 1 is equipped with NACA 0018 symmetric aerofoils, chosen for stall resilience (ie thick section), whose substantially lower drag factors presumably deliver correspondingly higher power factors. However, because of the exceedingly tight scheduling of SMART projects (one year each for SMART1 and SMART2) we have not found time to accommodate performance measurements with these streamline blades.

Transmission One crucial advantage of using a VAWT is the cost saving achieved by simple uni-axial transmission of shaft power. However, initially striving for the pinnacle of environmental idealism, we foolishly sacrificed this advantage with a complicated planetary action stirrer arrangement whose blade trajectories assured vigorous dispersion throughout the entire processing volume. The intention was sound enough: namely, to recirculate all of the particulate matter and so deliver adequate oxygenation without introducing bubbles whose disengagement is of emerging concern as a possible source of aerosolised viral contamination. Whilst the planetary arrangement proved entirely satisfactory under controlled test conditions in the laboratory (and has excellent prospects for industrial processing of rheological media), the geared drive-train achieving this motion proved to be a nightmare of unreliability in the field units.

Following this distractingly expensive diversion and with growing recognition of costing criticality we have now substituted the planetary stirrers with self-inducing drawdown agitator-aerators as a simple, cheap and adequate solution which simultaneously accords with established wisdom that blowing bubbles is energetically more favourable than pushing liquid! These developments, the subject of a recent patent application, will be reported in future papers. We merely remark here that the oxygen transfer performance of our primitive prototype 'snorkel tubes' is not only upwards of 1kg/kWh (ie in line with industry benchmarks) but potentially upgradable to perhaps 10kg/kWh with the 'introduction of streamline sections and membrane sparging surfaces. We caution that all model and field tests reported below were conducted using the earlier planetary action stirrers.

Performance With maintained fan-driven wind of 5 m/s, the 1/4m model was found to satisfactorily oxidise screened sewage (dirty water) as measured by BOD reduction from 250-300 mg/L and Amm-N reduction from 50-100 mg/L to dischargable quality (BOD 30 mg/L; Amm-N 10 mg/L) on time-scales of 250 hours or so (Janes & Thomas, 1992). Nitrification (ie oxidation of Amm-N via nitrite

to nitrate) was significantly slower and less assured than BOD oxidation- indeed was suppressed altogether at 2.5 m/s windspeed, an early symptom of what we now recognise to be the major biological consequence of species competition in the presence of oxygen deficiency. Boosting the aeration with higher windspeeds tended to increase the rate of BOD removal rather than the rate of nitrification. This response puzzled us at the time but with the benefit of subsequent systematic biological studies we can now confidently attribute it to the relatively sluggish metabolism of the nitrosomas and nitrobacter species (Bradley, Fowler & Thomas, 1993). There may also be an inhibitory toxic response associated with accumulation of nitrite due to incomplete oxidation to nitrate.

Any practical realisation of the WATER plant will incorporate provision for maintaining minimum levels of activated sludge as biocatalyst: ie rather than growing up populations from the low concentrations of microorganisms naturally present in screened sewage. Recognising this shortcoming in our first tests (above), all subsequent trials have been conducted with prior seeding at concentrations up to about 100% by volume. Our first such test (Thomas & Janes, 1992) in the ¼m model, again with 5m/s fan-driven wind, delivered bio-oxidation intervals of around 25 hours for screened sewage from the same rural source- here possessing initial BOD 130 mg/L and Amm-N 20 mg/L. These low starting values are perhaps attributable only in part to initial halving by the addition of an equal volume of activated sludge, the remainder probably due to increased rainwater content. In fact, with BOD and Amm-N both reduced to 5 mg/L, the water quality after 25 hours was significantly better than required for river dischargability in the UK.

Although the boosted levels of nitrifiers available from activated sludge were clearly sufficient to maintain effective nitrification in this case, we nevertheless started routine monitoring of nitrate as a closure on the Amm-N balance and, in particular, as a diagnostic for incomplete oxidation (nitrite). Consistent with the direct measurements, this test demonstrated that the Amm-N had indeed been completely oxidised to nitrate. However, as reported below, this encouraging outcome was not so readily reproduced in our first field trials using the 2m pilot machine- albeit under extremely stern conditions of severe cold and low wind in an unfavourably sheltered location. Moreover, we hasten to emphasise, the pilot plant was equipped at that time with essentially the same planetary actions stirrers employed in the ¼m laboratory model. As indicated earlier, we have since introduced snorkel tube agitator-aerators with very much higher oxygen transfer capacity, comparable with industry benchmarks. Indeed, very recent motor powered tests (to be reported) have convincingly validated this new arrangement for bio-oxidation performance with screened sewage.

#### 4. Field trialling

Set-up The trials were conducted at Severn Trent Water's Treatment Works in Newtown (mid-Wales) during February and March (1992). The process tank (2m diameter, 1¼m deep; 3500L process capacity) was recessed into the ground with the 2m VAWT mounted on a frame concentrically above the tank, as seen in figure 1 (identical machine; different site). Dictated by availability and safety considerations, its location at Newtown was far from ideal as a windy site what with the Works situated in a valley and the machine shielded by large digester tanks and a barn all within perhaps 50m. Scheduling, also not ideal (see below), was dictated by project workplan constraints on fabrication, installation and work-up including instrumentation. The latter included direct datalogging (STARLOG) of air temperature and windspeed measured at 1m elevation (1-4 hour intervals), also auto-sampling (EPIC1011) for subsequent analysis (5-20 hour intervals) of suspended solids (SS), COD (chemical oxygen deficit), BOD,



Amm-N and total oxidised nitrogen (TON; ie nitrification). The conditions and results of three batch trials, each for on-site municipal effluent (screened sewage: BOD 200-700 mg/L; Amm-N 50-100 mg/L) biocatalysed with activated sludge (3-10% by volume) from an on-site oxidation ditch, are reviewed below. These data as presented at the conference will be reported in Shrimpton, Bradley & Thomas, 1993).

Trial 1 Unfortunately, the weather during this 6-day interval was dominated by a sluggish anticyclone delivering seriously unfavourable cold conditions with air temperatures always less than 5°C and even down to -10°C: ie far below the preferred range of 20-40°C for vigorous biological activity. With windspeed always less than the 2½m/s cut-in threshold for our loaded VAWT, the absence of bio-oxidation is entirely as we would have expected. On the other hand, with such low temperatures prevailing, it is unlikely that conventional (continuous) treatment plant would have managed to sustain servicability without the benefit of thermal protection (if only by volume alone) and maintained supply of warm influent which apparently arrives year-round at 15°C or so. Indeed, nitrification is acknowledged to be problematical for existing treatment systems during extended periods of cold weather, less than 5°C or so. Nevertheless, this first field result was extremely depressing at the time and it certainly served to provide a salutary warning that practically acceptable operation of WATER as a marketed product would demand the utmost caution in site selection for wind supply, not to mention carefully worded disclaimers on fitness-for-purpose. We recall such sentiments are not uncommonly expressed by the wiser proponents of wind-powered electricity generating plant!

Trial 2 During this 10-day interval the weather was substantially warmer (2-10°C) and also windier (2-6 m/s) for the last 5 days. In fact, the test period here followed 5 days when conditions were essentially as in trial 1 and no biological activity was recorded, so trial 2 represents also a test of reactivation following extended dormancy. Strikingly correlated with the onset of wind energisation, the sampling records showed a large jump in SS and COD associated with upwards dispersion of previously settled matter, following by more gradual upwards ramping of BOD as organic material was desorbed from flocced particulates. Whereas these data gave no indications of bio-oxidation, the Amm-N and TON records together provided clear evidence of nitrifier recovery after a lag period of about 1 day from onset of wind excitation. Reinforcing this encouraging sign, the BOD time-trace also subsequently plateaued and dipped. Although we could not make any serious claims for quality recovery here, this biological resilience following extended dormancy was an encouraging sign that wind intermittency might after all be a manageable problem. Extensive and detailed subsequent laboratory evaluations have confirmed that it is indeed tolerable, especially when provisions are made to segregate the competitive carbonaceous and nitrifying species and sequentially oxidise the BOD and Amm-N, as now incorporated in current versions of the WATER treatent plant.

Trial 3 This 8-day period was characterised by lower winds than in trial 2, typically exceeding the 2½ m/s cut-in speed only for short periods daily and never more than 4 m/s. However, apart from cold overnight 'snaps', the temperature was generally higher than in the earlier trials, approximately ranging from 6-12°C throughout. In contrast to trials 1 and 2 conducted with 3% activated sludge, here we raised the seeding level to 10% so as to reduce the intial lag phase of population adjustment and thereby also provide conditions more closely approximating those for realistic plant operation. The sampling time-traces convey a rather confusing picture of large cyclic excursions in SS and COD associated with the intermittently wind-energised suspension and settling of solids. The BOD samples also mirrored these fluctuations for the

first 3 days, after which they followed a sustained fall from around 200 mg/L to 30 mg/L by day 8. However, the Amm-N stubbornly refused to budge from initial 75 mg/L except for one reading at the end of the trial showing a drop to 65 mg/L. Whilst naturally sceptical about ascribing undue significance to a single reading especially as the reduction was not mirrored in the TON test, we mention it here because this behaviour is precisely in line with our now much improved understanding (Bradley, Fowler & Thomas, 1993) of the main limitation on nitrification performance: namely, that the nitrifiers effectively compete for scarce oxygen only when the BOD has been reduced sufficiently as to cause nutrient inhibition of the carbonaceous species.

#### 5. Conclusions

FRED's SMART concept proposition that wind powered waste water treatment is not only environmentally attractive but also practically viable has received support from feasibility testing using a fan-driven  $\frac{1}{4}$ m model in the laboratory. Whilst the jury is still out on field trialling, our first results reported above show encouraging biological resilience in recovery from dormancy over extended periods of low wind, even in extremely cold weather. More recent work to be reported will not only confirm the broad interpretive picture outlined above but also show how plant component and configurational refinements have been combined with more sophisticated processing strategies to overcome the major limitations identified here.

#### Acknowledgements

NHT gratefully acknowledges DTI support with FRED's SMART Awards, also the ongoing help and guidance from Severn Trent Water and kind accomodation of Birmingham University in nurturing the new culture of academic enterprise.

#### References

1. Bradley, P, Fowler, P & Thomas, N. 1993. Nitrifier inhibition by competition in oxygen deficient waste water. In preparation.
2. Janes, DA & Thomas, NH. 1992. Wind power for waste water treatment - a viability evaluation. Proc 1992 Research Event, 140-142; I Chem E (Rugby).
3. Janes, DA & Thomas, NH. 1993. Pilot plant studies on FRED's 'WATER' process for wind powered treatment of waste water. J Wind Engrg & Indust Aerodynamics; submitted.
4. Shrimpton, JS, Bradley, PK & Thomas, NH. 1993. Wind-powered waste water treatment: field trialling experience with a 2m pilot plant. In preparation.
5. Thomas, NH & Janes, DA. 1992. Wind powered waste water treatment - FRED's 'WATER' process. Wind Engrg Soc Inaugural Conference (Cambridge, September 1992). Poster & extended abstract.



Fig 1. FRED's 'WATER' machine: the 2m field trialling pilot plant on test.

## Flow Visualization of a Rotating Wind Turbine Blade

Jan-Åke Dahlberg and Göran Ronsten  
The Aeronautical Research Institute of Sweden  
and  
He Dexin and Chen Ming  
China Aerodynamics Research and Development Center

**Abstract** The paper presents surface flow visualizations on a blade of a 5.35 m diameter horizontal axis wind turbine. The tests were carried out in the 12m×16m low speed wind tunnel at China Aerodynamics Research and Development Center (CARD C). Surface flow characteristics were observed at various tip speed ratios and yaw angles at Reynolds numbers up to 600000.

### 1 Introduction

When using Blade-Element/Momentum theory it is assumed that the flow around the rotating blade is two dimensional. However, as the actual flow around the blade is three dimensional, the computed results are not in good enough agreement with measured data. At low tip speed ratios this disagreement is mainly caused by poor modeling of the flow around the blade and not by uncertainties in the magnitude of the wind speed in the plane of rotation. At high tip speed ratios, however, the wake distribution and thus the wind speed in the plane of the disc is the largest unknown factor.

In order to investigate the 3D effects, pressure measurements on the blade of a wind turbine were performed 1989 in a joint project between CARD C and FFA [1]. At the time of these tests there were no intentions to go into deep stall as this was not considered of interest for large wind turbines. The test results at medium-low tip speed ratios, down to  $TSR=3.7$ , show that the measured loads at the root are higher than the results of the theoretical calculations while the tip loads are smaller when compared to calculations.

In March 1992, extensive tests were carried out at CARD C including wall pressure measurements for blockage corrections, yaw control tests, stall tests, yaw failure tests etc. In order to investigate if it would be possible and useful to visualize the 3D flow on the rotating blade, flow visualization tests were also carried out at CARD C during this test period. The paper presents the test method and the results from these tests.

### 2 Test set up

#### 2.1 Model

The model is a 5.35 m diameter, two bladed, upwind horizontal axis wind turbine, which was mounted on top of an 8m tower, Fig. 1. The 2.35m 5WPX blade from the Dutch manufacturer STORK (now AEROPAC) has NACA 4412-4424 airfoils. The twist angle at the root is 8 degrees while the tip is untwisted. The pitch angle and the coning angle were set to zero. The generator was an ordinary 1500 RPM 3-phase induction generator with a rated power of 7.5kW. The rotational speed was controlled using a frequency converter (AC-DC-AC).

#### 2.2 Wind Tunnel

The tests were carried out in the 12m×16m test section of CARD C's large low speed wind tunnel.

### 3 Test method

#### 3.1 Test Schedule

As the camera had to be mounted outside the main shaft, the test envelope was restricted by the maximum rotational speed (200 RPM) imposed by the maximum allowable acceleration of the camera. The upper limit for the free stream wind speed was restricted by the maximum torque produced by the generator and the maximum rotational speed attained in case the frequency converter would be disconnected from the generator. At one occasion the rotor accidentally spun up to 260 RPM as a fuse in the frequency converter broke but no damage occurred to any equipment.

#### 3.2 Test Method

##### 3.2.1 *Wind speed control and measurement*

The ordinary control system used in the CARDC large low speed wind tunnel was used during the tests in order to keep the free stream dynamic pressure constant while both the rotational speed and the yaw angle were varied. The wind speed was measured using a small ( $\phi=0.1\text{ m}$ ) propeller anemometer placed 11m upstream of the wind turbine. This wind speed indicator was compared to the sensor used when calibrating the wind tunnel. The difference in wind speed at 8 m/s was 1.3% ( $q\approx 2.6\%$ ) and at 10 m/s was 0.5% ( $q\approx 1\%$ ).

The indicated wind speeds in the flow visualization images are not corrected for blockage. This blockage is smaller at low tip speed ratios than at higher tip speed ratios where the indicated wind speed is too low and thus the indicated tip speed ratio too high. An example of the magnitude of the blockage correction can be taken from the tests carried out 1989. At an uncorrected tip speed ratio of 4.5, the wind speed was corrected for blockage from 7.75 m/s to 7.89 m/s (0.14 m/s). At an uncorrected tip speed ratio of 6.6, the wind speed was corrected for blockage from 7.76 m/s to 8.02 m/s (0.26 m/s). These numbers are mentioned to give the reader an idea of the magnitude of the corrections.

##### 3.2.2 *Rotational speed control and measurement*

The rotational speed of the wind turbine rotor was controlled using a frequency converter (AC-DC-AC link) connected to an induction generator. The rotational speed was measured using a small DC tachogenerator and displayed on screen as the current RPM.

##### 3.2.3 *Yaw angle control and measurement*

The turning of the turbine nacelle was accomplished by an hydraulic yaw servo drive inserted between the top of the tower and the nacelle, Fig. 2. Pulses from a yaw angle transducer were counted and converted to a DC-voltage in the control computer. This voltage was measured and displayed on screen as the current yaw angle.

##### 3.2.4 *Flow visualization method*

Ordinary white sewing thread ( $\phi\approx 0.5\text{mm}$ ) was used to observe the surface flow pattern on the rotating blade. One of the two blades was covered by tufts attached by glue to the downwind (pressure) side of the blade. The tufts were placed in 31 rows in the radial direction starting at  $r/R=25\%$ , 27.5%, 30% etc, ending at  $r/R=95\%$ , 97.5% and 99%. At each radial position there were 8 tufts in a row, Fig. 3. The chordwise distribution was:  $s/c=0\%$ , 12.5%, 25%, ..., 87.5%.

Close to the leading edge, the tufts will cause transition from laminar to turbulent flow which will grow in radial extension in the chordwise direction. Tufts normally have a stabilizing effect on the turbulent boundary layer as their motion transfers energy from outside the boundary layer into the boundary layer. The tufts act like vortex generators.

It is difficult to draw any wise conclusions about the magnitude of the radial flow in the separated region caused by the radial flow, the radial pressure gradient and the centrifugal force. The difficulty is to separate the effect of the pressure gradient, the centrifugal force and the initial curvature of the tuft from the influence of the flow field on the blade.

##### 3.2.5 *Image Processing Technique*

In order to obtain a uniform background, the first tests were carried at night. By covering the windows in the wind tunnel, good images were later obtained during day time. A TCZ-200E video camera (VHS-quality) was attached to the rotor shaft while two focusing light bulbs were mounted on the hub, Fig. 4.

The video signal of the blade was fed into a DVA-4000 video board from videologics inside a Macintosh II fx computer where the test parameters were put on top of the original image using LabVIEW, a data acquisition and analysis program from National Instruments. The computer screen was finally converted back to a VHS-PAL signal using a MEDIATOR box from videologics and recorded on a simple video cassette recorder.

The images shown in this report have been digitized and manipulated using a DVA-4000 plugin module to the image processing program Adobe Photoshop. All images of the blade have been rotated and the colors inverted in Adobe Photoshop to help the reader to better understand the images. Explanatory text and visualizations have been added by hand.

## 4 Discussion

### 4.1 Image recognition

The mirror images on the blade surface of the tufts should not be confused with the actual tufts. The tufts align with the surface of the blade in the chordwise direction in attached flow from about 60% radius and outwards at  $TSR=7$ . The tufts deviate in the spanwise direction from about 60% and inwards at  $TSR=7$  and the deviation from the chordwise direction increases as the flow travels in the chordwise direction. At lower tip speed ratios, when separated flow occurs on parts of the blade, the tufts create a blurred image when they vibrate. Normally, when testing a 2D model, a reasonable definition of separation is when the tufts do not align with the chord. In this case, however, as the balance between the centrifugal force and the force from the flow itself are unknown, this definition is not applicable. A definition of separated flow on the rotating blade will have to include a criteria for estimating the maximum allowed inclination between the tuft and the chord.

### 4.2 Angle-of-attack prediction

In order to help the analysis of the flow images of the blade, the local angle-of-attack on the blade at each radial section was predicted using Blade Element/Momentum theory. The calculated results at various tip speeds and yaw angles are shown in Fig. 5.

### 4.3 Analysis of flow

#### 4.3.1 Flow characteristics of NACA4415 at low Reynolds number

Turbulent separated flow at the trailing edge occurs on a NACA 4415 when the angle-of-attack is around  $10^\circ$  at  $Re=400000$ [2].

#### 4.3.2 Characteristics of the flow

##### 4.3.2.1 Flow patterns at different tip speed ratios

Fig. 6 shows the tufts and the blade both during increasing tip speed ratios (TSR) as well as decreasing tip speed ratios. The close up at the tip is not from the same occasion as the image covering the whole blade although the operating conditions are about the same.

There is a small time delay between the update of the operational data and the image of the blade as the images are recorded during acceleration and deceleration. Considering this and the possibility of "static" stall hysteresis it seemed adequate to include the images during deceleration as well.

At  $TSR \approx 2.7$  (increasing), only the 99% and 97.5% radial stations show attached flow and sporadically one can see a narrow trail of attached flow at 90% and a band of not completely separated flow around 75% radius.

At  $TSR \approx 3.1$  (increasing), the tufts at the outermost 7% and between 72.5% and 85% radius indicate a stable attached flow. In the latter area separation starts at  $s/c \approx 40\%$  at 72.5% radius while

separation seems to start later, at  $s/c=75\%$ , at  $85\%$  radius. At  $52.5\%$  and  $55\%$  radius there is an area of less separated flow.

At  $TSR \approx 3.5$  (increasing), there is no region of separated flow in the radial direction close to the tip. The outermost  $5\%$  indicate attached flow to the trailing edge while separation starts at  $s/c \approx 40\%$  from  $95\%$  to  $40\%$  radius. The tufts inside  $45\%$  radius do not align with the chord.

At  $TSR \approx 4.5$  (increasing), the outermost  $7.5\%$  indicate attached flow to the trailing edge while separation starts at  $s/c \approx 70\%$  from  $92.5\%$  radius to  $s/c=35\%$  at  $25\%$  radius. The tufts inside  $60\%$  radius do not align with the chord.

The area indicating attached flow grows at higher tip speed ratios.

#### 4.3.2.2 *Flow patterns at different yaw angles*

The video images show the tufts moving oscillatory, indicating separated and attached flow periodically. The reason is that the radial distribution of the local angle-of-attack is changing with azimuth position periodically when the wind turbine is yawed out of wind. Fig. 7 shows the maximum and minimum attached flow at various yaw angles at various tip speed ratios.

At  $TSR \approx 6.9$  and  $TSR \approx 4.1$ , the line of separation moves back and forth in the chordwise direction. Only with some imagination is it possible to see a separated region at the tip at  $TSR \approx 4.1$  at  $45^\circ$  yaw angle. No close ups of the tip were taken other than at  $TSR \approx 3.1$ .

At  $TSR \approx 3.1$ , a region of separated flow at the tip comes and goes as the azimuth angle changes. An interesting feature is that as the yaw angle increases the maximum area of attached flow increases as does the minimum area. The latter might be an effect of dynamic stall and/or high induction caused by the conditions on the opposite blade half a revolution earlier.

#### 4.3.2.3 *Comparison with pressure measurements*

Fig. 8 shows similar operating conditions for the whole blade, for the tip and the "corresponding" pressure distributions. At  $30\%$  radius, the flow deviation from the chord line is significant and increasing with decreasing tip speed ratio. At these angle-of-attacks, the non-rotating blade has stalled at the root while the rotating blade has a pressure distribution which corresponds more to the image of the rotating blade than the non-rotating blade. In general it seems like the tufts indicate separation earlier than the pressure distributions although two things should be considered. The first thing to bear in mind is the fact that none of the images nor the pressure distributions were recorded at the same occasion. The second issue effecting the flow image beside the distortion of the flow caused by the tuft itself is the view angle of a declined tuft at the trailing edge.

## 5 Conclusions

It is possible to observe flow patterns on a rotating wind turbine blade using a video camera and enlightened tufts. The results demonstrate that the real flow is highly three dimensional both at the root and at the tip. It should be considered repeating these tests using two S-VHS or better quality cameras, mini-tufts and ultraviolet light in order to enhance the resolution and to minimize the influence of the centrifugal force on the tuft.

## 6 Reference

- [1] G. Ronsten, J.-A. Dahlberg, S. Mejer, He Dexin and Chen Ming; Pressure Measurement on a 5.35 m HAWT in CARDC  $12m \times 16m$  Wind Tunnel Compared to Theoretical Pressure Distributions, FFA TN 1989-46.
- [2] E. Saliveros, R. A. Mc D. Galbraith and F. N. Conton; The Low Reynolds Number Performance of a NACA 4415 Aerofoil, 9th BWEA Conf. Edinb 1-3 April, PP287-294, 1987.

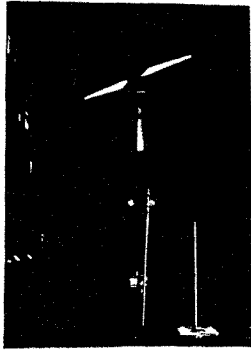


Fig. 1 Wind turbine in the 12m×16m wind tunnel test section



Fig. 2 Hub, nacelle and yaw mechanism

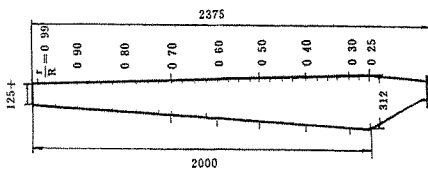


Fig. 3 Distribution of tufts on the blade

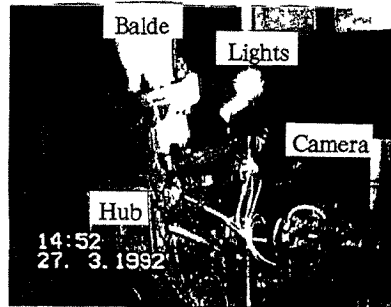


Fig. 4 Camera and light positions

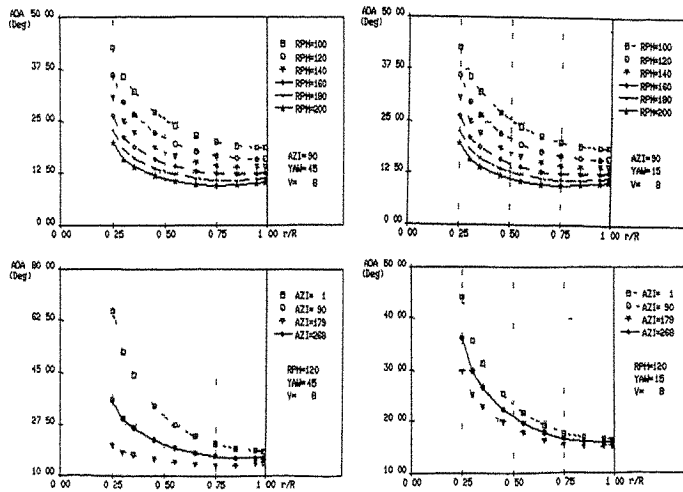
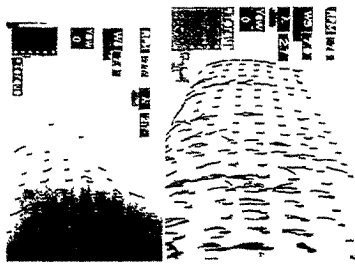
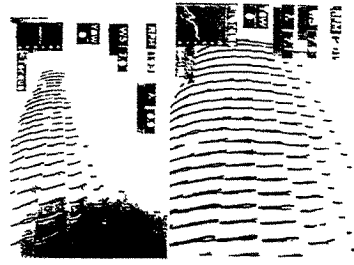


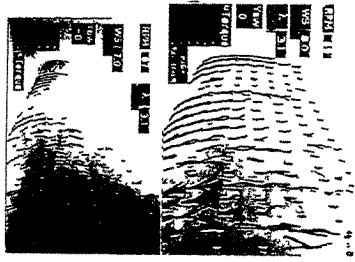
Fig. 5 Radial distribution of angle of attack as function of rotational speed, azimuth angle and yaw angle



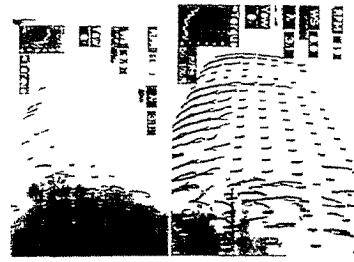
a. TSR = 2.7 increasing RPM



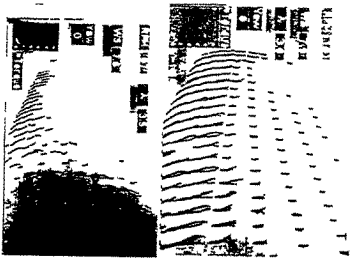
e. TSR = 7.0 increasing RPM



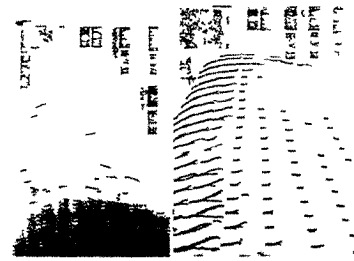
b. TSR = 3.1 increasing RPM



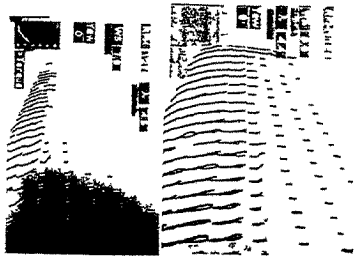
f. TSR = 3.1 decreasing RPM



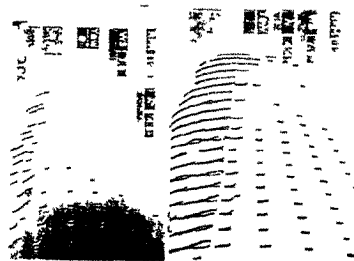
c. TSR = 3.5 increasing RPM



g. TSR = 3.5 decreasing RPM



d. TSR = 4.5 increasing RPM



h. TSR = 4.5 decreasing RPM

Fig. 6 Flow patterns at different tip speed ratios



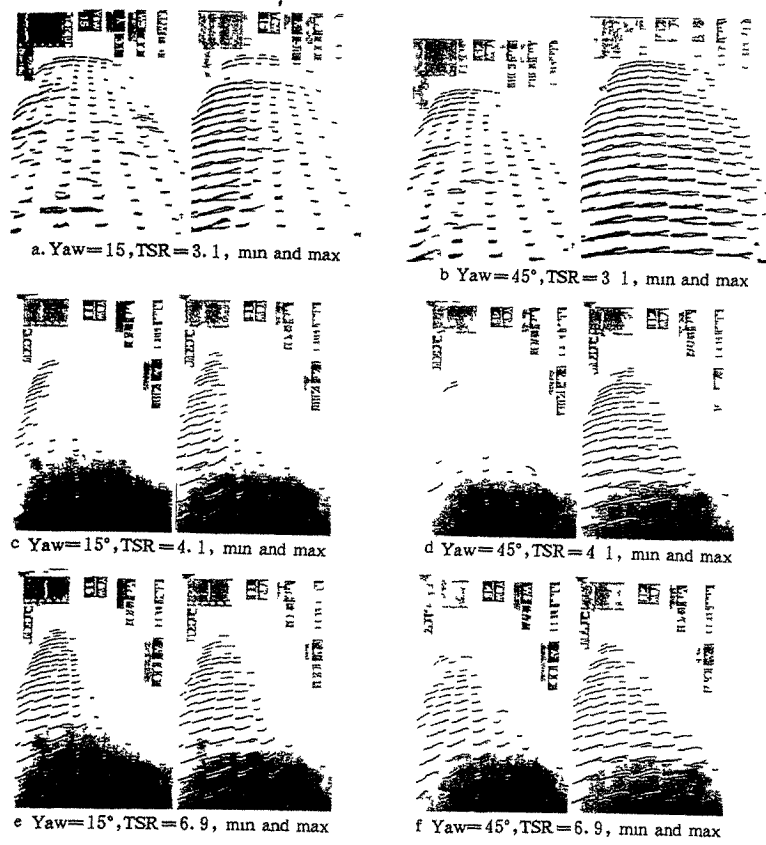


Fig. 7 Flow patterns at different yaw angles

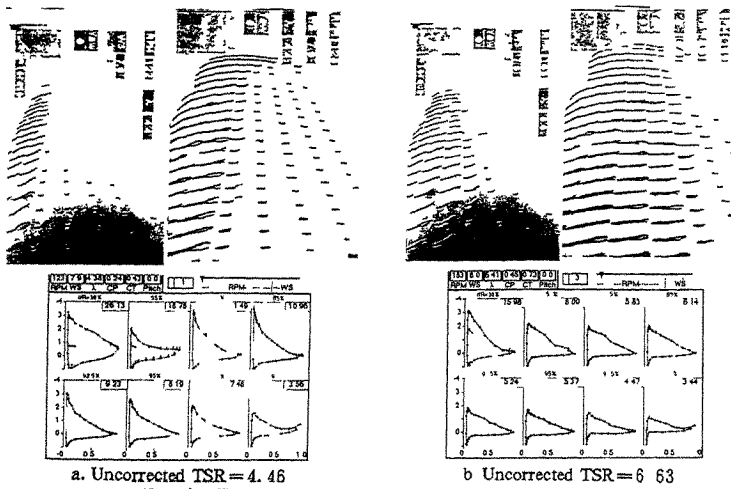


Fig. 8 Flow patterns compare with pressure distributions in similar operating conditions



## A research and exploitation on wind energy resources along the coast of Guangdong Province

Luo Jinlin

Applied Climate Institute, GRMC, Guangzhou, China

**Abstract:** On-the-spot data of 18 wind observing spots and ten years wind data in meteorological stations along the coast of Guangdong were used to investigate wind energy resources. An appraisal on the potentiality of exploitation and utilization of wind energy as well as its economic return were made in this paper, too.

### I. Introduction

With 4300 km coastline and numerous islands, the province is rich in wind energy resources. In order to programming and further exploitation of new kinds of energy, Planning Commission of Guangdong Province entrusted ACI to conduct an investigation on the distribution of wind energy along the coast. For these reason it became necessary for estimating wind energy resources objectively to select 18 observing spots along the coast area with representative location, terrain and island. Starting from in April 1989 to in April 1990, the observing experiment gained abundant data.

### II. Calculation method

#### 1. The extension of observing spots data

Taking adjacent meteorological station as a contrast point, each observing spot was calculated its average and maximum wind speed for many years, and then its wind energy parameter could be obtained by using Weibull distribution function. Considering factors as monthly average wind speed of observing spot and meteorological stations, daily maximum wind speed ( $>12\text{m/s}$ ) of observing spots and daily maximum wind speed of contrast points, respective correlation type and its formula could be established by optimum method.

The good result indicated that the reliability of correlation coefficient amounted to 0.05-0.001, and calculated value shad identical one with real observing values. Error of yearly average wind speed in most of contrast points were 0, error of maximum wind speed was less than and equal to absolute measurement of 1.0m/s.

#### 2. Calculation of wind energy

##### (1) Direct statistic method

Wind energy density was given by the following formula with a use of data of recording anemometer.

$$\bar{W} = (1/N) \sum_{i=1}^k (1/2) \rho N_i V_i^3 \quad (1)$$

where  $\bar{W}$  was the average wind energy density, that was the number of wind energy passing through unit area at unit interval;  $N_i$  was the number of wind speed  $V_i$  appearing at wind grade  $i$ ;  $N$  was the total number of observing wind speed;  $K$  was the number of wind grade;  $\rho$  was the air density (average air density value for years was adopted in the contrast point).

(2) Weibull double-parameters calculation method

Wind speed obey Weibull's probability distribution in the ground layer. It not only smoothed accidental error, but also obtained wind speed frequency and its wind energy parameters easily. In a special cases, the method was unreplaceable.

Weibull distribution function is:

$$P(v) = \int_0^v f(v) dv = 1 - \exp[-(v/c)^k] \quad (2)$$

here the calculating method of average wind speed and maximum wind speed was used to estimate the scale parameter  $c$  and shape parameter  $k$ .

$k, c$  by:

$$k = \ln(\ln T) / \ln(0.90 V_{ax} / \bar{V}) \quad (3)$$

$$c = \bar{V} / \gamma (1 + 1/k) \quad (4)$$

Where  $T$  was the number of time;  $V_{ax}$  was the maximum wind speed (mean of 10 min.);  $\bar{V}$  was the average wind speed;  $\gamma$  was the Gamam function; after  $c, k$  was given,  $\bar{W}, \bar{W}_e$  and  $t$  was calculated by:

$$\bar{W} = 0.5 \rho c^3 \cdot \gamma(3/k+1) \quad (5)$$

$$\bar{W}_e = \frac{0.5 \rho (k/c)}{\exp[-(v_1/c)^k] - \exp[-(v_2/c)^k]} \cdot \int_{v_1}^{v_2} V^3 \cdot (v/c)^{k-1} \cdot \exp[-(v/c)^k] \cdot dv \quad (6)$$

$$t = T \{ \exp[-(v_1/c)^k] - \exp[-(v_2/c)^k] \} \quad (7)$$

### III. Wind generator capacity factor

Capacity factor was rated power divided by average output power of wind generator. If wind probability distribution  $f(v)$  was known, actual output power of wind generator  $P$  could be obtained by the formular:

$$P = \int_0^{\infty} p(v) f(v) dv \quad (8)$$

after Weibull's parameters  $c, k$  was given,  $P$  was calculated by:

$$P = \int_{v_0}^{v_1} (A + Bv + cv^2) dv + P_r \{ \exp[-(v_1/c)^k] - \exp[-(v_2/c)^k] \} \quad (9)$$

$$\text{capacity coefficient was: } F_c = P/P_r \quad (10)$$

#### IV. Distribution feature of wind energy resource along coast area

##### 1. On-the-spot observing data

The following parameters of wind energy were obtained by direct statistic method.

##### (1) Yearly effective wind speed(3-20m/s) period

Except the west bank of Leizhou penisular was less than 6000 hours, the rest observing spots was above 6000 hours and islands and capes over 7000 hours. For example, Guishan island was 8017 hours. Observing spots were over 3000 hours on average more than that of in meteorological stations.

##### (2) Yearly effective wind energy density

The density of observing spots were mostly above  $150\text{w/m}^2$ , islands and capes above  $200\text{--}300\text{w/m}^2$ , such as Zhelang  $371.3\text{w/m}^2$ , Guishan island  $359.4\text{w/m}^2$ . The average of observing spots doubled that of meteorological stations, some 6 times as much as that of them.

##### 2. Average calculated value for many years

Weibull double parametrs probability distribution was used to investigate average value of wind energy for many years in each observing spot. The result showed that the values were significant greater than that of in real-observing period(due to be less-wind for the year of observing).

##### 3. Regionalization of wind energy

In light of conditions in Guangdong, yearly effective wind energy was used to be regionalization index according to national standard.

abundant area  $E > 1900$

less-abundant area  $900 < E < 1500$

exploitation area  $150 < E < 900$

deficient area  $E < 150$

##### (1) Abundant area

The area including offshore islands, capes along the coast and raised hillock had average wind speed  $> 5.5\text{m/s}$ , and yearly effective wind energy  $1500\text{--}3400\text{ kwh/m}^2$ . The period of daily generating energy in winter (Oct. - Mar.) was  $> 20$  hours, and 15-19 hours in summer (Apr. - Sep.). There were fit to install large - scale wind generator.

##### (2) Less-abundant area

The area 2 km away from the coastline had yearly average wind speed  $4.5\text{--}5.5\text{m/s}$  and yearly effective wind energy  $900\text{--}1500\text{ kwh/m}^2$ . It would generate electricity of 15-19 hours everyday in winter.

##### (3) Exploitation area

With  $3.0\text{--}4.5\text{m/s}$  yearly average wind speed and  $150\text{--}190\text{ kwh/m}^2$  yearly effective wind energy, the area 2-10 km away from the coastline would generate 10 hours electricity in season of strong wind.

##### (4) Deficient area

In addition to some hillock and wind gap, the coastbelt except for the above area had only yearly average wind speed  $< 3\text{m/s}$  and yearly effective wind energy  $< 150\text{ kwh/m}$  with low exploitaiton values.

## V. An appraisal on potential of exploitation and utilization of wind energy resources

### (1) Coast gross storage of wind energy resources

Coastline in Guangdong is so long as 4300 km that the area such as 2 km wide was taken as an example to demonstrate the storage. If a half of this area would install 10 m diameter blade wind generator, its effective gross storage of wind energy would have reached 41 billion kwh. Therefore 8.3 billion kwh electricity would be generated each year. So the potential of exploitation of wind energy resources along the coast of Guangdong has broad prospect.

### (2) Economic return evaluating

Distinct economic return was shown on this way. A wind generator with 10m diameter blade can generate 189 million kwh every year, 6 m diameter blade generator will raise 352,000 tons water 1 m higher or irrigate an rice area of 754 mu or refine 12,300 tons salts annually. A 200 w micro-generator cost will be recalled at 0.2-0.4 yuan for each kwh. Large and medium generators over 100 kw will recall their cost and interest in 6 -8 years(the imported generator price).

## Reference

1. Ye Qingkai, Wang Zhaoming, Calculation method of optimum control Science Press, 20 -29, 1986.
2. Zhu Ruizhao, Xue Yan, Applied Climate Handbook, Meteorological Press, 1992

## The stable position of a radar antenna system and application of the aerodynamic compensator to an array antenna

Bian Zongshan and Wu Zhicheng\*

Nanjing Research Institute of Electronic Technology,  
Nanjing 210013, China

\* Department of Aerodynamics  
Nanjing University of Aeronautics and Astronautics,  
Nanjing 210016, China

**Abstract:** In this paper the conditions for a radar antenna system to be in the stable equilibrium position under the action of wind are given when the system is in free rotation or unlocking state. Then some ideas of using aerodynamic compensators to change the stable position are presented to increase the security and wind resistance ability of the system. Finally some results are introduced from a wind tunnel experiment which is about using a flat-plate aerodynamic compensator in an array-antenna system. It has been proved to be effective in the practice for this study.

### Introduction

In this paper we will discuss some aerodynamics problems of a radar antenna system without *wind-break* cover under the action of natural winds. For the sake of convenience, here we choose the wind axis system  $oxyz$  (Seen in Fig.1). The load on the antenna can be decomposed into drag force  $X$ , lift force  $Y$  and side force  $Z$ . Besides these, there are also rolling moment  $M_x$ , azimuth wind moment  $M_y$ , overturning moment (pitch moment)  $M_z$  and the azimuth angle  $\beta$  which is between the normal direction of frontal projective plane of antenna and the  $x$  axis. The arrow direction in the figures is defined as positive direction.

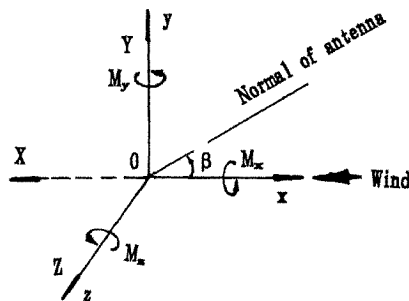


Fig.1 Wind axis system

Usually it is convenient to change those forces and moments into *non-dimensional* coefficients as follows,

$$c = \text{force} / (1/2 \rho V^2 S)$$

$$m = \text{moment} / (1/2 \rho V^2 SL)$$

where  $\rho$  is air density,  $V$  is wind speed,  $S$  and  $L$  represent the characteristic area and the characteristic length of antenna respectively.

According to the aerodynamics theory, it is considered to be an effective method for changing the stable position of antenna's system by using aerodynamic compensators in it, and this has been proved to be true in our wind tunnel experiment and some *actual* applications.

## 2. Stabilization conditions for the antenna system

When a radar antenna system is inoperative, especially in the case that the wind speed exceeds the allowed operating speed, usually it is always in the unlocking state for the system. The antenna may turn freely under the action of wind and achieve stability at some position. The stabilization condition for the antenna at some position ( $\beta_s = \beta_i$ ) is described as follows,

$$\begin{cases} (|m_y| - |m_{y_f}|)_{\beta_s = [\beta_a, \beta_b]} < 0 & (1) \\ (dm_y / d\beta)_{\beta_s = [\beta_a, \beta_b]} < 0 & (2) \end{cases}$$

where  $m_y$  is the azimuth moment coefficient. This coefficient is the function of azimuth angle  $\beta$ , which changes with the movement of antenna's angle  $\beta$ .  $m_{y_f}$  in the above formulation means the coefficient of maximum static friction moment of the system which has nothing to do with the angle  $\beta$ . If these two conditions are satisfied at the same time, the antenna system will be stabilized at one point in the region of  $[\beta_a, \beta_b]$ . Since it is instable of the wind speed and wind direction for the natural wind in the air, the antenna will have a small flapping movement near its stable position.

Fig 2 shows one antenna's  $m_y \sim \beta$  ( $0^\circ < \beta < 360^\circ$ ) relation curves. In the figure the two dash lines parallel to the  $\beta$  axis represent respectively the equivalent value of  $m_{y_f}$  when the wind speed is  $V_0$  and the equivalent maximum static friction moment  $M_{y_f}$ . These lines intersect ( $m_y \sim \beta$ ) curve separately at point  $\beta_1, \beta_2, \dots, \beta_n$ . According to the above stabilization conditions, it is sure that only region  $[\beta_n, \beta_1]$  and region  $[\beta_n, \beta_n]$  are stable for the system.

Generally the antenna's azimuth shaft lies in its symmetric plane. It can be seen from Fig 2 that when  $\beta = 0^\circ$  or  $\beta = 180^\circ$ , the azimuth moments at these two points are equal zero because of the antenna's symmetry. When the antenna turns for a small angle of yawing corresponding to the small change of wind direction, the produced aerodynamic azimuth moment will always make the antenna turn back to the stable position ( $\beta_s = 0^\circ$  or  $\beta_s = 180^\circ$ ) because of the twisting effect of stream to the antenna. Therefore there



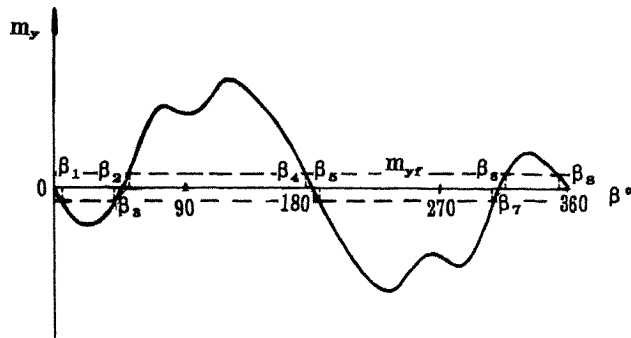


Fig 2 Stable position of antenna system

exist two stable points in the region near  $\beta_s=0^\circ$  and  $\beta_s=180^\circ$  ( i.e.  $[\beta_s, \beta_1]$  and  $[\beta_4, \beta_5]$  ).

In the case of heavy wind when the antenna's azimuth angle is at  $\beta_s=0^\circ$  or  $\beta_s=180^\circ$ , the windage and overturning moment at this time will be the biggest. So in order to ensure the security of system it is necessary to strengthen the antenna's structure, its transmission mechanism and its base pad in the designing. As a result the cost and weight of the system is certainly be increased.

### 3. Application of aerodynamic compensator

An aerodynamic compensator can change the stable position of antenna so as to make it in a position with smaller windage and smaller overturning moment. It is useful for structure designing and can also increase the security and wind resistance ability of the system.

The method of using a flat-plate aerodynamic compensator which is installed outside the antenna with its fixed angle adjustable is taken in the end after we have studied and compared several designing methods of using various aerodynamic compensators. The principal advantage of the method is as follows:

- (a) When using a flat-plate as compensator it is simple in structure, convenient in making and installation and can also provides a bigger aerodynamic force.
- (b) Being installed outside the antenna and far away from the antenna's azimuth shaft, the aerodynamic effect of the compensator is more remarkable. This is because the further away the compensator is from the azimuth shaft, the bigger azimuth moment it can supply for the antenna. And therefore the area of the aerodynamic compensator may be decreased a lot.
- (c) When the antenna system is in operative or inoperative state the compensator's fixed angle is at two different value and these two fixed angles can be changed into each other. In the normal working state the compensator is installed at one special

angle so that the azimuth wind moment on the antenna basically remains the same value as that of without compensator. In the inoperative state the compensator is adjusted at another fixed angle so that the compensator in this position can produce enough azimuth moment in order to change the stable position and increase the security and wind resistance ability of the system. By the way of changing compensator's fixed angle, it can not only make the system stable at one position with smaller windage and overturning moment when in inoperative state, but also can make it possible to increase no driving power for the antenna rotation when in operative state.

#### 4. Study of wind tunnel experiment

A wind tunnel experiment was made by using a flat-plate compensator on an array antenna. It was done in a 1.5m wind tunnel in Nanjing Research Institute of Electronic Technology. Fig. 3 shows a simplified model of array antenna used in the experiment. The ratio of length to width of compensator is 27, and its area is 6% of the antenna's frontal projective area. The compensator is installed at the edge of one side of antenna

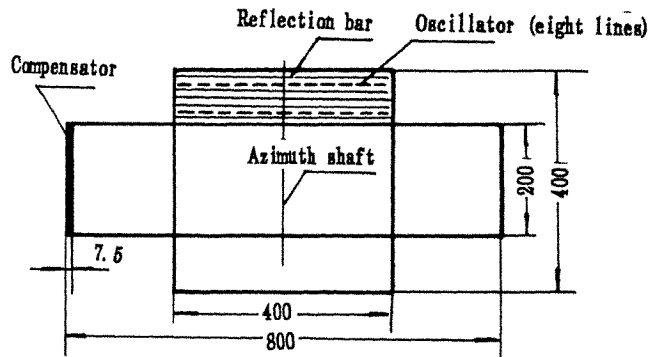


Fig. 3 Simplified model of antenna's outline

The fixed angle between the compensator's plane and the antenna's frontal projective plane is adjustable. A conclusion is drawn about the reasonable fixed angle according to the wind tunnel experiment. It is that if in normal operative state, the fixed angle is at  $90^\circ$  (vertical to the frontal projective plane of the antenna); if in inoperative state the fixed angle is at  $10^\circ$ .

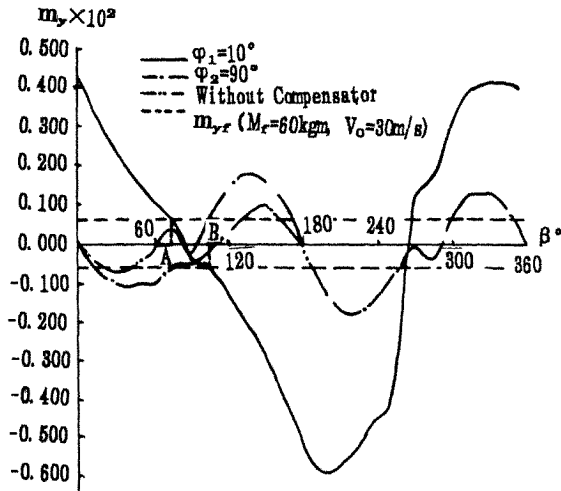


Fig 4 Antenna's  $m_y$ - $\beta$  curves with and without compensator

In Fig 4 the  $m_y$ - $\beta$  curves with compensators are given. It can be seen that when wind speed is  $V_0=30\text{m/s}$  and the maximum static friction moment is  $60\text{Kg-m}$ , the stable position of the system without compensator is near  $\beta_s=0^\circ$  or  $\beta_s=180^\circ$ . However when the compensator is installed with its fixed angle at  $\varphi_1 = 10^\circ$ , the stable position is moved to the region between [A, B], i.e. between  $\beta_s=75^\circ \sim 105^\circ$ . When the antenna is working normally and the fixed angle is adjusted to  $\varphi_2 = 90^\circ$ , the peak value of azimuth moment and its mean square root at this time are the same as those without compensator. It is also seen from Fig 5 that when the stable position moves from  $\beta_s = 0^\circ$  or  $180^\circ$  to  $\beta_s=75^\circ \sim 105^\circ$ , the windage on the antenna decreases at least more than 60% and the overturning moment also decreases correspondantly.

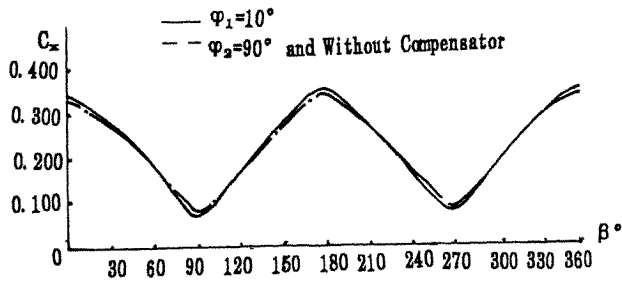


Fig 5 Antenna's  $C_x$ - $\beta$  curves with compensator (fixed angle is  $10^\circ$  and  $90^\circ$ )

It is worth noticing that in the instable region like  $[\beta_6, \beta_3]$  and  $[\beta_6, \beta_7]$  in Fig. 2, the antenna may stop turning in this region because of the action of static friction moment. So it is still necessary to consider the instable position even if the aerodynamic compensator has been installed. In Fig. 4 we find that the instable position will lie nearby  $\beta=270^\circ$  after the compensator installation and the windage and overturning moment are very small in this position. But the curves in this region are very steep. All this shows that the  $M_y$  value in instable position is very sensitive to the change of  $\beta$ . Once instability occurs in natural wind, a yawing moment bigger than static friction moment will be produced correspondant to any small changes of wind direction blown on the antenna and this can make the antenna turn back to the stable position from instable position rapidly.

## 5. Conclusions

The conditions given in this paper for judging whether the antenna system is in stable position under the action of wind in unlocking state are suitable for various types of antennas. For those antenna systems where the structure is symmetric and the azimuth shaft lies in the symmetric plane, their stable position is sure at  $\beta=0^\circ$  or  $180^\circ$ . In this position the windage and overturning moment on antenna are the biggest. It is an effective and simple way by using aerodynamic compensators to change the stable position of the system. Installing a flat-plate compensator outside the antenna with its fixed angle adjustable can have the advantages such like simple structure, remarkable effects, convenient making and using and no increasement of motor driving power. It can be widely used in many applications. The study results described in the paper have been verified in the wind tunnel experiment and practical use.

## Comparative study of the storm surge models proposed for Bangladesh : last developments and research needs

J.A. As-Salek and T. Yasuda<sup>+</sup>

Graduate Student, Dept. of Civil Engg.(Coastal), Gifu University, Japan  
<sup>+</sup>Professor, Dept. of Civil Engg.(Coastal), Gifu University, Japan

**Abstract:** The storm-surge models so far proposed for Bangladesh are discussed by emphasizing the new ideas developed and the deficiencies remaining. Numerical experiments are done by developing a model and a set of recommendations is made. The present status of storm-surge modelling activities for Bangladesh and the areas of research-needs are pointed out.

### 1. Introduction

Despite the loss of many lives every year, much is still remain to know the interactions among cyclone, astronomical tide and storm surge in the Bengal Bay. Need has also been arised to compare and combine the ideas developed in last storm-surge researches for Bangladesh.

A model has been developed by coupling two models of two different grid-spacings. The importance of 'Swatch of No Ground' (a deep gully situated about 24 km to the south of Bangladesh) and the effects of the coriolis force, sea-level rises and sedimentations on astronomical tide and storm surge are investigated. The results are also used to review the storm surge models proposed for Bangladesh and to formulate the recommendations.

### 2. Numerical Experiments

A typical numerical model of the astronomical tide and storm surge has been developed by integrating vertically the Navier-Stokes equation over the whole depth assuming hydrostatic pressure. The linear continuity equation is,

$$\frac{\partial \eta}{\partial t} + \frac{\partial M}{\partial x} + \frac{\partial N}{\partial y} = 0 \quad (1)$$

The momentum equations in the x-direction and y-direction are,

$$\frac{\partial M}{\partial t} + \beta \left( U \frac{\partial M}{\partial x} + V \frac{\partial M}{\partial y} \right) = -gd \left( \frac{\partial \eta}{\partial x} + \frac{1}{\rho g} \frac{\partial P_a}{\partial x} \right) + \frac{1}{\rho} (\tau_{sx} - \tau_{bx}) - \frac{1}{\rho} \left( \frac{\partial \tau_{xx}}{\partial x} + \frac{\partial \tau_{yx}}{\partial y} \right) + fN \quad (2)$$

$$\frac{\partial N}{\partial t} + \beta \left( U \frac{\partial N}{\partial x} + V \frac{\partial N}{\partial y} \right) = -gd \left( \frac{\partial \eta}{\partial y} + \frac{1}{\rho g} \frac{\partial P_a}{\partial y} \right) + \frac{1}{\rho} (\tau_{sy} - \tau_{by}) - \frac{1}{\rho} \left( \frac{\partial \tau_{xy}}{\partial x} + \frac{\partial \tau_{yy}}{\partial y} \right) - fM \quad (3)$$

Here,  $d$  is the total depth of water,  $h$  is the depth from the mean level,  $\eta$  is the water surface elevation,  $P_a$  is the atmospheric pressure,  $\rho$  is the water-density,  $f$  is the coriolis acceleration,  $\tau_{xx}, \tau_{xy}, \tau_{yx}$  and  $\tau_{yy}$  are the internal shear stresses,  $\tau_{sx}, \tau_{sy}$  are the surface wind stresses and  $\tau_{bx}, \tau_{by}$  are the bottom friction stresses.  $\beta$  is the momentum correction factor.  $M$  and  $N$  are the line discharges of  $x$  and  $y$  direction respectively, where  $U$  and  $V$  are the mean water velocities defined as,

$$M = \int_{-h}^{\eta} U dz, \quad N = \int_{-h}^{\eta} V dz \quad (4)$$

Fujita's Model [1] is used to simulate the cyclone assuming linear, steady state, non-anomalous, symmetrical flow of air and circular centric isobars of pressure and thereby calculating the gradient wind speeds, pressure gradients and the moving speeds of the cyclone.

Two-points finite-difference implicit schemes are used with equal-weights on upper and lower time-levels. ADI method is used to solve the schemes. The grid spacings are 1 minute-distance for larger-grid model and 1/2 minute-distance for finer-grid model. The models are stable for the Courant number  $\leq 1$ . B-spline interpolated bottom topographical data are used for finer-grid model. Tidal levels with  $M_2$  and  $K_1$  components in open boundary of larger-grid model are taken from Schwiderski [2]. Dirichlet-condition is assumed for boundary recurrence-relations in larger-grid model. The velocities and the water-levels calculated by larger-grid model in continental shelf areas are used as the boundary values of finer-grid model in shallow delta areas. The optimum model area is from  $89^\circ\text{E}$  Longitude and  $21^\circ\text{N}$  Latitude incorporating the 'Swatch of No Ground (SNG)' and worst effected coastal areas.

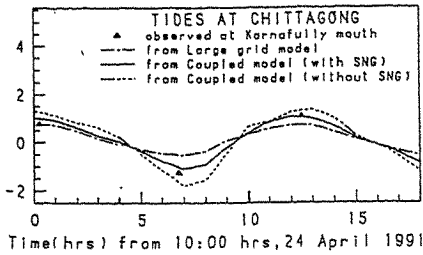


Fig.1. Simulated astronomical tides.

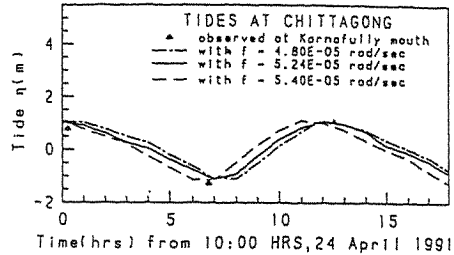


Fig.2.  $f$  effects wave propagation.

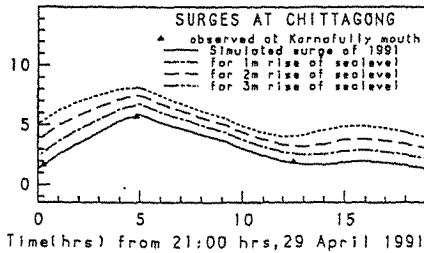


Fig.3. Effects of sea level rises in surges.

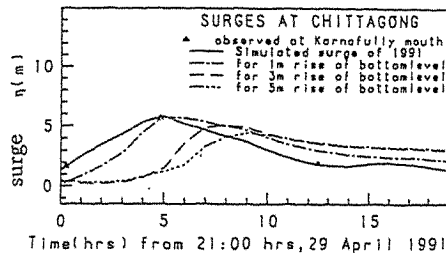


Fig.4. Effects of sedimentations in surges.

Simulated astronomical tide and storm surges fairly agree with the observed values for 1991 cyclone and results from coupled model agree better than results from a larger grid model applied for entire area (Fig.1). Thus patching the models with different grid spacings in accordance with the step formulations has been proved economical by the present study. In the model area,  $f$  varies from  $5.4 \times 10^{-5}$  rad/s in northern delta to  $4.8 \times 10^{-5}$  rad/s in southern open boundary. Present study suggests the optimum values of  $f$  to be  $5.24 \times 10^{-5}$  rad/s (Fig.2). The model predicts 0.8m, 1.5m and 2.3m increases of surge heights for a cyclone same as 1991 cyclone with 1m, 2m and 3m sea level rises (Fig.3). For slightest sea level rise in near future - the devastation of the storm surges will be more severe. Further study is needed to estimate the

surge propagation over the lands with the effects of sea level rises. The Bengal delta discharges 6000 million tons of sediments per year [3]. The speculated sedimentation or sea-bottom rises showed retardation of surge propagation for 1991 type cyclone. But peaks of almost same height with prolonged duration may be emerged (Fig.4). The inclusion of 'Swatch of No Ground' effects the wave propagations (Fig.5a) and velocity distributions (Fig.5b).

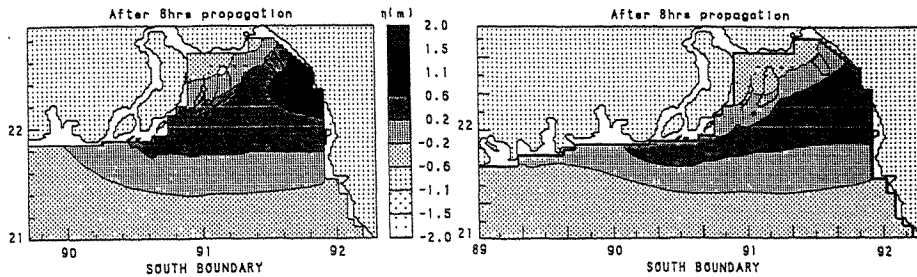


Fig.5a. Inclusion of 'Swatch of No Ground' (right Fig.) effects wave propagations.

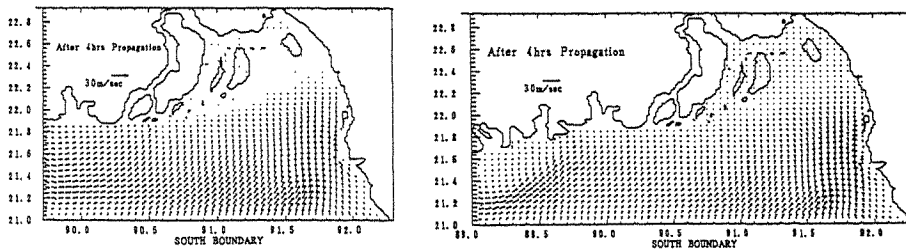


Fig.5b. Inclusion of 'Swatch of No Ground' (right Fig.) effects tidal currents.

### 3. Proposed Numerical Models

Flierl et al.[4] proposed nomograms of surge heights vs. landfall points and track angles of cyclone without considering the effect of barometric pressure. He used statical super impose of local tide with surge. Bottom friction term and island areas were omitted. Only 2 of his 5 simulated surge heights were agreed with the observed values.

Das et al. [5,6] used tidal forcing in open boundary and showed that superposition of surge on tide over-estimates the sea-level. But he manually smoothed the bottom topography, used very large grid of 15km~30km and omitted the island areas. Peak surge arrived within 2 hours of cyclone's hit and 30 km right to the centre for 1970 cyclone. He gave a formula relating the pressure drop and the translatory speed of cyclone with surge heights.

Dube et al. [7,8] developed a river-bay coupled model by using the Meghna as a pathway of surge for a i) definite and ii) no discharge and simulated 1970 cyclone. He considered unidirectional flow without meandering, no tide and constant river-discharges of 30,000 m<sup>3</sup>/sec by conditionally stable schemes. He used 'unrealistic' [7] extrapolated surge values with his grid spacings of 8km~30km. He showed short lived peak surge and used statical super impose of local tide with surge. Coriolis terms, island areas and wind stress terms were omitted.

Flather et al. [9] proposed a model with river modules but omitted the island areas.

Frank and Hussain [10] gave damage-analysis and some data of 1970 cyclone situation

John et al. [11,12] proved curvilinear boundary treatment is better than rectangular one, showed the interactions of tide and surge, simulated 1970 cyclone but discarded island areas

Yamashita et al. [13,14] simulated 1991 cyclone by a fractional step method with exchange depth and objective analysis of cyclone. Model run up test did not give good results. Simulated maximum astronomical tide showed a difference of 2.5m ~ 1.3m. The scheme for tidal propagation was stable for the Courant no.  $\leq 0.2$ . He used Holly and Preissmann scheme by adapting a cubic equation for nonlinear advection terms but achieved same results. He applied about 2 hours earlier (Fig.6) astronomical tide by approximating Schwiderski's T as  $T = (2.739 \times 10^4 + 1.000\bar{D})/3.653 \times 10^4$ . He also showed [14] 1/2 hourly cyclone positions as 1 hourly positions (Fig.7).

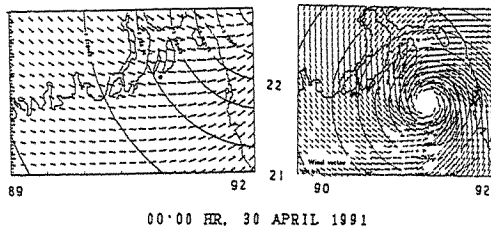
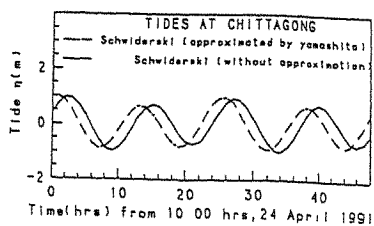


Fig.6. Approximated T imparts phase differences of 2 hrs. Fig.7. Cyclone's position; actual(left Fig.) and shown by Yamashita [14] (right Fig.)

Katsura et al. published a report [14] on storm surges and wind disasters caused by 1991 cyclone. Their objective analysis of the pressure pattern gave 'unreasonably low' [14] central pressures of 900 mb. They found 'over estimated' wind speeds by Fujita's model, 'discrepancies of wind direction' by Yoshizumi's model and used Mitsuta and Fujii's model. They reported intensified beach erosion, full inundation of islands during the peak and no hydrodynamical roughness against flooding in the coastal zones. Yasuda related the power of a cyclone, the damages and the risk to life. He pointed the dense populations in danger zones, insufficient countermeasures and high tide as the reasons of extensive damages.

Yamanaka [15] proved spatial scale of the Bengal Bay is bigger than the cyclone scales and wind distributions on the sea surface are not so influenced by the land

#### 4. Proposed Empirical Models

Chowdhury et al. [16] generated surge height data of various return periods from maximum wind speed and length of the continental shelf. He assumed linearly varying bottom topography, absence of astronomical tides and divided the coastal area into 3 regions.

S. Karmakar [17] calculated monthly and annual frequency of cyclone and their statistical aspects by dividing the coast into 4 parts according to the vulnerability of cyclone.

Chowdhury and Ah [18] proposed maximum storm surge heights including tide values against given pressure drops and wind speed. Ali [19] concluded that the contribution to surge height due to barometric forcing is small compared with that due to wind stress.

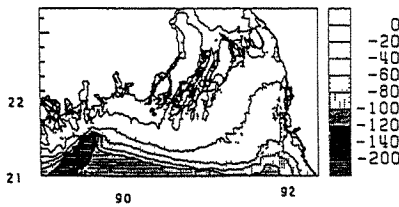


## 5. Coronaries

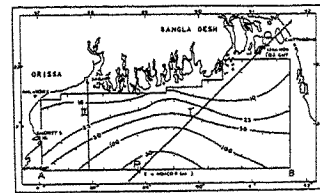
Dube and John recommended curvilinear boundary treatment. But rectangular boundary treatment, followed by Yamashita and present study, is suitable with data availability. Continuously contracting grid systems adjacent to coastal boundary may not be so practical as the bottom slope near the coastline is very small and the required data is not available.

A model for predicting local astronomical tide is still needed for Bangladesh. Approximate tidal forcings in the open boundary may lead to wrong calibration of the model. Schwiderski [2], popularly being used to specify astronomical tides in the open boundary, can not be used for calculating tidal levels and simulating storm surges before 1973.

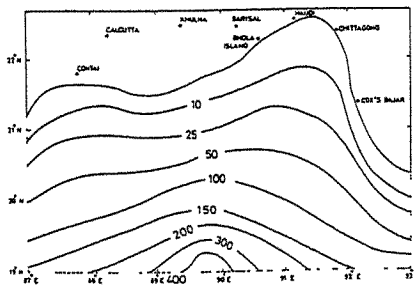
The sea-bottom of the proposed models are inconsistent with actual situations (Fig.8).



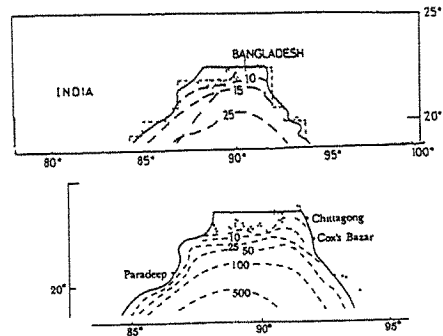
Present study (from BIWTA, Bangladesh)[20].



Bathymetry considered by Das [5,6].



Bathymetry considered by Dube [7].



Parts of the figures considered by John upper Fig from [11], lower Fig. from [12]

\* depths in all figures are shown in meters

Fig.8. Sea bottom bathymetry considered by various author

Simulated results from all authors for the surges differs from each other in peaks, phases, time of arrival and durations. The reasons include differences in bottom bathymetry considered by the authors, treatment of the cyclone, differences in tidal forcings considered in the open boundaries by the authors, the optimum model area considered by them and the treatment of the islands.

## 6. Recommendations

i) The simulation parameters should be well defined and based on physically realistic values with proper guidelines to use in various climatic and hydrologic situations.

ii) Patching of the models with different grid spacings in accordance with the step formulations of the Bengal Bay has proved efficient and recommended by the present study.

iii) Storm surge studies should incorporate the effects of the sea-level rises to wind velocity, bottom friction coefficient, model boundary, flooding mechanisms and surge-penetrability into the land. The effect of global warming on cyclone intensity should be investigated.

iv) 'Swatch of No Ground' should be included in the optimum model area.

v) Interactions between storm surges and the deltaic islands should be made clear. Inclusion of the effect of islands but allowing the flooding over the islands more than a certain level is kin to actual situations prevailing in the Bengal Bay.

vi) Studying the effect of river Karnafully is important as the damage of properties in Karnafully river mouth and the port area are always highest.

vii) Effect of sedimentation and bottom level rise should be given due attention.

viii) The present data collection activities should be strengthen. The orbit of the satellite GMS-4 may be modified to cover the Bengal delta. The modelling activities should take advantages of GIS, LANDSAT and SEASAT programs. Simulation of velocity may be a more sensitive indication of accuracy than water surface profiles. Verification of the models should be done by simulating more than one cyclone data of Bangladesh.

- For urgent protection and prevention works in Bangladesh against storm-surges a suitable model should be chosen by considering the aboves.

## References:

1. K. Wadachi (Editor): Tsunami, Storm Surge, Ocean Disaster, Kyoritsu Publishers, 377(1965).
2. E.W. Schwiderski, Atlas of Tidal Charts and Maps, (1979).
3. Open Univ. Oceanography Course Team, Waves, Tides and Shallow Water Processes,(1989).
4. G.R. Flierl and A. R. Robinson, Nature, 239 (1972) 213.
5. P.K. Das, Nature, 239 (1972) 211.
6. P.K. Das, M.C. Sinha and V. Balasubramanyam, Quart. J. R. Met. Soc. (1974) 437.
7. S.K. Dube, P.C. Sinha and G.D. Roy, Dyn. of Atmos. and Oceans, 9 (1985) 121.
8. S.K. Dube, P.C. Sinha and G.D. Roy, Proc. Coastal Engineering, 10 (1986) 85.
9. R.A. Flather and H. Khandakar, Proc. of Intl. Workshop on Climatic Change, Sea level, Severe Trop. Storms and Associated Impacts, Univ. East Anglia, Norwich, (1987) 1.
10. Frank and Hossain, Bull. Amer. Met. Soc. 52 (1971) 438.
11. B. Johns, S.K. Dube, U.C. Mohanty and P.C. Sinha, Quart. J. R. Met. Soc. 107 (1981) 919.
12. B. Johns, A.D. Rao, S.K. Dube and P.C. Sinha, Phil. Trans. R. Soc. Lond. 313 (1985) 507.
13. T. Yamashita, Proc. Coastal Engineering, JSCE, 39 (1) (1992) 236.
14. J. Katsura, T. Hayashi, H. Nishimura, M. Isobe, T. Yamashita, Y. Kawata, T. Yasuda and H. Nakagawa, Res. Rept. on Natl. Disasters, Jap. Ministry of Ed., Sc. and Culture, (1992).
15. H. Yamanaka, M.Sc. Engg. Thesis, Kyoto University, (1993).
16. J.U. Chowdhury and A.K.M. Tareque, Proc. Workshop on Coastal Zone Management in Bangladesh (1992).
17. S. Karmakar, Proc. Workshop on Coastal Zone Management in Bangladesh (1992).
18. A.M. Chowdhury and M.A. Ali, Nuc. Sc. and Applications, 7- B (1974) 118.
19. M.A. Ali, Mausam, 31 (1980) 517.
20. Department of Hydrography, BIWTA, Map of the Bay of Bengal, (1982).

Comparative Study for Assessment Code of Transport  
of Radioactive Material and Research of Model

Li Jikai and Wang Jiaming

China Institute for Radiation Protection

**Abstract:** The transportation of radioactive material is a issue which many countries and their people concern about very much. In this paper, a comparative calculation and study of radiological impact is carried out for a case of transportation of uranium hexafluoride (transport mode: rail, shipping distance: 4129 km) using INTERTRAN and RADTRAN 4.0 Code provided by IAEA (the International Atomic Energy Agency), and had been raised consideration to seek after for some defects in these assessment models.

1. Introduction

Since 1987, a large amount of work have been done on the development and application of INTERTRAN and RADTRAN 4.0 Code. On the basis of the work (e.g. the assessment of radiological impact of transportation in connection with uranium ore, UF<sub>4</sub>, UF<sub>6</sub> and other radioactive material), the comparative analysis has been carried out for two codes itself and the results show that it is necessary to augment new evaluation models into the Codes (i.e. wet deposition, diffusion in vertical wind direction, radioactive material dispersion in water and soil, etc). Especially, some defects in the Codes must be revised (e.g. radiological impact for the public at transfer station (or port), and various risks due to different radionuclide, etc).

2. Transportation and Application of computer Code

(1) Transportation of INTERTRAN Code

The transportation of INTERTRAN Code was accomplished in 1988, and the Code has been transported to a MICRO VAX- II /VMS system. During the transportation, some statements in the Code related to the characteristics of the computer have been revised accordingly (e.g. some format sentences), and some defects in the design of the code itself have been corrected (e.g. overflow of zero assignment).

(2) Transportation of RADTRAN 4.0 Code

The transportation of RADTRAN 4.0 Code was accomplished in 1991, and the Code has been transported to IBM-PC and MICRO VAX- II /VMS system, respectively. While transporting the Code, the following work was carried out, such as, revising source program, revising the input data file and revising the input format of the file, etc.

(3) Application of the Code

Right up to present, the assessment of many cases of transport of radioactive material have been carried out using the codes. It is believed that the codes will make a contribution to assessment of environment impact from transporting radioactive material in China.

### 3. Comparison analysis of the Codes

After comparison analysis for INTERTRAN and RADTRAN 4.0 Code itself, it is evident that RADTRAN 4.0 Code augmented the following features: ① The maximum individual dose is automatically calculated and printed out by the Code in the output for each run, ② The Code can deal with multiple isotope materials and permits direct analysis of multiple package shipments containing different packages, ③ The Code can calculate radiological impact both from transportation of alpha, beta and gamma-emitting radioactive materials and neutron-emitting ones, ④ It can calculate the radiological impact from transportation on one link, as well as on more links (less than 40, including road and water mode), ⑤ The accident severity category matrix has been expanded to permit the use of up to 20 accident severity categories, ⑥ The number of physical-chemical isotope groups have been expanded to permit the use of up to 15 physical-chemical isotope groups.

### 4. Comparative study of radiological impact

#### (1) A selected transport case for comparative study

For comparative study, a case of transport for  $UF_6$  (from northwest to northeast in China) was selected, the transport informations are listed in Table 1.

#### (2) Calculation results of radiological impact

In the paper, the comparative calculation of radiological impact had been made for a case of transport of uranium hexafluoride in China using INTERTRAN and RADTRAN 4.0 Code. The results are listed in Table 2, 3 and 4 respectively.

#### (3) Comparison of calculation Results

It can be seen from Table 2 that for collective dose equivalent to surrounding population while stops under normal conditions of transport, the result obtained by INTERTRAN is two orders of magnitude higher than RADTRAN 4.0. The others for both have same order of magnitude.

Table 3 and 4 show that under accident conditions of transport, two calculation results differs by one to two orders of magnitude. The radiological risk from the cloudshine is so small that it can be negligible.

#### (4) Analysis of the results

##### A. Normal conditions of transport

It is evident that the difference of the calculation results for collective dose equivalent of surrounding population while stop by INTERTRAN and RADTRAN 4.0 Code is due to different estimated model used in the two Codes. INTERTRAN Code calculates dose of person exposed using point source model based on the number of persons exposed and average exposure distance. However, in RADTRAN 4.0 Code, the persons exposed while stop within a corridor on either side of the transport link ranging from 10 m to 400 m in suburban zone is considered. The shielding effect of other vehicles and structure is also included. Shielding factor is supposed as 0.1 in the Code. Collective dose to crew is larger in RADTRAN 4.0 Code, because the dose to the train inspector is considered.

##### B. Accident conditions of transport

##### (I) Early effect

Calculation result is nil for two computer codes.

(II) Latent effect.

a. When compared two results, it can be seen that they made a great difference. Besides the calculation models exist certain difference, some parameters are also different in the Code. For instance, resuspension dose factor RDF is 1.13 for INTERTRAN Code, and 5.55 for RADTRAN 4.0 Code. Therefore, the ratio is given as:

$$\frac{[RDF(RADTRAN) - 1]}{[RDF(INTERTRAN) - 1]} = 35 \quad (1)$$

It is more concerned for the resuspension in the computation model of RADTRAN 4.0 Code. In addition, building dose factor BDF is 0.1 for INTERTRAN Code, and  $8.6 \times 10^{-3}$  for RADTRAN 4.0 Code. The final result is affected by the factor BDF.

b. Under accident conditions of transport, the difference for radiological risk of latent effect between the two Codes is rather evident.

c. The impact of cloudshine and ingestion is introduced in RADTRAN 4.0 Code. However, the impact of the former is rather small, and the impact of ingestion is temporarily not calculated in this paper.

(5) Conclusion of comparative study

a. Under normal conditions of transport, conservative theoretical values are more used in INTERTRAN Code, and more reliable experimental informations are used in RADTRAN 4.0 Code.

b. Under accident conditions of transport, latent cancer fatalities is over-severe in RADTRAN 4.0 Code.

c. It is very convenient to use RADTRAN 4.0 Code.

5. Research of model

In INTERTRAN and RADTRAN 4.0 Code, it have not been considered that impact of wet deposition, diffusion in vertical wind direction, radioactive material dispersion in water and soil, radiological impact for the public at transfer station (or port), and various risks is due to different radionuclide.

(1) Augmenting evaluation model to surrounding population exposed at transfer station (or port). The formula is:

$$D = 2\pi \cdot Q_0 \cdot F \cdot S \cdot P \cdot K \cdot TI \cdot IV \left( \frac{fr \cdot Pr \cdot Rr}{Vr} + \frac{fs \cdot Ps \cdot Rs}{Vs} + \frac{fu \cdot Pu \cdot Ru}{Vu} \right) \cdot Sh \quad (2)$$

where

D dose of surrounding population exposed, person · rem/a

Q<sub>0</sub> unit conversion factor, rem/mrem · km/m · h/s

F shipment distance, m

S shipments per year

P packages per shipment

TI transport index, mrem/h, at 1 meter

K TI to dose rate conversion factor, m<sup>2</sup>

IV general coefficient

Sh revision factor, h

fr, fs, fu fraction of travel in population zone (rural, suburban and urban)

Pr, Ps, Pu population density in population zone (rural, suburban and urban)

$r, R_s, R_u$  shielding factor in population zone (rural, suburban and urban)  
 $V_r, V_s, V_u$  velocity in population zone (rural, suburban and urban), m/s

(2) Augmenting evaluation model for diffusion in vertical wind direction. The equation is:

$$E = \frac{Q}{\pi U \sigma_y \sigma_z} \text{EXP}[-(y^2/2\sigma_y^2 + h^2/2\sigma_z^2)] \quad (3)$$

where

$E$  Air pollutant concentration Bq/m<sup>3</sup>  
 $E/Q$  dilution factor  
 $U$  wind speed, m/s  
 $\sigma_y, \sigma_z$  horizontal and vertical dispersion parameters, respectively, m  
 $y$  crosswind distance, m  
 $h$  calculated height, m

Equation (3) is called the Gaussian plume formula.

(3) Augmenting evaluation model for wet deposition. The equation is:

$$F = \text{EXP}(-WX/U) \quad (4)$$

where

$X$  downwind distance, m  
 $U$  wind speed, m/s  
 $W$  wet removal rate, 1/s

(4) Augmenting evaluation model for radioactive material diffusion in water. The equation is:

$$\frac{\partial C}{\partial t} + u \frac{\partial C}{\partial x} = K \frac{\partial^2 C}{\partial x^2} - K_1 C \quad (5)$$

where

$K$  dilution coefficient, km<sup>2</sup>/h  
 $K_1$  decay rate, 1/h  
 $C$  released concentration  
 $t$  diffusion time, h  
 $u$  flow speed, km/h  
 $x$  diffusion distance, km

(5) To the population exposed, radiological impact should be considered in accordance with different age (i. e. infant, child and adult) or different sex (i. e. male and female). But also, it should also be considered that the different radiological risk resulted from the various radionuclides. Especially, it should be carried out to study various exposure pathways for radioactive materials (such as the terrestrial food chain pathway and the aquatic food chain pathway).

Except for such evaluation models and discussions, it is also necessary to augment evaluation models and calculations into the codes for radioactive material dispersion in soil, as appropriate.

Transport mode	Rail
Typical package dimension (m)	2.22
Transport index (mrem/h)	0.6
Number of packages	9
Shipments per year	1
Transport distance (km)	4129
Fraction of travel in rural zone	0.450
Fraction of travel in suburban zone	0.359
Fraction of travel in urban zone	0.191
Velocity of travel in rural zone (km/h)	40
Velocity of travel in suburban zone (km/h)	40
Velocity of travel in urban zone (km/h)	40
Number of crew	5
Distance from source to crew (m)	150
Number of handlings	2
Stop time per 24 hours trip (h)	4
Number of persons exposed while stopped	16
Average exposure distance at stops (m)	20
Storage time (h)	24
Number of persons exposed at storage (m)	50
Average exposure distance at storage (m)	20
Number of persons per vehicle	1400
Traffic count in rural zone (1/h)	0.310
Traffic count in suburban zone (1/h)	0.670
Traffic count in urban zone (1/h)	2.690
Population density in rural zone (persons/km)	44
Population density in suburban zone (persons/km)	308
Population density in urban zone (persons/km)	1471

Table 1. Transport situation data

Name of code	INTERTRAN	RADTRAN 4.0
Crew (exclusive use)	4.60E-04	8.01E-04
Handler (exclusive use)	3.90E-02	4.76E-02
Surrounding population while underway	3.80E-03	3.83E-03
People traveling on transport line	6.72E-02	6.76E-02
Surrounding population while stops	1.30E-02	2.92E-04
Personal in warehouse storage	6.01E-02	6.01E-02
Totals	1.84E-01	1.80E-01

Table 2. Collective dose equivalent to different subgroups under normal conditions of transport, person-rem

Name of code	INTERTRAN	RADTRAN 4.0
Groundshine	2.80E-06	8.13E-08
Inhalation	9.00E-06	2.04E-04
Resuspension	1.20E-06	9.30E-04
Cloudshine	—	1.33E-12
Totals	1.30E-05	1.13E-03

Table 3. Expected radiological risk for the public under the transport accident (latent cancer fatalities)

Name of code	INTERTRAN	RADTRAN 4.0
Groundshine	1.80E-06	2.09E-07
Inhalation	2.50E-07	4.79E-08
Resuspension	3.20E-08	2.18E-07
Cloudshine	—	1.88E-07
Totals	2.08E-06	4.79E-07

Table 4. Expected radiological risk for the public under the transport accident (genetic effects)

References:

1. K. S. Neuhauser and F. L. Kanipe, RADTRAN 4.0 User Guide, IAEA, Vienna (1989).
2. IAEA-TECDOC-287, INTERTRAN, IAEA, Vienna (1983).
3. P. Pages and F. Rancillac, TRANSAT User Guide, France (1992).
4. Wang Jiaming and Li Jikai, et al., Transportation of RADTRAN 4.0 Code (will be published) (1992).



## The Mechanism of Unfavorable Effects of Wind on Efficiency of Dry Cooling Towers

WEI Qing-ding ZHANG Be-yin LIU Ke-qi  
DU Xiang-dong MENG Xian-zhong

(Department of Mechanics, Peking University, China)

**Abstract:** For clarifying the mechanism of unfavorable effects of wind on efficiency of dry cooling towers some full scale measurements and wind tunnel modelling were conducted. A hot water circulation system and fin-tubular radiators were used for simulating the thermodynamic process of dry cooling towers. A dimensionless value, wind effect coefficient  $C_w$ , was defined and measured to describe the wind effects on the efficiency of cooling tower radiators. The experimental results suggest that the natural wind makes the efficiency of dry cooling towers drop owing to three main reasons: (1) forming unfavorable pressure distribution at the tower entrance, (2) breaking the hot plume rising from cooling towers, (3) cool air induced by lee-edge separation entering cooling towers.

### 1 Introduction

The problem of the negative effects of wind on dry-cooling tower intakes has been researched by some scholars and engineers using wind tunnel modelling [1-4]. These research works contributed some interesting results, but have not yet clarified the mechanism thoroughly. The basic start points of this experimental research are to stress the essentials of the physical process and to consider the most important factors influencing this problem. For this purpose many kinds of experimental approaches including full scale measurement were adopted and some new physical parameters were introduced to describe the characteristics of the wind effects.

### 2 Similarity parameters and experimental principle

The complete coupled equations for describing the flow around and through a dry cooling tower and their boundary conditions are quite complex and a lot of similarity parameters can be induced from them. It is impossible to simulate all of the similarity parameters. In this experiment three most important similarity parameters have to be satisfied, they are as follows:

$$\text{indensity Froude number} \quad Fr = \frac{V_o^2}{(\Delta\rho/\rho)gH} \quad (1)$$

$$\text{speed ratio} \quad a = \frac{V_i}{V_o} \quad (2)$$

$$\text{Reynolds number} \quad Re = \frac{V_i H}{\nu} \quad (3)$$

Where  $V_o$  is the mean exit velocity of internal flow pass through a tower,  $V_i$  mean wind speed at the height of the tower tip,  $\Delta\rho = \rho_a - \rho_i$  difference between ambient air density  $\rho_a$  and internal air density of the tower  $\rho_i$ ,  $g$  gravity acceleration,  $H$  characteristic length,  $\nu$  kinetic viscosity.

In this experiment Froude number and speed ratio were satisfied. But because Reynolds number can not be reached seriously in wind tunnel testing at the same time to

meet the Froude number, only the efficient Reynolds number was met by increasing roughness of the cooling tower model.

A hot water circulation system and fin-tubular radiators with the same structure as that of prototype were used to simulate the heat exchange. In the test process a constant water temperature was kept at the entrance of radiators and the temperature dropping  $\Delta T$  of hot water past a radiator was measured.  $\Delta T$  is a function of the variables  $\Delta T_a$ ,  $\Delta T_i$ , and  $f$ ,  $\Delta T_a$  the difference between ambient temperature and entrance water temperature,  $V_i$ , mean draught speed pass radiators and  $f$  the hot water flow rate. It can be written as

$$\Delta T = \Delta T(\Delta T_a, V_i, f) \quad (4)$$

A dimensionless coefficient  $C_w$  called wind effect coefficient is defined as

$$C_w = \frac{\Delta T(\Delta T_a, V_i, f) - \Delta T(\Delta T_a, V_i^*, f)}{\Delta T(\Delta T_a, V_i^*, f)} \quad (5)$$

where  $V_i^*$  is mean draught speed on the condition  $V_i = 0$ , i. e. there is not wind. It is clear that if  $C_w$  is negative, wind gives a dry cooling tower unfavorable effects, if  $C_w$  is positive, wind effects are favorable, if  $C_w$  is equal to zero, wind does not effect on the efficiency of a cooling tower.

### 3. Full-scale measurement

A working dry cooling tower at shanxi province of China was measured using anemometers and temperature sensors controlled by remote devices. Fig. 1 shows the prototype of the cooling tower measured whose radiators vertically arranged. Fig. 2 shows the distribution of the mean draught speed  $V_i$  along annular radiator where  $\theta$  is latitude. It can be seen that when it was blowing with about 6m/s speed the mean draught speed  $V_i$  was decreased about 20% at a large part of the annular radiator except the part facing wind. Fig. 3 and Fig. 4 shows the temperature distribution above the annular radiator and along the central line of the cooling tower respectively. The measuring results reveal that wind with 6m/s speed made the temperature inside the tower rise about 26%. These results prove that the wind make the efficiency of a dry cooling tower dropping.

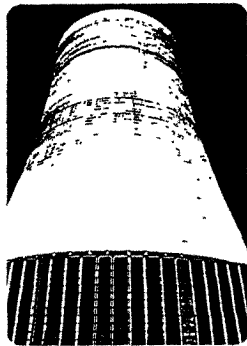


Fig. 1 The prototype of Shanxi dry cooling tower

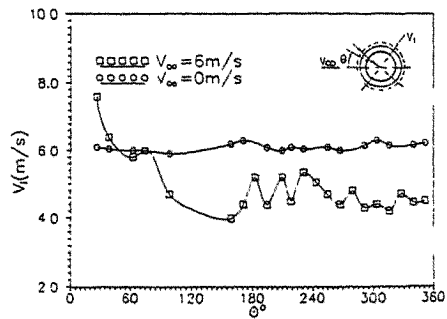


Fig. 2 Distribution of mean draught speed  $V_i$  of Shanxi dry cooling tower (wind speed about 6m/s at height 10m.

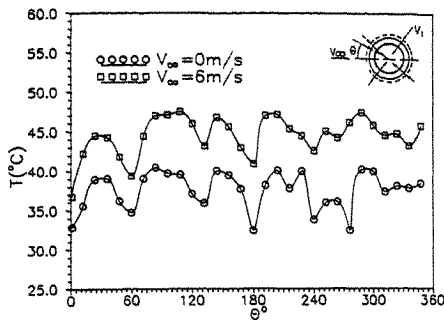


Fig. 3 Distribution of mean temperature above the annular radiator inside the prototype tower

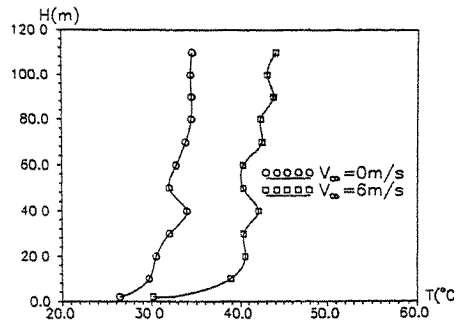


Fig. 4 distribution of mean temperature along the central axis of the prototype tower.

#### 4. Wind tunnel testing facilities.

##### 4.1 Model

A Scale 1/200 model of the Shanxi dry cooling tower was manufactured. The radiators have the same structure of the fin-tubular structure and the same drag coefficient as that of the prototype, but the different geometry. For simulating the prototype the annular radiators are divided equally to six segments which were numbered from No1 to No6. (Fig. 5).

A scale 1/800 cooling tower model without radiators was also used for testing the effect of lateral wind past the tower exit on the interflow past through the tower model. Fig. 6 shows the testing installation. The internal flow is produced by a fan.

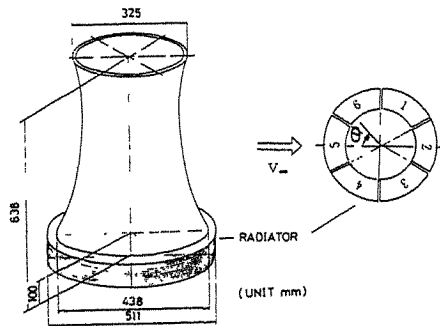


Fig. 5 Sketch of the model of Shanxi cooling tower

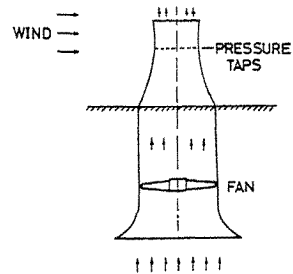


Fig. 6 Sketch of the model of a cooling tower — fan system

#### 4.2 Hot water circulation system

For simulating the heat exchange process a hot water circulation system was made. Its flow rate and output temperature can be regulated.

#### 4.3 Wind tunnel

A boundary wind tunnel with a test section 2.4m wide 1.8m high and 8.0m long was used. Using spires and roughness elements a artificial turbulent boundary layer simulating atmospherical boundary layer at site of Shanxi dry cooling tower was formed. The exponent of the mean velocity profile is about 0.24.

#### 4.4 Measurement devices

A hot-wire anemometer was employed for measuring the velocity field. Some pressure and temperature transducers were used for measuring the pressure and temperature of the air inside and outside the tower model and for measuring the temperature of circulation water at entrance and exit of the radiator segments.

### 5. Experimental results

#### 5.1 The wind effect coefficient $C_w$

The wind effect coefficients of radiator segment No  $i$  denoted by  $C_{wi}$  ( $i=1\sim 6$ ) are shown at Fig. 7. The radiator segment No 5 is just face to wind direction, therefore the wind effect coefficient  $C_{w5}$  is always positive regardless the wind speed. The radiator segment No 4 and No 6 are placed at the sideward wind direction. The wind effect coefficient  $C_{w4}$  and  $C_{w6}$  are just a little positive or negative. The radiator segment No 1, No 2 and No 3 are placed at the back wind direction. The wind effect coefficient  $C_{w1}$ ,  $C_{w2}$  and  $C_{w3}$  are all negative. The total wind effect coefficient of a dry cooling tower, denoted by  $C_w$ , is defined as

$$C_w = \frac{1}{6} \sum_{i=1}^6 C_{wi}$$

Fig. 8 shows the relationship between wind effect coefficient  $C_w$  and speed ratio  $V_t/V_o$ . It is shown that at a large range of speed ratio  $V_t/V_o$  the  $C_w$  is negative, and the curve  $C_w - V_t/V_o$  takes the shape of parabola, the minimum of which is about -8.8% occurring at about  $V_t/V_o=3.2$ , which will be dependent on the concret cooling tower and circumstance etc. When wind speed ratio exceed about 6.4 the wind effect coefficient becomes positive.

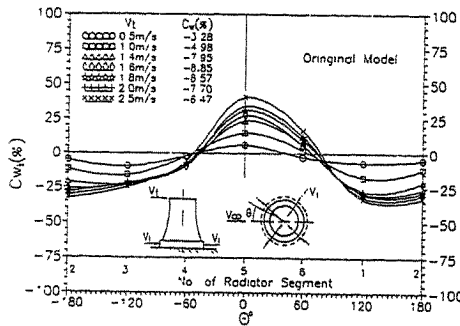


Fig. 7 Wind effect coefficient  $C_{wi}$  versus radiator segment No  $i$

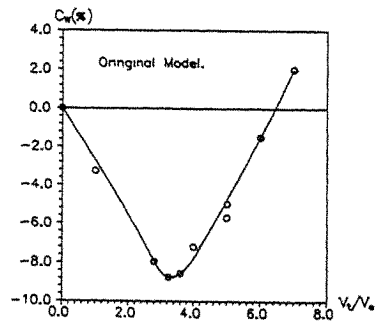


Fig. 8 Wind effect coefficient  $C_w$  versus wind speed ratio  $V_t/V_o$

**5.2 The distribution of the draft velocity and the static pressure along the annular entrance of the cooling tower model.**

The mean air speed pass through the entrance of the cooling tower model was measured by means of hot-wire anemometer. Fig. 9 shows the comparison of the results from full scale tower measuring and from wind tunnel modeling under probably the some conditions. In this figure  $\theta$  is latitude of the annular radiator, and  $\theta=0^\circ$  is wind direction angle,  $(V_t)_{\theta=0}$  is the maximum of draught speed, and break line indicates the value of  $V_t$  at the condition of no wind. It can be seen that the results of wind tunnel modeling is close to that of full scale measurement and that at most part of the annular radiator the draught speed decreases about 10~20% when there is blowing.

The distribution of the static pressure along the annular entrance is also drawn at Fig. 9. the strong correlativity of the draught velocity with static pressure reveals that the unfavorable pressure distribution caused by wind makes the mean draught velocity dropping.

**5.3 The effects of wind past the tower exit on the internal flow of the cooling tower model**

Fig. 10 shows the mean static pressure coefficient at the throat of the cooling tower model shown in Fig. 6. In this figure the abscissa is speed ratio  $V_t/V_o$ ,  $V_o=4.88\text{m/s}$  and  $7.0\text{m/s}$ . It can be seen that along with the  $V_t/V_o$  increases the throat static pressure increases rapidly and changes from minus to plus, then reaches maximum value at about  $V_t/V_o=1$ , after that reduces slowly near zero. This result suggests that the lateral wind breaks the hot plume of cooling towers and hinders the internal flow pass through the cooling tower. But if the bottom of the testing model is closed the negative static pressure coefficient about  $-0.4\sim-0.5$  can be caused by lateral wind. It suggest that the lateral wind can also increases tower's suction which is caused by separation of flow cross over the exit of the cooling tower. Fig. 11 shows pictures of visualization made by smoke wire method. Picture A and B show the internal flow patterns of a dry cooling tower model with working radiators under no blowing and blowing conditions respectively. It can be seen that when it is not blowing the hot air rises uniformly, and that when it is blowing some dropping flow occurs at the downstream part of throat section. The temperature measurement indicates the dropping flow has lower temperature. It is obvious that the dropping flow with lower temperature will reduce the draft of a cooling tower. It can be considered that the dropping flow is induced by Lee-dege separation vortex.

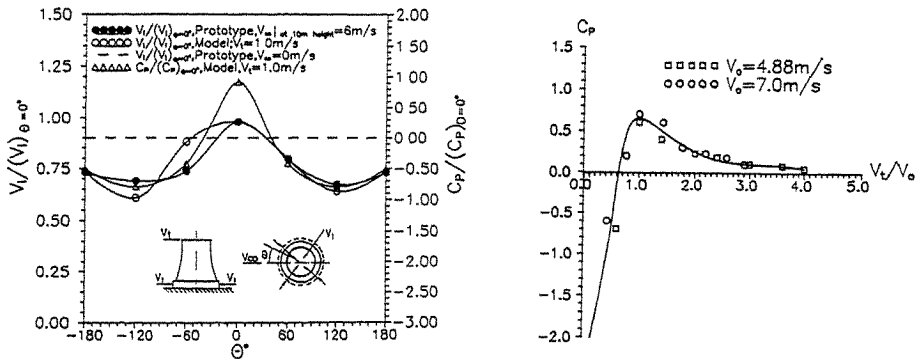


Fig. 9 Distribution of mean draft velocity and static pressure along the annular entrance

Fig. 10 Static pressure coefficient at the tower's throat versus speed ratio  $V_t/V_o$

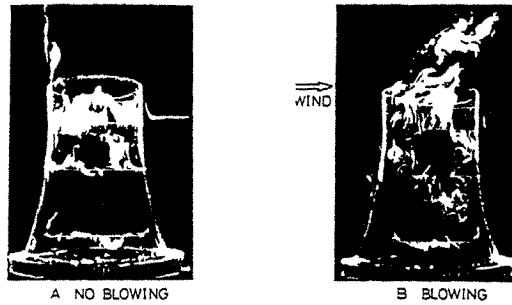


Fig. 11 Pictures of Visualization of wind effect

#### 6. Conclusions

1. At a quite big region of wind velocity natural wind reduces the efficiency of dry cooling towers. The relationship curve of wind effect coefficient  $C_w$  and wind velocity  $V$ , takes the shape of parabola.
2. Wind makes the temperature in dry cooling tower go up and makes the air velocity crossing radiator lower at about most part of tower entrance.
3. Natural wind makes the efficiency of dry-cooling towers lower owing to the next three main reasons :
  - (1)forming unfavorable pressure distribution at tower's entrance.
  - (2)breaking the hot plume rising from a cooling tower.
  - (3)cool air induced by lee-edge separation vortex of the exit of the tower entering the cooling tower.
4. The lee-edge separation of wind at tower's exit will increase tower's draft. When this favorable effect is weaker than the sum total unfavorable effects mentioned above, the wind will make the efficiency of a dry cooling tower dropping.

#### References :

1. Buchlin, J. -M. IAHR Cooling Tower workshop, Budapest, 1982
2. Ruscheweyh, H. Brennstopp-Warme-Kraft 34, 1982
3. Ribier, J. G IAHR Cooling Tower Workshop, San Francisco 1980
4. Chaboseau, J. IAHR Cooling Tower Workshop Budapest. 1982.

## WEAKLY NONLINEAR DEEP WATER WAVES UNDER WIND ACTION

John Z. Yim, C. R. Chou and P. E. Liu

Department of River & Harbour Engineering  
National Taiwan Ocean University  
Keelung, Taiwan R.O.C.

**Abstract:** Influences of wind on the evolutionary process of deep water wave groups were studied experimentally. Waves were first generated mechanically and then subjected to wind action. Comparing the results for cases both with and without wind action, the relative importance of nonlinearity and randomness can be identified quantitatively. It is found that, due to the presence of random waves agitated by the overlaying turbulent wind, the effect of nonlinearity was suppressed. As a result, wave spectra broaden with side-bands finally lost their identities altogether.

### 1. Introduction

Weakly nonlinear deep water waves are known to be unstable to perturbations. While developing, four possible outcomes can be identified. Waves of a particular mode can extract energy from the background field, grow exponentially, and, ultimately, dissipate their energies through breaking [1]. Cyclic modulation and demodulation, accompanied by repeatedly growth and subsidence, known as the Fermi-Pasta-Ulam (FPU) recurrence, can occur [2]. Depending on the initial conditions given, waves can either progress without any appreciable changes; or, they can accumulate energy and form in groups [3,4]. Of particular interest is the formation of wave group that has a shape of hyperbolic secant, i.e., the so-called envelope soliton [5].

Envelope soliton is the result of a subtle balance between two competitive effects. Dispersion tends to separate waves of different frequencies apart, while nonlinearity bonds them to form in groups [6]. Once formed, solitons have the remarkable character of being stable against perturbations. However, other (external) factors do affect their nature. When propagating in an inhomogeneous medium, waves will be modulated. Waves change their lengths due to temporal inhomogeneities, and spatial inhomogeneity modifies their periods [7]. One of such a flow field is caused by the wind.

Developments of mechanically generated waves under wind action were studied by many researchers, with the vast majority concentrated on the mechanism of momentum transfer between these two fluids [8,9,10,11,12]. Recently, three papers closely related with our objective have been published. Bliven et al. [13] compared the effects of wind and nonlinearity on the evolution of deep water wave trains. Nonlinearity is characterized by a pair of side bands located near the carrier frequency of the wave train. Wind was found to broaden the spectrum and thus blurred side band effects. However, since wave trains, not wave pulses, were used in their experiment, the nondispersive character of an envelope soliton is not studied. Pierson et al. [14] studied the evolution of wave pulses without wind action. It was found that, for wave pulses of moderate steepness,  $ka \leq 0.18$  ( $k$  is the wave number and  $a$  the amplitude), evolutionary process can be described satisfactorily by a model equation. Furthermore, they

found that during development, the spectra broaden and energy was shifted to both lower and higher frequencies. Chu et al. [15] studied interactions between a wave group and short wind waves. Their main interest was on the wind wave part. Vigorous breaking and rapid energy losses from short waves were found to occur in the front face of the wave group. After passage of the mechanical wave group, wind waves were suppressed, and a smoother water surface resulted. The characteristics and subsequent development of the wave group remain relatively unexplored in that paper.

In an attempt to understand the possible effects of wind on wave groups, series of experiments were conducted. This paper summarizes our present results. The paper is divided into four parts. A brief description of the experimental setups is given in Section 2. Section 3 contains some results of the experiments together with short discussion. Concluding remarks in Section 4 then closes this paper.

## 2. Experimental setups

Experiments were conducted in a wind-wave tunnel. The tunnel is located in the Laboratory for Ocean Engineering of the Department, with a dimension of 50x1.8x1.2 (length x width x height, meters). It has a glassy wall on one side and a reinforced concrete wall on the other. Approximately one-third of its total length is covered with metal roofs. When facing the tunnel, A programmable wave generator of piston type is installed on the left end of the channel, with a centrifugal type wind blower 10 m away from it. A transition plate, installed at the entrance of the wind blower, is used to suppress parasitic disturbances both in air and water. This plate also insures that pure wind waves were generated by fully turbulent wind. At the other end, a non-permeable type wave absorber with an inclination of 1 to 12 is installed to minimize reflection.

Six measuring stations, numbered 1 to 6, were used to record developments of the wave group. Locations of these stations are, with reference to the end of the transition plate, -8.0, 0.2, 6.0, 12.0, 18.0, 24.0 m, respectively. Station No. 1 is located between wave generator and air entrance. The second station, No. 2, is sited immediately at the end of the transition plate. At these two stations, waves are believed to be relatively unaffected by wind. Results of the first station were treated as initial conditions, and those of the second are considered as representing wave developments without wind action. Three amplitudes and three frequencies were chosen to generate waves mechanically. Wind velocities were limited below 10 m/s to avoid too strong interactions between wind and waves [16]. Table 1 lists the parameters used.

amplitude ( $a_0$ )	[cm]	3.5	3.8	3.9
frequency ( $f_0$ )	[Hz]	1.2	1.2	1.3
wind speed ( $U_0$ )	[m/sec]	1.92	5.24	7.06

Table 1 The experimental conditions

The experiments proceeded as follows: At first, wind blower was activated for a preset time interval. Air motion in the tunnel was then assumed to have reached the so-called statistical equilibrium state for the chosen velocity. Since fluctuating frequency, or the characteristic frequency of large eddies, in the free turbulent air motion was not determined, a typical time interval of 15 minutes was



selected rather arbitrarily. Wave generator was then motivated for a prescribed time, and set still for the rest of the experiment. Small residual waves are seen to be generated by the sudden halt of the generator. However, they are believed to have minor influences on the subsequent developments of the pulse, since the later possesses a group speed much larger than that of the residual waves.

Since evolution processes of nonlinear waves are more or less of stochastic nature, both with and without wind blowing, experiments were repeated several times. Recorded surface fluctuations are fast Fourier transformed. The surface elevations and their spectra of mechanical wave groups without wind action are then compared with corresponding cases of prevailing wind. Some selected results are presented in Section 3.

### 3. Results and discussion

We present only results of the first and last measuring stations in this section. Fig. 1 shows the development of a nonlinear wave pulse without wind action. Three soliton-like wave groups and an oscillating tail have formed. The corresponding spectra, Fig. 2, show that, while the lower side-band seems to have disappeared, the higher side-band still perseveres its integrity. A closer inspection indicates that, the lower side-band has actually grown to a state comparable with the dominant frequency, and has "consolidated" with it.

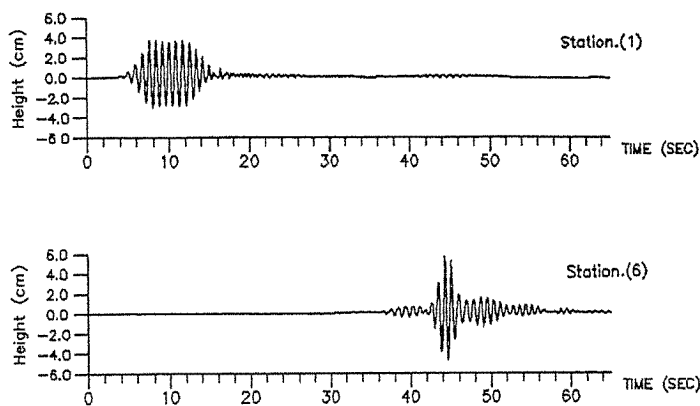


Fig. 1 Surface elevation of wave pulse at Stations 1 and 6. Case studied:  $a_0 = 3.9$  cm,  $f_0 = 1.2$  Hz,  $U_0 = 0.0$  m/sec.

With light wind, water surfaces are only ruffled, Figs. 3 and 4. The small fluctuations in front of the wave pulse previously seen in Fig. 1a have now become unappreciable. Comparing Figs. 2 and 4, it seems that, there are almost no detectable differences on the energy-containing part of the spectrum. On the high-frequency side, however, zigzags of spectral densities over small frequency intervals, typical for wind generated waves, can be detected. The first wave-like disturbances that can be distinctly detected by eye will occur at a wind speed of  $U_0 = 3.1$  m/s [17]. It seems reasonable to presume that, at least at this stage, wind generated capillary waves have no significant influence on wave evolution. The role of wind-induced

drift is not clear at present. More studies are in preparation.

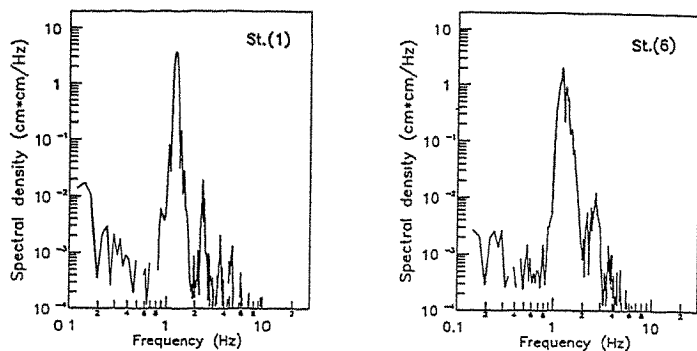


Fig. 2 Spectra of wave pulse at Stations 1 and 6. Case studied: same as Fig. 1.

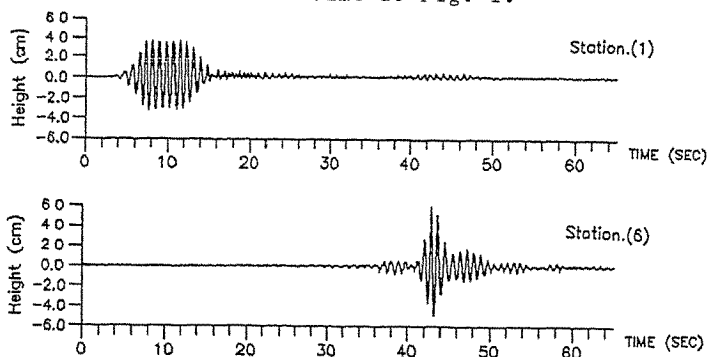


Fig. 3 Surface elevation of wave pulse at Stations 1 and 6. Case studied:  $a_0 = 3.9$  cm,  $f_0 = 1.2$  Hz,  $U_0 = 1.92$  m/sec.

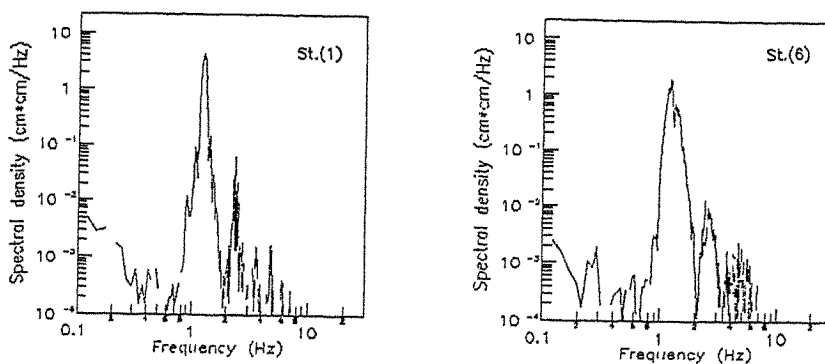


Fig. 4 Spectra of wave pulse at Stations 1 and 6. Case studied: same as Fig. 3.

Figs. 5 and 6 show the results of the strongest wind speed considered. As can be seen, at Station 6, amplitudes of wind-generated waves are now already comparable with the residual waves of the wave pulse (Fig. 1b). Waves within the group appear to be larger due to wind input, but this is not confirmed by the corresponding spectrum (Fig. 6b). Waves in front of the pulse interact strongly with wind generated waves and have lost their identities. The spectral peak of wind waves has down-shifted to a value that is comparable with the second harmonic of the pulse.

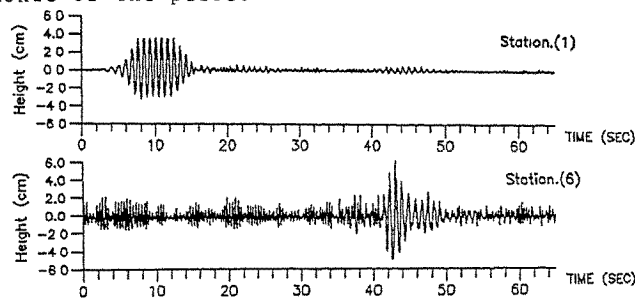


Fig. 5 Surface elevation of wave pulse at Stations 1 and 6. Case studied:  $a_0 = 3.9$  cm,  $f_0 = 1.2$  Hz,  $U_0 = 7.06$  m/sec.

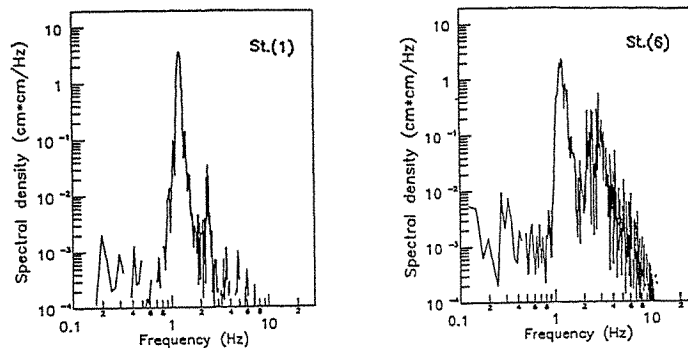


Fig. 6 Spectra of wave pulse at Stations 1 and 6. Case studied: same as Fig. 5.

#### 4. Conclusions

In a wind-wave flume, mechanical waves usually have a frequency much lower than that of wind waves. The density difference between these two fluids is approximately  $1/800$ . Considering these, and taken that nonlinearity is represented through irregularities of water surface, it seems reasonable to conjecture that, wind acts as a perturbative force to water waves, at least for light winds studied in this paper. With light wind, it is meant that wind speeds do not exceeding, say, 10 m/s. When a wave group has a fairly stable character, as the case with envelope soliton, the complex nature of wind-wave interaction seems to become somewhat tractable. This is because the problem is now reduced to the determination of the disturbances under which the waves are subjected to. We have set out our studies with this postulate in mind.

For the case without wind action, nonlinear waves are unstable to side-band perturbations. During their course of evolution, side-

bands receive energy from the primary wave (and its higher harmonics). Consequently, spectra of these nonlinear waves broaden, with a markedly decrease of energy content of the primary wave.

With wind acting, the water surface is ruffled. There is a considerable randomness on the high frequency side of the spectra. The spectral density of the peak frequency reduces its value, but there is no frequency down-shifting occurring. In the meantime, side-bands around the peak acquire energy rapidly, presumably as a result of both nonlinear wave-wave and wind-wave interactions. Energy of wind waves at the high frequency part of the spectrum is seen to be reduced considerably.

Wave developments are stochastic, irrespective of wind action. Experiments with same initial conditions were repeated, but spectra were not averaged, nor smoothed, as was common in wind wave studies. It is felt that, averaging could deprive characteristics of the wave group, which is the main interest of this study. This leads to the smeared spectra on the high frequency side representing wind waves. Digital filters are presently considered, which can hopefully resolve this dilemma in the near future.

The intention was to study the (presumably) stable nature of envelope solitons under wind action. However, even for the steepest wave considered, envelope profiles of the theoretical hyperbolic secant have not been successfully developed. A way out is to generate soliton-like wave groups directly in front of the generator. In this way, the relative importance of nonlinearity, dispersion, and randomness, could be investigated more thoroughly.

#### References

1. W.K.Melville, J. Fluid Mech., 115(1982) 165
2. H.C.Yuen and B.M.Lake, Adv. Appl. Mech., 12(1982) 303
3. H.C.Yuen and B.M.Lake, Phys. Fluids, 18(1975) 956
4. M.-Y.Su, Phys. Fluids, 25(1982) 2167
5. D.H.Peregrine, J. Austral. Math. Soc. B, 25(1983) 16
6. R.K.Dodd, J.C.Eilbeck, J.D.Gibbon & H.C.Morris, Solitons and nonlinear wave equations, Academic Press (1982) 495
7. G.B.Whitham, Linear and nonlinear waves, John Wiley & Sons (1974) 636pp
8. J.B.Bole and E.Y.Hsu, J. Fluid Mech., 35(1969) 657
9. M.Hatori, M.Tokuda and Y.Toba, J. Oceanogr. Soc. Japan, 37(1981) 111
10. H.Mitsuyasu and T.Honda, J. Fluid Mech., 123(1982) 425
11. Y.A.Papadimitrakis, E.Y.Hsu and R.L.Street, J. Waterway, Port, Coastal and Ocean Eng. ASCE, 113(1987) 39
12. W.S.Wilson, M.L.Banner, R.J.Flower, J.A.Michael and D.G.Wilson, J. Fluid Mech., 58(1973) 435
13. L.F.Bliven, N.E.Huang and S.R.Long, J. Fluid Mech., 162(1986) 237
14. W.J.Pierson, Jr., M.A.Donelan and W.H.Hui, J. Geophys. Res., C97(1992) 5607
15. J.S.Chu, S.R.Long and O.M.Phillips, J. Fluid Mech., 245(1992) 191
16. Y. Toba, 12th Symposium Naval Hydrodynamics, Washington D. C. (1978) 529
17. K.K.Kahma and M.A.Donelan J. Fluid Mech. 192(1988) 339

#### Acknowledgment

This paper is financially supported through a project of the National Science Council (NSC). Project number NSC-82-0209-E019-031

## Aspects of the wind energy potential in the former Soviet Union.

Nikolai N. Kukharin,

Center for Energy and Environmental Studies,  
Princeton University, Princeton, NJ 08544, U.S.A.

and

Russian Scientific Center "Kurchatov Institute",  
123182 Moscow, Russia

**Abstract:** This paper discusses the prospects of wind energy use for electricity supply in the former Soviet Union (fSU). The main focus is on the estimation of potential, but technological, economic and implementation issues are also considered. The option of grid-connected wind power production may benefit from the existence of the unique extensive Unified Power System. At the same time stand-alone wind power systems might be promising in the remote mountain and coastal regions which have large wind potential and are not connected to a grid. Western experience, research, and technologies could act as a catalyst to accelerate the introduction of wind energy.

### 1. Introduction.

Significant progress has been made in wind energy during the last decade. Both organizational and technological lessons learned from the field experience of the first installations have led to better prospects for wind. Total installed wind generating capacity in the world is now about 2,600 MW<sub>e</sub>, most of it is in California and Denmark, where wind already successfully competes with other energy sources.

The use of renewable energy generally and wind energy in particular is still considered to be exotic in the former Soviet Union (fSU). It is so despite the fact that fSU possesses large wind resources and, moreover, has substantial expertise in technology and theory of wind turbines. One of the reasons is a consequence of inertia, since huge sources of conventional fuels were available, and a giant fuel-energy complex of the fSU has been developed with a major focus on them. At present, it may be even more important that in the conditions of a so-called "transition economy", when costs mean almost nothing, there is simply no one interested in investments into renewables whatever advantages they would have.

The economic and political changes are so rapid now in the countries of the fSU that one should possess a talent of Nostradamus to foresee the situation even for several months ahead. Being unable to suggest such scenarios the author is not inclined to suggest prophecies. Therefore, the paper will focus on the potential for wind energy and provide an overview of the current situation and trends in the field of wind energy in the fSU and will not consider details of the economic constraints and incentives. Certainly, some of these issues will be touched upon to provide context.

### 2. Background of wind energy development in the fSU.

The use of wind energy in the fSU has a long history. To say nothing about the large number of windmills operating in the beginning of the XX<sup>th</sup> century, as early as in the 20s - 30s intensive research and design investigations were conducted in the Central Aero-Hydrodynamical Institute (TsAGI) in Moscow. The theory of real and ideal wind turbine was created there by N.E.Zhukovskii and others. In 1924 a 40 kW wind turbine was designed. In 1931 a wind power station (WPS) with installed capacity of 100 kW was built in Crimea. It was connected to the grid of the local utility Sevastopolenergo and reached an average annual electricity production of 270 MWh (capacity factor

of about 31%). In the period 1950-1956, about 30,000 wind turbines with wheel diameters from 2 to 12 m were built. The total installed capacity of WPS reached 100 MW. In the mid 60s, however, the construction of large thermal and hydro power plants and low oil prices led to the gradual curtailment of wind turbine production and operation. Only in the late 80s for various reasons did the rebirth of wind energy in the fSU become feasible.

### 3. Wind potential assessment.

A review of studies related to the assessment of wind energy potential shows that there is no consistent treatment of the "potential" for wind energy. The attempt to create some kind of a classification was made in [1]. There are following steps in this "potential staircase":

- ◆ meteorological potential is the total potential of wind energy over the territory;
- ◆ site potential is the potential after excluding regions that cannot be used due to various reasons (e.g. forested, build-up areas, inaccessible, unpopulated regions, etc.);
- ◆ technological potential takes into account the technology that can be applied in a given region;
- ◆ economical potential indicates the amount of energy that can be extracted in a profitable way, as indicated by cost-benefit analysis and market dictates;
- ◆ implementation potential is a part of the economic potential that will actually be implemented, and it is determined by different constraints and incentives like visual impacts, attitude of utilities and wind farm developers, knowledge transfer, etc.

The difference between meteorological and implementation potentials could be of several orders of magnitude. At the same time there are no strict borders between various kinds of potential, and numbers for technological, economical, and implementation potentials can change in time. Since there is a lot of uncertainty about the data even for the first two steps, the discrepancy could grow dramatically as one moves further. That is why the careful first step is indispensable when trying to estimate wind energy prospects in terms of real energy production in a particular region.

Below are some results of wind potential estimation in the fSU. ◆1. According to [2], the meteorological potential at the territory of the USSR constitutes about 3,000,000 TWh. ◆2. In 1989 the USSR estimated a technological potential of 2,000 TWh at the World Energy Conference. ◆3. NPO "Vetroen", one of the leading R&D organizations in the field of wind energy in the fSU, came out with an estimate of 3,500 TWh for the technological wind potential [3]. ◆4. The estimates for the North European part of Russia in [4] led to the technological potential value of about 2,000 TWh for this region only (the territory of the region, which is one of the most favorable for wind use in Russia, is about 200,000 km<sup>2</sup>, that is 1/80 of the all territory of Russia). It should be noted that there were no clear indications of what kind of potential it was in cases 1-3, and one can only assume this. In case 4, where all input data are available, it is possible to determine the kind of potential estimated. According to above classification, it is somewhere between the meteorological and technological potential, since the site constraints were not taken into account. For comparison, total annual electricity production in the fSU in 1988-1991 was about 1,700 TWh and that in Russia was about 1,070 TWh, so the figures show substantial wind resources regardless of all uncertainties.

### 4. Wind resources in the fSU: general data and methods for estimation.

The average wind power density in general case is determined as follows:

$$\langle N \rangle = \frac{1}{2} \rho \int_0^{v_{\max}} v^3 f(v) dv, \quad (1)$$

where  $f(v)$  is a wind frequency distribution. This function is given in the tables for particular regions and could be described in terms of special functions based on the analysis of experimental data. One of the most widely used functions is the Weibull distribution, which fits a wide variety of wind speed data from various locations

$$f(v) = \frac{b}{v_c} \left( \frac{v}{v_c} \right)^{b-1} \exp \left[ - \left( \frac{v}{v_c} \right)^b \right] \quad (b > 1, v \geq 0, v_c > 0). \quad (2)$$

Here the characteristic speed  $v_c$  is a scale parameter ( $v_c \approx 1.1 \langle v \rangle$ );  $b$  is a shape parameter. When information on the frequency distribution is not available, a special case of the Weibull distribution with  $b=2$  (known as the Rayleigh distribution) is often assumed. In [5,6] the values of  $\langle N \rangle$ , average wind speed  $\langle v \rangle$ ,  $f(v)$ ,  $v f(v)$ ,  $v^3 f(v)$  for various locations are given. The values of  $f(v)$  are given for fewer meteorological stations than those for  $\langle v \rangle$ . In this situation various methods are used to obtain approximate value of  $\langle N \rangle$  rather than just  $\langle N_R \rangle$  based on the Rayleigh distribution.

Intensive investigations of wind resources have been made in the fSU by various organizations, but the data have not been compiled and analyzed to produce a "Wind Energy Atlas". They are dispersed and sometimes unavailable because of institutional barriers. A map of the annual average wind speed on the territory of the fSU taken from [3] is shown in the Figure 1. These data are from meteorological stations recalculated for 10 m height. In [3] it is indicated that the use of wind turbines for mechanical purposes (such as water pumping) is expedient with  $\langle v \rangle > 3.5-4$  m/s, and for the electricity generation with  $\langle v \rangle > 4.5-6$  m/s. The latter estimation is roughly correspondent to the assumption given in [7], where the threshold of economic exploitation is indicated to be  $\langle N \rangle = 300$  W/m<sup>2</sup> at 50 m, which corresponds to  $\langle v \rangle = 5.1$  m/s at 10 m height if Rayleigh distribution is assumed. These background maps help make reasonable estimates of the specific power density for WPS located in the open terrain. If it is possible to deploy WPS in the same regions but at more favorable locations where the wind power density is higher (e.g. on tops of hills) then values of  $\langle N \rangle$  should be corrected according to the form of relief. If there is no data available from meteorological stations at the particular site, one can use mesoscale coefficients for wind speed changes at the most characteristic types of sites in the fSU. This coefficient is a ratio of the wind speed at the particular location to that on an open plain and may vary between  $\leq 0.4$  to 4.0 [8]. For example, if the wind speed at an open plain is 5 m/s, it may vary from 20 m/s at the tops of hills to 2 m/s at closed cavities. For the detailed estimates of wind resources the mesoscale data are not sufficient, and the roughness of the second order, given by microscale coefficients, should be taken into account (hills in the valleys, hollows, ponds etc.). Changes in wind speeds even at close distances may be significant. The field experience of Altamont Pass showed that changes in locations of wind turbines by a few meters had substantial impact on energy output.

Macroscale analysis indicates that the coasts of the Arctic and Pacific oceans are the most favorable regions for wind energy use. The use of microscale and mesoscale characteristics allowed to reveal local areas in the fSU which are characterized by very high wind potential. They are Dzhungar gates in Taldy-Kurgan region, Kazakhstan ( $\langle N \rangle$  up to 1,500 W/m<sup>2</sup>); the east coast of the Caspian Sea, Tamanskii peninsula at Crimea, Ukraine; the south edge of Kamchatka peninsula and Kuril islands at the Far East of Russia ( $\langle N \rangle = 1,000-1,200$  W/m<sup>2</sup>); mountain Taganai in the Urals; and coast areas of Baltic, Black and White seas.

##### 5. Status and trends in technology and wind power development in the fSU.

The leading R&D organizations in wind energy are NPO "Vetroen", NPO "Yuzhnoe", NII "Hydroproject", KB "Raduga"<sup>1</sup>. Until now industry in Russia produces only one type of wind turbines of 4 kW power for autonomous energy supply and water pumping (NPO "Vetroen" design).

<sup>1</sup> The acronyms mean: NPO - scientific production assoc.; NII - scientific research inst.; KB - design bureau. All R&D organizations used to be within a particular ministry, but after a lot of ministries were merged or eliminated during last several years, some of them either changed their pertain or became independent from ministries.

According to the decision of the Council of Ministers of the USSR in 1989 the R&D works in the field of renewable energy were united within the State Scientific and Technological Program "Ecologically Clean Energy". It consists of five subprograms: ♦1. Safe nuclear power. ♦2. Ecologically clean thermal power plant. ♦3. Non-conventional energy. ♦4. Fuel of the future. ♦5. Hydrogen energy. Initially six wind turbine projects were included into the subprogram for non-conventional energy: 0.25-1, 3-8, 30, 100, 250, and 1250 kW. Later, the projects of 30 kW and 1250 kW turbines were closed because of lack of financing. NPO "Vetroen" is developing the projects of horizontal axis wind turbines (HAWT) of 16, 30, 100, 250 kW. The design of another 250 kW HAWT is being carried out at the PO "Kirovskii zavod" in S.Petersburg. Several projects of powerful (1000, 1250 kW) vertical axis wind turbines (VAWT) for optimal wind speeds 15-20 m/s have been started. The construction of a test turbine at the isle of Dikson in the Arctic ocean was scheduled for 1993. However, these plans were not fulfilled.

There was a plan to build in 1991-95 four wind power plants with total installed power capacity 58 MW: near S. Petersburg - 25 MW; in Kazakhstan (Dzungar Gates) - 15 MW; East Crimea (Tamanskii peninsula) - 12 MW; Dagestan (west Caspian Sea coast) - 6 MW. There was also a project for construction of WPS in Maritime Cray. 250 kW ("Vetroen", "Yuzhnoe", "Raduga") and 1000 kW ("Raduga") HAWT were chosen as the basic equipment. It was planned to make a series of 60 turbines in 1991 and start tests at the sites of planned WPS near S.Petersburg, East Crimea, and Dagestan. However, most of these plans remain on paper. In 1991 feasibility studies for the East Crimean and Dagestan WPS were finished and sites were agreed with local authorities. Unfortunately, political issues interfered into the process after the collapse of the USSR. The problem is that the leading organization for implementation of this project was Samara branch of "Hydroproject", which is in Russia, while two of four planned WPS are outside Russia (Ukraine and Kazakhstan), and the third one is in Dagestan autonomous republic, where relations between local authorities and federal government are also tense.

At present the coordinating role of the subprogram for non-conventional energy seems to be reduced. The projects have uncertain financing and may not be funded directly by the Program. Some large projects (e.g. 1000 kW turbine) are not included in the program and conducted independently. At the same time permanent changes and reorganizations in the Russian Ministry of Fuel and Power and increasing activity of the former military enterprises in the sphere of producing equipment for energy production make the situation more complicated to coordinate.

Recently the project for the development of wind power in Crimea, Ukraine, was revived when, in late 1992, Kenetech/Windpower Corp. (S.Francisco, California) entered into a joint venture, Windenergo Ltd., with Krimenergo, the Ukrainian electric utility. The purpose of their ambitious project is to manufacture, install in four phases in 1993-96 (beginning with 25 MW in the summer of 1993), and operate a 500 MW windplant in Crimea. When complete, this will be the second largest wind power facility in the world after 740 MW Altamont Pass. The power will be sold to the local utility, Krimenergo. It is planned to use 250 Windpower's Model 56-100 wind turbines in the initial stage of the project. Most of the components will be manufactured in Ukraine and Russia under license. In case of success the project might be very important for Ukraine, which suffers from power and fuel shortages because of its dependence on Russia for fuel supply and the uncertainty with further nuclear power plants operation.

There are at least two reasons, which could contribute to implementation of wind energy in the fSU. First, the existence of a unique Unified Power System (UPS) that covered almost all the inhabited areas and interconnected over 98% of the total generating capacity of the fSU. In December 1992 the joint-stock company "Unified Energy System" was established in Russia in order to preserve the major part of the UPS. It united 70 energy systems and all large hydro (>300 MW) and thermal (> 1000 MW) power plants. In case of connection of windplants to the grid, the use of UPS would permit transfer of power from the windy areas to the industrialized and heavily populated regions with large demand. Another aspect is that 30 GW of installed capacity of the UPS



from total 220 GW in Russia are already used up. In order to meet additional capacity needs it is necessary to add about 150 GW by 2010 [9]. In this case even with measures in the field of demand side management it is important to use every possibility to develop renewable energy.

Second, the regions most favorable for wind use (North of Russia, Far East, and part of Kazakhstan) are not connected to the UPS or even to any local grid. Although these territories are less populated, they need energy for life and development. Currently the main energy source there is delivered fuel for diesel power stations. In this situation (some regions in the far North can be reached only by helicopters or during the few months of navigation by the Northern Sea Route) the price of energy is extremely high, to say nothing about the harm to very sensitive maritime and northern environment. In these conditions the use of stand alone windplants might be promising.

As one can see from the consideration in Sec.4 all the Pacific coast from Chukotka to Vladivostok is rich in wind. I would risk to assume that wind (together with geothermal) energy is one of the factors that might help to find an economical approach to solving the painful political puzzle of the Kuril islands. The introduction of wind energy in this region might be a good direction for all interested parties to start dialogue and to cooperate in the economic development of this area and the preservation of its nature.

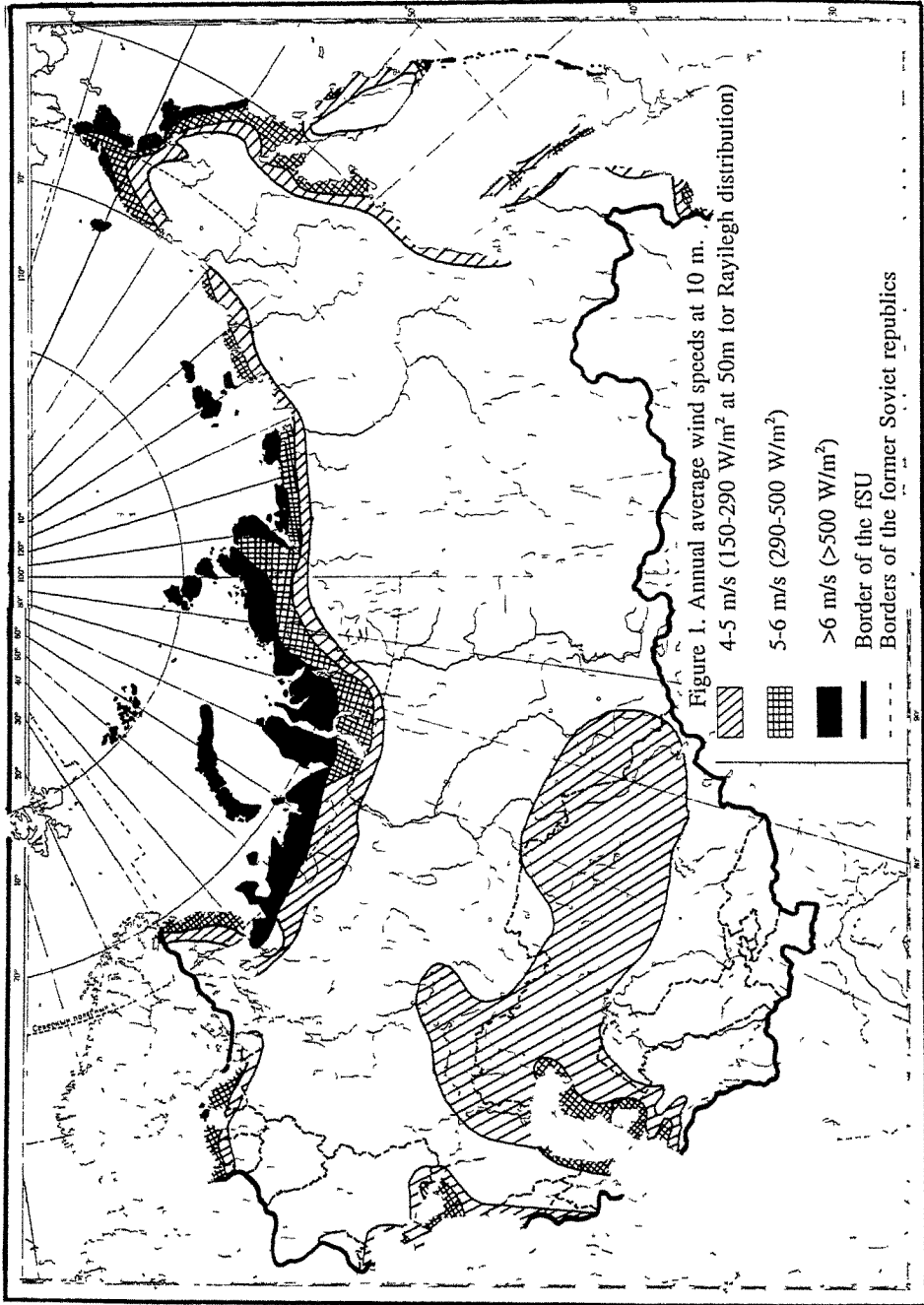
## 6. Conclusions.

The paper has outlined current trends and prospects for wind energy use in the fSU. The principal conclusions may be summarized as follows:

- ◆ Wind resources at the territory of the fSU are significant and may play an increasing role in electricity supply.
- ◆ The successful implementation of wind energy needs systematization of all collected but dispersed information on wind resources and publication of a "Wind Energy Atlas".
- ◆ The existence of the Unified Power System could promote the development of grid-connected windplants. On the other hand, the use of stand-alone wind power systems as well as use of local power grids might be promising in the Far North, along the Pacific coast, and in some other areas.
- ◆ The newly independent states of the fSU will benefit from preservation and joint use of the UPS and from close cooperation in the field of wind energy. However, it is unlikely that this cooperation can be effective without active coordinating institution.
- ◆ Cooperation with Western firms may promote technological leap-frogging, and, consequently, to avoid mistakes by taking into account lessons learned in the West at the first stage of wind power development. For Western firms the manufacturing of wind turbines in the fSU may decrease their cost and make them more competitive with other energy technologies. In the longer run, the West will also benefit from the developing experience in the countries of the fSU.

## References.

1. W.C.Turkenburg, Proc. of the EWEC'91, Part II, Amsterdam (1992).
2. A.Diakov, Energeticheskoye stroitel'stvo (Energy Construction), #3 (1991) 8 (in Russian).
3. I.Sidanov, B.Sukasyan, M.Kleinbok, Alternative Sources of Energy, #2 (1990) 12 (in Russian).
4. V.Zubarev, V.Minin, I.Stepanov, *The Use of Wind Energy in Northern Regions*, Leningrad, Nauka, 1989 (in Russian).
5. *Handbook on Climate of the USSR*, Leningrad, Gidrometeoizdat, 1965-1967 (in Russian).
6. *New Airclimate Handbook of Boundary Atmospheric Layer Over the USSR*, v. II, "Statistical Characteristics of Wind", books 1-10, Moskva, Gidrometeoizdat, 1986-1987 (in Russian).
7. T.Johansson, H.Kelly, A.Reddy, R.Williams (eds.), *Renewable Energy: Sources for Fuels and Electricity*, Island Press, 1993.
8. *Recommendations for Estimations of Wind Energy Resources*, Goskomgidromet SSSR, 1989 (in Russian).
9. A.Diakov, President of "Unified Energy System" joint stock company, *Izvestiya*, January 1993.



## Learning from Hurricane Iniki

Arthur N L Chiu

Professor of Civil Engineering  
University of Hawaii at Manoa  
Honolulu, Hawaii 96822, U S A

Gregory L F Chiu

Ph D Candidate  
Stanford University  
Stanford, California 94305, U S A

**Abstract:** Hurricane Iniki hit the island of Kauai, Hawaii on September 11, 1992. Major damage to buildings and structures resulted from the strong winds and also from the wind-driven waves. Roof failures were prevalent, the loss of windows and roof coverings of all types was common. Water then caused damage to the contents and interiors of the buildings. In many locales, topographic effects escalated wind speeds causing much damage to structures. The impact from Hurricane Iniki was much less on the other islands. The damage resulting from recent major hurricanes have contributed to the impetus for development of hurricane risk assessment tools.

### 1. Introduction

Hurricane Iniki hit Kauai, Hawaii on September 11, 1992, less than ten years after Hurricane Iwa grazed Kauai on November 23, 1982 (Chiu et al, 1983). Its intensity was much greater than Hurricane Iwa, it left a trail of devastation, mostly on Kauai, in excess of \$1.6 billion of property damage. Communications and lifeline utilities were severed on Kauai, and there was no direct telephone linkage with the other islands. Many parts of the island were without electricity for several weeks, and portable generators became prized possessions.

The southern coastline from Kekaha to Poipu (Fig 1) was subjected to severe flooding and suffered heavily from the hurricane-induced wave action. Damage from strong winds was widespread. Extremely complex wind-flow patterns resulted from the topography, resulting in much higher localized wind speeds. This condition in turn exacerbated the destruction to structures in certain areas. The loss of roofing, a common failure noted in all structures, permitted water intrusion which then damaged the interiors and contents. Damage to buildings ranged from minor to complete destruction.

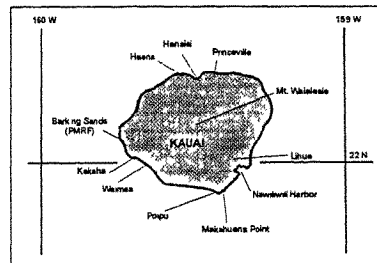


Figure 1 Site Locations on Kauai

Emergency legislative action was taken by the County Council of Kauai in the aftermath of the storm. The much more stringent provisions of Appendix Chapter 25, Section 2518, of the 1991 edition of the Uniform Building Code (ICBO, 1991) were adopted. The buildings and structures constructed in strict adherence to these provisions should have increased resistance capabilities of withstanding hurricane winds. Although much repair and reconstruction work have taken place, the scars from Hurricane Iniki have not healed completely. The resulting ripple effects from this storm on the community and the State's economy will continue to be felt.

## 2. The Storm

Figure 2 shows the “best track” for Hurricane Iniki which made landfall near Waimea (Fig 1) at about 2:30 p.m. on September 11, 1992. The National Weather Service reported that the wind speeds at that time were estimated to be 130 mph (58 m/s), with gusts to 160 mph (72 m/s), within a radius of five nautical miles (9.3 km) about the center of the hurricane (SEAOH, 1993). In less than two hours, the hurricane traversed northward over the center of the island and exited from Haena. Because of the topographic features of the island, the resulting wind patterns were extremely complex. These features contributed to the escalation of wind speeds over certain locales. The peak wind speeds were reported to be between 90-100 mph (40-45 m/sec) at 10 m AGL (WERC 1992).

Flooding from the wave action left debris lines that were much further inland than were noted during Hurricane Iwa. A detailed analysis of the marine overwash excursion distances and elevations at various parts of the coastline is presented by Fletcher (1993). Excursions ranged from 20-250 m and elevations were 4-8 m.

## 3. Wind-Induced Damage to Structures

The impact of Hurricane Iniki was much less on Oahu and Hawaii than on Kauai. Major damage to buildings and structures was caused by wind effects, primarily to light wood-frame construction. Almost all buildings were affected by the hurricane with damage varying from minor to total destruction. Roof failures occurred predominantly from inadequate hurricane connectors for resisting wind uplift forces. The loss of windows and roof coverings of all types was common to residences, hotels, as well as commercial and industrial buildings. This loss resulted in subsequent major water damage to the contents and interiors of the buildings.

Besides various agencies and groups, post-disaster damage surveys were also undertaken by the Structural Engineers Association of Hawaii (SEAOH) and the Wind Engineering Research Council (WERC). The findings and recommendations of the SEAOH team are presented in the SEAOH report, *A Survey of Structural Damage Caused by Hurricane Iniki* (SEAOH, 1993). The SEAOH was also requested by the Mayor of Kauai to provide advice during the emergency legislative deliberations and also in the rebuilding efforts. These activities comprise part of the continuing volunteer effort by the SEAOH to alert and educate the community-at-large regarding the devastation and havoc that can be wreaked by hurricane winds and the proper ways to build structures capable of resisting these strong winds. The Wind Engineering Research Council (WERC) also performed a post-disaster survey and published the findings in *Hurricane Iniki-Preliminary Observations of WERC Post-Disaster Team* (WERC, 1992). Other publications and reports pertaining to Hurricane Iniki are cited in the references listed at the end of this paper.

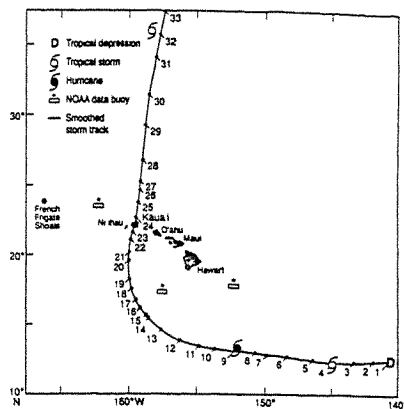


Figure 2: Track of Hurricane Iniki

#### **4. Damage to Residential Structures**

Single-family and multi-family residential buildings were particularly affected by the strong winds, and new as well as older buildings alike sustained damage. The reported figures (American Red Cross, 1993) showed that for single-family dwellings, 1,437 were destroyed, 5,189 sustained major damage, and 7,544 suffered minor damage. The corresponding figures for apartment units were 18 destroyed, 260 major damage, and 483 minor damage.

The SEAOK report (SEAOK, 1993) indicated that single-family houses are typically of light-framed timber construction, one-story or two-stories high. The newer houses usually are constructed with timber stud walls (double-wall construction), timber roof framing with plywood sheathing, and a concrete slab on grade. Most of the rafters or roof trusses are not attached with metal fasteners because these were not required until 1988. Older houses are typically of single-wall construction with timber roof framing and non-structural corrugated metal roofing. Metal fasteners were not used.

The loss of metal roofs was a notably common type of failure. Although the metal roofing is in popular use, this type of roofing and its connectors tend to corrode, leaving them vulnerable to damage by strong winds. The SEAOK report (SEAOK, 1993) also noted that failures of gable end roofs were very common.

Structures built along the edges of cliffs sustained heavy damage from strong wind effects. Damage could be initiated by the loss of the roof structure or by breaching of the structure's envelope. Roof failures occurred predominantly from connections inadequate for resisting uplift wind pressures. With the loss of the roof structure, progressive failure developed that led to complete destruction in many cases. A complete load path to hold a structure together, from the roof to the foundation, must be provided to mitigate this type of damage. The loss of the building envelope on the windward side permitted internal pressures to build up and this action contributed to the outward wind pressures on the walls and roofs.

The County of Kauai was still operating under the wind loads provisions of the 1985 edition of the Uniform Building Code (ICBO, 1985). After a long and arduous debate, the County of Kauai on December 7, 1992, adopted Emergency Ordinances (County of Kauai, 1992) for upgrading the provisions for post-Iniki repairs and reconstruction. One of the provisions incorporated Appendix Chapter 25, Section 2518 of the Uniform Building Code, 1991 Edition (ICBO, 1991), which explicitly prescribe a complete load path to resist uplift forces. The Structural Engineers Association of Hawaii also prepared a booklet entitled *Tips for Improving Wind Resistance for One-Story Single Family Dwelling Repairs on Kauai* (SEAOK, 1992) as a volunteer community effort to assist in the implementation of the new provisions.

Multi-family dwellings are usually two- and three-story structures constructed with reinforced concrete, reinforced masonry, and timber. Structural timber walls and roofs are used at the topmost levels of the reinforced concrete or masonry buildings. Those structures using heavy timber roofs performed better than light framing even in areas highly exposed to winds such as along the cliffs. However, many of these buildings suffered extensive glazing damage.

#### **5. Pre-Engineered Buildings**

Many pre-engineered metal buildings were extensively damaged. It was noted that numerous roll-up doors failed on the windward side which then led to failures of roofs and/or walls because of increased combined internal and external suction pressures on the leeward roofs and sides (WERC, 1992).

## **6. Selected Recommendations from SEAOH Report**

The following are some of the recommendations presented in the SEAOH (1993) report

1. Provide adequate uplift resistance of roofs to wind forces with complete load paths from the roof structures down to the foundations
2. Recommend adoption of the latest edition of the Uniform Building Code and the appropriate appendices (the 1991 edition Appendix Chapter 25, Section 2518, will be in force for all counties by 1994).
3. Establish appropriate basic wind speeds, consider topographic features which can escalate wind speeds, and microzone for extreme wind speeds.
4. Provide verification/inspection of construction for wind-resistant features.
5. Reevaluate roofing material specifications.
6. Evaluate pre-engineered metal buildings for adequacy of connections, fasteners, windows, and doors to resist hurricane winds

## **7. The Need for Hurricane Risk Assessment Tools**

Damage resulting from Hurricanes Iwa (Hawaii, 1982), Hugo (South Carolina, USA, 1989), Andrew (Florida, USA, 1992), Iniki (Hawaii, 1992) and Typhoon Omar (Guam, 1992) have contributed to the impetus for the development of hurricane risk assessment tools. Hurricane risk assessment (HRA) tools are an integral part of developing hurricane damage mitigation plans because of the need to answer such questions as:

- How much damage can be expected due to future hurricanes (typhoons),
- How much will damage be reduced by implementing a specific damage mitigation strategy;
- Given that a specific amount of damage or economic loss is "acceptable", will a particular damage mitigation strategy reduce losses to that "acceptable" threshold

The difficulty in answering these questions results from the lack of an integrated hurricane risk assessment system. The development of such a system requires the quantification of the hurricane hazard and relating that hazard to a state of damage (loss). Hurricane hazard comprises all of the variables which contribute to a site's exposure to the effects of a hurricane. The most common expression of hurricane hazard, used currently, is a hurricane's surface wind-field which must be generated synthetically for use in hurricane risk analysis. The current algorithms for establishing a synthetic wind-field are based upon the Monte-Carlo simulation procedures of Russell (1968). The method was improved by Georgiou (1984, 1985) and has been refined to its current state by Vickery and Twisdale (1993). The loss, or damage, is whatever topic of interest the analyst desires to study, such as, lifelines, insured losses, or fatalities. Using the synthetic wind-fields and a selected type of loss, knowledge-based expert systems, KBES, can be used to relate the wind-fields to loss or damage.

The development of KBES to assess potential hurricane damage requires the combination of analytical and heuristic knowledge. The analytical knowledge manifests itself in the form of the relations used in determining wind pressures from wind speeds, and basic strength of materials concepts used in the design and construction of structures. The heuristic knowledge is modeled through damage probability matrices, or fragility curves, to relate a site-specific wind-speed to a loss. Models of heuristic knowledge are required as the validation of damage models has not yet been performed due to a lack of properly catalogued damage databases.

The combination of the hurricane synthetic wind-field (the hazard) coupled with the wind-speed to damage-state relationships (the vulnerability) provides a typhoon risk assessment system which can be used to answer the questions raised previously. Further research is required to define properly the damage-state to hazard-state relations; the use of fuzzy mathematics provides a means of relating linguistic terms (heuristic knowledge) to an analytical tool.

## 8. Closure

The damage caused by Hurricane Iniki reemphasizes the need for structures to withstand lateral and uplift wind loads through adequate connectors. These loads in turn must be transmitted via a complete load path from the roofs through the structures down into their foundations. The random destruction from wind effects reinforces the need for recognizing that topography can escalate wind speeds exceeding those prescribed in the building codes.

Much of the damage from Hurricane Iniki could have been avoided if the various recommendations presented by the Structural Engineers Association of Hawaii (SEAOH, 1983) and the Committee on Natural Disasters (Chiu et al., 1983) had been implemented during the post-Iwa reconstruction and repair work. However, there were examples of good post-Iwa reconstruction and repair work which included corrective measures based on the lessons learned from the damage caused by Hurricane Iwa. Those properly repaired structures withstood adequately the onslaught of Hurricane Iniki.

The Structural Engineers Association of Hawaii is to be commended for its active volunteer efforts in promoting mitigation against damage to structures from strong winds.

A need exists to develop hurricane risk assessment tools as an integral part of hurricane damage mitigation plans. The lack of properly catalogued damage databases has hindered the validation of damage models.

## 9. Acknowledgments

Acknowledgment is made of the partial support from the National Science Foundation (Grant No BCS-9300961) as well as from the Structural Engineers Association of Hawaii (SEAOH) for the post-disaster studies.

## References

1. American Red Cross (1993) personal communication
2. Chiu, A.N.L., L.E. Escalante, J.K. Mitchell, D.C. Perry, T.A. Schroeder, and T. Walton (1983) *Hurricane Iwa, Hawaii, November 23, 1982*, National Research Council, National Academy Press, Washington DC 20418.
3. County of Kauai (October 1992) "Ordinance 607 and 608," Lihue, Kauai, Hawaii
4. Federal Emergency Management Agency (1992) *Hazard Mitigation Report, Hurricane Iniki*, FEMA-961-DR-HI, State of Hawaii.
5. Federal Emergency Management Agency (Jan 1993) *Building Performance: Hurricane Iniki in Hawaii*, FIA-23, Washington DC.
6. Fletcher, C.H., T.A. Schroeder, G.M. Barnes, B.M. Richmond, and M.A. Hampton (1993) "Estimation of  $V_{\theta \max}$  and Identification of the Iniki Overwash Line on Kauai," paper presented at ASCE Conference on Hurricanes of 1992, Dec 1-3, 1993, Miami, Florida.
7. Georgiou, P.N. (1984) "Simulation of Hurricane Wind Speeds", *Hurricane Alicia: One Year Later, Proceedings of the ASCE Specialty Conference*, Aug 16-17, 1984, Galveston, Texas

8. Georgiou, P.N. (1985) *Design Wind Speeds in Tropical Cyclone-Prone Regions*, Ph.D. Thesis in Civil Engineering, The University of Western Ontario, London, Ontario, Canada, Sep 1985.
9. Hayashida, K. K., and D. K. Hanatani (1993) "Improvements to Residential Construction on Kauai after Iniki," paper presented at ASCE Conference on Hurricanes of 1992, Dec 1-3, 1993, Miami, Florida.
10. International Conference of Building Officials (1985) *Uniform Building Code, 1985 Edition*, Whittier, California 90601.
11. International Conference of Building Officials (1991) *Uniform Building Code, 1991 Edition*, Whittier, California 90601.
12. Lau, H.K.C., and M.K.H. Yee (1993) "SEAOH Involvement in Post-Iniki Rebuilding and Recovery Efforts," paper presented at ASCE Conference on Hurricanes of 1992, Dec 1-3, 1993, Miami, Florida.
13. Russell, L.R. (1968) *Stochastic Models for Hurricane Prediction for the Texas Gulf Coast*, Engineer Thesis, Dept. of Civil Engineering, Stanford University, Stanford, California 94305.
14. Schroeder, T.A. (1993) "Hurricane Iniki and Omar Meteorology," paper presented at ASCE Conference on Hurricanes of 1992, Dec 1-3, 1993, Miami, Florida
15. Structural Engineers Association of Hawaii (May 1983) *A Survey of Major Structural Damage Caused by Hurricane Iwa, November 23, 1982*, P O Box 3348, Honolulu, Hawaii 96801.
16. Structural Engineers Association of Hawaii (October 1992) *Tips on Improving Wind Resistance for One-Story Single Family Dwelling Repairs on Kauai*, P.O. Box 3348, Honolulu, Hawaii 96801.
17. Structural Engineers Association of Hawaii (March 1993) *A Survey of Structural Damage Caused by Hurricane Iniki, September 11, 1992*, P O Box 3348, Honolulu, Hawaii 96801.
18. Vickery, P.J. and L.A. Twisdale (1993) "Prediction of Hurricane Windspeeds in the U.S.," *Proceedings, 7th U.S. National Conference on Wind Engineering*, UCLA, Los Angeles, California, Jun 27-30, 1993.
19. Wind Engineering Research Council (September 1992) "Hurricane Iniki, Preliminary Observations of WERC Post-Disaster Team," P O. Box 10029, College Station, Texas 77842.
20. Yee, M.K.H, and A.N.L. Chiu (1993) "Assessment of Building Damage Sustained During Hurricane Iniki (Comparison with Hurricane Iwa)," paper presented at ASCE Conference on Hurricanes of 1992, Dec 1-3, 1993, Miami, Florida.



## Author Index

### A

Ahuja, A.K.	747	Cheli, F.	137
Akins, R.E.	723	Chen, A.R.	223, 235
Al-Hatimi, H.K.R.	329	Chen, D.P.	241
Alam, M.J.	537	Chen, Feng	923
Albrecht, Pedro	193	Chen, Ming	1147
Andersen, H.	841	Chen, Qiang	1079
Andrews, R.J.	417	Chen, Qin hao	753
Appa Rao, T.V.S.R.	543, 811	Chen, W.	205
Aroussi, A.	655, 1135	Chen, Y.S.	1103
As-Salek, J.A.	1165	Chen, Yingjun	793
Asami, Yutaka	423	Cheng, Edmond D.H.	519
Asano, K.	587	Cheng, W.R.	865
Attou, M.	297	Cheng, Zhao	611

### B

Balaji Rao, K.	543	Cheong, H.F.	835
Balakrishna Rao, S.V.S.	385	Cheshire, Ronald H.	805
Balendra, T.	267, 835	Cheung, J.C.K.	1011
Bartoli, Gianni	429	Cheung, Y.K.	305, 379
Beard, A.S.	89	Chiu, A.Y.W.	593
Beneke, D.L.	341	Chiu, Arthur N.L.	519, 1195
Bian, Zongshan	1159	Chiu, Gregory L.F.	1195
Bienkiewicz, B.	711, 911	Choi, Edmund C.C.	311
Boonyapinyo, Virote	199	Chou, C.R.	1129, 1185
Bosch, Harold R.	193	Chou, J.H.	787
Brownjohn, J.M.W.	119, 217	Cigada, A.	131
Bruni, S.	137	Cochran, Leighton S.	873, 917

### C

Cai, Chun-Sheng	193	Coleman, S.A.	89
Cai, G.H.	353	Collina, A.	137
Cao, Hong	335, 347, 391	Cui, E.J.	679, 1097
Cermak, J.E.	3, 699, 873, 917	Curami, A.	143
Chan, J.	699		
Chan, Johnny C.L.	525		
Chang, S.P.	113		

### D

Dahlberg, Jan-Ake	1147
Damsgaard, A.	131
Danielson, S.L.	699
Davenport, A.G.	15
Diana, G.	137
Dielen, B.	557

Ding, C.H.	787	Hendel, S.	897
Dobrescu, M.	1005	Hibi, K.	711
Donat, J.	897	Hill, S. St.	1073
Du, Guoliang	493	Hou, Wen-Wei	247
Du, Xiangdong	1177	Hoxey, R.P.	759
Durga Prasad, J.	811	Hu, An-ding	1109
		Hu, Erbang	1041
F		Hu, Guofeng	923
Fa, Lixia	505	Huang, B.C.	305, 379
Facioni, R.J.	853	Hugh Ellis, J.	175
Falco, M.	131		
Fang, Furman F.M.	891	I	
Farrance, Geoff	879	Ibrahim Keser, H.	623
Ferreira, A.D.	483	Irwin, P.A.	107, 799, 961
Fevzi Unal, M.	623	Itoh, Y.	563
Flay, R.G.J.	417, 935	Iwamoto, M.	125
Fong, Clarence C.K.	525		
Fu, Guangming	1097	J	
Fujino, Y.	125, 637	Janes, D.A.	1141
		Ji, Juzhi	531
G		Jiang, W.M.	477, 1035, 1047
Galemann, Thomas	373	Jones, N.P.	71, 175
Gan, Kenny W.M.	891	Jong Lou, J.	291
Gao, L.	1103		
Ginger, J.D.	717, 973	K	
Glanville, M.J.	367	Kato, K.	581
Goldstein, Steven D.	513	Kawai, H.	323
Gong, G.Y.	1103	Kawase, A.	77
Gu, M.	205, 223, 235	Kawatani, M.	575
Gu, Zhifu	57, 1079	Kazama, K.	169
Guo, Yingjun	673	Kim, H.	575
Gupta, Rajeev	747	Kim, Y.S.	113
Gusella, Vittorio	429	Kimura, K.	637
		Kitamura, H.	279
H		Ko, N.W.M.	569, 593, 599
Ham, H.J.	711	Kobayashi, H.	83, 575
Handa, Virender K.	705	Koh, C.G.	267
Hatanaka, A.	83	Kot, S.C.	999
He, Dexin	1147	Krishna, P.	39

Kubo, Y.	581	Liu, H.N.	499
Kukharkin, Nikolai N.	1189	Liu, Jinfeng	1059
Kuwahara, K.	563	Liu, Keqi	1177
Kwan, A.K.H.	929	Liu, P.E.	1185
Kwok, K.C.S.	341, 367, 829, 853	Liu, Shangpei	255, 261
Kwon, K.J.	643	Lo, K.W.	599
Kwon, S.D.	113, 285, 447	Lopes, A.M.G.	483
L		Lou, Kang-Ning	291
Lai, M.	459	Lou, L.S.	947
Lai, M.L.	699	Lu, Guorong	953
Lakshmana Gowda, B.H.	685	Lu, Z.J.	787
Lakshmanan, N.	385	Luo, Jinlin	1155
Lam, K.M.	305, 379, 735, 929, 985	M	
Lam, K.S.	999	Ma, Shuhong	531
Larose, G.L.	131, 137, 823	Ma, Wendou	549
Larsen, A.	823, 841	Manabe, S.	77
Le, Junwang	397	Marukawa, H.	279, 605
Lee, B.E.	255, 261, 923	Mathur, G.C.	817
Lee, S.J.	643	Matsumoto, T.	587
Leffler, Russ D.	873	Mauroof, A.L.M.	329
Letchford, C.W.	717, 741, 973	Mehta, K.C.	513, 693, 805
Leung, A.Y.T.	305, 379	Melbourne, W.H.	27, 631, 1011
Leung, Y.C.	599	Meng, Xianzhong	1177
Levitan, Marc L.	917	Miau, J.J.	787
Li, Guiqing	335, 347, 391, 847	Miyagi, H.	885
Li, Jikai	1171	Miyashita, Koichi	423
Li, Q.C.	273	Miyata, Toshio	169, 187, 199, 211
Li, Q.F.	1103	Mochida, A.	41
Li, Qiusheng	335, 347, 391, 631	Modi, V.J.	1073
Li, Y.M.	447, 459	Mohamed Sitheeq, M.	685
Li, Z.Y.	847	Momomura, Y.	605
Liang, Shuguo	397, 847	Morais, M.J.S.	993
Lin, Kongguang	441	Murakami, S.	41
Lin, Y.K.	273	Murlidharan, T.L.	811
Lin, Z.X.	101	N	
Liu, Baozhang	1029	Nagahawatta, H. D.	155
		Nagao, F.	77, 587, 905

Naito, Syunichi	423	Richardson, G.M.	1117
Nakahara, T.	581	Ronsten, Goran	1147
Ng, C.W.	569	Ruscheweyh, H.	373, 557, 773
Nishi, A.	885		
Niu, Guangcheng	793	S	
Niu, Zhennan	489	Saathoff, P.J.	1005
Niwa, H.	279	Saffir, Herbert S.	781
Noda, M.	905	Samali, B.	829, 853
		Sang, Jianguo	489
O		Sankaran, R.	729
Ohkuma, T.	279, 605	Santhakumar, A.R.	537, 765
Okajima, Atsushi	649	Santos, Jovito C.	211
Oliveira, L.A.	993	Sarkar, P.P.	71
Ou, Siyuan	335, 347	Savage, M.G.	617
Ou, W.C.	661	Scanlan, R.H.	71, 95, 175
		Schatzmann, M.	897
P		Severn, R.T.	119
Padmanaban, K.	765	Shah, D.A.	661
Pan, Weiming	1085	Sheng, K.S.	847
Panzer, E.C.	723	Sheng, Senzhi	941
Park, S.Y.	113	Sheu, M.H.	787
Parthiban, J.	765	Shi, Tinghui	175
Paterson, D.A.	411, 879	Shi, Z.C.	679
Peng, Xi	953	Shiau, Bao-Shi	1123
Peterson, Richard E.	513	Shrimpton, J.S.	1141
Pirner, M.	161	Simpson, A.G.	89
Pun, P.K.F.	741	Singh, L.	71
		Smith, D.A.	693
Q		Soligo, Michael J.	961
Qamaruddin, M.	329	Song, J.Z.	101
Qi, Ying	465, 471	Song, San	1079
Qu, Weilian	181, 397, 847, 865	Sousa, A.C.M.	483
		Spinelli, Paolo	429
		Stathopoulos, T.	967, 979, 1005
R		Stephen, G.A.	119
Ramanathan, R.	267	Stroh, S.L.	95
Raggett, J.D.	95	Sun, Bingnan	229
Rediniotis, O.K.	723	Sun, Keming	835
Ren, Y.H.	403	Sun, T.F.	57, 1023, 1079
Richards, P.J.	759, 1117	Sun, Y.	911

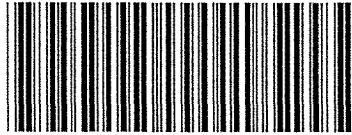
Suzuki, O.	575	Wang, Maoxun	1091
Svensson, E.	823, 841	Wang, Qizhi	255, 261
		Wang, Shufang	1017
T		Wang, W.G.	477
Tam, Paul W.M.	705	Wang, X.L.	447
Tamura, T.	563	Wang, Xianfu	1085
Tamura, Y.	711	Wang, Zhugao	505
Tamura, Yukio	423	Wanigaratne, B.S.	759
Tanaka, H.	617	Wei, Qingding	1177
Tang, Jinchun	229	Wenzel, Helmut	149
Tao, Qibin	359	Williams, Colin J.	961
Tao, Shuwang	1059	Winoto, S.H.	661
Teramoto, T.	279	Wong, C.H.	599
Thomas, K.C.	543	Wong, P.T.Y.	593
Thomas, N.H.	1141	Woo, H.G.C.	699
Thomas, P.	435	Wu, Hanqing	967, 979
Thung, D.K.T.	985	Wu, X.M.	499
Tieleman, H.W.	723	Wu, Xiaosong	505
To, A.P.	735, 985	Wu, Zhicheng	1159
Tsurumi, T.	605		
		X	
U		Xiang, H.F.	101, 181, 205, 223, 235
Ueda, H.	711	Xiao, M.K.	285
Ueda, T.	83	Xie, Changtian	255, 317
Uematsu, Y.	667	Xie, G.L.	1047
Ueno, Hisanori	649	Xie, J.	107, 799
Urano, D.	617	Xu, Cheng	505
Utsunomiya, H.	77, 587, 905	Xu, Youheng	611
		Xuan, Jie	1023, 1053
V			
Venkateswarlu, B.	385	Y	
Viegas, D.X.	483	Yamada, Hitoshi	169, 187, 199, 211
Vogt, S.	435	Yamada, M.	667
		Yamaguchi, H.	155
W		Yang, Zhongqin	453
Wada, A.	563	Yao, Rentai	1059
Wang, Han	1041	Yasuda, T.	1165
Wang, J.H.	447	Ye, Wenhui	1023, 1053
Wang, Jiaming	1171	Yeatts, B.B.	693
Wang, Kaichun	673		

Yeatts, Byron B.	917
Yi, Donglai	649
Yim, John Z.	1129, 1185
Yin, Jianming	793
Yip, D.Y.N.	935
Yokomizo, T.	1073
Yoshie, K.	279
Yoshimura, T.	617
Yu, C.C.	1129
Yu, H.B.	1035
Yu, Wenzhuo	453
Yu, X.T.	679
Yu, Xizhe	793

## Z

Zasso, A.	119, 143
Zen, S.K.	787
Zhang, Boyin	489, 1177
Zhang, Ch.	285
Zhang, Jianbo	1097
Zhang, Lianghang	317
Zhang, Maoshuan	1059
Zhang, R.C.	859
Zhang, Shaoqing	1085
Zhang, X.T.	859
Zhao, K.	947
Zhao, Q.	459
Zheng, Xiong	1065
Zheng, Zhihua	549
Zhou, Bicheng	359
Zhou, Jiangnan	465, 471
Zhou, Qiang	229
Zhou, Ruming	453
Zhou, Yuping	1091
Zhu, B.	241
Zhu, Guolin	673
Zhu, Ruizhao	531
Zhu, Wei,	1091
Zhu, X.Y.	679
Zhuang, Yongji	941

X09382678



624.175 A83 P03  
Asia Pacific Symposium on Wind  
Engineering (3rd : 1993 : Hong  
Kong)  
Proceedings of the third  
Asia-Pacific Symposium on Wind  
Engineering : December 13-15.

**Printed by The Central Printing Press Ltd.**  
**Tel: 562 0237 Fax: 565 8261**